Mol Imaging Biol (2021) 23 (Suppl 2):S991–S1738
DOI: 10.1007/s11307-021-01693-y

ID: GA2
Contrast and Resolution Enhancement in Clinical MRI Imaging

Nikolai Slavine, UT Southwestern Medical Center at Dallas, Texas, nikolai.slavine@utsouthwestern.edu

---

Category: Computational & Data Science

Abstract Body : Purpose: To demonstrate an application of fast iterative method to enhance contrast and image resolution in clinical MRI imaging. An efficient rapidly converging deconvolution algorithm with a novel resolution subsets-based approach RSEMD for improving the quantitative accuracy of previously reconstructed clinical MRI images by commercial system has been evaluated. Materials and Methods: The method was tested on ACR MRI phantom and DICOM clinical MRI data. Data acquisition was performed on a commercial Siemens MRI system. The method was applied to MRI images previously processed with clinical MRI software to determine improvements in resolution and contrast to noise ratio. Results: In all of the phantom and patients' MRI studies the post-processed images proved to have higher resolution and contrast as compared with images reconstructed by conventional methods. In general, the values of CNR reached a plateau at around 8 iterations with an average improvement factor of about 1.7 for processed MRI images. Improvements in image resolution after the application of the method have also been demonstrated. Conclusions: An efficient, iterative deconvolution algorithm with a novel resolution subsets-based approach that operates on patient DICOM images has been used for quantitative improvement in MRI clinical imaging. The method can be applied to clinical MRI images and will be crucial in order to facilitate diagnosis of tumor progression at the earliest stages. The method can be considered as an extended blind deblurring or Richardson-Lucy like algorithm with multiple resolution levels. The uncertainty caused in the system was modeled as an iterative deconvolution with resolution subsets to de-noise and enhance image resolution. This efficient extension of the blind deblurring algorithm iterates the MRI clinical image with different resolution parameters sigma and a corresponding number of iterations n (sigma) for each subset are taken in turn. In this case RSEMD method look similar to an extended Richardson-Lucy algorithm with multiple resolution levels (resolution subsets): RSEMD algorithm iterates the clinical image consistently with different resolution parameters (to maximize SNR/CNR) and a corresponding number of iterations for each resolution subset are taken in turn. During the iteration procedure the SNR is checked in each iterative step and this process can be repeated until the enhancement procedure reaches the highest SNR and resolution. The first parameter can be set as a small fraction of initial SNR. The second parameter is an initial resolution parameter (width). The original image is never revisited after the first iteration. For most clinical MRI cases, the total number of iterations for enhanced image quality is around 8 with a total number of resolution subsets around 4.

References: [1] "Magnetom Aera, transforming 1.5T economics". Siemens AG, www.siemens.com/aera (2012). [2] "Syngo MR E11, increase your efficiency, expand your MRI services" , www.usa.siemens.com/E11, (2015) [3] Robson MD, Gore JC, Constable RT, "

Measurement of the Point Spread Function in MRI Using Constant Time Imaging", Magn. Reson. Med 38, 733-740 (1997). [4] Panych LP, Lei Zhao, and Mulkern RV, " PSF-Choice: A Novel MRI Method for Shaping Point Spread Functions in Phase-Encoding Dimensions", Magn Reson Med 54, 159-168 (2005). [5] Kiarash Ahi, "Mathematical Modeling of THz Point Spread Function and Simulation of THz Imaging Systems IEEE Trans on Terahertz Science and Technology, 7, 747-754 (2017) [6] Fish, D, Walker, J., Brinicombe, A., Pike, E., "Blind deconvolution by means of the Richardson–Lucy algorithm," JOSA 12A, 58-65 (1995). [7] Richardson, WH ,"Bayesian-Based Iterative Method of Image Restoration," JOSA 62, 55-59 (1972). [8] Lucy, LB, "An iterative technique for the rectification of observed distributions," The astronomical journal 79, 745-750 (1974). [9] Slavine, NV, "Rapidly converging 3D Iterative Deconvolution Method for Quality Image Improvement from Different Clinical Modalities", Patent disclosure UT 3277 , UT Southwestern Medical Center at Dallas, TX (2020).

Image/Figure:

https://s3.amazonaws.com/amz.xcdsystem.com/1E8A4501-BB41-A02A-1D3B9882B798BFAA_abstract_File10351/GA2_ImageFigure_0218053617.png

Image/Figure Caption: The detail of the MRI kidney image enhancement with conventional algorithm (left) seen on axial view and followed enhancement with RSEMD method (right). The contrast to nose improvement factor is about 1.6 after the application of RSEMD image enhancement method.

First Name: Nikolai

Last Name: Slavine

Email: nikolai.slavine@utsouthwestern.edu

Organization: UT Southwestern Medical Center at Dallas, Texas

Country: United States

ID: GA3
Imaging pulmonary blood vessels and ventilation-perfusion mismatch in Covid–19

Dnyanesh Tipre, Children's Hospital Los Angeles, dnyanesht@yahoo.com

---

Category: Cardiovascular & Pulmonary

Abstract Body : Covid-19 hypoxemic patients despite sharing a single etiology (SARS–CoV–2 infection) present themselves quite different from one another. Patients respond differently to prescribed medicine and, prone or supine bed positions. A severe pulmonary ventilation-perfusion mismatch underlies the pathophysiology of moderate to severe Covid-19 cases. Although portable X-ray and ultrasound imaging are serving on the frontline to evaluate lung parenchymal abnormalities, they are unable to provide information about pulmonary vasculature and blood flow redistribution that is a consequence of hypoxemia in Covid-19. Advanced imaging modalities such as computed tomography, single-photon emission tomography, and electrical impedance tomography using a sharp algorithm visualize pulmonary ventilation-perfusion mismatch in the abnormal and in the apparently normal parenchyma. It helps to access the severity of infection, lung performance, ventilation-perfusion mismatch, and strategies for medical treatment. This review summarizes the contribution of various teams and applications of imaging modalities to assess pulmonary blood vessels and ventilation-perfusion mismatch in Covid-19. Despite having limitations, these modalities are providing vital information on blood volume distribution, pulmonary embolism, pulmonary vasculature and are useful to evaluate effective medical treatments in acute patients and recovered Covid-19 long haulers.

References: 1. Coagulopathy in COVID-19. J Thromb Haemost. 2020;18:2103-9. doi:10.1111/jth.14975. 2. Hypoxaemia related to COVID-19: vascular and perfusion abnormalities on dual-energy CT. Lancet Infect Dis. 2020;20:1365-6. doi:10.1016/S1473-3099(20)30367-4. 3. Functional respiratory imaging identifies redistribution of pulmonary blood flow in patients with COVID-19. Thorax. 2020. doi:10.1136/thoraxjnl-2020-215395. 4. Assessment of Small Pulmonary Blood Vessels in COVID-19 Patients Using HRCT. Acad Radiol. 2020;27:1449-55. doi:10.1016/j.acra.2020.07.019. 5. The vascular nature of COVID-19. Br J Radiol. 2020;93:20200718. doi:10.1259/bjr.20200718. 6. Pulmonary infarction secondary to pulmonary thromboembolism in COVID-19 diagnosed with dual-energy CT pulmonary angiography. Rev Esp Cardiol (Engl Ed). 2020;73:672-4. doi:10.1016/j.rec.2020.04.013. 7. COVID-19 pneumonia: microvascular disease revealed on pulmonary dual-energy computed tomography angiography. Quant Imaging Med Surg. 2020;10:1852-62. doi:10.21037/qims-20-708. 8. Ventilation/perfusion SPECT/CT findings in different lung lesions associated with COVID-19: a case series. Eur J Nucl Med Mol Imaging. 2020;47:2453-60. doi:10.1007/s00259-020-04920-w. 9. Tracheobronchitis signs observed on ventilation lung scintigraphy during the course of COVID-19 infection. Eur J Nucl Med Mol Imaging. 2020;47:2709-10. doi:10.1007/s00259-020-04834-7. 10. Bedside Electrical Impedance Tomography Unveils Respiratory "Chimera" in COVID-19. Am J Respir Crit Care Med. 2021;203:120-1. doi:10.1164/rccm.202005-1801IM.

First Name: Dnyanesh

Last Name: Tipre

Email: dnyanesht@yahoo.com

Organization: Children's Hospital Los Angeles

Country: United States

ID: GA4

Improving Oral Cancer detection using PARPi-FL: A Phase I Clinical Trial.

Paula Demetrio de Souza Franca, MSKCC, demetrip@mskcc.org

Category: Oncology

Abstract Body : INTRODUCTION: Despite their accessible location, oral cavity cancers are often diagnosed late, especially in low-resource areas where their incidence is typically high (1). In addition to poorer survival rates (2), patients with more advanced cancers also suffer from a poorer quality of life after treatment, requiring extensive surgery and postoperative adjuvant treatment. In this phase I, dose-escalation clinical trial, we have explored the use of a fluorescent imaging agent, PARPi-FL (3, 4), as a tool for non-invasive in vivo identification of malignant oral lesions in real-time. PARPi-FL is a molecularly specific, fluorescent contrast-based approach that may fill the unmet need for a simple, non-invasive, cost-effective, in vivo, method for the early diagnosis of oral cancer (5). Here, we explored the safety and feasibility of the imaging agent PARPi-FL used as a mouth-wash for oral cancer diagnosis. METHODS: In this study protocol we enrolled 12 patients on phase I and 1 patient on phase II. For the patients on phase I, we used 3 for each concentration level of the dose escalation (100 nM, 250 nM, 500 nM, and 1000 nM). Patients had a histologically proven oral squamous cell carcinoma. They gargled a PARPi-FL solution for 60 seconds followed by a clearing solution (30% PEG 300 in water). Fluorescence measurements of the lesion and surrounding mucosa were taken before, after PARPi-FL application, and after the clearing solution. Blood pressure, oxygen levels, clinical chemistry, and complete blood count were also obtained. The phase II patient was imaged after administration of 1000 nM of PARPi-FL and subsequent clearing. For this patient, a biopsy was taken in the operating room from the tumor and the free-of-disease margin for fluorescence microscopy and histopathological correlation. RESULTS: PARPi-FL was well-tolerated by all patients without safety concerns. All malignant lesions showed a significant contrast after administration of PARPi-FL, with the highest increase occurring at 1000 nM, where patients had an average tumor-to-margin fluorescence signal ratio of 3.3. A clearing step was essential to increasing signal specificity, as it clears unbound PARPi-FL trapped in normal anatomical structures. PARPi-FL specificity was confirmed by ex vivo tabletop confocal microscopy endorsing our macroscopic findings. Although outside the scope of a phase I study, several incidental findings suggested the approach is specific and sensitive. We observed one patient who did not show a significant increase in tumor-to-margin contrast ratio between pre and post-PARPi-FL administration. The patient had a pre-PARPi-FL lesion-to-margin ratio (LMR) of 1.20. The contrast increased after PARPi-FL administration (LMR: 2.24) but decreased after the clearing step (LMR: 1.53). This patient did not have any residual tumor in the definitive surgical specimen. PARPi-FL contrast also revealed a lesion on a patient with a previously unrecognized cancer on the contralateral side of the tongue based on the PARPi-FL contrast. This area did not present any clinical evidence of macroscopic tumor in the pre-surgical setting. This area had TMRs of 1.28 (pre-PARPi-FL), 1.33 (PARPi-FL pre-wash), and 1.71 (PARPi-FL post-wash). Post-wash, the TMR was significantly higher ($p = 0.03$) than pre-PARPi-FL. Based on the pre-operative PARPi-FL finding and surgeon's scrutiny after the patient was under anesthesia, an

intraoperative biopsy of this lesion was performed, conforming to be malignant. CONCLUSION: A PARPi-FL swish-and-spit solution is a rapid and non-invasive diagnostic tool that preferentially localizes fluorescent contrast to oral squamous cell carcinoma. This technique holds promise for the early detection of oral cancer based on in vivo optical evaluation and targeted biopsy of suspicious lesions in the oral cavity.

References: 1. Siegel RL, Miller KD, Jemal A. Cancer statistics, 2020. CA: a cancer journal for clinicians. 2020;70(1):7-30. 2. Bosetti C, Carioli G, Santucci C, Bertuccio P, Gallus S, Garavello W, et al. Global trends in oral and pharyngeal cancer incidence and mortality. International journal of cancer. 2020;147(4):1040-9. 3. Kossatz S, Brand C, Gutiontov S, Liu JT, Lee NY, Gonen M, et al. Detection and delineation of oral cancer with a PARP1 targeted optical imaging agent. Scientific reports. 2016;6:21371. 4. Demétrio de Souza França P, Guru N, Roberts S, Kossatz S, Mason C, Abrahão M, et al. Fluorescence-guided resection of tumors in mouse models of oral cancer. Scientific reports. 2020;10(1):11175.

Image/Figure: https://s3.amazonaws.com/amz.xcdsystem.com/1E8A4501-BB41-A02A-1D3B9882B798BFAA_abstract_File10351/GA4_ImageFigure_0401104856.pdf

Image/Figure Caption: Figure. Design of phase I dose-escalating study NCT03085147, concept of PARPi-FL imaging for delineation of oral cancer and inter-patient analysis and subcellular specificity of PARPi-FL. (A) Patients (n = 12) with biopsy-proven oral squamous cell carcinoma gargled a solution of PARPi-FL (step 1) at increasing concentrations (100 nM, 250 nM, 500 nM, and 1000 nM; each dose n = 3) for 1 min. Then, patients gargled a clearing solution for 1 min (step 2). Using a Quest Spectrum imaging device with an endoscopic camera and PARPi-FL optimized LED–filter system, the tumor area and surrounding margin of the patient were imaged before PARPi-FL administration, after PARPi-FL administration pre-wash, and after PARPi-FL administration post-wash. (B) Tumor-to-margin ratio of fluorescence imaging for dose groups (100 nM, 250 nM, 500 nM, and 1000 nM). Ratios were calculated from 5 ROIs per FOV and 3 FOVs of each patient. Displayed are individual data points, means, and SEM. (C) PARPi-FL macroscopic imaging of a patient sample from phase II (PARPi-FL post-wash, 1000 nM), which was selected for microscopic confirmation of PARPi-FL specificity. 1 = area of the tumor where the biopsy was taken from, 2 = area where the biopsy of the free-of-disease margin was taken from. (D) H&E and PARP1 IHC (overview and zoom-in) of the tumor and margin biopsies from the patient in panel B, demonstrating higher PARP1 expression in the tumor area compared to normal adjacent mucosa. (E) Microscopic analysis of the tumor and margin biopsies to evaluate the PARPi-FL accumulation following topical 1 min swish & spit application. Fresh tissues underwent nuclear counterstaining with Hoechst 33342 ex vivo prior to microscopy. Orange arrows point to the nuclei of tumor cells, red arrows point to nuclei of cells in a normal (benign) basal layer, and white arrows point to the interstitial layer (collagen autofluorescence). (F) Quantification of PARPi-FL fluorescence signal inside the nuclei of cells. Cell nuclei were identified using Hoechst 33342.

Full Name of Abstract's 1st Author : Paula Demetrio de Souza Franca

First Name: Paula

Last Name: Demetrio de Souza Franca

Email: demetrip@mskcc.org

Organization: MSKCC

Country: United States

ID: GA5
"Imaging surface marker expression and intratumoral heterogeneity with SERRS-NPs"

Lara Rotter, Dana-Farber Cancer Institute, Memorial Sloan Kettering Cancer Center, larak_rotter@dfci.harvard.edu

---

Category: Oncology

Abstract Body : Glioblastoma multiforme (GBM) is a highly lethal primary central nervous system cancer with a median overall survival of 12-15 months [1][2]. Tumor heterogeneity is considered to be a hallmark of GBM. In fact, the evaluation of heterogeneity is essential not only between different cases (intertumoral heterogeneity) but especially within individual tumors of the same patient (intratumoral heterogeneity) [2], [3]. Heterogeneous intratumoral composition is thought to augment the extensive therapy resistance and recurrence rate of GBMs [3, 4]. Specifically, epidermal growth factor receptor (EGFR), which controls cell growth, has gained much attention as a clinical marker in GBMs due to its reported connotation with survival and response to treatment [5-8]. EGFR is observed to be aberrant in up to 60% of GBMs leading to unrestrained cell growth, replication, and an increase in the cancer's aggressive potential. However, assessing the intratumoral heterogeneity and later on the therapeutic response in GBM remains clinically challenging and often involves brain biopsies, which are complex and invasive procedures. Additionally, one primary concern about using histology, the currently employed clinical gold standard for initial and subsequent treatment decisions, is that it only provides a static snapshot of heterogeneous tumors that often undergo longitudinal changes over time, especially under the selective pressure of ongoing therapy [9]. This work presents a promising step towards overcoming hurdles related to inter-and intra-tumoral heterogeneity. Focusing on the surface markers EGFR and Her2, which are well-known targets in cancer treatment, we show that it is possible with a single injection of a high-sensitivity surface-enhanced resonance Raman scattering nanoparticle (SERRS-NP) functionalized with cetuximab or trastuzumab to reliably delineate the difference between high and low expressing EGFR and Her2 tumors in mice. The targeted uptake of SERRS-NPs leads not only to a "yes" or "no" answer but also to an accurate representation of the extent of their expression. Additionally, among the high expressing EGFR tumors, the NPs even allowed the visualization of the tumors' intratumoral heterogeneity. SERRS NPs can offer quantifiable signals in the form of distinct spectra, whereas immunohistochemistry (IHC) is very hard to quantify and remains qualitative. Immunofluorescence can increase the quantitative sensitivity of conventional IHC but still has significant drawbacks due to tissue autofluorescence which negatively impacts its performance [9, 10]. SERRS-NPs could help to overcome this hurdle by their potential to provide quantitative information without interference from autofluorescence [11]. All tests were performed in immunodeficient mice (Institute for Cancer Research severe combined immunodeficient – ICR scid) implanted with high and low expressing EGFR and high and low expressing Her2 cell lines in the flanks and both brain hemispheres. The tumors were allowed to grow for 4-8 weeks, after which cetuximab or trastuzumab conjugated SERRS-NPs were administered via tail vein injection. Raman microscopy was performed using a commercial

Raman imaging system on the freshly excised tumors, and histological images were analyzed to verify that the targeted SERRS-NPs enabled not only the delineation of the main tumor but also were able to accurately differentiate between high and low expressing EGFR/Her2 tumors. This Raman spectroscopy-based nanoparticle-imaging technology holds promise to facilitate high precision visualization of a tumor's surface expression pattern in a minimally invasive manner, which could represent a new method for the improvement of quantitative in vivo IHC and therewith an essential step to overcome the hurdles of ordinary biopsies, bringing us one step closer to more personalized patient treatment.

References: 1. Tabatabai G, Wakimoto H (2020) Glioblastoma: State of the Art and Future Perspectives. MDPI 2. Website. Liesche-Starnecker F, Mayer K, Kofler F, et al (2020) Immunohistochemically Characterized Intratumoral Heterogeneity Is a Prognostic Marker in Human Glioblastoma. Cancers 12.: https://doi.org/10.3390/cancers12102964. Accessed 7 Mar 2021 3. Bergmann N, Delbridge C, Gempt J, et al (2020) The Intratumoral Heterogeneity Reflects the Intertumoral Subtypes of Glioblastoma Multiforme: A Regional Immunohistochemistry Analysis. Front Oncol 10:494 4. Lee J-K, Wang J, Sa JK, et al (2017) Spatiotemporal genomic architecture informs precision oncology in glioblastoma. Nat Genet 49:594–599 5. Saadeh FS, Mahfouz R, Assi HI (2018) EGFR as a clinical marker in glioblastomas and other gliomas. Int J Biol Markers 33:22–32 6. Vivanco I, Robins HI, Rohle D, et al (2012) Differential sensitivity of glioma- versus lung cancer-specific EGFR mutations to EGFR kinase inhibitors. Cancer Discov 2:458–471 7. Reardon DA, Wen PY, Mellinghoff IK (2014) Targeted molecular therapies against epidermal growth factor receptor: past experiences and challenges. Neuro Oncol 16 Suppl 8:viii7–13 8. Lee A, Arasaratnam M, Chan DLH, et al (2020) Anti-epidermal growth factor receptor therapy for glioblastoma in adults. Cochrane Database Syst Rev 5:CD013238 9. Sareen H, Garrett C, Lynch D, et al (2020) The Role of Liquid Biopsies in Detecting Molecular Tumor Biomarkers in Brain Cancer Patients. Cancers 12.: https://doi.org/10.3390/cancers12071831 10. Andreou C, Pal S, Rotter L, et al (2017) Molecular Imaging in Nanotechnology and Theranostics. Mol Imaging Biol 19:363–372 11. Andreou C, Neuschmelting V, Tschaharganeh D-F, et al (2016) Imaging of Liver Tumors Using Surface-Enhanced Raman Scattering Nanoparticles. ACS Nano 10:5015–5026

Image/Figure: https://s3.amazonaws.com/amz.xcdsystem.com/1E8A4501-BB41-A02A-1D3B9882B798BFAA_abstract_File10351/GA5_ImageFigure_0403110636.pdf

Image/Figure Caption: EGFR-targeted cetuximab-SERRS-NPs enable quantitative assessment of the surface marker EGFR and delineation between high and low EGFR expressing tumors. (a) Flow cytometry data of EGFR expressing GBM cell lines in decreasing EGFR expression A431, U87EGFR, U87, TS895. (b) ICR scid mice received flank injections of GBM cells. One flank was injected with a low expressing, and the other flank with a high expressing EGFR cell line. As high expressing EGFR cell lines A431 and U87EGFR were utilized. As low expressing EGFR cell lines, TS895 and U87 were applied. GBM flank-tumor-bearing animals were injected with cetuximab-SERRS-NPs. (c) Ex vivo Raman imaging was performed on the freshly extracted and halved tumor (thickness 2-4 mm) after cetuximab-SERRS-NPs were allowed to circulate for 18-24 hours. Shown are Raman images of the high-expressing EGFR tumor (cell line A431 and U87EGFR) and low expressing EGFR tumor (cell line U87 and TS895). (d) Raman-imaged tumors were then paraffin-embedded and sequential sections cut and processed

with H&E and immunohistochemistry staining for EGFR (target of the cetuximab-SERRS-NPs). The tumor shape between Raman images and IHC slides changed because paraffin embedding and staining procedures were performed after Raman imaging. (e) Raman spectra of the high-expressing EGFR tumor (turquoise (A431)) and dark green (U87EGFR)) and low expressing EGFR tumor (light green (U87) dark orange (TS895)).

Full Name of Abstract's 1st Author : Lara Kim Rotter

First Name: Lara

Last Name: Rotter

Email: larak_rotter@dfci.harvard.edu

Organization: Dana-Farber Cancer Institute, Memorial Sloan Kettering Cancer Center

Country: United States

ID: GA6

To target or not to target: Deconvoluting the nanomedicine tumor specificity puzzle with molecular imaging and nanoengineering

Girgis Obaid, University of Texas at Dallas, girgis.obaid@utdallas.edu

---

Category: Oncology

Abstract Body : Nanomedicines have been long-hailed as the future of cancer therapy owing to their ability to improve the efficacy and safety of anticancer drugs. Nanomedicines are frequently targeted towards tumor cell receptors in order to improve the specificity of the therapy applied. However, as the size of tumor targeted nanomedicines exceed beyond 50 nm, their capacity for tumor selective delivery becomes dominated by their size, and not by their specificity towards tumor cell receptors. As such, the role of targeting to tumor cell receptors becomes ambiguous, thereby undermining and confounding efforts for precision medicine. This study demonstrates the first use of quantitative molecular imaging to measure the degree of receptor binding by ligand targeted nanomedicines. This is demonstrated in three different glioblastoma tumors with varying degrees of EGFR expression. Results show that tumor selectivity of nanomedicines does not in fact correspond to their specificity for tumor EGFR, as quantified by molecular imaging. As such, a framework for rational and modular nanoengineering is proposed whereby nanomedicines for combination cancer therapy can achieve their truest potential as platforms for patient customizable precision medicine.

Image/Figure: https://s3.amazonaws.com/amz.xcdsystem.com/1E8A4501-BB41-A02A-1D3B9882B798BFAA_abstract_File10351/GA6_ImageFigure_0407110401.docx

Image/Figure Caption:

First Name: Girgis

Last Name: Obaid

Email: girgis.obaid@utdallas.edu

Organization: University of Texas at Dallas

Country: United States

ID: GA7
Relative efficacy of 225Ac-PSMA-617 and 177Lu-PSMA-617 in prostate cancer based on subcellular dosimetry

Hwan Lee, University of Pennsylvania Perelman School of Medicine, Hwan.Lee@pennmedicine.upenn.edu

---

Category: Computational & Data Science

Abstract Body : Purpose: Metastatic castration-resistant prostate cancer (mCRPC) carries a poor prognosis despite multiple approved existing therapies with antiproliferative, immunologic, and endocrine effects (1). More recently, targeted radionuclide therapy for mCRPC has gained much interest secondary to development of small molecules and antibodies targeting prostate-specific membrane antigen (PSMA) (2). The most commonly used radionuclide in PSMA-targeted therapy is the beta emitter lutetium-177, in the form of the small molecule 177Lu-PSMA-617 (2). Compared to beta therapy with 177Lu-PSMA-617, improved antitumor efficacy is seen with alpha-emitting 225Ac-PSMA-617 (3). To date, 225Ac-PSMA-617 therapy has primarily relied on empiric dosing (4), and the required radioactivity of 225Ac-PSMA-617 relative to 177Lu-PSMA-617 to produce comparable efficacy remains to be investigated from a dosimetry perspective. Methods: A 3-dimensional tumor model of prostate cancer was constructed for subcellular dosimetry in a single cell, micrometastsis, and macroscopic tumor. For each decay event of 225Ac-PSMA-617 and 177Lu-PSMA-617, the absorbed radiation dose to the tumor cell nuclei was calculated, with subsequent conversion to the equivalent dose using the relative biological effectiveness of 5 for alpha particles (4). The relative efficacy of 225Ac-PSMA-617 vs. 177Lu-PSMA-617 per administered activity was then estimated by taking into account the differences in residence time and previously published tumor uptake data (5). Results: As the tumor size increased, the absorbed dose from 225Ac-PSMA-617 initially increased linearly (R2 = 0.99), and reached an asymptote near the maximum range of the alpha particles (85 μm). In contrast, the absorbed dose from 177Lu-PSMA-617 continued to increase linearly beyond 100 μm (R2 = 0.99). For a decay event in each cell, the equivalent dose per decay was 2,320, 2,900, and 823-fold higher in favor of 225Ac-PSMA-617 compared to 177Lu-PSMA-617 in a single cell, 100 μm-radius micrometastasis, and macroscopic tumor, respectively. Per administered radionuclide activity, the relative efficacy of 225Ac-PSMA-617 compared to 177Lu-PSMA-617 in respective tumor sizes was at least 3,480, 4,350, and 1,230-fold higher, and possibly as high as 11,800, 14,900, and 4,200-fold higher considering differences in tumor uptake. Conclusion: Based on subcellular dosimetry, alpha therapy with 225Ac-PSMA-617 is more effective for treatment of measurable disease and especially for eradiation of micrometastatic disease compared to beta therapy with 177Lu-PSMA-617 at commonly used doses, which may explain the high efficacy of 225Ac-PSMA-617 in clinical studies.

References: 1. Mohler JL, Antonarakis ES, Armstrong AJ, et al. Prostate Cancer, Version 2.2019, NCCN Clinical Practice Guidelines in Oncology. J Natl Compr Canc Netw. 2019;17:479-505. 2. Sadaghiani MS, Sheikhbahaei S, Werner RA, et al. A Systematic Review and Meta-analysis of the Effectiveness and Toxicities of Lutetium-177-labeled Prostate-specific

Membrane Antigen-targeted Radioligand Therapy in Metastatic Castration-Resistant Prostate Cancer. Eur Urol. 2021. 3. Sathekge M, Bruchertseifer F, Vorster M, et al. Predictors of Overall and Disease-Free Survival in Metastatic Castration-Resistant Prostate Cancer Patients Receiving (225)Ac-PSMA-617 Radioligand Therapy. J Nucl Med. 2020;61:62-69. 4. Kratochwil C, Bruchertseifer F, Rathke H, et al. Targeted α-Therapy of Metastatic Castration-Resistant Prostate Cancer with (225)Ac-PSMA-617: Dosimetry Estimate and Empiric Dose Finding. J Nucl Med. 2017;58:1624-1631. 5. Current K, Meyer C, Magyar CE, et al. Investigating PSMA-Targeted Radioligand Therapy Efficacy as a Function of Cellular PSMA Levels and Intratumoral PSMA Heterogeneity. Clin Cancer Res. 2020;26:2946-2955.

First Name: Hwan

Last Name: Lee

Email: Hwan.Lee@pennmedicine.upenn.edu

Organization: University of Pennsylvania Perelman School of Medicine

Country: United States

ID: GA8
Y-86/Gd-EOB-DTPA for simultaneous PET/MRI in liver

Erik Shapiro, Michigan State University, shapir86@msu.edu

Category: New Chemistry, Materials & Probes

Abstract Body : Dynamic contrast enhanced-(DCE)-MRI employing the hepatospecific MRI contrast agent Gd-EOB-DTPA is under investigation for measuring hepatic function in a variety of acute and chronic liver diseases. Gd-EOB-DTPA is injected rapidly into patients and T1-weighted MRI is dynamically performed for 10-60 minutes. Parametric estimation techniques with physiologically-based pharmacokinetic models measures hepatic functional parameters such as kinflux – the rate constant of contrast agent influx into hepatocytes via OATPs, and kefflux – the rate constant of contrast agent efflux from hepatocytes to bile via MRP2. Accurate estimation of kinflux and kefflux are sensitive to hepatic diseases such as fibrosis, cirrhosis, NAFLD, and diabetes, and can potentially enable early disease detection. Furthermore, reporter gene molecular imaging applications employing OATPs will also require quantitative measurements of kinflux and kefflux. Tracer kinetic modeling and analysis for estimating kinflux and kefflux requires the conversion of MRI signal enhancement to contrast agent concentration, for both the vascular input function and the tissue signal. This calculation is rife with assumptions and prone to multiple large sources of error, in both preclinical and clinical scenarios, making the use of DCE-MRI to measure liver function prone to significant errors. This results in large uncertainty in estimating liver function and poor ability of DCE-MRI to discriminate liver disease stages (1). Encouraged by work employing 86Y-labeled chelates as surrogates for Gd-labeled chelates (2), we propose simultaneous PET/MRI employing both 86Y-EOB-DTPA and Gd-EOB-DTPA to solve these challenges, either using the PET signals to correct the MRI calculations or for standalone PET. Free EOB-DTPA was first generated by precipitating Gd with oxalic acid, followed by MPLC (2). Cold 89Y-EOB-DTPA was synthesized via chelation of the yttrium salt with free EOB-DTPA at pH 6.0, RT, 60min. Gd-EOB-DTPA was similarly resyntheszied. Gd-EOB-DTPA is transported into hepatocytes by OATPs. To confirm Y-EOB-DTPA cell uptake, experiments in OATP1B3-overexpressing HEK cells were performed, incubating 2.5 mM Y- or Gd-EOB-DTPA with cells for 1h, 37°C followed by metals analysis. Results confirm the uptake of Y-EOB-DTPA 1.6-fold higher than Gd-EOB-DTPA. Hot 86Y-EOB-DTPA was synthesized similarly as cold 89Y version. Radiolabeling was >95%, determined by radio-TLC. 86Y-EOB-DTPA (~50 μCi) was mixed with Gd-EOB-DTPA (0.025 mmol/kg) and co-injected as a bolus (200 μl over 30s). In vivo simultaneous PET/MRI was performed on a Bruker 7T PET/MRI for 1h after injection. PET: MLEM reconstruction with 0.5mm isotropic resolution, with time resolution ranging from 8sec post-injection to 6.5min at the end of the scan. MRI: 3D T1-weighted FLASH, with retrospective gating, TE/TR = 6/1.6ms, spatial resolution 0.5x0.5x1mm, temporal resolution 1min. 86Y multiple prompt gamma emissions affect the standard 511 keV ± 20% coincidence energy window, so in order to maximize S/N, 5% energy windows were used, and photopeak position was tracked. Both 86Y-EOB-DTPA and Gd-EOB-DTPA displayed hepatic and renal clearance, evidenced by PET signal and MRI contrast enhancement. No PET signals were visualized in bones due to the high stability of 86Y-EOB-DTPA. Figure 1 shows the

DCE-MRI time curve from the Gd-EOB-DTPA contrast in the liver overlayed with a time activity curve from 86Y-EOB-DTPA accumulation in the liver, and shows near perfect coincidence of the two curves. A second set of experiments where free 86Y was injected in addition showed accumulation in the bones, as expected. Concluding, 86Y-EOB-DTPA is a PET surrogate for Gd-EOB-DTPA, and directly measures tracer concentration from the image data. A scaling factor might be required to use this PET calculation to correct MRI-based calculations of Gd-EOB-DTPA concentration. Further, we hypothesize that an image-derived vascular input function can be obtained from the PET data, owing to the ease in measuring tracer concentration and the quick frame rate achievable in PET (< 3 s frame rate).

References: 1. Forsgren MF, et al. (2019) Model-inferred mechanisms of liver function from magnetic resonance imaging data: Validation and variation across a clinically relevant cohort. PLOS Computational Biology 15(6): e1007157. 2. Le Fur, M, et al. (2019) Yttrium-86 Is a Positron Emitting Surrogate of Gadolinium for Noninvasive Quantification of Whole-Body Distribution of Gadolinium-Based Contrast Agents. Angewandte Chemie 132(4) 1490-94.

Image/Figure:

https://s3.amazonaws.com/amz.xcdsystem.com/1E8A4501-BB41-A02A-1D3B9882B798BFAA_abstract_File10351/GA8_ImageFigure_0511121930.jpg

Image/Figure Caption: By using complementary pairs of PET and MRI contrast agents, we can improve non-invasive diagnosis of liver disease and probe the expression of hepatic transporters. In this work, we co-deliver Gd-EOB-DTPA, a clinically used hepatospecific MRI contrast agent, with a new PET analog, 86Y-EOB-DTPA, and perform dynmaic image simultaneously in both imaging modalities for 1 hour. Using the complementary information from both modalities enables us to mitigate deficiencies in the other imaging modality, and better calculate critical hepatic influx and efflux parameters.

First Name: Erik

Last Name: Shapiro

Email: shapir86@msu.edu

Organization: Michigan State University

Country: United States

ID: GA9

18F-FHBG PET Imaging Visualized the Distribution and Suicide Mechanism of Oncolytic Viruses in a Pre-clinical Tumor Model

Ziyue Karen Jiang, Pfizer, karen.jiang@pfizer.com

Category: Oncology

Abstract Body : Oncolytic viruses (OVs) are widely investigated as cancer immunotherapy platforms and are represented by a diverse group of DNA and RNA viruses. Almost all OVs have the properties of being replication-competent (selectively in the tumor), causing oncolysis and tumor debulking, acting as in situ vaccines, and inducing both innate and adaptive anti-tumor immune responses [1, 2]. Vaccinia viruses (VV) are double stranded DNA viruses and an attractive OV platform because of the proven potential for systemic delivery, rapid replication in permissive tissues, broad tumor tropism, and robust tumor cell lysis. Further, their large DNA genome enables insertion of foreign transgenes. We constructed a VV where a transgene encoding a variant of Herpes Simplex Virus (HSV) TK was inserted to 1) render the OV sensitive to readily available anti-HSV drugs (e.g., Cytovene or Acyclovir) to enable treatment of spontaneous skin lesions that can occur in some patients following VV treatment [3, 4], and 2) function as a PET imaging reporter when combined with the clinically used probe 18F-FHBG. This enables non-invasive monitoring of viral distribution in vivo and in patients [5, 6]. Here, we sought to assess the applicability of 18F-FHBG PET imaging as a companion non-invasive biomarker for tracking the distribution and activity of the oncolytic VV as well as monitoring the safety off-switch mechanism in a preclinical model. C57BL/6J mice with syngeneic MC38 tumors were enrolled to receive a single intravenous dose of a mouse surrogate OV or, as a comparator, a non-HSV TK-expressing OV. A separate group of mice was uninfected as control. Twice per day (BID) Cytovene (or vehicle control) treatment was initiated the following day and continued for a total of 4.5 days. Then, animals were subject to 18F-FHBG PET imaging and ex vivo gamma counting. Additionally, tumors were retrieved and snap frozen to enable DNA extraction and qPCR quantification of viral DNA. As shown in the Figure, HSV TK-expressing OV could infect and replicate in the tumor microenvironment, resulting in greater expression levels of this transgene and consequently significantly higher 18F-FHBG uptake compared to the background levels seen with uninfected control. In contrast, although the non-HSV TK-expressing OV still caused oncolysis and necrosis of the tumor, it did not express the reporter gene and therefore only showed nonspecific 18F-FHBG uptake coincident with necrosis. Further, Cytovene treatment successfully decreased viral load in the tumor and reduced imaging signal from the HSV TK-expressing OV. The non-HSV TK-expressing OV, however, showed no difference in tumor uptake of 18F-FHBG regardless of Cytovene. This was expected as expression of HSV TK is needed for conversion of Cytovene to its toxic metabolite. This data validated the function of the safety switch as well as the capability of 18F-FHBG PET imaging to faithfully detect such mechanism of action. Finally, PET imaging results were well corroborated by ex vivo gamma counting quantification of 18F-FHBG and qPCR assay of viral DNA at the tumor (data not shown in the Figure). Overall, this study showcased the ability of 18F-FHBG PET imaging to detect the oncolytic VV's in vivo distribution and to reflect the

safety mechanism. These proof-of-concept data provide a solid foundation for further clinical evaluation of this imaging modality to accompany not only this OV platform but other virus-based therapeutics as well.

References: 1. Lawler et al, JAMA Oncol 2017; 3(6):841-9. 2. Russel et al, Nat Biotechnol 2012;30(7):658-70. 3. Breitbach et al, Nature 2011; 477(7362):99-102. 4. Kung et al, BMC Cancer 2015; 15:704. 5. Yaghoubi et al, J Nucl Med. 2001; Aug;42(8):1225-34. 6. Yaghoubi et al, J Nucl Med. 2006; 47 (4) 706-715.

Image/Figure:

https://s3.amazonaws.com/amz.xcdsystem.com/1E8A4501-BB41-A02A-1D3B9882B798BFAA_abstract_File10351/GA9_ImageFigure_0427051657.jpg

Image/Figure Caption: Figure. Individual cross-tumor transverse MPR (multiplanar reformation) images of animals from indicated treatment groups. Thick yellow arrows indicate the tumor while, as exemplified in M1 (Mouse 1), the thin white arrows indicate several bones that were high in 18F uptake due to non-specific fluorine distribution. The red dashed line over the mouse skeleton on the right provides a reference location for these cross-section images. Group uptake by in vivo tumor ROI (Region of Interest) analysis was plotted on the right. Normality Test: Shapiro-Wilk Test (ns); Variance Test: Brown-Forsythe Test (ns); Significance Test: One-way ANOVA; Post-Hoc Test: Tukey's HSD Test; Alpha = 0.05; Error bars = SEM.

First Name: Ziyue Karen

Last Name: Jiang

Email: karen.jiang@pfizer.com

Organization: Pfizer

Country: United States

ID: GA10

Immuno-PET imaging of Siglec-15 using the therapeutic mAb, NC-318

Elaine Jagoda, Molecular Imaging Program, NCI/NIH, ejagoda@mail.nih.gov

---

Category: Oncology

Abstract Body : Objectives: Siglec-15 (S15), a cell surface immune inhibitory ligand, is over expressed on a variety of human cancer cells and tumor-infiltrating macrophages and capable of creating an immunosuppressive tumor micro-environment (TME) conducive to disease progression. In pre-clinical models antibody blockade of S15 resulted in tumor regression by reversing the immunosuppression in the TME thus exhibiting potential for clinical applications. NC318, a humanized IgG1 monoclonal Ab developed as an anti-S15 therapeutic Ab is currently undergoing evaluation in clinical trials and the development of an ImmunoPET imaging agent using NC318 could aid in selecting patients for these immunotherapeutics and monitoring responses [1]. NC318, which recognizes human and murine S15 was labeled with 89Zr (ZNC) and evaluated in vitro and in vivo in human S15 expressing cancer cells and mouse xenografts, respectively, for appropriate S15 targeting and potential for clinical translation. Methods: ZNC was synthesized by conjugating NC318 to desferrioxamine via an isothiocyanate linker (df-NC318). In vitro binding studies (Kd, Bmax) were performed using the human melanoma cancer cell lines, 624-MEL [wildtype (MEL) and S15 transduced (MEL+)] and LOX-IMVI (LOX). ZNC biodistributions studies were performed with MEL and MEL+xenograft mouse models at 1, 2, 3 and/or 6d post ZNC injections and NC318 dose escalation (coinjections of ZNC with 0, 20, 100 or 300 μg of NC318) biodistributions were done at 3d in MEL+ xenografts from which blood and tissue uptakes [%injected dose/g (%ID/g)] and tissue to muscle ratios (T:M) were determined. PET imaging studies were conducted at similar times using the MEL+xenografts. Results: In vitro ZNC exhibited high affinity (Kd~3 nM) and detected relative changes in S15 expression levels (Bmax) in MEL+ (moderate S15), LOX (low S15) and MEL (negligible S15) cells. In MEL+xenografts ZNC distributed rapidly in tissue with high uptakes occurring in lymph nodes (LN; 6.3 to 11.2%ID/g) and spleen (5.0 to 7.4%ID/g) at all time points which was expected as both have murine S15+ immune cells. MEL+tumor uptakes (2.9 to 5.5 %ID/g) were lower than the spleen and LN indicating decreased S15+ expression which was consistent with the modest S15+ levels found in vitro in MEL+cells. From 1 to 6d ZNC was retained in LN and spleen while tumor uptakes decreased at 3d (36%; 2.9%ID/g) and 6d (28%; 3.2%ID/g) compared to the uptake at 1d (4.5%ID/g). Femur uptakes ranged from 5.0 to 6.7%ID/g from 1 to 6d which likely represent both targeted uptake and free 89Zr. T:M for S15+tissues were highest for the LN (14 to 50) followed by the spleen (9 to 33) and the tumor (9 to 17) which steadily increased from 1 to 6d. Similiar studies with MEL xenografts at 3d had ~3-fold lower tumorT:M compared to MEL+tumorT:M indicating selective S15 uptake (Table 1). In NC318 dose escalation studies the T:M for LN, MEL+tumors and the femur were decreased (29 to 88%) when NC318 doses were ≥ 20 μg indicating that S15 binding is specific and dose dependent (Table 1). In contrast spleen T:M were increased ~2-fold at the 20 μg NC318 dose (Table 1) most likely from increased ZNC delivery to the spleen due to NC318 altered ZNC binding in the blood. From PET images

MEL+tumors could be discerned at 1d (Fig.1) and had tumor T:M of ~20 (3d) reflective of the higher ZNC activity imaging dose (20 μg) and comparable to the ≤ 20 μg NC318 coinjections (Table 1). Conclusions: ZNC exhibited specific and high affinity for S15 in vitro and had target tissue uptakes correlating with S15 expression levels in vivo. These results suggest that clinical ZNC PET imaging may have value in identifying patients who may benefit from S15+ targeted immunotherapies.

References: 1. Sun J, Lu Q, Sanmanmed MF, et al. Siglec-15 as an Emerging Target for Next-generation Cancer Immunotherapy. Clin Cancer Res 2021; 27: 680-688.

Image/Figure:

https://s3.amazonaws.com/amz.xcdsystem.com/1E8A4501-BB41-A02A-1D3B9882B798BFAA_abstract_File10351/GA10_ImageFigure_0512013608.jpg

First Name: Elaine

Last Name: Jagoda

Email: ejagoda@mail.nih.gov

Organization: Molecular Imaging Program, NCI/NIH

Country: United States

ID: GA11
Optical imaging and photopharmacology: towards light-activated therapy

Wiktor Szymanski, University Medical Center Groningen, w.szymanski@umcg.nl

---

Category: New Chemistry, Materials & Probes

Abstract Body : Direct combination of medical imaging and therapy offers unparalleled opportunities for precision and personalized medicine. This possibility is highlighted by image-guided therapy, surgery and theranostics, for example by employing molecules that are equipped with positron / gamma photon emitters for SPECT or PET imaging, and with therapeutic radionuclides that emit alpha or beta particles. Optical imaging (OI) offers certain advantages over nuclear imaging methods used commonly in theranostics, with its high resolution, more accessible instrumentation, and operation without the need for ionising radiation. However, exactly because it uses photons of lower energy, it is challenging to directly translate the optical output of OI to a therapeutic effect. This translation of low-energy photon flux into a pharmacological effect, on a molecular level, can be realized through photopharmacology. [1,2] This emerging field develops bioactive molecules whose activity can be controlled with light, both reversibly and irreversibly. The main molecular tools [3] of photopharmacology are photocleavable protecting groups (PPGs) and photoswitches. Those moieties are introduced into the structure of bioactive molecules in a way that enables the pronounced increase of the activity under irradiation with light. Especially in the reversible photopharmacology, employing photoswitches, local activation is enabled through the thermal relaxation of the photopharmacological agents to their less potent forms once they have left the irradiation zone. In the last decade, photopharmacological control has been established over chemotherapeutic agents, [4] antibiotics, [5] GPCR ligands [6] and many other classes of bioactive molecules [7] (see Persuasive Data File for examples). This presentation will focus on the recent developments in the fields of photopharmacology and molecular photoswitches / PPGs that advance those fields towards theranostic combination with OI. Specifically, developing and understanding [8-10] of molecular tools that can be activated with deep-tissue-penetrating red/NIR light, applying those in new photopharmacological agents [11-13], and creating new OI agents [14] will be highlighted. Finally, future prospects will be discussed from the perspective of photon fluxes (light intensity) needed from photopharmacology and available from optical imaging.

References: [1] M. M. Lerch et. al. Angew. Chem. Int. Ed. Engl. 55, 10978 (2016); [2] M. W. H. Hoorens et al. Trends. Biochem. Sci. 43, 567 (2018); [3] I. M. Welleman et al. Chem. Sci. 11, 11672 (2020); [4] W. Szymanski et al. Chem. Eur. J., 21, 16517 (2015); [5] M. R. Wegener et al. J. Am. Chem. Soc, 139, 17979 (2017); [6] M. Ricart-Ortega et al. Mol. Cell. Endocrin., 488, 36 (2019); [7] K. Hüll Chem. Rev. 118, 10710 (2018); [8] L. N. Lameijer et al. Angew. Chem. Int. Ed. 59, 21663 (2020); [9] M. W. H. Hoorens et al. Nature Comm. 10, 2390 (2019); [10] M. W. H. Hoorens et al. Chem. Sci. 12, 4588 (2021); [11] K. Sitkowska et al. ChemComm, 56, 5480 (2020); [12] V. Arkhipova et al. J. Am. Chem. Soc., 143, 1513 (2021); [13] D. Kolarski et al. J. Am. Chem. Soc. 143, 2078 (2021); [14] F. Reessing et al. ACS Omega 5, 22071 (2020).

Image/Figure:

https://s3.amazonaws.com/amz.xcdsystem.com/1E8A4501-BB41-A02A-1D3B9882B798BFAA_abstract_File10351/GA11_ImageFigure_0502104333.jpg

Image/Figure Caption: Figure. Using light as a bridge between optical imaging (emitting photons) and photopharmacology (absorbing photons to locally activate drugs) towards spatiotemporal control of bioactivity in personalized medicine.

First Name: Wiktor

Last Name: Szymanski

Email: w.szymanski@umcg.nl

Organization: University Medical Center Groningen

Country: Netherlands

ID: GA12

Imaging the fibrotic response in preclinical models of cardiovascular disease using newly characterised and developed collagen-binding probes

Nadia Chaher, King's College London, nadia.chaher@kcl.ac.uk

Category: Cardiovascular & Pulmonary

Abstract Body : Introduction: Cardiac and vascular remodelling, following myocardial infarction and vascular damage, are characterised by a fibrotic response. Pathologic fibrosis, however, may lead to the development of heart failure and affect the integrity of the vessel wall. Fibrosis is primarily characterised by the accumulation of two primary collagen types; collagen I and III [1]. However, non-invasive imaging techniques to selectively visualise and quantify collagen I and III and their crosslinking in vivo are currently lacking [2]. Herein, we identified and characterised two collagen I & III specific peptides, conjugated to a DOTA unit. A first MRI proof-of-concept study of a gadolinium conjugated(labelled)-Dota-peptide 1 (Gd-Dota-P1) in a preclinical model of aortic injury to study vascular remodelling is presented. Method: Two peptides (P1&P2) were selected based on reported interactions between collagen I (col1), collagen III (col3) and other proteins. To study selectivity and affinity, in vitro binding was determined by dissociation-enhanced lanthanide fluorescence immunoassay (DELFIA) using (Eu-DOTA)-peptide analogues. 96-well plates coated with col1, col3, albumin and elastin were incubated with different peptide concentrations (100nM-15μM), and the dissociation constants (Kd) and fractional occupancy were calculated. Gd-DOTA-P1 was administered (0.2mmol/kg) in a murine model of aortic wall injury. In vivo MRI was performed on a 3T clinical scanner and MR angiography and late gadolinium enhancement (LGE) images were obtained 30 min post-contrast administration. Results: In vitro binding assays showed that peptide 1 discriminates between col1 and col3 with a Kd value ~5-fold lower for col3 (5.3±1.3μM vs 26. 7±7.7μM) (Fig. 1A, E). The fractional occupancy (FO) was higher for col3 (72%) compared to col1 (40%). Peptide 2 binds equally to col1 and col3 with Kd values of 3.8±1.5 μM and 4. 8±0.6μM, respectively (Fig. 1C, E). Consequently, the FO was similar between col1 (78%) and col3 (75%) (Fig. 1D). None of the peptides bound to albumin or elastin (Fig. 1E). Magnetic resonance angiography and LGE images, after injection of Gd-DOTA-P1, showed contrast agent accumulation and vessel wall enhancement was confined within the injured segment of the aorta (Fig. 1F). No enhancement was observed in the control segment. To further validate in vivo findings ex vivo histological analyses and fluorescent microscopy colocalization experiments using rhodamine labelled peptide is underway. Conclusion We have identified and characterised two peptides specific for col1 and col3 that can be developed into targeted probes for in vivo imaging of fibrosis. Preliminary in vivo MRI results showed binding of the Gd-DOTA-P1 probe to diseased aortic segments. Biodistribution using PET/CT and further in vivo MRI studies in cardiovascular disease models are underway. This approach may expand our understanding of the role col1/3 play in the development of CVDs and may provide new imaging biomarkers for the diagnosis and prognosis of CVDs. Acknowledgement This work was supported by the following grants: (1) UK Medical Research Council (MR/N013700/1) and King’s College London member of the MRC Doctoral Training Partnership in Biomedical Sciences, (2) BHF

programme grant RG/20/1/34802 and (3) BHF Project grant RG/20/1/34802 (4) King's BHF Centre for Research Excellence RE/18/2/34213.

References: 1. Bateman, E.D.; et al. Thorax 1981, doi:10.1136/thx.36.9.645. 2. Jugdutt, B.I. Circulation 2003, oi:10.1161/01.CIR.0000085658.98621.49.

Image/Figure:

https://s3.amazonaws.com/amz.xcdsystem.com/1E8A4501-BB41-A02A-1D3B9882B798BFAA_abstract_File10351/GA12_ImageFigure_0503051805.png

Image/Figure Caption: Figure 1: Binding assays of Peptide 1 (A/B) and Peptide 2 (C/D) against immobilised proteins. The Kd values (E) show that Peptide 1 has a 5-fold higher binding affinity to collagen III compared to collagen I. The Kd values for Peptide 2 show that the peptide has a similar affinity for collagen I and III. Kd values are presented as mean±SD (3 independent experiments). (F) Preliminary in vivo analysis of DOTA-Peptide1 complexed with gadolinium (Gd) in a murine model of vessel wall injury.

Full Name of Abstract's 1st Author : Nadia Chaher

First Name: Nadia

Last Name: Chaher

Email: nadia.chaher@kcl.ac.uk

Organization: King's College London

Country: United Kingdom

ID: GA13
A Low Molecular Weight Multifunctional Molecule for the Treatment of Prostate Cancer

Xinning Wang, Case Western Reserve University, xxw171@case.edu

---

Category: Oncology

Abstract Body : Prostate cancer (PCa) is the most common malignancy and the second leading cause of cancer death in men in the United States [1]. It has been found that men with high-risk localized PCa have a high risk of biochemical recurrence that will ultimately develop into lethal metastatic disease [2-5]. Establishing an appropriate treatment strategy is particularly important for these patients, particularly a methodology that considers the use of a multimodal approach that includes both local and systemic therapies. Photodynamic therapy (PDT) is a minimally-invasive therapy used clinically in the treatment of cancers [6]. PDT kills cancer cells by generation of reactive oxygen species (ROS) induced by light activation. Due to the unique mechanisms of PDT, it has been utilized in combination with chemotherapy to achieve a synergistic therapeutic effect [7, 8]. However, PDT and chemotherapy are both limited by off-target tissue accumulation leading to cell death in normal tissue. Prostate specific membrane antigen (PSMA) is a PCa biomarker overexpressed by virtually all prostate cancers, and its expression is further increased in poorly differentiated, metastatic, and hormone-refractory carcinomas [9]. The goal of this study is to develop a selective and simultaneous delivery approach for both chemotherapeutic drugs and photosensitizers that will minimize side effects, generate a wider therapeutic window, and result in enhanced antitumor activity. Using a bifunctional PSMA ligand, we created a novel theranostic PSMA-targeting-drug-IR700 conjugate (PSMA-1-MMAE-IR700) that integrated both the photosensitizer IR700 and microtubular inhibitor monomethyl auristatin E (MMAE) in one simple molecule. PSMA-1-MMAE-IR700 showed a binding affinity of IC50 = 2.44 nM. Selective and specific uptake was observed in vitro using PSMA-positive PC3pip cells and PSMA-negative PC3flu cells. When exposed to 690 nm light in vitro, PSMA-1-MMAE-IR700 demonstrated greater cytotoxicity than either PSMA-1-IR700 or PSMA-1-MMAE in killing PC3pip cells, while no cell-killing effect was observed in PC3flu cells. In in vivo imaging studies, PSMA-1-MMAE-IR700 demonstrated selective uptake in PC3pip tumors. Further, therapeutic studies showed that PSMA-1-MMAE-IR700 with light irradiation significantly inhibited PC3pip tumor growth and prolonged survival time as compared to mice that received equimolar amounts of PSMA-1-IR700 with light irradiation, PSMA-1-IR700-MMAE without light irradiation or co-administration of PSMA-1-IR700 and free MMAE with light irradiation. In summary, we have synthesized a new PSMA-targeted theranostic agent that combines imaging (and potentially image guided surgery), chemotherapy and PDT, which may provide a new treatment option for advanced prostate cancer.

References: 1. Siegel, R. L.; Miller, K. D.; Jemal, A., Cancer statistics, 2019. CA Cancer J Clin 2019, 69, (1), 7-34. 2. Syndikus, I.; Pickles, T.; Kostashuk, E.; Sullivan, L. D., Postoperative radiotherapy for stage pT3 carcinoma of the prostate: improved local control. J Urol 1996, 155,

(6), 1983-6. 3. Pound, C. R.; Partin, A. W.; Eisenberger, M. A.; Chan, D. W.; Pearson, J. D.; Walsh, P. C., Natural history of progression after PSA elevation following radical prostatectomy. JAMA 1999, 281, (17), 1591-7. 4. Partin, A. W.; Yoo, J.; Carter, H. B.; Pearson, J. D.; Chan, D. W.; Epstein, J. I.; Walsh, P. C., The use of prostate specific antigen, clinical stage and Gleason score to predict pathological stage in men with localized prostate cancer. J Urol 1993, 150, (1), 110-4. 5. Chay, C.; Smith, D. C., Adjuvant and neoadjuvant therapy in prostate cancer. Semin Oncol 2001, 28, (1), 3-12. 6. Agostinis, P.; Berg, K.; Cengel, K. A.; Foster, T. H.; Girotti, A. W.; Gollnick, S. O.; Hahn, S. M.; Hamblin, M. R.; Juzeniene, A.; Kessel, D.; Korbelik, M.; Moan, J.; Mroz, P.; Nowis, D.; Piette, J.; Wilson, B. C.; Golab, J., Photodynamic therapy of cancer: an update. CA Cancer J Clin 2011, 61, (4), 250-81. 7. Canti, G.; Nicolin, A.; Cubeddu, R.; Taroni, P.; Bandieramonte, G.; Valentini, G., Antitumor efficacy of the combination of photodynamic therapy and chemotherapy in murine tumors. Cancer Lett 1998, 125, (1-2), 39-44. 8. Pasparakis, G.; Manouras, T.; Vamvakaki, M.; Argitis, P., Harnessing photochemical internalization with dual degradable nanoparticles for combinatorial photo-chemotherapy. Nat Commun 2014, 5, 3623. 9. Bostwick, D. G.; Pacelli, A.; Blute, M.; Roche, P.; Murphy, G. P., Prostate specific membrane antigen expression in prostatic intraepithelial neoplasia and adenocarcinoma: a study of 184 cases. Cancer 1998, 82, (11), 2256-61.

Image/Figure:

https://s3.amazonaws.com/amz.xcdsystem.com/1E8A4501-BB41-A02A-1D3B9882B798BFAA_abstract_File10351/GA13_ImageFigure_0504020753.png

Image/Figure Caption: (A) In vivo fluorescence imaging showed selective uptake of PSMA-1-MMAE-IR700 to PSMA-positive PC3pip tumors (red circles), but not to PSMA-negative PC3flu tumors (yellow circles). (B) PSMA-1-MMAE-IR700 with PDT significantly inhibited PC3pip tumor gowth. (C) PSMA-1-MMAE-IR700 with PDT significantly prolonged animal survival time. Greatest antitumor activity was observed in animals treated with PSMA-1-MMAE-IR700 with PDT. (*, $p < 0$ .05, PSMA-1-MMAE-IR700 vs other groups.)

First Name: Xinning

Last Name: Wang

Email: xxw171@case.edu

Organization: Case Western Reserve University

Country: United States

ID: GA14
The effect of chemical modifications of the Cyanine 5 dyes on the pharmacokinetic profile of nanobody-based tracers

Lukasz Mateusiak, Vrije Universiteit Brussel, lukasz.mateusiak@vub.be

---

Category: New Chemistry, Materials & Probes

Abstract Body : INTRODUCTION: Over the past two decades it has been shown that fluorescence molecular imaging is a valuable tool in preclinical research and that it also plays an important role in clinical applications such as image-guided surgery. The technology often relies on the use of targeted fluorescent agents that recognize specific biomarkers expressed by diseased tissue. Targeting moieties such as Nanobodies (Nbs), camelid-derived single-domain antibodies, are characterized by excellent kinetic parameters for molecular imaging due to their small size and robustness. However, as their pharmacokinetic profile is influenced by the chemical structure of the conjugated fluorescent dyes, in this study the biodistribution and tumor targeting of Nbs labelled with three derivatives of Cy5 were compared. METHODS: The chemical design of sulfoCy5 dye was modified by alkylation of the indole-nitrogen, resulting in three Cy5 variants with differences in charge (quaternary amine, methyl or sulfonate groups were introduced) [1][2]. The Cy5-derivatives were conjugated to the lysines of an anti-HER2 Nb (2Rs15dNOTAG) [3] via NHS chemistry. Compounds were characterized regarding purity, stability and serum protein binding; functionality was assessed via in vitro cell binding studies. After IV injection of the different Cy5-Nbs, their in vivo biodistribution and tumor targeting were evaluated over 24h by 2D fluorescence imaging in nude mice bearing either a HER2+ (SKOV3) or HER2- (MDA-MB-435) tumor (n=3 per group). Urine samples were collected to study the metabolism of the tracers. RESULTS: The three Cy5 variants were successfully conjugated to the Nb. All conjugates maintained their affinity and remained stable both in PBS and serum. However, some serum protein binding was observed for Nb-Cy5-Methyl. In vivo fluorescence imaging allowed clear visualization of the HER2+ tumors after 1h for Nb-Cy5-Sulfonate and -Cy5-QAmine (Fig.1). No tumor uptake was detected in HER2- tumors. Contrarily, for Nb-Cy5-Methyl sufficient contrast was only attained after several hours (> 3h) due to higher background signal (including the liver). Interestingly, while all Nb-tracers were eliminated through renal excretion, Nb-Cy5-Sulfonate showed significantly less kidney retention with almost no signal coming from kidneys after 6h (intense kidney signal was still visible for Nb-Cy5-QAmine at 24h). CONCLUSIONS: This study demonstrates that the chemical character of Cy5-derived dyes does significantly influence the biodistribution profile and tumor targeting of Nb-based tracers. The fluorescent dye sulfoCy5-Sulfonate was found to have the most promising properties to use in combination with Nbs, as the resulting conjugates showed good tumor binding with negligible background and rapid excretion from the kidneys.

References: [1] Bunschoten A, Willigen DM Van, Buckle T, et al (2016) Tailoring Fluorescent Dyes to Optimize a Hybrid RGD-Tracer. Bioconjug Chem 27:1253–1258 [2] Spa SJ, Hensbergen AW, Wal S van der, et al (2018) The influence of systematic structure alterations on the photophysical properties and conjugation characteristics of asymmetric cyanine 5 dyes. Dye

Pigment 152:19–28 [3] Vaneycken I, Devoogdt N, Gassen N Van, et al (2011) Preclinical screening of anti-HER2 nanobodies for molecular imaging of breast cancer. FASEB J 25:2433–46

Image/Figure:

https://s3.amazonaws.com/amz.xcdsystem.com/1E8A4501-BB41-A02A-1D3B9882B798BFAA_abstract_File10351/GA14_ImageFigure_0505072725.jpg

Image/Figure Caption: Fig.1. 2D fluorescence imaging of biodistribution and tumor targeting of anti-HER2 Nb (2RS15dNOTAG) randomly labeled with 3 distinct Cy5-derivatives in mice bearing subcutaneous HER2+ SKOV3 tumors on right hind limb evaluated over 24h after injection.

Full Name of Abstract's 1st Author : Lukasz Mateusiak

First Name: Lukasz

Last Name: Mateusiak

Email: lukasz.mateusiak@vub.be

Organization: Vrije Universiteit Brussel

Country: Belgium

ID: GA15
Photoacoustic imaging of oxygen saturation in the skeletal muscle of spontaneously hypertensive rats

Emily Lupton, University College London, emily.lupton1@gmail.com

---

Category: Cardiovascular & Pulmonary

Abstract Body : Introduction: Hypertension affects 1.1 billion people globally and increases the risk of heart, brain and kidney diseases1. Spontaneously hypertensive rats (SHR) are a well-established animal model of human essential hypertension. As such, SHRs develop increased peripheral resistance with age. Photoacoustic imaging (PAI) is a non-invasive method used to determine blood oxygen saturation (sO2) using measurements of deoxy- and oxy- haemoglobin. This study aims to use PAI to evaluate the effect of increased peripheral resistance on sO2 levels and capillary density in the hind limb of a hypertensive rat model. Methods: Hind limb sO2 measurements of SHR, SHR on high fat diet (HFSHR) and Wistar-Kyoto (WKY) control animals were used with histology to examine the effects of hypertension on sO2 and capillary density. Twelve-month old male SHR (n=5), HFSHR (n=5) and WKY rats (n=8) were anaesthetised with isoflurane in 1.5 L/min air (21% oxygen). Warmed ultrasound (US) gel was applied to shaved hind limbs. B-mode and power Doppler US was used to confirm blood flow (Fig 1a-c, Vevo3100 LazrX). PAI was used to measure deoxy- and oxy- haemoglobin (absorption 750 nm and 850 nm respectively). PA images were acquired for 2 minutes during inhalation of 21% O2 (Fig 1d-f) followed by 2 minutes inhalation of 100% O2 (Fig 1g-i). Capillary density in the hind limb was measured by semi-automated assessment of H&E stained cryosection. Results: SHRs had higher hind limb sO2 levels than HFSHR and control animals. Control animals consistently had the lowest sO2. While inhaling 21% O2, hind limb sO2 was significantly higher in SHRs than control animals (75.4 +/- 4.4% vs. 54.8 +/- 4.5%, p Conclusions: PAI has been used to demonstrate that SHRs have higher hind limb sO2 and a higher response to change in inhaled oxygen concentration than control animals, despite having significantly lower capillary density. This could be caused by inefficient oxygen coupling by the mitochondria in SHRs2. PAI provides a non-invasive method for assessing sO2 levels and will be useful for future work examining relationships between sO2 and vascular diseases.

References: 1. World Health Organization. Hypertension. Accessed 30th April 2021. https://www.who.int/news-room/fact-sheets/detail/hypertension#:~:text=An%20estimated%201.13%20billion%20people,cause%20of%20premature%20death%20worldwide. 2. De Cavanagh EM, Toblli JE, Ferder L, Piotrkowski B, Stella I, Fraga CG, Inserra F. Angiotensin II blockade improves mitochondrial function in spontaneously hypertensive rats. Cell Mol Biol (Noisy-le-grand). 2005 Nov 8;51(6):573-8. PMID: 16309582.

Image/Figure:

https://s3.amazonaws.com/amz.xcdsystem.com/1E8A4501-BB41-A02A-1D3B9882B798BFAA_abstract_File10351/GA15_ImageFigure_0505122427.png

Image/Figure Caption: Figure 1 (a-c) Example power Doppler and B-mode images of hind limb used to locate region of interest by locating region with highest flow measurements. Red indicates location of flow. (d-f) Example PA images of hind limb when inhaling 21% O2. Red and blue indicate oxy-haemoglobin and deoxy-haemoglobin respectively. (g-i) Example PA images of hind limb when inhaling 100% O2. Red and blue indicate oxy-haemoglobin and deoxy-haemoglobin respectively. (j-l) sO2 measurements over time. Anaesthesia was changed from 21% oxygen to 100% oxygen at 2 minutes. j) SHR, k) HFSHR, l) control. m) Change in sO2 for each group of animals when anaesthetic was changed from isoflurane with 21% O2 to isoflurane with 100% O2. n) Difference in sO2 measurements between each group of animals when inhaling isoflurane with 21% O2. o) Difference in sO2 measurements between each group of animals when inhaling isoflurane with 100% O2. p) Capillary density calculated from semi-automated assessment of H&E stained cryosections. (* = $p < 0.05$, ** = $p < 0.01$, *** = $p < 0.001$, **** = $p < 0.0001$)

Full Name of Abstract's 1st Author : Emily Lupton

First Name: Emily

Last Name: Lupton

Email: emily.lupton1@gmail.com

Organization: University College London

Country: United Kingdom

ID: GA16
Computed Tomography and [18F]-FDG PET imaging as a readout for COVID-19 pathophysiology, treatment and vaccine evaluation in Non-Human Primates

Thibaut Naninck, CEA, thibaut.naninck@cea.fr

Category: Immunology: Inflammation & Infection

Abstract Body : Background The current COVID-19 pandemic highlights the crucial need for preclinical infectious disease models to assess disease pathogenesis, but also to quickly evaluate the efficacy of vaccine or treatment candidates. Non-Human Primates (NHPs) such as cynomolgus or rhesus macaques harbour the closest genome compared to humans and are therefore particularly relevant as preclinical models for SARS-CoV-2 infection [1, 2]. Here we investigated the asset of in vivo imaging (CT and [18F]-FDG PET-CT) to monitor disease progression and to evaluate some treatments and vaccines in SARS-CoV-2 infected NHPs. Methods Cynomolgus and rhesus macaques (untreated, treated or vaccinated) were exposed to SARS-CoV-2 (Wuhan variant) by intranasal + intratracheal routes. Animals were monitored for viral load by classical nasopharyngeal and tracheal swabs and RT-qPCR, for analysis of complete blood count, for clinical parameters and by in vivo imaging (CT scans or [18F]-FDG PET-CT). CT scans were performed longitudinally during the first two weeks of infection. Pulmonary lesions were graded by semi-quantitative CT scoring by two independent people according to lesion type and extension. Percentage change of lung hyperdensity was also quantified. Longitudinal [18F]-FDG PET-CT in some animals allowed the evaluation of inflammation in several regions of interest such as lungs, lung-draining lymph nodes and spleen. Results Infected animals harbour asymptomatic to mild clinical symptoms as already described [3, 4]. All untreated animals showed characteristics of SARS-CoV-2 infection in the airways. All types of COVID-19 related pulmonary lesion patterns were found including, in the majority, peripheral Ground Glass Opacities but sometimes coupled to reticulations (crazy-paving patterns) or consolidations (Fig 1). CT scores also reflect the heterogeneity of lung lesions in infected animals. Around viral load peak (day 2), no statistical differences in CT scores were found between groups exposed with different inoculum doses or between cynomolgus and rhesus macaques. [18F]-FDG uptake evaluated by PET imaging was increased in lungs (not only in lesion sites) and in lung-draining lymph nodes (see persuasive data), allowing us to assess the inflammation process and cell activation occurring during the disease. Comparison of CT scores but also [18F]-FDG uptake allowed us to assess treatment and/or vaccination efficacy [3, 5]. Conclusion CT and [18F]-FDG PET-CT can be useful tools for longitudinal disease assessment in macaque models of COVID-19, representative of asymptomatic to mild clinical cases in humans. All COVID-19 typical pulmonary lesion patterns were found in these models allowing us to monitor disease progression but also to assess treatments and vaccines efficacy in macaques.

References: References: 1. Singh, D.K., et al., Responses to acute infection with SARS-CoV-2 in the lungs of rhesus macaques, baboons and marmosets. Nature Microbiology, 2021. 6(1): p. 73-86. 2. Lu, S., et al., Comparison of nonhuman primates identified the suitable model for

COVID-19. Signal Transduction and Targeted Therapy, 2020. 5(1). 3. Maisonnasse, P., et al., Hydroxychloroquine use against SARS-CoV-2 infection in non-human primates. Nature, 2020. 585(7826): p. 584-587. 4. Munster, V.J., et al., Respiratory disease in rhesus macaques inoculated with SARS-CoV-2. Nature, 2020. 585(7824): p. 268-272. 5. Brouwer, P.J.M., et al., Two-component spike nanoparticle vaccine protects macaques from SARS-CoV-2 infection. Cell, 2021: p. 2020.11.07.365726.

Image/Figure:

https://s3.amazonaws.com/amz.xcdsystem.com/1E8A4501-BB41-A02A-1D3B9882B798BFAA_abstract_File10351/GA16_ImageFigure_0505034253.jpg

Image/Figure Caption: Figure 1 : Chest Computed Tomography (CT) features detected in SARS-CoV-2 infected macaques. Lung CT representative transversal slices of SARS- CoV-2 infected cynomolgus macaques harbouring peripheral Groung-Glass Opacities (A, B, arrows), GGOs with reticulations (C) and focal consolidations (D). CT scores were assessed around the viral load peak (D2-D3) in cynomolgus macaques exposed with diverse inoculum doses (E) and between macaques species (F). Dpi : days-post-infection; PFU : plaque-forming unit.

First Name: Thibaut

Last Name: Naninck

Email: thibaut.naninck@cea.fr

Organization: CEA

Country: France

ID: GA17
Assessment of (R)- and (S)-18F-OF-NB1 as potential radiotracers for PET imaging of the GluN2B subunits of NMDA receptors

Mike (MingQiang) Wenn (Zheng), Yale University, ming-qiang.zheng@yale.edu

---

Category: Neuroscience

Abstract Body : Objectives The GluN2B subunit of the NMDA receptor is believed to be a therapeutic target for schizophrenia, Alzheimer's disease and brain injury. We have previously reported the radiosynthesis and evaluation of racemic 18F-OF-NB1 in rodents (1). Here we report a comprehensive evaluation and comparison of enantiopure (R)- and (S)-18F-OF-NB1 in rhesus monkeys. Methods. The enantiomeric purity of (R)- and (S)-18F-OF-NB1 was determined by chiral HPLC analysis. PET scans in three rhesus monkeys were conducted on the Focus 220 scanner. Blocking studies were performed after treatment of the animals with Co101,244, a GluN2B antagonist, or FTC-146, a sigma-1 receptor antagonist. Arterial blood samples were collected and assayed for radioactivity in whole blood and plasma. Blood samples at 5 min, 15 min, 30 min, 60 min, 90 min and 120 min were processed and analyzed to measure radiometabolites. Regional brain time-activity curves (TAC) were produced from regions of interest (ROIs) defined on a brain template. Volume of distribution (VT) was determined by kinetic modeling with one- and two-tissue compartment models (1TCM and 2TCM) and multilinear analysis-1 (MA1) using the metabolite-corrected arterial input function. Receptor occupancy for each blocking drug and non-displaceable volume of distribution (VND) were determined from the occupancy plots. Regional non-displaceable binding potential (BPND) was determined using VND estimates from GluN2B blocking scans (BPND = VT/VND – 1) Results (R)- and (S)-18F-OF-NB1 were synthesized and purified using semi-preparative chiral HPLC, and obtained in >99% radiochemical and enantiomeric purity (Figure 1A). Metabolism rate was similar between the two tracers in different monkeys, with ~50% parent compound remaining at 20-25 min after injection. Brain uptake was high for both tacers (Figure 1B). In brain regions (R)-18F-OF-NB1 displayed fast uptake and slower clearance comparing to (S)- 18F-OF-NB1 (Figure 1C). Both the 1TCM model and MA1 method gave reliable estimates of regional VT values, with MA1 VT (mL/cm3) in the same monkey, ranging from 27 and 20 in the centrum semiovale to 80 and 39 in the cingulate cortex for (R)- and (S)- 18F-OF-NB1, respectively. Blocking with 0.25 mg/kg of Co101,244 greatly reduced the uptake of (R)- and (S)- 18F-OF-NB1 across all brain regions (Figure 1B), resulting in an occupancy of 96% measured with (R)-18F-OF-NB1, and 88% when measured with (S)-18F-OF-NB1, and VND of 12.90 for (R)-18F-OF-NB1, and 9.32 for (S)-18F-OF-NB1, while 0.027 mg/kg of FTC-146 reduced tracer binding by 49% for (S)-18F-OF-NB1(Figure 1D). Average cortical BPND values for (R) and (S)-18F-OF-NB1 were 4.43 and 2.27, respectively (2.79 for (S)-18F-OF-NB1 in a different monkey). Graphs Figure 1 Conclusions In rhesus monkeys, (S)-18F-OF-NB1 showed faster kinetics compared to (R)-18F-OF-NB1 although with a smaller VT, and heterogeneous uptake across brain regions. Blocking study with GluN2B antagonist indicated binding specificity. Values of BPND were >2.0 in most brain regions, suggesting good in vivo specific binding signals. Taken together, results from our current study demonstrated the potential of (S)-18F-OF-

NB1 as a useful radiotracer for imaging GluN2B subunit of the NMDA receptor. Research support: NIH grant U01MH107803

References: 1. Ahmed H. et al. Preclinical development of 18F-OF-NB1 for imaging GluN2B-containing N-Methyl-D-Aspartate receptors and its utility as a biomarker for amyotrophic lateral sclerosis. jnumed.120.246785

Image/Figure:

https://s3.amazonaws.com/amz.xcdsystem.com/1E8A4501-BB41-A02A-1D3B9882B798BFAA_abstract_File10351/GA17_ImageFigure_0512035818.JPG

Image/Figure Caption: Figure 1. A. Chemical structures of (R)-18F-OF-NB1 and (S)-18F-OF-NB1, and their chromatograms from chiral HPLC analysis, along with that of non-radiolabeled racemic OF-NB1. B. Summed PET SUV images from 45-60 min after tracer injection, including baseline and Co-101,244 blocking for (R)-18F-OF-NB1(left) and baseline, Co-101,244 and FTC-146 blocking for (S)-18F-OF-NB1 (right). C. Time-activity curves from baseline scans of (R)- and (S)-18F-OF-NB1 (Black:Cerebellum; Red, Frontal cortex; Blue, Hippcampus; Green, Putamen; Purple, Cingulate cortex). D. Representative monkey brain regions from baseline and blocking studies with (S)-18F-OF-NB1.

First Name: Mike (MingQiang)

Last Name: Wenn (Zheng)

Email: ming-qiang.zheng@yale.edu

Organization: Yale University

Country: United States

ID: GA18
Prosaposin mediates inflammation in atherosclerosis

Mandy van Leent, Icahn School of Medicine at Mount Sinai, New York, mandyvanleent@gmail.com

---

Category: Cardiovascular & Pulmonary

Abstract Body : Introduction Macrophages play a central role in the pathogenesis of atherosclerosis1. The inflammatory properties of these cells are dictated by their metabolism, of which the mechanistic target of rapamycin (mTOR) signaling pathway is a key regulator2–5. Methods & results We formulated apoliprotein A1-based nanobiologics6 loaded with mTOR or ribosomal protein S6 kinase-1 (S6K1) inhibitors7 (Panel A) to specifically inhibit the mTOR signaling pathway in atherosclerotic plaques. As our model for atherosclerosis we used apolipoprotein E-deficient (Apoe-/-) mice that had been on a 12-week Western Diet. First, we evaluated the biodistribution of our therapeutic platform by near-infrared fluorescence (NIRF) imaging using DiR-labeled nanobiologics. Ex vivo imaging performed 24 hours after intravenous administration showed that mTOR inhibitor nanobiologics (mTORi-NB) and S6K1i-NB primarily accumulate in the liver, spleen and kidneys of Apoe-/- mice (Panel B). High DiR uptake was observed in the aortic sinus area, which is the preferential site of plaque development in this mouse model. Next, we treated Apoe-/- mice with 4 intravenous injections of either mTORi-NB, S6K1i-NB, unloaded nanobiologics or PBS over the course of one week and evaluated therapeutic efficacy using several methods (Panel C). Through histologic assessment we found that mice treated with mTORi-NB had a 14% (P mTORi-NB and S6K1i-NB therapies reduced the number of aortic macrophages (Panel D). To test the plaque's inflammatory activity, we performed in vivo fluorescence molecular tomography with computed tomography (FMT-CT) imaging to quantify protease activity in the aortic sinus area8. PBS and mTORi-NB-treated Apoe-/- mice received a single injection of an activatable pan-cathepsin protease sensor 24 hours before imaging. The protease sensor is taken up by activated macrophages and cleaved in the endolysosome, yielding fluorescence as a function of enzyme activity. mTORi-NB treatment reduced protease activity by 30% compared to PBS control (P = 0.03, Panel E). To gain insight into the mechanism by which mTOR-S6K1 signaling affects monocytes and macrophages in atherosclerosis, we used laser capture microdissection to isolate CD68+ cells from aortic sinus plaques of Apoe-/- mice that were treated for one week with either PBS, mTORi-NB or S6K1i-NB. Total RNA of these cells was isolated for transcriptome analysis. Using a systems biology approach of weighted gene co-expression network analysis we identified Psap, a gene encoding for the lysosomal protein prosaposin9, as closely related with mTOR signaling (Persuasive Data Panels D-I). Subsequent in vitro experiments on bone marrow derived macrophages revealed that Psap inhibition suppressed both glycolysis and oxidative phosphorylation. Transplantation of Psap-/- bone marrow to low-density lipoprotein receptor knock-out (Ldlr-/-) mice led to a reduction of atherosclerosis development and plaque inflammation (Panels F-I). Finally, we confirmed the relationship between PSAP expression and inflammation in human carotid atherosclerotic plaques10 (Panels J and K, Persuasive Data Panels J-L). Conclusion In this study we showed that myeloid cell-specific mTOR and S6K1

inhibition rapidly suppressed plaque inflammation in atherosclerotic mice. We identified prosaposin as a mediator of these anti-inflammatory effects and revealed prosaposin's regulatory role in immunometabolism. In humans we confirmed high PSAPexpression in plaque macrophages and found it to be related to mTOR signaling and inflammation.

References: 1. Tabas, I. & Lichtman, A. H. Monocyte-Macrophages and T Cells in Atherosclerosis. Immunity 47, 621–634 (2017). 2. O'Neill, L. A. J., Kishton, R. J. & Rathmell, J. A guide to immunometabolism for immunologists. Nat. Rev. Immunol. 16, 553–565 (2016). 3. Ketelhuth, D. F. J. et al. Immunometabolism and atherosclerosis: Perspectives and clinical significance: A position paper from the Working Group on Atherosclerosis and Vascular Biology of the European Society of Cardiology. Cardiovasc. Res. 115, 1385–1392 (2019). 4. Koelwyn, G. J., Corr, E. M., Erbay, E. & Moore, K. J. Regulation of macrophage immunometabolism in atherosclerosis. Nat. Immunol. 19, 526–537 (2018). 5. Weichhart, T., Hengstschläger, M. & Linke, M. Regulation of innate immune cell function by mTOR. Nat. Rev. Immunol. 15, 599–614 (2015). 6. Mulder, W. J. M. et al. High-Density Lipoprotein Nanobiologics for Precision Medicine. Acc. Chem. Res. 51, 127–137 (2018). 7. Pearce, L. R. et al. Characterization of PF-4708671, a novel and highly specific inhibitor of p70 ribosomal S6 kinase (S6K1). Biochem. J. 431, 245–255 (2010). 8. Nahrendorf, M. et al. Hybrid in vivo FMT-CT imaging of protease activity in atherosclerosis with customized nanosensors. Arterioscler. Thromb. Vasc. Biol. 29, 1444–1451 (2009). 9. Hazkani-Covo, E., Altman, N., Horowitz, M. & Graur, D. The Evolutionary History of Prosaposin: Two Successive Tandem-Duplication Events Gave Rise to the Four Saposin Domains in Vertebrates. J. Mol. Evol. 54, 30–34 (2002). 10. Depuydt, M. A. C. et al. Microanatomy of the Human Atherosclerotic Plaque by Single-Cell Transcriptomics. Circ. Res. 127, 1437–1455 (2020). 11. Van Leent, M. M. T. et al. Prosaposin mediates inflammation in atherosclerosis. Sci. Transl. Med. 1433, (2021).

Image/Figure: https://s3.amazonaws.com/amz.xcdsystem.com/1E8A4501-BB41-A02A-1D3B9882B798BFAA_abstract_File10351/GA18_ImageFigure_0506085844.pdf

Image/Figure Caption: Prosaposin mediates inflammation in atherosclerosis. (A) Schematic overview of the different components of mTORi-NB and S6K1i-NB. mTORi-NB was constructed by combining human apoA-I, the phospholipids 1,2-dimyristoyl-sn-glycero-3-phosphocholine (DMPC) and 1-myristoyl-2-hydroxy-sn-glycero-phosphocholine (MHPC) and the mTOR inhibitor rapamycin. S6K1i-NB consisted of apoA-I, the phospholipids 1-palmitoyl-2-oleoyl-sn-glycero-3-phosphocholine (POPC) and 1-palmitoyl-2-hydroxy-sn-glycero-3-phosphocholine (PHPC), and the S6K1 inhibitor PF-4708671. (B) IVIS imaging of organs of Apoe-/- mice, injected with DiR-labeled mTORi-NB (left) or DiR-labeled S6K1i-NB (middle). IVIS imaging of the aorta of DiR-labeled mTORi-NB injected Apoe-/- mice (right). Organs were harvested 24 hours after injection. (C-E) Apoe-/- mice were fed a Western diet for 12 weeks, followed by 1 week of treatment, while continuing the diet. Treatment consisted of 4 intravenous injections of PBS, mTORi-NB (rapamycin at 5 mg/kg), S6K1i-NB (PF-4708671 at 5 mg/kg) or unloaded nanobiologics (NB, at a comparable dose). See schematic in (C). (D) Aortic macrophages (CD11b+Lin-CD11c-F4/80+Ly6Clo) as assessed by flow cytometry (n = 8-10 mice/group). (E) FMT/CT imaging of protease activity in the aortic root of PBS or mTORi-NB-treated mice (n = 8-10 mice/group). (F-I) Ldlr-/- mice were lethally irradiated and transplanted with Psap+/+ or Psap-/- bone marrow cells. Mice were left to

reconstitute for 6 weeks after which they were put on a Western diet for 11 weeks (n = 10 mice/group), see schematic in (F). (G) Representative images of H&E-stained aortic roots. (H) Histologic quantification of plaque area at set distances from the aortic root, presented as mean ± SEM. (I) Lesion volume was calculated as area under the curve in H. (J) Representative images of CD68 (top) and prosaposin (middle and bottom) staining on a human carotid endarterectomy sample. (K) Single-cell RNA sequencing of human atherosclerotic plaques identifies 14 leukocyte subsets. (n = 18). Violin plot shows expression of PSAP in each leukocyte subset.

First Name: Mandy

Last Name: van Leent

Email: mandyvanleent@gmail.com

Organization: Icahn School of Medicine at Mount Sinai, New York

Country: United States

ID: GA19
Fe(deferasirox)2: A novel MRI contrast agent endowed with remarkable molecular and functional characteristics

Lorenzo Palagi, University of Torino, lorenzo.palagi@unito.it

---

Category: New Chemistry, Materials & Probes

Abstract Body : The search for alternatives to gadolinium-containing MRI contrast agents (CAs) addresses the field of Fe(III)-bearing species with the view that the use of an essential paramagnetic metal ion may avoid the issues raised by the exogenous Gd. Attention is currently devoted to highly stable, hexacoordinated Fe(III) complexes, in spite of the fact that they may lack any coordinated water molecule.[1] It has been found that the well-known hexacoordinated Fe(III) complex with deferasirox, a Fe(III) sequestering agent largely used in patients with iron overload, displays properties that can make it a viable alternative to Gd-based MRI CAs. Such complex, in which one metal ion is coordinated by two ligands, is normally formed in vivo upon the action of deferasirox as sequestering agent, that efficiently chelate the iron ions subtracted to the pool.[2] In this work, Fe(deferasirox)2 (chemical structure reported in Figure 1) was synthesized and its structural and relaxometric properties were investigated in vitro. In vivo studies on a tumor-bearing mouse model are also reported. Fe(deferasirox)2 owns an outstanding thermodynamic stability and a good relaxivity, comparable to the ones displayed by clinically used Gd-based CAs. The relaxation enhancement is due to second sphere water molecules likely forming H-bonds with the coordinating phenoxide ions. Furthermore, the high binding affinity to human serum albumin (HSA) enables, in serum, the formation of a slowly tumbling supramolecular adduct in which three units of complex are simultaneously bound to one protein. Upon the formation of such an adduct, a further relaxation enhancement was observed. The binding sites of Fe(deferasirox)2 on HSA have been characterized by relaxometric competitive assays. Preliminary in vivo imaging studies on a tumor-bearing mouse model indicated that, on a 3 T MRI scanner, the contrast ability of Fe(deferasirox)2 is well comparable to the one shown by the commercial Gd(DTPA), one of the most clinically used MRI CAs. ICP-MS analyses on blood samples withdrawn from healthy mice administered intravenously with a dose of 0.1 mmol/kg of Fe(deferasirox)2 showed that the complex is completely excreted in 24 h. The herein reported relaxation efficiency (with increasing relaxivity values in the range 20-80 MHz), the overall biodistribution and excretion properties and the expected good biocompatibility of Fe(deferasirox)2, make this system a promising candidate as an alternative to the Gd-based MRI CAs currently used in clinics. Furthermore, one may think of designing other systems based on the coordination cage of deferasirox with the introduction of substituents that may allow an improved control of the mobility of the second sphere water molecules, thus maintaining the interesting field-dependent properties shown by Fe(deferasirox)2.

References: [1] Wahsner, Jessica, et al. "Chemistry of MRI contrast agents: current challenges and new frontiers." Chemical reviews 119.2 (2018): 957-105 [2] Weiss, H. Markus, et al. "In vitro blood distribution and plasma protein binding of the iron chelator deferasirox (ICL670) and

its iron complex Fe-[ICL670] 2 for rat, marmoset, rabbit, mouse, dog, and human." Drug metabolism and disposition 34.6 (2006): 971-975.

Image/Figure:

https://s3.amazonaws.com/amz.xcdsystem.com/1E8A4501-BB41-A02A-1D3B9882B798BFAA_abstract_File10351/GA19_ImageFigure_0506102130.png

Image/Figure Caption: Figure 1. Chemical structure of the complex Fe(deferasirox)2

Full Name of Abstract's 1st Author : Lorenzo Palagi

First Name: Lorenzo

Last Name: Palagi

Email: lorenzo.palagi@unito.it

Organization: University of Torino

Country: Italy

ID: GA20
PET Imaging of the Acidic Tumor Microenvironment with Zirconium-89-labeled Membrane Inserting Peptides

David Bauer, Memorial Sloan-Kettering Cancer Center, bauerd1@mskcc.org

---

Category: Oncology

Abstract Body : Introduction: The pH low insertion peptides (pHLIP®) allow for the selective targeting of acidic extracellular environments in vivo due to their pH-dependent cellular membrane insertion. Imaging of acidity, a hallmark in the tumor microenvironment, can provide new information about tumor biology, progression, and cancer treatment responses. Initial preclinical studies indicated the feasibility of this approach by using 18F- and 64Cu-radiolabeled pHLIP® conjugates to visualize tumors in vivo via positron emission tomography (PET).[1,2] However, the short half-lives of 18F ($t_{1/2}$ = 1.8 h) and 64Cu ($t_{1/2}$ = 12.7 h) did not allow for long-term imaging. Additionally, the variation of the peptide sequence and the conjugating to chelators results in differing pharmacokinetics.[1,3] The use of radionuclides with longer half-lives, the optimization of pHLIP® conjugates, and a thorough investigation of their pharmacokinetics can lead to pHLIP® conjugates with improved properties for cancer imaging. Imaging using the pHLIP® technology will primarily benefit these cancer entities that do not necessarily overexpress specific molecular markers, e.g., triple-negative breast cancer. Method: Two variants of pHLIP®, the wild-type (WT) and the optimized Var3 sequence,[2] were compared for their use as PET tracers for cancer imaging. This study focuses on long-term PET imaging to investigate the pharmacokinetics of these peptides. For this purpose, both variations were labeled with zirconium-89 ($t_{1/2}$ = 3.3 d). Four chelators (DFO, DFO*, DFO-squaramide, and 3,4,3-LI(1,2-HOPO)) were compared on their influence on the resulting conjugate's biodistribution. In total, six 89Zr-labeled pHLIP® conjugates were synthesized and injected into athymic nude mice bearing subcutaneous RM-1 or 4T1 tumor allografts as a model for aggressive end-stage prostate and breast cancer, respectively. The mice were imaged 4, 24, 48, and 72 h p.i. to determine the pHLIP®-biodistribution in vivo. Tissue samples were collected for additional ex vivo biodistribution studies. Autoradiograms, hematoxylin & eosin and CD31 staining of tissue-slices were used to illuminate the conjugate's distribution inside the tumor. Results and Conclusion: Clear differences in biodistribution and chemical behavior were found among the six pHLIP® conjugates investigated. In vivo PET imaging revealed that the pHLIP®s accumulate in the tumor around 4 h p.i. and showed the best tumor-to-background ratio after 24 h p.i. The highest tumor uptake of (12.4 ± 4.7)%ID/g at 48 h p.i was observed for the DFO-squaramide-Var3 conjugate in the RM-1 mouse model. The elevated tumor uptake comes with a high accumulation of the pHLIP® in the kidneys' cortex (82.5 ± 14.2)%ID/g, visualizing the acidic region of the nephrons. Autoradiography, hematoxylin & eosin and CD31 staining indicated that the investigated 89Zr-labeled pHLIP®s target specifically the hypovascular region of the tumor. Anti-cancer drugs like chemotherapeutics do not usually reach these tumor areas. This can be the origin of chemoresistance. The 89Zr-labeled DFO-squaramide-Var3 conjugate shows excellent potential for indicating these regions, and with only a one-time administration, the tumor progression can be monitored over several days.

References: [1] D. W. Demoin, et al., Bioconjugate Chem 2016, 27, 2014. [2] P. Daumar, et al., Bioconjugate Chem 2012, 23, 1557. [3] D. Weerakkody, et al., Proc Natl Acad Sci USA 2013, 110, 5834.

Image/Figure: https://s3.amazonaws.com/amz.xcdsystem.com/1E8A4501-BB41-A02A-1D3B9882B798BFAA_abstract_File10351/GA20_ImageFigure_0506024801.jpeg

Image/Figure Caption: Biodistribution of 89Zr-labeled pH low insertion peptides (pHLIP®) in athymic male nude mice bearing subcutaneous RM-1 tumor allografts. A. Coronal in vivo PET images (maximum intensity projection) at 4 and 72 h p.i. of DFO-squaramide-Var3-pHLIP®. The pHLIP® accumulates in the acidic areas (kidney cortex and tumor). Scale: percent injected dose per gram of tissue (%ID/g). B. Ex vivo biodistribution (kidneys and tumor) 48 h p.i. of six pHLIP variations. C. (LTR) Autoradiogram, hematoxylin & eosin and CD31 staining of 10 μm-tumor slices (excised at 72 h p.i. of DFO-squaramide-Var3-pHLIP®) indicating the pHLIP's accumulation in the hypovascular regions of the tumors.

Full Name of Abstract's 1st Author : David Bauer

First Name: David

Last Name: Bauer

Email: bauerd1@mskcc.org

Organization: Memorial Sloan-Kettering Cancer Center

Country: United States

ID: GA23
Capturing the actin nucleation supercomplex in its entirety

Akira Chiba, University of Miami, akira.chiba@miami.edu

Category: Bioengineering, Synthetic Biology and Basic Biology

Abstract Body : Monomeric G protein Cdc42 binds nucleation promoting factor WASp. Activated WASp in turn associates with ubiquitous seven-part Arp2/3 complex, which then initiates autocatalytic dendritic nucleation of actin cytoskeleton. Not well understood in vivo, however, is how much time this sequence of events requires and how much space its ensuing structure(s) occupies. We developed multiplex Förster resonance energy transfer as a visual proxy to directly image fluorescently labeled Cdc42, WASp and Arp3 in vivo. Here, in an intact Drosophila embryo, we capture the instance at which the entire nine-part actin nucleation protein supercomplex assembles within a miniscule volume of twelve proteins.
Introduction: Proteins form complexes within cells, but visualizing them as fully assembled three-dimensional structures has been difficult. Arp2/3 (actin-related protein-2/3) is a seven-part protein complex found in every eukaryotic cell. Decades of work made clear that this ubiquitous protein complex has little catalytic activity of its own. This led to discovery of nucleation promoting factors such as WASp (Wiskott–Aldrich Syndrome protein). The central role of WASp is to help multimeric Arp2/3 complex adapt a form suitable for initiating auto-catalytic dendritic nucleation of actin filaments. However, WASp itself is in need of changing its default configuration. In most metazoans, what activates WASp is the small GTPase Cdc42 (cell division control protein 42 homolog). Hence, a total of nine proteins are proposed to amass this functionally pertinent structure that initiates and regulates the actin filament network. Yet, when, where and in what order these proteins, each encoded and synthesized separately, associate with one another remain unknown to date. Rationale: We sought to image this protein complexing event by exploiting Förster resonance energy transfer. We fluorescently tagged the three separate proteins Arp3, WASp and Cdc42 and allowed them to assemble in vivo in an optically transparent Drosophila embryo. Results: In our control trial, the three fluorescent proteins — eGFP, mCherry and nirFP — were expressed at the same concentrations as the experimental trial but left unfused. They did not spontaneously approach with each other, as judged by the complete absence of FRET. This was also true in other second control when one of the fluorescent proteins was fused to Cdc42. The localization of donor and/or acceptor do not usually predict when and where FRET would occur within the cytosol. In contrast, FRET occurred reproducibly between the pairs of Cdc42-WASp and WASp-Arp3 in the regions where cell bodies are devoid and axons and dendrites are abundant. This became apparent at hour 21:00 of embryogenesis as opposed to earlier hour 12:00 when neither axons or dendrites are present. The neuropil, known as the longitudinal connective, tended to show the highest interaction probability, followed by the commissures and the nerves. Swapping the fluorescent tags on the protein pairs for donor and acceptor of FRET did not alter the whereabouts of the FRET occurrence. Furthermore, FRET incidences were independent of whether the tag was inserted at the amino terminus or at the carboxyl terminus. Thus, the protein interactions were independent from the color or relative position of the fluorophore tag. Intriguingly, Cdc42 and Arp3, at both

ends of the allegedly sequential assembly events, was found to exhibit FRET. In the same animals, Arp3 was also seen to FRET with WASp. Conclusion: Approaches to isolate and then reconstruct a multimeric protein complex have necessarily sacrificed natural context. By instead adding fluorescent tags to individual proteins, we capture the very instance at which a protein supercomplex is built within an intact animal. We propose that direct FRET imaging offers a vital complement to the reconstructionist approaches that have been widely successful in cracking the proteome.

Image/Figure:

https://s3.amazonaws.com/amz.xcdsystem.com/1E8A4501-BB41-A02A-1D3B9882B798BFAA_abstract_File10351/GA23_ImageFigure_0506051021.jpg

Image/Figure Caption: FIG.1. Summary. (a) Polar-plot analysis reveals the tag-to-tag distance (left), and the size-free FRET probability (right). (b) Tag-to-tag distances between Cdc42's amino terminus and WASp's amino terminus, WASp's amino terminus and Arp3's amino terminus, and Arp3's amino terminus to Cdc42's amino terminus are shown. Arp3's 3D structure is shown together with other six proteins of the Arp2/3 complex. (c) Size-free FRET probabilities between the protein trio Arp3 (yellow circle), WASp (orange circle) and Cdc42 (white circle) in, counterclockwise, cortex, commissure, neuropil and nerve regions at 21:00 of embryogenesis are summarized

First Name: Akira

Last Name: Chiba

Email: akira.chiba@miami.edu

Organization: University of Miami

Country: United States

ID: GA24
Hypoxia-responsive CEST-MR and chemi-luminescence imaging agent for in vivo bacteria and tumor detection

Kwan Soo Hong, Korea Basic Science Institute, kshong@kbsi.re.kr

---

Category: Oncology

Abstract Body : Hypoxia-responsive CEST-MR and chemi-luminescence imaging agent for in vivo bacteria and tumor detection Sanu Karan,a,b Mi Young Cho,a Hyunseung Lee,a Jee-Hyun Cho,c and Kwan Soo Honga,b aResearch Center for Bioconvergence Analysis, Korea Basic Science Institute, Cheongju 28119, Korea bGRAST, Chungnam National University, Daejeon 34134, Korea cResearch Equipment Operations Division Center, Korea Basic Science Institute, Cheongju 28119, Korea Hypoxia enlargement in tumor is closely related with its expanded aggressiveness and strong resistance to therapy, leading to poor prognosis in several cancer types. Herein, we show a novel molecular antenna-based bimodal probe designed to improve MR/optical detection sensitivity. We designed and synthesized a novel chemi-luminescent probes for tumor hypoxia detection and cancer cell imaging, in which hypoxia activatable chemi-luminescent probe corporates DOTA with a nitroreductase (NTR)-sensing moiety, a 3-nitropthalimide group. In vitro response and mechanism of the NTR-catalysed reduction of probe have been investigated through UV, fluorescence, and CEST-MRI measurements. Also, optical imaging of live Escherichia coli and CEST-MRI studies in CT26 cells have been investigated to confirm the ability of detection of NTR activity at the cellular level and also in hypoxic tumors in a xenograft mouse model. This bimodal probe could provide a dual imaging hypoxia detection tool to guide tumor malignancy.

Image/Figure:

https://s3.amazonaws.com/amz.xcdsystem.com/1E8A4501-BB41-A02A-1D3B9882B798BFAA_abstract_File10351/GA24_ImageFigure_0506084721.jpg

Image/Figure Caption: Figure. (A) Schematic representation of active switching “On” of CEST-MR and luminescence under hypoxic condition with nitroreductase (NTR), (B-D) CEST-MR spectra shown by z-spectrum (B) and MTRasym plot (C), and representative color-map (D; sum of the MTRasym (%) from 1.5 to 6 ppm) acquired from probe phantom with (upper) and without NTR.

First Name: Kwan Soo

Last Name: Hong

Email: kshong@kbsi.re.kr

Organization: Korea Basic Science Institute

Country: Korea, Republic of

ID: GA25
Simulating Dose Reduction for Myocardial Perfusion SPECT Using a Poisson Resampling Method

Joon-Kee Yoon, Ajou University, jkyoon3@gmail.com

Category: Cardiovascular & Pulmonary

Abstract Body : Purpose: The purpose of this study was to determine the lowest Tl-201 dose that does not reduce the image quality of myocardial perfusion SPECT (MPS) by Poisson resampling simulation. Methods: One hundred and twelve consecutive MPS data from patients with suspected or known coronary artery disease were collected retrospectively. Stress and rest MPS data were resampled using the Poisson method with 33%, 50%, 67% and 100% count settings. Two nuclear medicine physicians assessed the image quality of reconstructed data visually by giving grades from -2 to +2. The summed stress score (SSS), summed rest score (SRS) and summed difference score (SDS) were obtained on the workstation. Image quality grades and semi-quantitative scores were then compared among these resampled images. Results: The proportions of “adequate” image quality were 0.48, 0.75, 0.92, and 0.96 for the groups of images with 33%, 50%, 67%, and 100% data, respectively. The quality of the resampled images was significantly degraded at 50% and 33% count settings, while the image quality was not different between 67% and 100% count settings. We also found that high body mass index further decreased image quality at 33% count setting. Among the semi-quantitative parameters, SSS and SRS showed a tendency to increase with a decline in count. Conclusion: Based on the simulation results, Tl-201 dose for MPS can be reduced to 74 MBq without significant loss of image quality. However, the SSS and SRS can be changed significantly, and it needs to be further verified under the different conditions.

References: 1. Ishihara M, Taniguchi Y, Onoguchi M, Shibutani T. Optimal thallium-201 dose in cadmium-zinc-telluride SPECT myocardial perfusion imaging. J Nucl Cardiol. 2018;25:947-54. 2. Bednarova V, Kincl V, Kaminek M, Vasina J, Panovsky R, Machal J. The prognostic value of ultra low-dose thallium myocardial perfusion protocol using CZT SPECT. Int J Cardiovasc Imaging. 2019;35:1163-7. 3. Jin M, Niu X, Qi W, Yang Y, Dey J, King MA, et al. 4D reconstruction for low-dose cardiac gated SPECT. Med Phys. 2013;40:022501. 4. Zafrir N, Solodky A, Ben-Shlomo A, Mats I, Nevzorov R, Battler A, et al. Feasibility of myocardial perfusion imaging with half the radiation dose using ordered-subset expectation maximization with resolution recovery software. J Nucl Cardiol. 2012;19:704-12. 5. White D, Lawson RS. A Poisson resampling method for simulating reduced counts in nuclear medicine images. Phys Med Biol. 2015;60:N167-76.

Image/Figure:

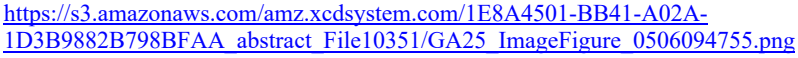
https://s3.amazonaws.com/amz.xcdsystem.com/1E8A4501-BB41-A02A-1D3B9882B798BFAA_abstract_File10351/GA25_ImageFigure_0506094755.png

Image/Figure Caption: The representative images for visual grades of the image quality in myocardial perfusion tomography and polar map

First Name: Joon-Kee

Last Name: Yoon

Email: jkyoon3@gmail.com

Organization: Ajou University

Country: South Korea

ID: GA26
18F-FDG-PET and CT Imaging Reveal Age-dependent Disease Progression in SARS-CoV-2-infected Golden Hamsters

Ji Hyun Lee, Integrated Research Facility at Fort Detrick, National Institute of Allergy and Infectious Diseases, National Institutes of Health, jihyun.lee@nih.gov

---

Category: Immunology: Inflammation & Infection

Abstract Body : Background As of April 27, 2021, there were 32,077,798 confirmed human cases of COVID-19 and 572,200 related deaths in the U.S. [1]. Animal models to assess the efficacy of medical countermeasures and elucidate pathogenesis are essential to ending the pandemic and mitigating impacts of endemic COVID-19, caused by SARS-CoV-2. Here, 18F-FDG PET and CT imaging techniques were applied to evaluate pulmonary disease progression in SARS-CoV-2-infected golden hamsters. Disease progression in young (≈5-6 weeks) and aged (≈1 year) hamsters was compared with human data to determine the validity of the hamster model of COVID-19. Methods 18F-FDG was used to longitudinally quantify the metabolic activity in young and aged golden hamsters pre-exposure (Day -7±3) and post-exposure (Day 2, Day 5, and Day 8) with serial sacrifice (Table 1). Animals were intranasally exposed to either high (105 PFU) or low (103 PFU) doses of SARS-CoV-2 and compared to a PBS-exposed group (mock). SARS-CoV-2 replicated in the lungs, causing pulmonary pathology that was consistent with the golden hamster model and human disease [2-3]. High resolution respiratory gated chest CT and 60-min-delayed static PET imaging were performed and reconstructed on a pre-clinical micro PET/CT (MR Solutions, England). MIM software version 7.0.3 (Cleveland, OH, USA) was used for imaging analysis. We measured consolidation CT scores by a board-certified radiologist, percent change in lung hyperdensity (PCLH), and SUVmax in the lung tissue were measured. Blood samples and lavage fluid were collected at necropsy to determine viremia, viral load, viral dissemination, and host response to infection through hematology, urinalysis, clinical chemistry, antibody responses to SARS-CoV-2, chemokine/cytokine profile, and histopathological analysis. Statistical analysis was performed using linear mixed-effect models for body weight change and image data with days post-exposure and treatment groups as factors. Data are expressed as predicted values with 95% confidence intervals. Results Virus-exposed young hamsters progressively lost weight and then recovered by Day 8 post-exposure in contrast to the mock-exposed animals, which gained weight throughout the experiment. Aged hamsters exhibited higher and more protracted weight loss relative to the young cohort. PET and CT imaging detected variable pulmonary responses to virus exposure and showed that aged hamsters developed more pronounced radiological lung abnormalities compared to the young animals. CT imaging suggested disease progression and regression that mimicked characteristics of SARS-CoV-2-infected human lungs, including severe bilateral, peripheral multilobular ground-glass opacities and regions of consolidations (Figure 1A). Both the CT consolidation score (Figure 1B) and PCLH (Figure 1C) data were statistically significant. Moreover, PET imaging assessments further supported the presence of lung inflammation and/or infection, detecting a significant increase in signal intensity in lesioned areas (Figure 2). SUVmax corresponded to the CT consolidation score and PCLH values. Gross pathology confirmed the radiological findings

(Figure 3). Image scores were correlated with clinical data (Table 2). In line with similar observations of immune response and histopathology, these results suggest a reliable assessment of disease by CT and PET for the hamster SARS-CoV-2 model [2-3]. Conclusions Aged hamsters developed more severe pulmonary disease than young hamsters. Viral load, viral distribution, and immune responses were similar to reports from other laboratories. In addition, it was observed that the human interferon-inducible protein 10 (IP-10) had strong positive correlations with PCLH, CT, and PET. ELISA had strong positive correlations with CT and PCLH scores while Interleukin-2 (IL-2) were strongly negatively correlated with PET and PCLH. Nasal viral load had significant positive correlation with PET but not with CT nor PCLH. In summary, mild to moderate non-lethal disease was observed in hamsters using CT and PET imaging, which may help assess countermeasure efficacy without serial sacrifice.

References: 1. https://coronavirus.jhu.edu/map.html 2. Chan JF, Zhang AJ, Yuan S, et al. Simulation of the Clinical and Pathological Manifestations of Coronavirus Disease 2019 (COVID-19) in a Golden Syrian Hamster Model: Implications for Disease Pathogenesis and Transmissibility. Clin Infect Dis 2020; 71(9): 2428-46. 3. Imai M, Iwatsuki-Horimoto K, Hatta M, et al. Syrian hamsters as a small animal model for SARS-CoV-2 infection and countermeasure development. Proc Natl Acad Sci U S A 2020; 117(28): 16587-95.

Image/Figure: https://s3.amazonaws.com/amz.xcdsystem.com/1E8A4501-BB41-A02A-1D3B9882B798BFAA_abstract_File10351/GA26_ImageFigure_0507084810.pdf

Image/Figure Caption: Table 1. Group distribution Table 2. Summary of statistically significant partial correlations (Days post-exposure, adjusted) between selected clinical variables and image scores Figure 1. A) Representative computed tomography (CT) images from mock, low-dose (1x10^3), and high-dose (1x10^5) groups of young (4–5 weeks) and aged (1 year) golden hamsters intranasally exposed to SARS-CoV-2: From top to bottom, images show disease progression (baseline to Day 8). The two columns on the left are lung images from young hamsters, and the two on the right are from aged hamsters. In the high-dose group, disease peaked in young hamsters on Day 5 and resolved on Day 8, whereas aged hamsters had mixed responses on Day 8 (yellow and red arrows). Both young and aged hamsters that received a mock dose had normal lungs, whereas hamsters exposed with the high dose developed ground-glass opacities and consolidations mimicking human disease. The scale bar indicates the radiodensity value (HU). BL = baseline; D2 = Day 2; D5 = Day 5; D8 = Day 8. B) CT consolidation scores per group show the separation among different groups at Day 5 and Day 8 is clear (p Figure 2. A) Fluorodeoxyglucose (FDG) positron emission tomography (PET) images from mock, low-dose (1x10^3), and high-dose (1x10^5) groups of young (4–5 weeks) and aged (1 year) golden hamsters intranasally exposed to SARS-CoV-2: From top to bottom, images show disease progression (baseline to Day 8). The two columns on the left are lung images from young hamsters, and the two on the right are from aged hamsters. Lesions correspond to those visible via computed tomography (CT). Metabolic activities peaked in young hamsters on Day 5 and resolved on Day 8, whereas aged hamsters had mixed responses on Day 8 (yellow and red arrows). The color bar indicates the maximum standardized uptake value (SUVmax). BL = baseline; D2 = Day 2; D5 = Day 5; D8 = Day 8. B). Mean SUVmax values per group showed a similar pattern as CT consolidation score and PCLH with statistical significance (p Figure 3. Gross pathology images from mock, low-dose (1x10^3), and high-dose (1x10^5) groups of

young (4–5 weeks) and aged (1 year) golden hamsters intranasally exposed to SARS-CoV-2: From top to bottom, images show disease progression (Day 2 to Day 8). The two columns on the left are lung images from young hamsters, and the two on the right are from aged hamsters. Histopathology scores indicate disease severity, which confirms radiographical imaging findings.

First Name: Ji Hyun

Last Name: Lee

Email: jihyun.lee@nih.gov

Organization: Integrated Research Facility at Fort Detrick, National Institute of Allergy and Infectious Diseases, National Institutes of Health

Country: United States

ID: GA27
18F-FDG PET Imaging Indicates Altered Cerebral Glucose Metabolism in SARS-CoV-2 infected Nonhuman Primates

Byeong-Yeul Lee, Integrated Research Facility at Fort Detrick, Division of Clinical Research, National Institute of Allergy and Infectious Diseases, National Institutes of Health, byeongyeul.lee@nih.gov

---

Category: Immunology: Inflammation & Infection

Abstract Body : Background As the coronavirus 19 (COVID-19) pandemic progresses, neurological symptoms of central nervous system (CNS) manifestations (including meningoencephalitis, stroke, seizures, and cognitive impairment) have been increasingly reported [1]. However, the mechanism and underlying pathophysiology of CNS involvement in COVID-19 remain elusive. In this study, 18F-FDG PET imaging was used to evaluate CNS involvement in nonhuman primates exposed to SARS-CoV-2 via intrabronchial instillation. Methods In two iterations, 12 young (4–5 years old) crab-eating (aka cynomolgus) macaques (Macaca fasciularis) were exposed to SARS-CoV-2 (n=6, four female and two male) or vehicle only (n=6, three female and three male) via intrabronchial instillation. The macaques were then observed for the development of clinical signs of infection. All 18F-FDG PET studies were conducted on a Gemini PET/CT scanner (Philips Healthcare). After a 60-min delay from 18F-FDG injection (0.5 mCi/kg), whole-body (WB) PET/CT scans were performed at baseline (pre-exposure) and on Day 2 and Day 6 post-exposure. Dwell time per bed position was 3 min with 50% overlap and a total duration of 21 min. PET data were reconstructed with 128x128 cubic, 2-mm-wide voxels. For quantitative analysis, all reconstructed PET images were corrected for radioactive decay during the scan, as well as uniformity, random coincidences, attenuation, and scattering of the PET radiation in the macaques' bodies [2]. Image processing of PET data and voxel-based statistical analysis were implemented with an in-house pipeline in MATLAB (MathWorks, Natick, MA, USA) and statistical parametric mapping (SPM12) software (www.fil.ion.ac.uk/spm), respectively. Briefly, each WB PET image was aligned to WB CT, and a brain PET/CT image was then extracted. The brain CT image was spatially normalized to a high-resolution D99 macaque template (0.5 mm) [3] and the transformation matrix was applied to the brain PET image to co-register it to the template. Subsequently, all registered PET images were smoothed with an isotropic Gaussian kernel of 1.5 mm full width at half-maximum. With a general linear model, a voxel-based statistical comparison was performed using the two-way repeated measure to test the hypothesis of differential longitudinal changes in cerebral glucose metabolism between mock-exposed and virus-exposed groups. A statistical significance was reported at p Results Compared to the pre-exposure baseline, a widespread decreased cerebral FDG uptake was noted on Day 2 after virus exposure (p (Fig. 1). By Day 6, this decreased FDG uptake partially recovered to baseline levels in the virus-exposed animals. Voxel-based statistical analysis further confirmed that the brain regions that had a significant temporal change in FDG uptakes (Fig. 2-3) included most of the cerebral cortex, insula, and putamen, bilaterally. In contrast, there were no significant changes in FDG uptake in mock-exposed animals (Fig. 1). the longitudinal changes in FDG uptake were highly correlated with serum cytokine concentration

(IL2, IL6, IL10) and changes in white blood cell count (|r|>0.5, p . The macaques did not show obvious neurologic signs during viral exposure. In three SARS-CoV-2-infected macaques euthanized at Day 8 after exposure, CNS histopathology was normal, and SARS-CoV-2 was not detected in brain tissues. Taken together, these preliminary results suggest that decreased glucose uptake may have resulted from systemic inflammatory changes occurring early in SARS-CoV-2-infected macaques [4] rather than direct viral invasion of the brain. The lack of complete recovery, however, raises the possibility of partially irreversible neuronal damage. Conclusions Our findings provide in vivo evidence of early altered CNS glucose metabolism in SARS-CoV-2-infected crab-eating macaques, which recovers only partially following the early stage of the disease. Incomplete recovery of brain glucose metabolism could thus underlie long-term neurological findings in COVID-19 patients and should be confirmed in long-term follow up of infected monkeys.

References: [1]. Zubair, A.S., et al., Neuropathogenesis and Neurologic Manifestations of the Coronaviruses in the Age of Coronavirus Disease 2019: A Review. JAMA Neurol, 2020. 77(8): p. 1018-1027. [2]. Zasadny, K.R. and R.L. Wahl, Standardized uptake values of normal tissues at PET with 2-[fluorine-18]-fluoro-2-deoxy-D-glucose: variations with body weight and a method for correction. Radiology, 1993. 189(3): p. 847-50. [3]. Reveley, C., et al., Three-Dimensional Digital Template Atlas of the Macaque Brain. Cereb Cortex, 2017. 27(9): p. 4463-4477. [4]. Huang, K.J., et al., An interferon-gamma-related cytokine storm in SARS patients. J Med Virol, 2005. 75(2): p. 185-94.

Image/Figure: https://s3.amazonaws.com/amz.xcdsystem.com/1E8A4501-BB41-A02A-1D3B9882B798BFAA_abstract_File10351/GA27_ImageFigure_0507120304.pdf

Image/Figure Caption: Figure 1. Averaged 18F-FDG SUV images for the mock-exposed group (n=6, left panel) and virus-exposed group (n=6, right panel). All images were registered to the standard template of D99 before averaging. Compared to the baseline (pre-exposure), the most significant changes in the FDG uptake value were found in the early days (DPE 2) in the virus-exposed macaques (right panel). In contrast, there was no noticeable change in FDG uptakes over the course of virus exposure In the mock-exposed group (left panel). The colorbars represent an absolute SUV value. DPE, day post-exposure. SUV, standardized uptake value. Figure 2. Voxel-based statistical comparison of 18F-FDG uptake changes between the virus-exposed and mock-exposed macaques. There were significant group differences in FDG uptake changes over the time course of infection in multiple brain regions (two-way repeated measure, corrected p 37.5), FWE correction, extent threshold of 25 voxels). The left and right panels display the coronal and axial view, respectively. The colorbars represent the F-value. Figure 3. Cluster analysis of temporal changes in 18F-FDG uptake value in the virus-exposed group during virus exposure. A similar temporal change in FDG uptake value was observed, showing an early decrease on Day 2 and partial recovery on Day 6 after virus exposure. DPE, day post-exposure. Error bars represent standard deviations.

First Name: Byeong-Yeul

Last Name: Lee

Email: byeongyeul.lee@nih.gov

Organization: Integrated Research Facility at Fort Detrick, Division of Clinical Research, National Institute of Allergy and Infectious Diseases, National Institutes of Health

Country: United States

ID: GA28

Detection and differentiation of pathophysiological changes in non-alcoholic steatohepatitis and inflammatory liver fibrosis in mice by multiparametric MRI

Ferhan Baskaya, RWTH Aachen University, ferhanbaskaya@gmx.de

Category: Systemic Diseases (Kidney, Liver and Pancreas)

Abstract Body : Purpose Chronic liver diseases (CLDs) have different causes. An early determination of etiology and initiation of the adequate therapy has a strong influence on the course of disease and can prevent liver failure. During CLD progression, various pathophysiological changes occur in the liver. These include changes in tissue structure, inflammation, fibrosis and fat degeneration, as well as alterations in cell functions such as hepatocyte and macrophage function. The goal of this study was to capture these biological processes by multiparametric MRI (mpMRI) and to investigate whether differentiation between inflammatory liver fibrosis and nonalcoholic steatohepatitis (NASH) is possible at early stage of disease. Methods Two animal models of different etiology were examined: In the inflammatory driven fibrosis model, mice were injected twice weekly intraperitoneally with CCl4 for 8 weeks. For the NASH model, mice received a high-fat diet over 24 weeks. Untreated animals were carried along as control group (CG). Longitudinal multiparametric imaging was performed at 7T MRI every 4 weeks. The structural assessment of the liver was examined by fat-selective imaging to determine fat content and by diffusion-weighted imaging to evaluate extracellular matrix composition and cellularity. T1- and T2-relaxometry provided quantitative information about fat content and inflammation-related edema, respectively. Additionally, dynamic contrast enhanced (DCE) MRI was applied to assess accumulation and elimination kinetics of Gadoxetic acid as a measure of hepatocyte function, and DSC-MRI with Ferucarbotran (SPION) was performed to assess macrophage activity. Imaging results were compared to serological and immunohistological data. Results In the NASH model, there was an early increase in fat deposition (wk4: 13±8a.u. vs CG: 4±0.6a.u., p=0.001), which was also reflected by a decreased T1 relaxation time (wk4: 1206±253ms vs CG: 1456±219ms; p=0.015). These changes were not present in the CCl4 model. A restricted diffusion could be observed in both models (wk8: NASH: 0.9 ± 0.3; p=0.0009, CCl4: 0.9 ± 0.1; p=0.042; CG: 1.1 ± 0.05). Inflammatory edema formation was reflected by increased T2 relaxation times in the NASH model (wk8: NASH: 24±3ms vs CG: 19±1ms; p=0.0002). In contrast, in the CCl4 model there was only a trend towards increasing T2 relaxation times. Interestingly, the uptake of Gadoxetic acid (wk4:423±174ms vs CG: 749±204ms; p=0.005) and SPIONs (wk8:1.3±1.6ms vs CG: 3.2±0.6ms; p=0.019) decreased significantly only in the NASH model suggesting either loss of vascularization or the loss of hepatocyte and macrophage function. ALT/AST levels were increased in both disease models. Conclusion This study shows that the mpMRI parameters describing the driving pathophysiological processes in the liver can distinguish NASH and inflammatory driven liver injury and are able to indicate the onset of the disease at an early stage. As all applied methods are clinically applicable our findings might be very helpful to improve early diagnosis of different CLDs, to better select and monitor therapy, and to reduce the number of biopsies. As a next step, we will try to unravel the relationships between the imaging

parameters using radiomics approaches to put our findings into a mechanistic context and to stratify the imaging protocol.

Full Name of Abstract's 1st Author : Ferhan Baskaya

First Name: Ferhan

Last Name: Baskaya

Email: ferhanbaskaya@gmx.de

Organization: RWTH Aachen University

Country: Germany

ID: GA29
Tracking proteins using eGFP-mCherry-nirFP trio

Akira Chiba, University of Miami, akira.chiba@miami.edu

Category: Instrumentation

Abstract Body : Förster resonance energy transfer is a useful technique for demonstrating protein-protein interactions within living animals. However, its usage has been confined to a pair at a time with the most popular FRET reporter being eGFP-mCehrry duo. We introduce eGFP-mCherry-nirFP trio to label proteins A, B and C, where mCherry serves at once as a FRET acceptor to eGFP and a FRET donor to nirFP. Importantly, A-to-B interaction and B-to-C interaction are separable in vivo. More globally, going from a fluorescing duo to trio is not a mere matter of economy but a means to expose the logic underscoring protein interactomics. Introduction: Proximity-based demonstration of protein-protein interactions is possible in their native environment. Technical basis, hence strength, of such an approach is in its sensitive detection of Förster resonance energy transfer between a pair of proteins that are each labeled with fluorescent tags ¾ eGFP as a FRET donor and mCherry as a FRET acceptor. With a 'nearfield' microscope capable of quantifying the fluorescence lifetime of eGFP while it is being fused to protein A, any diminution of proper distancing that may occur between this protein, protein A, and another protein, protein B, is documented. This is true irrespective of either the physical size or the local abundance of individual proteins as long as each is labeled fluorescently. To add a third fluorescent label to this, one could in theory go toward either the blue or the far-red side of this well-established FRET reporter duo. However, the former happens to be largely impractical because imaging any voluminous in vivo system requires a substantial depth of signal penetration, whereas most natural tissues contain a large amount of fluorescent matters of either a known or unknown origin as undesirable auto-fluorescence. We wish to exploit also the fact that FRET detection does not need the acceptor's emission being sensitized, making it hence sufficient to focus on the FRET donor only. We therefore opted for seeking a red-shifted fluorescence excitable through the emission of mCherry, i.e., toward the far-red side of the aforementioned FRET reporter. Rationale: We introduce nirFP as the third fluorophore of the fluorescing trio to label proteins A, B and C. Results: Using the in vivo system previously developed, we examined this eGFP-mCherry-nirFP trio's performance. First, we confirmed that eGFP without any FRET yields 2.56 ns of lifetime, while mCherry without any FRET produces 1.47 ns of lifetime. Second, we demonstrated that the mCherry-to-nirFP pair we introduce here would serve as a good FRET reporter. As expected, fusing eGFP to WASp and mCherry to Cdc42 results in all 99,960 pixels of the eGFP channel to display lifetime of 2.42 ns. And, this same protein-protien interacton causes a reduction of mCherry lifetime when WASp is fused to mCherry and Cdc42 to nirFP. Third, it would be important to establish that eGFP does not FRET with nirFP in vivo. For this reason, we used eGFP and nirFP to label, respectively, WASp and Cdc42, the same pair of proteins that we know have mutualy affinity to each other. These proteins indeed do co-localize in the embryonic brain of Drosophila. Nonetheless, little change in the eGFP's lifetime occurs as indicated by digital readout of the eGFP fluorescence lifetime. Conclusion: Using the eGFP-mCherry-nirFP trio is not a mere matter of economy for

FRET detection but is a means to expose the logic underscoring social networking among proteins within us humans and other animals.

Image/Figure:

https://s3.amazonaws.com/amz.xcdsystem.com/1E8A4501-BB41-A02A-1D3B9882B798BFAA_abstract_File10351/GA29_ImageFigure_0512083434.jpg

Image/Figure Caption: Figure 1. TRIO. (a) Fluorescing trio of complementary colors: green eGFP (G), red mCherry (R), and dark nirFP (B). At nearfield, the physical proximity causes Förster resonance energy transfer from eGFP to mCherry (GR FRET), whereas a similar proximity causes FRET from mCherry to nirFP (RB FRET). (b) Proteins A, B and C are fluorescently labeled and co-expressed in a Drosophila embryo. Co-expression is necessary but not predictive of their interaction. Genotype: elav'-GAL4 / UAS-eGFP::WASP UAS-mCherry::Cdc42 ; UAS-Pak1::nirFP. (c) One-on-one of a protein (gold star) to a genetically encoded fluorophore. Förster distance for the pair (FGR), green eGFP and red mCherry, is 5.2 nm. This miniscule distance is large enough to reach any pair of proteins that are each labeled fluorescently. (d) Concentration blindness in quantification of FRET results from frequency domain fluorescence lifetime imaging. Millions of flickering low-energy photons (white wave at left) are Fourier transformed into the exponential decay curve with a single fluorescence lifetime t (green dot at right). (e) Converting this to a size-free association probability (magenta arrow) assumes the singularity of affinity among interacting protein pairs, e.g., eGFP without FRET has 2.56 nm fluorescence lifetime, but with FRET it becomes as short as 1.00 nm or less. However, regardless of whether FRET occurs or not, the same fluorescence lifetime (green open dot) is obtained from the phase shift (f) and the modulation drop (M) of these flickering photons. The estimated lifetime t non-linearly decreases from infinity to zero according to the relationship of M*cos(f) and M*sin(f). (f) FRET from-eGFP-to-mCherry (magenta arrows, i.e., a reduction of lifetime) exposes the affinity between proteins A (WASp) and B (Cdc42). (g) Similarly, FRET from-mCherry-to-nirFP (magenta arrows, i.e., a reduction of lifetime) exposes the affinity between the same proteins A (WASp) and B (Cdc42). (h) However, no FRET occurs between eGFP-labeled protein A (WASp) and nirFP-labeled protein B (Cdc42). (i) Trio reveals the logic underscoring synergy or competition among interacting proteins. Triangulation of three proteins A, B and C from the spacetime 1 to (top) the spacetime 2 (bottom) can support protein interactomics that drives the development of a multicellular animal.

First Name: Akira

Last Name: Chiba

Email: akira.chiba@miami.edu

Organization: University of Miami

Country: United States

ID: GA30
HER2-targeted PET imaging to track endocytosis modulation as a novel pharmacologic approach to boost antibody efficacy

Patricia Ribeiro Pereira, WUSTL, ribeiropereirap@wustl.edu

Category: Oncology

Abstract Body : Objectives: Resistance mechanisms and heterogeneity in HER2-positive gastric cancers (GC) limit trastuzumab benefit in 32% of patients, and other targeted therapies, including the trastuzumab-drug conjugate TDM1, failed in clinical trials1. The cellular dynamics of HER2 could justify the failed studies in HER2+ GC. Indeed, endocytosis decreases HER2s available at the cell membrane for antibody-tumor binding. Receptor internalization also reduces natural killer (NK) cell-mediated antibody-dependent cellular cytotoxicity (ADCC)2, which is a major mechanism of clinical efficacy of IgG1 antibodies. We recently identified that caveolin-1 (CAV1), the major structural protein of caveolae-mediated endocytosis, negatively correlates with membrane HER2 and affects trastuzumab-tumor binding as visualized with immunoPET3. This study aimed to validate CAV1 as a complementary predictive biomarker to detect HER2 expression in the clinic and prognostic biomarker of targeted therapeutic response in GC. To achieve this, we determined CAV1 levels and HER2 surface availability by tumor-targeted molecular imaging. We then stratified the patient survival during trastuzumab therapy in CAV1-high and CAV1-low GC. Preclinical models of CAV1 modulation included a Tet-on inducible CAV1 knockdown or treatment studies with FDA-approved cholesterol-depleting drugs, statins. Lastly, preclinical and retrospective data validated the potential of acute CAV1 depletion combined with antibody therapies in GC. Methods: Retrospective studies: Medical record numbers of GC patients were analyzed from trastuzumab trials. Tumors' somatic alterations were determined by MSK-IMPACT data. HER2-positivity: IHC 2+/3+, HER2:CEP17 FISH ratio ≥ 2.0. CAV1 IHC: 0/1+ CAV1-low and 2+/3+ CAV1-high. Radiolabeling: Trastuzumab or TDM1 coupled with the DFO chelator were labeled with 89Zr. Imaging: PET/CT images and ex vivo biodistribution were acquired between 4 to 72 h post-injection of [89Zr]Zr-DFO-antibody (6.66–7.4 Mbq, 45–50 μg protein, >99% RCP). Animals: PDXs were s.c. implanted in NSG mice and grouped as CAV1-low versus CAV1-high. CAV1 knockdown mice were prepared by implanting NCIN87 Tet-On xenografts in athymic nude mice. For ADCC experiments, freshly isolated human NK cells were administered to NSG mice bearing GC xenografts2. Treatments: Mice received TDM1 (5 mg/kg, i.v.) or trastuzumab (5 mg/kg, i.p.) weekly. Lovastatin (4.15 mg/kg of mice), a cholesterol-depleting drug known to modulate CAV13, was orally administered 12 h prior and at the same time as the antibody. Results: Distinct signaling profiles were observed in CAV1-high versus CAV1-low HER2+ GC (Suppl. Fig1a). In retrospective analyses, the CAV1-low profile corresponds to tumors with homogeneous surface HER2s (Fig1A) and predicts favorable patient response to trastuzumab (n=51 patients, $p < 1 \times 10\text{-}4$, Fig1B). At 48 h post-injection of 89Zr-labeled TDM1, CAV1-low PDXs had uptakes ranging from 22.8±6.5 to 32.5±5.7 %ID/g, while uptakes in CAV1-high PDXs were from 9.7±3.6 to 13.3±3.0 %ID/g (Fig1C). CAV1 depletion induced by synthetic oligonucleotides or statins enhances TDM1 binding to HER2+/CAV1HIGH NCIN87 xenografts (Suppl. Fig1b, Fig1D).

Although TDM1 accumulation in CAV1-low PDXs was similar in control and lovastatin cohorts (Fig1C), TDM1-tumor accumulation was 1.8-fold and 1.4-fold higher in CAV1-high PDX #1 (CAV1, IHC 3+) and PDX #2 (CAV1, IHC 2+), respectively. Lovastatin enhances antibody efficacy and improved mice survival in a CAV1-high PDX (TP53 and KRAS mutant with HER2 IHC 3+) obtained from a patient who did not respond to trastuzumab therapy (Fig1E). ADCC experiments indicate that lovastatin enhances antibody efficacy, which depends on cytokine-mediated NK expansion and antibody's Fc domain (Suppl. Fig1c). The preclinical findings were further validated in the retrospective analyses showing that statin users treated with trastuzumab had higher survival than non-statin users ($p = 0.02$; Suppl. Fig1d). Conclusions: This study identifies how tumoral CAV1 expression and statin use relate to GC response in HER2-targeted imaging and therapeutic approaches. In addition to show the preclinical synergy of CAV1 depletion with anti-HER2 antibodies, we demonstrate that statin users had better clinical responses to antibody-based therapies in HER2+ heterogeneous GC.

References: 1. Oh DY and Bang YJ, HER2-targeted therapies - a role beyond breast cancer. Nat Rev Clin Oncol. 2020;17(1):33-48. 2. Chew HY, De Lima PO, Cruz JLG, et al. Endocytosis inhibition in humans to improve responses to ADCC-mediating antibodies. Cell. 2020;180(5): 895-914.e27. 3. Pereira PMR, Sharma SK, Carter LM, et al. Caveolin-1 mediates cellular distribution of HER2 and affects trastuzumab binding and therapeutic efficacy. Nat Commun. 2018;9(1):5137.

Image/Figure:

https://s3.amazonaws.com/amz.xcdsystem.com/1E8A4501-BB41-A02A-1D3B9882B798BFAA_abstract_File10351/GA30_ImageFigure_0507061312.png

Image/Figure Caption: Figure 1. (A) CAV1 IHC, confocal images, and quantification of immunofluorescence staining of HER2 (green color) and CAV1 (red color) in human HER2+GC. CAV1-high: CAV1 2+/3+, Patients #1, #2. CAV1-low: CAV1 1+/0, Patients #14, #3, #4, #5. The graphs plot protein intensity per unit area, calculated by quantifying IF images (mean ± S.E.M, n = 3). Scale bar, 50 μm. (B). (F) Kaplan-Meier analyses of CAV1 expression and GC disease outcome in patients treated with trastuzumab. Patients with HER2+/CAV1HIGH(blue color, n = 15 patients) phenotype have a worse survival than HER2+/CAV1LOW(red, n = 36 patients). Log rank; p< 1 □10-4. (C) [89Zr]Zr-DFO-TDM1 uptake in HER2+GC PDXs containing varying levels of CAV1 and administered PBS or statin. Points, n = 5 mice per group, mean ± S.E.M, **P< 0.01 based on a Student's t-test. %ID/g, percentage of injected dose per gram. (D) Coronal PET images at 4, 8, 24, and 48 h p.i. of [89Zr]Zr-DFO-TDM1 in athymic nude mice bearing s.c. NCIN87 tumors. Lovastatin (8.3 mg/kg of mice) was orally administrated 12 h prior and at the same time as the tail vein injection of 89Zr-labeled TDM1. Bars, n = 5 mice per group, mean ± S.E.M. *P< 0.05,**P< 0.01, ***P< 0.001 based on a Student's t-test. (E) Superior in vivo therapeutic efficacy of TDM1 combined with lovastatin when compared with TDM1 alone in a GC PDX with heterogeneous membrane HER2.

Full Name of Abstract's 1st Author : Patricia Manuela Ribeiro Pereira

First Name: Patricia

Last Name: Ribeiro Pereira

Email: ribeiropereirap@wustl.edu

Organization: WUSTL

Country: United States

ID: GA31

Synthesis and preclinical characterization of [11C]ROCK201 for PET imaging of the rho-associated protein kinase in brain

Chao Zheng, Yale School of Medicine - New Haven, CT, c.zheng@yale.edu

---

Category: Neuroscience

Abstract Body : Objectives: Rho-associated protein kinase (ROCK) and activation of the rho/rho-kinase pathway has been implicated in various central nervous system disorders 1. Development of a PET imaging agent for ROCK in the brain will facilitate the in vivo investigation of this protein kinase in diseases. Here we report the successful development and evaluation of the first ROCK specific PET imaging ligand, [11C]ROCK201, in rodents and nonhuman primates (NHPs). Methods: ROCK201 was reported as a selective ROCK inhibitor with IC50 values of 17 nM, 2 nM and 240 nM for ROCK1, ROCK2 and protein kinase A (PKA), respectively 2, and no appreciable affinity for more than 40 CNS targets. [11C]ROCK201 was synthesized via reaction of its phenol precursor with [11C]MeOTf or [11C]MeI. PET imaging studies in both rats and NHPs were conducted on the Focus-220 scanner, with arterial blood drawn for metabolite analysis and construction of plasma input function during the NHP scans. Self-blocking scans were performed at 10 min after the injection of 3.3 mg/kg (for rats) or 0.05 mg/kg (for NHP) of unlabeled ROCK201. Region of interests (ROIs) were extracted from brain atlas and regional time-activity curves (TACs) were obtained by applying template ROIs to the PET images. For NHP PET, regional brain TACs were fitted with one-tissue compartment (1TC) model to obtain volume of distribution (VT). Binding potential (BPND) was calculated using the nondisplaceable volume of distribution (VND) obtained from the blocking study, where BPND = (VT/VND)-1. Results: [11C]ROCK201(Fig. 1a) was prepared in >99.9% radiochemical purity and molar activity of 256 ± 103 GBq/μmol at the end of synthesis (n=8). The measured LogP value of [11C]ROCK201 was 2.9. Uptake of [11C]ROCK201 was observed throughout the rat brain, with peak SUV of 2.5. Higher levels of uptake in the striatum, thalamus, and hippocampus, and lower in the brain stem (Fig. 1b). In the self-blocking studies reduced uptake was observed in the brain of both rats and monkey, confirming specific binding of [11C]ROCK201 (Fig. 1b-1d). In NHPs the total radioactivity in the plasma showed a sharp increase within three minutes, followed by fast distribution and clearance phases. The tracer showed a relatively fast metabolism rate, with parent tracer fraction of 27% at 30 min after injection. High quality brain PET images were generated with [11C]ROCK201 in rhesus monkey (Fig. 1c). The tracer entered the brain quickly and reached peak uptake levels within 10 min p.i., with higher tracer uptake in the amygdala, putamen, cerebellum, frontal cortex (peak SUV ≥5), and lowest uptake in the white matter region, i.e., centrum semiovale (peak SUV ≈ 2) (Fig. 1d). TACs were well fitted with the 1TC model to derive regional VT values, which ranged from 5.7 to 12.4 mL/cm3. Based on the Lassen plot, ROCK occupancy was calculated to be 43% with VND being 2.62 mL/cm3. Regional BPND values calculated using VND as reference ranged to be 1.5 (brain stem) to 3.8 (occipital), indicating high level of specific binding signals. Conclusions: We have accomplished the radiosynthesis of the first ROCK radiotracer [11C]ROCK201 and evaluated its imaging characteristics in rat and rhesus monkey brains.

[11C]ROCK201 showed fast brain kinetics and good specific binding signals in rats and NHP, which allowed reliable estimation of kinetic and binding parameters using 1TC. Further validation studies are ongoing to confirm the correlation between the PET signal and ROCK protein levels in different brain regions.

References: 1. Koch JC, Tatenhorst L, Roser A-E, Saal K-A, Tönges L, Lingor P. ROCK inhibition in models of neurodegeneration and its potential for clinical translation. Pharmacology & Therapeutics 2018; 189: 1-21. 2. Hobson AD, Judge RA, Aguirre AL, et al. Identification of Selective Dual ROCK1 and ROCK2 Inhibitors Using Structure-Based Drug Design. Journal of Medicinal Chemistry 2018; 61(24): 11074-100.

Image/Figure:

https://s3.amazonaws.com/amz.xcdsystem.com/1E8A4501-BB41-A02A-1D3B9882B798BFAA_abstract_File10351/GA31_ImageFigure_0513062247.jpg

Image/Figure Caption: Figure 1: (a) Structure of [11C]ROCK201; (b) Whole brain TACs of [11C]ROCK201 in Sprague-Dawley under baseline and self-blocking (ROCK201, 3.33 mg/kg, i.v.) conditions; (c) Summed SUV PET images of [11C]ROCK201 in the brain of a rhesus monkey from 15 to 30 min imaging window under baseline and blocking (ROCK201,0.05 mg/kg, i.v.) conditions; (d) TACs from selected regions in the rhesus monkey brain under baseline and self-blocking (ROCK201, 0.05 mg/kg, i.v.) conditions.

Full Name of Abstract's 1st Author : Chao Zheng

First Name: Chao

Last Name: Zheng

Email: c.zheng@yale.edu

Organization: Yale School of Medicine - New Haven, CT

Country: United States

ID: GA32
3-D H-scan ultrasound imaging of cancer cell death during response to drug treatment

Kenneth Hoyt, University of Texas at Dallas, kenneth.hoyt@utdallas.edu

---

Category: Instrumentation

Abstract Body : Introduction: The use of noninvasive ultrasound (US) for in vivo tumor tissue characterization is an exciting prospect for anticancer treatment response monitoring. A new technology termed H-scan US imaging has been developed and links differences in the raw backscattered US signals to various-sized tissue structures. The purpose of this research was to develop a 3-dimensional (3-D) H-scan US imaging system and method for tissue characterization in volume space using a preclinical animal model of breast cancer. Further, the proposed H-scan US imaging technique has been validated using matched histological data. Statement of Contribution/Methods: Preliminary studies were conducted using female nude athymic mice (N = 15, Charles River Laboratories) implanted in the mammary fat pad with 1 million breast cancer cells (MDA-MB-231, ATCC). Once tumors reached about 1 cm in size, animals were sorted into three groups so that mean tumor size in each was comparable (N = 5 per group). Animals were then US imaged at baseline and before receiving intraperitoneal injections, namely: (1) 0.3 mg sterile saline (control), (2) 0.2 mg of agnostic TRA-8 monoclonal antibody to human death receptor 5 (DR5) + 0.1 mg sterile saline, and (3) 0.1 mg TRA-8 + 0.2 mg paclitaxel. Image data was acquired using a programmable US scanner (Vantage 256, Verasonics Inc) equipped with a volumetric imaging transducer (4DL7, Vermon) at baseline and again every 24 h for 3 d. To generate the H-scan US images, a set of Gaussian-weighted Hermite filters were convolved with the radiofrequency (RF) data to measure the relative strength of the received signals. Finally, the lower frequency backscattered signals were assigned to a red (R) channel and the higher frequency components to a blue (B) channel. The unfiltered original RF signal was assigned to the green (G) channel to complete the RGB colormap and 3-D H-scan US image display. After US imaging on day 3, animals were humanely euthanized and tumors excised for histological processing using immunofluorescent staining for DAPI. Result/Discussion: The in vivo results show that 3-D H-scan US imaging is considerably more sensitive to tumor changes after neoadjuvant treatment as compared to traditional B-scan US. While there was no difference at baseline ($p = 0.52$), repeat H-scan US results from treated tumors exhibited percentage decreases in percentage of image intensity (-19.8 ± 8.2 %, and -62.2 ± 11.7% for the TRA-8 and TRA-8 + paclitaxel treated animals at day 3, respectively; p 0.5, p Conclusions: 3-D H-scan US imaging is a promising technique that allows visualization of the heterogenous tumor tissue microenvironment and allows in vivo detection of an early treatment response within days of chemotherapy administration.

Image/Figure:

https://s3.amazonaws.com/amz.xcdsystem.com/1E8A4501-BB41-A02A-1D3B9882B798BFAA_abstract_File10351/GA32_ImageFigure_0510045733.png

Image/Figure Caption: Fig. 1. Segmented H-scan US volume reconstructions acquired at baseline (day 0), and again at days 1, 2 and 3 after systemic administration of a sham (control) or anticancer drug, namely, TRA-8 or TRA-8 + paclitaxel. Note that the blue channel in the H-scan US images becomes more dominant for the treated tumors, which suggests a decrease in US scatterer size like cancer cell nuclear condensation during apoptosis.

First Name: Kenneth

Last Name: Hoyt

Email: kenneth.hoyt@utdallas.edu

Organization: University of Texas at Dallas

Country: United States

ID: GA33
3-D focused ultrasound simulated drug delivery and validation using fluorescent imaging in a preclinical model of breast cancer

Kenneth Hoyt, University of Texas at Dallas, kenneth.hoyt@utdallas.edu

---

Category: Instrumentation

Abstract Body : Introduction: Near-infrared (NIR) fluorescent dyes have recently been utilized as a potential tool for tumor imaging and therapies. IR-780 dye, a NIR dye, has been used extensively due to its excellent optical properties for in vivo imaging and can be detected using fluorescent imaging. In this regard, IR-780 dye was used as a surrogate for a chemotherapeutic drug to evaluate the potential of a newly developed ultrasound (US) imaging-guided FUS (USgFUS) system and method for enhancing drug delivery in 3-dimensional (3-D) tumor space. Statement of Contribution/Methods: 3-D USgFUS therapy functionality was implemented on a programmable US research system (Vantage 256, Verasonics Inc) equipped with a dual transducer configuration for interleaved US imaging and 3-D therapy. The imaging and therapeutic transducers are both 128 element arrays with center frequencies of 3.5 and 2.0 MHz, respectively. The latter is a spherical phased array that enables focused beam steering in 3-D space. This study compared a new 3-D multi-focus treatment protocol to our previously developed 2-D US therapeutic approach [1]. The 3-D therapy consisted of overlapping focal zones distributed over an entire user-defined volume space whereas the 2-D treatment had the same distributed focal zones but only within a single plane. Using female athymic nude mice implanted with MDA-MB-231 breast cancer cells (N = 4), preliminary US therapy studies were conducted with a mechanical index of 0.5, pulse repetition frequency of 10 Hz, and duty cycle of 10%. Therapy was performed in mice immediately after a 100 μL bolus injection of microbubbles (DEFINITY®, Lantheus Medical Imaging, Inc. MA) and IR-780 dye. In vivo optical imaging (Pearl Trilogy, LI-COR Biotechnology) was performed at 0, 24, and 48 h. Following the 48 h timepoint, tumors were excised and additional ex vivo optical imaging (Odyssey CLx, LI-COR Biotechnology) was performed. Results/Discussion: While no differences existed at baseline, 3-D USgFUS treatment significantly increased IR dye extravasation into the tumor space at 24 (238.1%) and 48 h (202.4%) as compared to the 2-D US treatment protocol ($p = 0.03$). Ex vivo optical images revealed a similar trend with 3-D US treatment having a higher fluorescent signal per area than the 2-D approach. Overall, preliminary results suggest that 3-D USgFUS-mediated drug delivery is an exciting prospect for treatment of the entire cancer burden.

References: [1] L. Basavarajappa, G. Rijal and K. Hoyt, "Multifocused ultrasound therapy for controlled microvascular permeabilization and improved drug delivery," in IEEE Transactions on Ultrasonics, Ferroelectrics, and Frequency Control, vol. 68, no. 4, pp. 961-968, 2021.

Image/Figure:

https://s3.amazonaws.com/amz.xcdsystem.com/1E8A4501-BB41-A02A-1D3B9882B798BFAA_abstract_File10351/GA33_ImageFigure_0510050310.png

Image/Figure Caption: Fig. 1. Optical images comparing the 2-D and 3-D USgFUS-mediated drug delivery results at 0, 24, and 48 h after receiving treatment (left). A summary of optical imaging results is shown and highlights the advantage of using the 3-D US treatment protocol (right).

First Name: Kenneth

Last Name: Hoyt

Email: kenneth.hoyt@utdallas.edu

Organization: University of Texas at Dallas

Country: United States

ID: GA35
A modular approach toward producing nanotherapeutics targeting the innate immune system

Abraham Teunissen, Icahn school of medicine at mount sinai, bramteunissen@gmail.com

---

Category: Immunology: Inflammation & Infection

Abstract Body : A modular approach toward producing nanotherapeutics targeting the innate immune system Immunotherapies controlling the adaptive immune system are firmly established, but regulating the innate immune system remains much less explored. The intrinsic interactions between nanoparticles and phagocytic myeloid cells make these materials especially suited for engaging the innate immune system. However, developing nanotherapeutics is an elaborate process that typically needs to be repeated for each specific drug. Here, we demonstrate a modular approach that facilitates efficiently incorporating a broad variety of drugs in a nanobiologic delivery platform. Using a microfluidic formulation strategy, we produced 4 different sizes of apolipoprotein A1–based nanobiologics (20, 35, 65, 120 nm, only the 35 variant is shown; Fig. 1A). Radiolabeling these platforms with 89Zr facilitated monitoring their biodistribution and pharmacokinetics by a combination of PET imaging and ex vivo gamma counting (Fig. B and C). Flow cytometry was used to reveal their high myeloid cell uptake. Based on these results, we selected the 35 nm-sized nanocarrier for therapeutic studies. Subsequently, rapamycin and three small-molecule inhibitors were derivatized with lipophilic promoieties, ensuring their seamless incorporation and efficient retention in the lipid-based nanobiologics (only the rapamycin prodrug is shown; Fig. D). This lipophilic prodrug strategy facilitates incorporating a broad variety of drugs without modifying the nanocarrier, thereby establishing a modular approach for developing nanotherapeutics targeting the innate immune system. To test the rapamycin prodrug-loaded nanobiologics (mTORi-NB) we performed biodistribution, toxicity, and efficacy studies in a mouse model for heart allograft transplantation, revealing significant prolongation of graft survival (Fig 1E). Fig. 1 (A) Composition and morphology of the 35 nm-sized nanobiologic, formulated by microfluidic mixing. (B and C) C57BL/6 mice were intravenously injected with an 89Zr-labeled nanobiologic. (B) Representative maximum intensity projections of PET/CT scans performed 24 hours after injection. (C) Nanobiologic's blood pharmacokinetics was fitted with a biexponential decay function; n = 5. (D) Molecular structure of rapamycin and its lipophilic prodrug. (E) Allograft survival in mice treated with mTORi-NB, unloaded nanobiologics, or PBS, directly before as well as 2 and 5 days after transplantation (5 mg rapamycin/kg). A log-rank test was used. ****PTo pave the way for clinical translation, we also studied mTORi-NB in nonhuman primates. 89Zr-labeled mTORi-NB were intravenously administered and their distribution examined using a fully integrated three-dimensional PET/MRI protocol. Dynamic scanning revealed that within the first 20 min after administration, mTORi-NB accumulate in the spleen, liver, kidney, and bone marrow (Fig. 2A and 2B). Static PET/MRI performed 2 and 48 hours after injection allowed quantifying mTORi-NB's biodistribution. We found that mTORi-NB have a blood half-life of ~1 hour and mainly accumulate in the liver, spleen, kidney, and bone marrow 48 hours post injection (Fig. 2C-E). Blood analyses showed no signs of liver or kidney

damage, corroborating this immunotherapy's biocompatibility (Fig. 2F). This study has been recently published in Science Advances. Fig. 2. Two nonhuman primates weighing 5.99 and 10.13 kg were injected with 89Zr-labeled mTORi-NB. (A) Representative 3D-rendered images acquired in the first hour after injection using dynamic PET/MR. (B) Quantification of nanobiologic PET signal in liver, spleen, kidneys, and bone marrow. (C) Representative whole-body PET/MR images, 2 and 48 hours after nanobiologic injection. (D) PET-based quantification of nanobiologic uptake in various organs at 48 hours after injection. (E) Blood pharmacokinetics measured by ex vivo gamma counting of blood samples and the associated weighted blood half-life obtained by fitting the data with a biexponential decay function. (F) Aspartate aminotransferase (AST), creatinine, and blood urea nitrogen (BUN) levels before (Pre) and 48 hours after (Post) injection. White areas represent normal ranges for male cynomolgus monkeys. SUV, standardized uptake value.

First Name: Abraham

Last Name: Teunissen

Email: bramteunissen@gmail.com

Organization: Icahn school of medicine at mount sinai

Country: United States

ID: GA36

PRECLINICAL EVALUATION OF [11C]MPC-6827, A NOVEL PET TRACER FOR ALZHEIMER'S DISEASE IMAGING

Ramesh Neelamegam, UT Health San Antonio, neelamegam@uthscsa.edu

---

Category: Neuroscience

Abstract Body : Objective: Clinical trials for Alzheimer's disease (AD) lack a valid biomarker that can provide a surrogate endpoint. The existing positron emission tomography (PET) tracers used in AD have limited utility in prognosis and in revealing reliable clinicopathologic correlations of disease. Therefore, identifying novel biomarkers for neurodegeneration through PET imaging is a top priority in biomedical research. However, there is no such PET tracer available at present. We proposed to target microtubules (MTs) as an imaging target for neurodegeneration owing to established clinical studies that support the implication of altered regulation of MTs in a large spectrum of neurodegenerative disorders (NDs), including AD. Therefore, targeting brain MTs may be advantageous, as cumulative loss of MTs is the final common pathway for a variety of biochemical pathologies leading to neurodegeneration. At present, the blood brain barrier-penetrating PET tracers, [11C]MPC-6827, which we have developed is the only PET tracer available for in vivo imaging of MTs in brain.1,2 Herein, we present the head-to-head comparison of [11C]MPC-6827 with Aβ PET tracer [11C]PiB in Aβ over expressing J20 mice and tau PET tracer [18F]MK6240 in hTau mice model of AD expressing human tau isoforms and age matched controls. Methods: [11C]MPC-6827, [11C]PiB and [18F]MK62403,4 were synthesized, purified and formulated using GE Tracerlab modules. microPET imaging were performed in J20 and hTau mice and corresponding littermates (n=4 mice per group) using a Siemens Focus 220 microPET scanner for 30-minute dynamic acquisitions with the above mentioned three PET tracers. Image analyses were performed with vendor-provided software on reconstructed data. Results: PET analyses showed reduced whole brain (WB), hippocampus (HC) and prefrontal cortex (PFC) uptake of [11C]MPC-6827 in J20 and hTau mice groups, whereas, [11C]PiB and [18F]MK6240 modest higher binding in corresponding mice models than controls. [11C]MPC-6827 has higher standardized uptake value and effect size compared to [11C]PiB and [18F]MK6240 binding. Conclusion: Our studies show that binding of the MTs PET ligand, [11C]MPC-6827 is significantly reduced in WB, HC and PFC in J20 and hTau mice compared to control groups and is inversely correlated with [11C]PiB and [18F]MK6240 binding. Our pilot data indicate a likelihood of a higher binding difference of [11C] MPC-6827 than Aβ and tau tracers in human AD compared to control subjects. Therefore [11C] MPC-6827 can be used as a potential PET tracer for human brain imaging of AD and other NDs. Details of the preclinical evaluation of the radiotracers will be presented.
Acknowledgements: We acknowledge Center for Biomedical Neuroscience (CBN) 2020-21, UT Health San Antonio, Texas for generously providing funding for this research. We also thank Glenn Fulbright for isotope production and Katie Strychalski for technical support.

References: 1. Kumar JSD et al. J. Med. Chem., 2018, 61(5), 2118. 2. Kumar JSD et al. Bioorg. Med. Chem. Lett., 2020, 29(10), 126785. 3. Aguero C et al. Acta Neuropathol. Commun., 2019, 7(1), 37. 4. Coliier TL et al. J. Labelled Comp. Radiopharm., 2017, 60(5), 263.

Image/Figure: https://s3.amazonaws.com/amz.xcdsystem.com/1E8A4501-BB41-A02A-1D3B9882B798BFAA_abstract_File10351/GA36_ImageFigure_0509072718.pdf

Image/Figure Caption: Table 1. SUV comparison of [11C]MPC-6827, [11C]PiB and [18F]MK6240 in J20, hTau and control mice (n=4 per group).

First Name: Ramesh

Last Name: Neelamegam

Email: neelamegam@uthscsa.edu

Organization: UT Health San Antonio

Country: United States

ID: GA37
The additional value of PET-guided and navigated biopsies through analysis of dexterity and performance

Imke Boekestijn, Leiden University Medical Center, i.boekestijn@lumc.nl

---

Category: Instrumentation

Abstract Body : Introduction: In routine care at interventional radiology (IR), needle-based interventions (e.g. minimal-invasive biopsy and ablation) for soft-tissue organs are commonly performed under guidance of morphological imaging (US, CT, MRI). Unfortunately, these imaging technologies are only able to identify disease at an advanced stage, where information on a molecular level is limited. Here nuclear medicine, and in particular PET imaging, can create benefit by improving accuracy and diagnostic yield through targeting needles to the most metabolic-active sections of a lesion. The direct translation of such PET images to the patient in the intervention room can be complex. We studied in a phantom setup if PET-guidance and computer-assisted navigation strategies help guide percutaneous needle placement by both experts and novices. Methods: Using a custom-build abdominal biopsy phantom, we performed PET/CT-guided needle placements under US guidance. Needle placements were monitored using a fiducial-based near-infrared optical tracking system, able to record the trajectories of the intervention instruments used by every operator. To see how computer-assisted navigation impacts different user groups, we studied the effect on dexterity and performance of the experts (i.e. interventional radiologists) vs. novices. Needle trajectories were quantified for various features, including duration time, total pathlength, needle retractions and corrections, speed, acceleration and straightness index. Results: In all cases it was possible to record the traveled paths of both the biopsy needle and ultrasound probe . The paths travelled, either with or without navigation could be visualized in 4D (i.e., x, y, and z over time, with a time resolution of 20 Hz). Computer-assisted quantification of movement features indicated that the features, total pathlength, needle retractions and corrections, speed, acceleration and straightness index had most impact leading towards a successful biopsy. Comparing the groups based on experience indicated that computer-assisted navigation was most beneficial for novices. Conclusion: Using dedicated movement analysis on the dexterity and performance of biopsy procedures, we were able to quantify value of PET-navigated biopsies over using ultrasound only. These preclinical findings underline the potential that PET/CT guided, and possibly navigated, biopsies could provide. Something that needs to be further validated in clinical follow-up studies.

First Name: Imke

Last Name: Boekestijn

Email: i.boekestijn@lumc.nl

Organization: Leiden University Medical Center

Country: Netherlands

ID: GA38

In vivo study in healthy balb/c mice of the excretion of a macrocyclic Gadolinium Based Contrast Agent and its specific retention in bladder, spleen and bones.

Chiara Furlan, University of Turin, chiara.furlan@unito.it

Category: New Chemistry, Materials & Probes

Abstract Body : Gadolinium based contrast agents (GBCAs) are commonly employed at clinical settings to add relevant information to the anatomical resolution of the magnetic resonance images1. In recent years, concern on the use of GBCAs has raised as it has been found that tiny amount of Gd can be retained in brain and other tissues, also in patients without renal dysfunctions2–5. Whereas much work has been carried out to investigate the issue of Gd-retention in the brain, the aim of this work is to bring the attention to tissues less considered in the past such as bladder, spleen and bones. In order to evaluate the amount of Gd retained in the tissues, mice were administered with 20 doses of 0.6 mmol Gadoteridol/kg over a period of 4 weeks. The sacrifice time was set at four different time points (4, 15, 30 and 90 days) after the last injection. After sacrifice, urine, tissues and organs were collected. One tibia was weighted, mineralized and Gd quantified through ICP-MS. The other tibia was handled in order to separate bone matrix and bone marrow and Gd quantified separately. Spleen was processed as well, to measure the amount of Gd in the splenocytes and in its fibrous part. In bladder, beside ICP-MS total Gd quantification, UPLC-MS was performed to study the chemical form of the retained metal. Urine Gd concentration rapidly decreased over time to suggest that most of the administered GBCA is correctly excreted through the renal route. The quantification of Gd in the bladder showed the highest amount of metal retained, among all the investigated organs, at the shortest times (Figure 1A). Although the amount of retained Gd decresed over time, 3 months after injections, bladder resulted to be a major accumulation organ together with spleen and bones. In addition, the amount of Gd found in the spleen decreased in time, and, quite surprisingly, the metal found in the fibrous part was higher than that found in the splenocytes (Figure 1B). The quantitative analysis of the whole tibia showed a constant quantity of metal retained until 90 days after the last administration. The separate analysis of bone marrow and bone matrix, revealed that most of Gd is retained constantly by the bone matrix, while a very low, and time decreasing, amount of metal was found in the bone marrow (Figure 1C). The outcomes point out that bladder, which was never investigated for Gd retention in the past, could be an extremely specific organ for the metal retention. This result is likely related to the passage and stasis of urines, which contain a very large amount of GBCA starting from the hours immediately after the administration. In the spleen, the most of Gd is found in its fibrous part: likely due to the characteristic and unique composition of its extracellular matrix6, Gd could be stuck, after an initial washout. Indeed, after 90 days, the quantity of metal remains almost at the same level in both whole spleen and its fibrous part. The analysis on bones showed a very quick deposition of Gd: as a matter of fact, the excretion rate is very low, in particular in the bone matrix, where most of Gd is retained.

References: 1. Yousaf T, Dervenoulas G, Politis M. Advances in MRI Methodology. In: International Review of Neurobiology. Vol 141. Academic Press Inc.; 2018:31-76. doi:10.1016/bs.irn.2018.08.008 2. Errante Y, Cirimele V, Mallio CA, Di Lazzaro V, Zobel BB, Quattrocchi CC. Progressive increase of T1 signal intensity of the dentate nucleus on unenhanced magnetic resonance images is associated with cumulative doses of intravenously administered gadodiamide in patients with normal renal function, suggesting dechelation. Invest Radiol. 2014;49(10):685-690. doi:10.1097/RLI.0000000000000072 3. Kanda T, Ishii K, Kawaguchi H, Kitajima K, Takenaka D. High signal intensity in the dentate nucleus and globus pallidus on unenhanced T1-weighted MR images: Relationship with increasing cumulative dose of a gadoliniumbased contrast material. Radiology. 2014;270(3):834-841. doi:10.1148/radiol.13131669 4. Schlemm L, Chien C, Bellmann-Strobl J, et al. Gadopentetate but not gadobutrol accumulates in the dentate nucleus of multiple sclerosis patients. Mult Scler. 2017;23(7):963-972. doi:10.1177/1352458516670738 5. Di Gregorio E, Ferrauto G, Furlan C, et al. The issue of gadolinium retained in tissues: insights on the role of metal complex stability by comparing metal uptake in murine tissues upon the concomitant administration of lanthanum- and gadolinium-diethylentriamminopentaacetate. Invest Radiol. 2018;53:167-172. 6. Lokmic Z, Lämmermann T, Sixt M, Cardell S, Hallmann R, Sorokin L. The extracellular matrix of the spleen as a potential organizer of immune cell compartments. Semin Immunol. 2008;20(1):4-13. doi:10.1016/j.smim.2007.12.009

Image/Figure:

https://s3.amazonaws.com/amz.xcdsystem.com/1E8A4501-BB41-A02A-1D3B9882B798BFAA_abstract_File10351/GA38_ImageFigure_0510033505.jpg

Image/Figure Caption: Amount of Gd 4, 15, 30, and 90 days after the last administration of Gadoteridol (20 doses of 0.6 mmol Gadoteridol/kg over a period of 4 weeks) in: A) Bladder and Urine; B) Spleen and its fibrous part; C) Bone and bone matrix.

Full Name of Abstract's 1st Author : Chiara Furlan

First Name: Chiara

Last Name: Furlan

Email: chiara.furlan@unito.it

Organization: University of Turin

Country: Italy

ID: GA39
Adapting ADEPT: towards smart MRI contrast agents

Ilse Welleman, Universitair Medisch Centrum Groningen, I.M.welleman@UMCG.nl

---

Category: New Chemistry, Materials & Probes

Abstract Body : Introduction: While MRI is a powerful, safe, whole-body imaging technique, it suffers from low sensitivity. This hinders the imaging of molecular targets, such as enzyme/receptor (over)expression visualization of physiological processes in the human body.[1] Contrast agents (CAs) have been developed to improve the sensitivity of MRI, yet a considerable concentration of CA is still required for contrast, and this concentration is much higher than that of imaging targets. The goal of this project is to use establish a general, molecular platform for the local, biocatalytic and biorthogonal amplification of the MRI signal, by adapting the ADEPT prodrug activation strategy. Antigen-Directed Enzyme Prodrug Therapy (ADEPT) is a drug delivery modality, which has been developed for cancer treatment with the aim to activate the cytotoxic payload only at the tumor site to prevent damage to healthy tissue (figure 1.A).[2] In ADEPT, the activation if achieved through in a reaction catalyzed by an enzyme that is not naturally present in the human body, and that is directed to the disease site e.g. through a conjugation with a specific antibody. Carboxypeptidase G2 (CPG2) from Pseudomonas sp. (strain RS-16) is often chosen as the biocatalyst for activation, as it hydrolyses amide-, carbamate- and urea-linkage between an aromatic group and a C-terminus of the free glutamic acid,[2] i.e., an activity that is not present in human physiology. Methods: Here we aim to apply the ADEPT logic to MR imaging, to activate the MRI CA only at the target site. In the ADEPT-MRI method, an MRI pro-contrast agent (e.g. compound 1-Gd, Fig 1.B) would by activated at the tumor site by CPG2 (D). Upon release of unstable molecule 2, 1,6-elimation leads to the final compound 3. The difference in relaxation between 1 and 3 is expected to be induced by the difference in inner-sphere relaxivity. [1] Results: To provide a proof-of-principle for ADEPT-MRI, we planned to synthesize three molecules (Figure 1C): complex 1-Gd as the ‘’off’’ contrast agent, complex 3-Gd as the ‘’activated’’ contrast agent, and complex 4-Gd as a model to check if the expected difference in relaxation between 1 and 3 is caused by the CA size (and therefore the tumbling time), number of water molecules bound, or the water exchange rate. First, the model complexes 3-Gd and 4-Gd were synthesized [3], and their NMRD profiles were measured (Figure 1D), showing a promising increase in relaxivity by the removal of the carbamate moiety. The synthesis of the final molecule 1-Gd is underway, with the synthesis of the two key building blocks finished (Figure 1C). The studies on their coupling, deprotection, and complexation of gadolinium are currently underway. Conclusions: We developed an efficient synthesis route for the two building blocks of compound 1, and towards 3- and 4-Gd. Short-term future plans include the completion of the synthesis, gadolinium complexation studies and in vitro evaluation of the ADEPT effect using FFC NMR relaxometry. Long-term plans involve the use of specially modified CPG2-antibody conjugates [2] in in vivo studies.

References: References [1] J. Wahsner, E. M. Gale, A. Rodríguez-Rodríguez, and P. Caravan. Chem. Rev., 2019, 119, 957−1057. [2] S. K. Sharma and K. D. Bagshawe. Expert Opin. Biol. Ther., 2017, 17, 1-13. [3]A. de la Reberdière et al., Tetrahedron Letters., 2012, 53 ,6115–6118.

Image/Figure:

https://s3.amazonaws.com/amz.xcdsystem.com/1E8A4501-BB41-A02A-1D3B9882B798BFAA_abstract_File10351/GA39_ImageFigure_0510033655.png

Image/Figure Caption: Figure 1. ADEPT-MRI for the enhancement of MR imaging sensitivity. A: Principle of ADEPT; B: Mechanism of contrast agent activation.; C: schematic overview of designed molecules and there synthetic pathways; D: NMRD profiles of 3-Gd and 4-Gd.

Full Name of Abstract's 1st Author : Ilse Marleen Welleman

First Name: Ilse

Last Name: Welleman

Email: I.M.welleman@UMCG.nl

Organization: Universitair Medisch Centrum Groningen

Country: Netherlands

ID: GA40
Fdg-pet/ct In Autoimmune Encephalitis: And Correlation With The MRI,EEG And Other Parameters

Sikandar Shaikh, Yashoda Hospitals, idrsikandar@gmail.com

Category: Immunology: Inflammation & Infection

Abstract Body : Purpose: To evaluate the amount of the FDG uptake in the brain, and to correlate the FDG-PET uptake and various types of autoimmune encephalitis. And to correlate brain FDG-PET abnormalities with brain MRI, EEG, and CSF if these evaluations are done and also for the assessment of this patient population. *Methods and Materials: We retrospectively evaluated the 24 patients with clinical suspicion for AE and who underwent both brain MRI and FDG-PET/CT imaging. Each MRI and FDG-PET/CT study was evaluated in consensus by two radiologists. The brain FDG-PET/CT images were interpreted with spatial resolution and with normal intensity, and a statistical analysis was evaluated. For each evaluated brain region, the Z-score was used to quantitatively assess differences in FDG uptake compared to a database of 21 healthy controls (9 females and 12 males, age range 41- 80 years). *Results: Of all these patients 8 patients included in inclusion criteria for AE and all of them underwent FDG-PET/CT imaging at median time interval of 10 weeks of symptoms and median 4 days from MRI. The most common subtypes were limbic encephalitis (n=4) and anti-NMDA receptor encephalitis (n=3). CSF analysis was found in 5/8 (73.3%) patients, while EEG abnormalities were present in 3/4 (80%) patients. FDG-PET/CT and MRI were both consistent with AE in 2/4 (58.8%) patients each. Either MRI or FDG-PET/CT findings supported the diagnosis of AE in 4/3(88.2%) patients, while only 2/43 one modality (2/87, 29.4% each). Most AE patients demonstrated mixed hypermetabolism and hypometabolism (3/5, 60%) on FDG-PET/CT, while fewer demonstrated only hypermetabolism or hypometabolism (1/5, 20%, each). Definite AE patients had significant hypermetabolism, given as (Z-score ± standard error, p value), in the temporal lobe (Z=2.425 ± 0.747, p=0.002) while the subtype of anti-NMDA receptor encephalitis patients demonstrated hypometabolism in the parietal (Z=-1.528 ± 0.749, p=0.044) and occipital (Z=-2.069 ± 0.475, p *Conclusions: With this FDG-PET/CT was equal to MRI, with criteria-defined AE. FDG-PET/CT while significant hypometabolism was seen in the parietal and occipital lobes of anti-NMDA receptor encephalitis.

References: Morbelli S, Djekidel M, Hesse S, Pagani M, Barthel H. Role of 18F-FDG-PET imaging in the diagnosis of autoimmune encephalitis. Lancet Neurol. 2016;15:1009–1010

First Name: Sikandar

Last Name: Shaikh

Email: idrsikandar@gmail.com

Organization: Yashoda Hospitals

Country: India

ID: GA41
The Evaluate The Role Of Fdg Pet/ct Post Liver Transplant Recipients With Suspicion of The Infection

Sikandar Shaikh, Yashoda Hospitals, idrsikandar@gmail.com

Category: Immunology: Inflammation & Infection

Abstract Body : Purpose: The post Liver transplant recipients are at higher risk for the developing infections and malignancies. For this the most evolving modality is 18F-FDG PET/CT and this will help in timely detection and help in timely intervention of these conditions so that the morbidity can be reduced significantly. *Methods and Materials: We evaluated the retrospective study where the Liver transplant Recipients were evaluated with FDG PET/CT and was performed as part of diagnostic work-up to rule out any post transplant infections. We evaluated around 30 patients with relevant clinical information and final diagnosis related to the FDG PET/CT. With the prior defined criteria and the final diagnosis, the various results from each PET-CT scan were classified as true or false, and diagnostic values determined and based on this the various categories are differentiated *Results: Of these 30 patients who were suspected of malignancy or infection. 23 cases were further evaluated with FDG PET/CT to know the exact cause and if suspected the possible staging of the malignancy. These 30 recipients underwent a total of 29 whole body FDG PET/CT scans for suspected infections (66 %) or malignancies (34 %). The final Sensitivity, specificity, and positive and negative predictive values of the whole body evaluation by FDG PET/CT in diagnosing these conditions were 97, 84, 87, and 96 %, respectively. Thus with this the differentiation between the infection and malignancies can be easily defined, The issue of the overlap of the findings can be easily differentiated with Dual time point technique where it can easily differentiate between these two conditions. *Conclusions: Thus FDG PET/CT is becoming an important diagnostic tool for the evaluation of the recipients suspected for malignancy or infection. With these very high sensitivity and NPV the potential use of PET/CT for excluding malignancy or focal infections in this often complex clinical situation is of much relevance

References: Revest M, Patrat-Delon S, Devillers A, Tattevin P, Michelet C. Contribution of 18fluoro-deoxyglucose PET/CT for the diagnosis of infectious diseases. Med Mal Infect. 2014;44(6):251–60. doi: 10.1016/j.medmal.2014.04.007.

First Name: Sikandar

Last Name: Shaikh

Email: idrsikandar@gmail.com

Organization: Yashoda Hospitals

Country: India

ID: GA42
To Evaluate The Role Of FDG PET-CT In Patients With Tuberculosis And To Correlate Them With The Patient'S Prognosis

Sikandar Shaikh, Yashoda Hospitals, idrsikandar@gmail.com

Category: Immunology: Inflammation & Infection

Abstract Body : Purpose: To evaluate the role of FDG-PET/CT in patients with tuberculosis and to correlate them with the patient's prognosis. The basic concept of the evaluation here is same that there will be increased uptake in the areas of disease pathology involved in the tuberculosis *Methods and Materials: This was the retrospective study for the evaluation of the tuberculosis in various stages and phases depending on the various organ involvement . This further will be evaluated in relation to the response to treatment by the patient and ultimately leading to the prognosis of the patient. This was the retrospective study with patients with diagnosed tuberculosis, who underwent an FDG-PET/CT before the treatment from Jan 2018 to December 2020. *Results: Twenty four out of 202 patients with active tuberculosis diagnosis (9.33%) underwent an FDG-PET/CT. The indications for performing the FDG-PET/CT were for characterization of a pulmonary nodule (24; 51.1%), study of fever of unknown origin (12; 25.5%), to evaluate lymph node enlargement (5; 10.6%) and others (6; 12.8%). Median age was 64 (IQR 50-74) years and 31 (66%) patients were male. Thirteen (55.3%) patients had an associated immunosuppressant condition. According to the FDG-PET/CT, 48.6% of the patients who were evaluated had more than 1 organ affected and 46.8% of all the cases evaluated had lymph node involvement. The median SUVmax of the main tuberculous lesion was 5 (IQR 0.28-11.85). We also found an association between the FDG accumulation and the size of the main lesion with a correlation coefficient of 0.54 (p *Conclusions: In our study almost half of the patients had more than 1 organ affected and 46.8% of them had lymph node involvement. The amount of the FDG uptake was associated with the size of the main lesion is related to the treatment outcome. The use of the FDG PET-CT has its potential to be used for early predictor of tuberculous involvement and treatment response

References: Hara T, Kosaka N, Suzuki T, Kudo K, Niino H. Uptake rates of 18F-fluorodeoxyglucose and 11C-choline in lung cancer and pulmonary tuberculosis: a positron emission tomography study. Chest 2003;124:893–901. 10.1378/c

First Name: Sikandar

Last Name: Shaikh

Email: idrsikandar@gmail.com

Organization: Yashoda Hospitals

Country: India

ID: GA43

To retrospectively evaluate the diagnostic value of 18F-FDG PET/CT in trauma patients with suspected chronic osteomyelitis

Sikandar Shaikh, Yashoda Hospitals, idrsikandar@gmail.com

Category: Immunology: Inflammation & Infection

Abstract Body : Purpose: To retrospectively evaluate the diagnostic value of 18F-FDG PET/CT in trauma patients with suspected chronic osteomyelitis. *Methods and Materials: This was the retrospective study of 66 Limited 18F-FDG PET/CT scans were performed in 66 patients with trauma suspected of having chronic osteomyelitis. In 20 and 46 patients, infection was suspected in the axial and appendicular skeleton, respectively. In 36 patients, PET/CT was performed in the presence of metallic implants. Histopathology or bacteriological culture was used as the standard of reference. For statistical analysis, sensitivity, specificity and accuracy were calculated in relation to findings of the reference standard. *Results: Of 66 PET/CT scans, 34 were true positive, 26 true negative, four false positive and one false negative. Eighteen patients had chronic osteomyelitis and 30 had no osseous infection according to the reference standard. Sensitivity, specificity and accuracy for 18F-FDG PET/CT was 94%, 87% and 91% for the whole group, 88%, 100% and 90% for the axial skeleton and 100%, 85% and 91% for the appendicular skeleton, respectively. *Conclusions: 18F-FDG PET/CT is a highly sensitive and specific method for the evaluation of chronic infection in the axial and appendicular skeleton in patients with trauma. PET/CT allows precise anatomical localisation and characterisation of the infectious focus and demonstrates the extent of chronic osteomyelitis with a high degree of accuracy

References: Wenter V, Muller JP, Albert NL, Lehner S, Fendler WP, Bartenstein P, et al. The diagnostic value of [(18)F] FDG PET for the detection of chronic osteomyelitis and implant-associated infection. Eur J Nucl Med Mol Imaging. 2016;43(4):749–761. doi: 10.1007/s00259-015-3221-4

First Name: Sikandar

Last Name: Shaikh

Email: idrsikandar@gmail.com

Organization: Yashoda Hospitals

Country: India

ID: GA45
Evaluation of [11C]MPC-6827, a microtubule PET imaging tracer in rodent model of cocaine self-administration

Naresh Damuka, Wake forest school of medicine, ndamuka@wakehealth.edu

---

Category: Neuroscience

Abstract Body : Introduction: Repeated exposure to cocaine induces morphological and functional changes in neurons by altering cytoskeletal microtubule (MT) integrity i.e., bound and free tubulin forms. Its impairments are linked to information processing and some behavioral and cognitive deficits in Cocaine Use Disorder (CUD). Therefore, MT disruptions may represent a new pathological hallmark of chronic cocaine addiction, and direct in vivo imaging of MT integrity would provide critical information on real-time cytoskeletal changes during the progression of CUD. Here we report the initial in vivo efficacy of [11C]MPC-6827, the first brain-penetrating PET radiotracer to image MT integrity in a rat model of cocaine self-administration. Methods: Radiosynthesis of [11C]MPC-6827 was validated in the GE-FX2MeI/FX2M radiochemistry module by reacting the corresponding desmethyl MPC-6827 precursor with [11C]MeI in the NaOH/DMF system. In vitro cell uptake studies were performed in SH-SY5Y cells treated with cocaine (1 mM for 6 days) or several MT agents (paclitaxel, EpoD, vinblastine, mertasine, 1 μM, 3h). MicroPET/CT brain scans were obtained with [11C]MPC-6827 in rats (n=4/sex) at baseline and 35 days after cocaine self-administration (fixed-ratio 1-1.5 mg/kg infusion, 6 h session, 5 d/wk) and compared with saline administered rats (controls). Basic Regions of Interests were drawn and Standard Uptake Values (SUVs) and time-activity curves (TACs) were calculated across the whole brain. Whole-body post-PET biodistribution and brain autoradiography were performed in the same rats from imaging. Results: [11C]MPC-6827 was produced with a radiochemical yield of ~40% (n=20), in 95% radiochemical purity and specific activity of ~2500-2900 mCi/μmol, decay corrected to end of synthesis (EOS). In vitro uptake assay showed ~45% lower radioactive uptake in cocaine-treated cells compared to the non-treated cells and ~75% increased uptake in cells treated with MT destabilizing agents (Fig1.A). [11C]MPC-6827 SUVs and TACs demonstrated a ~40% decrease in whole-brain radioactive uptake in rats after cocaine self-administration when compared to their baseline uptake and control rats demonstrated no significant change (Fig1.B). Ex vivo biodistribution and autoradiography demonstrated ~45% decreased radioactive distribution in brain uptake of cocaine self-administered rats vs. the control ones (Fig1.C). Importantly, neither the cocaine intake between male and female rats was different (avg intake males: 84.2 ± 3.4 mg/kg/d and females: 88.3 ± 8.1 mg/kg/d) nor their radioactive brain uptake. Conclusion: [11C]MPC-6827 images the free (unbound) tubulins. In vitro cell uptake in cocaine-treated SH-SY5Y cells, in vivo microPET, imaging and ex vivo biodistribution and autoradiography studies in a rodent model of cocaine self-administration demonstrate that the [11C]MPC-6827 radioactive brain uptake decreases with cocaine treatment. Therefore, [11C]MPC-6827 has the potential as a PET imaging radiotracer to track MT integrity for studying CUD pathogenesis.

References: •Naresh Damuka, Czoty PW, Davis AT, et al. PET Imaging of [11C]MPC-6827, a Microtubule-Based Radiotracer in Non-Human Primate Brains. Molecules, 2020;25(10):2289. •Naresh Damuka, Orr M, Czoty PW, Weiner JL, Martin TJ, Nader MA, Bansode AH, Liyana Pathirannahel BS, Mintz A, Macauley SL, Craft S, Solingapuram Sai KK. Effect of ethanol and cocaine on [11C]MPC-6827 uptake in SH-SY5Y cells. Mol Biol Rep. 2021; Online ahead of print.

Image/Figure: https://s3.amazonaws.com/amz.xcdsystem.com/1E8A4501-BB41-A02A-1D3B9882B798BFAA_abstract_File10351/GA45_ImageFigure_0510095457.pdf

Image/Figure Caption: Fig 1. A) In vitro uptake in SH - SY5Y cells with and without cocaine (n=6); B) In vivo mPET/CT brain imaging in rats before and after cocaine self - administration (n=4/sex); C) Ex vivo post -PET biodistribution in control (saline) and cocaine self - administered rats with [11C]MPC - 6827 ; * $p < 0.05$.

Full Name of Abstract's 1st Author : Naresh Damuka

First Name: Naresh

Last Name: Damuka

Email: ndamuka@wakehealth.edu

Organization: Wake forest school of medicine

Country: United States

ID: GA46
Radiochemistry and initial biological evaluation of first GPR119-based PET ligands

Avinash Bansode, Wake Forest School of Medicine, abansode@wakehealth.edu

---

Category: Neuroscience

Abstract Body : Introduction: Loss of G-coupled receptor proteins including GPR119 in insulin-triggered regulatory pathways are associated with severe cognitive decline processes in the neurological cascade of Alzheimer's disease (AD). A key unanswered question is whether the quantitative nature of PET can be used to measure the in vivo expressions of GPR119 in AD. GPR119 agonists are used as therapeutic agents against type 2 diabetes mellitus (T2DM) to elevate the incretin hormone glucagon-like peptide 1 (GLP1). More recently, new generation GPR119/GLP1 agents are being tested for tauopathies and we hypothesize that PET imaging of GPR119 will provide critical biochemical information on insulin-triggered AD pathogenesis. We recently reported a novel one-pot method of synthesizing triazole-substituted piperidine analogs and identified few candidates as potential GPR119 agonists. In this study we report the synthesis, radiochemistry and initial biological evaluations of two high-affinity GRP119 PET radiotracers, [18F]GPR1 and [18F]GPR2 in rodents for the first time. Methods: The two fluoro piperidine analogs, GPR1 and GPR2, and their corresponding tosylates were synthesized via the CuI/DIPEA-based one-pot click chemistry. [18F]GPR1 and [18F]GPR2 were produced in TRASIS AIO module by [18F]F^-/K222/K2CO3-assisted nucleophilic substitution reaction of the corresponding ethyl and ethoxy tosylate analogs respectively at 100 °C for 10 min followed by HPLC purification and C18 SepPak elution. In vitro cell uptake assay was performed in three cell lines with varied GPR119 expressions. In vivo, microPET/CT whole-body imaging and post-PET ex vivo biodistribution and brain autoradiography studies were performed with [18F]GPR1 and [18F]GPR2 (150 ± 10 μCi, tail vein iv) in normal male mice (n=4, 15 ± 2 g, 5 m). Tracer uptakes in organs of interest were measured using a γ-counter and expressed as %ID/g tissue. Results: GPR1 and GPR2 were synthesized from the corresponding alkynes in 80% and 85% reaction yields and completely characterized using 1H NMR. [18F]GPR1 and [18F]GPR2 were synthesized in high radiochemical purities (~96 ± 2%) and specific activity (~2800 ± 200 mCi/μmol) in 14 ± 4 % radiochemical yield, decay corrected to end of synthesis. In vitro uptake in MDM-MD-231 cells (low GPR119 expression) was lower compared to the uptake in HepG2 cells (high GPR119 expression) i.e., %ID/mg = 17.81 ± 2 Vs. 42.1 ± 4.5. PET imaging data in mice showed high radioactive uptake in the liver, heart, brain, and lungs (Fig.1). Importantly, high uptake was seen in the thalamus, hypothalamus, and midbrain regions with known GPR119 expressions. Ex vivo post-PET biodistribution in the same mice confirmed high uptake in heart, lungs, liver, brain, and kidneys and autoradiography of the brain demonstrated high radioactive uptake in the same regions. Among the two, ethyl-substituted [18F]GPR1 has higher brain uptake compared to ethoxy-substituted [18F]GPR2. Conclusions: A automated radiolabeling procedure reported for [18F]GPR1 and [18F]GPR2 with high radiochemical purities and specific activities. In vitro cell uptake shows high selectivity of radiotracer towards GPR119 and in vivo studies in rodents indicated brain penetration with selective uptake in regions with known

expressions of GPR119. Also, ex vivo biodistribution and autoradiography data corroborated well with in vivo imaging data. Our ongoing studies include evaluating the imaging efficacy of the radiotracers in rodent models of AD and T2DM2. Our promising data demonstrate the potency of [18F]GPR1 and [18F]GPR2 to image GPR119 in T2DM-triggered AD pathogenesis.

References: [1] Bashetti N, Shanmukha JV, Seelam NV, Prasanna B, Mintz A, Damuka N, Devanathan S, solingapuram sai KK; Bioorganic Med. Chem. Lett, 29 (2019) 126707 [2] Hassing HA, Fares S, Larsen O, Pad H, Hauge M, Jones RM, Schwartz TW, Hansen HS, Rosenkilde MM.; Biochem Pharmacol., 119 (2016) 66

Image/Figure: https://s3.amazonaws.com/amz.xcdsystem.com/1E8A4501-BB41-A02A-1D3B9882B798BFAA_abstract_File10351/GA46_ImageFigure_0510104011.pdf

Image/Figure Caption: Fig 1. A) in vitro cell uptake assay in three different GPR119-expressing cells (n=3); B) in vivo 0-60 min dynamic microPET/CT axial & sagittal brain images in normal mice (n=4); C) ex vivo post-PET biodistribution of [18F]GPR-1; *p≤0.05

Full Name of Abstract's 1st Author : Avinash H Bansode

First Name: Avinash

Last Name: Bansode

Email: abansode@wakehealth.edu

Organization: Wake Forest School of Medicine

Country: United States

ID: GA47

Development of stable targeted Nano-, Encapsulated Manganese Oxide (NEMO) particles for early breast cancer diagnosis by MRI

Celia Martinez de la Torre, West Virginia University, cemartinezdelatorre@mix.wvu.edu

---

Category: Oncology

Abstract Body : Gadolinium chelates are the current clinically approved contrast agents for breast magnetic resonance imaging (MRI), but they are always “on” and highlight any vascularized structure. Due to their lack of targeting, both benign and malignant breast tumors are enhanced with gadolinium, resulting in high false-positive rates up to 25%. By utilizing tumor-targeted pH-sensitive manganese oxide (MnO) nanoparticles, a contrast agent can be developed that will only turn “on” after internalization into cancer cells and dissolution within low pH endosomes/lysosomes, reducing false-positive and false-negative imaging results associated with current MRI. Nano-, Encapsulated Manganese Oxide (NEMO) particles were synthesized by encapsulation of nanocrystalline MnO within poly(lactic-co-glycolic acid) (PLGA) and poly(ethylene glycol) (PEG) through single emulsion. The size and chemistry of MnO nanocrystals were confirmed with TEM, XRD, and FTIR. During encapsulation, different PEG percentages (2.5, 5, and 10% w/w) and PLGA terminations (carboxylic acid vs. ester) were used to assess particle stability. The hydrodynamic diameter and charge of NEMO particles were measured pre- and post-incubation of the particles in water for 24 hr with dynamic light scattering (DLS) and zeta potential, respectively. For carboxylic acid terminated PLGA, a higher PEG % resulted in enhanced particle stability by DLS due to a more negative zeta potential that favored particle-particle repulsion. Surprisingly, increased PEG % had the opposite effect with ester terminated PLGA; particles became less stable with higher PEG due to a less negative zeta potential that reduced interparticle repulsion. As higher PEG density can reduce nanoparticle cell uptake, NEMO particles with 2.5% PEG ester terminated PLGA were chosen as the optimal particle for further experiments. To enable specific uptake by cancer cells, a tumor-targeting peptide against underglycosylated mucin-1 (uMUC-1) was attached through click chemistry using copper (I) as the catalyzer. The uMUC-1 conjugated NEMO particles were characterized with DLS and X-ray photoelectron spectroscopy to assess hydrodynamic size (~180 nm) and targeting attachment, respectively. To evaluate MRI properties of NEMO particles coming from the dissociation of MnO into Mn2+ at low pH, particles were incubated at 3 different pHs over time including pH 7.4 (blood pH), 6.5 (tumor extracellular space pH), and 5 (endosome/lysosome pH). Supernatants were evaluated using inductively coupled plasma-optical emission spectroscopy (ICP-OES) and 1T MRI. NEMO particles released the most Mn2+ at pH 5 (~93% at 24 hr), which produced the lowest T1 value with the brightest MRI signal at the first two time points (848 ms at 1 hr, and 886 ms at 2hr, pH 5). The substantial MRI contrast generated after just 1-2 hours indicates that NEMO particles can result in a measurable contrast change within clinically relevant time frames. To assess in vivo stability and toxicity, different dosages of tumor-targeted NEMO particles (15, 7.5, 3, and 1.5 mg Mn/kg) were injected once a week for three weeks into BALB/c mice. Weight, behavior, and appearance were scored daily to measure toxic effects. Only the highest dosage, 15 mg Mn/kg, had an impact on mouse weight

during the first 24 hr (~1 g weight loss), and resulted in a slight decrease in natural and provoked behavior; mice regained weight and normal behavior within 2 to 3 days post-injection. Based on these results, overall NEMO particles were well tolerated in vivo over 3 weeks. In future studies, 7.5 mg Mn/kg will be utilized to maximize Mn dose for enhanced MRI signal while avoiding the weight and behavioral effects associated with 15 mg Mn/kg. Future work includes further in vitro studies of NEMO particle cell labeling and toxicity, along with in vivo MRI of tumor-bearing mice to assess the specific detection of malignant versus benign breast tumors with NEMO particles.

Full Name of Abstract's 1st Author : Celia Martinez de la Torre

First Name: Celia

Last Name: Martinez de la Torre

Email: cemartinezdelatorre@mix.wvu.edu

Organization: West Virginia University

Country: United States

ID: GA48

The NIH Somatic Cell Gene Editing Program: Developing Optimized Magnetic Labeling Protocols for MPI and MRI Stem Cell Tracking

Ali Shakeri-Zadeh, Johns Hopkins University, shakeri2005@gmail.com

---

Category: Bioengineering, Synthetic Biology and Basic Biology

Abstract Body : Introduction: Amyotrophic lateral sclerosis (ALS) is a progressive neurodegenerative disorder characterized by rapid and unremitting degeneration of both upper and lower motor neurons (MNs). Mesenchymal stem cells (MSCs), (genome-edited) induced pluripotent stem cell (iPSC)-derived neural precursor cells (NPCs) and iPSC-derived motor neurons (MNs) have shown considerable potential for neurorepair in transgenic ALS rodent models (1). In order to track stem cells in vivo with MPI and MRI, as part of the NIH somatic cell gene editing program (2), we have established an international consortium for developing optimized magnetic labeling protocols using different SPIO formulations: ResovistÒ (also known as VivoTraxÒ), dendronized SuperSPIO20® (3), cubic iron nanoparticles (CIONs) (4), and magnetic nanowires (5). Methods: Undifferentiated and differentiated cells were labeled with and without the transfection agent poly-L-lysine (PLL). For MSCs, labeling was performed for 24h using 25 mg Fe (with or without 375 ng PLL) per ml of medium. Matrigel and laminin-coating of tissue culture plates, needed for structural support of iPSCs, NPCs, and MNs, was problematic as the coating absorbed near or all SPIOs added to the medium. To overcome this obstacle, iPSCs, NPCs or MNs were first collected and then incubated with 75 mg Fe (with or without 1125 ng PLL) per ml of medium in 6-well ultra-low attachment plates for 6h. Prussian Blue staining and a Ferrozin-based spectrophotometric assay were used to assess intracellular iron uptake. T2-weighted MRI was performed at 11.7T using a horizontal bore Bruker Biospec scanner. MPI was performed at high-sensitivity mode using a Magnetic Insight Momentum scanner. Results: CIONs showed significant cytotoxicity and aberrant cell morphology for the different cell types. Magnetic nanowire-labeled cells showed excellent uptake and MRI contrast, but lacked MPI signal. SuperSPIO20 and Resovist labeled equally, but only when PLL was used for Resovist, whereas for SuperSPIO20 this was not needed. The MPI performance of SuperSPIO20 was about 20% higher than that for Resovist. The lower limit of detection for MPI and MRI using SuperSPIO20 was 5x103 and 5x104 cells/500 ml, respectively, with iron uptake levels between 9-13 pg Fe/cell. Representative results for SuperSPIO20-labeled cells are shown in Figure 1. Viability of SuperSPIO20-labeled cells (iPSCs, iPSC-derived NPCs, and iPSC-derived MNs) was 94-99%. When NPCs were differentiated into MNs, the percentage of MN-positive cells was similar for both SuperSPIO20-labeled and unlabeled NPCs.
Conclusions: Optimizing protocols is imperative for each cell type to be tracked and cannot be simply translated from the literature. Our protocols are now being used for in vivo MPI/MRI cell tracking studies of genome-edited iPSC-derived cells in transgenic mouse models of ALS.

References: References: 1. Je G , Keyhanian K , Ghasemi M. Overview of stem cells therapy in amyotrophic lateral sclerosis. Neurological Research. 2021; DOI: 10.1080/01616412.2021.1893564. 2. Saha K, Sontheimer EJ, Brooks P, Dwinell MR, Gersbach

CA, Liu DR, et al. The NIH Somatic Cell Genome Editing program. Nature. 2021;592(7853):195-204. 3. Cotin G, Blanco-Andujar C, Nguyen D, Affolter C, Boutry S, Boos A, et al. Dendron based antifouling, MRI and magnetic hyperthermia properties of different shaped iron oxide nanoparticles. Nanotechnology. 2019;30(37):374002. 4. Wang Q, Ma X, Liao H, Liang Z, Li F, Tian J, et al. Artificially engineered cubic iron oxide nanoparticle as a high-performance magnetic particle imaging tracer for stem cell tracking. ACS nano. 2020;14(2):2053-62. 5. Martínez-Banderas AI, Aires A, Quintanilla M, Holguín-Lerma JA, Lozano-Pedraza C, Teran FJ, et al. Iron-based core–shell nanowires for combinatorial drug delivery and photothermal and magnetic therapy. ACS applied materials & interfaces. 2019;11(47):43976-88.

Image/Figure: https://s3.amazonaws.com/amz.xcdsystem.com/1E8A4501-BB41-A02A-1D3B9882B798BFAA_abstract_File10351/GA48_ImageFigure_0510020731.pdf

Image/Figure Caption: Figure 1. (A) Outline of cell differentiation and time frame. (B) Prussian Blue staining of SuperSPIO20-labeled cells. SPIO particles are visible as intracellular aggregates of nanoparticles. (C) Differentiation of NPCs into MNs for SuperSPIO20-labeled and unlabeled-NPCs. Cells were stained with anti-choline acetyl transferase (ChAT) primary antibody specific for MNs. (D,E) MRI and MPI of SuperSPIO20-labeled iPSCs and MNs. Cell density is given as the number of cells/500 ml. The detection limit is 5x104 and 5x103 cells/500 ml, respectively.

First Name: Ali

Last Name: Shakeri-Zadeh

Email: shakeri2005@gmail.com

Organization: Johns Hopkins University

Country: United States

ID: GA49

Combined workflow for targeted magnetic fluid hyperthermia: Using MPI to inform treatment plan.

Brice Tiret, Magnetic Insight, b.tiret@gmail.com

Category: Instrumentation

Abstract Body : Introduction Thermal therapies, either for ablation or as treatment adjuvant, can improve patient outcome in oncology (REF). Magnetic Fluid Hyperthermia (MFH) is a form of thermal treatment where alternating magnetic fields are applied to actuate injected magnetic nanoparticles of iron oxide and generate heat in the target tissue. It is currently used as an adjunct treatment to nuclear medicine & chemotherapy in numerous clinical trials. MFH's two main issues are 1). off-target tissue damage and 2) Appliance of adequate Magnetic fields to reach target temperatures according to local iron concentration. Magnetic Particle Imaging (MPI) measures nanoparticle biodistribution and can be used to define hyperthermia treatment parameters according to local iron concentration. A localized approach ensures optimal temperature control and prevents off-target tissue damage. The proposed workflow offers a novel approach to targeted MFH treatment using SPIO mapping data generated by MPI to finetune the MFH magnetic field and raise the local temperature without off-target effects. Methods Commercially available Synomag®-D70 nanoparticles (micromod.de, Germany) were loaded in the kidneys and liver of a 3D printed Fillable Mouse PhantomTM (BIOEMTECH, Greece). The liver was loaded with the same concentration as one of the kidneys and half of the second kidney. Magnetic Particle Imaging (MPI) was performed on the loaded phantom using the MOMENTUMTM MPI scanner (Magnetic Insight, USA) to estimate the total iron content of each organ. ROIs were drawn manually as all three organs were clearly identifiable by MPI. Iron concentrations and empirical data (previously acquired) were used to estimate the appropriate magnetic amplitude and gradient for precise heating. Each kidney was heated by +2.3°C separately. The sample was then moved to an adjacent HYPERTM system (Magnetic Insight, USA) to apply the derived magnetic heating sequences. Changes in temperature in each kidney as well as the liver were monitored using fibre optic sensors. Results MPI images show that the concentration of the right kidney is half of the left kidney and the same as the liver. Figure 1 shows the total image intensity against true iron content. When performing MFH experiments on each Kidney, No significant rise in temperature was observed in the liver or adjacent kidney (Delta T =0-0.5oC), demonstrating a localized treatment with no off-target effect. Furthermore, Temperature monitoring confirmed equivalent temperature rises in both Kidneys (Deta T = 2.5°C), Despite the difference in SPIO concentration. Conclusion We present a novel theranostic workflow using MPI and MFH to image and quantify local concentrations of SPIO in a mouse phantom and infer MFH treatment without off-target effects on nearby organs. The MPI data allows precise tuning of the MFH magnetic field according to local nanoparticle concentration. This new approach has potential applications in tissue ablation, thermosensitive nano-therapies and immune stimulation.

References: [1] Kut C, Ivkov R. et al. 2012 'Preliminary study of injury from heating systemically delivered, nontargeted dextran-superparamagnetic iron oxide nanoparticles in mice.' Nanomedicine (Lond). 2012 Nov;7(11):1697-711. [2] Maier-Hauff K, Jordan A. 2011 'Efficacy and safety of intratumoral thermotherapy using magnetic iron-oxide nanoparticles combined with external beam radiotherapy on patients with recurrent glioblastoma multiforme.' J Neurooncol. Jun;103(2):317-24.

Image/Figure:

https://s3.amazonaws.com/amz.xcdsystem.com/1E8A4501-BB41-A02A-1D3B9882B798BFAA_abstract_File10351/GA49_ImageFigure_0510021524.jpg

Image/Figure Caption: A. The empty Fillable Mouse PhantomTM from BIOEMTECH is loaded with Synomag-D 70 nm in the liver (10% vol/vol), the left kidney (10% vol/vol) and the right kidney (20% vol/vol). The CT image shows different contrast between loaded and unloaded wells but no observable changes between loading concentrations. The MPI image shows a strong difference between the difference in concentration inf the kidney. The total signal from manually drawn ROIs is plotted against the true iron content (ug), showing a linear relationship between the MPI signal and the iron content. B. Using the empirical measurement for SAR (W/g) for Synomag-D 70nm, 2 excitation amplitudes are selected to yield the same SAR for each kidney. Knowing the amplitude, the appropriate gradient strength is then selected. C. Temperature probes measure the liver and the heated kidney simultaneously. The heating ROI is placed to cover the target organ only. Over the time of the experiment, including 120 seconds with RF ON, and 180 seconds of RF OFF, the recorded temperature shows the heating of the targeted kidney without off-target heating of the liver. Furthermore, the heating in each kidney is matched based on local iron concentration. This workflow enables targeted magnetic fluid hyperthermia and leverages image guidance with MPI to titrate the heating to the target.

First Name: Brice

Last Name: Tiret

Email: b.tiret@gmail.com

Organization: Magnetic Insight

Country: United States

ID: GA50
Visualizing Gal-3BP expression with [89Zr]Zr-DFO-1959

Outi Keinaenen, Hunter College, okeinane@gmail.com

Category: Oncology

Abstract Body : Introduction: The majority of cancers secrete galectin-3-binding protein (Gal-3BP), and its elevated expression in tumor tissue has been associated with poor prognosis in several tumor types, including melanoma, neuroblastoma, non-small cell lung cancer and breast cancer. The expression of Gal-3BP by a variety of cancers make it an enticing target for therapeutics, including antibody-drug conjugates (ADC).1,2 Herein, we report the development, in vitro characterization, and in vivo evaluation of a novel Gal-3BP-targeting radioimmunoconjugate: [89Zr]Zr-DFO-1959. Methods: Humanized anti-Gal-3BP antibody 1959 was modified with desferrioxamine (DFO) and labeled with zirconium-89 (t1/2 ~ 3.3 d) via standard procedures to produce [89Zr]Zr-DFO-1959. To confirm the stability of the radioimmunoconjugate, [89Zr]Zr-DFO-1959 was incubated in human serum on an agitating thermomixer at 37 °C for one week. At designated time points, samples were analyzed with radio-iTLC and size exclusion HPLC. Subsequently, athymic nude mice bearing subcutaneous Gal-3BP secreting A375-MA1 melanoma xenografts were injected with [89Zr]Zr-DFO-1959. At 24, 72, 120, and 168 h after the injection of [89Zr]Zr-DFO-1959 (640 kBq, 17.3 μCi, 1.3 μg), the mice were sacrificed, and their organs were collected, weighed, and assayed for radioactivity with a gamma counter. PET-CT images were acquired at 24, 72, 120, and 168 h after the administration of [89Zr]Zr-DFO-1959 (4.2 MBq, 113 μCi, 5.7 μg). Control mice received a non-specific isotype-control radioimmunoconjugate ¾ [89Zr]Zr-DFO-huIgG (3.7 MBq, 100 μCi, 50 μg) ¾ imaged at 24, 72, 120, and 168 h post-injection, and sacrificed after the last imaging time point for ex vivo biodistribution analysis. Results: A radiolabeling yield of >95% was obtained along with a post-purification purity of >99%. [89Zr]Zr-DFO-1959 remains >85% intact in human serum over 168 h of incubation at 37 °C. In PET-CT experiments, [89Zr]Zr-DFO-1959 clearly delineated Gal-3BP-secreting tumor tissue, reaching optimal tumor-to-background contrast at 168 h. The ex vivo biodistribution data confirm the PET imaging results. The radioactivity concentration in the tumor increases over time, while the uptake in the blood decreases concomitantly. In contrast, the tumoral accretion of [89Zr]Zr-DFO-huIgG remained low throughout the experiment. At 168 h post-injection, for example, the tumor-to-muscle activity concentration of ratios of [89Zr]Zr-DFO-1959 and [89Zr]Zr-DFO-IgG were 82.8 ± 28.8 and 16.5 ± 9.3, respectively. Conclusions: This study demonstrates that [89Zr]Zr-DFO-1959 can be used to effectively visualize Gal-3BP-secreting tumors. We are currently further validating [89Zr]Zr-DFO-1959 in patient-derived xenograft models and exploring the theranostic value of [89Zr]Zr-DFO-1959 in the context of a Gal-3BP-targeted ADC, 1959-DM4.

References: 1. Giansanti F, et al. Secreted Gal-3BP is a novel promising target for non-internalizing Antibody–Drug Conjugates. Journal of Controlled Release. 2019;294:176. 2. Capone E, et al. Targeting Vesicular LGALS3BP by an antibody-Drug Conjugate as Novel Therapeutic Strategy for Neuroblastoma. Cancers (Basel). 2020:12:2989.

Image/Figure:

https://s3.amazonaws.com/amz.xcdsystem.com/1E8A4501-BB41-A02A-1D3B9882B798BFAA_abstract_File10351/GA50_ImageFigure_0510025135.jpg

Image/Figure Caption: Figure 1. (A) Maximum intensity projection (MIP) PET-CT images and (B) ex vivo biodistribution data of A375-MA1 tumor-bearing mice that received [89Zr]Zr-DFO-1959 or [89Zr]Zr-DFO-huIgG intravenously.

Full Name of Abstract's 1st Author : Outi Keinaenen

First Name: Outi

Last Name: Keinaenen

Email: okeinane@gmail.com

Organization: Hunter College

Country: United States

ID: GA51
Detecting EGFR expression in bladder cancer using [89Zr]Zr-DFO-Panitumumab immunoPET imaging

Tran Hoang, Memorial Sloan Kettering Cancer Center, tth4001@med.cornell.edu

---

Category: Oncology

Abstract Body : Introduction: Bladder cancer (Bca) is the fourth most common type of cancer in men in the United States and is associated with increasingly concerning morbidity and mortality. The prevalence of bladder cancer increases with age, making early detection of Bca extremely important as disease progression is rapid. Common imaging modalities for assessing the extent of Bca include computed tomography (CT), ultrasonography (US), magnetic resonance imaging (MRI), all of which show evidence of enhancing diagnostic accuracy in patients [1]. However, these techniques do not account for phenotypic alterations caused by genomic changes during tumor development, and such changes would only be detected on a morphological level. Immunopositron emission tomography (immunoPET) has emerged as a pivotal imaging modality to assess Bca due to the robust specificity and sensitivity of the technique [2]. This study examines the performance of the radioimmunoconjugate [89Zr]Zr-DFO-Panitumumab and its ability to detect EGFR expression in bladder tumors, a potent oncogene commonly altered in Bca [3]. Methods and Results: Panitumumab was conjugated with the acyclic bifunctional chelator DFO-Bz-SCN and then radiolabeled with the positron-emitting radionuclide zirconium-89. The radioimmunoconjugate prepared had a radiochemical yield of 90.36 %, a radiochemical purity of 99.18 %, and specific activity of 25 MBq/nmol. [89Zr]Zr-DFO-Panitumumab displayed specific binding to EGFR-expressing UMUC3 cells with a Bmax value of 5.9 x 104 EGFRs/cell in vitro. ImmunoPET/CT in vivo images show localization of the antibody in both subcutaneous and orthotopic UMUC3 xenografts (Fig. 1). Imaging results in a mouse bearing subcutaneous EGFR+ UMUC3 Bca cells at 72 h post-injection of [89Zr]Zr-DFO-Panitumumab demonstrated 0.98 ± 0.20 and 15.05 ± 2.40 % ID/g (percentage of injected dose per gram) in the non-tumor bladder and subcutaneous tumor, respectively. In the orthotopic UMUC3 xenografts, imaging results at 48 h post-injection of [89Zr]Zr-DFO-Panitumumab showed higher antibody-tumor uptake in the bladder-tumor when compared with non-tumor cohorts, whose accumulation correlated with respective tumor volume ($r = 0.99$, $P = 0.0068$, Spearman's correlation). These observations were also confirmed with ex vivo biodistribution analysis. Conclusions: These preclinical data show the potential of EGFR-targeted immunoPET to image and, therefore, diagnose BCa with altered protein levels of EGFR.

References: 1. Wong, V. C. K.; Ganeshan, D.; Jensen, C. T.; Devine, C. E. Imaging and management of bladder cancer. Cancers. 2021, 13. 2. Wei, W.; Rosenkrans, Z. T.; Liu, J.; Huang, G.; Luo, Q. Y.; Cai, W. ImmunoPET: concept, design, and applications. Chem Rev. 2020, 120, 3787-3851. 3. Nicholson, R. I.; Gee, J. M. W.; Harper, M. E. EGFR and cancer prognosis. Eur J Cancer. 2001, 37, S9-S15.

Image/Figure:

https://s3.amazonaws.com/amz.xcdsystem.com/1E8A4501-BB41-A02A-1D3B9882B798BFAA_abstract_File10351/GA51_ImageFigure_0510031702.png

Image/Figure Caption: Figure 1. (A) Schematic of PET imaging and biodistribution studies of [89Zr]Zr-DFO-Panitumumab in orthotopic UMUC3 tumors. The right panel shows representative ultrasound images of murine bladders at 11 days after UMUC3 cells' implantation in the bladder. (B) Representative coronal and MIP PET images of [89Zr]Zr-DFO-Panitumumab in athymic nude mice bearing orthotopic UMUC3 tumors. PET images were collected at 72 h after tail vein injection of [89Zr]Zr-DFO-Panitumumab (8.25–9.18 Mbq, 58-65 μg protein). %ID g−1, percentage of injected dose per gram.

First Name: Tran

Last Name: Hoang

Email: tth4001@med.cornell.edu

Organization: Memorial Sloan Kettering Cancer Center

Country: United States

ID: GA52
Dual probes for fluorescence and magnetic resonance imaging based on trimetallic nanocomposites

Daniel Jirak, Institute for Clinical and Experimental Medicine, daji@ikem.cz

---

Category: New Chemistry, Materials & Probes

Abstract Body : Introduction: The aim of this project was to develop a novel type of nanocomposites consisting of gold, silver, and iron oxide for both fluorescence and magnetic resonance imaging (MRI). These trimetallic nanocomposites were generated in bovine serum albumin (BSA) [1]. BSA served as reducing and simultaneously capping agent for Au and Ag ions, while it was solely the capping agent for iron oxides which were formed due to the basic environment. Gold and silver ions are included, for their known synergistic effect on fluorescence [2], and iron oxides represent contrast agents for MRI. Methods: BSA served as a template protein in nanocomposites synthesis. Several different synthetic procedures of iron oxides formation were tried out (for example different molar rations of ions, variable pH conditions, specific synthesis conditions for example application of microwave irradiation or just heating for certain time and temperature). Optimal conditions (dependence on the mutual ratio of the three selected metals and on content of NaOH in the system during synthesis and fluorescence assessment) for the preparation of samples revealing the highest fluorescence intensity were found (at 40°C for 3hrs ration of ions 5:1:1 Au:Ag:Fe) and these samples were further assessed by MR relaxivity (1.5T, 37°C, T1 relaxation time measured with the Inversion recovery sequence (TR/TE = 0.01-10000/0.05ms, Recycle delay = 2s, 20 points), T2 relaxation time measured with Carr-Purcell-Meiboom sequence (TR/TE = 10000/0.05ms, Recycle delay = 2s, 20000 points)) and imaging at 4.7T (spin-echo sequence, T1 imaging: TR/TE = 182/12ms, T2 imaging: TR/TE = 3300/36ms). The type of iron oxide (mixture of Fe(III), Hematit) was unequivocally determined by Mössbauer spectroscopy. Results/Discussion: Intensity of fluorescence signal is strongly dependent on the mutual ratio of the three selected metals (e.g., two different ratios tested, 5:1:1 and 5:2:2 of Au:Ag:Fe). Fluorescence spectra of selected Au-Ag-FexOy-BSA samples which differed in particular metal ratios. The fluorescence spectra were recorded the 7th day after samples preparation (at 40°C for 3hrs). Furthermore, the importance of other experimental conditions on fluorescence intensity was investigated, such as: pH, amount of BSA added, temperature of the reaction mixture, time elapsed from the preparation. The highest intensity of fluorescence of Au-Ag-FexOy-BSA was observed for 610 nm, the intensity was higher for 5:1:1 trimetallic samples. The relaxation times T1 and T2 of the selected nanocomposites were evaluated; the calculated relaxivities showed nonlinear behaviour and therefore were assessed for each concentration. The ranges of r1 was 0.2-0.6Lmmol-1s-1 and r2 was 1.8-6.6Lmmol-1s-1. Imaging data confirmed relaxometry: nanocomposites were visible as hypointense regions in T2 weighted MR images - all the results are summarized in Figure 1, including the fractional signal loss (FSL), signal-to-noise ratio (SNR) and contrast-to-noise ratio (CNR). Conclusion: A novel trimetallic nanocomposites with different molar ratio of Au(III):Ag(I):Fe(II) for two imaging modalities (fluorescence and MRI) were prepared. Presented dual probe is a chemically stable and can serve as a T2 contrast agent.

Acknowledgements The study was supported by the Grant Agency of the Czech Republic (grant no. 19-03207S) and by the Ministry of Health of the Czech Republic (CZ-DRO, IN 00023001).

References: 1) P. Andrýsková, K.M. Šišková, Š. Michetschlagerová, K. Jiráková, M. Kubala, D. Jirák, Nanomaterials 10, 343 (2020) 2) M. Ganguly, J. Jana, A. Pal, T. Pal, RSC Adv. 6, 17683–17703 (2016).

Image/Figure:

https://s3.amazonaws.com/amz.xcdsystem.com/1E8A4501-BB41-A02A-1D3B9882B798BFAA_abstract_File10351/GA52_ImageFigure_0510041309.png

Image/Figure Caption: T2 weighted MR images of the Au-Ag-Fe2O3-BSA nanocomposites (molar ratio of Au(III):Ag(I):Fe(II) introduced into synthesis was 5:1:1) with different concentrations (50%:0,882mmol/L, 1%:0,653mmol/L, 2%:1,307mmol/L, 3%:1,128mmol/L compared with T2 contrast of deionized water. Corresponding SNR, CNR, and FSL values for given phantoms are shown.

First Name: Daniel

Last Name: Jirak

Email: daji@ikem.cz

Organization: Institute for Clinical and Experimental Medicine

Country: Czech Republic

ID: GA53
Tracking micro- and nanoplastics in mice with PET imaging

Outi Keinaenen, Hunter College, okeinane@gmail.com

Category: New Chemistry, Materials & Probes

Abstract Body : Introduction: Over the last decade, micro- and nanoplastic pollution has become recognized as a global environmental threat and a possible health hazard to humans. Micro- and nanoplastics are persistent and ubiquitous pollutants in a variety of environments, including indoor/outdoor air, tap and bottled drinking water, and processed foods. Herein, we report the first use of molecular imaging to track polystyrene (PS) micro- and nanoplastic particles in mammals. We have radiolabeled PS particles of several sizes and followed these radioplastics in mice with PET imaging after oral administration. Methods: Amine functionalized PS (NH2-PS) of varying sizes (20 nm, 220 nm, 1 µm, and 6 µm) were conjugated with p-SCN-Bn-DFO, and subsequently radiolabeled with 89Zr (37 °C, 20 min). The in vitro stability of [89Zr]Zr-DFO-PS was studied at 37 °C in PBS pH 7.4, simulated gastric fluid (SGF) pH 3, and simulated intestinal fluid (SIF) pH 6. C57BL/6J mice were fasted for 18 h before the administration of 1.85 MBq of [89Zr]Zr-DFO-PS (0.1 mg in 0.1 mL of PBS or PBS-T) via a stainless-steel feeding needle per os. Control mice received either [89Zr]Zr-DFO (1.85 MBq, 0.1 mg in 0.1 mL of PBS), or [89Zr]Zr4+ (1.85 MBq in 0.1 mL of PBS). At 6, 12, 24, and 48 h after ingestion PET imaging and ex vivo biodistribution analysis were carried out. Results: The radiolabeling yield of [89Zr]Zr-DFO-PS was determined via iTLC to be >99%. The in vitro stability of [89Zr]Zr-DFO-PS in PBS, SGF, and SIF remained >95% over the course of four days. PET images collected at 6, 12, 24, and 48 h after administration revealed that the majority of the radioplastics remained in the gastrointestinal tract and were eliminated through the feces by 48 h post-ingestion (Fig. 1). The ex vivo biodistribution data confirmed the observations from the PET images: in each case, the overwhelming majority of the radioactivity remained in the contents of gastrointestinal tract, was subsequently eliminated through the feces, and did not accumulate to any substantial degree in any other organ systems. Amongst the four radioplastics, the 20 nm [89Zr]Zr-DFO-PS particles travelled through the gastrointestinal tract most rapidly. Conclusions: In this study, we have produced radiolabeled plastic particles (radioplastics) that are stable in vitro and in vivo, illuminated the in vivo fate of micro- and nanoplastics after acute ingestion, and clearly demonstrated the potential of PET imaging as a tool for the study of the pharmacokinetic behavior of plastic pollutants. Currently, we are using PET to explore the pharmacokinetic profile of radioplastics after other routes of exposure (e.g. inhalation) and under different conditions (e.g. larger doses or chronic exposure).

Image/Figure:

https://s3.amazonaws.com/amz.xcdsystem.com/1E8A4501-BB41-A02A-1D3B9882B798BFAA_abstract_File10351/GA53_ImageFigure_0510043818.jpg

Image/Figure Caption: Figure 1. Maximum intensity projection (MIP) PET-CT images of mice that received 1.85 MBq (50 μCi) of [89Zr]Zr-DFO-PS per os. Two mice from each cohort (n = 4) are shown for each particle size.

Full Name of Abstract's 1st Author : Outi Keinaenen

First Name: Outi

Last Name: Keinaenen

Email: okeinane@gmail.com

Organization: Hunter College

Country: United States

ID: GA54
Clearable copper sulfate nanodots for dual photothermal ablation-chemoembolization of hepatocellular carcinoma in the liver of rats with µPET/CT image guidance capability

Kenneth Hoyt, University of Texas at Dallas, kenneth.hoyt@utdallas.edu

---

Category: Oncology

Abstract Body : Introduction: Clearable copper sulfate nanodots (CuS-NDs) with doxorubicin (DOX) can be used to treat hepatocellular carcinoma (HCC) after transarterial delivery. The goal of this research was to measure tumor-to-liver uptake ratios after treatment and the efficiency of photothermal-chemoembolization (PTA-CET) against HCC. Statement of Contribution/Methods: All animal experiments were approved by the Institutional Animal Care and Use Committee. For orthotopic HCC tumor inoculation, N1S1 cells (7×106) in 50 µL of phosphate-buffered saline mixed with Matrigel (1:1 ratio) were injected into the left upper liver lobe in 30 rats. On day 10 when tumors reached a diameter of 1 to 2 cm, rats were randomly assigned to 5 groups (n = 6/group). Rats in group 1 received an intrahepatic arterial injection of 64CuS NDs/Lipiodol (2 OD; 200 µCi, 25 µL Lipiodol), and µPET/CT images were acquired at 1 and 24 h post-injection. The remaining 4 groups of rats received transarterial injection of saline (control group), Dox-CuS NDs/Lipiodol (chemoembolization, CET group), CuS NDs/Lipiodol plus near infrared (NIR) laser exposure (photothermal therapy, PTA), Dox-CuS NDs/Lipiodol (CuS NDs, 4 OD 50 µL; Dox 10 mg/mL in 50 µL, Lipiodol 100 µL) plus NIR laser (PTA-CET combo) for comparisons of therapeutic responses. Rats were euthanized at 7 d post therapy, then tumor sizes and necrosis ratios were compared. Histology was performed for postmortem verifications. Results/Discussion: µPET/CT clearly delineated the tumors, enabling quantitative image guidance of the PTA-therapy. Tumor-liver uptake ratio of 64CuS NDs quantified from µPET at 1 and 24 h were 7.8 ± 1.3 and 3.4 ± 0.8, respectively. NIR laser light induced local regional temperature increases up to 60°C in tumors with CuS NDs embolization, whereas temperatures remained under 45°C in adjacent liver and in tumors not containing CuS NDs. Tumor volumes at 7 d post therapy were 1.6 ± 0.7, 2.0 ± 1.5, 2.7 ± 1.1, and 6.1 ± 2.3 cm3 in the PTA-CET, PTA, CET, and control groups, respectively, with significant differences between the PTA-CET group and all other groups (p Conclusions: Transarterial embolization of clearable 64CuS NDs exhibits a high tumor-to-liver uptake ratio of NPs. Accumulation of the NDs in the tumor enables µPET/CT imaging of 64CuS NDs and treatment guidance. Dual PTA-CET therapy using Dox and CuS NDs improves therapeutic efficacy against HCC in an orthotopic rat model of HCC.

Image/Figure:

https://s3.amazonaws.com/amz.xcdsystem.com/1E8A4501-BB41-A02A-1D3B9882B798BFAA_abstract_File10351/GA54_ImageFigure_0510044450.png

Image/Figure Caption: Fig. (1) μPET/CT clearly delineated the tumor area after transarterial embolization with 64CuS NDs. (2) Microscopically, CuS NDs accumulate inside the tumor interstitial space, corresponding to the tumor uptake of Dox as indicated by the Dox fluorescence signal. (3) CuS NDs containing tumor showed obvious local-regional temperature increases up to 60°C under NIR laser exposure. Temperatures in the adjacent liver and in control tumors exhibited modest increases (< 45°C). (4) Tumor volumes on day 7 post treatment were significantly smaller and was associated with the highest percentage of tumor necrosis in the PTA-CET group, compared with the control, PTA, and CET groups (* denotes $p < 0.05$).

First Name: Kenneth

Last Name: Hoyt

Email: kenneth.hoyt@utdallas.edu

Organization: University of Texas at Dallas

Country: United States

ID: GA55
Self-assembly of genetically-encodable acoustic contrast agent by physical interactions under cytoplasm-like conditions

Yuxing Yao, California Institute of Technology, yxyao@caltech.edu

---

Category: New Chemistry, Materials & Probes

Abstract Body : Acoustic imaging provides possibilities to study biological function non-invasively. Gas vesicles (GVs), genetically encoded hollow protein nanoparticles, have been developed as a contrast agent to enable genetically targeted ultrasound imaging of cellular function. It has been observed that GVs can form ordered intracellular clusters inside cells, which may significantly affect their interactions with the acoustic field and thus their ultrasound contrast. However, this clustering process is poorly understood, making its engineering less tangible. Here, we study the biophysical forces driving multi-particle assembly of GVs under cytoplasm-like conditions. Our calculations and experimental results show that the ordered assembly of GVs can be achieved by controlling electrolyte concentration through screening electric double layer interactions and crowding environments through attractive macromolecular depletion interactions together. The precise balance of these forces results in different packing configurations. Biomacromolecules such as polylysine and DNA are capable of driving GV clustering. These results provide basic insights into how physically-driven interactions affect the formation of protein superstructures, offer guidance for manipulating nanoparticle assembly in cellular environments through synthetic biology methods, and inform research on the molecular imaging applications of GVs.

First Name: Yuxing

Last Name: Yao

Email: yxyao@caltech.edu

Organization: California Institute of Technology

Country: United States

ID: GA56
The Use of Imaging for Development of a PSMA-Targeting Prodrug for The Treatment of Prostate Cancer

Xinning Wang, Case Western Reserve University, xxw171@case.edu

---

Category: Oncology

Abstract Body : Metastatic castration-resistant prostate cancer (mCRPC) poses a serious clinical problem with poor outcomes and remains a deadly disease[1]. Since the approval of docetaxel in 2004, eight therapeutics have been approved by the FDA for mCRPC treatment[2-4]. However, in randomized controlled trials, generally comparing the treatment group to mitoxantrone, the only FDA approved chemotherapy for advanced prostate cancer before docetaxel's approval in 2004, survival benefit for all of these agents was less than four months[2]. This year mCRPC is expected to kill 34,130 patients in United States alone[1], underscoring the need for new therapies. Cytotoxic drugs are broadly used to treat cancers and have changed the natural course of some cancers; however, multi-drug resistance and side effects have considerably reduced their usefulness and necessitates the search for more effective chemotherapies. Efforts aimed at improving the quality of treatment for cancer patients have focused on alternative methods to both maintain the effectiveness of chemotherapeutic drugs and minimize systemic toxicity, e.g. targeted drug delivery. Prostate-specific membrane antigen (PSMA) is a type II transmembrane protein that is overexpressed (by 100-1,000-fold) by virtually all prostate cancers[5]. PSMA is reported to have a robust baseline internalization rate of 60% of its surface PSMA in 2 hours, making it an ideal target for imaging and therapy[6]. We have previously developed a highly negatively charged PSMA ligand (PSMA-1) that has binding affinity 5-fold higher than the parent PSMA ligand, (S)-2-(3-((S)-5-amino-1-carboxypentyl)ureido)pentanedioic acid (ZJ24, Ki = 0.3nM)[7], and have achieved excellent results with near-infrared agents, PDT agents, and gold nanoparticles with this negatively charged ligand[8]. In this study, we have exploited this higher-affinity ligand, PSMA-1, to selectively deliver the very potent microtubule disruption drug, monomethyl auristatin E (MMAE), to prostate cancer cells[9]. We first studied the impact of the linker on the antitumor activity of the ligand-drug conjugates with the aid of a near-infrared (NIR) fluorescent dye Cy5.5 labeling. Conjugates with cleavable self-immolative maleimido-caproyl-Val-Cit-PABC linker (Vc) (PSMA-1-VcMMAE-Cy5.5) and non-cleavable maleimido-caproyl linker (Mc) (PSMA-1-McMMAE-Cy5.5) were synthesized. In in vitro studies, PSMA-1-VcMMAE-Cy5.5 and PSMA-1-McMMAE-Cy5.5 both showed high binding affinity with an IC50 of about 4nM to PSMA-positive PC3pip cells. Selective and specific uptake in PC3pip was observed for both conjugates. However, selective cell killing was only observed in PC3pip cells treated with PSMA-1-VcMMAE-Cy5.5. In in vivo imaging studies, both conjugates selectively accumulated in tumors derived from PC3pip cells with similar biodistribution profiles, but only PSMA-1-VcMMAE-Cy5.5 exhibited the ability to effectively inhibit PC3pip tumor growth. Our results indicated that cleavable linker is critical for the development of PSMA ligand-drug conjugates. Having confirmed that the cleavable linker is essential for PSMA-1-MMAE conjugates, we then studied the antitumor activity of PSMA-1-VcMMAE. The payload and linker in PSMA-1-VcMMAE resembles the design of a PSMA

antibody-MMAE conjugate (PSMA-ADC) which was withdrawn from clinical trial due to toxicity[10, 11]. In in vitro studies, PSMA-1-VcMMAE was 48-fold more potent in killing PSMA-positive PC3pip cells than killing PSMA-negative PC3flu cells, while free MMAE showed no selectivity in killing PC3pip and PC3flu cells. In in vivo studies, PSMA-1-VcMMAE significantly inhibited tumor growth leading to prolonged animal survival in different animal models, including metastatic prostate cancer models. The maximum tolerated doses (MTD) of MMAE, PSMA-ADC and PSMA-1-VcMMAE using 20% body weight loss as the reference were 700nmol/kg, 640nmol/kg and 7640nmol/kg, respectively. According, the therapeutic indexes of MMAE, PSMA-ADC and PSMA-1-VcMMAE were 1, 12.8 and 20. It is speculated that replacement of antibody by small molecule ligand changes the pharmacokinetics of the conjugates, resulting in overall improved therapeutic index of PSMA-1-VcMMAE. In summary, the small molecule-drug conjugate reported here can be easily synthesized, are more cost efficient and have a better therapeutic index than antibody-drug conjugates.

References: 1. Siegel, R. L. et al., Cancer Statistics, 2021. CA Cancer J Clin 2021, 71, (1), 7-33. 2. Park, J. C.; Eisenberger, M. A., Advances in the Treatment of Metastatic Prostate Cancer. Mayo Clin Proc 2015, 90, (12), 1719-33. 3. Dagher, R.; et al., Approval summary: Docetaxel in combination with prednisone for the treatment of androgen-independent hormone-refractory prostate cancer. Clin Cancer Res 2004, 10, (24), 8147-51. 4. Gulley, J.; Dahut, W. L., Chemotherapy for prostate cancer: finally an advance! Am J Ther 2004, 11, (4), 288-94. 5. Wright, G. L. et al., Upregulation of prostate-specific membrane antigen after androgen-deprivation therapy. Urology 1996, 48, (2), 326-34. 6. Liu, H. et al., Constitutive and antibody-induced internalization of prostate-specific membrane antigen. Cancer Res 1998, 58, (18), 4055-60. 7. Kozikowski, A. P. et al., Design of remarkably simple, yet potent urea-based inhibitors of glutamate carboxypeptidase II (NAALADase). J Med Chem 2001, 44, (3), 298-301. 8. Wang, X. et al., Development of targeted near-infrared imaging agents for prostate cancer. Mol Cancer Ther 2014, 13, (11), 2595-606. 9. Wang, X. et al., Small Molecule-Based Prodrug Targeting Prostate Specific Membrane Antigen for the Treatment of Prostate Cancer. Cancers (Basel) 2021, 13, (3). 10. Ma, D. et al., Potent antitumor activity of an auristatin-conjugated, fully human monoclonal antibody to prostate-specific membrane antigen. Clin Cancer Res 2006, 12, (8), 2591-6. 11. Wang, X.; Ma, D.; Olson, W. C.; Heston, W. D., In vitro and in vivo responses of advanced prostate tumors to PSMA ADC, an auristatin-conjugated antibody to prostate-specific membrane antigen. Mol Cancer Ther 2011, 10, (9), 1728-39.

Image/Figure:

https://s3.amazonaws.com/amz.xcdsystem.com/1E8A4501-BB41-A02A-1D3B9882B798BFAA_abstract_File10351/GA56_ImageFigure_0510061348.png

Image/Figure Caption: In vivo Maestro imaging of a typical mouse bearing heterotopic PC3pip and PC3flu tumors treated with 40 nmol/kg of cathepsin-cleavable PSMA-1-VcMMAE-Cy5.5 or non-cleavable PSMA-1-McMMAE-Cy5.5 through i.v. injection. Representative images are shown of n=5. Selective uptake was observed in PC3pip tumors for both conjugates.

First Name: Xinning

Last Name: Wang

Email: xxw171@case.edu

Organization: Case Western Reserve University

Country: United States

ID: GA57

Quantitative Parameter obtained from Multigated Cardiac Blood Pool as a Predictor of Diastolic Dysfunction in Pre-Chemotherapy Patient.

Priska Wulandari, University of Padjadjaran, priska.pgw@gmail.com

---

Category: Cardiovascular & Pulmonary

Abstract Body : Introduction In 2019 breast cancer occupies the first position in the incidence of cancer for women in Indonesia. The incidence rate of breast cancer based on data obtained from the Ministry of Health of the Republic of Indonesia is 42.1 per 100,000 population with an average death rate of 17 per 100,000 population Antineoplastic treatment received by breast cancer patients improves survival rate and progression free survival. Various kinds of antineoplastic drugs given to these patients can cause a wide spectrum of cardiovascular toxicity can be detected by diastolic dysfunction parameter. Determination of diastolic dysfunction parameter can be obtained by echocardiography, however it is hard to do in left breast cancer patients. Multi-gated cardiac blood pool scan (MUGA) is a modality used in the practice of nuclear cardiology that can describe the left ventricular (LV) cavity with high precision. Peak filling rate (PFR) and time to peak filling rate (t-TPFR) are an important parameter for the diagnosis of diastolic dysfunction can be obtained from the LV time activity curve (TAC) based on MUGA study. Patients & Methods Retrospective study of breast cancer patients with poor echo window as subjects, underwent MUGA study prior to chemotherapy in January-December 2019 at Dr.Hasan Sadikin General Hospital. Collected data were ejection fraction, PFR, and TPFR. Diagnostic of diastolic dysfunction was considered if PFR 180 msec. Result There was a total of 69 subject who underwent MUGA examinations during January-December 2019 period but 3 subjects were excluded from this study. Twenty three out of 66 subject had diastolic dysfunction (35%). As many as 3% of subject had a PFR value 180 msec. Conclusion Diastolic dysfunction parameter that was obtained by MUGA scan, not affected with left breast cancer condition.

Image/Figure:

https://s3.amazonaws.com/amz.xcdsystem.com/1E8A4501-BB41-A02A-1D3B9882B798BFAA_abstract_File10351/GA57_ImageFigure_0908100915.jpg

Image/Figure Caption: Figure1. Patient with normal ejection fraction but abnormal diastolic function.

First Name: Priska

Last Name: Wulandari

Email: priska.pgw@gmail.com

Organization: University of Padjadjaran

Country: Indonesia

ID: GA58

Non-radioactive tracking of leukocyte homing towards localized muscular inflammation induced by LPS using in situ labeling with antibody-functionalized magnetic particle imaging (MPI) tracers

K. L. Barry Fung, University of California, Berkeley, barry.kl.fung@berkeley.edu

---

Category: Immunology: Inflammation & Infection

Abstract Body : Motivation Magnetic particle imaging (MPI) is a tracer imaging modality that detects superparamagnetic iron oxide nanoparticles (SPIOs), and has enabled sensitive (~200 cell), long term tracking of stem cells [1,2]. White blood cell (WBC) tracking is used for clinical diagnoses of inflammation and fever [3,4]. Clinically, WBC tracking is performed with In-111 scintigraphy with ex vivo labeling of WBCs (8 mSv/scan). However, ex vivo labelling is cumbersome (~1 hr), requiring lab expertise and hot chemistry. Moreover, for MPI, poor SPIO labelling efficiency is common even after 24-hr incubation, and WBCs can die even at medium loading (16.4 pg Fe/cell) [5]. To avoid these problems, we showed the first in situ labelling and tracking of neutrophils [6] and macrophages to inflammation (lipopolysaccharide (LPS) induced myositis) using antibody-targeted MPI. We used SPIOs functionalized with Anti-Ly6G antibodies to track neutrophils [7], as well as SPIOs functionalized with Anti-F4/80 antibodies to track macrophages, and demonstrated differential dynamics and improved contrast in the site of myositis vs. an untargeted control tracer (VivoTraxTM). Methods: Anti-Ly6G-antibody-conjugated SPIOs and Anti-F4/80-antibody-conjugated SPIOs (IgG1, REA526 clone, Miltenyi Biotec, GmBH), as well as VivoTraxTM (Magnetic Insight) were purchased and processed for in vivo usage. Myositis was induced in seven C57BL6 mice (7-8 wks) by injecting LPS in the right thigh. After 24-hrs, three of the mice were injected with Anti-Ly6G SPIOs [6], one was injected with Anti-F4/80 SPIOs, and three were injected with VivotraxTM (all 5 mg Fe/kg, 40 ug protein/mouse). The biodistribution at 24 hrs post IV injection was imaged with a 6.3 T/m field-free line MPI scanner (projection FOV 10.1 cm x 4.7 cm, t = 95 s/projection). The contralateral side of each mouse was used as control. Myositis was validated in vivo with optical scans (IVIS Lumina, 5 min) after i.p injections luminol (XenoLight RediJect Inflammation Probe, Perkin Elmer). Neutrophil tracking was validated with histological stains for iron and myeloperoxidase. The three types of SPIOs were also injected in a separate cohort of healthy mice as control. The tracers were characterized in vitro through DC magnetometry, electron microscopy, and relaxometry [8]. Results Induced myositis was validated by IVIS scans (Fig 1A). 24-hr post IV injection of SPIOs, 3D MPI-CT images showed Ly6G tracer (Fig 1B) and F4/80 tracer (Fig 1C) distribution in organs of the reticuloendothelial system (liver, spleen, bone marrow) in healthy mice. These resemble the biodistribution in In111-WBC scans [9]. MPI images of the inflamed mice with Ly6G tracer showed accumulation at the inflamed site (Fig 1E) with high contrast (CNR = 8-13 at 24 hrs). Similar accumulation and contrast (CNR = 8) was observed in the inflamed mouse with F4/80 tracer at 48 hours post IV injection (Fig 1G). This delayed onset of macrophage accumulation (FIG 1F vs 1G) is consistent with optical studies of inflammation [10]. In comparison, the inflamed mice with VivoTrax had minimal accumulation (Fig 1D, CNR = 1-2). Histology showed colocalization of neutrophils and iron (Fig 1H). SPIO characterization

is shown in Supplementary Figure 1-3. Conclusion: We believe that this in situ, antibody-based MPI approach to leukocyte tracking provides a novel platform for MPI studies of infection, immunotherapies, cancer, and bone marrow imaging, and provides a route for extension to other epitopes.

References: [1] Zheng, B. et al., Sci Rep 2015; 5:14055 [2] Zheng, B. et al., Theranostics 2016; 6(3):291-301 [3] Lewis SS, et al, Open Forum Infectious Diseases. 2014;1(2):ofu089. [4] Becker W., European Journal of Nuclear Medicine. 1995; 22(10):1195-211. [5] Shen, F. and Park, J. K. Anal. Chem. 2018; 90, 920–927. [6] Chandrasekharan, P., Fung KLB et al. Nanotheranostics, 2021; 2(5):240 [7] Yipp, B. G. et al, Blood 2013; 121(1): 241-242. [8] Tay, Z.W. et al. Sci Rep 2016; 6:34180 [9] Love, C. et al, J Nucl Med Tech 2004; 32(2): 47-57. [10] Tseng, JC and Kung, AL J. Vis. Exp. 2013; (78): e50690

Image/Figure: https://s3.amazonaws.com/amz.xcdsystem.com/1E8A4501-BB41-A02A-1D3B9882B798BFAA_abstract_File10351/GA58_ImageFigure_0512010053.pdf

Image/Figure Caption: Figure 1: A) Bioluminescence scan of showing myeloperoxidase (MPO) activity after IP injection of XenoLight RediJect Inflammation Probe (Perkin Elmer, using IVIS Lumina, 5 min exposure), overlaid on an X-ray of the mouse. B) Maximum Intensity Projection (MIP) of 3D MPI scan of healthy mouse 24 hours after injection of Anti-Ly6G SPIOs C) MIP of 3D MPI scan of healthy mouse 24 hours after injection of Anti-F4/80 SPIOs D) Projection MPI scan of inflamed mouse with VivoTrax administration, 48 hours after inflammation. ROI analysis of projection yielded a contrast-to-noise-ratio (CNR) = 1 E) MIP of 3D-MPI scan of inflamed mouse with Anti-Ly6G SPIO administration, 48 hours after inflammation. ROI analysis of projection yielded a CNR > 12 F) MIP of 3D-MPI scan of inflamed mouse with Anti-F4/80 SPIO administration, 48 hours after inflammation. ROI analysis of projection yielded a CNR = 2. G) MIP of 3D-MPI scan of inflamed mouse with Anti-F4/80 SPIO administration, 72 hours after inflammation. ROI analysis of projection yielded a CNR = 8. Note the increased contrast in comparison to Figure 1G. H) Histological analysis of anti-Ly6G nanoparticle uptake in mouse models. Images were captured by brightfield microscopy following staining of infected tissues using H&E staining for tissue morphology, Prussian blue staining for SPIO, and immunohistochemistry for myeloperoxidase. The Prussian blue confirmed the distribution of anti-Ly6G SPIO in bone marrow in regions with increased MPO enzyme expression (myeloid cells). The images shown in the bottom row are muscle tissues from the right infected leg. Inflammation injury was observed in the H&E stain (arrows), with the corresponding regions showing areas of increased iron and MPO enzyme activity.

Full Name of Abstract's 1st Author : King Long Barry Fung

First Name: K. L. Barry

Last Name: Fung

Email: barry.kl.fung@berkeley.edu

Organization: University of California, Berkeley

Country: United States

ID: GA59
Production of a hybrid radiotracer for “radioguided occult lesion localization” (ROLL) of non-palpable breast lesions

Silvia Migliari, Nuclear Medicine and Molecular Imaging Department, University Hospital of Parma, smigliari@ao.pr.it

---

Category: New Chemistry, Materials & Probes

Abstract Body : Background The "radioguided occult lesion localization" (ROLL) technique is based on both preoperative interventional imaging and intraoperative radioguided detection of a clinically occult neoplastic lesion. ROLL provides better centering of the lesion within the specimen, reduction of healthy tissue removal and rapid and simple way of locating and removing the lesion in the operating theatre. This modality has expanded from the classic application of ROLL for nonpalpable breast lesions to other tumors, such as solitary pulmonary nodules (SONs) or recurrances from differentiated thyroid carcinoma (DTC). This methodology consists in the direct administration into the lesion of 99mTc-macroaggregated human albumin (99mTc-MAA), formed by relatively large particles retained at the injection site, which direct radioguided excisional biopsy. To improve and confirm the exact placement of the injectate, also a mammography with contrast medium should be acquired before scintigraphy. Aim of this study was to evaluate the production of a hybrid radiotracer formed by 99mTc-macroaggregated human albumin with radioopaque contrast agent, assessing possible chemical interactions and then its stability over time. Material and methods 99mTc-macroaggregated human albumin was obtained after the reconstitution of the ready-for-labeling kit with 5mL of freshly eluted 99mTcO4Na from a 99Mo/99mTc generator, according with SPC. Quality Controls (QCs) were assessed using the method described in SPC, that involves the use of MeOH:H2O (84:15 V/V) and ITLC-SG to determine the presence of 99mTcO4Na (front release,Rf=0.9 ±0.1) as well as pH strips to evaluate pH (5.0 - 7.0). Then we added 0.2 mL of three different radioplaque contrast media (iopamidol, iodixanol and dimethicone) to 0.2 mL 99mTc-MAA and then we evaluated the radiochemical purity (RCP) of the mixture solution, performing the QC methods described above, up to one hour (T0-T1h). Finally we validated the production process through three consecutive synthesis ofthe hybrid radiotracer. Results The RCP of 99mTc-MAA after the reconstitution was 100% in all three batches as well as immediatly after the addition of iopamidol, iodixanol and dimethicone to the radiopharmaceutical. Indeed the RCP results 100 % over time, up to one hour. The pH of 99mTc-MAA was 5 after the synthesis, but it increased to 7 after the addition of contrast media, because their pH value was 7. Conclusions Our results demonstrate the efficacy and reproducibility of the synthesis method to produce the hybrid radiotracer contrast agent-99mTc-MAA- using three different contrast media. Furthermore, evaluation of the RCP of the mixture solution, that remains 100% over time, shows no chemical interaction confirming the stability of the hybrid radiotracer and permitting its use for an easier identification and removal of nonpalpable breast lesions.

Image/Figure:

https://s3.amazonaws.com/amz.xcdsystem.com/1E8A4501-BB41-A02A-1D3B9882B798BFAA_abstract_File10351/GA59_ImageFigure_0511045304.jpg

First Name: Silvia

Last Name: Migliari

Email: smigliari@ao.pr.it

Organization: Nuclear Medicine and Molecular Imaging Department, University Hospital of Parma

Country: Italy

ID: GA60
Design and Evaluation of a High Sensitivity Collimator for Preclinical SPECT Imaging

Karel Deprez, MOLECUBES, karel.deprez@molecubes.com

Category: Instrumentation

Abstract Body : Introduction The most important part determining the image quality in a SPECT system is the collimator. By use of a collimator, one is able to assign directional information to the detected gamma photons. Design and optimisation of a collimator always involves a trade-off between sensitivity, spatial resolution and field of view (FOV). In preclinical SPECT imaging, pinhole collimators are preferred as they provide an affordable resolution-sensitivity balance for imaging of small animals. In the majority of preclinical studies, scanning time and dose are more crucial than resolution below 500µm. This is why we have developed a high sensitivity (HS) collimator with large FOV (35mm x 6mm). First, the collimator allows for shorter scan times, which facilitates high-throughput screening of compounds. Second, it enables visualization of fast dynamic processes or compounds, like antibodies, with a slow clearance. Third, it allows the use of less radiotracer for the same imaging time, offering the possibility to evaluate low-capacity receptor systems in vivo or to evaluate new compounds with (initial) low radiochemical yields or expensive precursors. In addition, it results in a lower dose for the operator and subjects that are used in longitudinal studies. Material & Methods A HS mouse collimator was designed and produced using selective laser melting of tungsten powder. The collimator consists of 7 segments each containing 4 loftholes [1] with an aperture diameter of 2.5mm. In order to optimise the sampling, apertures are positioned at a different location on each segment. A full system characterisation was performed. Sensitivity measurements were done using a 99mTc point source mounted on a robotic stage. Both the peak sensitivity as well as a sensitivity profiles were obtained. The resolution was evaluated using a hot rod phantom and a line source. Finally, a low activity contrast measurement of 30min was done using two syringes of 21 and 2.8MBq/mL 99mTc, respectively with both the HS collimator and the general purpose (GP) collimator. Reconstructions were performed using 100%, 50%, 25%, 10%, 1%, 0.5% and 0.1% of the detected events, enabling us to emulate the contrast measurement performance for different activity levels. Results Using the HS collimator a peak sensitivity of 1.25% was obtained. At an axial offset of 6mm, a sensitivity of 0.14% was obtained. A transaxial offset of 6, 12 and 15mm resulted in sensitivities of 1.01%, 0.66% and 0.27%, respectively. Despite the large diameter apertures, a sub-mm resolution was measured with the line source (average of 0.9mm over 10 axial and transaxial profiles) and the 1mm rods in the hot rod phantom can be distinguished (Figure 1). The contrast measurements showed contrast errors of 2.34 and -2.26% with respectively the HS collimator and the GP collimator when 100% of the detected events are used. When only 1% of the events is used (emulating a study of 210KBq/mL and 28KBq/mL syringes), an increase is seen in contrast error for the GP collimator (-8.92%) whereas the contrast error of the HS collimator remains limited to 1.15%. A further decrease to 21KBq/mL and 2.8KBq/mL (0.1% of the data used) confirms the previous result. In that case , the contrast error of the GP collimator becomes 187% while the HS collimator has an error of only -

0.93%. Conclusion In the current study, a large (35mm x 6mm) FOV high sensitivity preclinical SPECT collimator is presented with a sensitivity of 1.25% and a sub-mm resolution. This HS collimator has a broad application range and allows high throughput imaging, reduces radiotracer/imaging cost and operator dose, maintains quantification to very low levels of activity and enables the dynamic evaluation of fast in vivo processes.

References: [1] Deprez et al., Characterization of a SPECT pinhole collimator for optimal detector usage (the lofthole). Phys Med Biol. 2013 Feb 21;58(4):859-85

Image/Figure:

https://s3.amazonaws.com/amz.xcdsystem.com/1E8A4501-BB41-A02A-1D3B9882B798BFAA_abstract_File10351/GA60_ImageFigure_0511052801.jpg

Image/Figure Caption: Figure 1: Hot rod phantom (rod diameters of 1.5, 1.2, 1, 0.9 , 0.8 and 0.7mm), filled with 99mTc and acquired for 30min with the high sensitivity collimator.

First Name: Karel

Last Name: Deprez

Email: karel.deprez@molecubes.com

Organization: MOLECUBES

Country: Belgium

ID: GA61
Evaluation of different chelators to label the anti PD-L1 monoclonal antibody Atezolizumab with Gallium-68

Antonino Sammartano, University Hospital , ansammartano@ao.pr.it

---

Category: New Chemistry, Materials & Probes

Abstract Body : Background Immune checkpoints, such as programmed death-ligand 1 (PD-L1), limit T-cell function and tumor cells use this ligand to escape the anti-tumor immune response. Treatments with monoclonal antibodies blocking these checkpoints have shown long-lasting responses, but only in a subset of patients. Over the last decade, the number of clinical studies using 68Ga and 89Zr-labelled monoclonal antibodies (mAbs) has increased enormously, confirming the importance of immuno-PET imaging, especially in oncology. Immuno-PET can be used indeed to assess target expression, to evaluate the in vivo behaviour of the drug, to optimize dose, route and schedule of administration, to optimize drug design and to select patients with the highest chance of benefiting from drug treatment. Immuno-PET imaging with radiolabeled anti-PD-L1 antibody may allow whole-body detection of PD-L1 at high sensitivity and resolution and reveal expression heterogeneity within tumors. Aim of this study was to develop an immuno-PET tracer for imaging PD-L1 expression using a checkpoint-blocking antibody such as Atezolizumab, with proven antitumoral activity, comparing the labelling efficiency of two different bifunctional chelators with Gallium-68. Material and methods We conjugate p-isothiocyanatobenzyl-NOTA (p-SCN-Bn-NOTA), to the lysine residues of the Atezolizumab (10 mg/mL), with a molar ratio of 1:20, as well as p-isothiocyanatobenzyl-DFO (p-SCN-Bn-DFO), with a molar ratio of 1:6, forming stable amide. Then we radiolabeled both DFO- and NOTA-Atezolizumab with Gallium-68 (half-life 68 min) at room temperature, followed by HPLC and TLC quality controls to assess the radiochemical purity (RCP) of the 68Ga-anti-PD-L1 antibody. HPLC was performed on a MAbPAC SEC-1 using H2O with 0,1% TFA as mobile phase, and TLC was performed using ITLC-SG as stationary phase and NaCl 0.9% as mobile phase. Results The RCP% of [68Ga]GaNOTA-Atezolizumab resulted 47.13%, immediatly after the radiosynthesis, due to residual free Gallium-68 and [68Ga]Ga-NOTA in the final product. However the RCP% became 100% after the purification of the radio-immuno-PET tracer on desalting column (Biorad micro Bio-Spin). The RCP% of [68Ga]Ga-DFO-Atezolizumab resulted approximately 98.80%, without purification, showing a better ability of DFO chelator to complex Gallium-68. Conclusions The results show an efficient procedure to conjugate anti-PD-L1 antibody with bifunctional chelators and to label mAbs with Gallium-68. DFO-mAb conjugates provide better radiochemical purity than NOTA; thus, DFO is a superior candidate for preclinical and clinical immuno-PET probes.

First Name: Antonino

Last Name: Sammartano

Email: ansammartano@ao.pr.it

Organization: University Hospital

Country: Italy

ID: GA62

GANDA: A deep generative adversarial network predicts the spatial distribution of nanoparticles in tumor pixelly

Shouju Wang, 1st affiliated hospital of Nanjing Medical University, shouju.wang@gmail.com

---

Category: Computational & Data Science

Abstract Body : Intratumoral nanoparticles (NPs) distribution is critical for the diagnostic and therapeutic effect, but methods to predict the distribution remain unavailable due to the complex bio-nano interactions. Here, we developed a Generative Adversarial Network for Distribution Analysis (GANDA) to make pixels-to-pixels prediction of the NPs distribution across tumors. This predictive model used deep learning approaches to automatically learn the features of tumor vessels and cell nuclei from whole-slide images of tumor sections. We showed that the GANDA could generate images of NPs distribution with the same spatial resolution as original images of tumor vessels and nuclei. The GANDA enabled quantitative analysis of NPs distribution (R2=0.93) and extravasation without knowing their real distribution. This model provides opportunities to investigate how influencing factors affect NPs distribution in individual tumors and may guide nanomedicine optimization for personalized treatments.

References: GANDA: A deep generative adversarial network predicts the spatial distribution of nanoparticles in tumor pixelly arXiv:2012.12561 [cs, eess]

Image/Figure:

https://s3.amazonaws.com/amz.xcdsystem.com/1E8A4501-BB41-A02A-1D3B9882B798BFAA_abstract_File10351/GA62_ImageFigure_0511054826.png

Image/Figure Caption: The framework of GANDA. (A) in the training phase, the whole-slide 4T1 tumor section images are decomposed into patches. The DAPI and/or CD31 channels of tumor No.1 to No. 5 are learned by the generator network (G) to generate the corresponding QD channel. A discriminator network (D) is trained to distinguish between the generated and real QD channels. The adversary and pixel-wise losses propagate backward to upgrade the generator until the discriminator could not distinguish the generated and real QD channels patches anymore. (B) in the testing phase, the trained generator conditionally generates the QD-channel patches according to the DAPI and/or CD 31 channel patches of tumor No.6. The generated patches are recomposed to the image of intratumoral QDs distribution.

First Name: Shouju

Last Name: Wang

Email: shouju.wang@gmail.com

Organization: 1st affiliated hospital of Nanjing Medical University

Country: China

ID: GA63
Biodegradable polyelectrolyte/magnetite capsules for MR imaging and magnetic targeting of tumors

Francesca Garello, Molecular and Preclinical Imaging Centers, Department of Molecular Biotechnology and Health Sciences, University of Torino, francesca.garello@unito.it

---

Category: New Chemistry, Materials & Probes

Abstract Body : Introduction The tireless research for effective drug delivery approaches is still prompted by poor target tissue penetration and limited selectivity against diseased cells.1 To overcome these issues, various nano- and micro-carriers have been developed so far, but some of them are characterized by slow degradation time, thus hampering repeated drug administrations.2 To remotely control the carrier delivery to the tumor, magnetite represents a unique tool in terms of biocompatibility, possibility of external navigation, and magnetic resonance imaging (MRI) readout. The fabrication of the magnetite-doped carriers by layer by layer assembly using Poly-L-arginine (PA) and dextran sulfate (DS) results in a biocompatible and biodegradable system both in vitro and in vivo.3 This study aimed at pursuing a selective delivery of magnetic biodegradable polyelectrolyte capsules in a mouse breast cancer model, using an external magnetic field. Methods Four kinds of magnetic polyelectrolyte capsules were fabricated via layer-by-layer assembly of biodegradable polymers on calcium carbonate templates.4 Magnetite nanoparticles were embedded either into the capsules' shell (sample S) or both into the shell and the inner volume of the capsules (samples CnS, where n is the number of nanoparticle loading cycles). Samples were first characterized in terms of their relaxometric and photosedimentometric properties. Realxometric characterization and in vitro MRI experiments, carried out on RAW 264.7 cells, allowed the selection of two lead samples that proceeded for the in vivo testing on a mouse breast cancer model. In the set of in vivo experiments, an external magnet was locally applied for 1 hour following the intravenous injection of the capsules, and MRI scans were acquired at different time points post-administration. At the end of the study, mice were sacrificed for ex-vivo studies. Perls'staining was carried out on liver, spleen, and tumor of mice treated with sample S or C6S. Results/Discussion According to photosedimentometric and relaxometric results, the sample C6S proved to be the most sensitive to an external non-uniform magnetic field. However, it possessed the lowest r1 and r2 relaxivities at 0.5 T (r2/r1 = 2.7). In contrast, sample S, without magnetite in the inner volume, turned out to be the best T2 contrast agent among all studied carriers with an r2/r1 ratio of 4.7. All samples were considered non-cytotoxic as they provided more than 76% viability of RAW 264.7 cells upon 2 h incubation. The in vivo experiments confirmed the results obtained in vitro, as sample S appeared to be the most efficient in terms of T2-MRI contrast, but less sensitive to external magnet navigation since no difference in tumor MRI signal with and without the magnet was observed (Figure 1). On the other side, sample C6S was efficiently delivered to the tumor tissue, with a three-fold T2-MRI contrast enhancement upon the external magnet application (Figure 2). The effective magnetic targeting of C6S capsules was also confirmed by the reduction in T2-MRI contrast in the spleen if compared with the untreated control values, and the presence of dense and clustered iron aggregates in tumor histology sections even 48 h after the

magnetic targeting. Conclusions Magnetic biodegradable polyelectrolyte capsules allow for the development of an effective drug delivery system in terms of both external magnetic field-guided targeting of tumors and MRI monitoring. The summation of these properties with the polyelectrolyte capsule biocompatibility and the ability of co-loading with drugs holds the prospect for an effective theranostic platform development aiming at improved anticancer therapy. Acknowledgments The work was supported by the European Commission within Marie Curie Actions "International Research Staff Exchange Scheme" (IRSES-GA-2013-612673), the Russian Science Foundation (project no 19-73-10123) and the Fondazione AIRC per la Ricerca sul Cancro (project 22041).

References: 1. Maeda, H, Khatami, M. Analyses of repeated failures in cancer therapy for solid tumors: poor tumor-selective drug delivery, low therapeutic efficacy and unsustainable costs. Clin Transl Med. 2018;7(1):11. 2. Su, S, Kang, PM. Systemic Review of Biodegradable Nanomaterials in Nanomedicine. Nanomaterials. 2020; 10(4):656. 3. De Koker S, De Geest BG, Cuvelier C. et al. In vivo Cellular Uptake, Degradation, and Biocompatibility of Polyelectrolyte Microcapsules. Adv Funct Mater. 2007;17:3754-63 4. Svenskaya Y, Garello F, Lengert E, Kozlova A, Verkhovskii R, Bitonto V, Ruggiero MR, German S, Gorin D, Terreno E. Biodegradable polyelectrolyte/magnetite capsules for MR imaging and magnetic targeting of tumors. Nanotheranostics 2021; 5(3):362-377. doi:10.7150/ntno.59458.

Image/Figure:

https://s3.amazonaws.com/amz.xcdsystem.com/1E8A4501-BB41-A02A-1D3B9882B798BFAA_abstract_File10351/GA63_ImageFigure_0511055202.png

Image/Figure Caption: Figure 1. A) Comparison of T2 signal change in the mice tumors with and without magnet application following sample S administration. (B) Representative T2-weighted axial MR images of mice acquired before (pre) and 1 hour after the injection. Tumors are marked with blue circles and presented in pseudo colors. Figure 2. A) Comparison of T2 signal change in the mice tumors with and without magnet application following sample C6S administration. (B) Representative T2-weighted axial MR images of mice acquired before (pre) and 1 hour after the injection. Tumors are marked with blue circles and presented in pseudo colors.

Full Name of Abstract's 1st Author : Francesca Garello

First Name: Francesca

Last Name: Garello

Email: francesca.garello@unito.it

Organization: Molecular and Preclinical Imaging Centers, Department of Molecular Biotechnology and Health Sciences, University of Torino

Country: Italy

ID: GA64
Non-invasive blood half-life determination of a fluorinated nanoemulsion by 19F MRS

Francesca Garello, Molecular and Preclinical Imaging Centers, Department of Molecular Biotechnology and Health Sciences, University of Torino, francesca.garello@unito.it

---

Category: New Chemistry, Materials & Probes

Abstract Body : Introduction The blood half-life time of some fluorinated systems has been already evaluated in the past.1,2 However, invasive techniques consisting of blood collection followed by ex-vivo 19F Magnetic Resonance Imaging (MRI)/Magnetic Resonance Spectroscopy (MRS) were applied. The low sensitivity of the method, in fact, requires the collection of large blood volumes, reducing the sampling and the time window in which the blood clearance can be studied. In the present work, an innovative and non-invasive method to estimate the blood half-life of a perfluorocarbon-based compound is presented. Methods C57BL/6J healthy mice were anesthetized and a catheter was inserted into the tail vein. The mice were positioned into a 7 T Bruker MRI scanner. Allocation of animals in the scanner was performed accurately to ensure that positioning and imaging could be consistent through all imaging sessions. A perfluorocarbon-based nanoemulsion (PFCE-NE, with particle mean size around 135 nm) was prepared by sonication3 and injected via the tail vein (1 mmol/kg b.w). Immediately after the injection, 19F MR spectra were acquired every 43 s for 1h. Additional spectra were acquired 3,24, 48, and 72 h after the injection. A standard reference tube containing trifluoroacetic acid (TFA) was used to normalize the signal acquired during each imaging session. The same procedure was carried out 10 minutes after the intravenous administration of empty liposomes, to check if any variations in the blood half-life of PFCE-NE could be detected. Empty liposomes, in fact, are expected to partially saturate the reticuloendothelial system (RES system),4 thus allowing longer circulation time for the PFCE-NE. Results/Discussion Since no extravasation of fluorinated particles has been reported in the brains of healthy mice, by placing in the volume coil only the head of the animal, all the signal detected by 19F MRI/MRS merely referred to the particles circulating in blood vessels. In this way, a large amount of data can be acquired, performing a precise sampling. The acquired spectra were integrated, and the resulting values were expressed in terms of % injected dose and plotted against time. Data obtained were fitted with a bi-exponential fitting curve. Resulting blood half-life times were respectively t1/2 fast = 46 min and t1/2 slow = 11.4 h, R2 = 0.99 (Figure 1), comparable to that reported for fluorinated liposomes (8.6–12.8 h).1,2 When liposomes were pre-injected to saturate Kupffer cells, blood circulating PFCE-NE was significantly higher only in the first hours post-injection (82.3 vs. 60.4% of the injected dose, 3 h post PFCE-NE injection, p Conclusions The 19F-MRS method herein proposed for determining the blood half-time of fluorine-based systems in vivo has the advantage of allowing an assiduous sampling, for long time windows and without blood collection. This method could be applied to a wide range of fluorinated compounds and systems. However, in order to obtain a valid measurement, the absence of extravasation in the central nervous system of healthy mice is required. Acknowledgement The authors acknowledge the

Italian Ministry of Research for FOE contribution to the Euro-BioImaging MultiModal Molecular Imaging Italian Node (www.mmmi.unito.it).

References: References [1] Santaella, C, Frézard, F, Vierling, P, Riess, J.G. Extended in Vivo Blood Circulation Time of Fluorinated Liposomes. FEBS Lett. 1993, 336, 481–484 [2] Vierling, P.; Santaella, C.; Greiner, J. Highly Fluorinated Amphiphiles as Drug and Gene Carrier and Delivery Systems. J. Fluor. Chem. 2001, 107, 337–354. [3] Garello F, Boido M, Miglietti M, Bitonto V, Zenzola M, Filippi M, Arena F, Consolino L, Ghibaudi M, Terreno E. Imaging of Inflammation in Spinal Cord Injury: Novel Insights on the Usage of PFC-Based Contrast Agents. Biomedicines. 2021; 9(4):379. [4] Liu, T.; Choi, H.; Zhou, R.; Chen, I.-W. RES Blockade: A Strategy for Boosting Efficiency of Nanoparticle Drug. Nano Today 2015, 10, 11–21.

Image/Figure:

https://s3.amazonaws.com/amz.xcdsystem.com/1E8A4501-BB41-A02A-1D3B9882B798BFAA_abstract_File10351/GA64_ImageFigure_0511062052.png

Image/Figure Caption: Figure 1 Blood half-life time calculation of PFCE-NE in healthy mice carried out by 19F MRS (n = 3). Data points fitted a bi-phasic exponential decay (R2 = 0.99). Figure 2 Blood clearance of PFCE-NE with (green squares) or without (black circles) pre-injection of liposomes in order to pre-saturate Kupffer cells, calculated by 19F MRS in healthy mice (n = 6, * $p < 0.05$).

Full Name of Abstract's 1st Author : Francesca Garello

First Name: Francesca

Last Name: Garello

Email: francesca.garello@unito.it

Organization: Molecular and Preclinical Imaging Centers, Department of Molecular Biotechnology and Health Sciences, University of Torino

Country: Italy

ID: GA65
Multicenter experience in >1900 patients of the surgical benefits of hybrid tracers in image-guided surgery

Tessa Buckle, Leiden University Medical Center, t.buckle@lumc.nl

---

Category: Oncology

Abstract Body : Introduction: Hybrid image-guided surgery concepts using combined radio- and fluorescence-image guidance are increasingly gaining interest. However, most of these efforts are pursued in the preclinical setting or in small first-in-human trials only. The bimodal tracer ICG-99mTc-nanocolloid has already been extensively applied at multiple clinical sites in sentinel node (SN) biopsy procedures. This study aimed to evaluate if and how hybrid approaches based on ICG-99mTc-nanocolloid can help realize improvements beyond the current state-of-the-art of radioguided approaches. Methods: 1910 patients that underwent SN procedures guided by ICG-99mTc-nanocolloid (500 Prostate, 700 penis, 60 vulva, 20 breast, 20 cervical, and 590 head and neck cancer (melanoma and oral cavity) cancer patients) were retrospectively included. Preoperative SNs were identified based on lymphoscintigraphy and single-photon emission computed tomography combined with computed tomography (SPECT/CT). Intraoperatively, SNs were detected via gamma tracing and fluorescence imaging. The use of hybrid guidance was compared to conventional radioguidance methods based on results obtained in the same patient. Outcome was based on reported surgical complications, overall survival, LN recurrence free survival (5yr follow up), and false negative rates (FNR). Results: Interim analysis of all combined results for prostate, penile, vulva, breast and head and neck cancer showed that between 98 and 100% of preoperatively identified SNs could be intraoperatively detected with a combination of radio- and fluorescence guidance. The synergistic hybrid approach yielded enhanced intraoperative find rates. Herein radioguidance allowed rough indication of the location of the SN, while fluorescence provided visual validation of the exact location of the SN and accurate SN resection. Furthermore, identification of aberrant drainage patterns outside the standard dissection template (revealed in 29.4% of patients, containing metastases in 22.2% of cases) allowed adaptation of the resection template during surgery. Inability to intraoperatively detect a radioactive signal (in 2% of preoperatively defined SNs) was linked to low tracer uptake and radioactive decay. Overall, the preoperative SPECT/CT roadmap was shown to be indispensable for accurate guidance towards the SNs. Use of ICG-99mTc-nanocolloid was not associated with increased risk of postoperative complications (Clavidien-Dindo >- II, $p>0.041$) and no tracer-related (allergic) reactions were reported. No significant difference FNR or overall operation time was seen, compared to the routine radioguided approach. At 5 yr follow up the hybrid approach revealed lower rates of biochemical recurrence (0.79, 95%CI 0.63-0.98) and clinical recurrence (HR 0.76, $p=0.035$). Conclusion: Large scale implementation of the hybrid SN tracer ICG-99mTc-nanocolloid, indicates that intraoperative fluorescence imaging complements preoperative lymphoscintigraphy/ SPECT/CT as well as intraoperative gamma tracing. This helps make detailed nodal identification more intuitive for the operating surgeon.

First Name: Tessa

Last Name: Buckle

Email: t.buckle@lumc.nl

Organization: Leiden University Medical Center

Country: Netherlands

ID: GA66
Radiological Evaluation of Implanted Materials for Long-term Biomedical Monitoring using Nanoparticle Contrast Agents

Kendell Pawelec, Michigan State University, paweleck@msu.edu

Category: Bioengineering, Synthetic Biology and Basic Biology

Abstract Body : Implantable medical devices from polymeric materials have been developed to stabilize and repair tissue after trauma or disease. While their use is widespread, it remains difficult to evaluate devices after implantation to ensure proper positioning and determine subsequent damage to the device, potentially preventing life-threatening complications. Incorporating radiopaque materials into device design might improve clinical functionality by allowing in situ monitoring by radiologists. Polymers visible in computed tomography (CT) and magnetic resonance imaging (MRI) have been made by chemically reacting radiopaque elements directly to the polymer chain, but this can negatively affect other materials properties [1]. In contrast, nanoparticles offer a facile way of adding radiopacity in a variety of imaging modalities [2-3]. This study was designed to assess the utility of nanoparticle contrast agents for improving radiological assessment of implantable devices, in a standard clinical setting, with three common imaging modalities: CT, MRI, and ultrasound. Methods: To mimic the range of devices available, phantoms from hydrophobic poly(lactide co-glycolide)(PLGA) films and hydrophilic agarose gels were constructed, with and without CT- visible TaOx (50mM) and clinically available MRI-visible Fe3O4 (Vivotrax, 1mM) nanoparticles. Some phantoms were purposely damaged by nick or transection prior to implantation into ex vivo tissue (lamb shanks) along with sham controls. The tissue + phantoms were imaged with CT, MRI and ultrasound, using clinical protocols and machines. The blinded data sets were evaluated independently by radiologists to assess whether 1) implants were present, 2) determine the implant type, and 3) diagnose whether the implant was damaged or intact. Results & Discussion: In CT and MRI, only implants incorporating a nanoparticle matching the imaging modality were easily visible, while ultrasound was agnostic to nanoparticle incorporation. Radiologists were far more likely to successfully identify implant placement and type when nanoparticles were present. This correlated to a success rate of >90% with nanoparticles present compared to a 85% when a nanoparticle contrast agent was present. The imaging results were validated in a physiologically relevant model, by implanting films as nerve wraps. Conclusion: Contrast agents were critical for the ability of radiologists to identify implant features. The capability of monitoring implants accurately over time provides radiologists the opportunity to identify potential device damage before catastrophic failure, which can expose the patient to life-threatening consequences. With benefits and drawbacks to all three clinical imaging modalities, future implants should be engineered to be visible in the imaging modality which best fits with the tissue being treated, the physical location of the implant, and the type of information which is required.

References: [1] Erol, A.; Rosberg, D. B. H.; Hazer, B.; Goencue, B. S. Biodegradable and biocompatible radiopaque iodinated poly-3- hydroxy butyrate: synthesis, characterization and in vitro/in vivo xray visibility. Polym. Bull. 2020, 77, 275−289. [2] Baetke, S. C.; Lammers, T.;

Kiessling, T. Applications of nanoparticles for diagnosis and therapy of cancer. Br. J. Radiol. 2015, 88, No. 20150207. [3] Wolf, F.; Paefgen, V.; Winz, O.; Mertens, M.; Koch, S.; Gross-Weege, N.; Morgenroth, A.; Rix, A.; Schnoering, H.; Chalabi, K.; Jockenhoevel, S.; Lammers, T.; Mottaghy, F.; Kiessling, F.; Mela, P.MR and Pet-CT monitoring of tissue-engineered vascular grafts in the ovine carotid artery. Biomaterials 2019, 216, No. 119228.

Image/Figure:

https://s3.amazonaws.com/amz.xcdsystem.com/1E8A4501-BB41-A02A-1D3B9882B798BFAA_abstract_File10351/GA66_ImageFigure_0511101619.jpg

Image/Figure Caption: Figure: Radiological evaluation of phantoms with nanoparticle contrast agent (Fe3O4 or TaOx), mimicking biomedical devices. (a) Hydrophilic nanoparticles embedded in agarose (schematic) to mimic a gel for cartilage repair. Gels, visualized macroscopically and via 3D CT reconstructions, were implanted intact, cut or gouged. (b) Hydrophobic nanoparticles were added to poly(lactide co-glycolide) films (schematic) to simulate nerve wraps. Porous films (imaged via white light microscopy) were wrapped around tissue to create intact and damaged constructs (3D reconstructions and macroscopically). (c) Phantoms were implanted into a lamb shank and scanned with (d) CT, (e) MRI and (f-g) ultrasound, for independent evaluation by radiologists. (d) Phantoms with TaOx nanoparticles were visible in CT, while (e) phantoms with Fe3O4 nanoparticles appeared dark in MRI. Images in (d-e) are of the same lamb shank with inset transverse views of a gel and film; white arrows: implants without nanoparticles, blue arrows: Fe3O4 implants, orange arrows: TaOx implants. Ultrasound images of a representative (f) film and (g) gel with arrows marking implant location. Scale bars: 5 mm.

First Name: Kendell

Last Name: Pawelec

Email: paweleck@msu.edu

Organization: Michigan State University

Country: United States

ID: GA67
Cholesterol-depleting drugs for HER2-targeted radioimmunotherapy of heterogenous gastric cancer

Yi Rao, MSKCC, raoy@mskcc.org

Category: Oncology

Abstract Body : In 2018, more than 1,000,000 new cases of esophagogastric (EG) cancer were diagnosed and 783,000 death worldwide 1. Human epidermal growth factor receptor 2 (HER2) overexpression occurs in 10 — 20% of EG and associates with poor overall patient survival 2. HER2-targeting trastuzumab is used as first-line therapy to treat HER2+ EG cancer patients. However, intrinsic and acquired resistance to trastuzumab can develop over time. Although HER2 exists in both plasma membrane-bound and cytosolic forms, only cell-surface receptors are viable targets for trastuzumab therapy. Caveolin1 (CAV1), which anchors on plasma membrane cholesterol, can internalize and degrade surface HER2. In previous studies, cholesterol-lowering drugs were shown to temporarily modulate CAV1 levels, which further result in ~2-fold increase in half-lives of cell surface-associated HER2 in genetically engineered NCI-N87 cells 3. In the present study, we demonstrated that increasing doses of lovastatin from 2.1 – 8.3 mg/kg temporarily elevate [89Zr]Zr-DFO-trastuzumab uptake up to ~2-fold compared to saline treated control group in NCI-N87 xenografts. Furthermore, we have shown that the increase in antibody-tumor binding was accompanied by the depletion of tumoral cholesterol and CAV1 while enhancement of HER2 density at the cell surface via immunofluorescence imaging. In addition, tumor-targeted radionuclide approaches are less susceptible to tumors' resistance compared to receptor-targeted therapy. We radiolabeled Trastuzumab-DOTA conjugate with 177Lu in 250 mM NH4Ac at pH 5.5 with > 99% purity and > 90% stability in serum for up to 6 days for endoradiotherapy. Herein, the combination of radioimmunotherapy and modulating cell membrane HER2 with lovastatin could enhance therapeutic efficacies for heterogeneous EG resistant to trastuzumab-based treatments.

References: 1. Bray, F., et al. Global cancer statistics 2018: GLOBOCAN estimates of incidence and mortality worldwide for 36 cancers in 185 countries. CA: A Cancer Journal for Clinicians 68, 394-424 (2018). 2. Iqbal, N. & Iqbal, N. Human Epidermal Growth Factor Receptor 2 (HER2) in Cancers: Overexpression and Therapeutic Implications. Mol Biol Int 2014, 852748 (2014). 3. Pereira, P.M.R., et al. Caveolin-1 mediates cellular distribution of HER2 and affects trastuzumab binding and therapeutic efficacy. Nature Communications 9(2018).

Full Name of Abstract's 1st Author : Yi Rao

First Name: Yi

Last Name: Rao

Email: raoy@mskcc.org

Organization: MSKCC

Country: United States

ID: GA68
Predictive Models for Nonhuman Primate COVID-19 Imaging Research Using Machine Learning

Jeffrey Solomon, Clinical Monitoring Research Program Directorate, Frederick National Laboratory for Cancer Research sponsored by the National Cancer Institute, jeffrey.solomon@nih.gov

---

Category: Computational & Data Science

Abstract Body : Background The coronavirus 19 (COVID-19) pandemic, has resulted in more than 153 million confirmed cases and over 3 million deaths [1], along with morbidities. Infection of the SARS-CoV-2 virus produces a wide variability of outcomes, ranging from asymptotic to loss of life. Predicting the occurrence and severity of COVID-19 is an important area of research. COVID-19 disease is primarily a respiratory one. Computed tomography (CT) imaging of the lungs has elucidated aspects of the disease including peripheral ground-glass opacities, crazy-paving pattern and consolidation that relate to severity. Polymerase chain reaction (PCR) testing has become ubiquitous for detection of disease, but CT imaging can demonstrate abnormalities in the lungs prior to positive PCR results [2]. In this study, a combination of CT imaging radiomic features and clinical pathology features were selected as input to machine learning based (ML-based) predictive models to classify SARS-CoV-2 exposure versus mock exposure in nonhuman primates (NHPs). Methods Across three experiments, 12 crab-eating macaques (Macaca fasciularis) were exposed to SARS-CoV-2 and another 12 were instilled with vehicle only (mock). The macaques were observed for development of clinical signs of infection. Scans by CT (Gemini PET/CT, Philips Healthcare) were performed prior to exposure and on Day 2, Day 4, Day 6 and Day 8. Blood sampling, performed on the same days as CT scanning, provide concomitant serum chemistry, hematology and immunology laboratory values. CT and clinical pathology data from Day 2, Day 4 and Day 6 were selected for building machine learning models. The lung field was automatically segmented from the CT scan using a deep learning-based method that was initially developed for liver and modified for lungs [3]. Using PyRadiomics within 3D slicer, 110 radiomic features were extracted from the lung [4]. 61 clinical pathology features were collected. Due to the limited number within this study's sample set (72; 24 NHPs with three timepoints each), the minimum redundancy, maximum relevance (MRMR) [5] feature selection was employed to reduce the features to the 10 most relevant and least redundant for each category (radiomics, clinical pathology). Multiple ML algorithms were trained (Figure 2) using these selected features to determine which had the best predictive power. Eighty percent of the samples were used for training while the remainder was reserved for testing. During training, six-fold cross validation was performed, and the following measurements of predictive power were estimated: accuracy, sensitivity, and specificity. Results While disease severity was mild, showing no cage-size changes in behavior, Day 2, Day 4 and Day 6 demonstrated the largest abnormalities on CT. Figure 1 shows an axial CT section of the lung with the deep learning-based lung segmentation in blue and lesion segmentation in cyan [3]. Figure 2 shows the 10 radiomic and clinical pathology features selected by the MRMR algorithm and the overall accuracy, sensitivity and specificity of the 5 machine learning algorithms

evaluated. Random forest using radiomic selected features had an accuracy of 92.86%, sensitivity of 100% and specificity of 85.71%. Conclusions The SARS-CoV-2 virus exposure elicited mild disease in crab-eating macaques, making prediction analysis difficult. The selected radiomic features outperformed the selected clinical pathology features in predicting which samples were from SARS-CoV-2-exposed versus mock exposed NHPs. The random forest ML model outperformed the four other algorithms evaluated. Future efforts will focus on combining radiomic and clinical pathology features into a single predictive model as well as exploring additional feature selection techniques and ML models, such as least absolute shrinkage and selection operator (LASSO). Furthermore, we hope to use these observations to interrogate the predictive relationships between imaging features and disease heterogeneity and outcome, including histopathology, as more severe disease models become available.

References: 1. https://covid19.who.int, May 5, 2021 2. Q. Cai et al, A model based on CT radiomic features for predicting RT-PCR becoming negative in coronavirus disease 2019 (COVID-19) patients, BMC Med Imaging, 20(118), 1-10 (2020). 3. S. Reza et al, Deep Learning for Automated Liver Segmentation to Aid in the Study of Infectious Diseases in Nonhuman Primates, Academic Radiology, 14 September, 2020. http://doi.org/10.1016/j.acra.2020.08.023 4. J.J.M. Griethuysen, et al, Computational Radiomics System to Decode the Radiographic Phenotype. Cancer Research, 2017, 77(21), e104–e107. https://doi.org/10.1158/0008-5472.CAN-17-0339 5. H. Peng, et al, Feature Selection Based on Mutual Information: Criteria of Max-Dependency, Max-Relevance, and Min-Redundancy, IEEE Transactions on Pattern Analysis and Machine Learning, Vol. 27, No. 8, August 2005.

Image/Figure: https://s3.amazonaws.com/amz.xcdsystem.com/1E8A4501-BB41-A02A-1D3B9882B798BFAA_abstract_File10351/GA68_ImageFigure_0511104700.docx

Image/Figure Caption: Figure 1. Axial CT section of NHP lung. Blue and green borders represent the deep learning-based automated whole lung and lung lesion segmentation respectively. Figure 2. Table illustrates list of top 10 selected features using mRMR technique from radiomic and clinical pathology data sets. Accuracy measurements for 5 machine learning algorithms (linear discriminant analysis (lda), k-nearest neighbor (knn), random forest (rf), support vector machine (svm) and classification and regression trees (cart)) are shown on the right. Random forest (rf) classifier had the best performance. MIP1 alpha is macrophage inflammatory protein; IL is interleukin; IFN is interferon.

First Name: Jeffrey

Last Name: Solomon

Email: jeffrey.solomon@nih.gov

Organization: Clinical Monitoring Research Program Directorate, Frederick National Laboratory for Cancer Research sponsored by the National Cancer Institute

Country: United States

ID: GA69
Adventures in Radiochemistry

Peter Scott, University of Michigan, pjhscott@umich.edu

Category: New Chemistry, Materials & Probes

Abstract Body : Since the 1990s, PET infrastructure at academic medical centers and commercial nuclear pharmacies has been put in place primarily for the production, distribution and scanning of [18F]fludeoxyglucose. However, the PET landscape is rapidly changing and, in the last decade, >10 new PET radiopharmaceuticals have received FDA approval including a number of imaging agents with theranostic applications at the same time as research use of PET to support drug disocvery is rapidly expanding. This is creating an unprecedented demand for PET imaging which is beginning to stress exisiting infrastructure and present new challenges for PET drug manufacturers. Radiochemists need to produce larger numbers of more diverse radiotracers laebeld with different radionuclides each day (e.g. 11C, 18F, 64Cu, 68Ga) for clinical use at the same time as they are asked to label more complex chemical space (e.g. proprietary pharmaceutical assets, new imaging targets, and radiopharmaceutical discovery). At the same time, cGMP is increasing the regulatory burden, complexity and cost of PET drug manufacturing. Addressing these challenges needs fundamental new approaches and technology for conducting PET radiochemistry and our group is motivated to simplify the design, syntheses and quality control of PET radiopharmaceuticals. This presentation will describe a mutlipronged approach to meeting todays radiopharmaceutical production demands including translation of the latest cyclotron targets for production of high demand radionuclides like 68Ga [1], new approaches to radiochemistry automation [2], radiochemistry methodology allowing new chemcial space to be radiolabeled (e.g. late-stage radiofluorination) [3], approaches for streamlined quality assurance and regulatory compliance [4], and application of machine learning and artificial intelligence to radiochemistry in order to streamline the design and synthesis of new PET drugs [5]. The latest developments in each of these priority areas will be described, as well as the regualtory strategies for translation of each into clinical use including, for example, compatibility with current Good Manufacturing Practice (cGMP) and current Good Machine Learning Practice (cGMLP).

References: [1] Rodnick et al., EJNMMI Radiopharm Chem, 2020, 4, 24. [2] Frank et al., EJNMMI Radiopharm Chem, 2019, 5, 25. [3] Wright et al., Clin. Trans. Imaging 2020, 8, 167–206. [4] Jackson et al., EJNMMI Radiopharm Chem, 2020, 5, 24. [5] Webb et al., PET Clinics, 2021, In Press.

Image/Figure:

https://s3.amazonaws.com/amz.xcdsystem.com/1E8A4501-BB41-A02A-1D3B9882B798BFAA_abstract_File10351/GA69_ImageFigure_0511112149.png

Image/Figure Caption: Artificial intelligence and the radiochemistry workflow

First Name: Peter

Last Name: Scott

Email: pjhscott@umich.edu

Organization: University of Michigan

Country: United States

ID: GA70

Longitudinal Characterization of Biohybrid Tissue-Engineered Vascular Grafts Scaffold Resorption and Tissue Remodelling via Molecular MR and US

Elena Rama, RWTH Aachen University, erama@ukaachen.de

Category: Bioengineering, Synthetic Biology and Basic Biology

Abstract Body : The longitudinal monitoring of the remodelling and the pathological dysfunctions of implanted vascular prosthesis remains challenging. To overcome this issue, novel approaches toward the incorporation of MR contrast agents into the textile scaffold of vascular prostheses have already been explored [1,2]. Nonetheless, the transition from late-in-vitro bioreactor maturation to early-in-vivo implantation of vascular implants remains inadequately investigated. Therefore, this study aimed to further develop in vitro non-invasive imaging methods to monitor the passage between these two critical phases. For this purpose, we developed a biohybrid tissue-engineered vascular graft (TEVG) consisting of biodegradable poly(lactic-co-glycolic acid) (PLGA) fibers labeled with ultrasmall superparamagnetic iron oxide nanoparticles (USPIO), non-degradable polyvinylidene fluoride (PVDF) scaffold, and fibrin gel containing endothelial and smooth muscle cells. The degradation of the USPIO-labeled PLGA fibers was longitudinally monitored via MRI. Moreover, the deposition of newly synthesised extracellular matrix (ECM) components, as replacement of the degraded PLGA fibers, was assessed in TEVGs by molecular MR (mMR) using elastin- and collagen type I-targeted Gd-containing MR molecular probes (Gd-DTPA-ESMA and EP-3533) in comparison to untargeted Gd-DTPA (Magnevist). The tissue response was additionally investigated in terms of endothelial coverage by molecular US (mUS) using RGD-targeted poly(butyl cyanoacrylate) microbubbles (RGD-MB) targeting αvβ3 integrin as a marker of inflammatory reaction and thrombus formation. RGD-MB binding was longitudinally evaluated in TEVGs and compared to RAD-control MB used as control. A competition study was also performed by injecting free RGD before the injection of RGD-MB. The longitudinal monitoring of the degradation of USPIO-labeled PLGA fibers was performed by embedding the fiber sheets in fibrin gel and incubating them at 37°C for 8 weeks and at 70°C for 3 weeks. Furthermore, their degradation was evaluated in hybrid conditions. First, USPIO-labeled PLGA fibers were monitored in combination with the PVDF non-degradable scaffold for 3 weeks and, subsequently, combined with cellular components for 7 days (A). Quantitative R2 analysis reflects the correlation between the degradation of the USPIO-labeled PLGA fibers and the decrease of their relaxation rate values over time due to the release of the USPIO. Interestingly, the degradation rate of the PLGA fibers accelerated in combination with the PVDF scaffold and, subsequently, became even faster in combination with cells (B-C). mMR monitoring of the deposition of newly synthesised ECM components showed no Gd-DTPA-ESMA binding in TEVGs that was, furthermore, confirmed through immunofluorescence microscopy (D,J). A 3-fold +/- higher binding of the Gd-DTPA-ESMA probe was instead detected in human umbilical arteries (HUA) used as positive control. In contrast, a strong signal, given by the binding of EP-3533 to collagen type I, was observed in TEVGs and, subsequently, validated by histology(E-F,J). αvβ3 integrin expression was longitudinally monitored via mUS after 0, 3, and 14 days of bioreactor maturation of the TEVGs

(G). Of great relevance, no difference between RGD-MB and RAD-control MB binding was observed showing that the shear stress used during the bioreactor conditioning of the TEVGs did not cause distress to the endothelial cells (H). Therefore, TNF-α was used for pre-activating the endothelium and to mimic an inflammatory state. In this respect, RGD-MBs showed a 70-fold +/- higher binding expressed as differential targeted enhancement (d.T.E.) (I). Further histological analyses confirmed the expression of αvβ3 integrin only after TNF-α preconditioning (J). Herein, we present in vitro and non-invasive imaging approaches to monitor the late-in-vitro maturation phase as well as the early-in-vivo implantation phase of biohybrid tissue-engineered vascular grafts. Moreover, our findings demonstrate the replacement of the PLGA fibers by deposition of collagen type I and the detectability of endothelial inflammation via RGD-MB targeting. To conclude, the presented imaging methods may be highly valuable to foster the clinical translation of TEVGs.

References: [1] Wolf, Frederic, et al. "MR and PET-CT monitoring of tissue-engineered vascular grafts in the ovine carotid artery." Biomaterials 216 (2019): 119228. [2] Mertens, Marianne E., et al. "USPIO-labeled textile materials for non-invasive MR imaging of tissue-engineered vascular grafts." Biomaterials 39 (2015): 155-163.

Image/Figure:

https://s3.amazonaws.com/amz.xcdsystem.com/1E8A4501-BB41-A02A-1D3B9882B798BFAA_abstract_File10351/GA70_ImageFigure_0511114144.png

Image/Figure Caption: Figure 1: Longitudinal MR and US monitoring of USPIO-labeled PLGA fibers degradation and tissue remodelling. A: MR longitudinal investigation of USPIO-labeled PLGA fibers combined with the PVDF tubular structure and cell components. Quantitative R2 analyses reflect the PLGA fibers degradation through the decrease over time of their relaxation rate values (B) and show the higher detectability of the degradation process in comparison to the unlabeled control (C). D: ECM characterization via Gd-DTPA-ESMA and EP-3533 in comparison with an untargeted Gd-DTPA probe (Magnevist). E-F: No Gd-DTPA-ESMA binding and, therefore, no elastin is observed in TEVG. In contrast, strong EP-3533 binding to collagen type I is observed in TEVG (E) and HUA (F). G: TEVG molecular US investigation comparing RGD-MB to RAD-control MB binding in untreated and TNF-α treated TEVGs. Images of the competition study are also shown. H: Longitudinal US monitoring of untreated TEVG shows no difference between RGD-MB and RAD-control MB binding, and no changes in d.T.E. are observed in RGD-MB binding after free-RGD pre-injection. I: 70-fold higher binding for RGD-MBs is observed after TNF-α treatment of TEVGs. J: Immunofluorescence representative images of elastin, collagen type I, and αvβ3 integrin expression in TEVGs and HUA. (*p < 0 .05, **p < 0 .001 and ***p < 0 .0001) (Stars indicate the TEVGs lumen).

Full Name of Abstract's 1st Author : Elena Rama

First Name: Elena

Last Name: Rama

Email: erama@ukaachen.de

Organization: RWTH Aachen University

Country: Germany

ID: GA71

Pulsed Focal ultrasound as a non-invasive method to deliver exosomes in the brain/stroke

Ahmet Alptekin, Augusta University, aalptekin@augusta.edu

Category: Cardiovascular & Pulmonary

Abstract Body : Exosomes, a component of extracellular vesicles, are shown to carry important small RNAs, mRNAs, protein, and bioactive lipid from parent cells and are found in most biological fluids. Investigators have demonstrated the importance of mesenchymal stem cells derived exosomes in repairing stroke lesions. However, exosomes from endothelial progenitor cells have not been tested in any stroke model, nor has there been an evaluation of whether these exosomes target/home to areas of pathology. Targeted delivery of intravenous administered exosomes has been a great challenge, and a targeted delivery system is lacking to deliver naïve (unmodified) exosomes from endothelial progenitor cells to the site of interest. Pulsed focused ultrasound is being used for therapeutic and experimental purposes. There has not been any report showing the use of low-intensity pulsed focused ultrasound to deliver exosomes to the site of interest in stroke models. In this proof of principle study, we have shown different parameters of pulsed focused ultrasound to deliver exosomes in the intact and stroke brain with or without intravenous administration of nanobubbles. The study results showed that administration of nanobubbles is detrimental to the brain structures (micro bleeding and white matter destruction) at peak negative pressure of >0.25 megapascal , despite enhanced delivery of intravenous administered exosomes. However, without nanobubbles, pulsed focused ultrasound enhances the delivery of exosomes in the stroke area without altering the brain structures.

Full Name of Abstract's 1st Author : Ahmet Alptekin

First Name: Ahmet

Last Name: Alptekin

Email: aalptekin@augusta.edu

Organization: Augusta University

Country: United States

ID: GA72
A Proof-of-concept study: Simultaneous Hyperpolarized 129Xe MRI and [15O]-water PET Measurements

Ramanpreet Sembhi, The University of Western Ontario, rsembhi@uwo.ca

---

Category: Neuroscience

Abstract Body : INTRODUCTION: Inhaled hyperpolarized (HP) 129Xe magnetic resonance imaging (MRI) is a non-invasive imaging method, which is currently used to measure lung structure and function.1,2 This MRI approach provides a way to obtain simultaneous ventilation/perfusion (V/P) lung measurements of functional gas exchange within the lungs due to high natural solubility of xenon in lung tissue compared to other imaging gases. Due to various physical properties of the 129Xe isotope, it can serve as a new probe for brain blood flow, grey and white matter mapping3,4 and functional measurements. These measurements are possible due to distinct and large range of chemical shifts (~200ppm) of 129Xe when residing within lung tissue, brain tissue and red blood cells compared to the gas phase. 129Xe-based imaging aims to improve sensitivity where traditional MRI may fall short, and by reaching beyond the resolution limitations of positron emission tomography (PET). [15O]-water PET is the gold standard imaging method for determining cerebral perfusion.5,6 In this study, simultaneous 129Xe-based MRI and [15O]-water PET images were collected and compared. METHODS: For the initial validation phase in phantoms, in a 60mL plastic syringe, 30mL of hyperpolarized 129Xe gas was dissolved in (30mL) of [15O]-water solution. After dissolving, all leftover xenon gas was removed from the syringe. Hyperpolarized 129Xe gas was obtained from a turn-key, spin- exchange polarizer system (Polarean 9820 129Xe polarizer). 129Xe dissolved phase images were acquired in a 3T PET/MRI (Siemens Biograph mMR) scanner with RF coil tuned to 34.09 MHz. A fast Gradient Recalled Echo sequence was utilized using the following parameters: Matrix Size=104x48; Slice thickness=250mm; TE/TR=2.04/20ms; BW=660Hz/pixel; Flip angle= 110 (a Constant Flip Angle approach was used); and FOV= 150x150mm2. [15O]-water PET data (half-life time of 2min; Matrix size=344x344; 10x60sec frames and OSEM with 3 iterations) were acquired simultaneously with 129Xe MRI for 600sec using the integrated PET system in a 3T PET/MRI. RESULTS: Figure 1 A, B, C, D respectively shows two consecutive 2D axial 129Xe MRI images and two (2D and 3D) [15O]-water PET images acquired simultaneously. 129Xe/PET images indicate that the diameter of the phantom from both PET and MRI images are similar clearly indicating the feasibility of the simultaneous hyperpolarized 129Xe MRI and [15O]-water PET measurements. 129Xe images demonstrate a sufficient SNR level suggesting that 3D 129Xe imaging is possible. DISCUSSION AND CONCLUSIONS: As per knowledge, this is the first ever demonstration of the simultaneous 129Xe MRI and [15O]-water PET scans. This demonstration will enable the next step, namely, in-vivo double tracer brain perfusion imaging. Important validation work for 129Xe-based brain perfusion techniques, directly and simultaneously with [15O]-water PET will be performed using a small animal model. The comparison results show similarity between both imaging modalities and tracers, moving towards the next step in validating the xenon imaging technique as a potential for brain perfusion measurement. The ability to use 129Xe as a

non-radioactive tracer, providing similar and complimentary information as [15O]-water PET may be a much more cost-effective alternative to PET for imaging stroke, brain cancer and other brain diseases and will significantly increase the number of the 129Xe MRI clinical applications.

References: 1 Kaushik, S. S. et al. Single-breath clinical imaging of hyperpolarized (129)Xe in the airspaces, barrier, and red blood cells using an interleaved 3D radial 1-point Dixon acquisition. Magn Reson Med 75, 1434-1443, doi:10.1002/mrm.25675 (2016). 2 Kaushik, S. S. et al. Probing the regional distribution of pulmonary gas exchange through single-breath gas- and dissolved-phase 129Xe MR imaging. J Appl Physiol (1985) 115, 850-860, doi:10.1152/japplphysiol.00092.2013 (2013). 3 Kershaw, J. et al. Confirming the existence of five peaks in 129Xe rat head spectra. Magn Reson Med 57, 791-797, doi:10.1002/mrm.21186 (2007). 4 Wakai, A., Nakamura, K., Kershaw, J. & Kanno, I. In vivo MR spectroscopy of hyperpolarized Xe-129 in rat brain. International Congress Series 1265, 139-143, doi:10.1016/j.ics.2004.04.063 (2004). 5 Fan, A. P., Jahanian, H., Holdsworth, S. J. & Zaharchuk, G. Comparison of cerebral blood flow measurement with [15O]-water positron emission tomography and arterial spin labeling magnetic resonance imaging: A systematic review. J Cereb Blood Flow Metab 36, 842-861, doi:10.1177/0271678X16636393 (2016). 6 Ssali, T., Anazodo, U. C., Thiessen, J. D., Prato, F. S. & St Lawrence, K. A Noninvasive Method for Quantifying Cerebral Blood Flow by Hybrid PET/MRI. J Nucl Med 59, 1329-1334, doi:10.2967/jnumed.117.203414 (2018).

Image/Figure:

https://s3.amazonaws.com/amz.xcdsystem.com/1E8A4501-BB41-A02A-1D3B9882B798BFAA_abstract_File10351/GA72_ImageFigure_0511120045.png

Image/Figure Caption: Figure 1. (A) and (B) shows Two consecutive 2D axial 129Xe MRI images obtained for xenon dissolved in [15O]-water inside the syringe phantom. The MRI data acquisition was synchronized with the PET data acquisition. The SNR of the first 129Xe image (A) is 80 and the SNR of the second 129Xe image (B) is 10. (C)2D axial and (D)3D [15O]-water PET images obtained with the syringe phantom.

First Name: Ramanpreet

Last Name: Sembhi

Email: rsembhi@uwo.ca

Organization: The University of Western Ontario

Country: Canada

ID: GA73
Bioluminescent Genetically Encoded Indicators for Molecular Imaging of Neuronal Activity

Eric Petersen, MICHIGAN STATE UNIVERSITY, PETE1346@MSU.EDU

Category: Neuroscience

Abstract Body : Objective: Genetically encoded optical sensors and advancements in microscopy have revolutionized the scientific toolbox used for answering complex biological questions especially in terms of studying brain activity. Most optical sensors currently used are based on fluorescence and are very useful for single cell imaging in superficial brain regions. However, there remains a need to develop new tools for reporting neuronal activity in vivo within deeper structures without the need for hardware to be implanted within the brain such as lenses or fibers. We expect this can be achieved by replacing the fluorescent elements of the existing biosensors with bioluminescent producing elements (Figure 1A). This will bypass the need of external light sources to illuminate the sensor and overcome limitations such as limited light penetration depth, light diffraction and tissue heating that are all associated with the excitation light used for fluorescent imaging. We are developing neurotransmitter and voltage indicators based on bioluminescent light emission that have robust changes in light output in response to neurotransmitter presentation or membrane depolarization that do not photobleach (figure 1B). The neurotransmitter indicators will allow neuroscientists to monitor activity associated with a specific neurotransmitter as it relates to behavior in a variety of psychiatric disorders. We are building on recent advancements in two fields: genetically encoded optical sensors for real-time sensing changes in neurotransmitter levels; and genetic evolution of new enzymes that produce biological luminescence at unprecedented intensities. Methods and Results: We have bioengineered the first bioluminescent neurotransmitter indicators using a multistep screening approach. First rational design using a variety of split luciferases and linker variants to fuse the luciferases to a sensing protein. Then an automated workflow to screen for improved variants in mammalian cells. The variants were cloned using Gibson assembly with primers that incorporate randomized amino acids in the linker regions between the two NanoLuc halves and the glutamate binding protein Glt1. Then used automation for high throughput mini preps and transfection of mammalian cells. Currently, we have produced the first bioluminescent neurotransmitter indicators by adapting sensing domains used in fluorescent indicators and incorporating bioluminescent producing luciferases. As a result, we created a BioLuminescent Indicator of the Neurotransmitter Glutamate (BLING). Using our protein evolution approach in mammalian cells, we were able to improve our BLINGs response by 2.5x from screening 1200 variants (Figure 1D). Our improved glutamate indicator demonstrated a 255% +/-50 increase in response to neurotransmitter presentation when expressed in mammalian cells (HEK cells), can successfully report changes in extracellular glutamate when used in a plate reader and outperforms the fluorescent sensors iGluSnFr and GCamP6 in plate reader assays (Figure 1C-E). Finally, to test the feasibility of imaging BLING we used real-time microscopy (Figure 1F and 1G) which demonstrated up to a 310% increase in light emission detectable at the single cell level. Conclusion: We expect these indicators to perform well for molecular imaging neuronal

activity in deep brain structures with imaging equipment that is readily accessible to researchers. We are also continuing with our protein engineering strategy to improve BLING, other neurotransmitter indicators, to develop improved voltage indicators and spectral variants. These indicators will be able to immediately benefit ongoing research efforts to study the mechanisms that give rise to a wide array of psychiatric disorders and provide researchers with significantly improved approaches to study neuronal activity at the level of the cell, network, and behaving animals longitudinally. Furthermore, since these reporters produce their own light, they can be used as activators for light sensitive proteins to carry out a variety of downstream functions within a cell.

Image/Figure:

https://s3.amazonaws.com/amz.xcdsystem.com/1E8A4501-BB41-A02A-1D3B9882B798BFAA_abstract_File10351/GA73_ImageFigure_0511124739.png

Image/Figure Caption: A. Schematic of the BioLuminescent Indicator of the Neurotransmitter Glutamate (BLING) with a split luciferase (blue) and glutamate sensing domain (tan) displayed on the cell surface. B. Comparison of bioluminescent vs fluorescent imaging in superficial and deep brain regions. Bioluminescence light is able to be detected because no excitation light is needed and there is nearly no background noise or autofluorescence. C. Trace of BLINGs response to glutamate when expressed in HEK cells using a plate reader. D. High throughput screening of BLING linker variants produced a new optimized BLING. E. Optimized BLING sensor has 2.5x the response amplitude compared to the parental BLING and outperforms existing fluorescent indicators of glutamate iGluSnFr response and the response of GCamp6m to calcium. F. Example trace of a single cell response to 1000uM glutamate addition at 120 seconds. G. Bioluminescent microscopy comparing background luminescence to luminescence with 1000uM glutamate.

Full Name of Abstract's 1st Author : Eric Petersen

First Name: Eric

Last Name: Petersen

Email: PETE1346@MSU.EDU

Organization: MICHIGAN STATE UNIVERSITY

Country: United States

ID: GA75
Utilizing Magnetogenetics to Control Optical Imaging Reporters

Connor Grady, Michigan State University, gradycon@msu.edu

Category: Bioengineering, Synthetic Biology and Basic Biology

Abstract Body : Objective: The creation of a novel synthetic circuit based on a "switch" that is controlled in a non-invasive manner can become a valuable tool for the fields of synthetic biology and molecular imaging. Many circuit designs rely on external light or the injection of a chemical to stimulate the circuit. These methods can be limited in their stimulation of systems due to light having poor penetration in tissue and chemicals lacking spatial and temporal control due to variability in diffusion and cellular uptake. A circuit activated by magnetic fields can overcome these challenges as fields are able to penetrate deep into tissue and create a homogenous stimulation to cells. The "switch" for this novel circuit design is based on the Electromagnetic Perceptive Gene (EPG; GenBank: MH590650.1) which was discovered in Kryptopterus vitreolus (glass catfish). When EPG is expressed in mammalian cells, electromagnetic fields (EMF) can elicit a measurable response in the cell 1. Here we introduce a novel method of controlling enzymes used in molecular imaging simply by applying EMF. Methods: All cloned constructs were produced using the EPG gene and Gibson Assembly creating fusion proteins attached to the C and N terminal of EPG. For bacterial expression we used pET101 plasmid and BL21 E. Coli and expression was induced using Magic Media (Thermo Fisher). For Mammalian cells expression we used pcDNA 3.1 plasmid and HeLa and HEK293T cells. FRET readings were done using VICTOR Nivo (Perkin Elmer), NanoLuc imaging was performed using IVIS (Perkin Elmer), and APEX2 was read using Cytation 5 (BioTek). Results: Utilizing Förester Resonance Energy Transfer (FRET) with NanoLuc and mVenus fused to either terminus of EPG, we observed in HeLa cells a change of 2-4% in N=15 wells the DF/F (change in ratio of mVenus to Nanoluc after stimulus) following constant static magnet stimulation in contrast to controls without stimulation in a single copy EPG (Persuasive data Figure P1A) and a 10-15% in N=15 wells an increase in a DF/F when two copies of EPG were cloned in tandem (double EPG; Persuasive data Figure P1B). An EPG split Nanoluc2 fusion protein was cloned using Gibson Assembly with the EPG fused inside of the split NanoLuc fragments. This construct was expressed in BL21 cells and measured using the IVIS with EMF induction from an electromagnet (~35 mTesla). Reads were taken every 10 seconds with an open filter for 10 minutes with stimulation period of constant EMF for 2 minutes after 2 minutes of initial reads. In this EPG split NanoLuc construct we observed a 40% increase in photon flux with cell lysates (Fig 1A) and 70% increase with whole cell Fig 1B during stimulation with EMF and decreased after EMF stimulation was removed. The effect of this protein has also shown promising results when fused to the split peroxidase APEX23. HEK 293FT cells that were stimulated for 30 minutes with a static magnet show an increase in enzyme activity over the non-stimulated control (Persuasive data Figure P2). Conclusion: We were able to demonstrate through FRET and a split protein approaches, the potential to control enzymes by using EPG as a "biological hinge" that allows bringing together two proteins or two parts of a split protein by remote EMF induction. This is the first step toward engineering a new platform

technology for remote control of enzyme activity with EMF that can be immensely beneficial for noninvasive molecular imaging.

References: 1 Krishnan, V. et al. Sci Rep 8, 8764, (2018). 2 Nelson, T. J. et al. Methods in enzymology 622, 55-66, (2019). 3 Han, Y. et al. ACS Chem Biol 14, 619-635, (2019).

Image/Figure: https://s3.amazonaws.com/amz.xcdsystem.com/1E8A4501-BB41-A02A-1D3B9882B798BFAA_abstract_File10351/GA75_ImageFigure_0511022241.pdf

Image/Figure Caption: Figure 1: EPG split NanoLuc experiment in E. coli BL21 cells. Readings were taken on IVIS every 10 seconds with open filter. Electromagnetic stimulus applied to cells for 2 minutes and shown as shaded region. Lysate EPG (A) showed a 40% increase in luminescence and the Whole Cell EPG (B) showed a 70% increase in luminescence. Results shown are duplicate experiments with N=6 in each trial.

Full Name of Abstract's 1st Author : Connor Grady

First Name: Connor

Last Name: Grady

Email: gradycon@msu.edu

Organization: Michigan State University

Country: United States

ID: GA76
Imaging of olfactory nerve using a selective Nav1.7 sodium channel inhibitor In the diagnosis of smell disorders

Dauren Adilbay, Memorial Sloan-Kettering Cancer Center, dr.dauren@gmail.com

---

Category: Neuroscience

Abstract Body : Background: Sense of smell (olfaction) provides a range of information that enriches our lives and, in some cases, protects us from harm or saves our lives. Disorders of smell can be observed in a wide range of severity from minor parosmia's to total loss of smell or anosmia. Anosmia/hyposmia affects 13.3 million people in the US alone according to the recent U.S. National Health and Nutrition Examination Survey (NHANES) [1]. Hundreds of thousands more people with persistent smell issues will be added to this number due to the COVID pandemic [2]. Currently, smell disorders are assessed using self- or physician-administered smell tests that are mostly subjective and unable to describe the level of dysfunction. Nav1.7 sodium channels are abundantly expressed in the olfactory nerve, both in the epithelium and the olfactory bulb. Patients with loss-of-function in SCN9A, the gene encoding Nav1.7, experience anosmia in addition to congenital insensitivity to pain [3]. Hsp1a is a recently discovered peptide that binds to Nav1.7 with high potency and selectivity [4]. We examined whether a fluorescent-tagged version of Hsp1a could be used to visualize normal and damaged mouse olfactory nerves. Methods: We first assessed the possibility of visualizing the olfactory nerve in normal mice using Hsp1a-IR800, a tracer in which Hsp1a is covalently conjugated to the fluorescent dye IR-800. Athymic nude mice were intravenously injected with Hsp1a-IR800 (1 nmol, 100μL PBS), phosphate-buffered saline (PBS), or a combination of Hsp1a-IR800 and unmodified Hsp1a. To assess the difference in radiance efficiency in the normal and damaged olfactory nerve mouse model, we conducted a second experiment in which mice were injected with methimazole to model olfactory damage [5]. All mice were restrained using intraperitoneal ketamine/xylazine cocktail injection and in-vivo epifluorescence images obtained using an IVIS Spectrum (PerkinElmer) using a filter set (excitation 745 nm, emission 810 nm). Animals were sacrificed and olfactory nerve/bulb, muscle, heart, spleen, kidney, and liver were removed and imaged ex vivo using an IVIS imaging system. Autofluorescence was removed through spectral unmixing. Semiquantitative analysis of the Hsp1a-IR800 signal was conducted by measuring the average radiant efficiency (in units of [p/s/cm2/sr]/[μW/cm2]) in regions of interest (ROIs) that were placed on the region of olfactory epithelium/bulb. Results: Immunohistochemistry performed using a Nav1.7 antibody confirmed that mouse olfactory epithelium sensory neurons, axon bands, and olfactory bulb abundantly express Nav1.7 (Figure 1). In epifluorescence in-vivo images in mice receiving imaging agent, the area of olfactory epithelium/bulb were clearly visible. The radiant efficiency was significantly less in both mice injected with PBS and in mice injected with the unmodified peptide in combination with imaging agent (blocking, Fig. 1). We observed a 150-fold increase in radiant efficiency compared to mice injected with PBS and a 61-fold increase compared to blocking mice. Mice with damaged olfactory nerve had a visibly diminished radiance. The olfactory nerve area of methimazole-treated mice had a statistically significant 7-fold decrease in radiant efficiency compared to normal mice. Ex vivo images

showed a similar statistically significant difference between mice groups in the olfactory epithelium/bulb region. The heart and kidneys are the only internal organs with higher fluorescence signals compared to control and blocked mice. Conclusion: We demonstrated that it is possible to image the mouse olfactory epithelium/bulb using Hsp1a-IR800, a fluorescent peptide that targets Nav1.7. Radiance efficiency was reduced in mice with a damaged olfactory epithelium/bulb suggesting that Hsp1a tracers hold promise in the diagnosis of smell disorders.

References: 1. Hoffman, H.J., et al., New chemosensory component in the US National Health and Nutrition Examination Survey (NHANES): first-year results for measured olfactory dysfunction. Reviews in Endocrine & Metabolic Disorders, 2016. 17(2): p. 221-240. 2. Whitcroft, K.L. and T. Hummel, Olfactory Dysfunction in COVID-19 Diagnosis and Management. Journal of the American Medical Association, 2020. 323(24): 2512-2514. 3. Weiss, J., et al., Loss-of-function mutations in sodium channel Nav1.7 cause anosmia. Nature, 2011. 472(7342): 186-190. 4. Gonzales, J., et al., Fluorescence imaging of peripheral nerves by a Nav1.7-targeted inhibitor cystine knot peptide. Bioconjugate Chemistry, 2019. 30(11): p. 2879-2888. 5. Rupasinghe, D.B., et al., Localization of Nav1.7 in the normal and injured rodent olfactory system indicates a critical role in olfaction, pheromone sensing and immune function. Channels, 2012. 6(2): 103-110.

Image/Figure: https://s3.amazonaws.com/amz.xcdsystem.com/1E8A4501-BB41-A02A-1D3B9882B798BFAA_abstract_File10351/GA76_ImageFigure_0511030714.jpeg

Image/Figure Caption: Figure 1. Hsp1a-IR800 accumulation in the olfactory epithelium/bulb of naïve mice and those treated with methimazole to induce olfactory damage. (a) Epifluorescence images of animals injected with PBS, Hsp1a-IR800 (1 nmol, Hsp1a-IR800 in 100 µL PBS) and Hsp1a-IR800/Hsp1a formulation, respectively. Images were taken 30 min after tail vein injection. (b) Fluorescence intensity quantification of panel a. (c) Epifluorescence images of animals. Control – normal mice injected with Hsp1a-IR800; Experimental – animals treated with methimazole 50 mg/kg on day 0, day 3 and injected with Hsp1a-IR800 on day 8; Block – Hsp1a-IR800/Hsp1a formulation respectively. Images were taken 30 min after tail vein injection (d) Fluorescence intensity quantification of panel c. (e) Histological confirmation of NaV1.7 expression in olfactory bulb and epithelium. The first row is the overview of the olfactory epithelium IHC slide, epithelium with 20x magnification, and IgG control. The second row is the overview slide with the cut at the level of the olfactory bulb, the slide with 20x magnification, and the IgG control.

First Name: Dauren

Last Name: Adilbay

Email: dr.dauren@gmail.com

Organization: Memorial Sloan-Kettering Cancer Center

Country: United States

ID: GA77
Image-Guided Drug Delivery for Cancers Using H-Dots

Hak Soo Choi, Massachusetts General Hospital, Harvard Medical School, HCHOI12@mgh.harvard.edu

---

Category: Oncology

Abstract Body : H-Dot is a nonsticky and renal clearable theranostic nanoplatform designed to target various human diseases including gastrointestinal stromal tumors and lung cancers. The H-Dots include a near-infrared (NIR; 650-900 nm) fluorescent moiety which enables us to monitor targeting, pharmacokinetics, drug delivery, and therapeutic efficacy in vivo following surgical resection. H-Dots not only target tumorous tissue for image-guided surgery but also tailor the fate of anticancer drugs to the tumor site precisely, resulting in the treatment of unresectable tumors without nonspecific uptake of off-target H-Dots. When delivered by H-Dots, anticancer drugs show lower uptake into the immune system, improved tumor selectivity, and increased tumor suppression compared to free drugs. Using the state-of-the-art TriFoil InSyTe FLECT/CT imaging device, the fate of H-Dots could be followed in real-time in full 3D in tumor-bearing animal models. H-Dots are a promising theranostic nanoplatform for both image guidance and drug delivery with the ability to reduce the adverse effects associated with previous theranostic systems.

References: 1. Kang H, Gravier J, Bao K, Wada H, Lee JH, Baek Y, El Fakhri G, Gioux S, Rubin BP, Coll JL, Choi HS. Renal clearable organic nanocarriers for bioimaging and drug delivery. Adv Mater. 2016; 28(37):8162-8. 2. Kang H, Stiles WR, Baek Y, Nomura S, Bao K, Shuang H, Park GK, Jo MJ, I H, Coll JL, Rubin BP, Choi HS. Renal clearable theranostic nanoplatforms for gastrointestinal stromal tumors. Adv Mater. 2020;32(6):1905899.

Image/Figure:

https://s3.amazonaws.com/amz.xcdsystem.com/1E8A4501-BB41-A02A-1D3B9882B798BFAA_abstract_File10351/GA77_ImageFigure_0511031039.png

Image/Figure Caption: Figure 1. Renal clearable theranostic nanoplatforms for image-guided cancer interventions

First Name: Hak Soo

Last Name: Choi

Email: HCHOI12@mgh.harvard.edu

Organization: Massachusetts General Hospital, Harvard Medical School

Country: United States

ID: GA78
The first clinically relevant PET/MRI reporter gene system for cell tracking

Nourhan Shalaby, Western University, nshalaby@uwo.ca

Category: Bioengineering, Synthetic Biology and Basic Biology

Abstract Body : Introduction: Cell-based therapies, particularly cancer immunotherapies, have shown remarkable clinical success; however, there has been significant differences among patients in terms of treatment response and side effects. Non-invasive methods for monitoring the distribution, migration, viability and persistence of cellular therapies are in need. A multi-modal imaging approach would combine the benefits of more than one imaging tool to provide more comprehensive information on the fate of therapeutic cells. Hypothesis: The development of a clinically translatable, multi-modal reporter gene system using MRI and PET reporter gene system has the potential for safe, sensitive and longitudinal cell tracking purposes. This system would combine the quantification and sensitivity advantages of PET with the superior spatial resolution, relative feasibility and non-irradiative longitudinal tracking benefits of MRI. Methods: Human MDA-MB-231 (231) triple negative breast cancer cells were engineered with lentivirus to co-express zsGreen (zsG), a human organic anion transporter polypeptide 1B3 (OATP1B3), which promotes intracellular accumulation of the paramagnetic MRI contrast agent Gd-EOB-DTPA (Primovist). Cells were also co-engineered to express the human sodium iodide symporter (NIS), which promotes the intracellular uptake of the PET tracer, 18F-tetrafluoraborate (18F-TFB). In-vitro characterization was performed to confirm the transduction efficiency, protein expression, and functionality of both reporter proteins. Mice implanted with naïve and dual NIS/OATP1B3- expressing cells into contralateral mammary fat pads were imaged with PET and MRI, after administration of their respective imaging probes. Results: Flow cytometry revealed no zsG fluorescence in naive control cells, while 93% of the transduced cells were zsG-positive. ZsG presence was confirmed by fluorescence microscopy. Protein expression of NIS and OATP1B3 was confirmed with western blots at their respective band sizes (90 and 120 kDa for OATP1B3 and NIS, respectively). Reporter gene function was tested with MRI of cell pellets and showed approximately a 30% increase (p Primovist compared to naïve cells. Next, we measured a 45-fold increase in 18F-TFB tracer uptake in MRI/PET cells compared to naïve control cells (p 18F-TFB SUV in NIS-expressing tissue as well as the NIS-OATP1B3 tumour compared to the naïve tumour with dynamic PET imaging. Similarly, T1-weighted MRI images showed significantly higher (p Conclusion: We have developed the first dual PET and MRI reporter gene system for in-vivo cell tracking. Our system uses human-derived reporter genes in combination with clinically approved imaging contrast agents, underscoring the high translational potential of our system.

Image/Figure:

https://s3.amazonaws.com/amz.xcdsystem.com/1E8A4501-BB41-A02A-1D3B9882B798BFAA_abstract_File10351/GA78_ImageFigure_0513051642.png

Image/Figure Caption: Figure 1: No zsG in naïve cells (A) and 93% transduction efficiency in MRI/PET cells expressing zsG (B). Western blots confirmed the presence of OATP1B3 at 90 kDa and NIS at 120 kDa in MRI/PET cells (C). Functional tests with MRI showed over a 30% increase in average R1 of MRI/PET cells than in naive cells ($p < 0.05$) (D). Significantly higher ($p < 0.001$) 18F-TFB tracer uptake in MRI/PET cells as opposed to naïve cells (E). A PET MAP showing uptake of 18F-TFB uptake in NIS expressing tissues as well as our MRI/PET tumour (F). A T1-weighted MRI image showing contrast enhancement in the MRI/PET tumour and no contrast enhahncement in the naive tumour (G).

Full Name of Abstract's 1st Author : Nourhan Shalaby

First Name: Nourhan

Last Name: Shalaby

Email: nshalaby@uwo.ca

Organization: Western University

Country: Canada

ID: GA79
3D optical imaging of intravesicular infusion distribution

Andrei Molotkov, Columbia University PET center, am3355@cumc.columbia.edu

---

Category: Oncology

Abstract Body : Purpose: Bladder cancer is a prevalent disease with high morbidity and mortality. Intravesicular therapy is a modality of treatment that injects therapeutic agents directly into the bladder to minimize systemic effects. Recent targeted agents have shown potential against bladder cancer. Our goal is to develop a preclinical modality that can be used to evaluate real-time distribution of potential intravesicular therapies. We hypothesize that 3-dimensional optical/CT of optically labeled therapies can be used as a preclinical tool to determine systemic exposure of locoregionally delivered agents. To validate real-time 3D optical/CT for distribution studies, we used Cy7 labeled albumin as a therapeutic surrogate to validate this technique for future use with optically labeled therapeutics. Material and Methods: Mouse albumin (ALB) (Sigma, MO) was labeled with Cy7 according to manufacture instruction (Lumiprobe, MD). MB49 (ATCC, VA) mouse urothelial carcinoma cells stably expressing the fly luciferase were implanted orthotopically into the bladder of C57BL/6 mice (B6). MB49 tumor growth was detected by bioluminescence imaging (3D optical CT scanner, MILabs, Netherlands) and mice were injected intravesicularly with Cy7-labeled ALB (Cy7ALB). 3D optical scans with microCT for anatomical reference were done 24h, 3 and 5 days after Cy7ALB injection. To confirm Cy7 tracer uptake by MB49 cells some animals were dissected 24h, 3 and 5 days after tracer injection, bladders were sectioned and imaged using RVL-100G Echo Revolve microscope (Echo, San Diego, CA). Results: We found that 80-90% of the mice injected orthotopically with MB49 murine tumor cells developed bladder cancers, as confirmed by bioluminescent imaging as early as 7 days after implantation. We infused Cy7ALB intravesicularly for 2 hours and imaged real-time distribution with 3D optical/CT imaging and found expected high concentration of NIR activity in the bladder but not other tissues, which was confirmed post-necropsy. Interestingly, we found trace fluorescent activity in the region of the bladder cancer after extended imaging if we did not wash out the Cy7ALB after treatment, possibly due to macropinocytosis. Conclusion: Our study demonstrated that 3D optical/CT is a promising way to evaluate real-time distribution of NIR-labeled intravesicular proteins. Furthermore, using optically labeled probes allows evaluation of tumor accumulation versus urothelial uptake, which is important when developing targeted therapeutics. Thus, Cy7-labeled therapeutic candidates in conjunction with 3D optical/CT can play a valuable role in preclinical screening of candidate therapies being considered for intravesicular delivery.

Full Name of Abstract's 1st Author : Alessandra Ali

First Name: Andrei

Last Name: Molotkov

Email: am3355@cumc.columbia.edu

Organization: Columbia University PET center

Country: United States

ID: GA80

89Zr-labeled Trojan horse peptides for direct cell labeling: direct comparison with the state-of-the-art tracer [89Zr]Zr-oxine

Laura Lechermann, University of Cambridge, lmtl2@cam.ac.uk

Category: New Chemistry, Materials & Probes

Abstract Body : Introduction: In vivo imaging and tracking of cells can be used to non-invasively improve the accuracy, efficacy and safety of novel immune-modulatory treatments and cell therapies. Zirconium-89 has a long half-life (t1/2 = 78.4 h) and has therefore been applied for direct cell labeling and imaging of cells in vivo using positron emission tomography (PET), in particular with the tracer [89Zr]Zr-oxine [1]–[3]. However, the water insolubility of [89Zr]Zr-oxine and challenging synthesis method required may limit its implementation as a routine clinical imaging tool. This work has evaluated a novel cell labeling approach employing the desferrioxamine (DFO) chelator, commonly used to label antibodies for immuno-PET, attached to the cell penetrating peptide MPG ([89Zr]Zr-DFO-MPG△NLS) which is a fusion peptide with a nuclear localization sequence (△NLS), in direct comparison to [89Zr]Zr-oxine (Fig.1). Methods: DFO-MPG△NLS peptide was produced via solid phase peptide synthesis. [89Zr]Zr-oxine was synthesized according to a published procedure using 0.9-2.4 MBq of [89Zr]Zr(oxalate)4 [4]. DFO and DFO-MPG△NLS were labeled by adding 1.4-2.2 MBq neutralized [89Zr]Zr(oxalate)4, that was also used as a control for cell labeling, to 10-20 µg DFO and DFO-MPG△NLS, respectively. All 89Zr-labeled compounds were incubated at room temperature (RT). [89Zr]Zr-DFO-MPG△NLS was purified via a preconditioned Sep-Pak Plus light C18 cartridge. Complete chelation of zirconium-89 for all compounds was observed using instant thin layer chromatography (iTLC) and in addition high performance liquid chromatography (HPLC) in the case of [89Zr]Zr-DFO-MPG△NLS. Jurkat T-cells, human peripheral blood mononuclear cells (PBMCs), isolated human T-cells and sheep mesenchymal stem cells (MSCs) at 5×106 cells/mL were labeled with 94-902 kBq [89Zr]Zr-oxine, 60-842 kBq [89Zr]Zr-DFO-MPG△NLS, 151-669 kBq [89Zr]Zr(oxalate)4, 97-844 kBq [89Zr]Zr-DFO in a 1.5 mL Eppendorf vial in 500 µL phosphate buffered saline (PBS) by a 10-30 min incubation at RT. The cell associated activity and uptake were determined after 2 washes with PBS. Cell pellets were resuspended in the appropriate complete cell medium and cellular activity retention was examined at different time points post-labeling alongside viability by trypan blue exclusion. Results: All 89Zr-labeled compounds were synthesized at a radiochemical yield of >90%. The recovery of [89Zr]Zr-DFO-MPG△NLS after C18 cartridge purification was >90 % (n = 6). Both [89Zr]Zr-oxalate and [89Zr]Zr-DFO showed no significant uptake into Jurkat T-cells ([89Zr]Zr-DFO-MPG△NLS and [89Zr]Zr-oxine were 37.9 ± 6.1 % and 40.7 ± 13.0 %, respectively (Fig. 2 A). [89Zr]Zr-DFO-MPG△NLS exhibited fast cellular uptake kinetics in Jurkat T-cells cells independent of the incubation time as could be shown and has been described previously for [89Zr]Zr-oxine [2],[5] (Fig. 2 B). [89Zr]Zr-DFO-MPG△NLS showed significantly higher retention in PBMCs and sheep MSCs at 24 h and a non-significant difference in cellular retention in T-cells and Jurakt T-cells compared to [89Zr]Zr-oxine (Fig. 3 A); there was no difference in the cellular retention within Jurkat T-cells over 4 days, compared to [89Zr]Zr-oxine

(Fig. 3 B). No significant loss of viability was observed throughout all experiments as indicated by trypan blue exclusion. Conclusion: This work is the first to show that 89Zr-labeled DFO can be utilized for intracellular cell labeling via conjugation to the cell penetrating peptide MPG and that similar or superior performance, compared to the state-of-the-art tracer [89Zr]Zr-oxine could be achieved. [89Zr]Zr-DFO-MPG△NLS offers significant advantages over [89Zr]Zr(oxinate)4: excellent aqueous solubility, high specific activity of [89Zr]Zr-DFO, the additional purification step, and the potential to transfer the synthesis to an automated synthesis module. Future work will investigate the in vivo cell tracking over several days.

References: 1. Asiedu KO, Koyasu S, Szajek LP, Choyke PL, Sato N. Bone marrow cell trafficking analyzed by 89Zr-oxine positron emission tomography in a murine transplantation model. Clin Cancer Res. 2017;23(11):2759-2768. 2. Man F, Lim L, Volpe A, et al. In Vivo PET Tracking of 89 Zr-Labeled Vγ9Vδ2 T Cells to Mouse Xenograft Breast Tumors Activated with Liposomal Alendronate. Mol Ther. 2019;27(1):219-229. 3. Weist MR, Starr R, Aguilar B, et al. PET of adoptively transferred chimeric antigen receptor T Cells with 89Zr-Oxine. J Nucl Med. 2018;59(10):1531-1537. 4. Man F, Khan AA, Carrascal-Miniño A, Blower PJ, T.M. de Rosales R. A kit formulation for the preparation of [89Zr]Zr(oxinate)4 for PET cell tracking: White blood cell labelling and comparison with [111In]In(oxinate)3. Nucl Med Biol. 2020;90-91:31-40. 5. Sato N, Wu H, Asiedu KO, Szajek LP, Griffiths GL, Choyke PL. 89Zr-oxine complex PET cell imaging in monitoring cell-based therapies. Radiology. 2015;275(2):490-500.

Image/Figure: https://s3.amazonaws.com/amz.xcdsystem.com/1E8A4501-BB41-A02A-1D3B9882B798BFAA_abstract_File10351/GA80_ImageFigure_0511043138.pdf

Image/Figure Caption: Fig. 1 Molecular structure of (A) [89Zr]Zr-oxine and (B) [89Zr]Zr-DFO-MPG△NLS peptide using one letter amino acid code.

Full Name of Abstract's 1st Author : Laura Melanie Tessa Lechermann

First Name: Laura

Last Name: Lechermann

Email: lmtl2@cam.ac.uk

Organization: University of Cambridge

Country: United Kingdom

ID: GA81
Novel 31P-MR contrast agent based on phosphorus chemical shift

Natalia Ziółkowska, First Faculty of Medicine, Charles University, n.l.ziolkowska@gmail.com

---

Category: New Chemistry, Materials & Probes

Abstract Body : Introduction Presented metal-free MR contrast agent is based on phosphorus-containing polymer with phosphorothioate group (pTMPC), which is extremely rare in living organisms [1]. This feature ensure 31P MR signal chemical shift from the biological phosphorus-containing compounds, presented here by a polymer with phosphoester group (pMPC) and rat mesenchymal stem cells (rMSC). MR properties of the polymer were investigated using 4.7 T MR scanner with 1H/31P custom-made dual coils and 1.5 T relaxometer. Methods Presented probes pTMPC and pMPC were synthesized by controlled radical polymerization technique of the corresponding zwitterionic monomer. MR imaging and spectroscopy of probes were performed on 4.7 T scanner using dual 1H/31P radiofrequency surface coil intended for small laboratory animals. 1H-MR imaging (RARE sequence, TR/TE=2500/12 ms, FOV=10 cm) was applied for localization of phantom (1 mL, cP = 100 mmol L−1). T1 (single pulse sequence, TR=200–4000 ms) and T2 (CPMG spin lock sequence, TE=2–1200 ms) phosphorus relaxation times were measured. For 31P-MRI chemical shift imaging was used (CSI, TR=500 ms, scan time ST=15 min–3 h, field of view FOV=3.6 cm, resolution 2.25×2.25×3.6 mm). The same parameters were used to compare the signal from pTMPC (200 μL, cP = 100 mmol L−1) and rMS cells (200 μL, 1.25×108 mL−1) using more sensitive 1H/31P solenoid coil. 1H/31P-MRI overlapping and phosphorus MRI processing were obtained using ImageJ software. Signal-to-noise ratio (SNR) was calculated for MRI and MRS data. 1H relaxation times were obtained using 1.5 T relaxometer (cP = 10–100 mmol L−1). AlamarBlue Assay was used for cytotoxicity testing of the polymer (cP = 10–0.01 mg mL−1) using primary human fibroblasts (HF) and rMSC. Results and Discussion Results confirm that pTMPC do not influence 1H-MR T1/T2relaxation times (2510/2067.2 ms). 31P-MR T1/T2 relaxation times (2018.3/119.9 ms) were found to be adequate for further MR experiments. Between the polymers with phosphorothioate and phosphoester group, 31P-MR spectroscopy showed a chemical shift of 56.07 ppm, which enable to acquire 31P images from both phantoms during one CSI measurement by frequency selection (Figure 1-I). SNR calculated from 31P spectra results in 13.1–195.1 (ST=2 min–3 h) for pTMPC probe and 12.5–163.7 for pMPC. Imaging analyses results in SNR of 6.3–13.6 (ST=15 min–3 h) and 3.1–5.4, respectively. Measurement of the pTMPC and rMSC solution resulted in two clearly distinguishable signals (Figure 1-II). The difference in chemical shift between these the two peaks (Δδ=54.5 ppm) was similar to what we observed for phantoms. Imaging of both cells and polymers was possible to perform within short acquisition time (ST=2 min). Cytotoxicity testing confirms that pTMPC is not influencing cells viability. High phosphorus concentration and SNR within a short scan time is beneficial for further application in various in vivo animal models. Conclusion Preliminary results of a novel phosphorus-containing pTMPC contrast agent based on 31P-MR chemical shift proved high sensitivity of the probe. Large chemical shift from biological 31P signal, resulting in clearly

separated two 31P signals, was observed in spectroscopy and imaging. This outcome, together with great biocompatibility, indicate that pTMPC could serve as an efficient phosphorus in vivo contrast agent. Acknowledgements The study was supported by the Charles University Grant Agency GA UK (project number 358119); Ministry of Health of the Czech Republic (project number NU20-08-00095); Institute for Clinical and Experimental Medicine IKEM, IN00023001.

References: [1] Petkowski JJ, Bains W, Seager S. Natural Products Containing 'Rare' Organophosphorus Functional Groups. Molecules. 2019; 24(5):866. https://doi.org/10.3390/molecules24050866

Image/Figure:

https://s3.amazonaws.com/amz.xcdsystem.com/1E8A4501-BB41-A02A-1D3B9882B798BFAA_abstract_File10351/GA81_ImageFigure_0511043143.jpg

Image/Figure Caption: Figure 1. (I) 31P-MR CSI measurement with a reference 1H-MRI of pTMPC and pMPC. (A) 1H-MRI of pTMPC on the left and pMPC on the right with water reference between. (B, C) 31P-MR CSI measurements (ST=3 h) of pTMPC and pMPC, respectivelly. (D) Overlapped 1H/31P-MRI of pTMPC and pMPC; (II) 31P-MR CSI measurement of pTMPC (upper row) and rMSC (lower row) solution at different scan times: (A) 2 min, (B) 10 min, (C) 30 min, (D) 60 min, (E) 180 min and (F) overlapped 1H/31P-MR images. 31P signal is highlighted by green color. The scale bar represents 10 mm.

Full Name of Abstract's 1st Author : Natalia Ziółkowska

First Name: Natalia

Last Name: Ziółkowska

Email: n.l.ziolkowska@gmail.com

Organization: First Faculty of Medicine, Charles University

Country: Czech Republic

ID: GA82

Organelle topology is a new breast cancer cell classifier: classification of 3D rendered organelle objects using high resolution imaging and machine learning

Ling Wang, Albany Medical College, wangl3@amc.edu

Category: Computational & Data Science

Abstract Body : Breast cancer is a highly heterogenous disease, both phenotypically and genetically. Of critical importance, a correlation between intra-tumoral heterogeneity, drug resistance and negative clinical outcome has been established. Previously, quantity or subcellular location of protein biomarkers have been compared to identify tumor tissue types. To-date, mass cytometry and single-cell sequencing studies have been used to assess spatial intra-tumor heterogeneity by identifying a range of phenotypic and genetic alterations across different regions of a single tumor. Recently, cell morphology has been indicated as a direct readout of the functional phenotypic state of an individual cancer cell. Here, the hypothesis was proposed that the spatial context of organelles within cancer cells, specifically their subcellular location and inter-organelle relationships (topology), can be used to inform breast cancer cell classification. Since numerous correlations between biologic behaviors and pathologic findings have been well-established, organelle topological heterogeneity reveals the long-term adaptation of organelles and cytoskeletal networks to match breast cancer cell type status. Thus, Organelle Topology-based Cell Classification Pipeline (OTCCP) was introduced as a novel approach that quantifies, for the first time, the topological features of subcellular organelles, removing the bias of visual interpretation, to classify different breast cancer cell lines using a machine learning method. This study aims to investigate the heterogeneity of organelle topology and morphology in breast cancer cells to increase our basic understanding of breast cancer biology on a subcellular level. OTCCP is a novel approach that quantifies, for the first time, the feature of organelles in breast cancer cells, removing the bias of visual interpretation to classify different cell lines based on organelle morphology and topology. This method was tested on three different organelle datasets: mitochondria, early endosomes and recycling endosomes in a panel of human breast cancer cells, including T47D (estrogen receptor-positive), MDAMB231, MDAMB436 and MDAMB468 (triple negative) and AU565 (HER2 positive), as well as non-cancerous mammary epithelial MCF10A cells. High resolution Airyscan microscopy was used to collect z-stacks across cells labeled with fluorescently labeled-transferrin uptake (ERC) and immunostained with anti-Tom20 (Mito) and anti-EEA1 (EEC) to label the recycling and early endosomal and mitochondria networks, respectively. Subsequently, 3D surface rendering of organelle objects was performed using IMARIs image analysis software. A morphometric evaluation of mitochondrial and endosomal compartments resulted in 34 topology and morphology parameters. Application of Random Forest machine learning based classification to 18 of these 34 parameters generated the highest accuracy in breast cancer cell classification using MATLAB software. We systematically evaluated how different parameter combinations affected the machine learning-based cancer cell classification and discovered that topology parameters were crucial to achieve the highest classification accuracy. Based on organelle spatial distribution and their interaction with neighbor organelles (topology) a classification accuracy over 95% was

achieved to distinguish between a variety of human breast cancer cell lines of differing subtype and aggressiveness. Topology parameters generated the highest accuracy (97.1%) in breast cancer classification, indicating that organelle topology is a novel, highly precise classifier to differentiate cell lines of differing subtype and aggressiveness. These findings lay the groundwork for using quantitative topological organelle features as an effective method to analyze and classify breast cancer cell phenotypes.

References: Wang, L., Ward, J., Bouyea, M., and Barroso, M., 2020. "Heterogeneity of mitochondria morphology in breast cancer cells", Proc. SPIE 11216, Multiscale Imaging and Spectroscopy, 112160P; https://doi.org/10.1117/12.2546594

Full Name of Abstract's 1st Author : Ling Wang

First Name: Ling

Last Name: Wang

Email: wangl3@amc.edu

Organization: Albany Medical College

Country: United States

ID: GA83
High Throughput Dynamic Imaging in a Total Body Preclinical PET/CT System

Cesar Molinos Solsona, Bruker BioSpin , cesar.molinos@bruker.com

---

Category: Instrumentation

Abstract Body : Background and Motivation: High throughput capabilities can be useful in preclinical imaging to promote larger sample sizes while limiting experimental durations and costs. High throughput imaging facilitates the efficient use of experimental radiotracers, which tend to be available in small yet expensive batches and often use radionuclides with short half-life. Although multi animal imaging is a frequent practice, animal welfare and consistent imaging conditions (e.g. stable body temperature in [18F]FDG imaging, Ref. [1]) can be overlooked where multi-animal imaging platforms lack the ability to monitor physiological signals, stabilize temperature and adjust the concentration of anesthetic gas for individual subjects. A system for high throughput total body dynamic imaging in mice is presented here. It comprises a PET/CT system and a new 3-mouse cradle, enabling monitoring of physiological signals and dedicated anesthetic gas supply. This set up facilitates stable imaging conditions for consistent PET imaging, even with prolonged acquisition times. Methods: A new animal cradle with capacity for 3 mice was used. The cradle enables individualized monitoring of body temperature and respiration in each subject (figure 1). The cradle also includes animal warming using warm air, anaesthesia gas exhaust and the option to separately adjust anaesthesia for each animal. Two animals are located on the lower deck and the third is positioned above these on a removable tray for easier access and 2-mouse imaging. This animal cradle features an interface for quick connection of all lines on multiple imaging platforms (PET/CT, PET/SPECT/CT and PET/MR instruments). The animal cradle was tested with a PET/CT system with 150 mm FOV for total body imaging in a single cradle position. The CT performance of the system was assessed in Ref. [2] and the PET NEMA characterization can be found here [3]. The cradle and scanner combination was tested in a multi mouse [18F]FDG dynamic PET experiment using 3 healthy mice. Each mouse was injected via the tail vein with 10 MBq of [18F]FDG at the start of acquisition. 1% isoflurane was used for maintenance of anaesthesia and the scan lasted for 2 hrs. The LM file was rebinned after the acquisition using this scheme: 1x20 s, 8x5 s, 8x10 s, 8x60 s, 8x300 s and 7x600 s. The image was reconstructed with MLEM using 12 iterations and a 0.5 mm voxel size. PMOD was used for organ segmentation and statistical analysis. Results: The resulting images show the typical murine biodistribution of [18F]FDG. despite the prolonged acquisition, no signs of motion or brown adipose tissue uptake were apparent (figure 2). This indicated stable animal conditions and proper temperature control. Regions of interest were drawn in the vena cava to derive a surrogate of the blood tracer concentration as well as in the myocardium. The chart provided in the Persuasive Data section shows the time activity curves for each animal in each region of interest. Conclusion: A system comprising the Si78 PET/CT and a 3-mouse high throughput imaging cradle was tested in a dynamic [18F]FDG PET experiment. Physiological monitoring and controlled temperature in all positions of the 3-mouse bed allowed stable conditions to be maintained for as long as 2 h during the measurement. The system will facilitate high throughput imaging while maintaining gold-standard imaging

conditions. This will particularly benefit core facilities, pharma, and centers with high workloads.

References: 1. Mannheim et al. “Standardization of Small Animal Imaging – Current Status and Future Prospects” Molecular Imaging and Biology (2017) 2. Molinos et al, “Low-Dose Imaging in a New Preclinical Total-Body PET/CT Scanner” Front. Med., 03 May 2019 3. Gsell et al. “Characterization of a preclinical PET insert in a 7 tesla MRI scanner: beyond NEMA testing”. 2020 Phys. Med. Biol. 65 245016

Image/Figure: https://s3.amazonaws.com/amz.xcdsystem.com/1E8A4501-BB41-A02A-1D3B9882B798BFAA_abstract_File10351/GA83_ImageFigure_0511053334.pdf

Image/Figure Caption: Figure 1. 3-mouse cradle. Direct access to each animal is possible. Figure 2. Dynamic frames at different time points of the [18F]FDG acquisition. Initial frame shows injection moment

First Name: Cesar

Last Name: Molinos Solsona

Email: cesar.molinos@bruker.com

Organization: Bruker BioSpin

Country: United States

ID: GA84

Synthesis and Characterization of [11C]AZD1283: a Novel P2Y12R PET Radiotracer for Highly Specific Imaging of Microglial Function

Isaac Jackson, Stanford University, isaacmj3@stanford.edu

Category: Neuroscience

Abstract Body : Objectives: Microglia, the resident innate immune effector cells of the central nervous system (CNS), carry out a wide range of functions from passively surveilling the brain to contributing to the post-injury healing process, and play a critical role as first responders to brain injury. Despite the contribution of prolonged microglial activation and aberrant function to deleterious neuroinflammation seen in chronic neurological diseases such as Alzheimer's Disease (AD) and neuropathic pain, there are no readily available methods for specifically tracking these cells and their function in vivo. Positron Emission Tomography (PET) is a highly sensitive functional imaging modality well-suited to non-invasive, longitudinal visualization of these molecular processes. A recent gene profiling study identified P2Y12R as an important gene strongly associated with homeostatic microglia1. P2Y12R protein expression in the CNS is exclusively on microglia at constant levels in healthy adults, but quickly and significantly declines with the onset of a pro-inflammatory state (e.g, surrounding dense, mature Ab plaques in AD)2,4,5. While P2Y12R is an extremely promising functional PET biomarker of microglial function, the only published tracer is not suitable for in vivo use4. Here, we seek to develop the first P2Y12R PET radioligand amenable to in vivo imaging. Methods: We identified P2Y12R antagonist AZD1283 as a promising CNS tracer candidate based on its high affinity (KD = 11nM) and favorable lipophilicity (LogD=2.8)3. [11C]AZD1283 was labeling using the radioactive precursor [11C]NH4CN, which was obtained from cyclotron produced [11C]CO2 using the automatic module GE ProCab (Fig. 1A). [11C]NH4CN was delivered to a TRACERlab FX-FN module and trapped in a solution of 0.5M aqueous KOH (2mL) and K2.2.2 (3mg in 1mL tetrahydrofuran) in a glass reactor. A solution of 1mg synthetic precursor and 2mg palladium tetrakis-triphenylphosphine in 500mL THF was added to the reactor, and the resulting mixture heated and stirred at 90oC for 5 minutes. This crude reaction mixture was purified via semipreparative HPLC to afford pure [11C]AZD1283. Final product was reformulated via plus-lite C18 cartridge to yield [11C]AZD1283 in saline/EtOH, and analyzed via analytical HPLC at 0 and 90 minutes after reformulation to confirm both tracer identity and stability in formulation. Stability of [11C]AZD1283 was assessed in human plasma via HPLC at 0, 5, 15, 30, 60, and 90 minutes. In vitro incubation with mouse and human liver microsomes and a Caco-2 monolayer assay were performed to assess metabolic stability and passive permeability, respectively. Finally, key physiochemical parameters (e.g. cLogP, pKa, total polar surface area) were calculated and a published Multi-Parameter Optimization (MPO) scoring tool used to predict potential for CNS uptake6. Results: AZD1283 was radiolabeled for the first time with carbon-11 to afford [11C]AZD1283 in a yield of 9.17 mCi with high chemical and radiochemicaly purity (>99%) and molar activity of 395 mCi/mmol(average of n=3). In vitro stability of [11C]AZD1283 was found to be high with >99% intact tracer present after 90 minutes incubation in formulation and human serum as demonstrated by HPLC chromatograms (Fig. 1B-

D). Half-life in mouse and human liver microsomes was found to be 37 and >160 minutes, respectively, and Caco-2 assay predicts passive CNS uptake with a small amount of active efflux. AZD1283 received an MPO score of 4.2, indicating over-all alignment with known CNS penetrant druglike molecules, and high potential for in vivo CNS uptake. Conclusions: Herein we describe the successful synthesis of [11C]AZD1283, and demonstrate its high stability in both formulation and human plasma. Our new P2Y12R tracer can be reliably synthesized in ample yield and purity for in vivo imaging. Future PET imaging and metabolism studies in mice and non-human primates will further elucidate the in vivo behavior and translational potential of this very promising compound.

References: 1. Butovsky et al. Nat. Neurosci, 2014. 17:131-143. 2. Haynes et al. Nat Neurosci. 2006, 19(12): 1512–9. 3. Bach et al. J. Med. Chem, 2013, 56(17): 7015-7024 4. Villa et al. Theranostics, 2018, 8(19): 5400-18. 5. Walker et al. Int J Mol Sci. 2020, 21:687. 6. Wager et al. ACS Chem. Neurosci. 2010, 1:435-49.

Image/Figure: https://s3.amazonaws.com/amz.xcdsystem.com/1E8A4501-BB41-A02A-1D3B9882B798BFAA_abstract_File10351/GA84_ImageFigure_0513080852.pdf

Image/Figure Caption: Figure 1. Palladium catalyzed [11C]cyanation of synthetic bromo-precursor was carried out in THF at 90 oC for 5 minutes to yield [11C]AZD1283 (A). Identity and radiochemical purity of [11C]AZD(1B, green) was confirmed via co-injection with cold reference standard(1b, blue) onto analytical HPLC (B). [11C]AZD1283 is stable in formulation at 90 minutes post end of synthesis(C). [11C]AZD1283 was incubated in human plasma, with aliquots quenched and analyzed at 0 (1D,red), 5 (1D,blue), 15 (1D,green), 30 (1D,pink), and 90 (1D, brown) minutes to confirm stability in human plasma for 90 minutes (D).

Full Name of Abstract's 1st Author : Isaac Mackenzie Jackson

First Name: Isaac

Last Name: Jackson

Email: isaacmj3@stanford.edu

Organization: Stanford University

Country: United States

ID: GA85
A Novel Three-Pronged In Silico Approach for Revolutionizing CNS PET Tracer Design and Enhancing Translational Success

Isaac Jackson, Stanford University, isaacmj3@stanford.edu

Category: Neuroscience

Abstract Body : Objectives: Predicting central nervous system (CNS) uptake and binding specificity of positron emission tomography (PET) tracers prior to in vivo testing remains a significant challenge. For this reason, developing and translating a single CNS PET tracer for clinical use is an extremely resource intensive endeavor, often requiring synthesis and evaluation of numerous candidate molecules without a reliable way to predict likelihood of success in advance. While in silico methods exist to augment the therapeutic drug development process by efficiently screening candidates for potential pitfalls early in development, there is a paucity of such tools tailored to PET tracer design and translation1. In this work, we address this unmet need by generating a unique three-pronged in silico approach to rapidly predict the potential value of candidate CNS PET tracers for clinical use by 1) building a large database of successful and unsuccessful CNS PET tracers following an in-depth meta-analysis of published work, 2) leveraging this database to develop complementary in silico methods to determine multi-parameter scoring functions for quantifying likelihood of tracer success and 3) utilizing machine learning (ML) approaches to differentiate successful and unsuccessful tracers. Methods: Following an extensive literature analysis, we collated a diverse library of 75 successful CNS tracers (defined as approved for clinical research) and 65 unsuccessful tracer candidates (most commonly due to insufficient blood-brain barrier permeability or prohibitively high non-specific binding (NSB)). Eight key physiochemical parameters were computed for all tracers: clogP, clogD, molecular weight, topological polar surface area (tPSA), pKa, number of hydrogen bond donors (HBD) of the neutral species, HBD at physiological pH, and net charge at pH 7.4. Tracers were categorized as ‘successful’ or ‘unsuccessful’, with the latter further subdivided (Fig 1a). Based on published methods, physiochemical data was used to create a multi-parametric scoring function for quantifying a tracer’s likelihood of success in vivo, with the aim of distinguishing between successful and unsuccessful tracers2. In parallel, a random subset of the physiochemical and classification data (70%) was used to train several ML models that were then evaluated by classifying the remaining tracers (30%). Results: Evaluation of 8 physicochemical parameters showed distinct trends, indicating significant potential for in silico differentiation of successful vs. non-CNS penetrant tracers (Fig 1b). These distinctions were effectively captured by our novel scoring function, which distinguished successful from non-permeable molecules with 96.7% specificity, 49.3% sensitivity, and positive (PPV) and negative (NPV) predictive values of 97.4 and 43.3, respectively. In particular, the PPV reflects the function’s high potential utility for identifying nonpermeable molecules early in development. Conversely, overall physicochemical property profiles of high NSB tracers were strikingly similar to successful tracers, discouraging use of an analogous function for distinguishing these two populations of tracers(Fig 1c). In comparison, application of a Support Vector Machine learning model showed a 16% increased probability of correct classification for both positive and non-permeable categories (79% vs.

63%), despite access to only a portion of the data (Fig. 1d-e). Conclusion: Analysis of physicochemical properties of 140 successful and unsuccessful CNS PET radiotracers revealed key differences that we believe significantly impact CNS uptake in vivo. Our proof-of-concept method based on both a manually constructed quantitative function and ML models show promise for ab initio prediction of CNS tracer viability prior to resource intensive in vivo imaging studies. Future work will include expansion of the tracer library in addition to optimization and comparison of our scoring function with ML-derived models. Integration of these complimentary approaches will enable design of a high throughput, easy to use computational tool for CNS PET tracer design, ultimately facilitating translation of high impact tracers for clinical use in a time- and cost-effective manner.

References: 1. Zhang et al. J. Med. Chem. 2013, 56, 4568-4579. 2. Wager et al. ACS Chem. Neurosci. 2010, 1, 435-49.

Image/Figure: https://s3.amazonaws.com/amz.xcdsystem.com/1E8A4501-BB41-A02A-1D3B9882B798BFAA_abstract_File10351/GA85_ImageFigure_0513083312.pdf

Image/Figure Caption: Figure 1. The radiotracer library we used to generate this data, depicted in (A), is comprised of successful (n = 75) and unsuccessful (n = 65) radiotracers, with the latter further subdivided into tracers without CNS uptake(n=30), tracers with prohibitively high NSB (n = 25), and tracers that failed for other reasons (n = 10). Head-to-head comparison of the average physiochemical property profile of successful CNS tracers vs. non-permeable PET tracers (B), and tracers with high NSB (C). A Support Vector Machine learning model identified distinct attributes between successful vs. non-permeable negatives allowing for high probability of correct classification on a test set when compared with manual assignment (79% correct assignment) (D). Just as manual scoring failed to distinguish between positives and high non-specific binders, the same model also found little distinction and classified all tracers as positive (E).

Full Name of Abstract's 1st Author : Isaac Mackenzie Jackson

First Name: Isaac

Last Name: Jackson

Email: isaacmj3@stanford.edu

Organization: Stanford University

Country: United States

ID: GA86
Diagnostic Value of Lung Perfusion Scintigraphy In COVID-19 Patients

Mushref Algarni, KFMMC, fresh20033@hotmail.com

Category: Cardiovascular & Pulmonary

Abstract Body : Aim/Introduction: To make describe radiographic imaging findings of perfusion single-photon emission computed tomography (SPECT)/CT for diagnosing pulmonary embolus (PE) and other important imaging finding in patients hospitalized with Coronavirus disease 2019 (COVID-19). Materials and Methods: This retrospective study was carried in the Nuclear Medicine Department, King Fahad Military Medical Complex, Dhahran between March to December 2020 (10 months). All patients undergoing evaluation for suspected PE admitted with COVID-19 imaged with Lung Perfusion SPECT/CT where CT angiogram was contraindicated (such patient with a renal problem or severe contrast reaction). Imaging findings were interpreted by 2 dual qualification physicians in both clinical radiology (CR) and nuclear medicine and consensus reporting was made. Results: Out of 53 patients, majority were males (n=41, 77.4%). Lung Perfusion SPECT/CT demonstrate multiple segmental pulmonary in 6 (8.8%) of patients. Twenty-three patients (43.3%) had other abnormal imaging findings in associated CT of SPECT/CT with mostly peripheral GGO (56.5%), followed by consolidations (34.7%), and others imaging finding (such as atelectasis, reticulation, peribronchovascular thickening, lymphadenopathy, plural effusion and pneumomediastinum) (26%). All patients with unfavorable outcomes were above 65 years having comorbidities or complications (p Conclusion: Coronavirus disease 2019 is seen mostly affecting males. Elderly patients with co-morbidities may show unfavorable outcomes. Lung Perfusion SPECT/CT had important role during this time in diagnosis PE as well as interrupting other associated SPECT CT scan finding with peripheral ground glass opacities are the most common imaging findings.

First Name: Mushref

Last Name: Algarni

Email: fresh20033@hotmail.com

Organization: KFMMC

Country: Saudi Arabia

ID: GA87
Correlation of Acute Pancreatitis with Hyperparathyroidism Confirmed By Scintigraphy

Mushref Algarni, KFMMC, fresh20033@hotmail.com

Category: Systemic Diseases (Kidney, Liver and Pancreas)

Abstract Body : Aim/Introduction: Acute necrotizing pancreatitis is a severe condition with a high mortality rate. In the Western world, alcohol and biliary stones are the main causes of acute pancreatitis. The epidemiology of pancreatitis in Saudi Arabia is greatly different from that in Western Countries. Increasing prevalence of pancreatitis and its association with primary hyperparathyroidism (PHPT) is controversial and highly prevalent in Saudi Arabia. Materials and Methods: Retrospective study included 38 patients aged 26 - 87 years (mean age 49±7). Female to male ratio was 4:1. We including all patients diagnosed as primary hyperparathyroidism and revealed to had an acute pancreatitis attack. In all cases of clinically and biochemically confirmed pancreatitis. Records of 38 hypercalcemic patients with raised parathormone (PTH) were analyzed. All patients underwent dual phase (99m) Technetium SESTAMIBI parathyroid scintigraphy between January 2017and 2021. PHPT was confirmed scintigraphy which was performed with SPECT/CT (GE model 670pro NM/CT). Results: Our study shows 15.7% (6/38 patients) incidence of pancreatitis in patients with PHPT. No direct association between severity of pancreatitis and PHPT was noted in our series. Parathyroid adenoma was the most common underlying pathology. These patients' clinical outcome improved post parathyroidectomy. Conclusion: The prevalence of acute pancreatitis in patients with PHPT is estimated 7% worldwide. In Kingdome of Saudi Arabia, there is increase 2-fold incidence of pancreatitis (15.7%) in patients with PHPT confirmed scintigraphy.

References: 1. Bess MA, Edis AJ, Hyperparathyroidism and pancreatitis. Chance or a causal association? JAMA. 1980;243:246-7. 2. Zuidema PJ. Cirrhosis and disseminated calcification of the pancreas in patients with malnutrition. Trop Geogr Med. 1959;11:70-4. 3. Chandraprasert S, Diabetes mellitus and tropical form of chronic calcific pancreatitis in Thailand. Aust N Z J Med. 1976;6:316-20. 4. Bhatia E, Durie P et al. Mutations in the cystic fibrosis transmembrane regulator gene in patients with tropical calcific pancreatitis. Am J Gastroenterol. 2000;95:3658-9. 5. Balakrishnan V, Tropical pancreatitis — a distinct entity, or merely a type of chronic pancreatitis? Indian J Gastroenterol. 2006;25:74-81. 6. Pitchumoni CS. Familial pancreatitis. In: Pai KN, Soman CR, Varghese R, editors. Pancreatic Diabetes. Trivandrum: Geo Printers; 1970. pp. 46-8. 7. Mohan V. Fibrocalculous pancreatic diabetes. Diabetes Metab Rev. 1998;14:153-70. 8. Govindarajan M. Histopathology and immunohistochemistry of pancreatic islets in fibrocalculous pancreatic diabetes. Diabetes Res Clin Pract. 2001;51:29-38. 9. Cook MR. rising in PTH level immediately after parathyroid resection: Are additional hyperfunctioning glands always present? An application of the Wisconsin Criteria. Ann Surg. 2010;251:1127-30.

First Name: Mushref

Last Name: Algarni

Email: fresh20033@hotmail.com

Organization: KFMMC

Country: Saudi Arabia

ID: GA89
PARP1 expression differentiates melanoma from benign melanocytic lesions: towards PARPi-FL based molecular diagnosis of melanoma

Aditi Sahu, MSKCC, aditisahu@gmail.com

Category: Oncology

Abstract Body : Background: Melanoma is the most aggressive skin cancer with the highest associated mortality[1]. The 5-year survival rates range from 98.3% (stage I) to 16% (stage IV) emphasizing the importance of diagnosis at an early stage[2]. Non-invasive morphological imaging approaches such as dermoscopy and high-resolution, morphological reflectance confocal microscopy demonstrate high sensitivity but moderate and variable specificity[3]. Noninvasive gene assays based on PRAME (PReferentially expressed Antigen in MElanoma) expression show similarly high sensitivity but moderate specificity[4]; neither of these approaches have shown potential in stratifying lesions based on malignant potential. Noninvasive molecular imaging using targeted fluorophores such as PARPi-FL (targets PARP1, overexpressed in cancers[5]), can enable functional evaluation of PARP1 expression to stratify lesions which are malignant and/or have a higher propensity for malignant transformation[6], thereby improving diagnostic specificity for melanoma detection and prognosis. As a first step towards PARPi-FL imaging in vivo, we investigated PARP1 expression as a biomarker to differentiate melanoma, atypical melanocytic proliferation and benign nevi. Methods: We investigated PARP1 and PRAME expression using immunohistochemistry (IHC) in a spectrum of 132 melanocytic lesions (73-melanoma, 51-benign nevi, 8-atypical intraepidermal melanocytic proliferation) in 5 μm-thin formalin-fixed paraffin-embedded serial sections. IHC was performed on an automated Leica-Bond stainer platform. Both IHC and H&E slides were digitized. Automated quantification for PARP1 area positivity and intensity was performed using Aperio Positive Pixel Algorithm (Leica Biosystems, Germany) on whole slides annotated for tumor, benign and epidermis (used as control) by a pathologist using histology and PRAME expression as gold standard, The quantification was performed using fixed optimized parameters for hue value, hue width and color saturation threshold. Strong positive pixels were selected for analysis which was performed for total area positivity and normalized intensity. Descriptive statistics was performed for three groups- atypical intraepidermal melanocytic proliferation (AIMP), benign nevi and melanoma. ROC analysis was performed only on nevi versus melanoma. All statistics were performed on GraphPad Prism version 8.0. Results: PARP1 expression was found in all benign and melanoma tissues at different levels. Area positivity (%) was highest in melanoma (31±13), followed by AIMP (25±17) and benign nevi (13±16). One-way ANOVA demonstrated statistically significant differences between benign and melanoma groups (p Conclusions: Our results on a large dataset demonstrate statistically higher PARP1 expression in melanoma as compared to benign melanocytic lesions. Therefore, PARPi-FL will potentially serve as a robust biomarker for identification of malignant and potentially malignant lesions, which will be tested subsequently in excised tissues. A multimodal reflectance and fluorescence confocal microscopy approach will also be tested to further improve the diagnostic accuracy. Given the IND status of PARPi-FL for use in humans, the next set of results on

PARPi-FL staining will establish the basis for subsequent in vivo clinical imaging studies for molecular melanoma diagnosis in patients. Acknowledgements: Supported by Melanoma Research Foundation (Dermatology Fellow Award) and National Institutes of Health grants P30 CA008748-50 and R01EB020029.

References: 1. Karimkhani, C., et al., The global burden of melanoma: results from the Global Burden of Disease Study 2015. British Journal of Dermatology, 2017. 177(1): p. 134-140. 2. Nikolaou, V. and A. Stratigos, Emerging trends in the epidemiology of melanoma. British journal of dermatology, 2014. 170(1): p. 11-19. 3. Guitera, P., et al., In vivo confocal microscopy for diagnosis of melanoma and basal cell carcinoma using a two-step method: analysis of 710 consecutive clinically equivocal cases. Journal of investigative dermatology, 2012. 132(10): p. 2386-2394. 4. Gerami, P., et al., Development and validation of a noninvasive 2-gene molecular assay for cutaneous melanoma. Journal of the American Academy of Dermatology, 2017. 76(1): p. 114-120. e2. 5. Ossovskaya, V., et al., Upregulation of poly (ADP-ribose) polymerase-1 (PARP1) in triple-negative breast cancer and other primary human tumor types. Genes & cancer, 2010. 1(8): p. 812-821. 6. Kossatz, S., et al., Validation of the use of a fluorescent PARP1 inhibitor for the detection of oral, oropharyngeal and oesophageal epithelial cancers. Nature Biomedical Engineering, 2020. 4(3): p. 272-285.

Image/Figure:

https://s3.amazonaws.com/amz.xcdsystem.com/1E8A4501-BB41-A02A-1D3B9882B798BFAA_abstract_File10351/GA89_ImageFigure_0513080607.png

Image/Figure Caption: Higher PARP1- expression was found in melanoma and AIMP as compared to benign nevi suggesting PARP1 expression estimation using PARPi-FL can help identify malignant and potentially malignant lesions A. IHC quantification of area positivity and normalized intensity was higher for melanoma (p These results suggest the importance of PARP1 expression and potentially PARPi-FL staining in improving diagnosis of melanoma in vivo in patients.

Full Name of Abstract's 1st Author : Aditi Sahu

First Name: Aditi

Last Name: Sahu

Email: aditisahu@gmail.com

Organization: MSKCC

Country: United States

ID: GA90
Whole-body imaging of senescence with ImmunoPET

Edwin Pratt, Memorial Sloan Kettering Cancer Center, pratte@mskcc.org

---

Category: Oncology

Abstract Body : year overall survival rate of 10%. Treatment options with the greatest overall survival include chemotherapeutics such as gemcitabine or combination regimens such as FOLFIRINOX. Treating pancreatic cancers with gemcitabine or other cytostatic drugs has been known to induce senescence, a type of cell arrest, and to make the cancer refractory to additional therapy. Senescent tissue secretes numerous inflammatory markers, inducing increases in vascular access as part of the senescence associated secretory phenotype (SASP), and is considered tumorigenic. Here, we used clinically available antibodies such as Bevacizumab (VEGF-A), Crizanlizumab (P-selectin), Siltuximab (IL-6), and ADAM17 to target some of these secreted markers in order to identify senescent tissue. Current methods for determining senescence are limited to lysosomal activity of beta-galactosidase, which is not unique to senescent tissue and utilizes a small molecule agent that is widely distributed and rapidly cleared, lowering specificity. These SASP-targeting antibodies were radiolabeled using the established 89Zr-Desferoxamine isotope-chelator, with purities greater than 99%, to produce precision ImmunoPET versions of these clinically tested antibodies. We were able to induce SASP with daily administration of trametinib and palbociclib in both orthotopic and subcutaneous models of pancreatic cancer with the MiaPaCa2 cell line. By imaging four different components of SASP in mice undergoing senescence therapy, a greater visualization of chemotherapy induced senescence can achieved with immunoPET. In Figure 1, variation in tumor uptake was seen, showing not only differences in antibody tumor penetrance, but also injected dose per gram for the four antibodies. By quantifying tumor uptake of each SASP factor, the presence of senescent and resistant pancreatic cancer can be detected earlier, providing time for next-line therapy, and possibly a new therapeutic stratagem.

Image/Figure Caption: Figure 1: ImmunoPET of MiaPaCa2 subcutaneous tumors under TP therapy targeting markers of SASP. Tumor heterogeneity between markers identify SASP factor location and intensity (optimization needed).

Full Name of Abstract's 1st Author : Edwin C. Pratt

First Name: Edwin

Last Name: Pratt

Email: pratte@mskcc.org

Organization: Memorial Sloan Kettering Cancer Center

Country: United States

ID: GA92

Retrospective prognostic investigation using harmonized radiomic FDG PET features acquired by multiple scanners in the cohort of pancreatic cancer who underwent complete surgery

Masao Watanabe, Department of Diagnostic Radiology, Kobe City Medical Center General Hospital, d7he4ng@gmail.com

---

Category: Oncology

Abstract Body : Objectives: Textural features of FDG PET/CT can be used to clarify the tumor heterogeneity and to predict the patients' outcome (1,2). However, the textural features are sensitive to the acquisition and reconstruction PET parameters, i.e., "batch effect". The mitigation of the batch effect is critical in the retrospective study, especially when multiple PET scanners were used. Orlhac et al. successfully mitigated the batch effect and normalized the textural features by using the R software "Combat" (3-7). Patients with pancreatic cancer have low survival rate, and thus the curative R0 surgery is essential for the long survival (8). Moreover, the classification of the patients into the group with long survival and the group with short survival is important in the viewpoint of precision medicine to provide best treatment option. In this study, we aimed to reveal the promising prognostic factor including the harmonized radiomic features of the pancreatic cancer patients who underwent curative R0 surgery. Methods: From July 2011 to March 2020, 61 consecutive patients (35 males and 26 females) with localized pancreatic ductal carcinoma underwent FDG PET/CT scan by using various PET modalities. We retrospectively evaluated the primary lesions in terms of SUVmax, MTV, TLG, histograms and the other textural features by using LIFEx software version 6.30 (3,4). For tumor segmentation, we used Nestle's method ($\alpha = 0.3$) (9). The quantitative lesions' parameters were harmonized by referring the corresponding parameters of the background liver by means of "Combat". For univariate analysis using Cox proportional hazard regression, we evaluated the clinical information in terms of age, sex, histology, TNM stage, tumor location, the presence of arterial invasion, the presence of neural invasion and the completion of the adjuvant chemotherapy (10), as well as the quantitative PET parameters stated above. Next, we clarified the promising prognostic factor using Akaike's information criterion (AIC). Concerning ROC analysis, we determined the cut-off to be 300 days in PFS and 730 days in OS from the date of surgery, respectively (11), followed by Kaplan Meier analysis. Results: As for univariate analysis, the significant prognostic parameters were the presence of nodal metastasis, the presence of neural invasion, the completion of the adjuvant chemotherapy, GLCM Contrast, GLRLM LGRE, GLRLM SRLGE, NGLDM Contrast, GLZLM LGZE, GLZLM SZLGE in PFS; and the presence of nodal metastasis, the presence of neural invasion, the completion of the adjuvant chemotherapy, SUVmax, GLCM Contrast, GLCM Dissimilarity, GLRLM SRHGE, GLZLM HGZE in OS. Concerning AIC analysis, the revealed prognostic factors were the presence of nodal metastasis, the presence of neural invasion, the completion of adjuvant chemotherapy, GLCM Contrast and GLZLM SZLGE in PFS; and the presence of nodal metastasis, the presence of neural invasion, the completion of adjuvant chemotherapy and SUVmax in OS. The AUCs were more than 0.6 and the p values were less than 0.05 in the

Kaplan Meier analysis in GLRLM LGRE, GLRLM SRLGE, GLZLM LGZE and GLZLM SZLGE regarding PFS; and in SUVmax regarding OS. The p values were also under 0.05 in the Kaplan Meier analysis in the presence of neural invasion and the completion of adjuvant chemotherapy concerning PFS; and in the presence of nodal metastasis, the presence of neural invasion and the completion of adjuvant chemotherapy concerning OS. Conclusions: We have investigated the promising prognostic factor in PFS and OS using the univariate Cox proportional hazard regression, AIC, ROC and Kaplan Meier analyses. To mitigate the bias of our retrospective nature, the sub-analysis of the cohort who completed the adjuvant chemotherapy might be optimal. Besides, the application of interval censoring technique may reveal the true recurrent time point, which might strengthen our statistical power.

References: 1, Ha S, et al. Metabolic radiomics for pretreatment 18F-FDG PET/CT to characterize locally advanced breast cancer: histopathologic characteristics, response to neoadjuvant chemotherapy, and prognosis. Sci Rep. 2017;7:1556 2. Beukinga RJ, et al. Predicting response to neoadjuvant chemoradiotherapy in esophageal cancer with textural features derived from pretreatment 18F-FDG PET/CT imaging. J Nucl Med. 2017;58:723-729 3, Orlhac F, et al. A postreconstruction harmonization method for multicenter radiomic studies in PET. J Nucl Med. 2018;59:1321-1238 4, Nioche C, et al. LIFEx: A freeware for radiomic feature calculation in multimodality imaging to accelerate advances in the characterization of tumor heterogeneity. Cancer Res. 2018;78:4786-4789 5, Johnson WE, et al. Adjusting batch effects in microarray expression data using empirical Bayes methods. Biostatistics. 2007:8:118-127 6, Fortin JP, et al. Harmonization of multi-site diffusion tensor imaging data. Neuroimage. 2017;161:149-170 7, Fortin JP, et al. Harmonization of cortical thickness measurement across scanners and sites. Neuroimage. 2017;167:104-120 8, Strobel O, et al. Optimizing the outcome of pancreatic cancer surgery. Nat Rev Clin Oncol. 2019;16:11-26 9, Maisonobe JA, et al. Comparison of PET metabolic indices for the early assessment of tumour response in metastatic colorectal cancer patients treated by polychemotherapy. Eur J Nucl Med Mol Imaging. 2013;40:166-174 10, Yamamoto T, et al. Long-term survival after resection of pancreatic cancer: A single-center retrospective analysis. World J Gastroenterol. 2015;21:262-268 11, Groot VP, et al. Use of imaging during symptomatic follow-up after resection of pancreatic ductal adenocarcinoma. J Surg Res. 2018;221:152-160

Image/Figure:

https://s3.amazonaws.com/amz.xcdsystem.com/1E8A4501-BB41-A02A-1D3B9882B798BFAA_abstract_File10351/GA92_ImageFigure_0512063920.png

Image/Figure Caption: Kaplan Meier analysis of representative parameters in PFS and OS. GLZLM SZLGE in PFS and SUVmax in OS were significant or promising prognostic factors in the univariate Cox proportional hazard regression, AIC, ROC and Kaplan Meier analyses.

Full Name of Abstract's 1st Author : Masao Watanabe

First Name: Masao

Last Name: Watanabe

Email: d7he4ng@gmail.com

Organization: Department of Diagnostic Radiology, Kobe City Medical Center General Hospital

Country: Japan

ID: GA93
Etiology and Renogram Pattern of Congenital Hydropnephrosis: A Retrospective Study in Hasan Sadikin Hospital (2012-2019)

Rian Hidayatullah, Hasan Sadikin General Hospital, riandayat@gmail.com

---

Category: Systemic Diseases (Kidney, Liver and Pancreas)

Abstract Body : Background Congenital Hydronephrosis (CH) etiology is related with pelviureteric junction obstruction (PUJO), vesicoureteric reflux (VUR), vesicoureteric junction obstruction (VUJO), polycystic kidney disease (PCKD), ectopic kidney (EK), double collecting system (DCS), and others.1 Renography may precisely evaluate kidney function impairment in Congenital Hydronephrosis cases.2 This study aims to determine Congenital Hydronephrosis etiologies and their renogram pattern. Methods Medical records of Congenital Hydronephrosis patients underwent 99mTc-DTPA renography and GFR examination between January 2012 and July 2019 at Nuclear Medicine and Molecular Imaging Department Hasan Sadikin Hospital was retrospectively analyzed. If indicated, diuretic renography protocol was F+15.3 GFR 65 ml/minute were used to define kidney function as “poor”.4 Kidneys with GFR 5 Results One hundred ninety two kidney units from 119 CH patients (74 male, 45 female; mean age 9.2 years old (range: 1-18 years old)) were diagnosed as CH according to ultrasound (US) study. Among those, 91 (47.4%) were remain functioning, but most of them (n=89) were poor. The most common CH etiology were PUJO (82.8%), followed by VUJO (10.4%), VUR (4.2%), ectopic kidney (1.6%), PCKD (0.5%), and DCS (0.5%). The renogram obstructive patterns were observed in 74 (81.3%) functioning kidneys. We found that poor kidney function in non-obstructive pattern group is as prevalent as in obstructive pattern group (94% vs 98%) (Table 1). This finding emphasizes the importance of renography in continous monitoring of such patients.2 Representative renogram patterns are presented in Figure 1. Conclusion PUJO was the most prevalent CH etiology. Poor kidney function (65 ml/minute) in non-obstructive pattern group is as prevalent as in obstructive pattern group.

References: 1. Nguyen HT, et al. The Society for Fetal Urology consensus statement on the evaluation and management of antenatal hydronephrosis. J Pediatr Urol. 2010; 6:212 – 31. 2. Sinha A, et al. Revised guideline on management of antenatal hydronephrosis. Ind J Nephrol. 2013; 23(2): 83 – 97. 3. Gordon I, et al. Guidelines for standard and diuretic renogram in children. Eur J Nucl Med Mol Imaging. 2011; 38: 1175-88. 4. Du L, et al. Pediatric reference ranges for glomerular filtration rate determined by a single injection of Tc-99m DTPA. J Nucl Med. 2009; 50(2): 1375. 5. Nam JK, et al. Comparison of the Effectiveness of the Renogram, the Serial Renal Scan and the Diuretic Half Time according to the Renal Function for Interpreting a Diuretic DTPA Scan following Pyeloplasty Korean J Urol. 2006;47: 402-406.

Image/Figure:

https://s3.amazonaws.com/amz.xcdsystem.com/1E8A4501-BB41-A02A-1D3B9882B798BFAA_abstract_File10351/GA93_ImageFigure_0512121347.jpg

Image/Figure Caption: Renogram curve pattern of bilateral PUJO patient. Obstructive pattern is observed in the right kidney curve, while non-functioning left kidney showed a minimal radioactivity uptake (flat curve).

First Name: Rian

Last Name: Hidayatullah

Email: riandayat@gmail.com

Organization: Hasan Sadikin General Hospital

Country: Indonesia

ID: GA94
99mTc-Tilmanocept SPECT imaging as a potential non-invasive method to quantify CD206+ tumor-associated M2-like macrophages

Alexanne Bouchard, Université de Bourgogne UMR INSERM 1231, bouchard.alexanne@gmail.com

---

Category: Oncology

Abstract Body : In the era of personalized medicine in oncology, progress regarding the modulation of tumor microenvironment (TME) and its follow-up by molecular imaging is of crucial importance because of its central role in the development of cancer. Among immunosuppressive cells of the TME, M2-like macrophages have been associated with cancer aggressiveness, therapy resistance and poor prognosis. The aim of this study was to assess if M2-like macrophages (i) could be tracked in vivo into the TME with SPECT imaging and (ii) could be modulated by the inhibition of Gp96, an endoplasmic reticulum chaperone involved in inflammatory processes that we have previously shown to be expressed at the cell membrane of human primary M2 macrophages (Chaumonnot et al, 2021). Tissues from mouse triple negative breast cancer (TNBC, 4T1 cell line) and colon cancer (CC, CT26 cell line) were analyzed by immunohistochemistry (IHC) to detect the presence of Gp96 and CD206 (a marker of M2 macrophages) into the TME. Specific CD206 in vivo imaging on 4T1- and CT26-tumor bearing mice receiving or not a specific inhibitor of Gp96 (PU-WS13) was performed with 99mTc-Tilmanocept SPECT (i.v injection, 15MBq/mouse). Images were performed at 1h, 4h and 24h post-injection. Ex vivo gamma counting of tumors was performed after the last imaging. Radioactivity content measured with gamma counting or on images was expressed as percentage of the injected dose per gram of tissue (% ID/g). For 4T1 tumors, tumor growth and collagen content were also assessed. IHC experiments demonstrated an overexpression of Gp96 in tumor cells as well as the presence of M2-like macrophages expressing both CD206 and Gp96 in 4T1 tumors while CT26 tumors only showed an upregulation of Gp96. These results are confirmed with in vivo SPECT imaging. 99mTc-Tilmanocept tumor uptake was significantly higher in 4T1- compared to CT26-tumor bearing mice (2.53 %ID/g and 1.08 %ID/g respectively, p=0.009). Based on these results, the 4T1 model was chosen to study the impact of Gp96 inhibition. Interestingly, PU-WS13 induced a significant decrease in 99mTc-Tilmanocept tumor uptake compared to untreated mice (1.12 %ID/g and 0.78 %ID/g respectively, p=0.0011) as well as a lower number of CD206+ M2-like macrophages compared to untreated mice. These results correlated with a reduced tumor growth and collagen content in 4T1 tumors. 99mTc-Tilmanocept SPECT imaging might represent an innovative non-invasive strategy to quantify CD206+ tumor-associated macrophages as a biomarker relevant for prognosis, therapeutic prediction and/or monitoring of solid tumors. The potential effects of PU-WS13 on the modulation of M2-like macrophages are currently investigated.

References: Chaumonnot K, Masson S, Sikner H, Bouchard A, Baverel V, Bellaye P-S, et al. The HSP GRP94 interacts with macrophage intracellular complement C3 and impacts M2 profile during ER stress. Cell Death Dis. 22 janv 2021;12(1):114.

First Name: Alexanne

Last Name: Bouchard

Email: bouchard.alexanne@gmail.com

Organization: Université de Bourgogne UMR INSERM 1231

Country: France

ID: GA95
Quantifying Myocardial Metabolic Adaptive Changes of Mice in Simulated Weightlessness Environment by Dynamic 18F-FDG PET/CT

Min Yang, The Fifth Affiliation Hospital, Sun Yat-sen University, yangminyycm@sina.com

---

Category: Cardiovascular & Pulmonary

Abstract Body : Introduction: There has been a lack of real-time intravital quantitative research on cardiovascular adaptive changes of astronauts in weightlessness environment. In this study, the dynamic 18F-FDG PET/CT was used to explore the myocardial metabolic adaptive changes in hindlimb unloading (HU) model of weightlessness. Methods: Twelve healthy Balb/c mice aged 8 weeks were randomly divided into the control group (Ctrl, n = 6) and the HU group (HU, n = 6). The preparation of the simulated weightless model was mainly based on the classic tail-suspension method proposed and improved by Morey-Holton and Chen Jie et al. After 1/2/3/4 weeks of modeling, dynamic 18F-FDG PET/CT myocardial metabolic imaging was performed for 60 min including 31 frames (10×3s; 3×10s; 4×60s; 6×150s; 8 ×300s). The dynamic raw data was analyzed by Carimas software to obtain polar bull 's-eye map of myocardial metabolism (The American Heart Association 17-segment method). With the time activity curve (TAC) of left ventricular as the input function, the original TAC of 17 myocardial segments was fitted by Patlak model to obtain 18F-FDG net uptake rate constant Ki of each segment. Unpaired t test was used to compare Ki of each segment between the Ctrl group and the HU group, and p Results: After 1 week of HU modeling, the Ki of the seg 5 (0.01108 ± 0.00530 vs 0.01750 ± 0.00395, p and seg 6 (0.00985 ± 0.00323 vs 0.01564 ± 0.00221, p ± 0.00515 vs 0.02831 ± 0.00706, p ± 0.00390 vs 0.02230 ± 0.00766, p Conclusions: After short-term simulated weightlessness (suspension 1-2 weeks), Ki of the partial myocardial segments (seg 5, 6, 11, 16) supplied by left circumflex artery (LCX) was significantly reduced, indicating the decrease of glucose metabolism in the myocardial segment supplied by LCX was an important adaptive change. After mid-term simulated weightlessness (suspension 3-4 weeks), Ki of the most myocardial segments was significantly reduced, suggesting the heart was in a low metabolic state. The result of this study for guiding the astronauts to adapt to the weightlessness was that seg 5 and 6 were the myocardial regions with the most significant changes in glucose metabolism during the early weightless simulation, while glucose metabolism of the whole heart reduced during the later weightless adaptation.

Image/Figure:

https://s3.amazonaws.com/amz.xcdsystem.com/1E8A4501-BB41-A02A-1D3B9882B798BFAA_abstract_File10351/GA95_ImageFigure_0512032010.jpg

Image/Figure Caption: Figure 1. Myocardial metabolic adaptive changes in simulated weightless environment were quantified by real-time 18F-FDG PET/CT A-B: Representative PET myocardial metabolic imaging of control group (A) and HU group (B). C-F: PET quantitative analysis results of myocardial glucose metabolism by Patlak modeling after 1/2/3/4

(C/D/E/F) weeks of suspension. Key: LAD: left anterior descending; LCX: left circumflex artery; RCA: right coronary artery.

Full Name of Abstract's 1st Author : Min Yang

First Name: Min

Last Name: Yang

Email: yangminyycm@sina.com

Organization: The Fifth Affiliation Hospital, Sun Yat-sen University

Country: China

ID: GA96
Truly tiny acoustic protein nanostructures for molecular ultrasound imaging

Bill Ling, California Institute of Technology, blling@caltech.edu

---

Category: New Chemistry, Materials & Probes

Abstract Body : The molecular imaging capabilities of ultrasound are limited by the large size and low residence time of typical microbubble-based contrast agents. Here, we describe bicone gas vesicles, the smallest known ultrasound agent with a hydrodynamic diameter of 68 nm. Bicones are immature gas vesicles—hollow protein nanostructures produced in certain aquatic microbes. Like other gas vesicles, bicones comprise a 2-nm thick protein shell which stably encapsulates a pocket of air. They are heterologously produced in E. coli and easily isolated by centrifugation. The purified particles have lengths of 72.28±11.89 nm and diameters of 39.69±4.48 nm, as measured by cryo-electron microscopy. They are colloidally stable in 20% bovine serum albumin for at least one week, with no significant changes in size distribution detected by dynamic light scattering. Using collapse-based imaging methods, we detected bicones in vitro at concentrations below 15 nM. When intravenously administered into C57BL/6 mice, bicones circulated with a half-life of 17 minutes, as determined by the kinetics of transcranial Doppler signal enhancement. Finally, we determined the composition of the particles by MALDI-TOF, Western blot, and immunogold electron microscopy, finding at least two proteins which are amenable to peptide fusion. Due to their extremely small size, facile synthesis, inherent stability, enhanced circulation time, and ease of functionalization, we believe bicones are a versatile platform for molecular detection by ultrasound imaging.

Image/Figure: https://s3.amazonaws.com/amz.xcdsystem.com/1E8A4501-BB41-A02A-1D3B9882B798BFAA_abstract_File10351/GA96_ImageFigure_0512072106.pdf

Full Name of Abstract's 1st Author : Bill Ling

First Name: Bill

Last Name: Ling

Email: blling@caltech.edu

Organization: California Institute of Technology

Country: United States

ID: GA97

Perfusion Patterns in Patients with Chronic Limb-Threatening Ischemia versus Control Patients using Near-Infrared Fluorescence Imaging with Indocyanine Green

Pim Van Den Hoven, Leiden University Medical Center, p.van_den_hoven@lumc.nl

---

Category: Cardiovascular & Pulmonary

Abstract Body : Introduction: In assessing the severity of lower extremity arterial disease (LEAD), physicians often rely on clinical judgement, thereby supported by conventional measurements of macrovascular blood flow including the ankle-brachial index or toe pressure measurement. However, these techniques provide no information about regional tissue perfusion and have shown to be of limited value in patients with chronic limb-threatening ischemia (CLTI) (1). Near-infrared (NIR) fluorescence imaging using indocyanine green (ICG) has been used extensively in perfusion studies and has shown valuable results in prediction of tissue viability in patients with LEAD. However, with regards to diagnosing LEAD, inconsistency is seen between different Fontaine stages and it is unclear whether advanced stages of LEAD alter the in- and outflow of ICG (2). Furthermore, there is limited information about the perfusion patterns of ICG NIR fluorescence imaging in control patients. In the search for providing valid and reliable cut-off values for tissue perfusion, it is an essential step to define these perfusion patterns of ICG NIR fluorescence imaging in controls too. Methods: This prospective cohort study was registered at the Dutch Trial Register with number NL7531 and included patients with CLTI and control patients. Patients were excluded based on contra-indications for ICG. The Quest Spectrum Platform® was used to perform ICG NIR fluorescence imaging. Upon intravenous administration of ICG, the NIR fluorescence intensity in both feet was recorded for 10 minutes. The NIR fluorescence videos were analyzed using the Quest Research Framework®. The dorsum of the foot was selected as region of interest and subsequently a time-intensity curve was created. An example of the measured NIR fluorescence intensity with the corresponding time-intensity curve is shown in Figure 1. Fourteen parameters were extracted from the time-intensity curves. Results: Successful ICG NIR fluorescence imaging was performed in 35 patients with a total of 60 limbs included for analyses. Nineteen patients presented with LEAD of whom 28 limbs were classified as CLTI. The control group consisted of 16 patients with a total of 32 limbs. The mean maximum intensity was significantly lower in the control group (37.9 vs 25.8, p=0.000). Furthermore, the time to maximum intensity (i.e. Tmax) was reached earlier in the CLTI group (90.5 vs 143.3, p=0.002). When looking more closely at inflow parameters, the maximum slope, the normalized maximum slope and the ingress rate were all significantly higher in the CLTI group (2.0 vs 0.6, p=0.000; 4.2 vs 2.4, p=0.000; 1.0 vs 0.2, p=0.000). For outflow parameters, a significant difference was seen for the maximum slope egress, which was higher in the control group (0.5 vs 0.2, p=0.005). No significant difference was observed for the normalized maximum slope egress (1.0 vs 0.8, p=0.733). Normalization of the time-intensity curves displayed a more narrow distribution for the time-intensity curves in both groups. Conclusion: This study demonstrates the different perfusion patterns as seen on ICG NIR fluorescence imaging between patients with CLTI and control patients. Interestingly, most inflow parameters

observed in patients with CLTI were superior to the control group. No significant differences were observed regarding outflow. Possible explanations for the increased inflow include damage to the regulatory mechanisms of the microcirculation, arterial stiffness and transcapillary leakage. In the search for providing cut-off values for adequate perfusion, more research is needed on in- and outflow patterns for control patients and various stages of LEAD.

References: 1. Misra S, Shishehbor MH, Takahashi EA, Aronow HD, Brewster LP, Bunte MC, et al. Perfusion Assessment in Critical Limb Ischemia: Principles for Understanding and the Development of Evidence and Evaluation of Devices: A Scientific Statement From the American Heart Association. Circulation. 2019;140(12):e657-e72. 2. Terasaki H, Inoue Y, Sugano N, Jibiki M, Kudo T, Lepantalo M, et al. A quantitative method for evaluating local perfusion using indocyanine green fluorescence imaging. Ann Vasc Surg. 2013;27(8):1154-61.

Image/Figure:

https://s3.amazonaws.com/amz.xcdsystem.com/1E8A4501-BB41-A02A-1D3B9882B798BFAA_abstract_File10351/GA97_ImageFigure_0512035056.jpg

Image/Figure Caption: ICG NIR fluorescence imaging in a control patient showing the near-infrared fluorescence intensity (above) and the corresponding time-intensity curves for the right (red) and left (green) foot (below).

First Name: Pim

Last Name: Van Den Hoven

Email: p.van_den_hoven@lumc.nl

Organization: Leiden University Medical Center

Country: Netherlands

ID: GA98
Translation of targeted image-guided surgery solutions based on ex vivo tissue analysis

Tessa Buckle, Leiden University Medical Center, t.buckle@lumc.nl

---

Category: Oncology

Abstract Body : Introduction: Intraoperative tumour identification (e.g., tumour extension, margins or presence of metastases) via receptor specific targeting is one of the ultimate promises of fluorescence-guided surgery. The translation of receptor-specific fluorescence tracers into clinical trials forms a critical component in maturing this treatment concept. This step is often hindered by differences in physiology and dosing in the preclinical and clinical setting, as well as differences between the imaging equipment used in both situations. To close the gap between preclinical studies and first-in-human trials the potential of topical tracer application on surgical specimens was evaluated, in order to assess both tracer and (clinical grade) camera performance. Methods: Ex vivo tracer performance was assessed via incubation of freshly excised penile squamous cell carcinoma (pSCC; N=10) and oral squamous cell carcinoma (OSCC; N=10) specimens in a solution containing the c-Met targeting tracer EMI-137 (500 nM; (1)). Three prostate specimens were incubated with the PSMA-targeting tracer EuK-(SO3)Cy5-mas3 (500 nM; (2)). Both tracers contained Cy5 as fluorescent label. All specimens were analysed using a Cy5-compatible prototype clinical grade laparoscopic camera system. In-house developed image processing software allowed video-rate/real-time tumour identification and assessment of the tumour-to-background ratio (TBR). Fluorescence imaging results were related to standard pathological tumour evaluation and immunohistochemistry. The in vivo potential of c-MET targeting, and intraoperative tumour visualization was confirmed following intravenous administration of EMI-137 in five pSCC patients using the same camera system as used for ex vivo measurements. Results: After incubation with EMI-137 or EuK-(SO3)Cy5-mas3 91.3% of tumours could be fluorescently illuminated and detected (9/10 OSCC, 10/10 pSCC and 2/3 prostate tumours). Immunohistochemistry revealed overlap between the fluorescence staining and c-Met or PSMA receptor expression in all illuminated specimens. Non-visualization (2/23, 8.7%) could be linked to lesions that resided deeper below the resection surface (OSCC; limited tissue penetration) or highly diffuse, low grade tumour with very low density of PSMA positive cells (limited local signal). Tumour margin assessment was improved using video-rate representation of the TBR (median TBR: 2.5 +/- 0.2; range 1.9-4.2). This visualization technique also allowed recognition of heterogeneity in receptor expression within the lesion. With regard to EMI-137, studies on surgical specimens successfully translated to in vivo fluorescence-guided surgery, confirming the potential of the topical evaluation steps. Conclusion: Ex vivo evaluation on fresh tumour specimens helps 1) evaluate the ability of fluorescent tracers to target tumour specific receptors in human tissue and 2) highlights the possible limitations for in vivo use (e.g., tissue penetration, low/diffuse receptor expression). Initial data obtained with EMI-137 indicate that successful ex vivo staining could be predictive for successful in vivo use.

References: 1) Burggraaf et al, Nat Med 2015 2) Hensbergen et al, JNM 2020

First Name: Tessa

Last Name: Buckle

Email: t.buckle@lumc.nl

Organization: Leiden University Medical Center

Country: Netherlands

ID: GA99
Fluorescent FAPI, does it stain FAP or something else?

Tessa Buckle, Leiden University Medical Center, t.buckle@lumc.nl

---

Category: Oncology

Abstract Body : Introduction: In recent years imaging of the fibroblast activate protein has emerged as a high potential extension of the tracer arsenal within nuclear medicine for visualization of tumor tissue. Based on the success stories of FAPI-PET one may argue that the same target may also help advance the field of image-guided surgery. Therefore, a family of fluorescent FAPI-tracers was created based on the known FAP targeting vector Gly-Pro (GP; (1)) and its variant ERGTGP. As a first step towards assessment of their suitability as FAP-targeting tracer in fluorescence-based image-guided surgery in vitro performance was assessed, wherein focus was placed on their sub-cellular accumulation. Methods: Four different GP-fluorescent FAPI tracers were synthesized by functionalizing GP or ERGTGP with QAmine(SO3)Cy5, resulting in QAmine-(SO3)Cy5-GP, QAmine-(SO3)Cy5-ERGETGP, and QAmine-(SO3)Cy5-CPGTEGRE. MCF7 (known FAP positive human breast cancer cells; (1)) cells and three control cell lines (MDAMB231 (human breast carcinoma), RT4D12 (rat schwannoma), GeB3 (dog epithelial)) were incubated with 1uM of tracer, either alone or in competition with the FAP inhibitor Ac-Gly-BoroPro. Incubation with non-functionalized dye variants and blocking with a mitochondrial tracer (1nM) were performed as control. Fluorescence confocal microscopy was used to assess the cellular distribution of the tracer signal (Cy5). Nuclear, lysosomal and mitochondrial counter stains were used as reference for intracellular localization. Immunohistochemical staining with an anti-FAP antibody was applied to confirm the presence of FAP within the different cell cultures. Results: QAmine-(SO3)Cy5-GP, QAmine-(SO3)Cy5-ERGETGP and QAmine-(SO3)Cy5-CPGTEGRE showed intracellular tracer uptake in all cell lines, with a staining pattern similar to literature reports (1). Non-functionalized dyes did not show cellular uptake. Neither incubation time (1 or 4 hours) nor temperature (4 or 37 degrees) influenced the staining of QAmine-(SO3)Cy5-GP, QAmine-(SO3)Cy5-ERGETGP or QAmine-(SO3)Cy5-CPGTEGRE. Interestingly, blocking experiments with the FAP inhibitor Ac-Gly-BoroPro (1000-fold excess) revealed a 62% decrease in fluorescence in RT4D12 cells, while uptake in MCF-7 and Geb3 cells was unaffected. Blocking with a mitochondrial stain affected uptake of the FAPI tracers in MCF-7 (60% signal decrease) but not Geb3 cells while lysosomal and mitochondrial counterstains were completely diminished. In contradiction to fluorescence imaging, FAP-specific immunohistochemistry showed intracellular presence of FAP in MCF-7, but not in RT4D12, MDAMB231 and GEB3 cells. Conclusion: The fluorescent FAPI-tracers were able to stain a wide range of cells, but the observed staining patterns did not seem to correlate with FAP IHC. At this point this discrepancy is unexplained, but the bulky nature of the fluorescent dyes could play a role.

References: 1) Brennen et al, JNCI, 2012

First Name: Tessa

Last Name: Buckle

Email: t.buckle@lumc.nl

Organization: Leiden University Medical Center

Country: Netherlands

ID: GA100
Assessment of Tissue Viability following Amputation Surgery using Near-Infrared Fluorescence Imaging with Indocyanine Green

Pim Van Den Hoven, Leiden University Medical Center, p.van_den_hoven@lumc.nl

---

Category: Cardiovascular & Pulmonary

Abstract Body : Introduction: Patients with chronic limb-threatening ischemia have a risk of undergoing a major amputation within 1 year of nearly 30% with a substantial risk of re-amputation since wound healing is often impaired (1). Quantitative assessment of regional tissue viability following amputation surgery can identify patients at risk for impaired wound healing. For the assessment of regional perfusion, near-infrared (NIR) fluorescence imaging using Indocyanine Green (ICG) has already shown promising results in reconstructive surgery (2). Prospective studies on the predictive value of ICG NIR fluorescence imaging in healing of amputation wounds have yet to be performed. Methods: This prospective cohort study included adult patients undergoing lower extremity amputation surgery due to peripheral artery disease or diabetes mellitus. ICG NIR fluorescence imaging was performed within 5 days following amputation surgery using the Quest Spectrum Platform®. Following intravenous administration of ICG, the NIR fluorescence intensity of the amputation wound was recorded for 10 minutes. The NIR fluorescence intensity videos were analyzed and if a fluorescence deficit was observed, this region was marked as “low fluorescence”. All other regions were marked as “normal fluorescence”. Results: Successful ICG NIR fluorescence imaging was performed in 10 patients undergoing a total of 15 amputations. No “low fluorescence” regions were observed in 11 out of 15 amputation wounds. In 10 out of these 11 amputations, no wound healing problems occurred during follow-up. Regions with “low fluorescence” were observed in 4 amputation wounds. Impaired wound healing corresponding to these regions was observed in all wounds and a re-amputation was necessary in 3 out of 4. An example of a patient where a “low fluorescence” region was observed is depicted in Figure 1. When observing time-related parameters, regions with low fluorescence had a significantly longer time to maximum intensity (113 seconds versus 32 seconds, p=0.003) and a significantly lesser decline in outflow after five minutes (80.3% versus 57.0%, p=0.003). Conclusion: ICG NIR fluorescence imaging was able to predict postoperative skin necrosis in all four cases. Quantitative assessment of regional perfusion remains challenging due to influencing factors on the NIR fluorescence intensity signal, including camera angle, camera distance and ICG dosage. This was also observed in this study, contributing to a large variety in fluorescence intensity parameters among patients. To provide surgeons with reliable NIR fluorescence cut-off values for prediction of wound healing, prospective studies on the intra-operative use of this technique are required. The potential prediction of wound healing using ICG NIR fluorescence imaging will have a huge impact on patient mortality, morbidity as well as the burden of amputation surgery on health care.

References: 1. Mustapha JA, Katzen BT, Neville RF et al. Disease Burden and Clinical Outcomes Following Initial Diagnosis of Critical Limb Ischemia in the Medicare Population. JACC Cardiovasc Interv. 2018;11(10):1011-2. 2. Driessen C, Arnardottir TH, Lorenzo AR et al.

How should indocyanine green dye angiography be assessed to best predict mastectomy skin flap necrosis? A systematic review. J Plast Reconstr Aesthet Surg. 2020;73(6):1031-42.

Image/Figure:

https://s3.amazonaws.com/amz.xcdsystem.com/1E8A4501-BB41-A02A-1D3B9882B798BFAA_abstract_File10351/GA100_ImageFigure_0512051627.png

Image/Figure Caption: ICG NIR fluorescence imaging in a 76-year old male patient showing the visual, near-infrared fluorescence and merged imaged following transtibial amputation on the right side. A region of low fluorescence is seen in the middle and lateral wound region. The demarcation of the skin was clearly visible 3 weeks postoperatively and corresponded with the area of low fluorescence.

First Name: Pim

Last Name: Van Den Hoven

Email: p.van_den_hoven@lumc.nl

Organization: Leiden University Medical Center

Country: Netherlands

ID: GA101
Near-Infrared Fluorescence Imaging with Indocyanine Green for Quantification of Changes in Tissue Perfusion following Revascularization

Pim Van Den Hoven, Leiden University Medical Center, p.van_den_hoven@lumc.nl

---

Category: Cardiovascular & Pulmonary

Abstract Body : Introduction: Current diagnostic modalities for patients with peripheral artery disease (PAD) mainly focus on the macrovascular level and are unable to quantify regional tissue perfusion (1). For quantitative assessment of tissue perfusion, near-infrared (NIR) fluorescence imaging using indocyanine green (ICG) seems promising. In this prospective cohort study, ICG NIR fluorescence imaging was performed pre- and post-revascularization to assess changes in foot perfusion. Methods: ICG NIR fluorescence imaging was performed in patients with PAD pre- and postintervention. After intravenous bolus injection of 0.1mg/kg ICG, the camera registered the NIR fluorescence intensity over time on the dorsum of the feet for 15 minutes using the Quest Spectrum Platform®. Time-intensity curves were plotted for 3 regions of interest (ROIs): 1. The dorsum of the foot, 2. The forefoot and 3. The hallux. Time-intensity curves were normalized for maximum fluorescence intensity. Extracted parameters were the maximum slope, area under the curve (AUC) for the ingress and the AUC for the egress. The non-treated contralateral leg was used as a control group. Results: Successful revascularization was performed in 32 patients. There was a significant increase for the maximum slope and AUC egress in all three ROIs. The most significant difference was seen for the maximum slope in ROI 3 (3.7 %/s to 6.6 %/s, p Conclusions: This study shows the potential of ICG NIR fluorescence imaging in assessing changes in foot perfusion following successful revascularization. The perfusion of the non-treated leg does not appear to be influenced by a revascularization procedure on the contralateral side. Future studies should incorporate normalized parameters and focus on the value of ICG NIR fluorescence imaging in predicting favorable outcome following revascularization.

References: 1. Misra S, Shishehbor MH, Takahashi EA, Aronow HD, Brewster LP, Bunte MC, et al. Perfusion Assessment in Critical Limb Ischemia: Principles for Understanding and the Development of Evidence and Evaluation of Devices: A Scientific Statement From the American Heart Association. Circulation. 2019;140(12):e657-e72.

Image/Figure:

https://s3.amazonaws.com/amz.xcdsystem.com/1E8A4501-BB41-A02A-1D3B9882B798BFAA_abstract_File10351/GA101_ImageFigure_0512055229.png

Image/Figure Caption: NIR fluorescence intensity before (above) and after (below) an endovascular revascularization on the left side in a 76-year old male patient. The time-intensity curves of the treated left side (red) and control side (green) are shown on the right side. Hence the increased inflow on the left side.

First Name: Pim

Last Name: Van Den Hoven

Email: p.van_den_hoven@lumc.nl

Organization: Leiden University Medical Center

Country: Netherlands

ID: GA103
Preclinical Evaluation of [18F]Talazoparib as Next Generation PARP Imaging Agent.

Sophie Stotz, University of Tuebingen/Werner Siemens Imaging Center, sophie.stotz@med.uni-tuebingen.de

---

Category: Oncology

Abstract Body : PURPOSE The clinical importance of poly (ADP-ribose) polymerase (PARP) as a tumor biomarker warrants the development of novel PARP imaging probes with improved pharmacological properties. PARP inhibitors serve as lead structures for the development of PARP-targeted optical and nuclear imaging probes. The most prominent among such imaging agents are PARPi-FL, an optical probe; its radiolabeled analogue [18F]PARPi; and [18F]FTT, the first clinically applied PARP radiotracer. We present the preclinical in vivo evaluation of 18F-labeled talazoparib, the as-of-yet most potent PARP inhibitor, as second-generation PARP radiotracer. METHODS Enantiomerically pure [18F]talazoparib (>99% enantiomeric excess, >99% radiochemical purity, 45-176 GBq/µmol molar activity; n = 4) was used for this study. Binding of [18F]talazoparib to PARP1 was demonstrated by uptake assays in the HR-deficient cell line HCC1937 and compared to the inactive enantiomer [18F]LT-674. In a pilot in vivo study, HCC1937-xenograft bearing female NOD.CB17-Prkdcscid/J mice (n = 5) were subjected to 1 hour dynamic PET imaging and a 10 minute static PET scan 2 hours after injection of [18F]talazoparib, followed by an anatomical MR scan. Biodistribution was assessed from dynamic PET data as well as ex vivo by gamma-counting of selected organs in order to further investigate the pharmacological properties of the molecule. PARP1 immunofluorescence microscopy confirmed PARP1 expression in the xenograft tissue. RESULTS [18F]Talazoparib was stable in both mouse and human serum over 240 minutes. The radiotracer demonstrated excellent binding to HCC1937 cells in vitro that was blockable by >99% with excesses of both talazoparib and olaparib. As expected, the inactive enantiomer [18F]LT-674 showed only low uptake in HCC1937 cells. Talazoparib was found to block substantially more of the radiotracer signal than olaparib, a phenomenon that was also observed in a cell-based competition assay. In vivo, [18F]talazoparib exhibited balanced clearance by both hepatobiliary and renal excretion pathways and fast blood clearance with a calculated blood half-life of 3.3 minutes. Most radiotracer signal was observed in the excretion-related abdominal tissues (liver, kidney, spleen, and intestine). Moderate bone and muscle uptake was observed, in line with reported specific uptake of previous PARP radiotracers.[1] The HCC1937 xenografts showed [18F]talazoparib signal that intensified over time, resulting in a mean tumor-to-muscle ratio (TMR) of 1.82 ± 0.44 3 hours post injection. The 5.6-fold higher (10.23 ± 1.51) tumor-to-blood ratio underlines the rapid clearance of the tracer, combined with specific muscle uptake. Our data approve feasibility of [18F]talazoparib-PET in mice and warrants exploration of [18F]talazoparib imaging in other cell and animal models. CONCLUSION [18F]Talazoparib presented with rapid and balanced excretion, relatively high bone and muscle uptake, and a TMR that is comparable to [18F]FTT in the same xenograft model (1.9 after 1 hour uptake)[2]. The distinct mode of action compared to first-generation PARP inhibitors suggests that [18F]talazoparib may allow us to study PARP

enzymes from a different angle beyond PARP1.[3] To shed light on this hypothesis will be within the scope of future studies.

References: [1] Carney et al., Mol Imaging Biol, 2016 [2] Edmonds et al., Am J Nucl Med Mol Imaging, 2016 [3] LaFargue et. Al., Lancet Oncol, 2019

Full Name of Abstract's 1st Author : Sophie Stotz

First Name: Sophie

Last Name: Stotz

Email: sophie.stotz@med.uni-tuebingen.de

Organization: University of Tuebingen/Werner Siemens Imaging Center

Country: Germany

ID: GA104
Quantification of Perfusion in DIEP and PAP Flaps Using Near Infrared Fluorescence and Indocyanine Green

Lisette van Capelle, Leiden University Medical Center, lisette@vancapelle.com

---

Category: Instrumentation

Abstract Body : Abstract— Background: One of the complications in a deep inferior epigastric artery perforator (DIEP) flap or profunda artery perforator (PAP) flap is the occurrence of fat necrosis, which occurs in 12-45% of all reconstructions. [1,2] Intra-operative use of near-infrared fluorescence (NIR) imaging with indocyanine green (ICG) is a technique that has proven its potential to predict fat necrosis, since the use of ICG NIR fluorescence imaging reduces its incidence by more than halve. [3-7] For the interpretation of the observed NIR fluorescence intensity, the surgeon relies on qualitative assessment of the signal. The aim of this study is to provide a first step in quantification of the NIR fluorescence intensity by gaining insight in the observed perfusion patterns in DIEP and PAP flaps. Method: In this pilot study, NIR fluorescence with ICG was performed in patients undergoing DIEP - or PAP flap reconstruction. After arterial and venous anastomosis, 7.5mg ICG was administered intravenously as a bolus. To prevent autofluorescence, the operation room was cleared of ambient light and gauzes were placed around the flap to limit interfering fluorescence from the thoracic skin. The NIR fluorescence intensity over time was measured with the Quest Spectrum platform®. Postoperatively, four regions were selected by a plastic surgeon based on the NIR fluorescence images: perforator, well-perfused, questionably perfused and poorly perfused. The location of the perforators was selected based on an intra-operatively placed marker. Time-intensity curves were analyzed within these four regions with the Quest Spectrum Framework®. For the quantification, four parameters were extracted from the time-intensity curves: Tmax (seconds), ingress (arbitrary units/seconds), T max slope (seconds) and the max slope (arbitrary units/seconds). Results: During the study period, 14 DIEP flaps and 3 PAP flaps were performed in 14 patients. Thirteen perforators, 17 well-perfused, 8 questionably perfused and 3 poorly perfused regions were identified. The well-perfused regions matched the perforator curves and showed a fast inflow. The questionably perfused regions were more similar to the poorly perfused regions and demonstrated a slow inflow. Outflow was only seen in the perforator and well-perfused regions. There was a significant difference in three of the four measured parameters between the four groups: Tmax: p Conclusion: In the search for the quantitative assessment of tissue perfusion using ICG NIR fluorescence imaging, this study demonstrated well-perfused and perforator regions show a significantly faster inflow. Moreover, within these regions, the outflow phase was reached in all cases, in contrary to the questionably and poorly perfused regions. These results are a first step towards the quantification of tissue perfusion in free flap surgery. To more accurately predict fat necrosis, future studies on ICG NIR fluorescence imaging during free flap surgery, should incorporate quantitative assessment of the measured NIR fluorescence intensity.

References: 1. Bhullar, H., Hunter-Smith, D.J. & Rozen, W.M. Fat Necrosis After DIEP Flap Breast Reconstruction: A Review of Perfusion-Related Causes. Aesth Plast Surg 44, 1454–1461 (2020). 2. Peeters WJ, Nanhekhan L, Van Ongeval C, Fabré G, Vandevoort M. Fat necrosis in deep inferior epigastric perforator flaps: an ultrasound-based review of 202 cases. Plast Reconstr Surg. 2009 Dec;124(6):1754-1758. 3. Hembd AS, Yan J, Zhu H, Haddock NT, Teotia SS. Intraoperative Assessment of DIEP Flap Breast Reconstruction Using Indocyanine Green Angiography: Reduction of Fat Necrosis, Resection Volumes, and Postoperative Surveillance. Plast Reconstr Surg. 2020 Jul;146(1):1e-10e. 4. Momeni A, Sheckter C. Intraoperative Laser-Assisted Indocyanine Green Imaging Can Reduce the Rate of Fat Necrosis in Microsurgical Breast Reconstruction. Plast Reconstr Surg. 2020 Mar;145(3):507e-513e. 5. Malagón-López P, Vilà J, Carrasco-López C, García-Senosiain O, Priego D, Julian Ibañez JF, Higueras-Suñe C. Intraoperative Indocyanine Green Angiography for Fat Necrosis Reduction in the Deep Inferior Epigastric Perforator (DIEP) Flap. Aesthet Surg J. 2019 Mar 14;39(4):NP45-NP54. 6. Gorai K, Inoue K, Saegusa N, Shimamoto R, Takeishi M, Okazaki M, Nakagawa M. Prediction of Skin Necrosis after Mastectomy for Breast Cancer Using Indocyanine Green Angiography Imaging. Plast Reconstr Surg Glob Open. 2017 Apr 7. Parmeshwar N, Sultan SM, Kim EA, Piper ML. A Systematic Review of the Utility of Indocyanine Angiography in Autologous Breast Reconstruction. Ann Plast Surg. 2020

Image/Figure:

https://s3.amazonaws.com/amz.xcdsystem.com/1E8A4501-BB41-A02A-1D3B9882B798BFAA_abstract_File10351/GA104_ImageFigure_0512075930.png

Image/Figure Caption: Output of the Quest software. A, real time view with selected regions of interest. Red and spring green are well-perfused regions. Magenta and chartreuse show perforator regions. Blue and orange show questionably perfused regions and cyan is a poorly perfused region. B, fluorescence image with identical regions of interest as in A. C, time-intensity curves corresponding to the selected regions of interest. Time in seconds and intensity in arbitrary units. The perioperatively marks on the flap are not decisive in this study.

First Name: Lisette

Last Name: van Capelle

Email: lisette@vancapelle.com

Organization: Leiden University Medical Center

Country: Netherlands

ID: GA105

A convenient labeling strategy for the preparation of fluorescent/radioactive single-label tracers carrying 99mTc[Tc] and IRDye800CW for intra-operative decision making

Noemi Declerck, Vrije Universiteit Brussel, Noemi.Berte.Declerck@vub.be

---

Category: Oncology

Abstract Body : Introduction: Cancer surgery is applied in the treatment of solid tumors and aims for the total removal of tumor lesions and complete remission of the patient. Yet, intra-operative identification of tumor margins remains difficult, frequently resulting in positive resection margins and a necessity for adjuvant therapies. Intra-operative guidance using fluorescence molecular imaging has been proven to improve the identification of tumor margins and thus support complete resections. However, insufficient tissue penetration of the fluorescent signal hinders the identification of deep or occult tumor lesions. The combination of fluorescence imaging with intra-operative gamma-probing provides an ideal balance of the deep signal penetration of gamma rays for tumor localization and a fluorescent signal for precise tumor resection.[1],[2] Preferentially, both modalities are combined in a site-specifically labeled bimodal single-label tracer. In this study we propose a convenient way to label targeting moieties, such as nanobodies, with 99mTc[Tc] and IRDye800CW. 99mTc[Tc] is a gamma-emitting radioisotope which can be used pre- and intra-operatively for tumor detection using SPECT/CT or gamma-probing respectively. The near infra-red dye IRDye800CW shows high in vivo signals enabling accurate identification of tumor margins. Methods: Specific nanobodies were engineered to carry a carboxy-terminal hexahistidine- and cysteine-tag separated by a 14 amino acid linker. First, nanobodies were site-specifically labeled with IRDye800CW-maleimide on the cysteine-tag and subsequently with 99mTc[Tc](CO)3 on the hexahistidine-tag.(Figure 1A) Quality controls were conducted for each step via size-exclusion chromatography and hydrophobic interaction chromatography. (Photo)stability was assessed in function of time and added activity via absorbance and fluorescence measurements. The influence of the bimodal label on in vivobiodistribution and tumor targeting was evaluated. Tumor-bearing mice were imaged using SPECT/CT and fluorescence imaging one hour after intravenous injection of 2 nmol of labeled compound. Ex vivo analysis on organs of interest was performed using fluorescence imaging and gamma-counting. Results: The site-specific labeling of the nanobodies with IRDye800CW and subsequently 99mTc[Tc](CO)3 was successful. However, the labeling strategy was shown to be influenced by the amount of activity used in the second labeling step. Labeling of 25 µg nanobody-IRDye800CW with up to 74 MBq 99mTc[Tc](CO)3 resulted in good preservation of the fluorescent signal. Higher activities led to a decrease in or the loss of the fluorescent signal. Up-scalability of the labeling was proven to be possible by labeling 200 µg nanobody-IRDye800CW with 220 MBq 99mTc[Tc](CO)3 for the in vivo experiments without any consequences for the fluorescent signal. The IRDye800CW/99mTc[Tc] tracers showed an in vivo and ex vivo biodistribution profile with rapid blood clearance, renal clearance, no unexpected background signals, and specific tumor uptake for the targeted nanobody as compared to a non-targeting control nanobody.(Figure 1B-D) Thus, the bimodal label shows no

signs of influencing the in vivo biodistribution of the tracer negatively. Conclusion: The bimodal labeling was successfully optimized and could be implemented as a standard bimodal labeling strategy for other nanobodies. Furthermore, the in vivo biodistribution of the tracer is not negatively influenced by the addition of the bimodal label. Therefore, this new bimodal fluorescent/radioactive nanobody-based tracer has the potential to be translated and implemented into clinical practice.

References: [1] Hekman MC, Rijpkema M, Muselaers CH, et al. Tumor-targeted Dual-modality Imaging to Improve Intraoperative Visualization of Clear Cell Renal Cell Carcinoma: A First in Man Study. Theranostics. 2018;8(8):2161-2170. doi:10.7150/thno.23335 [2] Weissleder R, Ntziachristos V. Shedding Light Onto Live Molecular Targets. Nat Med. 2003;9(1). doi:10.1038/NM0103-123

Image/Figure:

https://s3.amazonaws.com/amz.xcdsystem.com/1E8A4501-BB41-A02A-1D3B9882B798BFAA_abstract_File10351/GA105_ImageFigure_0512082258.png

Image/Figure Caption: Figure 1: A. Schematic representation of the site-specifically labeled nanobody-99mTc[Tc](CO)3-IRDye800CW tracer. B, C & D. In vivo axial (B) and sagital (C) SPECT/CT and dorsal fluorescence (D) imaging 1h post-injection of a targeting nanobody-99mTc[Tc](CO)3-IRDye800CW tracer. Signal in the tumor (T) can be observed with both modalities. Signal in the kidneys (Kds) is present due to renal clearance of the tracer.

Full Name of Abstract's 1st Author : Noemi Berte Declerck

First Name: Noemi

Last Name: Declerck

Email: Noemi.Berte.Declerck@vub.be

Organization: Vrije Universiteit Brussel

Country: Belgium

ID: GA106
Robot assisted PSMA-targeted prostate cancer surgery – a multi-center experience

Matthias van Oosterom, Leiden University Medical Center, m.n.van_oosterom@lumc.nl

---

Category: Oncology

Abstract Body : Aim: During open salvage surgery, Prostate-Specific Membrane Antigen (PSMA)-targeting has shown to be a valuable approach for the detection and removal of prostate cancer (PCa) recurrences using radioguidance [1]. Especially within the field of Urology, the rapid adoption of robot-assisted surgery has generated the need for robot-compliant image-guided surgery techniques. To this end, we recently translated a miniaturized DROP-IN gamma probe which has promised to connect radioguidance with robotic surgery [2]. Building on these developments, we set out to evaluate the feasibility and short-term outcomes of robot-assisted PSMA radioguided surgery (RGS) in PCa patients using a dedicated radiotracer and DROP-IN gamma probe. Methods: 30 patients were included in this study with either primary or recurrent prostate cancer, divided over three different high-volume centers in PCa surgery (i.e., Amsterdam – The Netherlands; Hamburg – Germany; Sydney - Australia). Patients were selected based on a positive PSMA positron emission tomography (PET)/CT, where patients with a biochemical recurrent cancer (PSA ≥ 0.2 ng/ml) had either nodal or local recurrent PCa (a maximum of 2 recurrences). Roughly 21 hours before surgery, all participants received an intravenous injection of 99mTc-PSMA I&S (~550 MBq), which was followed by a SPECT/CT, serving as a quality control for successful tracer distribution, where correlation with diagnostic PET/CT was recorded. Robotic PSMA-targeted surgery was realized using the DROP-IN gamma probe. The primary endpoint was feasibility to identify and resect PCa (including recurrences or remnants) in this setting. Secondary endpoints included the comparison between radioactive observations of removed tissue samples and final histopathology, the reduction in prostate-specific antigen (PSA) and the obtainment of a complete biochemical response (i.e., PSA Results: In these PSMA-targeted procedures, the preoperative SPECT/CT images indicated tracer accumulation in lesions as well as background signal in clearance organs. During surgery, interference signals were observed from background tissues (i.e., blood, urine, bladder, and bowel). Due to these background signals, the maneuverability of the DROP-IN seemed to be instrumental for successful target definition in vivo. In both the primary and recurrent setting, nodal and local metastases could be retrieved. Interestingly, in some cases of the primary tumor setting, tumor remnants were still found in the prostate resection bed after an incomplete tumor resection, despite urine contamination. Ex vivo scanning of the specimens excised with a gamma probe, helped to immediately confirm a successful lesion retrieval in all cases. At pathology, nodal metastasis had a median size of 8.7 mm, IQR 3.8-15.0. Postoperatively, no high-grade complications (Clavien-Dindo ≥ grade 3) were observed. Conclusion: PSMA-targeted surgery has proven useful for the intraoperative detection and resection of local and nodal PSMA-avid PCa (recurrences). Based on these initial successes, the multicenter study is being expanded to include more patients and centers.

References: [1] T. Horn, et al. "Single lesion on prostate-specific membrane antigen-ligand positron emission tomography and low prostate-specific antigen are prognostic factors for a favorable biochemical response to prostate-specific membrane antigen-targeted radioguided surgery in recurrent prostate cancer." European urology 76.4 (2019): 517-523. [2] P. Dell'Oglio, et al. "A DROP-IN Gamma Probe for Robot-assisted Radioguided Surgery of Lymph Nodes During Radical Prostatectomy." European Urology 79.1 (2021): 124-132

First Name: Matthias

Last Name: van Oosterom

Email: m.n.van_oosterom@lumc.nl

Organization: Leiden University Medical Center

Country: Netherlands

ID: GA107

Hyperpolarized [1-13C]Lactate Production in Human Prostate Cancer is Driven by the Decoupling of Tumor-Stroma Lactate Shuttle and a Shift From Oxidative to Glycolytic Metabolism

Nikita Sushentsev, University of Cambridge, nikitasushentsev@gmail.com

---

Category: Oncology

Abstract Body : Background. Hyperpolarized [1-13C]pyruvate MRI (HP 13C-MRI) is an emerging clinical imaging technique for visualizing tumor lactate production in vivo1. Previous studies have shown elevated [1-13C]lactate production in metastatic prostate cancer (PCa)2 and established the relationship between Gleason grade and increasing [1-13C]lactate3. However, the specific biological mechanisms behind [1-13C]lactate production in human PCa are still not well characterized. Objective. This study used HP 13C-MRI in patients with low-, intermediate-, and high-risk PCa to identify molecular drivers of [1-13C]lactate production in prostate tumors of varying aggressiveness. Methods. Patients with biopsy-proven tumors visible on proton MRI (1H-MRI) who were also scheduled for radical prostatectomy, underwent 3T HP 13C-MRI following intravenous injection of hyperpolarized [1-13C]pyruvate. Tumor-derived signal-to-noise ratios (SNR) for pyruvate, lactate, and total carbon were calculated in addition to the [1-13C]pyruvate-to-[1-13C]lactate conversion rate (kPL). Whole-mount surgical sections were stained with hematoxylin and eosin, with tumor grade and percent Gleason pattern 4 (%GP4) evaluated by an experienced genitourinary pathologist. The same sections were used for the immunohistochemical analysis of monocarboxylate transporters (MCT) 1 and 4 membrane expression. We also used RNAscope to quantify mRNA expression of lactate dehydrogenase (LDH) subunits A and B as well as pyruvate dehydrogenase E1 subunit alpha 1 (PDHA1). A random forest classifier was used to quantify the overall, tumor-, and stroma-derived expression of these metabolic biomarkers. Results. The study included 10 patients with 15 lesions, of which 2, 11, and 2 harbored Grade Group 1, 2, and 3 disease, respectively. Lactate SNR showed a strong positive correlation with %GP4 (rs = 0.65, P = 0.03), tumor-stroma MCT4 ratio (rs = 0.90, P = 0.002), and LDHA/LDHB ratio (rs = 0.80, P = 0.005). Total carbon SNR demonstrated a strong positive correlation with LDHA/PDHA1 ratio (rs = 0.89, P 10%), the latter demonstrated a significantly higher median tumor-stroma MCT4 ratio (0.37 vs 0.05, P = 0.01), LDHA/LDHB ratio (2.60 vs. 0.31, P = 0.006), and LDHA/PDHA1 ratio (2.20 vs 0.31, P = 0.006), respectively. When the analysis was repeated in single malignant glands harboring clear Gleason pattern 3, 4, and 5 disease, the described ratios were significantly higher in GP5 glands compared to GP3 and GP4 disease (P-value range, Conclusions. We demonstrated differential [1-13C]lactate production in intermediate-risk PCa which contained varying percentages of Gleason pattern 4 disease, confirming that the metabolic signature derived from HP 13C-MRI can provide further stratification of disease aggressiveness. This was associated with increased tumor lactate efflux via MCT4 that was likely driven by a switch from oxidative to glycolytic metabolism as evidenced by the concomitant increase in both the LDHA/LDHB and LDHA/PDHA1 ratios. A single-gland assessment of the described ratios also indicated the presence of two distinct metabolic phenotypes: oxidative and lactate-consuming (Gleason

patterns 3 and 4) compared to glycolytic and lactate-producing (Gleason pattern 5) states. These findings provide the potential mechanistic evidence for the increasing [1-13C]lactate production in severe disease, which underpins further clinical translation of HP 13C-MRI as a non-invasive risk-stratification tool to differentiate indolent from aggressive PCa.

References: 1. Kurhanewicz, J. et al. Hyperpolarized 13C MRI: Path to Clinical Translation in Oncology. Neoplasia (United States) vol. 21 1–16 (2019). 2. Chen, H. Y. et al. Hyperpolarized 13C-pyruvate MRI detects real-time metabolic flux in prostate cancer metastases to bone and liver: a clinical feasibility study. Prostate Cancer Prostatic Dis. 23, 269–276 (2020). 3. Granlund, K. L. et al. Hyperpolarized {MRI} of Human Prostate Cancer Reveals Increased Lactate with Tumor Grade Driven by Monocarboxylate Transporter 1. Cell Metab. 31, 105--114.e3 (2020).

Full Name of Abstract's 1st Author : Nikita Sushentsev

First Name: Nikita

Last Name: Sushentsev

Email: nikitasushentsev@gmail.com

Organization: University of Cambridge

Country: United Kingdom

ID: GA108

High-yield Synthesis of Clinically Relevant DOTA-based Tracers Using Cyclotron-produced Gallium-68

Emma Jussing, Karolinska Institutet, emma.jussing@ki.se

Category: New Chemistry, Materials & Probes

Abstract Body : Background: With increasing demand for gallium-68 (68Ga) labeled radiopharmaceuticals, alternative sources of 68Ga to the low activity output 68Ge/68Ga-generators are strongly desirable. By using liquid or especially solid targets mounted to medical cyclotrons, it is possible to produce larger amounts of 68GaCl3 via the 68Zn(p,n)68Ga reaction (1,2). Purification of the 68Ga from the enriched 68Zn target material and other metal ion impurities is a critical step as these metals compete with 68Ga in the complexation with different chelators, that negatively effects the radiolabeling yields. Predominantly, the metal ion of concern is obviously the dominant Zn2+ present after irradiation, but also the trivalent Fe3+, which, for example, has a higher stability constant (log KML) than Ga3+ for the commonly used chelator DOTA. It was hypothesized that by decreasing the amount of Fe3+ in the cyclotron-produced 68GaCl3 eluate, the 68Ga-radiopharmaceutical yield and its' apparent molar activity (AMA) will consequently increase. In this work, an improved purification methodology is presented, generating low level of Fe3+ in the 68GaCl3 eluate, that can be utilized for high-yield radiolabeling of clinically relevant DOTA-based tracers, such as DOTA-TOC and FAPI-46. By titrations the potential improvement for radiolabelings based on NOTA- and HBED-based tracers was also investigated. Materials and methods: Enriched zinc-68 (68Zn) foils (approx. 120 mg 68Zn, Isoflex USA) were irradiated in a cyclotron with 25 μA, 12.6 MeV protons in a solid target cyclotron system (GE PETtrace 800 and Comecer PTS). The produced 68Ga was purified in an automated purification module (Taddeo PRF, Comecer) using a 2 x UTEVA resin (Triskem) method, as previously described (2). Modifications of the dilution and wash solutions before purification were performed to decrease the levels of Fe3+ in the final 68GaCl3 eluate. The 68GaCl3 eluate was analysed for metal content by Inductively Coupled Plasma-Mass Spectrometry (ICP-MS), and by titrations (evaluated with radio-iTLC) with three commonly used chelators (DOTA, NOTA, and HBED). The resulting 68GaCl3 eluate was utilized for GMP-radiolabeling of the DOTA-based tracer molecules DOTA-TOC and FAPI-46 using an automated synthesis module (Eckert & Ziegler). Full quality controls (QC) were performed and as an evaluation of the modification's impact, the amount radiolabeled activity, yields, and AMA were determined. Results: Compared to the earlier cyclotron produced 68GaCl3 eluates, the new modifications yielded a 5-fold decrease of Fe impurity levels, and 68Ga titrations with the chelators DOTA, NOTA, and HBED showed an increased AMA of >2-, >3-, and >15-fold, respectively. Notable; compared to earlier investigated generator eluted 68GaCl3, the AMA for DOTA was >40-fold higher (2). GMP-compliant, radiochemically pure, and stable products of [68Ga]Ga-DOTA-TOC (>5 h stability tested) and [68Ga]Ga-FAPI-46 (>4 h stability tested) were achieved. The final product activity at end of synthesis (EOS) of ~6 GBq/batch of [68Ga]Ga-DOTA-TOC or [68Ga]Ga-FAPI-46 after 68 min bombardment was significant higher, compared to the corresponding batches of ~0.6 GBq/batch, obtained from the generator produced 68GaCl3

eluate (see Table 1). Conclusions: In this study, a new improved purification approach was demonstrated to decrease the levels of competing metal ions (i.e., Fe3+) in the cyclotron solid-target produced 68GaCl3 eluate, which enabled GMP-compliant high-yield DOTA-peptide synthesis of clinically relevant tracers. To our knowledge, this is the first data showing the highest yields obtained for DOTA-based tracers with cyclotron-produced 68Ga. Titrations indicate that radiolabelings of NOTA- or HBED-based tracers may give even better yields using this cyclotron-produced 68GaCl3 eluate.

References: 1. IAEA-TECDOC-1863 (2019). Gallium-68 Cyclotron Production. Vienna, INTERNATIONAL ATOMIC ENERGY AGENCY. 2. Jonathan Siikanen. Emma Jussing, Stefan Milton, Carsten Steiger, Johan Ulin, Erik Samén, Thuy A. Tran. Cyclotron Production of 68Ga Using Enriched 68Zn Foils. Conditionally accepted Journal of Applied Radiation and Isotopes (11 April 2021)

Image/Figure: https://s3.amazonaws.com/amz.xcdsystem.com/1E8A4501-BB41-A02A-1D3B9882B798BFAA_abstract_File10351/GA108_ImageFigure_0512090901.pdf

Image/Figure Caption: Table 1. Results from radiopharmaceutical productions. All values are presented as non-decay corrected at end of synthesis. *GalliaPharm (Eckert & Ziegler) **GalliaPharm or GalliAd (IRE Elit)

First Name: Emma

Last Name: Jussing

Email: emma.jussing@ki.se

Organization: Karolinska Institutet

Country: Sweden

ID: GA109
Improved intraoperative localization for magnetic nanoparticles with fluorescence imaging and 3D freehand magnetic particle imaging

Samaneh Azargoshasb, Department of Radiology, Leiden University Medical Center, s.azargoshasb@lumc.nl

---

Category: Instrumentation

Abstract Body : Introduction: In penile cancer, sentinel lymph node biopsy is a routine procedure for nodal staging. Most commonly, radiocolloids are used to provide various forms of preoperative imaging and intraoperative guidance in this procedure. This has been further extended with intraoperative fluorescence imaging by introduction of hybrid radio- and fluorescence-tracers, such as ICG-99mTc-nanocolloid. In parallel, an alternative magnetic-particle based approaches has been introduced that uses superparamagnetic iron-oxide nanoparticles (SPIONs). In this magnetic approach, intraoperative localization is currently limited to detection with a handheld-magnetometer-detection probe only. In an attempt to improve intraoperative localization in the magnetic approach, this study investigates a novel 3D magnetic particle imaging (MPI) and navigation modality (freehand MPI) in procedures that use a combination of magnetic and indocyanine-green (ICG) fluorescence guidance. Methods: The freehand MPI modality was built using a surgical navigation device, optical tracking system, magnetometer probe and dedicated reconstruction software. The combined use of magnetic and fluorescence guidance was facilitated by administering a hybrid cocktail of both SPION and ICG tracers. The use of both the 3D freehand MPI modality and the tracer mixture were investigated in phantoms, in human skin explants and during porcine surgery. Results: The phantom and human skin studies showed that the current freehand MPI modality had a depth penetration up to 1.5 cm, a resolving power of at least 7 mm and a sensitivity of 2.2*10-2 mg/mL SPIONsa. Evaluation during porcine surgery showed that freehand MPI could improve intraoperative target identification by allowing for an augmented reality visualization of the localized tracer uptake directly on the surgical field. Furthermore, the sites of SPION accumulation found in the fhMPI scans could be used as target for virtual reality navigation and depth estimation prior to incision. This boosted surgical confidence, as opposed to using magnetic tracing only. Furthermore, in analogy to the hybrid approach used in radioguided surgery, fluorescence imaging provided a real-time visual confirmation of the sentinel lymph nodes during the actual excision. Conclusion: 3D freehand MPI is feasible in vivo, supporting a better identification of SPION accumulation and providing subsequent surgical navigation. Furthermore, the additional use of ICG provides the option for direct real-time confirmation of the localized lymph nodes.

First Name: Samaneh

Last Name: Azargoshasb

Email: s.azargoshasb@lumc.nl

Organization: Department of Radiology, Leiden University Medical Center

Country: Netherlands

ID: GA110
Co-registration of OPT and MRI enables detailed anatomical brain mapping of tick-born flavivirus infection in mice

Stefanie Willekens, Umeå Universitet, stefanie.willekens@umu.se

---

Category: Immunology: Inflammation & Infection

Abstract Body : Within the past decade, the incidence of tick-born encephalitis virus (TBEV) infection has risen significantly and medically speaking, it has become the most important arthropod-born virus in Europe. TBEV is a neurotropic flavivirus that potentially causes lethal encephalitis while among survivors, long-term neurological sequelae are often observed (1). At present, our knowledge regarding viral tropism and its distribution along specific anatomical brain regions remains limited. In this study, we aimed to visualize flavivirus infection within the mouse brain using Optical Projection Tomography (OPT) (2) and investigated the possibility to map viral spread to specific brain regions by co-registering OPT to anatomical Magnetic Resonance Images (MRI). Immunocompromised mice were intracranially inoculated with Langat virus, a BSL-2 flavivirus closely related to TBEV and at endpoint, brains were harvested and processed for whole-organ OPT. After immunofluorescent labelling of nonstructural protein 5 (NS5), viral and autofluorescent OPT images were acquired and reconstructed into DICOM format. Afterwards, volumetric T1-weighted (MDEFT, TR/TE/TI 3000/3/950 ms, 40 mm3 voxel size) MR images were acquired. Voxel-to-voxel affine transformation matrices were calculated using the autofluorescent OPT images and applied to those displaying viral NS5 signal. Finally, fusion images were created, and virus-containing brain regions were determined according to the Turone mouse brain atlas (3). Affine registration successfully resulted in fusion images delineating viral signal in a detailed anatomical context provided by high-resolution MRI and revealed infection in gray matter (GM), white matter (WM) and the entire ventricular system. For GM specifically, we observed viral signal in entorhinal cortex, dorsal endopiriform nucleus, piriform area, primary visual field and primary somatosensory cortex (upper limb and barrel field). As for WM, the olfactory limb of the anterior commissure, anterior forceps of corpus callosum and supra-callosal WM contained viral signal. Interestingly, the choroid plexus of the lateral ventricle, subventricular zone and olfactory limb of the anterior commissure, all part of the rostral migratory stream, suggest the specific infection of the ventriculo-olfactory neurogenic system in this mouse model. In this study we demonstrated, for the first time, the successful creation of OPT-MRI fusion images and their value for anatomical brain mapping of flavivirus infection. In the future, the proposed method may significantly contribute to unraveling the tropism of TBEV and provide novel insights regarding its neurotropic properties.

References: 1. Lindquist L. et al. Tick-borne encephalitis. Lancet (2008) 371:1861-71 2. Sharpe J. et al. Optical Projection Tomography as a tool for 3D microscopy and gene expression studies. Science (2002) 296:541-545 3. Barrière DA. et al. Brain orchestration of pregnancy and maternal behavior in mice: A longitudinal morphometric study. Neuroimage (2021) Apr 15, 230:117776

First Name: Stefanie

Last Name: Willekens

Email: stefanie.willekens@umu.se

Organization: Umeå Universitet

Country: Sweden

ID: GA111
Near Infrared Molecular Imaging of the Alternatively Spliced D Domain of Tenascin C in Preclinical Models of Inflammatory Bowel Disease

Liang Zhang, AbbVie, liangzhang89@gmail.com

Category: Immunology: Inflammation & Infection

Abstract Body : Purpose: Inflammatory bowel diseases (IBD) are progressive disorders of the gastrointestinal tract that hinder patient quality of life if untreated. Systemic treatments have yielded mixed results in mouse models and the clinic, where a lack of selective delivery has yielded low drug concentrations in the colon. Thus, it is fruitful to identify potential drug delivery targets through targeted molecular imaging. Extracellular matrix (ECM) proteins are upregulated in a variety of inflammatory diseases due to increased tissue remodeling and have served as attractive delivery targets 1–4. Tenascin C, in particular, is a glycoprotein with multiple functional isoforms within the ECM. While various tenascin C targeting proteins have been specific in several oncology models5, it remains largely unexplored in IBD. Methods: In this work, colon immunohistochemistry from mice provided with dextran sulfate sodium (DSS) in drinking water revealed expression of the alternatively spliced D domain of tenascin C (TNC D). Novel proteins with sub-micromolar binding affinity to TNC D were generated. Using amine chemistry, we labeled these proteins with IRDye 800CW, a commonly used near infrared (NIR) fluorophore. After confirming minimal changes in binding affinity after bioconjugation via in vitro binding assays, the reagents were dosed in murine DSS colitis. Results: We report evidence of in vivo specificity by dosing the imaging antibody with and without a high molar dose of unlabeled antibody as shown through macroscopic organ-level imaging with a NIR scanner as well as a custom NIR endoscope. Our imaging data revealed TNC D expression in punctate lesions ranging from the distal to proximal ends of the colon. Subsequent ex vivo biodistribution via total organ digest helped quantify the absolute uptake in the diseased colons between blocked and unblocked groups and revealed significant differences in colon uptake and undetectable specific uptake in non-disease organs. Following ex vivo imaging, cellular level specificity was confirmed via IHC and microscopy. Conclusion: It is beneficial to be mindful of delivery applications in addition to imaging. Thus, it's fruitful to identify ECMs with high absolute local expression unique to disease tissue early on in preclinical research. The murine blocking experiments estimate absolute expression of TNC D at the site of lesions is likely greater than 100 nM. This estimate is similar to cell surface molecular imaging targets present in autoimmune diseases such as type 1 diabetes and various cancers with high reported imaging target to background ratio (TBR).

References: 1. Doll, F., Schwager, K., Hemmerle, T. & Neri, D. Murine analogues of etanercept and of F8-IL10 inhibit the progression of collagen-induced arthritis in the mouse. Arthritis Res Ther 15, R138 (2013). 2. Villa, A. et al. A high-affinity human monoclonal antibody specific to the alternatively spliced EDA domain of fibronectin efficiently targets tumor neo-vasculature in vivo. International Journal of Cancer 122, 2405–2413 (2008). 3. Schwager, K. et al. Preclinical characterization of DEKAVIL (F8-IL10), a novel clinical-stage immunocytokine which inhibits

the progression of collagen-induced arthritis. Arthritis Res Ther 11, R142 (2009). 4. Bootz, F., Ziffels, B. & Neri, D. Antibody-Based Targeted Delivery of Interleukin-22 Promotes Rapid Clinical Recovery in Mice With DSS-Induced Colitis: Inflammatory Bowel Diseases 22, 2098–2105 (2016). 5. Brack, S. S., Silacci, M., Birchler, M. & Neri, D. Tumor-Targeting Properties of Novel Antibodies Specific to the Large Isoform of Tenascin-C. Clin Cancer Res 12, 3200–3208 (2006).

First Name: Liang

Last Name: Zhang

Email: liangzhang89@gmail.com

Organization: AbbVie

Country: United States

ID: GA112
In-house v. commercialized cores for Nano-, Encapsulated, Manganese Oxide (NEMO) particles as MRI contrast agents

Kasey Freshwater, West Virginia University, kaf0005@mix.wvu.edu

---

Category: Oncology

Abstract Body : Over the last 40 years, gadolinium (Gd)-based contrast agents have served as the gold-standard for contrast enhancement in magnetic resonance imaging (MRI). Unfortunately, Gd chelates retain high false-positive rates and can lead to harmful side effects, such as nephrogenic systemic fibrosis and Gd-deposition in the brain. Although there has been substantial research using superparamagnetic iron oxide nanoparticles (SPIONs) as contrast agents due to their robust dark T2* MRI signal, these particles suffer from some limitations. SPIONs produce a constant dark signal that is always “on” and can be easily confounded by the negative contrast produced by natural iron stores. Here, we propose poly(lactic-co-glycolic acid) (PLGA) Nano-, Encapsulated, Manganese Oxide (NEMO) particles due to their ability to convert from an “off” to “on” state in low-pH environments, such as tumor microenvironments, rendering the particles pH-activatable. Three types of manganese oxide cores (MnO, Mn2O3, and Mn3O4) were either synthesized through thermal decomposition of manganese(II) acetylacetonate or purchased from Company A or Company B. The composition of the nanocrystals was confirmed using X-Ray diffraction (XRD), which showed impurities in cores from Company A that corresponded to calcium, sodium, and zinc. Transmission electron microscopy (TEM) results showed that the true nanocrystalline sizes directly contradict the reported diameters with up to a 30nm and 60nm difference than reported for Company A and Company B, respectively. Company A’s nanocrystals presented with a consistent, non-uniform distribution with some rod-like figures, while Company B’s nanocrystals presented with an unknown substance creating a persistent film across all TEM images. The diameters for in-house nanocrystals were ~35nm and ~11nm for MnO and Mn3O4, respectively, with uniform distributions. All manganese oxide cores were then encapsulated within PLGA to form NEMO particles using a single emulsion technique. To produce bright signal on MRI, MnO must degrade to produce Mn2+ ions at low pH. To assess Mn2+ release and resulting MRI signal via controlled release, NEMO particles were incubated at pH 7.4, 6.5, and 5 to mimic pH in blood, tumor extracellular space, and intracellular endosomes, respectively. Supernatants were analyzed by inductively coupled plasma - optical emission spectrometry (ICP-OES) for released Mn content and 1T MRI for T1 signal enhancement. After encapsulation of the first of three replicates, controlled release showed greater than 100% release of Mn2+ at 24h in pH 5 buffer for Company A Mn2O3, Company B MnO, and Company B Mn3O4, which was attributed to impurities and poor encapsulation efficiency. According to scanning electron microscopy (SEM), micron-sized particles were synthesized when encapsulating cores from both Company A and Company B. In-house NEMO particles showed a uniform nano-sized distribution with ~94% Mn2+ release for MnO and ~41% Mn2+ release for Mn3O4 after 24h at pH 5. In general, the T1 MRI signal of particle supernatants increased with decreasing pH as expected due to greater release of Mn2+ under acidic conditions. Specifically, In-house MnO and Company A Mn3O4

presented with the maximum T1 MRI signal. Contrarily, both samples of Company B Mn_2O_3 presented with no discernable signal change with varying pH indicating that these particles were very poor contrast agents. Based on our preliminary assessment, it appears that in-house synthesis of smaller batches of manganese oxide nanocrystals is currently preferable to commercialized sources to ensure sample purity, a tight size distribution, and maximum T1 MRI signal. Ultimately, determining a precise and reliable way to synthesize commercially available manganese oxide nanocrystals at large scales will allow for reproducibility of NEMO particles bringing them one step closer to being used in a clinical setting.

Image/Figure:

https://s3.amazonaws.com/amz.xcdsystem.com/1E8A4501-BB41-A02A-1D3B9882B798BFAA_abstract_File10351/GA112_ImageFigure_0512093219.jpg

Image/Figure Caption: Figure 1. Scanning Electron Microscopy of PLGA-NEMO particles. First Column: In-house PLGA MnO and PLGA Mn_3O_4 NEMO particles with scale bars 1.0µm and 3.0µm, respectively. Second Column: Company A PLGA Mn_2O_3 and PLGA Mn_3O_4 NEMO particles with scale bars 5.0µm and 3.0µm, respectively. Third/Fourth Columns: Company B PLGA MnO, (1) PLGA Mn_2O_3 (small nanocrystals), (2) PLGA Mn_2O_3 (large nanocrystals), and PLGA Mn_3O_4 NEMO particles with scale bars 10.0, 2.0, 3.0, and 5.0µm, respectively. Note the micron-sized particles formed after PLGA encapsulation of nanocrystals from Company A and B, with unencapsulated rod-like structures also shown with nanocrystals originating from Company A. In-house NEMO particles are more uniform with a nano-sized distribution.

Full Name of Abstract's 1st Author : Kasey Freshwater

First Name: Kasey

Last Name: Freshwater

Email: kaf0005@mix.wvu.edu

Organization: West Virginia University

Country: United States

ID: GA113
A PSMA-targeted probe for NIRF-guided surgery and photodynamic therapy: synthesis and in vivo biodistribution

Martina Capozza, University of Turin, martina.capozza@unito.it

---

Category: Oncology

Abstract Body : Introduction 20% to 50% prostate cancer (PCa) patients leave the surgery room with positive tumor margin.1 The intraoperative combination of fluorescence-guided surgery and photodynamic therapy (PDT) may be very helpful for improving tumor margin delineation and cancer therapy.2,3 PSMA is a trans-membrane protein overexpressed in 90-100% of PCa cells.4 The goal of this work is to develop a PSMA-targeted Near InfraRed Fluorescent probe to offer surgeon a valuable intraoperative tool for allowing a complete tumor resection with the possibility of killing the residual cancer cells by PDT. Methods PSMA-617 binding motif was synthetized as reported5 and conjugated to IRDye700DX-NHS. The PSMA affinity of the dye was examined in human PCa cells with different PSMA expression (LNCaP, PC3, PC3-PIP, and PC3-FLU) by FACS, whereas cellular uptake and dye localization (endolysosomal pathway) was studied by fluorescence confocal microscopy. IRDye700-PSMA-617 photodynamic properties were evaluated in PC3-PIP and PC3-FLU cells after irradiation with a laser at 635 nm (100 J/cm2). MTT assay was performed 1h post irradiation. Finally, PC3-PIP tumor bearing mice were injected with two doses (1 and 5 nmol) of IRDye700-PSMA-617 and imaged at 1h, 4h and 24h post injection. After imaging mice were sacrificed and organs harvested to detect the fluorescence signal. Results and discussion The conjugation of IRDye700DX with PSMA-617 did not affect the exc/em wavelengths of the fluorophore (Persuasive data). As expected, the affinity of IRDye700-PSMA-617 towards PCa cells followed the order of their PSMA expression, i.e. PC3-PIP>LnCap >PC3, PC3-FLU (Fig1.A). Confocal microscopy images confirmed these results (Fig.1C), and showed a co-distribution of the probe and endolisosomal markers in the perinuclear region (Persuasive data). PDT experiments showed a concentration-dependent decrease of cell viability (from 75% at 10 nM to 12% at 500 nM), whereas controls did not show any cytotoxicity (Fig.1B). NIRF imaging on mice bearing PC3-PIP tumors showed a significant tumor uptake after the injection of both 1 or 5 nmol (Fig.1D) at any time points. The maximum tumor-to-muscle ratio (ca. 60) was observed, for both doses (Persuasive data), 24h post-injection. Importantly, urine, healthy prostate, and bladder were not fluorescent at 24h post injection (Fig.1E). Conclusion A novel PSMA-targeted NIRF dye with dual imaging-PDT capabilities was synthetized. The probe displayed cellular uptake and photo-induced cytotoxicity proportional to the PSMA expression. NIRF imaging, performed on a mouse model with high PSMA expression, displayed an excellent and specific tumor uptake with a significantly high tumor-to-background ratio at 24 h post injection, when healthy prostate, kidneys and bladded were not fluorescent. Acknowledgements The PSMA positive (PSMA+) PC3-PIP and PSMA negative (PSMA−) PC3-FLU were kindly provided by Prof. Martin G. Pomper (Johns Hopkins Medical School, Baltimore, MD)

References: 1. Iczkowski KA, Lucia MS. Frequency of positive surgical margin at prostatectomy and its effect on patient outcome. Prostate Cancer 2011;2011:673021. 2. Bařinka C, Rojas C, Slusher B, Pomper M. Glutamate carboxypeptidase II in diagnosis and treatment of neurologic disorders and prostate cancer. Curr Med Chem 2012;19(6):856-870. 3. Maurer T, Graefen M, van der Poel H, Hamdy F, Briganti A, Eiber M, Wester HJ, van Leeuwen FWB. Prostate-Specific Membrane Antigen-Guided Surgery. J Nucl Med 2020;61(1):6-12. 4. van Leeuwen FWB, Schottelius M, Brouwer OR, Vidal-Sicart S, Achilefu S, Klode J, Wester HJ, Buckle T. Trending: Radioactive and Fluorescent Bimodal/Hybrid Tracers as Multiplexing Solutions for Surgical Guidance. J Nucl Med 2020;61(1):13-19. 5. Benešová M, Bauder-Wüst U, Schäfer M, Klika KD, Mier W, Haberkorn U, Kopka K, Eder M. Linker Modification Strategies To Control the Prostate-Specific Membrane Antigen (PSMA)-Targeting and Pharmacokinetic Properties of DOTA-Conjugated PSMA Inhibitors. J Med Chem 2016;59(5):1761-1775.

Image/Figure:

https://s3.amazonaws.com/amz.xcdsystem.com/1E8A4501-BB41-A02A-1D3B9882B798BFAA_abstract_File10351/GA113_ImageFigure_0512093300.jpg

Image/Figure Caption: Figure 1. A) FACS affinity of IRDye700-PSMA-617 (500nM), IRDye700-PSMA-617 and PSMA-617 100X, IRDye700DX (500nM) to PSMA positive cells PC3-PIP, LnCap and PSMA negative PC3 and PC3-FLU; B) targeted photodynamic therapy efficacy of IRDye700-PSMA-617 at different concentration (range 10nM-500nM) on PC3-PIP (green) and PC3-FLU (red); C) Confocal microscopy of on PC3-PIP, LnCap, PC3 and PC3-FLU incubated with IRDye700-PSMA-617; D) In vivo biodistribution and tumor uptake in PC3-PIP tumor bearing mice after 1h, 4h and 24h post administration of 1 nmol or 5 nmol of IRdye700-PSMA; E) ex vivo fluorescent signal of organs harvested 1h, 4h and 24h post administration of 1nmol or 5nmol.

Full Name of Abstract's 1st Author : Martina Capozza

First Name: Martina

Last Name: Capozza

Email: martina.capozza@unito.it

Organization: University of Turin

Country: Italy

ID: GA114

The impact of a novel Click-On gamma probe design on surgical dexterity and surgical decision-making during robot-assisted radioguided surgery

Samaneh Azargoshasb, Department of Radiology, Leiden University Medical Center, s.azargoshasb@lumc.nl

---

Category: Instrumentation

Abstract Body : Introduction: Decision-making and dexterity are considered the hallmark features for improving surgical performance. With the advances in (robot-assisted) minimally-invasive surgery and image-guided surgery, improving the surgical performance features is becoming increasingly more important. Recently, DROP-IN gamma probes were introduced to facilitate radioguidance in robotic surgery. This study investigates if robotic radioguidance could be further improved with a novel tethered Click-On gamma probe design, which further integrates the detection modality with the robotic instruments themselves. This is done using a thorough investigation of decision-making and dexterity in both a phantom setting and during porcine surgery. Methods: Using computer-assisted design, 3D print prototyping and precision machining, we created a miniaturized gamma probe that can be integrated with a robotic instrument using a clicked concept. To allow for a quantified investigation on the surgical performance, fiducial markers were integrated in the Click-On gamma probe housing and a custom computer-vision algorithm was built to track the gamma probe movements via the robotic laparoscope, allowing for a reconstruction of the probe movement trajectory. Using a dexterity phantom, the tasks performed with the Click-On prototype were compared to those performed with the parental DROP-IN probe using the completion time of the specific-tasks and the quantified features of the extracted movements. To investigate the impact of radioguidance on surgical decision-making, we also performed a blinded study during porcine surgery, wherein surgeons had to localize a hidden radioactive 57Co-source using either palpation or Click-On radioguidance. Results: A fully functional Click-On gamma probe was fabricated, which allowed for a successfully integration with the robotic forceps instrument, while preserving the grasping function and rotational freedom of the instrument. With a diameter procedural time, and a more focused movement.. Conclusion: The integration of gamma probe designs within the surgical instruments themselves provides a next step forwards in the optimization of minimal-invasive surgery using radioguidance. The value of this approach was highlighted by its impact observed on surgical decision-making and dexterity.

First Name: Samaneh

Last Name: Azargoshasb

Email: s.azargoshasb@lumc.nl

Organization: Department of Radiology, Leiden University Medical Center

Country: Netherlands

ID: GA115
Inflammation Imaging in Spinal Cord Injury: Novel Insights on the Usage of PFC-Based Contrast Agents

Francesca Garello, Molecular and Preclinical Imaging Centers, Department of Molecular Biotechnology and Health Sciences, University of Torino, francesca.garello@unito.it

---

Category: Immunology: Inflammation & Infection

Abstract Body : Introduction Perfluorocarbon(PFC)-based compounds have been largely used to label immune system cells and track the inflammatory process by Magnetic Resonance Imaging (MRI).1 However, information is still lacking about the impact of these agents on the monocyte/macrophage polarization towards one of their cell subsets and on the best way to image them. In the present work, a PFC-based nanoemulsion (PFCE-NE) was developed to monitor the course of inflammation in a model of spinal cord injury (SCI), a pathology in which the understanding of immunological events is of utmost importance to select the optimal therapeutic strategies.2 Moreover, as in the literature there is not a standard protocol for fluorinated system-based imaging (single or multiple administrations, 19F MRI or PRESS, etc…), the various protocols adopted have been compared in terms of signal quantification, amount of contrast agent delivered to the diseased region, information gained. Finally, the influence of PFCE-NE over macrophage polarization was investigated both in vitro and in vivo. Methods The PFCE-NE was prepared by sonication of a mixture of Perfluoro-15-crown-5 ether, the fluorescent phospholipid Rhodamine-DOPE, and 10 % w/v Kolliphor P188. The effects of PFCE-NE over macrophage polarization were studied in bone marrow-derived macrophages extracted from C57BL/6J mice. Experiments were carried out on M0, M1, or M2 macrophages, incubated with PFCE-NE (40 mM in fluorine) for 1, 6, or 24 h. Then, the PFCE-NE was injected in SCI mice (20 mmol F/Kg) and different cell tracking protocols were tested (single and multiple PFCE-NE administrations, 19F-MRI or MRS detection, and the option of pre-saturating Kupffer cells through a pre-injection of phospholipid-based vesicles) (Figure 1). At the end of the MRI study, spinal cords were excised and the impact of PFCE-NE over macrophage polarization was investigated ex-vivo. Results/Discussion M0, M1, and M2 cells avidly took up the nanoemulsion (mean diameter 135 nm), even if with different rates. A switch towards M2 (anti-inflammatory) phenotype was observed, especially for M0 cells. The administration of PFCE-NE to SCI mice allowed to monitor by 19F MRI the ongoing inflammation (Figure 2), individuating a possible therapeutic window for stem cell transplantation, around day 8 to 11 post-injury. Pre-saturation of Kupffer cells with liposomes allowed for significantly higher contrast agent accumulation at the lesion site (1038.4 ± 160.6 nmol 19F with saturation, 463.3 ± 45.5 nmol w/o saturation, p Conclusions In conclusion, this work demonstrates that PFCE-NEs can be used as probes to non-invasively track the monocytes/macrophages infiltration in a SCI model by 19F-MRI. Moreover, the influence exerted by PFCE-NE on macrophage phenotypes, with a prevailing switching towards the M2 profile, suggests a possible theranostic function, with tremendous potential future applications. Nevertheless, extensive behavioral and toxicity tests are still required. Acknowledgement The authors acknowledge the Italian Ministry of Research for FOE contribution to the Euro-BioImaging MultiModal Molecular Imaging Italian Node

(www.mmmi.unito.it), the Open Lab of Advanced Microscopy (OLMA) at the Molecular Biotechnology Center (MBC) for support.

References: [1] Wu, L, Liu, F, Liu, S, Xu, X, Liu, Z, Sun, X. Perfluorocarbons-Based 19F Magnetic Resonance Imaging in Biomedicine. Int J Nanomedicine. 2020;15:7377-7395. [2] Nakamura, M.; Okano, H. Cell Transplantation Therapies for Spinal Cord Injury Focusing on Induced Pluripotent Stem Cells. Cell Res. 2013, 23, 70–80.

Image/Figure:

https://s3.amazonaws.com/amz.xcdsystem.com/1E8A4501-BB41-A02A-1D3B9882B798BFAA_abstract_File10351/GA115_ImageFigure_0512095739.png

Image/Figure Caption: Figure 1 . Schematic representation of the different experimental groups. Figure 2. A-F) 1H and 1H/19F MR images of the spinal cord at the lesion level following different protocols of PFCE-NE administration, summarized in Figure 1. L) 19F MRI signal trend for group A and C. M) Comparison between the MRI signal of a SCI (group D) and healthy (group F) mouse (L stands for liver, yellow arrows indicate spinal cord).

Full Name of Abstract's 1st Author : Francesca Garello

First Name: Francesca

Last Name: Garello

Email: francesca.garello@unito.it

Organization: Molecular and Preclinical Imaging Centers, Department of Molecular Biotechnology and Health Sciences, University of Torino

Country: Italy

ID: GA117
PET imaging of serotonin transporter and synaptic vesicle protein 2A for potential monitoring of neuroregeneration in the spinal cord

David Reuter, AbbVie, david.reuter@abbvie.com

Category: Neuroscience

Abstract Body : Background: AbbVie is evaluating the repulsive guidance molecule A (RGMa) inhibitor monoclonal antibody Elezanumab for the treatment of spinal cord injury. There is preclinical evidence suggesting a correlation of motor function recovery after spinal cord injury with regeneration of serotonin axons. The presynaptic serotonin transporter (SERT) has been shown to be modulated after injury and in response to treatment, and the synaptic vesicle glycoprotein 2A (SV2A), expressed on the membrane of synaptic vesicles and present in spinal cord grey matter, may both serve as biomarkers for the evaluation of neuroregeneration in the spinal cord. Here we report the evaluation of two high affinity SERT radioligands and one SV2A radioligand for imaging uninjured spinal cord in nonhuman primates (NHPs). Materials and methods: Precursors and standards for fluorine-18 labeled (S)-2'-(3-fluoropropoxy)methyl)-6-nitroquipazine ((S)-[18F]1, hSERT Ki: 0.46 ± 0.08 nM)1 and (R)-[18F]1 (hSERT Ki: 0.12 ± 0.01 nM)1 were prepared by a 5-step synthesis. Radiolabeling of 1 was established by direct fluorination using the tosylate-precursor. The SV2A radioligand [18F]SynVesT-1 was prepared by Cu-mediated radiofluorination of the trimethyltin precursor.2 The distribution and density of SERT and SV2A in the NHP and human brain and spinal cord were evaluated by autoradiography and tissue homogenate binding assays using radioligands (S)-[18F]1, [3H]UCB-J and [3H]SynVesT-1. A total of eight PET measurements were performed in six cynomolgus macaques. Baseline and pretreatment PET measurements with the SERT inhibitor escitalopram (2 mg/kg) were performed in a FOCUS-220 PET system for (S)-[18F]1 with the brain or spinal cord in the field of view. Binding of (R)-[18F]1 in brain and spinal cord and [18F]SynVesT-1 in spinal cord (n=2) was also evaluated. Blood samples were collected for evaluation of metabolism of the radioligand and computation of the arterial input function. PET images were evaluated using MRI and CT-based regions of interest for the brain and spinal cord, respectively. Results: Both [18F]1 enantiomers and [18F]SynVesT-1 could be prepared with high chemical yield and molar activity. The SV2A density in the NHP and human spinal cord was 5-10 fold lower than in brain (cortical grey matter). Metabolism of [18F]1 was moderate to slow, with ~40% remaining at 60 min post-injection. (S)-[18F]1 binding was highest in the cervical part of the spinal cord. Binding of (S)-[18F]1 was reliably quantified in brain, and specific binding was reduced by ~70% following administration of escitalopram. Similar results were observed in cervical spinal cord with escitalopram pretreatment. Baseline PET measurements with (R)-[18F]1 and [18F]SynVesT-1 demonstrated binding in the cervical spinal cord. The binding kinetics of (R)-[18F]1 in the brain and spinal cord were slow and not suitable for quantification using compartmental modeling. Spinal cord binding of [18F]SynVesT-1 was reversible and could be quantified using a two-tissue compartment model. Conclusion: In vitro and pre-clinical imaging studies indicate that quantitative molecular imaging of SERT and SV2A, in the spinal

cord, may serve as a potential translational biomarker for the evaluation of neuronal regeneration.

References: 1 Gerdes J., Zheng M.-Q., Braden M., Holden D., Ropchan J., Lin S., Carson R., Huang Y. Novel F-18 labeled 6-nitroquipazine derivatives as high affinity tracers for the serotonin transporter. 2012 Journal of Nuclear Medicine, 53:S1, 291. 2 Li S., Cai Z., Wu X., Holden D., Pracitto R., Kapinos M., Gao H., Labaree D., Nabulsi N., Carson R.E., Huang Y. Synthesis and in vivo evaluation of a novel PET radiotracer for imaging of synaptic vesicle glycoprotein 2A (SV2A) in nonhuman primates. 2019 ACS Chem Neurosci, 10:3, 1544-1554.

First Name: David

Last Name: Reuter

Email: david.reuter@abbvie.com

Organization: AbbVie

Country: United States

ID: GA118

Endogenous Magnetic Particle Imaging of Intraplaque Hemorrhage Highlights Unstable Plaques in Atherosclerotic Mice and Human Carotid Tissues

Wei Tong, Department of Cardiology, the Sixth Medical Centre, Chinese PLA General Hospital, waynetong_301@163.com

---

Category: Cardiovascular & Pulmonary

Abstract Body : Background: Intraplaque hemorrhage (IPH) is a pivotal driver of atherosclerotic plaque progression, instability and rupture [1, 2] and is an imaging predictor of stroke and myocardial infarction [3, 4]. Advanced imaging techniques were required to accurately detect IPH for risk stratification of patients and early intervention of unstable plaques [5]. We aimed to use magnetic particle imaging (MPI) combined with computed tomographic angiography (CTA) for precise detection of IPH in vivo. Methods: Twenty-two human carotid atherosclerotic samples were collected from the patients undergoing carotid endarterectomy (CEA) and imaged using the MPI/CT scanner. Histological examinations were used to analyze the source of MPI signals in human tissues. Six-week-old ApoE-/- mice were used to establish the tandem stenosis (TS) mouse model, which provided comparative arteries of unstable plaques with IPH, stable plaques and normal arterial wall in the same mouse [6, 7]. TS ApoE-/- mice were performed with MPI and CTA imaging. 7.0 T T1-weighted fat-suppression MRI and Prussian blue staining were performed to confirm the presence of IPH. Results: Human CEA samples exhibited strong endogenous MPI signals ex vivo. Histological examinations found that MPI signals were related to the presence of IPH and particularly hemosiderin, the degradation product of IPH. In vivo MPI/CTA images of TS ApoE-/- mice revealed that endogenous MPI signals were detected in the unstable plaques rather than stable plaques and normal arterial wall. Quantitative analysis indicated that MPI signals were significantly higher in unstable plaques (7.29 ± 4.48) compared with stable plaques (2.63 ± 1.12) and normal arterial wall (2.09 ± 0.79) (P 1.34 ± 0.08) than stable plaques (1.00 ± 0.06) and normal arterial wall (0.96 ± 0.02) (P Conclusions: MPI/CTA is a novel technology that allows in vivo detection of atherosclerotic plaques with IPH and holds great promise for identification of unstable plaques in humans.

References: 1. Saba L, Moody AR, Saam T, Kooi ME, Wasserman BA, Staub D, et al. Vessel Wall-Imaging Biomarkers of Carotid Plaque Vulnerability in Stroke Prevention Trials: A viewpoint from The Carotid Imaging Consensus Group. JACC Cardiovascular imaging. 2020;13(11):2445-56. 2. Kolodgie FD, Gold HK, Burke AP, Fowler DR, Kruth HS, Weber DK, et al. Intraplaque hemorrhage and progression of coronary atheroma. N Engl J Med. 2003;349(24):2316-25. 3. Schindler A, Schinner R, Altaf N, Hosseini AA, Simpson RJ, Esposito-Bauer L, et al. Prediction of Stroke Risk by Detection of Hemorrhage in Carotid Plaques: Meta-Analysis of Individual Patient Data. JACC Cardiovascular imaging. 2020;13(2 Pt 1):395-406. 4. Bos D, Arshi B, van den Bouwhuijsen QJA, Ikram MK, Selwaness M, Vernooij MW, et al. Atherosclerotic Carotid Plaque Composition and Incident Stroke and Coronary Events. Journal of the American College of Cardiology. 2021;77(11):1426-35. 5. Saba L, Saam

T, Jager HR, Yuan C, Hatsukami TS, Saloner D, et al. Imaging biomarkers of vulnerable carotid plaques for stroke risk prediction and their potential clinical implications. The Lancet Neurology. 2019;18(6):559-72. 6. Chen YC, Bui AV, Diesch J, Manasseh R, Hausding C, Rivera J, et al. A novel mouse model of atherosclerotic plaque instability for drug testing and mechanistic/therapeutic discoveries using gene and microRNA expression profiling. Circulation research. 2013;113(3):252-65. 7. Htun NM, Chen YC, Lim B, Schiller T, Maghzal GJ, Huang AL, et al. Near-infrared autofluorescence induced by intraplaque hemorrhage and heme degradation as marker for high-risk atherosclerotic plaques. Nature communications. 2017;8(1):75.

Full Name of Abstract's 1st Author : Wei Tong

First Name: Wei

Last Name: Tong

Email: waynetong_301@163.com

Organization: Department of Cardiology, the Sixth Medical Centre, Chinese PLA General Hospital

Country: China

ID: GA120
Imaging Tumour Hypersialylation Using Metabolic Oligosaccharide Engineering

Daniel Parle, University of Cambridge Department of Chemistry, drp45@cam.ac.uk

---

Category: New Chemistry, Materials & Probes

Abstract Body : Introduction: Aberrant cell surface glycosylation has been described as one of the key hallmarks of cancer, with hypersialylation the most commonly observed alteration.1 Changes in the glycome of cells can be monitored by incorporating unnatural sugars bearing bioorthogonal chemical reporters. Monitoring hypersialylation could provide an insight into tumour progression, proliferation and potentially be used for monitoring treatment response.2,3 We describe here improved in vitro imaging of hypersialylation using a novel triacetylated cyclopropene mannosamine (Ac3ManNCyoc) derivative. Methods: Mannosamine was functionalised with a carbamate linked cyclopropene handle. The monosaccharide was synthesised with different degrees of acetylation (Ac1 to Ac4), which we expected to show different diffusion rates across the cell membrane due to varying hydrophobicity as well as variable aqueous solubility. Ac4ManNCyoc has limited aqueous solubility as a result of its high clogP (2.20). A tetrazine-PEG11-DyLight649 probe was synthesised and used to label the methyl cyclopropene moiety. The extent of incorporation of the sugar analogues was assessed in three cell lines (COLO205, MDA-MB-231, PANC-1) by flow cytometry. Results: Varying the levels of sugar acetylation resulted in significant differences in measured fluorescence intensity, indicating that there was an optimum level of acetylation that balanced sugar solubility and membrane penetration. In COLO205 cells, this optimum was found with tri- and diacetylated sugar derivatives (SBR 16.6 and 17.4 respectively). The hydrophobicity of Ac4ManNCyoc results in poor aqueous solubility limiting the substrate availability. Ac3ManNCyoc and Ac2ManNCyoc strike a balance, whereas the hydrophilicity of Ac1ManNCyoc results in poor cellular uptake. The improved labelling with Ac3ManNCyoc and Ac2ManNCyoc was also observed in MDA-MB-231 and PANC-1 cell lines (Fig 1B-C). Ac3ManNCyoc yielded the highest signal-to-background ratio in both (97.6 and 52.8 respectively) with the increased labelling demonstrating the increased hypersialylation in these tumour lines. Ac3ManNCyoc Labelled PANC-1 cells were visualised using fluorescent microscopy (Fig 1D-E). Conclusions: Ac3ManNCyoc is a novel candidate for probing tumour hypersialylation by metabolic labelling and subsequent in vivo imaging in murine models. The triacetylated sugar represents the optimal compromise between sugar solubility and membrane penetration.

References: 1. Pinho S.S., Reis C.A. Glycosylation in cancer: mechanisms and clinical implications. Nat. Rev. Cancer. 15, 540-555 (2015). 2. Neves, A. A., Stoeckmann, H., Wainman, Y. A., Kuo, J. C., Fawcett, S., Leeper, F. J. & Brindle, K. M. Imaging cell surface glycosylation in vivo using ‘double click’ chemistry. Bioconjug. Chem. 24, 934–941 (2013). 3. Neves, A. A., Wainman, Y. A., Wright, A., Kettunen, M. I., Rodrigues, T.B., McGuire, S., Hu, D. E., Bulat, F., Geninatti Crich, S., Stoeckmann, H., Leeper, F. J. & Brindle, K. M. Imaging Glycosylation in

Vivo by Metabolic Labeling and Magnetic Resonance Imaging. Angew. Chemie - Int. Ed. 55, 1286–1290 (2016).

Image/Figure:

https://s3.amazonaws.com/amz.xcdsystem.com/1E8A4501-BB41-A02A-1D3B9882B798BFAA_abstract_File10351/GA120_ImageFigure_0512101707.png

Image/Figure Caption: Figure 1 - COLO 205 (A) MDA-MB (B) and PANC-1 (C) cells were incubated in the presence or absence of the appropriate ManCyoc sugar 125μM (Ac1, Ac2, Ac3 or Ac4) for 24 hours. They were subsequently treated with the dye solution (5 μM Tz-Dylight647 + 50 nm Sytox green cell death stain) for 1 hour. Statistical analysis was performed using an unpaired t test with Welch correction (**** P≤0.0001,*** P≤0.001, ** P≤0.01, * P≤0.05). Data are median ± SEM (n = 3, per group). Fluorescence microscopy of PANC-1 cell glycans. Cells were cultured with (D) or without (E) Ac3ManNCyoc (125 μM) for 24 h and then incubated with a 5 μM solution of Tz-AF647, Red: AF647, Blue: DAPI nuclear stain, scale bar 50 μm.

First Name: Daniel

Last Name: Parle

Email: drp45@cam.ac.uk

Organization: University of Cambridge Department of Chemistry

Country: United Kingdom

ID: GA121
In Vivo Longitudinal Molecular Contrast-Enhanced Ultrasound Imaging of Vascular Growth and Remodeling of the Placenta During Preeclampsia

Carolyn Bayer, Tulane University, carolynb@tulane.edu

Category: Cardiovascular & Pulmonary

Abstract Body : New-onset hypertension during pregnancy, termed preeclampsia, is a leading cause of maternal mortality and a probable risk factor predisposing both the mother and offspring to cardiovascular disease. While inadequate growth and remodeling of the placental vasculature, beginning at the earliest stages of pregnancy, is the likely cause of preeclampsia, little is understood about the in vivo, longitudinal progression of placental development. The establishment of methods for longitudinal, in vivo molecular imaging of markers of placental angiogenesis and vascular remodeling, therefore, was the objective of this work. Using an established in vivo rat model of preeclampsia and molecularly targeted microbubbles (MBs), we acquired longitudinal contrast-enhanced ultrasound (CEUS) images of placental development. Timed-pregnant Sprague Dawley rats were surgically modified on gestational day (GD) 14 using the reduced uterine perfusion pressure technique (RUPP) to induce preeclampsia [1]. Vevo Target-Ready MicroMarkers (FUJIFILM, VisualSonics) were used for CEUS imaging. MBs were conjugated with biotinylated arginine-glycine-aspartate (RGD), a peptide that binds to αvβ3, a marker of angiogenesis. A full video loop of nonlinear contrast images was acquired before MB administration to obtain a baseline measurement of the nonlinear background signal from tissue. Then, a 200 μL bolus of MBs was administered followed by a 150 μL saline flush while continuously recording nonlinear CEUS images. At 10-minutes after MB injection, a destructive US burst was applied and an additional two minutes of nonlinear CEUS images were acquired. Thirty minutes later, a second bolus of MBs conjugated with biotinylated L-arginine-glycine-glutamic acid-serine (RGES), a nontargeted isotype control of RGD, was administered and the same imaging sequence was implemented. All injections were administered via tail vein catheter on GD14 and through the indwelling jugular vein catheter on GD16 and 18. We used a bicompartmental model to evaluate αvβ3-targeted microbubble binding, placental microvasculature architecture, and placental perfusion in both a normal pregnant and a rat model of preeclampsia. A linearized time intensity curve was extracted from each pixel of the images of each CEUS sequence and fitted to the bicompartmental model using nonlinear iterative least-squares curve fitting [2]. The parameters of molecular expression and perfusion were confirmed with histology. Using the developed imaging methods and models, we have demonstrated in vivo, longitudinal imaging of the reduced expression of the angiogenic marker as well as reduced microvasculature development and perfusion in the preeclamptic animals in comparison to the controls. The imaging methods and the bicompartmental model allow for the assessment of the complex development of the placenta, which has previously not been demonstrated longitudinally and in vivo. The developed imaging and analysis methods will enable the discovery and validation of novel therapeutics for preeclampsia.

References: [1] B. T. Alexander et al., "Reduced uterine perfusion pressure during pregnancy in the rat is associated with increases in arterial pressure and changes in renal nitric oxide," Hypertension, vol. 37, no. 4, pp. 1191-1195, Apr 2001. [2] S. Turco, I. Tardy, P. Frinking, H. Wijkstra, and M. Mischi, "Quantitative ultrasound molecular imaging by modeling the binding kinetics of targeted contrast agent," Physics in Medicine

Image/Figure:

https://s3.amazonaws.com/amz.xcdsystem.com/1E8A4501-BB41-A02A-1D3B9882B798BFAA_abstract_File10351/GA121_ImageFigure_0512101739.png

Image/Figure Caption: Figure 1: (a) B-mode ultrasound images of the placental environment in a normal pregnant animal on GD18. (b) The nonlinear CEUS signal in the placenta shows the placenta (p) is fully perfusion approximately one-minute after microbubble administration. After fitting the CEUS signal in each pixel to the bicompartmental model, parametric maps of Kb (c), κ (d), and relative blood flow (e) were generated and overlaid on the B-mode US image of anatomy for visualization. Scale bar = 3mm.

First Name: Carolyn

Last Name: Bayer

Email: carolynb@tulane.edu

Organization: Tulane University

Country: United States

ID: GA122
Phase-changing nanodroplets for combined fluorescence and ultrasound imaging

Catalina Spatarelu, Dartmouth College, catalina-paula.spatarelu.th@dartmouth.edu

---

Category: Oncology

Abstract Body : Phase-changing nanodroplets (PCNDs) are nanosized constructs with perfluorocarbon liquid cores that can be remotely vaporized to form highly echogenic gaseous microbubbles. After vaporization, the presence of the microbubbles within the tissue allows for ultrasound images of the agents to be obtained. The PCND nanometric size results in better biological stability and longer circulation times than conventional microbubble ultrasound contrast agents. Beyond their role as ultrasound contrast agent precursors, the PCNDs can be loaded with fluorophores, to allow for techniques such as near-infrared (NIR) fluorescence imaging to be employed to follow their biodistribution. These probes are particularly useful in studying the dynamics of nanoparticle circulation, accumulation and on-target release1, but also to overcome the limits of fluorophore photostability. A standing challenge in the fabrication of nanoparticle-encapsulated dyes, however, is the aggregation-induced quenching that is associated with large dye loadings. This decreases the quantum yield and severely limits the brightness of dye-loaded nanoparticles2. In this study, we employ a lipophilic carbocyanine DiOC18(7) (DiR) NIR dye to produce NIR-sensitive fluorescent PCNDs. Apart from DiR, the PCNDs are loaded with Epolight 3072, a NIR-absorbing dye with a maximum absorption near 1064 nm. This chromophore absorbs pulsed laser light, resulting in localized heating and pressure waves that cause the liquid perfluorocarbon core to vaporize. In the inactivated (liquid) PCND phase, the loaded DiR dye is in a self-quenched state, as a large number of fluorophore molecules are confined to a small space. When activated, the PCNDs undergo a liquid-to-gas phase transition and increase in diameter approximately 5-fold, allowing for the dye molecules to disperse and un-quench and resulting in increased fluorescence intensity. This phenomenon was observed by varying the amount of loaded DiR and studying the fluorescence intensity change in polyacrylamide phantoms containing the PCNDs. An example of such a phantom is presented in Fig.1, where panel A shows the 800-nm channel and the white light channel of the phantom activated with an “FMI” stencil, and panel B is an ultrasound frame of a portion of the same phantom. The ratio between the fluorescence signal intensity in activated regions and fluorescence signal intensity in the non-activated, background region was used as a measure of fluorescence enhancement. A fluorescence enhancement of up to 1.5x was observed in the cases of DiR-lipid molar ratios between 1 x 10-3 and 6 x 10-3. Batches with dye-lipid ratios lower than 1 x 10-3 did not show a self-quenching effect, while batches where the lipid-dye ratio exceeded 6 x 10-3 showed a lower enhancement due to the unquenching being only partially achieved. Several nanodroplets concentrations in phantoms are studied, to elucidate whether inter-particle interactions play a role in the quenching process. Overall, these probes are promising in achieving an increased tumor-to-background ratios (TBR) in NIR fluorescence techniques. Non-targeted agents generally suffer from high background signals, lowering their TBR. Even for targeted agents, that offer molecular insights into the tumor microenvironment, unbound agent in the blood can hamper imaging2. Combining the possibility of on-demand fluorescence

enhancement like shown herein with molecular targeting could provide new avenues for diagnosis or monitoring of cancer progression.

References: (1) Cheng, X.; Li, H.; Chen, Y.; Luo, B.; Liu, X.; Liu, W.; Xu, H.; Yang, X. Ultrasound-Triggered Phase Transition Sensitive Magnetic Fluorescent Nanodroplets as a Multimodal Imaging Contrast Agent in Rat and Mouse Model. PLoS One 2013, 8 (12), e85003. https://doi.org/10.1371/journal.pone.0085003. (2) Reisch, A.; Klymchenko, A. S. Fluorescent Polymer Nanoparticles Based on Dyes: Seeking Brighter Tools for Bioimaging. Small 2016, 12 (15), 1968–1992. https://doi.org/10.1002/smll.201503396.

Image/Figure:

https://s3.amazonaws.com/amz.xcdsystem.com/1E8A4501-BB41-A02A-1D3B9882B798BFAA_abstract_File10351/GA122_ImageFigure_0512101906.png

Image/Figure Caption: Figure 1. A. Fluorescence and white images of phantom with 3% v/v concentration of droplets activated through an “FMI” stencil. B. Ultrasound frame capturing the contrast in the same phantom due to the presence of microbubbles.

Full Name of Abstract's 1st Author : Catalina-Paula Spatarelu

First Name: Catalina

Last Name: Spatarelu

Email: catalina-paula.spatarelu.th@dartmouth.edu

Organization: Dartmouth College

Country: United States

ID: GA123

Investigating the Translational Potential of a Humanized MUC16-Targeted Antibody Conjugate for Fluorescence-Guided Surgery of Pancreatic Cancer

Madeline Olson, University of Nebraska Medical Center, madeline.olson@unmc.edu

---

Category: Oncology

Abstract Body : Pancreatic cancer (PC) is an extremely lethal disease, with an overall survival rate of 10% [1]. Surgical resection remains the only potentially curative option, but resections are complicated by infiltrative disease, proximity of critical vasculature, peritumoral inflammation, and dense stroma [2, 3]. Furthermore, translating preoperative images to the intraoperative setting poses additional challenges for tumor detection, and can result in undetected lesions. Thus, PC has high rates of incomplete resections, and disease recurrence [4]. Fluorescence-guided surgery (FGS) has emerged as a method to improve intraoperative detection of cancer and ultimately improve surgical outcomes. Initial clinical trials have demonstrated feasibility of FGS for PC, but there are limited targeted probes under investigation for FGS in PC. Because of the heterogeneity of PC, it is essential to investigate other targets for FGS, either in combination with existing probes, or independently [5]. Mucin16 (MUC16) is a glycoprotein overexpressed in 60-80% of PCs, yet this biomarker has not been investigated for FGS of this disease. Our previous work demonstrated initial feasibility for targeting MUC16 for FGS in subcutaneous and orthotopic mouse models with a murine antibody conjugate, muAR9.6-IRDye800 [6]. Herein, we investigate the translational potential of the humanized variant of this antibody, huAR9.6-IRDye800, for fluorescence-guided surgery of PC. The objective of this project is to develop preclinical evidence to support the clinical translation of huAR9.6-IRDye800, and to investigate the role of antigen expression and tumor microenvironment on accumulation and contrast. Our hypothesis is that huAR9.6-IRDye800 is a non-toxic fluorescent probe that improves the intraoperative detection of PC with FGS in MUC16-expressing tumors. AR9.6 was humanized via complementarity determining region grafting. Humanization did not impact binding of the antibody to MUC16 (Figure 1A). HuAR9.6 was conjugated to IRDye800 via amide coupling synthesis at dye to protein ratios of 0.3, 1, 2, and 4 (Figure 1B). An ELISA confirmed that the conjugation ratio did not impact antibody affinity for MUC16 (Figure 1C). Western blotting confirmed binding of the humanized conjugate to human PC cell lines (Figure 1D). While in vitro binding was not impacted by conjugation ratio, in vivo studies in healthy CD-1 mice, shown in Figures 2A and 2B, demonstrated that increased dye to protein ratios resulted in increased liver signal at 48 hours after injection, consistent with other studies in the literature [7]. Dynamic contrast enhancement observed after injection of 50 μg of huAR9.6-IRDye800 in MUC16-expressing subcutaneous xenografts showed that tumor to background ratios (TBRs) continued to increase up to 9 days after injection (peak TBR 6.95 ±0.392, N=4), as shown in Figure 3A and C. Necropsies conducted at 9 days post-injection showed 5.92 times greater signal in the tumor as compared to the liver (Figure 3B), suggesting the potential to differentiate tumor from key background organs in PC, and detect metastatic lesions. Results of the dynamic contrast enhancement were consistent with previous dynamic imaging conducted with muAR9.6-IRDye800 [6]. HuAR9.6-IRDye800 localization within tumors was observed with fluorescence

microscopy (Figure 5). A 28-day safety and biodistribution study (not pictured) of both high (80µg) and low (20µg) dose huAR9.6-IRDye800 compared to saline control showed no indication of long-term toxicity from the conjugate, evidenced by no significant changes in animal weight over time, and no significant differences in blood chemistry. Future work will assess the impact of antigen expression on contrast. To that end, patient-derived xenograft models were screened for expression of MUC16, and three models were identified that express low, moderate, and high levels of MUC16 (Figure 4). Our results demonstrate that huAR9.6-IRDye800 binds to MUC16, preferentially accumulates and identifies tumors with high tumor to background ratios, and does not exhibit long-term toxicity.

References: 1. Siegel RL, Miller KD, Fuchs HE, Jemal A (2021) Cancer Statistics, 2021. CA Cancer J Clin 71:7–33 . doi: 10.3322/caac.21654 2. Lu G, van den Berg NS, Martin BA, et al (2020) Tumour-specific fluorescence-guided surgery for pancreatic cancer using panitumumab-IRDye800CW: a phase 1 single-centre, open-label, single-arm, dose-escalation study. Lancet Gastroenterol Hepatol 5:753–764 . doi: 10.1016/S2468-1253(20)30088-1 3. Tummers WS, Miller SE, Teraphongphom NT, et al (2018) Intraoperative Pancreatic Cancer Detection using Tumor-Specific Multimodality Molecular Imaging. Ann Surg Oncol 25:1880–1888 . doi: 10.1245/s10434-018-6453-2 4. Strobel O, Neoptolemos J, Jäger D, Büchler MW (2019) Optimizing the outcomes of pancreatic cancer surgery. Nat Rev Clin Oncol 16:11–26 . doi: 10.1038/s41571-018-0112-1 5. Hoogstins CES, Boogerd LSF, Sibinga Mulder BG, et al (2018) Image-Guided Surgery in Patients with Pancreatic Cancer: First Results of a Clinical Trial Using SGM-101, a Novel Carcinoembryonic Antigen-Targeting, Near-Infrared Fluorescent Agent. Ann Surg Oncol 25:3350–3357 . doi: 10.1245/s10434-018-6655-7 6. Olson MT, Wojtynek NE, Talmon GA, et al (2020) Development of a MUC16-Targeted Near-Infrared Fluorescent Antibody Conjugate for Intraoperative Imaging of Pancreatic Cancer. Mol Cancer Ther 19:1670–1681 . doi: 10.1158/1535-7163.MCT-20-0033 7. Cilliers C, Nessler I, Christodolu N, Thurber GM (2017) Tracking Antibody Distribution with Near-Infrared Fluorescent Dyes: Impact of Dye Structure and Degree of Labeling on Plasma Clearance. doi: 10.1021/acs.molpharmaceut.6b01091

Full Name of Abstract's 1st Author : Madeline Olson

First Name: Madeline

Last Name: Olson

Email: madeline.olson@unmc.edu

Organization: University of Nebraska Medical Center

Country: United States

ID: GA124
Visualizing Small Cell Lung Cancer via PET with a CD133-Targeted Radioimmunoconjugate

Samantha Sarrett, CUNY Hunter College, ssarrett@gradcenter.cuny.edu

---

Category: Oncology

Abstract Body : Introduction: Small cell lung cancer (SCLC) is a notoriously aggressive disease, presenting with a 5-year survival rate of only 7%1. Low-dose computed tomography, the gold-standard in lung cancer screening, is unable to detect early SCLC when interventions are most effective2. Thus, the identification of biomarkers for SCLC and the subsequent creation of targeted therapeutics remain unmet clinical needs. CD133 is a transmembrane protein with minimal expression in normal tissue but overexpression on the surface of a variety of tumors, including SCLC, making it a promising target for imaging and therapy3. Here, we report the development of a novel CD133-targeting radioimmunoconjugate ¾ [89Zr]Zr-DFO-PROM1 ¾ and its in vivo evaluation in a murine model of SCLC via PET imaging and ex vivo biodistribution studies. Methods: The CD133-targeting mAb PROM1 was modified with desferrioxamine (DFO) using p-SCN-Bn-DFO, and the resultant DFO-PROM1 immunoconjugate was subsequently labeled with [89Zr]Zr4+ under basic conditions (pH 7.4) and purified via size exclusion chromatography. The immunoreactivity of [89Zr]Zr-DFO-PROM1 was determined via an in vitro assay with CD133-expressing NCI-H82 human small cell lung cancer cells. To interrogate the performance of the radioimmunoconjugate in vivo, either [89Zr]Zr-DFO-PROM1 (90 µCi, 36 ug) or an isotype-control radioimmunoconjugate ([89Zr]Zr-DFO-hIgG1, 90 µCi, 36 ug) were administered via tail vein to 5-7 week old BALB/c female mice bearing subcutaneous NCI-H82 tumors. PET images were collected 24, 48, 72, 96, and 120 h post-injection, and the mice were sacrificed for ex vivo biodistribution analysis after the final imaging timepoint. Results: [89Zr]Zr-DFO-PROM1 was synthesized in >99% radiochemical yield and >99% radiochemical purity. The radioimmunoconjugate was found to have a post-purification specific activity of 11.1 GBq/µmol and an immunoreactive fraction of >70% with CD133-positive NCI-H82 SCLC cells. PET imaging and biodistribution experiments revealed the in vivo specificity of [89Zr]Zr-DFO-PROM1 for its target. Selective uptake of the radioimmunoconjugate was observed in CD133-positive NCI-H82 xenografts as early as 24 h post-injection. Over the course of 5 days, the activity concentration in the tumor grew to a maximum of 22.4 %ID/g (± 6.45 %ID/g), while the uptake in healthy compartments such as the blood, liver, and bone decreased or remained at relatively lower levels. Critically, only low levels of accretion of [89Zr]Zr-DFO-hIgG1 were observed in the tumor, reinforcing the specificity of the CD133-targeted radioimmunoconjugate. Conclusion: We have synthesized and characterized a novel CD133-targeting radioimmunoconjugate ¾ [89Zr]Zr-DFO-PROM1 ¾ and clearly demonstrated its efficacy for the non-invasive delineation of antigen-expressing tumor tissue in a murine model of SCLC. We are currently working to leverage the PROM1 platform for theranostic PET imaging as well as radioimmunotherapy.

References: 1. Byers, L. A.; Rudin, C. M., Small cell lung cancer: where do we go from here? Cancer 2015, 121 (5), 664-72. 2. National Lung Screening Trial Research, T.; Aberle, D. R.; Adams, A. M.; Berg, C. D.; Black, W. C.; Clapp, J. D.; Fagerstrom, R. M.; Gareen, I. F.; Gatsonis, C.; Marcus, P. M.; Sicks, J. D., Reduced lung-cancer mortality with low-dose computed tomographic screening. N Engl J Med 2011, 365 (5), 395-409. 3. Li, Z., CD133: a stem cell biomarker and beyond. Exp Hematol Oncol 2013, 2 (1), 17. µ

Image/Figure:

https://s3.amazonaws.com/amz.xcdsystem.com/1E8A4501-BB41-A02A-1D3B9882B798BFAA_abstract_File10351/GA124_ImageFigure_0512103817.png

Image/Figure Caption: Fig 1. (A) Representative PET images acquired over 24, 48, 72, 96, and 120 h after the administration of [89Zr]Zr-DFO-PROM1 (90 µCi, 36 µg) and [89Zr]Zr-DFO-hIgG1 (90 µCi, 36 µg) to athymic nude mice bearing subcutaneous NCI-H82 SCLC xenografts (n = 4 for each antibody). Images on the left are coronal slices, whereas the last image on the right is a maximum intensity projection (MIP) collected at 120 h p.i. (B) Ex vivo biodistribution results. Following the final PET imaging timepoint at 120 h, the mice were sacrificed via CO2 asphyxiation. Selected organs were collected in pre-weighed tubes, and the activity in each tissue was measured using a gamma counter and subsequently normalized to the mass of each tissue. Statistical significance was determined using 2way ANOVA analysis with GraphPad Prism 8 (****$p < 0.0001$).

Full Name of Abstract's 1st Author : Samantha M. Sarrett

First Name: Samantha

Last Name: Sarrett

Email: ssarrett@gradcenter.cuny.edu

Organization: CUNY Hunter College

Country: United States

ID: GA125
A bioresponsive near-infrared fluorescent molecular probe for imaging cell hypoxia

Janeala Morsby, University of Notre Dame, jmorsby@nd.edu

Category: Oncology

Abstract Body : Hypoxia, the diminished availability of molecular oxygen in bodily tissues is the hallmark of many solid tumors which often results in chemoresistance in different types of cancers. Over the last decade a variety of bioresponsive off-on molecular probes have been designed to specifically monitor changes in nitroreductase (NTR) and azoreductase enzymes that are overexpressed under hypoxic conditions. Although several probes have been shown to respond to these reductase enzymes, there is still a great need for fluorescent near infrared (NIR), water soluble probes with favorable pharmaceutical properties that enable clinical translation. Here we report a novel off – on water soluble fluorogenic probe that indicates cell hypoxia. The probe is a heptamethine cyanine dye that is selectively triggered by NTR to undergo self-immolative cleavage (1,6-elimination) to produce a large enhancement in NIR fluorescence signal at 780 nm. Additionally, the probe enables microscopic imaging of cell hypoxia with "turn on" fluorescence with no cytotoxicity effects. Michaelis Menten kinetic measurements, NTR blocking studies and colocalization studies are also reported. The probe has excellent photophysical properties and a chemical structure which can be easily manipulated to produce other NIR fluorescent probes that monitor changes in other reductase enzymes elevated under hypoxic conditions.

References: 1. Org. Biomol. Chem., 2021,19, 4100-4106. 2. L. Štacková , P. Štacko and P. Klán , J. Am. Chem. Soc., 2019, 141 , 7155 —7162.

Image/Figure Caption: A sulfonated bioresponsive near-infrared fluorescent molecular probe for imaging cell hypoxia

First Name: Janeala

Last Name: Morsby

Email: jmorsby@nd.edu

Organization: University of Notre Dame

Country: United States

ID: GA126

The Formulation of the Thermosensitive Sol–Gel/ Protease Substrate Probe Mix for the Rapid Visualization of Tumor Margin in the Breast Surgical Wound

Ethan Walker, Case Western Reserve University, yvv@case.edu

Category: Oncology

Abstract Body : Introduction: Breast cancer (BCa) is the second most common cancer in American women. Surgical removal of the primary BCa is the standard of care for this disease. Currently, ~75% of BCa surgeries in the USA are breast conserving surgery (BCS). Positive surgical margins, cancer tissue at the surface of a resected lumpectomy specimen, are found in 20-40% of all BCS resections. Among patients treated by BCS and radiation therapy, positive surgical margins are associated with a 2-fold increase in the risk of local recurrence when compared with negative margins1. Pathological examination is a current gold standard to confirm positive margins. However, microscopic evaluation of tissue samples only assesses about 1/10 of 1% of the entire volume of the removed specimen leading to margin undersampling and local recurrence of patients with pathologically clean margins, i.e. false negative margins. Innovation: Development of a simple real-time imaging technique to rapidly and precisely identify excisional BCa margins of the surgical wound would significantly improve the quality of care and reduce costs associated with incomplete excisions and consequent multiple visits. Exploiting increased protease expression at the edge of BCa, we propose in vivo topical administration of an imaging probe to identify BCa that may remain in the surgical cavity after standard-of-care resection. Methodology: Based on years of preclinical and clinical studies2-4 we have formulated a small molecule, fluorescently-quenched-protease-substrate probe, 6QC-ICG5, as a tool for imaging the surgical cavity after resection of tumor tissues. Different formulations of thermosensitive sol–gel Poloxamer-407, DMSO, and 6QC-ICG were tested to identify the best characteristics for topical application of the imaging probe. Results: Thermosensitive gel mixtures were utilized to allow easy fluid application and solidification once applied to prevent “dripping”. Initially, to assess the viscosity and time-to-solidification of gel mixtures, more than forty formulations with different concentration of the gel and DMSO were tested. Results suggested that poloxamer-407/DMSO mixes (with ~20% concentration of each) possessed the best characteristics for “no drip” topical applications of 6QC-ICG. The formulations were tested using mouse animal models including: 1) orthotopic human MDA-MB-468 BCa xenografts in nude mice; or 2) human BCa xenografts in NSG PDX mice. We found that these mixes were good solvents for 6QC-ICG (>100-μM) with a desirable thermoreversible sol–gel transition and a weak mechanical strength that was important for distribution of 6QC-ICG on the surface of tissue. They demonstrated excellent ability to detect cancer tissue after 10-min exposure that led to high signal-to-noise ratio (4.5) without pooling on the surface (Spectrum, Perkin-Elmer or Curadel-FLARE, Curadel, imaging cameras, 800-nm filter sets). H&E histology and fluorescence imaging (Odyssey, Li-Cor) of the tumor and surrounding normal tissue samples confirmed that Poloxamer-407/DMSO/6QC-ICG mix penetrated into the 120-μm in 10-min. To assess an efficacy of gel-carrier/prob formulation to detect cancerous tissue in vivo, half of tumor xenograft along with surrounding tissue was excised under

anesthesia followed by 10-min topical application of the gel-carrier/probe mix. ICG fluorescent “hot-spots” in animals were inked to indicate the regions of fluorescence during histology. Correlation between the inked areas, i.e. fluorescence, in H&E slides, and the areas of pathologically confirmed cancer was determined. This analysis revealed a per-spot sensitivity=1.0 [95% CI 0.059-1.000] and specificity=0.933 [95% CI 0.765-0.988] for 24 spots in 12 nude mice that corroborated with a sensitivity=1.0 [95% CI 0.791-1.000] and specificity=0.941 [95% CI 0.692-0.997] for 36 spots in 10 PDX mice. Conclusion: Utilization of Poloxamer-407/DMSO/6QC-ICG mix topically to detect BCa in vivo in the surgical wound has the potential to reduce re-excisions as well as the false negative rate from pathology undersampling, with a consequent savings in healthcare costs and enhancement in patient quality of life.

References: 1. PMID: 20817513; 2. PMID: 27876303; 3. PMID: 32132111; 4. PMID: 24705781; 5. PMID: 26039341.

First Name: Ethan

Last Name: Walker

Email: yvv@case.edu

Organization: Case Western Reserve University

Country: United States

ID: GA127
Simultaneous optogenetic [18F]FDG-fPET/fMRI to study brain circuits in rats

Sabrina Buss, Eberhard Karls University of Tuebingen, sabrina.buss@med.uni-tuebingen.de

---

Category: Neuroscience

Abstract Body : Introduction Optogenetic functional magnetic resonance imaging (ofMRI) combines a precise neuronal stimulation technique, with fMRI as indirect readout of neuronal activation1. This enables a cell-type specific mapping of the whole brain dynamic response to the activation or inhibition of neuronal circuits. Despite the advantage of using fMRI to map functional changes of whole brain activity, molecular changes after optogenetic activation have mainly been measured using invasive techniques, such as fast-scan cyclic voltammetry or genetic fluorescence sensors. Although both techniques have been shown to have a high temporal resolution and specificity, they are restricted to a small, preselected region in the brain. In contrast, positron emission tomography (PET) offers the great potential to assess metabolic and molecular changes on whole brain level in vivo. While static [18F]FDG-PET provides no information on metabolic changes induced by a stimulation during the acquisition, functional PET (fPET) enables the detection of metabolic changes with high temporal resolution on single subject level via a continuous [18F]FDG infusion2. In this study, a simultaneous [18F]FDG-fPET/BOLD-fMRI protocol was established in rats subjected to optogenetic stimulation of the nigrostriatal pathway. Material&Methods Male rats (n=4, 329±24 g), were stereotactically injected with 2 µL of an adeno-associated virus vector overexpressing channelrhodopsin-2 into the right substantia nigra compacta (rSNc). Five to six weeks post-surgery, a [11C]methylphenidate PET scan was performed to control for neuronal cell death induced by protein overexpression. Ten weeks post-surgery, an optical fiber (diameter: 200 µm) connected to a 473 nm laser was implanted through a drilled hole into the rSNc. A constant infusion of α-chloralose (20 mg/kg/h) and pancuronium bromide (1 mg/kg/h) was used as anesthesia. [18F]FDG-fPET/BOLD-fMRI scans were performed on a 7T small-animal MRI equipped with a PET insert. [18F]FDG (98±29 MBq) was infused using a bolus plus constant infusion protocol and fMRI data were simultaneously acquired using an EPI-BOLD sequence (TR: 2 s, TE: 18 ms). 20 Hz light stimulation protocols were used for optimized readouts. fMRI data were preprocessed and analyzed using SPM12. For PET data analysis, time activity curves (TACs) were generated and the difference between right (rSTR) and left striatum (lSTR) over time was calculated. To exclude temperature induced artifacts from optical stimulations, two non-injected control rats were stimulated and scanned using the protocol described above. Results [11C]Methylphenidate TACs and binding potential values were indistinguishable between the rSTR and lSTR, confirming that protein overexpression did not induce neuronal death. Optogenetic stimulation of the nigrostriatal pathways resulted in BOLD signal changes of 3.6±1.0% in the rSTR, while no changes were detected on the contralateral side. BOLD signal changes highly correlated to the stimulation paradigm and maximum t-values of 7.5±0.4 were observed in the dorsal rSTR on single animal level. [18F]FDG uptake in the rSTR gradually increased over time and the uptake pattern followed the stimulation paradigm. In the rSTR, an

increased tracer uptake of 12.0±4.0% compared to the contralateral side was calculated in the last 5-minute time-interval of the PET acquisition. In contrast to the fMRI activation, metabolic activation was more pronounced in the medial part of the rSTR. Light stimulated, non-injected rats did not show BOLD signal changes or right-left differences in [18F]FDG uptake in the STR. Conclusion Here, we present for the first time simultaneous, dynamic [18F]FDG-fPET/BOLD-fMRI data during optogenetic stimulation in rats. We established a protocol to detect brain activation induced by light stimulation of nigrostriatal neurons projecting to the dorso-medial part of the STR. Our data show a clear spatial and temporal mismatch between activity patterns observed with BOLD-fMRI and [18F]FDG-fPET, which may be related to the complementary readouts of both. Further experiments are ongoing to increase the animal number and determine functional connectivity changes on group level.

References: (1) Lin, P., Fang, Z., Liu, J., & Lee, J. H. (2016). Optogenetic Functional MRI. Journal of visualized experiments : JoVE, (110), 53346. https://doi.org/10.3791/53346 (2) Villien, M. Simultaneous functional imaging using fPET and fMRI. EJNMMI Phys 2, A66 (2015). https://doi.org/10.1186/2197-7364-2-S1-A66

First Name: Sabrina

Last Name: Buss

Email: sabrina.buss@med.uni-tuebingen.de

Organization: Eberhard Karls University of Tuebingen

Country: Germany

ID: GA128
Shortwave infrared detection of Cerenkov Luminescence from radioisotopes

Ben Mc Larney, Memorial Sloan Kettering Cancer Center, mclarneb@mskcc.org

---

Category: Oncology

Abstract Body : Cerenkov luminescence (CL) is produced by radioisotopes predominantly when beta (β) particles travel faster than light in a given medium i.e. tissue.[1] The emitted CL is continuous, blue weighted, and proportional to the reciprocal wavelength.[2] CL has been characterized across the visible spectrum of light and into the near infrared region. The wide availability of highly sensitive visible light detectors such as IVIS based systems has allowed CL imaging to be established as a cheap alternative to PET, especially in the preclinical field.[3] However, the scattering and absorption of visible light is a major limitation of CL. Light above 650nm and into the NIR spectrum is absorbed an order of magnitude less than wavelengths in the 400 – 600 nm regime.[4] SWIR wavelengths furthermore undergo minimal to no absorption or scattering and detection of CL in this spectrum would have significant benefits.[5] It should be further noted that the human eye does not detect light past ~700nm and LED bulbs are optimized for visible light emission with no emission in the SWIR spectrum. CL has previously been detected in the SWIR regime from medical linear accelerators (LINACs) where particles are accelerated to a magnitude higher energy than radioisotopes.[6] Proportionally they produce an order of magnitude more-light than that of radioisotope CL.[1] In this work we show for the first time that SWIR CL detection can also be performed with radioisotopes. SWIR CL is detected using an InGaAs based detector from five medical radioisotopes. The current setup's sensitivity (0.05 μCi/μl) is characterized along with and the SWIR CL radioisotope spectrum. Furthermore, the pre-clinical applicability of SWIR CL is shown using xenograft models. This work has implications for the rapid adoption of CL for both clinical screening and resection. The advantages of SWIR CL imaging for radioisotopes would include no need for ambient light removal along with reduced scattering, absorption and increased penetration depths in comparison to visible based CL.

References: 1. Glaser, A.K., et al., Cherenkov radiation fluence estimates in tissue for molecular imaging and therapy applications. Physics in Medicine & Biology, 2015. 60(17): p. 6701. 2. Ruggiero, A., et al., Cerenkov luminescence imaging of medical isotopes. Journal of Nuclear Medicine, 2010. 51(7): p. 1123-1130. 3. Spinelli, A.E., et al., Multispectral Cerenkov luminescence tomography for small animal optical imaging. Optics Express, 2011. 19(13): p. 12605-12618. 4. Jacques, S.L., Optical properties of biological tissues: a review. Physics in Medicine & Biology, 2013. 58(11): p. R37. 5. Thimsen, E., B. Sadtler, and M.Y. Berezin, Shortwave-infrared (SWIR) emitters for biological imaging: a review of challenges and opportunities. Nanophotonics, 2017. 6(5): p. 1043-1054. 6. Cao, X., et al., Observation of short wavelength infrared (SWIR) Cherenkov emission. Optics letters, 2018. 43(16): p. 3854-3857.

Image/Figure:

https://s3.amazonaws.com/amz.xcdsystem.com/1E8A4501-BB41-A02A-1D3B9882B798BFAA_abstract_File10351/GA128_ImageFigure_0512110850.jpg

Image/Figure Caption: Schematic outlining the SWIR setup of isotope imaging. Imaging was carried out in a dark enclosure with the radioactive source located within a lead ingot (pig) for shielding. The camera was fitted with a 16mm $f/1.4$ SWIR lens and located ~20 cm from the source with a field of view of ~15x15 cm. Camera control and recordings were managed from the camera software on a laptop.

First Name: Ben

Last Name: Mc Larney

Email: mclarneb@mskcc.org

Organization: Memorial Sloan Kettering Cancer Center

Country: United States

ID: GA130
Low field NMR relaxometry for intraoperative tumour margin assessment in breast-conserving surgery

Valeria Bitonto, University of Turin, valeria.bitonto@unito.it

---

Category: Instrumentation

Abstract Body : Introduction. Breast cancer is the most commonly diagnosed cancer for women and clear margins in breast-conserving surgery (BCS) are essential for preventing recurrence1,2. About 20% to 40% of BCS procedures result in margins, which are either positive or suspected of having malignant cells at the margins of the resection region3. The aim of this study is to develop an alternative diagnostic method, based on Nuclear Magnetic Relaxation (NMR) relaxometry and Fast field cycling (FFC) technique, able to identify the presence of tumour tissue in in small tissue samples cut from the surgical specimens, at the margins of tumour resection, before the histopathological analysis. Water proton's T1 relaxation, measured at very low magnetic fields, can be exploited to support the surgeon in real time margin assessment during BCS. Methods. Forty-one patients (aged between 40 and 90 years, mean age 65±15 years) undergoing quadrantectomy or mastectomy for breast cancer were enrolled in the study. From each surgical specimen between two and three samples (weight between 16-114 mg and with a diameter between 2.5-8.9 mm) were obtained, leading to a total of 104 freshly excised breast tissue samples. The individual tissue samples were analyzed by relaxometric methods and then transferred to the pathology laboratory for standard histopathological evaluation (H&E staining). The acquisition of proton longitudinal relaxation time (T1) as a function of the magnetic field strengths (the so-called Nuclear Magnetic Resonance Dispersion, NMRD, profile) was performed on the Stelar SpinMaster Fast Field Cycling (FFC)-NMR relaxometer (Stelar S.n.c., Mede (PV), Italy), endowed with a microcoil of 10 mm diameter. The NMRD profiles (7 points) were acquired at 10°C, in the range of low magnetic field strength from 0.01 to 1 MHz proton Larmor frequencies (corresponding to B0 = 0.24 mT-24 mT). The overall acquisition time was 20’34’’. Results/Discussion. The histological analysis allowed to classify the investigated specimens as follows: 40 healthy (H), 21 tumours (T), and 43 mix (M, containing both tumor and healthy tissue), respectively. Both H and T tissues relaxation rates increase when the magnetic field strengths decrease but the relative values and slopes of the two curves are significantly different. This finding appears to be associated with the different water content and water mobility characteristics of the tissues. Tumour tissue has a protein/fat/water ratio that is highly altered in respect to healthy breast tissue in which adipocytes are predominant. As previously reported 4, 5, lipid protons relaxation rates are significatively less dependent than water/protein protons from the magnetic field strength in the range 0.02-10 MHz. Accordingly, we identified two relaxometric criteria, namely i) the slope of the line joining the R1 values measuread at 0.02 and 1 MHz and ii) the sum of the R1 values measured at 0.39 and 1 MHz, that reflect this peculiar behavior and can allow to assess the presence of tumour cells in a breast tissue specimen (sensitivity of 92% and specificity of 85%) (Fig.1). Conclusion. The relaxometric method proposed is low cost, fast and it does not rely on the expertise of a pathologist or cytologist as it can be highly authomatised. Its application can allow intraoperative surgical breast specimen

margin evaluation by providing the surgeon real time information about the presence of residual tumour tissue. This can lead to a more precise surgical resection of breast cancer in BCS, reducing the need for re-excision. Acknowledgments. This work was performed in the frame of the COST Action AC15209 (EURELAX). This project has received funding from the European Union Horizon 2020 research and innovation program under grant agreement No 668119 (project "IDentIFY") and from AIRC under IG 2019, ID 23267 project (PI Geninatti Crich Simonetta).

References: 1. Sung, H. et al. Global cancer statistics 2020: GLOBOCAN estimates of incidence and mortality worldwide for 36 cancers in 185 countries. CA. Cancer J. Clin. (2021) doi:10.3322/caac.21660. 2. Fajdic, J., Djurovic, D., Gotovac, N. & Hrgovic, Z. Criteria and procedures for breast conserving surgery. Acta Inform. Medica 21, 16–19 (2013). 3. Elmore, L. C. & Margenthaler, J. A. A tale of two operations: Re-excision as a quality measure. Gland Surg. 8, 593–595 (2019). 4. Di Gregorio, E., Ferrauto, G., Lanzardo, S., Gianolio, E. & Aime, S. Use of FCC-NMRD relaxometry for early detection and characterization of ex-vivo murine breast cancer. Sci. Rep. 9, 1–8 (2019). 5. Broche, L. M., Ross, P. J., Davies, G. R., MacLeod, M. J. & Lurie, D. J. A whole-body Fast Field-Cycling scanner for clinical molecular imaging studies. Sci. Rep. 9, 1–11 (2019).

Image/Figure:

https://s3.amazonaws.com/amz.xcdsystem.com/1E8A4501-BB41-A02A-1D3B9882B798BFAA_abstract_File10351/GA130_ImageFigure_0512115213.jpg

Image/Figure Caption: Box chart of the Ratio (A) and 2R1 (B) values calculated for the 104 investigated tissue samples. The box is determined by the mean ± SD. The line inside each box represents the 50th percentile (median). The thick red line represent the cut-off value (see text). Statistical significance was determined by Student's t-test (*** $p < 0.01$).

Full Name of Abstract's 1st Author : Valeria Bitonto

First Name: Valeria

Last Name: Bitonto

Email: valeria.bitonto@unito.it

Organization: University of Turin

Country: Italy

ID: GA131
Modulation of neutrophil extracellular trap formation through polymer coating of metal oxide nanoparticles

Dhruvi Panchal, West Virginia University, dp00016@mix.wvu.edu

---

Category: New Chemistry, Materials & Probes

Abstract Body : Given that 1 in 8 women develop breast cancer throughout their lifetime, the disease is a substantial public health burden. Patient morbidity and mortality occur primarily due to metastatic spread but are compounded by thrombosis or the formation of blood clots. Recently, neutrophils activated by the inflammatory tumor microenvironment have been observed to release web-like DNA fibers known as neutrophil extracellular traps (NETs). NETs have been linked to several negative downstream effects including thrombosis, damage to vascular endothelial cells, and capture of circulating tumor cells to promote metastasis. Due to the pathogenic role of NETs in breast cancer, it is critical to ensure that contrast agents used in diagnostic imaging do not elicit this response. Breast MRI is often used as a supplement to mammography for high-risk women, as it detects breast cancers that may be missed by mammography and provides superior soft-tissue contrast; however, the standard MRI contrast agents used in the clinic (e.g. gadolinium chelates) cause high false-positive rates, as high as 25%. Thus, alternative contrast agents to improve diagnostic accuracy are being developed, including metal oxide nanoparticles such as iron oxide (Fe3O4) and manganese oxide (MnO). Prior studies have demonstrated that certain nanoparticle formulations may promote NETosis, which could encourage cancer progression. This study aimed to evaluate the effect of altered polymer coating of MnO nanoparticles on NET formation. MnO nanocrystals were synthesized using thermal decomposition of Mn (II) acetylacetonate in dibenzyl ether and oleylamine at 280°C. Nanocrystal size and chemistry were evaluated with TEM, XRD, and FTIR. Hydrophobic MnO nanocrystals were encapsulated with biodegradable poly(lactic-co-glycolic acid) (PLGA) and increasing amounts of polyethylene glycol (PEG) including 0%, 2.5%, 5%, and 10%. Hydrodynamic particle size was evaluated by DLS and confirmed to be ~180 nm. Neutrophils were isolated from the bone marrow of healthy female BALB/c mice femurs via density gradient. Neutrophils were stained with CellTracker Deep Red, plated, and stimulated for 3 hours with either media only (negative control), phorbol-12-myristate-13-acetate (PMA) (positive control), unencapsulated MnO nanoparticles, or PLGA MnO nanoparticles with 0-10% attached PEG. DNA was stained with Hoechst and plates were imaged with an inverted confocal fluorescence microscope to evaluate the total NET formation. Nikon General Analysis software was used to quantify the number of neutrophils and NETs per field of view. The greatest NET formation resulted from PMA stimulated neutrophils with an average of 35.83 NETs per 100 neutrophils. Unstimulated neutrophils caused the second-highest amount of NET formation at 19.28 NETs per 100 neutrophils. Bare MnO nanocrystals and PLGA MnO nanoparticles without PEG attached resulted in similar NETosis to unstimulated controls, whereas particles coated with a low PEG percentage provoked fewer NETosis than did stimulated neutrophils; 2.5% PEG PLGA nanoparticles had the smallest response of 11.06 NETs per 100 neutrophils. These results indicated that polymer-coated MnO nanoparticles do not enhance NETosis, supporting their

safety as future breast cancer MRI contrast agents. Future studies will elucidate the mechanism responsible for the observed reduced NETotic response with nanoparticle PEG coating, including assessing nanoparticle stability, particle uptake into neutrophils, neutrophil activation, and reactive oxygen species as a result of nanoparticle exposure.

First Name: Dhruvi

Last Name: Panchal

Email: dp00016@mix.wvu.edu

Organization: West Virginia University

Country: United States

ID: GA133
Feasibility of Simplifying Imaging-Based Personalized Dosimetry with Machine Learning

Qing Liang, Actinium Pharmaceuticals, qliang@actiniumpharma.com

---

Category: Computational & Data Science

Abstract Body : Objectives: This work is investigates the feasibility of utilizing machine learning (ML) to predict the optimal level of I-131 injected activity which could allow reducing the number of time points required for dosimetry calculation for the SIERRA phase III clinical trial. Background: Personalized dosimetry in targeted radiopharmaceutical therapy provides a methodology to estimate the dose for each patient. Dosimetry can guide the amount of administered activity to patients maximizing the radiation dose to the tumor without causing toxicity in healthy organs. Currently, the methodology of the Committee on Medical Internal Radiation Dose (MIRD) to estimate the radiation dose involves imaging at multiple timepoints over a period of several days, which is not always feasible or practical. The SIERRA trial uses an iodine-131 labelled antibody (Apamistamab, Iomab-B) to deliver high doses of radiation to leukemia cells of older patients (55 years and older) with relapsed or refractory acute myeloid leukemia. This is done as a conditioning regimen for bone marrow transplant. Machine learning has become a powerful tool for predictive modelling within healthcare and nuclear medicine imaging. The availability of demographic, anatomic structural, and lab test information within the context of SIERRA opens the possibility to improve dosimetric prediction using machine learning. Methods: 74 patients who received the Iomab-B treatment were retrospectively analyzed in this work. The therapeutic infused activity was personalized based on an initial dosimetric dose with a low activity (7-20 mCi) Iomab-B infusion followed by 3 gamma camera imaging acquisitions performed immediately after infusion is complete, at 24 h, and at 72-96 h post infusion. The biodistribution information at the different imaging timepoints was used to calculate the dose to the liver following the MIRD formalism. 212 features (organ uptake and volume from planar and CT images respectively, demographic information, blood, and marrow tests) were evaluated. Features with greater than 20% of entries missing were discarded. Other remaining missing values were replaced with the median. Interquartile range of features was scaled using the RobustScaler preprocessing method using Python's scikit-learn library. A novel feature selection pipeline was designed and implemented using Python's mlxtend library (SequentialFeatureSelector method). The LASSO linear regression method (α=0.3) was used to train and test the model (70/30 train/test split). The model was used in combination with a single timepoint image (first image) to predict the injected activity required to achieve a 24 Gy maximum dose to the liver. Results: Liver mass, initial liver uptake, serum aspartate aminotransferase value (pre and post dosimetric infusion), body surface area (BSA), serum lactase dehydrogenase, lymphocyte count, and neutrophil count were robust features observed to account for variations in prescribed activity. The machine learning model had r2 = 0.71 and RMSE=179.8 mCi (mean prescribed activity=716.4 mCi). Error of less than 30% was reported in 63.6% of patients, which represents the fraction of patients within the uncertainty threshold of optimized gamma-camera imaging. SIERRA-specific constraints (maximum manufactured

activity is 1030 mCi) led to further reduced model error within the clinical setting (RMSE=167.4 mCi). Our ML model outperformed conventional single-variable methods, such as those based on body or liver mass (RMSE=337.2 mCi or 278.3 mCi, respectively). Furthermore, the current method appears to significantly improve upon the predictive capability of liver dosimetry using the single initial time point (RMSE=331.8 mCi). Conclusion: Our results suggest that with carefully selected features, it is feasible to train a ML model that reduces the number of images to predict a personalized I-131 injection for the SIERRA trial.

Image/Figure:

https://s3.amazonaws.com/amz.xcdsystem.com/1E8A4501-BB41-A02A-1D3B9882B798BFAA_abstract_File10351/GA133_ImageFigure_0512121226.JPG

Image/Figure Caption: Table 1: Test set performance metrics for Iomab-B dose prediction, using models of varying complexity.

First Name: Qing

Last Name: Liang

Email: qliang@actiniumpharma.com

Organization: Actinium Pharmaceuticals

Country: United States

ID: GA135
Investigations Into functional Red and Near-Infrared Emitting Fluorescent Probes for Facile Radiolabeling and Tracing in Living Prostate Cancer Cell Lines

Rüdiger Exner, University of Bath, R.M.Exner@bath.ac.uk

Category: New Chemistry, Materials & Probes

Abstract Body : In recent years, the synthesis and modification of functionalized indocyanine dyes incorporating cypate frameworks, denoted Cy5 and Cy7 dyes, has received a lot of academic and commercial interest. Fluorescent probes based on these are of particular interest in in vivo imaging, for instance in fluorescence guided surgery, because their photophysical properties allow for imaging in the near-infrared (NIR) window, ranging from ca. 650 to 1350 nm[1] and more recently for photoacoustic imaging investigations [REF]. In the far-red and NIR spectral range, overall attenuation in biological tissues reaches a local minimum, allowing for higher penetration depths of the emitted light. Most of the Cy5 and Cy7 dyes used in ongoing clinical studies bear sulfonates as peripheral substituents as these modifications are typically associated with higher tumor-to-background ratio in vivo, higher brightness due to reduced aggregation to protein surfaces and faster excretion of corresponding optical imaging probes from healthy tissues.[2-5] Hereby we report on our investigations into the synthesis and spectroscopic characterization of a new family of sulfonated cyanine dyes incorporating carboxylic acids as design elements of choice for a straightforward conjugation to multiple functional molecules. These yielded access a variety of novel compounds equipped with multiple targeting vectors including moieties suitable for conjugation to biomolecules and/or ligands or prosthetic groups for radiolabeling with metal isotopes of relevance for nuclear medicine applications, such as 89Zr ions, which were fully characterized. Furthermore, the in vitro characteristics of the as-synthesized novel compounds were assessed in vitro in PC3, DU145 or LNCaP cell lines cultured under normoxic or hypoxic conditions, and the vector-driven cellular uptake was rationalized. We envisage that the general design principles, as well as new insights into the chemistry of these dyes, will allow for the practical, facile, and rapid realization of highly modular building blocks of interest in a range of imaging applications including in multimodality regimes.

References: [1] A. M. Smith, M. C. Mancini, S. Nie, Nature Nanotechnology 2009, 4, 710-711. [2] M. Koller, S.-Q. Qiu, M. D. Linssen, L. Jansen, W. Kelder, J. de Vries, I. Kruithof, G.-J. Zhang, D. J. Robinson, W. B. Nagengast, A. Jorritsma-Smit, B. van der Vegt, G. M. van Dam, Nature Communications 2018, 9, 3739. [3] L. M. Randall, R. M. Wenham, P. S. Low, S. C. Dowdy, J. L. Tanyi, Gynecologic Oncology 2019, 155, 63-68. [4] S. J. Spa, A. W. Hensbergen, S. van der Wal, J. Kuil, F. W. B. van Leeuwen, Dyes Pigm. 2018, 152, 19-28. [5] A. Bunschoten, D. M. van Willigen, T. Buckle, N. S. van den Berg, M. M. Welling, S. J. Spa, H.-J. Wester, F. W. B. van Leeuwen, Bioconjugate Chem. 2016, 27, 1253-1258.

Image/Figure:

https://s3.amazonaws.com/amz.xcdsystem.com/1E8A4501-BB41-A02A-1D3B9882B798BFAA_abstract_File10351/GA135_ImageFigure_0512124249.png

Image/Figure Caption: General structure of the designed probes, and preliminary in vitro imaging data (top left: Uptake of a Cy5 conjugate in PC3 cells, bottom right: Time correlated single photon counting (TCSPC) image of a Cy7-biotin conjugate binding to streptavidin-decorated polymer beads).

First Name: Rüdiger

Last Name: Exner

Email: R.M.Exner@bath.ac.uk

Organization: University of Bath

Country: United Kingdom

ID: GA136
Tracking the Accumulation of Self-assembled Iron(III) Cages in Murine Tumor Models by MRI

Janet Morrow, University at Buffalo, SUNY, jmorrow@buffalo.edu

---

Category: New Chemistry, Materials & Probes

Abstract Body : Transition metal-based MRI contrast agents are of interest as alternatives to gadolinium-based contrast agents. High spin Fe(III) complexes have shown promising proton r1 relaxivity and enhanced contrast in mice MRI studies.1-3 A rational approach to increase the relaxivity of Fe(III) MRI probes is to connect multiple iron centers together in a rigid framework by using aromatic linkers. Such an approach produces self-assembled tetrahedral cages with six-coordinate Fe(III) centers bound to three catechols each. Such cages have been used for chemical catalysis4-5 but their solution chemistry is not well-studied.6 Our investigations confirm that that rigidly linked self-assembled Fe(III) centers are robust towards dissociation and produce strong T1 proton relaxation.7 The self-assembled structures produce four kinetically inert iron catechol centers. Tetrahedral Fe(III) cages (Fe4L6) remain intact in solution when challenged with phosphate, carbonate or rat serum and show inertness towards acid, unlike tris-catechol complexes that dissociate under similar conditions. Proton relaxivity at neutral pH in PBS buffer, 37 °C at 4.7 T is 6.5 mM-1s-1 per molecule. In the presence of human serum albumin (HSA), relaxivity increases to 14 mM-1s-1, consistent with strong binding to serum albumin. Variable temperature 17O NMR studies are consistent with the absence of rapidly exchanging inner-sphere water ligands. The efficient proton relaxation is attributed to second-sphere water interactions at the Fe(III) centers that are tightly connected in a slowly tumbling assembly. Characterization of the iron cage by EPR spectroscopy and NMR spectroscopy experiments of Ga(III) analogs provide additional support for the structure of the cage in solution. MRI studies in mice show that Fe4L6 produces enhanced contrast of the vasculature with a half-life of approximately 4 hours for clearance. The iron cage accumulates over a period of several minutes to several hours into different murine tumor models including subcutaneous tumors from murine colon cancer and from ovarian cancer cell lines. Contrast enhancement of the ovarian tumor upon injection with 0.025 mmol/kg iron cage is even greater than that with injection of covalently linked HSA-Gd(III) complexes. This accumulation is attributed in part to the enhanced permeability retention effect of the Fe4L6-bound HSA and to the active uptake of serum albumin into tumor tissue by transcytosis through the vasculature and enhanced uptake at the cellular level. These hypotheses are being addressed by tuning the binding affinity of the cage to serum albumin.

References: 1. Snyder, E. M.; Asik, D.; Abozeid, S. M.; Burgio, A.; Bateman, G.; Turowski, S. G.; Spernyak, J. A.; Morrow, J. R., Angew. Chem. Int. Ed. 2020, 59, 2414-2419. 2. Wang, H.; Jordan, V. C.; Ramsay, I. A.; Sojoodi, M.; Fuchs, B. C.; Tanabe, K. K.; Caravan, P.; Gale, E. M. J. Am. Chem. Soc. 2019, 141, 5916-5925. 3. Bales, B. C.; Grimmond, B.; Johnson, B. F.; Luttrell, M. T.; Meyer, D. E.; Polyanskaya, T.; Rishel, M. J.; Roberts, J. Contrast Media Mol Imaging 2019, doi.org/10.1155/2019/8356931. 4. Caulder, D. L.; Raymond, K. N. Acc. Chem.

Res. 1999, 32, 975-982. 5. Hong, C. H.; Bergman, R. G.; Raymond, K. N.; Toste, F. D. Acc. Chem. Res. 2018, 51, 2447-2455. 6. Wang, R.; An, L.; He, J.; Li, M.; Jiao, J.; Yang, S. J. Mat. Chem. B 2021, 9, 1787-1791. 7. Morrow, J. R.; Cook, T. R.; Sokolow, G.; Rivera, A. PCT, 12/30/2020; WO 2020/263761 A1.

First Name: Janet

Last Name: Morrow

Email: jmorrow@buffalo.edu

Organization: University at Buffalo, SUNY

Country: United States

ID: GA138
A single-sided magnetic particle imaging scanner for in vivo human imaging

Alexey Tonyushkin, Oakland University, tonyushkin@oakland.edu

---

Category: Instrumentation

Abstract Body : Magnetic Particle Imaging (MPI) is an emerging molecular imaging modality that visualizes the distribution of magnetic nanoparticles (MNPs) with an extraordinary sensitivity providing high spatial and temporal resolutions [1]. MPI could address clinical needs for safe diagnostic and therapeutic applications such as cancer detection, cell tracking, and angiography. MNPs may be functionalized to serve as specific tumor markers, which would allow the MPI device to be used for in vivo screening of cancer [2]. In MPI, the continuous excitation of the MNP is provided by the external ac magnetic field with rf frequencies. The nonlinear magnetization response to the excitation is detected by a receive coil. The spatial encoding of the signal is produced by selective saturation of the MNPs with the superimposed magnetic field gradient. Scanning the field-free region (FFR) across the imaging volume senses the local concentration of MNPs that allows a tomographic reconstruction of the tracer distribution inside the volume. The two different FFR are field-free point (FFP) and field-free line (FFL). Scanners with the FFP geometries have a more robust hardware consisting of a smaller number of coils to generate the required field configuration; however, the FFL geometry provides signals that are a factor of ten higher and benefits from a more robust and time saving backprojection image-reconstruction technique [3]. Thus, the FFL scanners may be beneficial to the future clinical applications. To date, a few small-bore MPI systems have been developed, including the commercial preclinical systems; however, human-size MPI scanner has yet to be built. The major challenges are the requirements of high power and safety concern due to high-field gradient being scanned across large cylindrical bore. These cylindrical geometry constraints prevent scaling up the MPI hardware to accommodate full-size human subject. Single-sided geometry, on the other hand, has all the hardware located on one side providing an unrestricted imaging volume, which would allow the MPI device to be used locally for in vivo screening of pathologies and in interventional procedures [4]. Previous state-of-the-art single-sided MPI scanner had an FFP geometry [5]. The major drawback of any single-sided devices is inherently non-homogeneous magnetic fields and nonlinear gradient, which diminishes the performance of the scanner. Our single-sided prototype of the MPI scanner utilizes a unilateral geometry with an FFL that offers higher signal and more robust image reconstruction technique than the corresponding single-sided scanner with the FFP geometry. In our device, a strong excitation magnetic field is generated by a single elongated transmission coil and the MNP response is simultaneously detected by a surface gradiometer receive coil. Here, progress toward the development of a single-sided MPI scanner for in vivo human imaging is presented. In particular, the simulation's results of the 2D image reconstruction imply an achievable spatial resolution of 2 mm. The experimental results from the sensitivity studies show the highest to date MNP detection limit in a single-sided scanner of up to 100 ng of iron that is a factor of 50 better sensitivity than the estimated limit of small tumor detection.

References: [1] B. Gleich and J. Weizenecker, “Tomographic imaging using the nonlinear response of magnetic particles,” Nature, vol. 435, no. 7046, pp. 1214–1217, Jun. 2005. [2] H. Arami, et al., “Tomographic magnetic particle imaging of cancer targeted nanoparticles,” Nanosc., vol. 9, no. 47, pp. 18723–18730, Dec. 2017. [3] J. Weizenecker, B. Gleich, and J. Borgert, “Magnetic particle imaging using a field free line,” J. Phys. D, Appl. Phys., vol. 41, no. 10, Art. no. 105009, May 2008. [4] C. Kaethner, et al., “Asymmetric scanner design for interventional scenarios in magnetic particle imaging,” IEEE Trans. Magn., vol. 51, no. 2, Art. no. 6501904, Feb. 2015. [5] K. Grafe, et al., “2D images recorded with a single-sided magnetic particle imaging scanner,” IEEE Trans. Med. Imag., vol. 35, no. 4, pp. 1056–1065, Apr. 2016.

First Name: Alexey

Last Name: Tonyushkin

Email: tonyushkin@oakland.edu

Organization: Oakland University

Country: United States

ID: GA140
Albumin-binding vs conventional Lutetium-177-labeled LLP2A derivatives as theranostics for metastatic melanoma

Michael Pun, University of Missouri, michael.pun@missouri.edu

---

Category: New Chemistry, Materials & Probes

Abstract Body : Very late antigen-4 (VLA-4) is a trans-membrane integrin protein that is highly expressed in aggressive forms of metastatic melanoma. This integrin plays a key role in tumor growth, angiogenesis and metastasis by facilitating cancer cell adhesion and migration. LLP2A, a small-molecule high affinity, peptidomimetic, itself does not inhibit cancer cell proliferation and survival, and therefore is an ideal candidate for imaging and delivery of therapeutic payloads. We previously demonstrated the utility of 177Lu-DOTA-LLP2A as a therapeutic agent against metastatic melanoma in mice in combination with immune checkpoint inhibitors, although tumor growth was only inhibited with no cures. We hypothesize that failure to diminish tumor burden after 177Lu-DOTA-LLP2A therapy was due to the rapid renal clearance of the dose from the blood and tumor thereby decreasing efficacy. To improve the pharmacokinetic profile, we designed and synthesized novel analogs of DOTAGA-LLP2A with a 4-(p-iodophenyl)butyric acid (pIBA) albumin binding moiety. We demonstrate the feasibility of this albumin binding strategy by comparing in vitro cell binding assays and in vivo biodistribution performance of 177Lu-DOTAGA-PEG4-LLP2A (1) to the albumin binding 177Lu-DOTAGA-pIBA-LLP2A (2). In vitrocell binding assay results for 1 and 2 showed Kd of 0.4 and 1.75 nM and Bmax of 200 and 315 fmol/mg respectively. Preliminary in vivo biodistribution data for both tracers exhibited specific uptake in tumor, spleen, thymus and bone due to endogenous organ expression of VLA-4. Tumor uptake for 1 was highest at 1 h (~15 %ID/g) and 2 at 24 h (~27 %ID/g). Clearance from the tumor for 1 occurs at 24 h (< 5 %ID/g) while 2 is retained for greater than 96 h (~10 %ID/g). Compound 2 also exhibited longer blood circulation time compared to 1. Collectively, the in vitro and in vivo data suggest that modifying LLP2A with an albumin binder (pIBA) offers similar VLA-4 receptor binding qualities as the non-albumin binding molecule and provides a remarkable improvement in renal clearance and tumor retention. Efficacy studies are underway.

Full Name of Abstract's 1st Author : Michael Pun

First Name: Michael

Last Name: Pun

Email: michael.pun@missouri.edu

Organization: University of Missouri

Country: United States

ID: GA141
Development and characterization of targeted near-infrared I/II fluorophores for canine and human lung cancer imaging

Michael Hart, University of Pennsylvania, mihart@pennmedicine.upenn.edu

---

Category: Oncology

Abstract Body : Lung cancer is the leading cause of cancer-related death in the United States. Non-small cell lung cancer (NSCLC) accounts for 85% of all diagnosed lung cancers and is treated primarily by surgical resection (1). In order to preserve lung function, surgeons attempt to remove the minimum amount of lung tissue required, but intraoperative identification of NSCLC is difficult. Surgeons utilize tissue palpation and visual inspection to identify tumor margins leading to disease recurrence in approximately 40% of patients (2). More specific methods for delineating tumor margins intraoperatively need to be developed to improve the rates of complete resections (3). Fluorescence-guided surgery (FGS) is an emerging technology for aiding surgeons in the specific detection of tumors in real-time using fluorophores targeted to overexpressed tumor markers (4). Fluorophore development for in vivo imaging has largely focused on the synthesis and characterization of near-infrared (NIR) I fluorophores due to longer wavelength emitters exhibiting increased tissue penetration and decreased light scattering, but longer wavelength fluorophores have further increased signal-to-noise ratios compared to emitters in the visible spectrum due to lower tissue autofluorescence in the NIR-II window (5). This project focuses on the development of NIR-I/II fluorophores targeted to cytosolic phospholipase A2 (cPLA2) and choline kinase α (ChoKα), two enzymes overexpressed in NSCLC (6,7). DDAO-arachidonate is a cPLA2-activatable fluorophore. In the presence of cPLA2, DDAO is released from arachidonate and has a measurable fluorescence with maximum emission at 660 nm and extending into the NIR-I window. For this project, freshly resected canine (n=1) and human (n=5) lung tumor and normal lung tissues were obtained from surgeries for operable lung cancers and painted ex vivo with 20 nmol of DDAO-arachidonate. The canine tissue for this project contained baseline fluorescence from ChoKα-targeted JAS239 (700 and 800 nm emission - LI-COR Pearl), and two human tissues contained baseline fluorescence from a folate receptor-targeted fluorophore (800 nm emission - LI-COR Pearl). Tissues were incubated with DDAO-arachidonate, and the fluorescence determined using the LI-COR Pearl (700 nm emission) or PerkinElmer IVIS Spectrum (680 nm emission). Fluorescence in tumor tissue was then compared to normal to determine tumor-to-normal ratios (TNR). Tumor was considered distinguishable from normal tissue if the TNR was greater than 2:1. TNRs for human tissues ranged from just over 1.5:1 to over 5:1 with three of the tumors distinguishable from the normal tissues. TNR for the canine tissue increased from 1.48:1 to 2.17:1 following treatment with DDAO-arachidonate. These data suggest that tumor heterogeneity may be overcome in FGS by employing fluorophores targeted to different enzymes commonly overexpressed in lung cancers with differentiable emissions. To improve the TNR for intraoperative NSCLC imaging, we synthesized a novel family of NIR-II fluorophores targeted to ChoKα by choline mimetic groups. These fluorophores are constitutively active with Stokes shifts over 40 nm and maximum emissions between 980 nm and 1020 nm. The fluorescence tails of these probes

extend well past 1200 nm. In this project, we have shown that DDAO-arachidonate is a promising fluorophore for lung cancer imaging in human and canine patients, and we have developed prototype ChoKα-targeted probes with emissions in the NIR-II window making them strong candidates for in vivo lung cancer imaging.

References: (1) Cancer Facts & Figures. Atlanta, Georgia: American Cancer Society; 2020. (2) Crandall K, Maguire R, Campbell A, Kearney N. Exercise intervention for patients surgically treated for Non-Small Cell Lung Cancer (NSCLC): A systematic review. Surg. Onc. 2014; 23(1):17-30. (3) Kelsey CR, Clough RW, Marks, LB. Local recurrence following initial resection of NSCLC. Cancer J. 2006; 12(4):283-288. (4) Okusanya OT, DeJesus EM, Jiang JX, Judy RP, Venegas OG, Deshpande CG, Heitjan DF, Nie S, Low PS, Singhal S. Intraoperative molecular imaging can identify lung adenocarcinomas during pulmonary resection. J. Thorac. Cardiovasc. Surg. 2015; 150(1):28-35. (5) Hong G, Antaris AL, Dai H. Near-infrared fluorophores for biomedical imaging. Nat. Biomed. Eng. 2017; 1:1-22. (6) Molina A, Sarmentero-Estrada J, Belda-Iniesta C, Taron M, Ramirez De Molina V, Cejas P, Skrzypski M, Gallego-Ortega D, De Castro J, Casado R, Garcia-Cabezas M, Sanchez J, Nistal M, Rosell R, Gonzalez-Baron M, Lacal JC. Expression of Choline Kinase Alpha to Predict Outcome in Patients with Early-stage Non-small-cell Lung Cancer: A Retrospective Study. Lancet Oncol. 2007; 8(10):889-897. (7) Linkous AG, Yazlovitskaya EM, Hallahan DE. Cytosolic phospholipase A2 and lysophospholipids in tumor angiogenesis. J. Natl. Cancer Inst. 2010;102(18):1398-1412.

Image/Figure:

https://s3.amazonaws.com/amz.xcdsystem.com/1E8A4501-BB41-A02A-1D3B9882B798BFAA_abstract_File10351/GA141_ImageFigure_0512025431.png

Image/Figure Caption: Human neuroendocrine lung tumor and normal lung tissue from the same patient were sliced into four sections each. All tissue slices were thoroughly rinsed in DPBS to remove blood from the tissue surface. Slices were then placed in 1 mL each of phenol-red free DMEM in a 24-well clear plate. Slices were then treated with 50 µL of 400 µM DDAO-A (+ DDAO-AA) or 50 µL DPBS (- DDAO-AA). Slices were incubated at 37°C in 5% CO2 for 3 hr. Tissue was rinsed with DPBS twice prior to imaging using the IVIS Spectrum with 640 nm excitation and measuring 680 nm emission. Fluorescence was quantified using Living Image for two trials of the experiment, one using the neuroendocrine lung tumor, and one using a NSCLC, also donated by the Singhal lab. Fluorescence in the tumor tissue was significantly higher than in the normal tissue with an associated tumor-to-background ratio of approximately 4.9:1. *p-value < 0 .05 (unpaired t-test)

Full Name of Abstract's 1st Author : Michael Cameron Hart

First Name: Michael

Last Name: Hart

Email: mihart@pennmedicine.upenn.edu

Organization: University of Pennsylvania

Country: United States

ID: GA142
MALDI imaging identification of CEST MRI biomarkers that detect disease activity in a mouse model of multiple sclerosis

Aline Thomas, Johns Hopkins University School of Medicine, athom110@jhu.edu

---

Category: Neuroscience

Abstract Body : Introduction Chemical exchange saturation transfer (CEST) MRI is sensitive to many of the biomolecules in the central nervous system (CNS) altered in multiple sclerosis (MS) that cannot be detected using conventional MRI. Changes in CEST signal generated from two complementary methods, continuous wave (CW) and on resonance variable delay multiple pulse (onVDMP), were recently shown to occur during the progression of the mouse model experimental autoimmune encephalomyelitis (EAE)1,2. Here we investigated the cells and metabolites responsible for these CEST MRI signal changes in MS-associated lymph nodes using matrix-assisted laser desorption/ionization (MALDI) mass spectrometry imaging, correlating the molecular information from MALDI imaging with CEST signal and conventional EAE metrics. Methods EAE: The model was induced in C57Bl/6 mice by injection of pertussis toxin (250 ng, i.p.) and MOG35-55 (300 μg, s.c.) in IFA supplemented with tuberculin (4 mg/ml) on days 0 and 2. Mice were assessed for model progression using a standard 0-5 disability scoring rubric. MRI: Mice were imaged 13-14 days after model induction (DPI) using a horizontal bore Biospec 11.7T scanner with a 2x2 phased array coil and 72-mm volume resonator at 0.14 mm resolution. For onVDMP CEST MRI, we used 32 pulse-exchange modules with 8 delays (mixing times from 1.14 to 100 ms; B1 of 46.8 μT). For CW CEST MRI, we used a saturation time of 3 s with a B1 of 1 μT. Maps of magnetization transfer asymmetry ratio (MTR) were investigated at frequencies 0.4-6.0±0.2 ppm upon B0 correction using the WASSR method. MALDI imaging: Metabolite data was obtained with Bruker Rapiflex MALDI TOF/TOF instrument at 0.1 mm resolution. Tissue was extracted 13-14 days post induction, flash frozen, cryo-sectioned (10 μm thick), and placed on indium tin oxide (ITO)-coated slides that were sprayed with 1,5-diaminonaphthalene (1,5-DAN, 10 mg/mL). Metabolite identification was confirmed using MS/MS fragmentation spectral analysis. Histology: Adjacent sections were stained with hematoxylin and eosin (H&E) for anatomical referencing of MALDI images. Flow cytometry: Cellular staining was quantified using a MACSQuant 10 flow cytometer and data was analyzed in FlowJo software using a standard gating scheme as reported before3. Results Changes in CW and onVDMP CEST MRI signal were observed in the CNS-draining superficial cervical lymph nodes (cLNs). These changes corresponded with active stages of model progression, wherein the paralysis is increasing (13-14 DPI). We compared CEST MRI signals to cellular composition in these lymph nodes, and found significant correlation to CD11b+/CD86+ antigen-presenting cells and CD4+/IL-17+ T-cells, both recognized progressors of this model. We then compared CEST MRI signals to metabolite composition in these lymph nodes. Of metabolites confirmed thus far, 5 correlated significantly to CW and onVDMP CEST MRI signal: alanine, lactate, leucine, malate, and phenylalanine. H&E staining revealed regional, i.e. cortex and medulla, differences in metabolite presence, e.g. leucine, within these lymph nodes (Figure 1). Conclusions We linked changes in the CEST MRI signal of MS-associated

lymph nodes to cellular and metabolic alterations using flow cytometry and MALDI imaging, a label-free approach for screening a wide-array of biomolecules directly from tissue sections.

References: (1) Thomas, A. M.; Xu, J.; Calabresi, P. A.; van Zijl, P. C. M.; Bulte, J. W. M. NeuroImage 2020, 204, 116245. (2) Thomas, A. M.; Li, S.; Chu, C.; Shats, I.; Xu, J.; Calabresi, P. A.; van Zijl, P. C. M.; Walczak, P.; Bulte, J. W. M. Exp Neurol 2020, 329, 113316. (3) Kirby, L.; Jin, J.; Cardona, J. G.; Smith, M. D.; Martin, K. A.; Wang, J.; Strasburger, H.; Herbst, L.; Alexis, M.; Karnell, J.; Davidson, T.; Dutta, R.; Goverman, J.; Bergles, D.; Calabresi, P. A. Nature communications 2019, 10, 3887.

Image/Figure:

https://s3.amazonaws.com/amz.xcdsystem.com/1E8A4501-BB41-A02A-1D3B9882B798BFAA_abstract_File10351/GA142_ImageFigure_0512030148.png

Image/Figure Caption: Figure 1. MALDI imaging of the top 5 most significantly altered metabolites that correlate with CEST MRI signal in EAE-induced mice (13-14 DPI). Visualization of alanine, lactate, leucine, malate and phenylalanine maps in two representative cLNs each of (top row) control and (middle row) EAE mice. Bottom row: Average (N=5 each) relative signal intensity of these metabolites at their characteristic mass-to-charge ratio (m/z). Optical imaging is shown to highlight the location of the cLNs. H&E staining is shown to highlight intra-nodal regions (medulla and cortex). Arrows highlight a prominent example of these regional differences.

Full Name of Abstract's 1st Author : Aline M. Thomas

First Name: Aline

Last Name: Thomas

Email: athom110@jhu.edu

Organization: Johns Hopkins University School of Medicine

Country: United States

ID: GA144
CUB domain containing protein 1 is a target for radioligand therapy in PSMA null prostate cancer

Michael Evans, UCSF, michael.evans@ucsf.edu

Category: Oncology

Abstract Body : Purpose: Radioligand therapy (RLT) is a promising treatment option in metastatic castration resistant prostate cancer (mCRPC), although much of the focus has been on bone seeking radionuclides and PSMA-directed RLT. Herein, we evaluated if CUB domain containing protein 1 (CDCP1) can be exploited to treat mCRPC with RLT, particularly for subsets like small cell neuroendocrine prostate cancer (SCNC) that would not be expected to respond to bone seeking radionuclides or PSMA directed RLT. Experimental Design: CDCP1 mRNA levels were evaluated in the RNA-seq data from 119 recent mCRPC biopsies. Protein expression was assessed in twelve SCNC and adenocarcinoma patient derived xenografts. Saturation binding assays were performed with 4A06, a recombinant human antibody that targets the CDCP1 ectodomain. The feasibility of imaging and treating mCRPC in vivo was tested with 89Zr-4A06 and 177Lu-4A06. Results: CDCP1 mRNA expression was observed in over 90% of mCRPC biopsies, including SCNC and in adenocarcinoma with low FOLH1 (PSMA) levels. A modest anticorrelation was observed between CDCP1 and PTEN. Overall survival was not significantly different based on CDCP1 mRNA levels, regardless of PTEN status. Full length and/or cleaved CDCP1 was expressed in ten of twelve PDX samples . Bmax values of ~22,000 and ~6,200 fmol/mg were calculated for two human prostate cancer cell lines. Five prostate cancer models were readily detected in vivo with 89Zr-4A06. 177Lu-4A06 significantly suppressed the growth of DU145 tumors compared to control. Conclusions: The antitumor data and the overexpression of CDCP1 reported herein provide the first evidence promoting CDCP1 directed RLT as a treatment strategy for mCRPC. Combined with low expression in normal human tissues, these data provide a compelling scientific rationale for testing CDCP1 directed RLT clinically in mCRPC patients alone or in combination with other systemic therapies.

First Name: Michael

Last Name: Evans

Email: michael.evans@ucsf.edu

Organization: UCSF

Country: United States

ID: GA145
Using CD69 PET Imaging to Monitor Immunotherapy-Induced Immune Activation

Kimberly Edwards, University of Pennsylvania,
Kimberly.Edwards@pennmedicine.upenn.edu

Category: Oncology

Abstract Body : Cancer immunotherapies have had transformative success and durable clinical responses in patients with intractable malignancies. Immune checkpoint inhibitors (ICIs) have been effective in treating refractory solid tumors like non-small cell lung cancer and melanoma. Still, these treatments can have significant toxicities and there are many patients whose cancers do not respond. Thus, there is a clear need for translational tools that allow for early assessment of a favorable response.1–3 Preclinical evidence shows that immunologically active tumors, containing high levels of CD3+/CD8+ T cell infiltrates, correlate with favorable responses to immunotherapy.2,3 As a result, efforts have been made to image and monitor immune activity, particularly within the tumor microenvironment (TME). These efforts include the direct imaging of global T cell activation markers (eg. Granzyme B and ICOS), as indicators of T cell-mediated immune response.4,5 Still, none of these approaches have yet developed into widespread clinical application and each has a different temporal expression pattern relative to the cell type and immunogen. Our approach uses CD69, the canonical early-activation marker expressed in a variety of activated immune cells including cytotoxic T cells and NK cells, and applies this approach as a biomarker of response to cancer immunotherapy. Here, we show CD69-targeted PET imaging can characterize immune cell activation in the TME in response to checkpoint blockade therapy. The PET imaging probe was produced by conjugating an anti-mouse CD69 monoclonal antibody (H1.2F3) to deferoxamine (DFO) and labeling with Zr-89 ([89Zr]-DFO-H1.2F3). To test this probe in vitro, an uptake study was conducted comparing PMA/Ionomycin-stimulated primary mouse T cells and an untreated control. [89Zr]-DFO-H1.2F3 detected a 15-fold increase in CD69 expression between stimulated and unstimulated T cells. To model an in vivo system, the probe was tested using an immunocompetent immune checkpoint inhibitor preclinical model.6 Adult, female, Balb/c mice bearing CT26 syngeneic tumors were injected with [89Zr]-DFO-H1.2F3 on day 15 post tumor inoculation, and were then imaged or sacrificed for organ harvest on day 18 post tumor inoculation, i.e. 72 hours post radiotracer injection. The in vivo PET/CT imaging study showed increased uptake in tumors from responder mice (18.0 ± 2.4 %ID/g, n = 8), relative to tumors from nonresponders and untreated controls (11.8 ± 0.4 %ID/g, n = 2; and 13.3 ± 0.6 %ID/g, n = 5, respectively). In a separate experiment, ex vivo biodistribution validation showed compelling increased tumor uptake in responders (43.1 ± 12.8 %ID/g; n = 6) relative to that of nonresponder and untreated control cohorts (10.3 ± 1.2 %ID/g; n = 4, and 12.6 ± 1.8 %ID/g; n = 5, respectively). The spleens of responder mice also had higher uptake (34.03 ± 2.66 %ID/g) than those of nonresponders and untreated controls (24.21 ± 0.52 %ID/g and 22.84 ± 2.80 %ID/g, respectively). Autoradiography corroborated biodistribution analyses showing increased uptake (%ID/mm2) for responders relative to nonresponders and untreated control mice. Using chromogenic detection methods, immunohistochemistry staining

detected increased expression of CD69, OX40, Granzyme B, ICOS, and CD3 expression in tumor sections of responder mice relative to tumor sections from nonresponders and untreated controls. This CD69 PET imaging approach detected CD69 expression with sufficient sensitivity to quantify immune cell activation in a syngeneic mouse immunotherapy model, in which increased tumor uptake correlated with response.

References: (1) Ponomarev, V.; Doubrovin, M.; Lyddane, C.; Beresten, T.; Balatoni, J.; Bornman, W.; Finn, R.; Akhurst, T.; Larson, S.; Blasberg, R.; Sadelain, M.; Tjuvajev, J. G. Imaging TCR-Dependent NFAT-Mediated T-Cell Activation with Positron Emission Tomography in Vivo. Neoplasia N. Y. N 2001, 3 (6), 480–488. https://doi.org/10.1038/sj.neo.7900204. (2) Gooden, M. J. M.; de Bock, G. H.; Leffers, N.; Daemen, T.; Nijman, H. W. The Prognostic Influence of Tumour-Infiltrating Lymphocytes in Cancer: A Systematic Review with Meta-Analysis. Br. J. Cancer 2011, 105 (1), 93–103. https://doi.org/10.1038/bjc.2011.189. (3) Pagès, F.; Galon, J.; Dieu-Nosjean, M.-C.; Tartour, E.; Sautès-Fridman, C.; Fridman, W.-H. Immune Infiltration in Human Tumors: A Prognostic Factor That Should Not Be Ignored. Oncogene 2010, 29 (8), 1093–1102. https://doi.org/10.1038/onc.2009.416. (4) Larimer, B. M.; Wehrenberg-Klee, E.; Dubois, F.; Mehta, A.; Kalomeris, T.; Flaherty, K.; Boland, G.; Mahmood, U. Granzyme B PET Imaging as a Predictive Biomarker of Immunotherapy Response. Cancer Res. 2017, 77 (9), 2318–2327. https://doi.org/10.1158/0008-5472.CAN-16-3346. (5) Xiao, Z.; Mayer, A. T.; Nobashi, T. W.; Gambhir, S. S. ICOS Is an Indicator of T Cell-Mediated Response to Cancer Immunotherapy. Cancer Res. 2020. https://doi.org/10.1158/0008-5472.CAN-19-3265. (6) Duraiswamy, J.; Kaluza, K. M.; Freeman, G. J.; Coukos, G. Dual Blockade of PD-1 and CTLA-4 Combined with Tumor Vaccine Effectively Restores T-Cell Rejection Function in Tumors. Cancer Res. 2013, 73 (12), 3591–3603. https://doi.org/10.1158/0008-5472.CAN-12-4100.

Full Name of Abstract's 1st Author : Kimberly J. Edwards

First Name: Kimberly

Last Name: Edwards

Email: Kimberly.Edwards@pennmedicine.upenn.edu

Organization: University of Pennsylvania

Country: United States

ID: GA146
Novel Probes for Bladder Urothelial Carcinoma Imaging

BORIVOJ GOLIJANIN, MINIMALLY INVASIVE UROLOGY INSTITUTE, BORA.GOLI31@GMAIL.COM

Category: Oncology

Abstract Body : Introduction: Fluorescence guided surgery is a promising direction of modern robotic surgery. The development of near infrared fluorescent (NIRF) probes that specifically target cancer cells, thus enabling the visualization of cancer lesions in surgeries, can provide improvement in diagnostics and management of disease, particularly in cases of bladder cancer. Urothelial carcinomas are a heterogenous malignancy, which can be difficult to identify on the bladder surfaces. Despite the heterogeneity, the urothelial carcinomas have common characteristics: the acidic microenvironment. pH low insertion peptides (pHLIP) are a class of pH specific transmembrane peptides that target the acidic microenvironment of cancer cells [1, 2]. It has been shown that pH on the surface of cancer could be much lower than in bulk extracellular solutions [3]. In this work, pHLIP variant-3 (Var3-pHLIP) was conjugated to NIRF dyes to evaluate specificity and sensitivity as a tumor targeting molecular imaging probe and the fluorescent signal emitted by in post-cystectomy bladder cancer specimens was analyzed. Materials and methods: Thirty-eight ex-vivo bladder specimens, from patients undergoing robotic assisted laparoscopic radical cystectomy for bladder cancer, underwent intravesical incubation for 15 minutes with Var3-pHLIP conjugated to indocyanine green (ICG) or IRDye® 800CW. Samples were placed under NIR laser to excite the fluorophore. The number of lesions visible under NIRF were compared with the number identified under white light. Expression of NIRF signal and identification of lesions under white light by urologic oncology pathologist were compared to histopathologic diagnosis. An image analysis protocol was used to identify clusters of cells with characteristic fluorescence signals. Histograms of fluorescent images showed the distinct peaks of fluorescent signals, which corresponded to different areas on internal bladder area. Each peak could be fitted with Gaussian function that showed mean value and dispersion of fluorescence intensity for the cell clusters. This method allowed to identify malignant and non-malignant areas. Results and Conclusions: White light cystoscopy identified 47/58 (81%) and NIRF cystoscopy identified 57/58 (98.3%) of lesions selected for histopathological processing. Var3-pHLIP NIRF demonstrated 98% sensitivity and 100% specificity in identification of UC. NIRF Var3-pHLIP improved diagnosis by 17.3% ($p=0.003$). On signal intensity analysis, mean peak intensity of malignant cases was 99.96 relative fluorescent units (RFU) and nonmalignant cases had average peak of 46.88 RFU ($p < 0 .001$). Corrected average signal intensity of malignant lesions demonstrated an average of 52.9 RFU/μm2 and nonmalignant lesions showed an average of 25 RFU/μm2 ($p < 0 .001$). NIRF Var3-pHLIP identified UC irrespective of subtypes, previous treatment, and stage. All CIS cases missed by white light cystoscopy were diagnosed using Var3-pHLIP NIRF imaging. Var3-pHLIP NIRF enhanced visualization and improved diagnosis of urothelial carcinoma in this series of ex-vivo bladder specimens. In addition, categorizing into broader categories of malignant and nonmalignant, NIRF pHLIP is able to differentiate between the two groups based

on both peak signal intensity and mean intensity per unit area of lesion. Readily available imaging analysis software can help differentiate between malignant and nonmalignant lesions. Additional work into digital, automated analysis of NIRF pHLIP signal and development of a fluorescent signal analysis capable cystoscope can lead to diagnosis of bladder cancer at the time of cystoscopy.

References: [1] Golijanin, et al., Proc Natl Acad Sci U S A., 113(42):11829; [2] Crawford, et al., Sci Rep., 2020, 27, 10(1), 18356; [3] Anderson, et al., Proc Natl Acad Sci U S A., 2016, 113, 8177.

Image/Figure:

https://s3.amazonaws.com/amz.xcdsystem.com/1E8A4501-BB41-A02A-1D3B9882B798BFAA_abstract_File10351/GA146_ImageFigure_0512033925.jpg

Image/Figure Caption: Figure: (A) Fluorescence Intensity based color diagram of bladder image, where red color shows high intensity cluster 2 and green area corresponds cluster 1, yellow indicates on transition area between clusters 1 and 2, blue is mostly healthy area. (B) Color photograph of the corresponding tissue. (C) Histogram plot of fluorescence image revealed two clusters, which correspond to green (cluster 1) and red (cluster 2). Both clusters showed Gaussian distribution with well-defined mean values. High intensity (red area, cluster 2) corresponds to malignant lesions as confirmed by histopathology. (D) Histograms of number fluorescence images taken at the same settings from different cases were analyzed. Statistically significant difference between malignant, non-malignant and control tissues were found.

First Name: BORIVOJ

Last Name: GOLIJANIN

Email: BORA.GOLI31@GMAIL.COM

Organization: MINIMALLY INVASIVE UROLOGY INSTITUTE

Country: United States

ID: GA147
Necrosis Binding of Ac-Lys0(IRDye800CW)-Tyr3-octreotate: A Consequence from Cyanine-labeling of Small Molecules

Marcus Stroet, Erasmus MC, Rotterdam, The Netherlands, m.stroet@erasmusmc.nl

---

Category: New Chemistry, Materials & Probes

Abstract Body : Background. There is a growing body of nuclear contrast agents that are repurposed for fluorescence-guided surgery. New contrast agents are obtained by substituting the radioactive tag with, or adding a fluorescent cyanine to the molecular structure of antibodies or peptides. This enables intra-operative fluorescent detection of cancerous tissue, leading to more complete tumor resection. However, these fluorescent cyanines can have a remarkable influence on pharmacokinetics and tumor uptake. Earlier research has pointed out that cyanines have a considerable affinity towards dead cells [1]. This study aims to investigate the effect of the IRDye800CW-mediated dead cell-binding on the physiological properties of 800CW-TATE. These dead cell-binding properties can be interfering with routine experiments. For instance, some of the experimental procedures used to study radioactively labeled compounds make use of cells with disrupted cell membranes. These experimental procedures cannot be applied to study the binding of cyanine-labeled agents as the binding to these disrupted cells interferes with the experiment. Methods. Cultured U2OS cells (alive or dead, with or without SSTR2-expression) were incubated with Ac-Lys0(IRDye800CW)-Tyr3-octreotate (800CW-TATE, 10 nM), washed, and fluorescence binding was determined macroscopically and microscopically. Blocking experiments were included by co-incubation with DOTA0-Tyr3-octreotate (DOTA-TATE). Frozen tumor tissue sections of NCI-H69 (SSTR2 positive) and CH-157MN (SSTR2 negative) were incubated with 800CW-TATE and increasing amounts of DOTA-TATE blocking, washed, and fluorescence binding was determined. 800CW-TATE was then injected into NCI-H69-tumor-bearing mice. Paraffin sections of the resected tumors were imaged for near-infrared fluorescence and TUNEL cell death staining was performed. Results. The binding of 800CW-TATE could be blocked with DOTA-TATE on SSTR2-positive U2OS cells and was absent in SSTR2 negative U2OS cells. However, strong binding was observed to dead cells, which could not be blocked with DOTA-TATE and was also present in dead SSTR2 negative cells. No SSTR2-mediated binding was observed in frozen tumor sections, possibly due to disruption of the cells in the process of sectioning the tissue before exposure to the contrast agent. DOTA-TATE blocking resulted in an incomplete reduction of 61.5±5.8% fluorescence uptake by NCI-H69-tumors in mice [2]. Near-infrared imaging and dead cell staining on paraffin sections from resected tumors revealed that fluorescence uptake persisted in necrotic regions upon blocking with DOTA-TATE. Conclusions. Labeling peptides with cyanines can result in dead cell binding, which may aid the purpose of fluorescence-guided surgery. Binding to necrosis in solid tumors can increase the overall tumor uptake. Moreover, necrotic tissue should be removed as much as possible as it cannot be salvaged, causes inflammatory responses, and even releases tumorigenic factors. However, this dead cell binding can resemble non-specific binding when performing binding experiments on cells with disrupted membrane integrity. This study can benefit the development of fluorescent contrast agents.

References: [1] Stroet MCM, de Blois E, Stuurman DC, et al 2020, In Vivo Evaluation of Indium-111-Labeled 800CW as a Necrosis-Avid Contrast Agent. Mol Imaging Biol. 22(5):1333-1341. doi:10.1007/s11307-020-01511-x [2] Dijkstra BM, de Jong M, Stroet MCM, et al 2021, Evaluation of Ac-Lys0(IRDye800CW)Tyr3-octreotate as a novel tracer for SSTR2-targeted molecular fluorescence-guided surgery in meningioma. J Neurooncol. doi:10.1007/s11060-021-03739-1

Image/Figure:

https://s3.amazonaws.com/amz.xcdsystem.com/1E8A4501-BB41-A02A-1D3B9882B798BFAA_abstract_File10351/GA147_ImageFigure_0512034634.png

Image/Figure Caption: A: NIR-fluorescence imaging of alive or dead U2OS cells with and without SSTR2-expression, exposed to 800CW-TATE (10 nM in culturing medium). Blocking is performed by co-incubation with DOTA-TATE (10 µM). SSTR2+ = U2OS cells transfected with SSTR2; SSTR2- = wild-type U2OS cells without SSTR2-expression; 800CW-TATE = Ac-Lys0(IRDye800CW)-Tyr3-octreotate; DOTA-TATE = DOTA0-Tyr3-octreotate. B: Consecutive sections of paraffin-embedded NCI-H69 tumor xenografts from mice, tumors resected 4 hours post-injection with either 3 µg 800CW-TATE (top) or 3 mg DOTA-TATE (as a blocking agent from SSTR2) and 3 µg 800CW-TATE (bottom). From left to right are depicted H&E staining, fluorescent cell death staining (TUNEL), NIR-fluorescent signal from 800CW-TATE uptake, and a merging of dead cell staining and NIR-fluorescence.

Full Name of Abstract's 1st Author : Marcus C.M. Stroet

First Name: Marcus

Last Name: Stroet

Email: m.stroet@erasmusmc.nl

Organization: Erasmus MC, Rotterdam, The Netherlands

Country: Netherlands

ID: GA148
Magneto-motive ultrasound imaging of magnetically functionalized gas vesicles

Whee-Soo Kim, California Institute of Technology, wheesoo@caltech.edu

---

Category: New Chemistry, Materials & Probes

Abstract Body : A major goal of molecular imaging is to enable the visualization of specific molecular targets and tissue properties such as stiffness. Among molecular imaging modalities, ultrasound has significant advantages such as a high spatiotemporal resolution, low cost and portability. Recently, gas-filled proteins called gas vesicles (GV) were introduced as a new type of ultrasound contrast agent, which are thermodynamically stable and engineerable at the genetic level, allowing their multiplexed detection, functionalization and use as reporter genes [1, 2]. However, in some circumstances it is challenging to differentiate the ultrasound scattering produced by GVs from tissue background. To enhance the signal specificity of ultrasound, previous work has introduced magneto-motive ultrasound (MMUS) imaging [3, 4], in which magnetic nanoparticles are moved by the applied magnetic field, resulting in unique time-locked ultrasound contrast. However, to produce this contrast, a high concentration of nanoparticles had to be used due to the poor echogenicity of magnetic nanomaterials. In this study, we combine the unique properties of GVs and magnetic nanoparticles to greatly enhance the sensitivity of MMUS and thereby enhance the contrast to noise ratio (CNR) of molecular imaging. Magnetic nanoparticle labeled GVs (MGVs) were constructed using click chemistry, resulting in approximately 186 magnetic nanoparticles attached to each GVs, and the hydrodynamic size was about 800 nm. After constructing the MGVs, MMUS imaging was conducted in hydrogel phantomes, demonstrating a strong signal uniquely produced by MGVs rather than either GVs or MNPs alone. Interestingly, we found that the MMUS signal was stronger in lower stiffness gels than at higher stiffness, which indicated that MGVs could be used as stiffness sensor. To further determine the effects of stiffness, several different concentrations of agarose and Matrigel were used. Lowering the stiffness in both materials led to stronger ultrasound signal. This result indicated that higher surrounding stiffness lowers the MGVs' movement by the magnetic force. We hypothesized that this stiffness dependence could be exploited to visualize biologically driven changes in tissue mechanics. To test this concept, we imaged an organoid model in which stiffness increases when fibrosis occurs. We found that MMUS signal decreased in the fibrosis model while in control organoids the signal was maintained. These results indicate that MGVs are a contrast agent with uniquely advantageous properties for MMUS imaging, which could be used as a tool for diagnostic and therapeutic applications.

References: 1. Lu, G.J., et al., Acoustically modulated magnetic resonance imaging of gas-filled protein nanostructures. Nat Mater, 2018. 17(5): p. 456-463. 2. Bourdeau, R.W., et al., Acoustic reporter genes for noninvasive imaging of microorganisms in mammalian hosts. Nature, 2018. 553(7686): p. 86-90. 3. Mehrmohammadi, M., et al., In vivo pulsed magneto-motive ultrasound imaging using high-performance magnetoactive contrast nanoagents. Nanoscale, 2013. 5(22): p. 11179-86. 4. Mehrmohammadi, M., et al., Pulsed magneto-acoustic imaging. Conf Proc IEEE Eng Med Biol Soc, 2009. 2009: p. 4771-4.

First Name: Whee-Soo

Last Name: Kim

Email: wheesoo@caltech.edu

Organization: California Institute of Technology

Country: United States

ID: GA149

Intraoperative c-Met targeted fluorescent imaging for the detection of lymph node metastases in papillary thyroid cancer

Pascal Jonker, Department of Surgery, University Medical Center Groningen, Groningen, The Netherlands, p.k.c.jonker@umcg.nl

---

Category: Oncology

Abstract Body : Background: Prophylactic central compartment lymph node dissection (CLND) for patients with papillary thyroid cancer (PTC) remains controversial due to its variable risk-benefit ratio. Molecular fluorescence-guided imaging (MFGI) and quantitative spectroscopy can differentiate tumor from normal tissue after intravenous injection of a near-infrared fluorescent (NIRF) tracer and may help to improve detection of true negative nodal compartments in patients with PTC. However, target antigens for NIRF-tracers in PTC are unknown and no study previously reported about the feasibility MFGI and quantitative spectroscopy in PTC management. Objectives: 1) To identify a PTC-specific antigen targeted by a clinical available NIRF-tracer; 2) associate protein overexpression of the selected antigen with PTC tumor characteristics and locoregional recurrence rates 3) assess in vitro selective binding of the selected NIRF-tracer and 3) evaluate safety and efficacy of the selected NIRF-tracer for the first in-human detection of PTC nodal metastases (NM) using MFGI and quantitative spectroscopy. Methods: The highest-ranked overexpressed gene targeted by a clinically available NIRF-tracer1 was selected by class comparison between PTC and normal thyroid tissue using Functional Genomic mRNA profiling2 of publicly available microarray expression data. Target antigen protein expression was quantified using the H-score calculated from a tissue microarray with primary PTC (n=741) and normal thyroid tissue (n=108) that was immunohistochemically stained with 8189S, a c-Met targeting antibody. An H-score ≥ 150 was considered as positive. Staining intensities were correlated with tumor characteristics and ten-year locoregional recurrence free survival (LRFS). Fluorescence microscopy of a c-Met positive PTC (TPC1) and MET negative cell line (T47D) were performed to assess selective binding of the c-Met targeting NIRF-tracer EMI-137. A multicenter phase 1 dose-escalation study (NCT03470259) of patients receiving intravenous EMI-137 prior to surgery was conducted to evaluate 1) safety; 2) optimal dosage for the ex vivo detection of PTC NM using the IVIS Spectrum and IVIS Lumina II; 3) feasibility ex-vivo PTC NM detection with multidiameter single-fiber reflectance and single-fiber fluorescence (MDSFR/SFF) spectroscopy and 4) in vivo selective binding using fluorescence microscopy and immunohistochemical staining with 8189S of PTC NM and normal lymph nodes (NLN). A p-value Results: MET (ranked 11 of 1,702 overexpressed genes) was selected as the most promising antigen and is targeted by the NIRF-tracer EMI-137. A higher c-Met expression was observed in primary PTC compared to normal thyroid tissue (200.0 (IQR 150.0-258.0) versus 68.0 (IQR 20.0-100.0); p Patients with a positive c-Met expression (n=364) of primary PTC were more frequently diagnosed with pT3 or pT4 PTC (40.7% versus 28.3%; p = 0.02), NM (42.4% versus 25.9%; p = 0.005), extrathyroidal extension (38.2% versus 21.7%; p=0.001) and positive BRAFV600E status (73.4% versus 22.5%; p A worse LRFS (81.9% versus 93.2%; p=0.02) was observed in patients with positive

(n=364) versus negative c-Met expression (n=120). In vitro specific binding of EMI-137 to c-MET was confirmed. 19 patients received 0.09 mg/kg (n=3), 0.13 mg/kg (n=10) or 0.18 mg/kg (n=6) EMI-137 intravenously prior to surgery. No adverse events related to EMI-137 administration occurred. 0.13 mg/kg EMI-137 was selected as optimal dosage to differentiate PTC NM from NLN using MFGI (8.2x107 p/sec/cm2/sr [IQR 1.2x108] versus 1.6x107 p/sec/cm2/sr [IQR 3.6x107]; p) and MDSFR/SFF spectroscopy (3.2x10-3 Q.µafaxmm-1 [IQR 1.3x10-3] versus 1.7x10-3 Q.µafaxmm-1 [IQR 7.5x10-4]; p 0001; figure 1C-D). MFGI identified 5/19 levels without nodal metastases, potentially reducing the number of negative prophylactic CLNDs with 26.3%. In vivo selective binding of EMI-137 to c-Met was confirmed in PTC NM. Conclusion: MET is overexpressed in PTC and may identify biologically aggressive variants. Perioperative intravenous administration of EMI-137 is safe and suitable to detect PTC NM with MFGI and quantitative spectroscopy, potentially reducing negative prophylactic CLNDs by a quarter.

References: 1. Zhang RR, Schroeder AB, Grudzinski JJ, et al. Beyond the margins: real-time detection of cancer using targeted fluorophores. Nat Rev Clin Oncol 2017; 13: 653–18. 2. Fehrmann RSN, Karjalainen JM, Krajewska M, et al. Gene expression analysis identifies global gene dosage sensitivity in cancer. Nat Genet 2015; 47: 115–25.

Image/Figure: https://s3.amazonaws.com/amz.xcdsystem.com/1E8A4501-BB41-A02A-1D3B9882B798BFAA_abstract_File10351/GA149_ImageFigure_0512040742.pdf

Image/Figure Caption: Figure 1A provides an overview of fluorescent intensities per dosage cohort of grossed formalin fixed PTC nodal metastases and normal lymph nodes imaged with the IVIS spectrum. Figure 1B shows the fluorescence intensities of PTC nodal metastases and normal lymph nodes of patients in the 0.13 mg/kg dosage cohort imaged using the IVIS Lumina. An overview of the intrinsic fluorescence measured with quantitative spectroscopy in fresh (1C) and formalin fixed (1D) PTC nodal metastases and normal lymph nodes respectively. Abbreviations: CT = connective tissue; NLN = normal lymph node; NM = nodal metastases; PTC = papillary thyroid cancer.

Full Name of Abstract's 1st Author : Pascal Klaas Christiaan Jonker

First Name: Pascal

Last Name: Jonker

Email: p.k.c.jonker@umcg.nl

Organization: Department of Surgery, University Medical Center Groningen, Groningen, The Netherlands

Country: Netherlands

ID: GA150
Pharmacokinetic comparison of two glycosylated tetrazines as radiotracer candidates for pretargeted PET imaging

Tatsiana Auchynnikava, Turku PET Centre, Department of Chemistry, University of Turku, tatauc@utu.fi

---

Category: New Chemistry, Materials & Probes

Abstract Body : Objectives: In vivo chemistry driven by bioorthogonal reactions has attracted considerable attention in the past decade, which has led to an exponential increase in pretargeted positron emission tomography (PET) studies. In turn, tetrazine based in vivo chemistry is a promising direction in pretargeted PET due to its instantaneous reaction rates and versatility.1 However, the success of pretargeted PET, in this case, relies on tetrazine radiolabeling, in which [18F]fluoroglycosylation has demonstrated great potential. It was previously reported that 5-[18F]fluoro-5-deoxyribose ([18F]FDR) conjugated tetrazine oxime ether ([18F]FDR-Tz) exhibits favorable pharmacokinetic properties for pretargeted PET imaging.2 [18F]FDR-Tz was synthesized via oxime formation between an aminooxy functionalized tetrazine and [18F]FDR. 2-[18F]fluoro-2-deoxy-D-glucose ([18F]FDG) is the most widely used radiopharmaceutical for PET imaging and therefore would have better availability as a starting material for the production of [18F]fluorinated tetrazines. Here, were report pharmacokinetic comparison of [18F]FDG and [18F]FDR conjugated tetrazine oxime ethers ([18F]FDG-Tz and [18F]FDR-Tz) in mice. Methods: [18F]FDG-Tz and [18F]FDR-Tz were synthesized as previously reported.2,3 Ex vivo studies for [18F]FDG-Tz and [18F]FDR-Tz were performed in healthy mice (female Balb/cOlaHsd, 9-14 weeks and male Balb/cOlaHsd, 11-12 weeks, respectively). Anesthetized animals (0.4 L/min O2, induction 4-5%, maintenance 1.5-2.5% isoflurane) were sacrificed at 15, 30, and 60 min, respectively, after intravenous tracer administration. The number of animals per time point varied from 2 to 4 (15 min n=3/3, 30 min n=4/4, 60 min n=2/3, [18F]FDG-Tz / [18F]FDR-Tz). Glucose transporter 1 (GLUT1) binding affinities of FDG-Tz and FDR-Tz were determined as described previously.4 Results: [18F]FDR-Tz showed higher uptake in blood, heart, spleen, lungs, and skeletal muscle than [18F]FDG-Tz at 15 min post-injection. In the blood and heart, [18F]FDR-Tz exhibited almost 2 times higher radioactivity concentration than [18F]FDG-Tz, the average %ID/g in blood being 5.9 vs 2.9 and in the heart being 2.9 vs 1.6. These differences are statistically significant (P Half-maximal inhibitory concentration IC50 for FDG-Tz was 324.4 μM and for FDR-Tz was 22.4 μM. Higher GLUT1 affinity for FDR-Tz correlates with higher observed binding of radiolabeled tracer in organs with high GLUT1 expression. Conclusions: We can conclude, that from the two investigated 18F-labeled glycosylated tetrazines, the [18F]FDR conjugated candidate exhibited higher binding in the blood and heart, which can be explained by its higher affinity to GLUT1 transporter.

References: 1. Stéen EJL, Jørgensen JT, Denk C, et al. Lipophilicity and Click Reactivity Determine the Performance of Bioorthogonal Tetrazine Tools in Pretargeted in Vivo Chemistry. ACS Pharmacology and Translational Science. 2021;4:824-833. 2. Keinänen O, Li XG, Chenna NK, et al. A New Highly Reactive and Low Lipophilicity Fluorine-18 Labeled Tetrazine

Derivative for Pretargeted PET Imaging. ACS Medicinal Chemistry Letters. 2016;7:62-66. 3. Keinänen O, Partelová D, Alanen O, Antopolsky M, Sarparanta M, Airaksinen AJ. Efficient cartridge purification for producing high molar activity 18F-glycoconjugates via oxime formation. Nuclear Medicine and Biology. 2018;67:27-35. 4. Matović J, Järvinen J, Sokka IK, et al. Exploring the Biochemical Foundations of a Successful GLUT1-Targeting Strategy to BNCT: Chemical Synthesis and in Vitro Evaluation of the Entire Positional Isomer Library of ortho-Carboranylmethyl-Bearing Glucoconjugates. Molecular Pharmaceutics. 2021;18(1):285-304.

Image/Figure:

https://s3.amazonaws.com/amz.xcdsystem.com/1E8A4501-BB41-A02A-1D3B9882B798BFAA_abstract_File10351/GA150_ImageFigure_0512041157.png

Image/Figure Caption: Figure 1. Ex vivo biodistribution of [18F]FDG-Tz and [18F]FDR-Tz in mice 15 min post-injection; time activity curves for up to 60 min post-injection and chemical structures of [18F]FDG-Tz and [18F]FDR-Tz.

Full Name of Abstract's 1st Author : Tatsiana Auchynnikava

First Name: Tatsiana

Last Name: Auchynnikava

Email: tatauc@utu.fi

Organization: Turku PET Centre, Department of Chemistry, University of Turku

Country: Finland

ID: GA151
Non-invasive and Simultaneous Temperature and Viscosity Estimation in Magnetic Particle Imaging via Relaxation Characterization of Iron Oxide Nanoparticles

Mustafa Utkur, Bilkent University, mustafa.utkur@bilkent.edu.tr

---

Category: Instrumentation

Abstract Body : Introduction: Magnetic Particle Imaging (MPI) is a tracer-based molecular imaging modality with applications such as angiography [1], cancer imaging [2], and catheter steering for cardiovascular interventions [3]. The superparamagnetic iron oxide nanoparticle (SPION) tracers suffer from relaxation effects that deteriorate their MPI signal response. On the other hand, by exploiting these relaxation effects, MPI's capability can be extended to detect functional parameters such as viscosity [4], [5] or temperature [6], [7]. Exiting techniques for temperature measurements during magnetic fluid hyperthermia (MFH) rely on invasive discrete temperature probes [8]. MPI, on the other hand, is noninvasive, compatible with MFH, and can further enable focused application of MFH in vivo [9]. A hybrid MPI-MFH configuration has the potential to enable cancer imaging, while substantially increasing the efficacy of thermal therapy via real-time temperature mapping. To map the temperature in vivo, however, the viscosity levels must be also taken into account due to the confounding effects of the two parameters on the MPI signal [10]. This work demonstrates proof-of-concept experiments of simultaneous estimation of temperature and viscosity in MPI. Experimental results for temperatures between 25-45°C and viscosities between 0.9-3.6 mPa·s show that our novel relaxation-based MPI technique can enable the simultaneous estimation of these two parameters. Materials and Methods: A total of 20 samples of a commercially available SPION (Perimag, Micromod GmbH) were prepared using water/glycerol mixtures and divided into four groups. For each group, a fixed viscosity level could be achieved at 5 different temperatures. An in-house magnetic particle spectrometer setup was used to acquire SPION responses under 60 different drive (i.e., excitation) field amplitude-frequency pairs ranging between 5-25 mT and 1-7 kHz for all 20 samples. The time-domain SPION responses were analyzed using our novel technique to estimate the effective relaxation time constant at each drive field amplitude-frequency pair. The estimated relaxation time constants were normalized by the period of the drive field at each frequency. This enables a fair comparison of the relaxation effect on the time-domain SPION responses at different frequencies. Results: The percentage changes in the normalized time constants with respect to 1°C change in temperature and 1 mPa·s change in viscosity are shown in Fig.1. These plots demonstrate the sensitivity of MPI for temperature and viscosity estimation at different drive field settings. The sensitivity for temperature estimations in Fig.1.A show a relatively mild change with respective to frequency and amplitude, with higher sensitivities seen at higher field amplitudes. The sensitivity for viscosity estimations in Fig.1.B, on the other hand, show a dramatic change with respective to frequency, with the highest sensitivity observed at relatively low frequencies of around 1-2 kHz. At around 3-4 kHz, the sensitivity for viscosity estimations rapidly falls down and flattens out, making it possible to directly estimate the temperature at those frequencies, preferably using high field amplitudes. Therefore, by

performing two measurements at two different drive field parameters (e.g., at a fixed field amplitude of 20 mT and at two different frequencies of 1 kHz and 4 kHz), both the viscosity and the temperature information of the environment can be simultaneously estimated. Conclusions: The benefits of simultaneously mapping temperature and viscosity make MPI a very promising modality for cancer imaging and treatment monitoring in combination with therapeutic hyperthermia. The novel relaxation-based MPI technique presented in this work utilizes the time-domain SPION signal and can be directly extended to estimate temperature and viscosity for multi-dimensional imaging in MPI.

References: [1] J. Weizenecker, B. Gleich, J. Rahmer, H. Dahnke, and J. Borgert, "Three-dimensional real-time in vivo magnetic particle imaging.," Physics in medicine and biology, vol. 54, no. 5. England, pp. L1–L10, Mar-2009. [2] E. Yu et al., "First Murine in vivo Cancer Imaging with MPI," in 6th International Workshop on Magnetic Particle Imaging (IWMPI), 2016, p. 148. [3] J. Haegele et al., "Magnetic particle imaging: visualization of instruments for cardiovascular intervention.," Radiology, vol. 265, no. 3, pp. 933–938, Dec. 2012. [4] M. Möddel, C. Meins, J. Dieckhoff, and T. Knopp, "Viscosity quantification using multi-contrast magnetic particle imaging," New J. Phys., vol. 20, no. 8, p. 083001, Aug. 2018. [5] M. Utkur, Y. Muslu, and E. Saritas, "Relaxation-based color magnetic particle imaging for viscosity mapping," Appl. Phys. Lett., vol. 115, no. 15, Oct. 2019. [6] J. B. Weaver, A. M. Rauwerdink, and E. W. Hansen, "Magnetic nanoparticle temperature estimation," Med. Phys., vol. 36, no. 5, pp. 1822–1829, May 2009. [7] C. Stehning, B. Gleich, and J. Rahmer, "Simultaneous magnetic particle imaging (MPI) and temperature mapping using multi-color MPI," Int. J. Magn. Part. Imaging, vol. 2, no. 2, Dec. 2016. [8] G. F. Baronzio and E. D. Hager, Hyperthermia in Cancer Treatment: A Primer. Springer, Lander Bioscience, 2006. [9] Z. W. Tay et al., "Magnetic Particle Imaging-Guided Heating in Vivo Using Gradient Fields for Arbitrary Localization of Magnetic Hyperthermia Therapy," ACS Nano, vol. 12, no. 4, pp. 3699–3713, Apr. 2018. [10] M. Utkur, Y. Muslu, and E. U. Saritas, "Confounding Effects of Temperature and Viscosity Towards Relaxation Mapping," in 9th International Workshop on Magnetic Particle Imaging (IWMPI), 2019, p. 1.

Image/Figure:

https://s3.amazonaws.com/amz.xcdsystem.com/1E8A4501-BB41-A02A-1D3B9882B798BFAA_abstract_File10351/GA151_ImageFigure_0512041645.png

Image/Figure Caption: The temperature (top row, A) and viscosity (bottom row, B) sensitivity plots, showing the percentage change in the normalized time constants with respect to 1°C change in temperature (A) and 1 mPa□s change in viscosity (B). The results are shown for the drive field frequencies ranging between 1-7 kHz with 1 kHz increments, and field amplitudes ranging between 5-25 mT with 2.5 mT increments. Each subplot in (A) corresponds to a distinct viscosity levels (left to right: 0.9 mPa·s, 1.8 mPa·s, 2.7 mPa·s, and 3.6 mPa·s), and each subplot in (B) corresponds to a distinct temperature (left to right: 25°C, 30°C, 35°C, 40°C, and 45°C). The normalized time constants with respect to viscosity show the highest slope (i.e., highest sensitivity) at lower frequencies of around 1-2 kHz, and falling down to almost zero beyond 3-4 kHz. According to the temperature plots, on the other hand, the highest sensitivity is achieved at lower frequencies and higher field amplitudes. As a result, due to the different trends in these

sensitivity plots, the temperature and viscosity levels can be simultaneously estimated by performing two measurements at different drive field parameters.

First Name: Mustafa

Last Name: Utkur

Email: mustafa.utkur@bilkent.edu.tr

Organization: Bilkent University

Country: Turkey

ID: GA152
In Vivo Imaging of Allografted Glial-Restricted Progenitor Cell Survival and Hydrogel Scaffold Biodegradation

Shreyas Kuddannaya, Cellular Imaging Section, Institute for Cell Engineering and Russell H. Morgan Department of Radiology and Radiological Science, Johns Hopkins University School of Medicine, Baltimore, MD, USA, shreyas10@jhu.edu

---

Category: Bioengineering, Synthetic Biology and Basic Biology

Abstract Body : Background: Neuroregenerative cell therapies of the central nervous system are hampered by high initial cell death and a host anti-graft immune response due to which >90% of transplanted cells can be lost within 1 week of transplantation1,2. We hypothesized that scaffolding cells in composite hyaluronic acid (HA)-based hydrogels of tunable mechanical strengths can significantly improve transplanted cell survival as evidenced by serial in vivo bioluminescence imaging (BLI). Concurrently we aim to quantitatively and directly assess hydrogel degradation post transplantation via chemical exchange saturation transfer (CEST) MRI by virtue of abundant high amide protons of the gelatin component of the hydrogels without necessitating any exogeneous labels. Methods: Allogeneic (mouse) GRPs (mGRPs) carrying proteolipid protein-green fluorescent protein (PLP-GFP) and transduced with a lentiviral vector carrying firefly luciferase (pLenti4-CMV-Luc) genes were derived from fetal forebrain tissue of (E13) transgenic mice. Composite hydrogels were formulated by mixing thiolated HA (HA-S), thiolated gelatin (Gel-S) and poly (ethylene glycol) diacrylate (PEGDA) crosslinker in a ratio of 2:2:1 at various concentrations and their rheological properties were tested. Based on optimal hydrogel stiffness, injectability and high cell viability, a 10 mg/ml formulation was chosen and 2x105 mGRPs were transplanted intracerebrally with/without hydrogel scaffolding into immunocompetent BALB/c mice brain striatum (Fig.1a). MRI was performed using a 11.7T horizontal bore Bruker Avance scanner equipped with a 15 mm birdcage transmit/receive coil and a rapid acquisition and relaxation enhancement (RARE) pulse sequence. Imaging parameters were: slice thickness=1.5 mm, averages= 2, echo time=19 ms, repetition time= 1500 ms, matrix dimensions=128x128, field of view (FOV)=17x17 mm2 and RARE factor=16. For CEST imaging, a saturation power of B1 = 3.6 μT was used with -5.5 to 5.5 ppm offset range. MTRasym values were derived from fixed regions of interest (ROI) using MATLAB. Results: The survival of scaffolded vs. naked mGRPs transplanted in brain striatum was serially assessed by BLI up until 32 days post injection (Fig.1b). The BLI signal gradually decreased over 32 days in both groups, but the decrease was significantly higher in the saline group post-day 7 (p Conclusion: We demonstrated that hydrogel morphology and biodegradation can be concurrently monitored in vivo with T2-w MRI and CEST MRI respectively, with the hydrogel acting as a barrier for infiltrating host immune cells. In parallel, serial in vivo BLI revealed a 4.5-fold enhancement in the survival of transplanted Luc+ allogeneic mGRPs in immunocompetent mice brain.

References: 1. Marquardt, L. M.; Heilshorn, S. C., Design of Injectable Materials to Improve Stem Cell Transplantation. Curr Stem Cell Rep 2016, 2, 207-220. 2. Kim, H.; Walczak, P.; Muja,

N.; Campanelli, J. T.; Bulte, J. W., ICV-transplanted Human Glial Precursor Cells are Short-lived Yet Exert Immunomodulatory Effects in Mice with EAE. Glia 2012, 60, 1117-1129

Image/Figure:

https://s3.amazonaws.com/amz.xcdsystem.com/1E8A4501-BB41-A02A-1D3B9882B798BFAA_abstract_File10351/GA152_ImageFigure_0512043844.png

Image/Figure Caption: Figure 1: (a) Scheme of transplantation of scaffolded Luc+ mGRPs in mouse brain striatum (b) Representative serial BLI images and (c) quantification of 2x105 mGRPs with and without scaffolding in 10 mg/ml hydrogel transplanted in the brain striatum region of immunocompetent BALB/c mice (n=8). (d) Cell numbers at endpoint as calculated from BLI intensity readouts. (e) Percentage cells of day 0 surviving at day 32 as calculated from BLI intensity. (f) T2-w (top) and CEST MR (bottom) maps of immunocompetent BALB/c mouse brain transplanted with either scaffolded or unscaffolded (saline control) mGRPs in the right striatum. Yellow and black arrows indicate T2 hyperintense region and CEST contrast at the cell transplant region. (g) MTRasym spectra and (h) Normalized CEST contrast at 3.6 ppm on the transplant site (black arrows) at different time points until day 32. *p < 0 .05.

Full Name of Abstract's 1st Author : Shreyas Kuddannaya

First Name: Shreyas

Last Name: Kuddannaya

Email: shreyas10@jhu.edu

Organization: Cellular Imaging Section, Institute for Cell Engineering and Russell H. Morgan Department of Radiology and Radiological Science, Johns Hopkins University School of Medicine, Baltimore, MD, USA

Country: United States

ID: GA153
Tracking FLASH Radiotherapy Oxygen Dynamics In Vivo

Brian Pogue, Dartmouth College, brian.w.pogue@dartmouth.edu

Category: Oncology

Abstract Body : Delivery of radiation at ultrahigh dose rates has become known as FLASH radiotherapy, and this technique has recently been shown to preferentially spare normal tissues from radiation damage, while preserving as compared to tumor tissue. However, the underlying mechanisms of this phenomenon remain unclear at this time, but perhaps the most widely proposed hypothesis about the biological origin is that the effect stems from substantial oxygen depletion during the FLASH radiation pulse. This oxygen depletion would reduce the radiochemical damage during irradiation becuase the presence of oxygen is well known to fix and enhance radiation damage. This is particularly important in normal tissues, as they are highly oxygenated, and so the reduction in normal tissue damage is thought to be from this depletion process. The radiation responses tumor tissue is largely unchanged in FLASH, presumably due to the fact that the tissue is already nearly hypoxic. Testing of this hypothesis was teh goal of this work, by direct measurement of tissue oxygen in vivo during and after FLASH irradiation. Oxygen measurements were performed in vitro and in vivo using the phosphorescence quenching method and a water-soluble molecular probe Oxyphor 2P. Lifetime fitting of the phosphorescnece emission provides a direct prediction of the in situ oxygen level. The changes in oxygen per unit dose (g-values) were quantified in response to irradiation by 10 MeV electron beam with both ultra-high dose rates of 300 Gy/sec or with conventional radiation therapy rates of 0.1 Gy/sec. In vitro experiments with 5% BSA acqueous solutions resulted in g-values for oxygen consumption of 0.19-0.21 mmHg/Gy (0.34-0.37 mM/Gy) for conventional irradiation and 0.16-0.17 mmHg/Gy (0.28-0.30 mM/Gy) for UHDR irradiation. In vivo, the total decrease in oxygen after a single fraction of 20 Gy FLASH irradiation was 2.3±0.3 mmHg in normal tissue and 1.0±0.2 mmHg in tumor tissue (p-value These molecular imaging observations suggest that oxygen depletion to radio-biologically relevant levels of hypoxia is unlikely to occur under FLASH irradiation, despite this being the leading hypothesis for the protective effect of FLASH. FLASH irradiation appears to induce less total oxygen consumption than conventional irradiation in vitro, which may be related to the FLASH sparing effect. This latter discovery was not expected but could agree with radical-mediated oxygen depletion effects. The difference in oxygen depletion between FLASH and conventional irradiation was not quantified in vivo, because measurements of oxygen depletion under conventional irradiation are hampered by the continuous resupply of oxygen from the blood.

References: X Cao, R Zhang, TV Esipova, SR Allu, Petr Bruza 4, PJ Hoopes, SA Vinogradov, BW Pogue, Quantification of oxygen depletion during FLASH irradiation in vitro and in vivo, Int J Radiat Oncol Biol Phys 2021 Apr 9;S0360-3016(21)00358-8. doi: 10.1016/j.ijrobp.2021.03.056.

Image/Figure:

https://s3.amazonaws.com/amz.xcdsystem.com/1E8A4501-BB41-A02A-1D3B9882B798BFAA_abstract_File10351/GA153_ImageFigure_0512044326.png

Image/Figure Caption: Oxygen measurements in vivo. Oxygen transients in normal tissue upon application of FLASH (a) and conventional radiation (b). Oxygen transients in tumors upon application of FLASH (c) and conventional radiation (d). (e) Quantification of oxygen depletion in normal tissues and tumors upon FLASH irradiation (20 Gy). Statistical analysis was performed using two-sample student's t-test, for n = 6.

First Name: Brian

Last Name: Pogue

Email: brian.w.pogue@dartmouth.edu

Organization: Dartmouth College

Country: United States

ID: GA154
In vivo evaluation of Cerenkov radiation excited ultrasmall downconverting nanoparticles for cancer imaging.

Qize Zhang, Memorial Sloan Kettering Cancer Center, zhangq@mskcc.org

---

Category: New Chemistry, Materials & Probes

Abstract Body : Lanthanide nanoparticles always exhibit excellent fluorescent properties which have been widely used as probes or sensors in biomedical engineering[1]. Among the various known probes, europium oxide exhibiting strength luminescence that can be excited with Cerenkov light, are advantageous over other lanthanide oxides nanoparticles[2]. In our work, a square-shaped ultra-small Europium nanoparticle (uEuNP) was synthesized through thermal hydrolysis of the precursor Europium(III) acetate. Next, we radiolabeled the uEuNP with FDA-approved PET tracer 89Zr and injected it into health mice for biodistribution behavior evaluation. After 48h, significantly reduced uptake was observed both in the liver and spleen, which could be attributed to the nanoparticles' hepatic clearance based on its ultra-small size. To further verify the cytotoxicity of the uEuNP, three different cell lines CT26, KCL22, and HS578 were exposed to different concentrations of uEuNP. Up to 24h, there is no major cytotoxicity observed through variety concentration. To investigate the effectiveness of the uEuNP as an enhanced Cerenkov light agent for tumor imaging in vivo, we tested it on a CT26 subcutaneous tumor mice model. The result revealed the tumor site successfully lit up by the Cerenkov excited nanoparticle. Impressively, under the 620 nm light filter (emission of Eu2O3), we observed significantly reduced liver signal comparison with the tumor signal. This unusual event of signal quenching on the liver was further elucidated and could help to prove the ultra-small Europium oxide nanoparticle as an excellent molecular imaging agent for clinic translation in the future.

References: [1]D'Aléo, A., et al., Charge transfer excited states sensitization of lanthanide emitting from the visible to the near-infra-red. Coordination Chemistry Reviews, 2012. 256(15): p. 1604-1620. [2]Dong, H., et al., Lanthanide Nanoparticles: From Design toward Bioimaging and Therapy. Chemical Reviews, 2015. 115(19): p. 10725-10815.

Image/Figure:

https://s3.amazonaws.com/amz.xcdsystem.com/1E8A4501-BB41-A02A-1D3B9882B798BFAA_abstract_File10351/GA154_ImageFigure_0512052155.png

Image/Figure Caption: a-b) 48h Cerenkov imaging post-injection under open and 620nm filter b-c) 48h ex-vivo organ imaging under open and 620 nm filter. e) 48h Tumor site ROI measurement spectrum vs regular Cerenkov spectrum, normalized.

First Name: Qize

Last Name: Zhang

Email: zhangq@mskcc.org

Organization: Memorial Sloan Kettering Cancer Center

Country: United States

ID: GA156
Comparison of cRGDfK Peptide Probes with Appended Shielded Heptamethine Cyanine Dye (s775z) for Near Infrared Fluorescence Imaging of Cancer

Rananjaya Gamage, University of Notre Dame, rgamage@nd.edu

Category: Oncology

Abstract Body : Recently our lab introduced a sterically shielded heptamethine cyanine dye 775c (previously called s775z) that has no propensity for aggregation and highly photostable and showed that cyclic-RGD (Arg-Gly-Asp) bioconjugation using standard amide bond chemistry (775cRGD) selectively target integrin receptors for tumor accumulation in a A549 lung adenocarcinoma tumor-bearing mouse model.1As the tumor-targeting is mediated by the interaction of the targeting ligand and the macromolecular target, it is critical to assure minimum interference from cyanine conjugation for favorable binding affinity. In this study, the conjugation scope of 775c to cyclic-RGD has been extended using different linker chemistries to demonstrate effective non-invasive bioconjugation and compare targeted cancer imaging performance. Reactive duos 775mRGD and 775aRGD were developed using maleimide-thiol coupling and strain promoted azide-alkyne cycloaddition chemistries respectively. Spectroscopy data obtained in phosphate-buffered saline (pH 7.4) for 775cRGD, 775mRGD and 775aRGD at room temperature show similar photophysical properties and no aggregation. Non-specific protein binding analysis using a series of dye/bovine serum albumin associations found a Ka value of 2.7 x 104M-1 for 775c which increased to 4.0 - 7.0 x 104M-1 upon cyclic RGD conjugation. This is about 20-40-fold lower serum albumin association compared to FDA-approved heptamethine cyanine analog, Indocyanine Green. Cell cytotoxicity studies using four different cancer cell lines (A549 lung adenocarcinoma, U87 human glioblastoma, HT1080 human fibro carcinoma, and CHO-K1 Chinese hamster ovary) showed no significant descend in cell viability for each peptide conjugate at low micromolar concentrations common for biological imaging studies. For cellular uptake studies, A549 lung adenocarcinoma cells which were previously reported for αvβ5-type integrin overexpression was exploited.2 A comparative set of fluorescence microscopy studies incubated separate A549 cell samples with each peptide conjugate of 775c for one hour and observed similar cellular uptake. In each case, targeted probe uptake was successfully blocked by pre-incubating the cells with free cyclic RGD peptide that indicates integrin selective binding and endocytosis. For in-vivo studies, an innovative paired-agent imaging strategy was followed where a binary mixture of targeted peptide and passively accumulating control fluorophore was injected into a single A549 subcutaneous tumor-bearing mouse model. A retro-orbital injection of each targeted peptide conjugate and the control (pentamethine cyanine dye 650c without cyclic RGD peptide, 10nmol of each probe) was given to nude mice (N=5) bearing a tumor in the right rear flank and imaged periodically over three hours. All three peptide conjugates showed high tumor-to-background ratios and slower washouts compared to the transient uptake of the control fluorophore over three hours suggesting integrin selective tumor accumulation. Ex-vivo tumor spheroid analysis revealed a heterogenic binding potential for each peptide conjugate and a significantly higher tumor accumulation of 775cRGD than remaining duo given to its inheritably strong amide bond nature. Subsequent

biodistribution analysis of excised major mouse organs strongly indicated low background tissue retention and promoted renal clearance of the peptide conjugates at three hours indicating effective excretion of the fluorophores. These results strongly suggest effective cyclic RGD bioconjugation of 775c using three highly utilized linker chemistries, superior tumor targeting for diagnosis, and potential applications for cancer fluorescence-guided surgery.

References: 1. Li et al. Angw. Chem. Int. Ed. 2020, 59, 12154-12161 2. Shaw et al. Bioorg. Med. Chem. 2018, 26, 2085-2091

First Name: Rananjaya

Last Name: Gamage

Email: rgamage@nd.edu

Organization: University of Notre Dame

Country: United States

ID: GA157
A dual wavelength fluorescence probe for monitoring active Aβ plaques in Alzheimer's brain

Biyue Zhu, Massachusetts General Hospital, 413897689@qq.com

Category: Neuroscience

Abstract Body : Alzheimer's disease (AD) is a neurodegenerative disorder that closely associated with high concentrations of reactive oxygen species (ROS) in the brain. However, a powerful tool to monitor cerebral ROS concentration is not at hand. Previously, we have reported CRANAD-61, a fluorescence probe for detecting cerebral ROS at micro- and macro levels in brains of AD mice. However, the short emission wavelength (570 nm) of CRANAD-61 after ROS reaction hampers it's in vivo applications due to limited penetration depth and background interference. In the present study, we designed, synthesized and characterized an oxalate-curcumin-based probe CRANAD-122 that enables noninvasive dual wavelength near-infrared fluorescence (NIRF) imaging in vivo. CRANAD-122 showed an emission wavelength at 740 nm and 620 nm before and after reacting with ROS, which enables in vivo ratiometric quantification of cerebral ROS from the near-infrared dual-imaging channels. Real-time in vivo imaging studies with CRANAD-122 showed with higher signal ratio of short wavelength to long wavelength of transgenic mice compared with wild-type mice within 180 min, indicating fast brain uptake and excellent ROS-responsive capability of CRANAD-122. In summary, CRANAD-122 is a fast responsive, BBB-permeable, dual-wavelength imaging probe that could provide a simple, fast and effective tool to noninvasively monitor ROS levels in AD brains.

References: 1. Perry G, Cash AD, Smith MA. Alzheimer disease and oxidative stress. J Biomed Biotechnol. 2002;2:120–123. 2. Meyer-Luehmann M, et al. Rapid appearance and local toxicity of amyloid-beta plaques in a mouse model of Alzheimer's disease. Nature. 2008;451:720–724. 3.Xie H, et al. Rapid cell death is preceded by amyloid plaque-mediated oxidative stress. Proc Natl Acad Sci USA. 2013;110:7904–7909. 4. Yang J, Zhang X, Yuan P, et al. Oxalate-curcumin–based probe for micro-and macroimaging of reactive oxygen species in Alzheimer's disease. Proc Natl Acad Sci USA, 2017, 114(47): 12384-12389. 5. Hong G, Antaris A L, Dai H. Near-infrared fluorophores for biomedical imaging. Nat. Biomed. Eng., 2017, 1(1): 1-22.

Image/Figure:

https://s3.amazonaws.com/amz.xcdsystem.com/1E8A4501-BB41-A02A-1D3B9882B798BFAA_abstract_File10351/GA157_ImageFigure_0923090529.png

Image/Figure Caption: Figure 1. In vivo two-photon imaging with CRANAD-123 to identify active plaques and CAAs. a-c) Representative images of plaques and CAAs labelled by CRANAD-123 from red channel (a) and green channel (b) and merged image (c). Arrowhead indicates inactive plaques, in which red signals are dominated, while the yellow spots are active plaques, in which red and green signals both exist. d) quantification of plaques and CAAs

through the ratio of intensities from red/green channels. It is clear that two distinct groups of plaques, and lower group is the active plaque group. While CAAs has no apparent separation. c-g) Representative images of CAAs labelled by CRANAD-123 from red channel (e) and green channel (f) and merged image (g). Arrowhead indicates inactive CAAss, in which red signals are dominated. Arrow indicates active CAAs, in which the merged red/green into yellow color can be seen. h) quantification of CAAs through the ratio of intensities from red/green channels. It is clear that two distinct groups of CAAs, and lower ratio group is the active CAA group.

Full Name of Abstract's 1st Author : Biyue Zhu

First Name: Biyue

Last Name: Zhu

Email: 413897689@qq.com

Organization: Massachusetts General Hospital

Country: United States

ID: GA158
Image-Guided Ultrasound-Activated Drug Delivery in the GI Tract Using Gas Vesicle Microgels

Maria Paulene Abundo, California Institute of Technology, paulene@caltech.edu

---

Category: New Chemistry, Materials & Probes

Abstract Body : Oral administration is unequivocally the most accessible mode of drug delivery, requiring minimal expertise and invasiveness. However, this route is unable to accommodate the delivery of most biological therapeutics such as antibodies and peptides. In addition, it is challenging to target oral delivery to specific segments of the gastrointestinal (GI) tract, for example to treat inflammation or cancerous lesions. Existing approaches to enable this via the protection, imaging and targeting of the payload following intake are lacking in translational value as they compromise on the convenient formulation and dosing of ingestible drugs. Here, we will present a platform that leverages the simple addition of protein nanoparticles called gas vesicles (GVs) to equip oral drug delivery vehicles with in vivo tracking and release capabilities to safely transport biomolecular cargo. This is possible because GVs function simultaneously as in vivo ultrasound contrast agents1–3 and steric blockers of molecular diffusion that can be ultrasonically "erased" to trigger a rapid outflow diffusion of the payload from within the material (Fig. 1). We demonstrate the utility of this approach in releasing protein therapeutic payloads in the GI tract of rodent models of experimental colitis. This platform has the potential to modernize existing oral drug delivery systems by enabling the convenient transportation of potent small molecules, biologics or gene therapy treatments to specific anatomical locations in complex tissues such as the gastrointestinal (GI) tract.

References: 1. Bourdeau, R. W. et al. Acoustic reporter genes for noninvasive imaging of microorganisms in mammalian hosts. Nature 553, 86–90 (2018). 2. Farhadi, A. et al. Recombinantly expressed gas vesicles as nanoscale contrast agents for ultrasound and hyperpolarized MRI. AIChE J. 64, 2927–2933 (2018). 3. Farhadi, A., Ho, G. H., Sawyer, D. P., Bourdeau, R. W. & Shapiro, M. G. Ultrasound imaging of gene expression in mammalian cells. Science 365, 1469–1475 (2019).

Image/Figure:

https://s3.amazonaws.com/amz.xcdsystem.com/1E8A4501-BB41-A02A-1D3B9882B798BFAA_abstract_File10351/GA158_ImageFigure_0512062928.png

Image/Figure Caption: Figure 1 | Gas vesicles as diffusion steric blockers and in vivo contrast agents. Illustration depicting GVs as diffusion steric blockers to hinder transport of internally embedded payload. Upon ultrasound application, GVs are shown to collapse and liberate excluded volume within the gel, triggering the rapid outflow diffusion of payload.

First Name: Maria Paulene

Last Name: Abundo

Email: paulene@caltech.edu

Organization: California Institute of Technology

Country: United States

ID: GA159
Copper-64 Labeled Metallophore for Targeted PET Imaging of Pathogenic and Probiotic Bacteria in vivo

Nabil Siddiqui, University of Cincinnati, siddiqnb@mail.uc.edu

---

Category: New Chemistry, Materials & Probes

Abstract Body : There is an emerging need to accurately identify both infectious and noninfectious bacteria noninvasively in the body to achieve multiple biomedical objectives. This can be challenging given the current lack of clinically available probes that can reliably distinguish bacteria from mammalian cells. Thus, a comprehensive understanding of bacterial physiology and genetics is required to develop probes for targeted imaging. Since bacteria are evolutionarily and phylogenetically distinct from mammalian cells, fundamental differences in metabolism and cellular structures can be leveraged to develop bacteria-specific imaging agents. Metal transport is a distinct pathway in bacteria that can be exploited to develop specific probes. For instance, Escherichia coli UTI89 utilizes the metallophore, yersiniabactin (YbT) to sequester Cu (II) from the extracellular environment and transport it inside specifically through the outer membrane protein receptor, FyuA (ferric yersiniabactin uptake A)1. We hypothesized that 64Cu-labeled YbT can facilitate targeted positron emission tomography (PET) imaging of FyuA-expressing bacteria in vivo. To optimize the radiolabeling process, we labeled YbT with four different transition radiometals – 55Co, 64Cu, 68Ga, and 89Zr – in various physicochemical conditions. High performance liquid chromatography analysis revealed highest complexation of YbT with 64Cu. The presence of a single well-defined radio-peak with >95% purity at pH 7 and 37°C (Figure 1A) motivated us to choose these conditions for our probe preparation. For in vitro stability assessment, we incubated the probe in mouse serum for 0, 0.5, 1, 2, and 4 hrs, and confirmed the presence of at least 60% of intact 64Cu-YbT 4 hrs after the initial incubation (Figure 1B). When we administered 64Cu-YbT intravenously (i.v.) in mouse models harboring bacteria in their hind limb muscles, we observed distinctly higher PET signals from muscles infected with FyuA-expressing bacteria: E. coli UTI89, E. coli Nissle wild-type (WT) and Klebsiella pneumoniae compared to those infected with negative control bacteria: Staphylococcus aureus and FyuA-knockout mutant E. coli Nissle (ΔfyuA) (Figures 1, C – E). We then proceeded to investigate whether 64Cu-YbT can be used to monitor antibiotic treatment outcomes. We administered 64Cu-YbT i.v. in mice following intramuscular injection of E. coli UTI89 and K. pneumoniae. Bioluminescence imaging of luciferase-expressing E. coli UTI89 indicated reduction in bacterial burden, while PET imaging revealed a corresponding reduction in signal intensity in mice that received two oral doses of ciprofloxacin, compared to untreated mice (Figures 1, F and G). Finally, we aimed to track FyuA-expressing bacteria in diverse, yet clinically relevant in vivo environments. We used 64Cu-YbT to selectively locate K. pneumoniae in the lungs of mice that received intranasal administration of bacteria (Figure 1H). P. aeruginosa, which can also infect the lungs as an opportunistic pathogen but does not encode the FyuA transporter, served as the negative control for the study (Figure 1I). Furthermore, 64Cu-YbT allowed us to specifically identify probiotic E. coli Nissle, which is a popular bacterial template for various bioengineering applications, in two distinct hypoxic

microenvironments – subcutaneous 4T1 tumor and ischemic heart (Figures 1, J-M). For both models, we first performed i.v. administration of E. coli Nissle or PBS and rested the mice for three days for the bacteria to localize and proliferate in the respective hypoxic cores. Subsequent administration of 64Cu-YbT i.v. yielded significant PET signals only in mouse models that received E. coli Nissle. In conclusion, we have validated that 64Cu-YbT, a metal-metallophore complex, can be prepared with high purity and stability under physiological conditions within an hour. We have demonstrated how this single PET probe can potentially be used to identify specific bacterial populations, monitor antibiotic treatment outcomes, and track pathogenic and probiotic bacteria in diverse niches in vivo.

References: Koh, EI., Robinson, A., Bandara, N. et al. Copper import in Escherichia coli by the yersiniabactin metallophore system. Nat Chem Biol 13, 1016–1021 (2017).

Image/Figure: https://s3.amazonaws.com/amz.xcdsystem.com/1E8A4501-BB41-A02A-1D3B9882B798BFAA_abstract_File10351/GA159_ImageFigure_0512071208.docx

Image/Figure Caption: Figure 1. 64Cu-YbT specifically identifies FyuA-expressing bacteria in vivo. (A) Radio-chromatogram and (B) serum stability of 64Cu-YbT at various time-points after incubation. PET/CT images of infectious mouse myositis models harboring (C) S. aureus and E. coli UTI89 (D) E. coli Nissle wild-type (WT) and E. coli Nissle FyuA-knockout mutant (ΔfyuA) (E) S. aureus and K. pneumoniae. Bioluminescence followed by PET/CT images of ciprofloxacin (F) untreated and (G) treated mice infected with bacteria – red arrows indicate K. pneumoniae and blue arrows indicate E. coli UTI89 injection sites. PET/CT images of mice with intranasal administration (sites indicated by yellow arrows) of (H) K. pneumoniae and (I) P. aeruginosa. PET/CT images of mice with subcutaneously developed 4T1 tumors (J) without and (K) with E. coli Nissle administration. PET/CT images of mice with ischemic hearts (L) without and (M) with E. coli Nissle administration. All images were taken 24 hrs post-administration of 64Cu-YbT.

Full Name of Abstract's 1st Author : Nabil A. Siddiqui

First Name: Nabil

Last Name: Siddiqui

Email: siddiqnb@mail.uc.edu

Organization: University of Cincinnati

Country: United States

ID: GA160

Dynamic monitoring and evaluation of therapeutic effectiveness of PD-1 in triple negative breast cancer by PD-L1 fluorescence / MRI dual-mode probe

Guo-Jun Zhang, Xiang'an Hospital of Xiamen University, guoj_zhang@yahoo.com

---

Category: Oncology

Abstract Body : Introduction: Breast cancer is the most common malignant tumor in women, especially triple negative breast cancer (TNBC) which has relatively worse outcome involved in high pathological grade and invasive ability.. Recently, several clinic trials show that immune checkpoint blockade therapy (ICBT) can increase both survival rates and pathologic complete response (PCR), and it is expected to provide effective treatment strategies of TNBC. However, some of studies demonstrated the clinical response rate of ICBT is only 20-30%.Therefore, how to screen out the beneficiaries of ICBT is crucial to improve the prognosis of patients. Nowadays, the predictive biomarkers of anti-PD-1 or anti-PD-L1 antibody response are usually detected by immunohistochemistry (IHC) in clinic, which is confounded by multiple unresolved issues: invasive operation; static detecting; complex IHC kits with different detection platforms. Recently, a recent study has shown that molecular signal is highly correlated with PD-L1 status and the sensitivity of predicting clinical response compared with IHC. Noteworthy, the second near-infrared (NIR-II) fluorescence and magnetic resonance (MR) imaging has the advantages of high spatial resolution, deep penetration depth and no ionizing radiation, which is more suitable for monitoring PD-L1 in real-time, noninvasively and dynamically in vivo imaging. We have successfully synthesized a targeting PD-L1 probe GdDTPA-HSA@ICG-Atezoilzumab (NPs-Ate), composed of a MR contrast agent (GdDTPA) and fluorescence dye (indocyanine green, ICG), was used for FL/MR dual-modality imaging. By using the tail emission of ICG in NIR-II and T1 contrast capability enhanced by GdDTPA-HSA, the probe improved the signal-to-noise ratio and tumor specific targeting in vitro and vivo imaging. From vivo to vitro, from macro to microscopic, we investigated the feasibility of dynamically evaluating the PD-L1 expression and the correlation between the probe signal and PD-1 therapeutic effect in TNBC. Methods: 1. Appearance, dispersibility, particle size, stability, light absorption spectrum, fluorescence emission spectrum, fluorescence penetration and relaxation efficiency are performed to investigate the characterization of the probe. 2. Cytotoxicity assay, blood biochemical and, pathology of important organs are examined to verify probe safety. Biological distribution of the probe is examined. 3. Human TNBC cell line MDA-MB-231 (high PD-L1 expression) and mouse breast cancer cell line 4T1 (low PD-L1 expression) are transfected with PD-L1 plasmid, respectively, to analyze the sensitivity of the NPs-Ate in vitro. Isotype control probe NPs-IgG and free Atezoilzumab blocking assays are used to examine the specificity. 4. Different PD-L1 expression tumor-bearing mouse modal is performed to investigate the characterization of the probe. 5. Dynamic FL/MR imaging is respectively used to monitor the PD-L1 upregulation induced by PD-1 blockade therapy combining with radiotherapy, chemotherapy (Nanoparticle albumin-bound, nab-paclitaxel) and interferon-γ(INF-γ) therapy in 4T1 mouse model. Analyze the correlation between FL/MR signal and PD-1 blockade therapy effectiveness. Results: 1. NPs-Ate was successfully synthesized with good dispersibility, stability with high intensity of NIR-II

fluorescent and high quality signal of MRI imaging. 2. NPs-Ate could specifically target different expression level of PD-L1 in TNBC cell line compared with NPs-IgG. 3. NPs-Ate was able to detected different expression level of PD-L1 tumor-bearing mouse models with a tumor-to-muscle ratios of ~8, correspondingly, 2 fold FL signal decrease was detected while blocked by unlabeled Atezoilzumab. 4.NPs-Ate could respectively detect the upregulation of PD-L1 induced by radiotherapy, chemotherapy and INF-γtherapy with the FL signal increasing. Summary: Our results demonstrate that NPs-Ate FL/MR dual-modality imaging can monitor PD-L1 in real-time, noninvasively and dynamically. More importantly, we have established the correlation between FL/MR signal intensity and PD-1 blocking treatment effect.We believe that these results are conducive to more accurate prediction of the efficacy of ICBT combined with radiotherapy or chemotherapy in the treatment of TNBC and achieve rapid clinical transformation in the near future.

References: No.

First Name: Guo-Jun

Last Name: Zhang

Email: guoj_zhang@yahoo.com

Organization: Xiang'an Hospital of Xiamen University

Country: China

ID: GA161
Fluorescence Imaging-guided Identification of Thymic Masses Using Low-Dose Indocyanine Green

Yu Hua Quan, College of Medicine, Korea University, hwa1983418@gmail.com

---

Category: Oncology

Abstract Body : Background. Indocyanine green (ICG) fluorescence imaging has been used to detect many types of tumors during surgery. However, there are few studies on thymic masses, and the dose and time of ICG injection have not been optimized. We aimed to evaluate the optimal ICG injection dose and timing for detecting thymic masses during surgery. Method. Forty-nine consecutive patients diagnosed with thymic masses on preoperative computed tomography (CT) and scheduled to undergo thymic cystectomy or thymectomy were included. The patients were administered 1, 2, or 5 mg/kg of ICG at different times. Thymic masses were observed during and after surgery using a near-infrared fluorescence imaging system, and the fluorescence signal tumor-to-normal ratio (TNR) was analyzed. Results. Among the 49 patients, 14 patients with thymic cysts showed negative fluorescence signals, 33 patients with thymoma or thymic carcinoma showed positive fluorescence signals, and 2 patients showed insufficient fluorescence signals. The diagnosis of thymic masses based on chest CT was correct in 32 (65%) of 49 cases. However, the differential diagnosis of thymic masses based on NIR signals was correct in 47 of 49 cases (94%); these included 14 cases of thymic cysts (100 %) and 33 cases of thymomas or thymic carcinomas (94%). In addition, the TNR was not affected by the time or dose of ICG injection, histological type, stage, and tumor size. Conclusions. Low-dose intravenous injection of ICG at flexible times can detect thymic masses. In addition, thymic cysts could be distinguished from thymomas or thymic carcinomas during surgery.

References: 1. Tomiyama N, Honda O, Tsubamoto M, et al. Anterior mediastinal tumors: diagnostic accuracy of CT and MRI. European journal of radiology. Feb 2009;69(2):280-288. 2. Kurup A, Loehrer PJ, Sr. Thymoma and thymic carcinoma: therapeutic approaches. Clinical lung cancer. Jul 2004;6(1):28-32. 3. Predina JD, Keating J, Newton A, et al. A clinical trial of intraoperative near-infrared imaging to assess tumor extent and identify residual disease during anterior mediastinal tumor resection. Cancer. Mar 1 2019;125(5):807-817.

Image/Figure Caption: FIG. 1. Fluorescence assessment of thymic masses with intravenously injected ICG. (A) Representative images of thymic masses (thymic cysts, thymomas, and thymic carcinomas) by computed tomography, intraoperative thoracoscopic color and merged image (color + NIR), and postoperative color, and merged image (color + NIR). (B) Graph showing the TNR of thymic masses. The error bars represent the SD values of the TNR (**P < 0.001). ICG, indocyanine green; NIR, near-infrared; SD, standard deviation; TNR, tumor-to-normal ratio.

Full Name of Abstract's 1st Author : Yu Hua Quan

First Name: Yu Hua

Last Name: Quan

Email: hwa1983418@gmail.com

Organization: College of Medicine, Korea University

Country: South Korea

ID: GA162
Characterization of Pancreatic Cancer Stroma in GEM Models by MRI and IHC

Miguel Romanello, University of Pennsylvania, miguelrj@seas.upenn.edu

---

Category: Oncology

Abstract Body : The desmoplastic (dense) stroma is a dynamic and diverse microenvironment resulting from the interaction of numerous cells and is a signature of pancreatic ductal adenocarcinoma (PDAC). This unique tumor microenvironment (TME) is immune suppressive and impedes delivery of chemotherapies. Paradoxically, genetic deletion of carcinoma-associated fibroblasts (CAF) or the entire sonic hedgehog pathway that drives formation of a fibroblast-rich desmoplastic stroma induces a more aggressive PDAC phenotype [1, 2]. In contrast, conversion of activated pancreatic stellate cells in PDAC to quiescent phenotypes [3] or targeted inhibition of focal adhesion kinase have led to increased gemcitabine accumulation and immune infiltration [4], respectively in GEM model of PDAC with reduced levels of fibrosis. The great extent of intra- and inter-tumor heterogeneities and dynamic change of stroma during tumor progression and during the course of treatment could contribute to limited clinical efficacy of stroma-direct drug such as PEGPH20 [5] due to a lack of clinical markers to guide patient selection and assess target impact. Therefore, imaging-based biomarkers which can assess the entire tumor area would be helpful for identifying patients whose tumors are suitable for stroma-directed treatment and for monitoring stroma changes during treatment since prolonged treatment can induce the development of resistance [6]. KPC (KrasG12D:Trp53R172H:Pdx1-Cre) mice are a well characterized GEM model of PDAC [7]. Meanwhile, SMAD4 is deleted in ~50% of PDAC patients and a CKS model (KrasG12D:Smad4L/L:Ptf1a-Cre) was developed recently to represent this genetic signature along with prevalent KrasG12D mutation in PDAC [8]. Our goal is to compare the diffusion-weighted (DW)-MRI and dynamic contrast enhanced (DCE)-MRI derived parameters of KPC vs. CKS tumor in reference to the degree of fibrosis (Trichrome and Sirius Red staining), microvasculature (CD31), morphology and fraction of necrosis (H&E) in each model. We developed pixel classifiers in QuPath [9] for quantitative analysis of stained sections - this approach allows unbiased assessment using whole slide scanned images in svs format as opposed to selected fields. Our data suggest that KPC tumors represent aggressive PDAC whereas tumors from CKS mice retain differentiated histological features resembling intraductal papillary mucinous neoplasia (IPMN). We found that apparent diffusion coefficient (ADC) values estimated from DW-MRI of KPC tumors are in the range of ADC measured from human PDAC [10]. Furthermore, DCE-MRI derived markers obtained from KPC model are sensitive to changes in TME induced by stroma-directed PEGPH20 [11]. Our ongoing studies compare imaging biomarkers of CKS vs KPC model and underlying differences in their stromal architecture.

References: [1] Andrew D. Rhim et. al, Stromal Elements Act to Restrain, Rather Than Support, Pancreatic Ductal Adenocarcinoma, Cancer Cell 25(6) (2014) 735-747. [2] Berna C. Özdemir et. al, Depletion of Carcinoma-Associated Fibroblasts and Fibrosis Induces Immunosuppression and Accelerates Pancreas Cancer with Reduced Survival, Cancer Cell 25(6) (2014) 719-734. [3]

Mara H. Sherman et. al, Vitamin D Receptor-Mediated Stromal Reprogramming Suppresses Pancreatitis and Enhances Pancreatic Cancer Therapy, Cell 159(1) (2014) 80-93. [4] H. Jiang, S. Hegde et. al, Targeting focal adhesion kinase renders pancreatic cancers responsive to checkpoint immunotherapy, Nat Med 22(8) (2016) 851-60. [5] L. Zheng, A. Hendifar et. al, Abstract CT066: Global phase 3, randomized, double-blind, placebo-controlled study evaluating PEGylated recombinant human hyaluronidase PH20 (PEGPH20) plus nab-paclitaxel and gemcitabine in patients with previously untreated, hyaluronan (HA)-high, stage IV pancreatic ductal adenocarcinoma, Cancer Res 77(13 Suppl) (2017) CT066. [6] H. Jiang, X. Liu et. al, Development of resistance to FAK inhibition in pancreatic cancer is linked to stromal depletion, Gut 69(1) (2020) 122-132. [7] S.R. Hingorani et. al, Trp53R172H and KrasG12D cooperate to promote chromosomal instability and widely metastatic pancreatic ductal adenocarcinoma in mice, Cancer Cell 7(5) (2005) 469-83. [8] N. Bardeesy et. al, Smad4 is dispensable for normal pancreas development yet critical in progression and tumor biology of pancreas cancer, Genes & development 20(22) (2006) 3130-46. [9] P. Bankhead et. al, QuPath: Open source software for digital pathology image analysis, Scientific reports 7(1) (2017) 16878. [10] J. Cao, et. al, Respiratory Motion Mitigation and Repeatability of Two Diffusion-Weighted MRI Methods Applied to a Murine Model of Spontaneous Pancreatic Cancer, Tomography : a journal for imaging research 7(1) (2021) 66-79. [11] J. Cao, et. al, Dynamic Contrast-enhanced MRI Detects Responses to Stroma-directed Therapy in Mouse Models of Pancreatic Ductal Adenocarcinoma, Clin Cancer Res 25(7) (2019) 2314-2322.

First Name: Miguel

Last Name: Romanello

Email: miguelrj@seas.upenn.edu

Organization: University of Pennsylvania

Country: United States

ID: GA163
Chemical Strategies Enable the Development of Near-Infrared and Water-Soluble Nerve-Binding Fluorophores for Surgical Navigation

Lei Wang, Oregon Health & Science University, wanglei@ohsu.edu

---

Category: New Chemistry, Materials & Probes

Abstract Body : Accidental nerve transection or injury is major morbidity associated with many surgical interventions, resulting in persistent postsurgical numbness, chronic pain, and/or paralysis. Nerve-sparing can be a difficult task due to patient-to-patient variability and the difficulty of nerve visualization in the operating room. Fluorescence-guided surgery (FGS) to aid in the precise visualization of vital nerve structures in real-time during surgery could greatly improve patient outcomes. Currently, almost all clinical FGS systems have an “800 nm” channel designed to image the U.S. Food and Drug Administration (FDA) approved indocyanine green, which is mainly used to assess blood flow or detect sentinel lymph nodes during surgery as a non-specific fluorescent contrast agent. After nearly two decades, only a limited number of fluorescent molecules have been developed to image nerve tissue, where the vast majority are plagued with high non-specific uptake in surrounding tissues and mostly fluoresce at visible wavelengths. Developing a nerve binding agent that has near-infrared (NIR) fluorescent properties has been a complex and challenging task. While nerve-specific fluorophores must be of sufficiently low molecular weight to cross the blood-nerve-barrier (BNB), the degree of conjugation (e.g., number of unsaturated hydrocarbons) requisite for long-wave fluorescence emission necessarily increases molecular weight. Here we applied medicinal chemistry and modern organic synthesis to create two classes of nerve-specific fluorescent contrast agents with excitation and emission profile comparable to US FDA approved methylene blue (MB) and indocyanine green (ICG), respectively, allowing for real-time intraoperative imaging using clinical-grade surgical systems. Additionally, we successfully engineered the lead candidates with substantially improved water-solubility, fully negating the need for formulation development with the added advantage of improved safety profiles for patient use in the clinic as well as decreased overall cost of clinical translation. Utilization of these novel NIR nerve binding fluorophores during FGS will significantly improve nerve visualization, providing an immediate benefit to both patients and surgeons. Additionally, our study design and results demonstrate the feasibility of our molecular engineering approach, which can be readily adapted to create other tissue-specific fluorophores for clinical use.

Full Name of Abstract's 1st Author : Lei Garrett Wang

First Name: Lei

Last Name: Wang

Email: wanglei@ohsu.edu

Organization: Oregon Health & Science University

Country: United States

ID: GA164
Activatable dual fluorescence probe for quantitative hypoxia imaging in vivo

Xin Feng, Institute of Automation, Chinese Academy of Sciences, xin.feng@ia.ac.cn

---

Category: Oncology

Abstract Body : Tumor microenvironment plays an important role in cancer development. Hypoxia, one of the key microenvironment factors, is a common feature of many solid tumors, which is caused by the rapid proliferation of cancer cells. Hypoxia is closely related to tumor growth and metastasis, and is believed to be associated with resistance to chemotherapy and radiotherapy. Therefore, hypoxia has become an important target in cancer imaging. Visualization of the hypoxic tissue region and quantification of the level of hypoxia will be helpful to detect cancer at early stage and to monitor the therapeutic responses. Early hypoxia imaging probes are mostly single-emission molecules, whose fluorescence intensity is greatly affected by the local probe concentration and heterogeneous delivery efficiency. Current studies focus on ratiometric probes that have hypoxia sensitive and non-sensitive fluorescence emission peaks, and the ratio of the two can predict hypoxia quantitatively. However, most of these probes lack the ability to actively target cancer cells and require intratumoral injection, which greatly limits their application in small lesions and metastases. The goal of this study was to combine hypoxia sensitive fluorescent dye, nanocarrier, and tumor targeting molecule together to improve the efficiency and specificity of hypoxia imaging in breast cancer. A near-infrared nitroreductase (NTR) activated fluorescent dye Cy7-1 and a “always-on” fluorophore FITC were conjugated to polyamidoamine (PAMAM) dendrimers (PAMAM-FITC-Cy7-1) to allow for quantitative imaging. The conjugates were further modified with low molecular weight hyaluronic acid (LWHA) to form LWHA@PAMAM-FITC-Cy7-1 nanoparticles (NPs). LWHA was used to target CD44 that is overexpressed on the surface of breast cancer cells. The proposed NPs were negatively charged with size ~80nm. The NPs are stable in physiological environment and selectivevly release Cy7-1 in acidic environment, presumably due to the conformational change of PAMAM. In vitro result shows that ratio between Cy7-1 fluorescence and FITC fluorescence (ICy7-1/ IFITC) presents good linear relationship with NTR level and is unaffected by the NPs concentrations. 4T1 breast cancer cells were used to investigate the cellular uptake of the probe. Confocal imaging results show that LWHA@PAMAM-FITC-Cy7-1 NPs were internalized into cancer cells through CD44 mediated endocytosis, and accumulated in cytoplasm after entering the cells. To test the performance of LWHA@PAMAM-FITC-Cy7-1NPs in living cells, CoCl2 was used to induce hypoxia in 4T1 cell culture. Confocal imaging results show that ICy7-1 were significantly higher in hypoxia cells, while IFITC remained similar between hypoxia and normoxia cells. Ratio images ICy7-1/ IFITC were generated and allow for quantitative evaluation of NTR level. The ability of LWHA@PAMAM-FITC-Cy7-1 in hypoxia imaging in vivo was investigated in subcutaneous tumor model. When administered intravenously, fluorescence of Cy7-1 was observed in tumor region with very low background. Fluorescence of FITC was helpful for monitoring the dynamic change of NPs concentration within the tumor region. Unlike ICy7-1 and IFITC that fluctuated with time, ratio of ICy7-1/ IFITC remained stable for ~10 hours, which provides sufficient imaging window and quantitative assessment of

tissue hypoxia. Overall, this study successfully developed a hypoxia imaging technique for breast cancer, which could serve as an in vivo imaging tool for assessing tumor microenvironment. This imaging technique could account for variability of NPs delivery and uptake, providing subjective evaluation of tumor hypoxia. Further studies are underway to investigate its ability to detect lymph node metastases and other micro-metastases lesions.

First Name: Xin

Last Name: Feng

Email: xin.feng@ia.ac.cn

Organization: Institute of Automation, Chinese Academy of Sciences

Country: China

ID: GA165
In Vivo Molecular Imaging with Granzyme B PET for Immunotherapy Response Assessment in Triple Negative Breast Cancer Mouse Models

Tiara Napier, University of Alabama at Birmingham, tnapier@uab.edu

---

Category: Oncology

Abstract Body : Objective: Monitoring and predicting patient-specific response to immunotherapy in triple negative breast cancer (TNBC) as there are variable clinical response rates. Using advanced positron emission tomography (PET) imaging to probe the tumor microenvironment for T-cell activation, we aim to predict early response to immunotherapy for in mouse models of TNBC tumors. Methods: Female Balb/c or C57/Bl6 mice bearing 4T1 (cohort 1) or E0771 (cohort 2) mammary carcinoma cell tumors, respectively, were administered paclitaxel (PTX; 10 mg/kg), immunotherapy [IMT, anti-PD1 (200 µg/mouse as a high dose or 66 µg/mouse as a low dose) + anti-CTLA4 (100 µg/mouse as a high dose or 33 µg/mouse as a low dose), PTX plus IMT, or vehicle (saline) intraperitoneally. Two mouse models were used as Balb/c mice are genetically biased to Th2 immune response and C57/Bl6 mice are biased to Th1 response. Treatments were given every 3 days and granzyme B specific (GZP) PET imaging (T-cell activation) was performed. Tumors were extracted for histological validation at endpoint and stained with etc, etc, etc. Standard uptake value (SUV) was quantified and heterogenity of SUV through histogram analysis were performed. Statistical analyses were performed with unpaired Mann-Whitney and t-tests. Results: In cohort 1, non-responders to treatment had a significantly higher tumor volume compared to responders starting on day 6 (p Discussion: Preliminary results reveal that chemotherapeutic treatment results in T cell activation when compared to treatment with immunotherapy alone. Non-invasive PET imaging of the tumor microenvironment can provide data on T cell activation and hypoxic response predicting response to combination immunotherapy and chemotherapy. Utilizing clinically available advanced imaging strategies to understand biologically distinct features of the TNBC tumor microenvironment can aid in personalizing anti-cancer therapies.

Full Name of Abstract's 1st Author : Tiara Napier

First Name: Tiara

Last Name: Napier

Email: tnapier@uab.edu

Organization: University of Alabama at Birmingham

Country: United States

ID: GA166

Simultaneous evaluation of macrophage and Gd distribution in a murine model of glioblastoma therapy response using magnetic resonance fingerprinting (MRF)

Kimberly Brewer, Dalhousie University, brewerk@dal.ca

Category: Oncology

Abstract Body : Introduction: Glioblastoma is a highly aggressive primary brain tumour with a poor long term survival outlook1. Currently, care for this type of cancer involves chemotherapy, radiation, and surgical intervention; however, survival is typically less than a year after diagnosis1, with a two year survival rate of 26-33%2. The use of novel immunotherapies, particularly in combination with the chemotherapy temozolomide (TMZ), shows promise and represents one of the first treatment advances in more than 10 years1,2. Tumour associated macrophages (TAMs) are implicated in tumour growth and poor prognostic outcome3, and preferentially take up systemically-injected iron oxide contrast agents, making them an ideal target for imaging. Additionally, gadolinium (Gd) contrast agents extravasate into brain tissue when the blood brain barrier (BBB) is damaged. In this work, a novel Magnetic Resonance Fingerprinting (MRF) sequence4 capable of simultaneous T1, T2 and T2* relaxation measurements was used to make concentration maps of iron-labeled TAMs and a Gd agent. We used MRF and traditional T2-weighted MRI anatomical scans to assess survival and tumour immunodynamics in response to two immunotherapy combinations in a mouse orthotopic glioblastoma model. Methods: Fifteen C57BL/6 mice (N=5/group) were intracranially implanted with 5x104 glioblastoma cells. Mice were 1) untreated, 2) treated with anti-PD-1 (200µg/mouse/treatment), or 3) treated with a combination of anti-PD-1 and TMZ (25µg/kg/mouse/treatment). All mice received MRI brain scans twice weekly (pre and post contrast) until the tumours reached endpoint for a maximum of 6 weeks. Both weekly scans included anatomicals and MRF. Mice received an IV tail vein injection of 100µL SPIO Rhodamine B (Biopal) 24 hours before the post-contrast scan. During the post-contrast scan, mice received injections of MultiHance (gadobenate dimeglumine, Bracco) prior to MRF imaging. Upon termination, flow cytometry (FC) was performed on the brains and spleens to compare macrophage populations to the MRF data and investigate cell populations in the brain. Results: As expected, treated mice survived the longest. Initial data obtained from analysis of a MRF scan subset indicates variable macrophage uptake between mice (Figure 1). There was no immediately observable link between overall uptake and treatment group, with one mouse in group 2 demonstrating a moderate infiltration of cells, some mice from groups 1 and 3 showing high levels throughout the brain, and others having no discernible macrophages. The MRF image for the mouse from group 2 corresponds with the FC data, with 13.3% of the identified brain cells being macrophages. This is in contrast to the overall mean of 3.0%. The group 1 mouse also showed high levels of iron in the brain, with 9% of cells identified as macrophages. One mouse in group 3 had no visible macrophages with MRF and very few in the FC analysis. We are still analysing maps, particularly Gd maps. Further analysis is required to determine if a correlation exists between imaging and FC data. Early analysis indicates differences in the location of

macrophages within the brain tissue at different time points, with later points having higher levels of putative TAMs, and treated mice with tumours having higher levels of macrophage and lymphocyte infiltration in tumours than untreated mice. There are deposits of iron in the ventricles of the brain at later time points, suggesting the early spread of tumour cells (assisted by TAMs) via the cerebral vasculature. Conclusions: To our knowledge, this is the first time MRF has been used in vivo to quantitatively image Gd and SPIO simultaneously. We are able to evaluate macrophage distributions and their longitudinal response to tumour growth using MRF. Further analysis is needed to determine the correlation between imaging and FC data and evaluate BBB damage indicated by Gd maps.

References: 1. Walid M. Prognostic Factors for Long-Term Survival after Glioblastoma. Perm J. 2008;12(4). doi:10.7812/TPP/08-027 2. Fernandes C, Costa A, Osorio L, et al. Current Standards of Care in Glioblastoma Therapy. In: Glioblastoma. Codon Publications; 2017:197-241. doi:10.15586/codon.glioblastoma.2017.ch11 3. Buonfiglioli A, Hambardzumyan D. Macrophages and microglia: the cerberus of glioblastoma. Acta Neuropathol Commun. 2021;9(1):54. doi:10.1186/s40478-021-01156-z 4. Marriott A, Bowen C, Rioux J, Brewer K. Simultaneous quantification of SPIO and gadolinium contrast agents using MR fingerprinting. Magnetic Resonance Imaging. 2021 Mar;79:121-129. doi: 10.1016/j.mri.2021.03.017.

Image/Figure:

https://s3.amazonaws.com/amz.xcdsystem.com/1E8A4501-BB41-A02A-1D3B9882B798BFAA_abstract_File10351/GA166_ImageFigure_0512090117.png

Image/Figure Caption: Figure 1 – MRF maps of iron-labeled macrophages and FC analysis of macrophages in the brain. Macrophage migration into the brain varied significantly between mice and groups (full analysis still ongoing). In the MRF maps overlaid on the FSE anatomical in these sample mice, tumours are circled in green and colour scales indicate cellular density (cells/mm3). The group 3 mouse with a tumour had far more visible macrophages in the tumour compared to other groups, whereas the group 3 mouse with no tumour had almost no macrophages visible on the MRI or in the flow cytometry. The mouse from group 2 had macrophages visible throughout the brain, whereas the mouse from group 1 had some macrophages visible in the tumour and some in the rest of the brain (not all shown on the single slice).

First Name: Kimberly

Last Name: Brewer

Email: brewerk@dal.ca

Organization: Dalhousie University

Country: Canada

ID: GA167
Zwitterionic nanogel coated acoustic nanostructures for long term functional ultrasound imaging

Bill Ling, California Institute of Technology, blling@caltech.edu

---

Category: New Chemistry, Materials & Probes

Abstract Body : Contrast-enhanced transcranial functional ultrasound imaging is a powerful technique for non-invasive visualization of neural activity. However, microbubbles and other commonly used ultrasound contrast agents are highly unstable in the bloodstream, necessitating repeated administration during a brief imaging session. Here, we describe nanoscale ultrasound reporters which circulate in mice for at least 2h, enabling prolonged imaging sessions with a single injection. These particles are based on gas vesicles (GVs), a unique class of air-filled protein nanostructure biosynthesized in certain aquatic microbes as a means to regulate buoyancy. GVs comprise a 2-nm thick protein shell encapsulating air which is in equilibrium with the surrounding media. Despite this inherent stability, intravenously injected GVs are rapidly sequestered by liver macrophages. We show that by coating the GV surface with a zwitterionic hydrogel, particle recognition and uptake pathways are disrupted, greatly enhancing circulation time. Acrylate groups are first biochemically attached to primary amines on the GV shell via N-hydroxysuccinimide chemistry. Next, these acrylate groups are used as anchors for radical polymerization with zwitterionic monomers and cross-linkers, forming a thin hydrogel on the GV surface. This process increases the hydrodynamic diameter of the particles from 235 nm to 348 nm, while reducing the zeta potential from -51 mV to -6 mV. The in vitro phagocytosis kinetics of these particles, as measured by flow cytometry, are significantly slower than that of unmodified particles. Upon intravenous administration, the coated GVs circulate with a half-life of approximately 1h, and share the same biodistribution as unmodified GVs. We believe such long-circulating ultrasound contrast agents to be of great practical utility in functional neuroimaging, and may be adapted for molecular detection and drug delivery applications as well.

Image/Figure: https://s3.amazonaws.com/amz.xcdsystem.com/1E8A4501-BB41-A02A-1D3B9882B798BFAA_abstract_File10351/GA167_ImageFigure_0512093004.pdf

Full Name of Abstract's 1st Author : Bill Ling

First Name: Bill

Last Name: Ling

Email: blling@caltech.edu

Organization: California Institute of Technology

Country: United States

ID: GA169

Optimization of Hyperpolarized Carbon-13 pH Imaging Method in Preparation for Clinical Translation in Prostate Cancer

Changhua Mu, University of California, San Francisco, changhua.mu@ucsf.edu

---

Category: New Chemistry, Materials & Probes

Abstract Body : Prostate cancer (PCa) is a prevalent cancer and leads to the second-highest rate of cancer death in men in the United States.1 Although some advanced non-invasive imaging technologies like MRI, CT, and PET/CT, have become standards of care for the management of localized PCa, their sensitivity and specificity remain limited and possibly lead to overtreatment of indolent cancer, while undertreating aggressive disease. Therefore, there is an unmet clinical need for better imaging methods to enable the discrimination between indolent and aggressive PCa. Recently, we developed a method of imaging the tissue pH using hyperpolarized (HP) 13C MRI for characterizing PCa.2 It relies on the polarization of [1-13C]1,2-glycerol carbonate (13C-GLC) using dissolution Dynamic Nuclear Polarization, and subsequent hydrolysis to HP 13C bicarbonate (Bic) (Figure 1a) that rapidly establishes a chemical equilibrium with HP 13CO2 in tissues.3 The detectable signals can be used to image tissue pH using the Henderson-Hasselbalch equation pH = pKa + logSBic/SCO2, where S hyperpolarized 13C NMR signal and pKa is known in vivo.2 Solid tumors commonly developed an acidic interstitial microenvironment with pH 6.5 – 7.2, in contrast to pH 7.4 in normal tissues, owing to heterogeneous perfusion, high metabolic activity, and rapid cell proliferation.4 We demonstrated this pH imaging method can distinguish between low- and high-grade prostate cancer in the TRAMP model of prostate cancer according to the level of extracellular acidification (Figure 1b and 1c). These data suggest that HP 13C MRI could be used to discriminate between indolent and aggressive PCa in humans, motivating clinical translation of the method. Therefore, we have developed optimized methods for polarization and breakdown of 13C-GLC to form HP 13C bicarbonate in preparation for clinical translation. First, we used NMR to identify the optimal conditions for 13C-GLC hydrolysis through systematically varying temperature, amount of base, reaction time, and amount of acid for neutralization (Figure 2). We then investigated the reaction kinetics to determine the reaction rate constants under these different conditions (Figure 3). These data showed GLC breaks down through an exponential kinetic profile of hydrolysis reaction with a time constant of 11 s catalyzed by 2.0 eq of NaOH at 60 °C (Figure 3b,3c). Subsequently, we polarized a mixture of 13C-GLC and GE trityl radical at 0.8 K with the human clinical GE 5T SPINlab polarizer for ~5 hours, where the frozen HP sample is dissolved immediately by 130°C hot water. We replaced H2O with D2O for dissolution to avoid the dipolar-dipolar interaction raised from the intermediate species of 13C-GLC breakdown, which caused a profound loss of polarization during the breakdown and neutralization process (Figure 4). We found that the percentage of polarization was significantly increased to 40% in D2O in comparison to 1% in H2O (Figure 5, Table 1). We established a standard operating procedure, including cooling down, neutralization, removal of radical, and sterilization of the dissolution, to ensure the safety for patient injection (Figure 6). We obtained a human injectable HP 13C-bicarbonate solution with a high polarization ~ 20% at 90 sec of dissolution and long T1 – 128 sec at 1.4 T (Table 2).

Using a human 3T clinical MRI scanner, we demonstrated the excellent accuracy and precision of this pH imaging method in in vitro phantom studies (Figure 7). We currently are characterizing it in vivo mouse models and investigating the toxicity in rats. Taken together, these data suggest that the high polarization and purity of the resulting hyperpolarized 13C-bicarbonate will enable the clinical translation of this method.

References: 1 Siegel, R. L., Miller, K. D. & Jemal, A. Cancer statistics, 2019. CA Cancer J Clin 69, 7-34, doi:10.3322/caac.21551 (2019). 2 Korenchan, D. E. et al. Hyperpolarized in vivo pH imaging reveals grade-dependent acidification in prostate cancer. Oncotarget 10, 6096-6110 (2019). 3 Korenchan, D. E. et al. Dynamic nuclear polarization of biocompatible 13C-enriched carbonates for in vivo pH imaging. Chemical Communications 52, 3030-3033, doi:10.1039/C5CC09724J (2016). 4 Gatenby, R. A., Gawlinski, E. T., Gmitro, A. F., Kaylor, B. & Gillies, R. J. Acid-mediated tumor invasion: a multidisciplinary study. Cancer Res 66, 5216-5223, doi:10.1158/0008-5472.Can-05-4193 (2006).

Image/Figure:

https://s3.amazonaws.com/amz.xcdsystem.com/1E8A4501-BB41-A02A-1D3B9882B798BFAA_abstract_File10351/GA169_ImageFigure_0512091400.jpg

Image/Figure Caption: Standard operating procedure of processing dissolution for human patient injection. (a) picture of GE Health 5T SPINlab polarizer, components, and procedure of processing dissolution solution. (1) cryovial in the SPINlab receiving microwave irradiation at 0.8 K for the buildup of polarization; (2) dissolution syringe loaded with D2O; (3) receiver vessel loaded with NaOH; (4) transfer; (5) neutralization with acid and cooling down; (6) syringe pump; (7) C18 cartridges installed on two manifolds; (8) 0.2 μm syringe filter; and (9) Solution ready for injection. (b) The first observed HP 13C NMR spectrum of the dissolution solution processed for patient injection. HP 13C-bicarbonate (161.09 ppm), two HP intermediate species (160.17 ppm and 159.7 ppm), HP CO2 (125.5 ppm). % polarization of 13C-bicarbnate = 19.7% at 94s, T1 = 128.2 s at 1.4 T

First Name: Changhua

Last Name: Mu

Email: changhua.mu@ucsf.edu

Organization: University of California, San Francisco

Country: United States

ID: GA172

Assessment of nanoparticle accumulation as a potential non-invasive method for imaging of endometriosis

Nazanin Talebloo, Michigan State University, talebloo@chemistry.msu.edu

---

Category: New Chemistry, Materials & Probes

Abstract Body : Introduction: Endometriosis is a gynecological disorder that commonly occurs in 10-15% of women of reproductive age and up to 30% of women suffering from infertility. This disease is defined by the presence of endometrial-like tissue (lesions) outside the uterus in the ovaries and peritoneum. It is accompanied by various symptoms such as cyclic menstrual pain, chronic pelvic pain, dyspareunia, and infertility which all negatively affect patient's quality of life [1]. Retrograde menstruation is thought to contribute to its etiology [2] though hormonal, inflammatory milieu, or immune dysfunction may cause the lesion deposition [3-5]. Since no symptom is pathognomonic for endometriosis, it is hard to determine whether pain or infertility are the results of this disorder. Even today the final diagnosis for the disease is only established at laparoscopy, which is a painful procedure for which anesthesia is required and multiple side effects (bleeding, infection, etc) are common. Most importantly, the stage of endometriosis on laparoscopy correlates poorly with the extent and severity of pain [1]. Therefore, there is an unmet clinical need for developing novel non-invasive methods for early/reliable detection of endometriosis. Magnetic resonance imaging (MRI) is a technique for diagnostic imaging before treatment planning [6]. However, with MRI different lesions like superficial or deep infiltrating lesions can be easily overlooked because of lack of adequate resolution [7]. The goal of this study was to investigate whether iron oxide nanoparticles can accumulate in endometriotic lesions in a mouse model of endometriosis. We expect to observe nanoparticle accumulation in the lesions largely due to the enhanced permeability and retention effect similar to that in tumors. We believe that this method can help to reduce the number of overlooked lesions by MRI. In future, these nanoparticles can also be used as a potential platform for the delivery of therapeutics to lesions. Methods: Dextran-coated iron oxide nanoparticles (NP, 32.6±4 nm, zeta potential: 27.5 mv) were synthesized with a co-precipitation method. NPs were labeled with a fluorescent dye (Cy5.5) to yield a multimodal MRI/optical imaging probe (Cy5.5-NP). Here, in vivo Pgrcre/+Rosa26mTmG/+ endometriosis mouse model was utilized. Endometriosis was induced by removing one uterine horn, mincing it in sterile PBS, and injecting back minced uterine tissues into the peritoneal cavity. This unique Pgrcre/+Rosa26mTmG/+ mouse model of induced endometriosis provides an opportunity to visualize the progesterone receptor (Pgr) - positive cells which express green fluorescent protein GFP (mG). In contrast, the Pgr-negative cells express red fluorescent mTomato (mT), allowing accurate localization and visualization of the endometriotic lesions under fluorescent imaging. Cy5.5-NP (10 mg Fe/kg) was injected intravenously in mice with endometriotic lesions. The animals were imaged with fluorescence imaging (IVIS) pre-injection and 24 hours post-injection followed by ex vivo imaging. Results: Ex vivo images showed fluorescent signal from Cy5.5-NP which was co-localized with the GFP signal from the lesions. NP accumulation was not detected in the muscle tissue, which was used as control (Fig. 1). We realize that GFP-expressing model is not ideal for in vivo imaging due to

the weak signal and abundance of tissue autofluorescence in the green channel. In the future, we will utilize a recently developed model where endometriotic lesions express luciferase and can be detected by a significantly more sensitive bioluminescence imaging (BLI). Conclusion: In this work, we employed a dual-modal, MR/NIRF imaging probe to visualize endometriotic lesions in a mouse model of endometriosis by passive targeting. Cy5.5-NP accumulated and were visible with ex vivo fluorescence imaging 24 hours following administration. Future work is focused on performing MRI studies and exploring different ligands for a targeted delivery approach, which can enhance the specific accumulation of NPs in lesions as a potential theranostic probe.

References: 1. Hsu, A.L., I. Khachikyan, and P. Stratton, Invasive and noninvasive methods for the diagnosis of endometriosis. Clin Obstet Gynecol, 2010. 53(2): p. 413-9. 2. Bulun, S.E., Endometriosis. N Engl J Med, 2009. 360(3): p. 268-79. 3. Sourial, S., N. Tempest, and D.K. Hapangama, Theories on the pathogenesis of endometriosis. International journal of reproductive medicine, 2014. 2014. 4. Child, T.J. and S.L. Tan, Endometriosis. Drugs, 2001. 61(12): p. 1735-1750. 5. Parasar, P., P. Ozcan, and K.L. Terry, Endometriosis: epidemiology, diagnosis and clinical management. Current obstetrics and gynecology reports, 2017. 6(1): p. 34-41. 6. Foti, P.V., et al., Endometriosis: clinical features, MR imaging findings and pathologic correlation. Insights into imaging, 2018. 9(2): p. 149-172. 7. Zhang, H., et al., Hyaluronic acid-modified magnetic iron oxide nanoparticles for MR imaging of surgically induced endometriosis model in rats. PLoS One, 2014. 9(4): p. e94718.

Image/Figure:

https://s3.amazonaws.com/amz.xcdsystem.com/1E8A4501-BB41-A02A-1D3B9882B798BFAA_abstract_File10351/GA172_ImageFigure_0512093231.png

Image/Figure Caption: Fig 1. A) GFP signal from the uterus and endometriotic lesion in a mouse model of endometriosis. B) Cy5.5 signal from accumulated Cy5.5-NP in the GFP-expressing endometriotic lesions compared to control tissue (muscle). C) Confirmation of GFP-expressing endometriotic lesion by fluorescence imaging.

First Name: Nazanin

Last Name: Talebloo

Email: talebloo@chemistry.msu.edu

Organization: Michigan State University

Country: United States

ID: GA173

A highly modular activatable synthetic biology system to visualize in vivo cell-cell communication

TianDuo Wang, Robarts Research Institute, twang342@uwo.ca

Category: Bioengineering, Synthetic Biology and Basic Biology

Abstract Body : INTRODUCTION: Cell-cell communication is central to the development and homeostasis of multicellular organisms. In recent years, it has also been leveraged for the development of targeted cellular immunotherapies for a variety of biomedical problems such as infectious diseases, autoimmune diseases, and cancer. Cell-based cancer immunotherapies harness the innate tumour-homing ability of immune cells to better accumulate within and kill malignant lesions. To improve cancer killing, immune cells can also be engineered with receptors, such as chimeric antigen receptors (CAR)1, to recognize specific cancer antigens. CAR-T cells have shown remarkable clinical success in treating B-cell cancers, with potential for many other cancer types on the horizon. However, some patients still suffer from inadequate efficacy or serious side effects, thought to be due to sub-optimal tumour homing and off-targeting of normal tissues. This study aims to develop a specific and non-invasive imaging tool to visualize when immune cells interact with its targeted antigen – the prerequisite for inducing cancer cell killing. The synthetic notch (SynNotch) receptor is a uniquely versatile system that signals cell-cell contact via activated transcriptional expression of desired transgenes2 (Fig. 1A). Here we engineered immune cells with a new SynNotch system that activates the expression of imaging reporter genes in response to cancer binding and validated this system in vitro and in vivo. METHODS: We engineered a human T cell line (Jurkat) via sequential lentiviral transduction of two components: (1) a SynNotch receptor directed against the B-cell surface antigen CD193, and (2) a response element containing tdTomato (tdT) for fluorescence, firefly luciferase (Fluc) for bioluminescence, and organic anion transporting polypeptide 1B3 (OATP1B3) for MRI4 (Fig. 1B). Successfully engineered Jurkat cells were isolated using fluorescence-activated cell sorting. To validate this system in vitro, Jurkat cells were co-cultured in well plates with CD19+ or CD19- Nalm6 B-cell leukemia cells. Twenty-four hours later, tdT and Fluc expression in Jurkat cells were assessed using fluorescence microscopy and bioluminescence imaging (BLI), respectively. Moving this system in vivo, Nod-scid-gamma (NSG) mice were implanted with either CD19+ or CD19- Nalm6 cells subcutaneously. Once tumours reached ~100mm3, mice received an intratumoural injection of engineered Jurkat cells (1x107), and Fluc BLI was performed to assess reporter activation. RESULTS: Co-culturing of engineered Jurkat cells with CD19+ Nalm6 cells resulted in higher tdTomato and Fluc signal compared to CD19- Nalm6 cells (Fig. 1C). Reporter expression was not observed when Jurkat cells engineered with only the response element or naïve Jurkat cells were co-cultured with CD19+ cells. In vivo evaluation revealed no bioluminescence signal from Nalm6 tumours prior to cell injection (Fig. 1D). Excitingly, as soon as 12 hours post-injection, CD19+ tumours (n=2), but not CD19- tumors (n=3), exhibited considerably elevated BLI signal, with observable differences in signal between groups still present 10 days post-injection. DISCUSSION: We have developed a new SynNotch system to non-invasively visualize antigen-specific

communication between immune and cancer cells for the first time. This system demonstrated antigen-dependent activation of reporter genes in immune cells when engaging CD19 on cancer cells, with minimal off-target activity. Continuing our work in animals, we plan to image this immune-cancer interaction via MRI, a clinically relevant modality, as well as co-engineer cells with a CD19-targeted CAR. We have also begun to broaden the antigens we can target with the highly modular SynNotch system, so that this system can be applied across various cancer cell types. Further development of this system will provide a broadly applicable tool for monitoring cell-based immunotherapies and beyond. We posit these tools will ultimately improve our ability to develop better cell therapies and to understand response/non-response and side effects in individual patients.

References: [1] Maude et al., NEJM, 2014, 371: 1507-1517. [2] Morsut et al., Cell, 2016, 164: 780-791. [3] Sadelain et al., J Clin Invest, 2015, 125(9): 3392-3400. [4] Nystrom et al., Invest Radiol, 2019, 54(5): 302-311.

Image/Figure: https://s3.amazonaws.com/amz.xcdsystem.com/1E8A4501-BB41-A02A-1D3B9882B798BFAA_abstract_File10351/GA173_ImageFigure_0512094918.pdf

Image/Figure Caption: Figure 1. Assessment of SynNotch reporter system. (A) Schematic of SynNotch system. CD19 binding by the CD19-targeted SynNotch receptor induces intracellular cleavage of a GAL4-VP64 transactivator, which binds to an upstream activating sequence (UAS) to initiate transcription of genes of interest encoded in the response element. (B) Jurkat cells were engineered with CD19-targeted SynNotch driven by the phosphoglycerate kinase 1 promoter (pPGK), and a response element containing reporter genes as well as a pPGK-driven blue fluorescence protein (BFP) for sorting. (C) TdTomato fluorescence with brightfield overlay and Fluc bioluminescence images of 105 Jurkat cells 24 hours after co-culturing with Nalm6 cells at a 1:1 ratio. (D) Representative bioluminescence images of Firefly luciferase (Fluc) from mice pre- and post-injection of Jurkat cells with quantification. NSG mice with similarly sized subcutaneous CD19+ (n=2) and CD19- (n=3) Nalm6 tumours were injected with 10 million engineered Jurkat cells intratumourally.

Full Name of Abstract's 1st Author : TianDuo Wang

First Name: TianDuo

Last Name: Wang

Email: twang342@uwo.ca

Organization: Robarts Research Institute

Country: Canada

ID: GA174
Biodistribution and Targeting of Near-Infrared Labeled Anti-CD38 Antibody-Drug Conjugate in Preclinical Multiple Myeloma

Nicholas Cho, Washington University in St. Louis School of Medicine, ncho@wustl.edu

---

Category: Oncology

Abstract Body : Introduction: Daratumumab (DARA) is an FDA approved high-affinity monoclonal antibody targeting CD38 that has shown promising therapeutic efficacy in double refractory multiple myeloma (MM) patients [1]. Despite the well-established clinical efficacy of DARA, not all heavily pretreated patients respond to single-agent DARA, and the majority of patients who initially respond eventually progress [2]. This may be due to upregulation of pathways that inhibit DARA-mediated tumor killing [3]. Antibody-drug conjugates (ADCs) combine the highly targeted tumor antigen recognition of antibodies with the cell killing properties of chemotherapy for effective internalization and processing of the drug. In this study, we evaluated the antitumor efficacy of DARA conjugated to the maytansine derivative, emtansine (DM1), linked via a non-cleavable bifunctional linker. The ADC was labelled with the near-infrared (NIR) fluorophore IRDye800CW (DARA-DM1-IR) to evaluate the biodistribution and pharmacokinetics of the ADC. We hypothesize: 1) the conjugation of DM1 will enhance tumor-killing efficacy of the native DARA and 2) the conjugation of IRDye800CW will not affect the biologic activity or tumor targeting ability of the ADC. Materials and Methods: Daratumumab (Janssen Biotech) was generously provided by the Siteman Cancer Center pharmacy. IRDye800CW (Li Cor) was conjugated following the manufacturer's protocol. Cell viability was evaluated with native and fluorescently labelled DARA (DARA-IR) and DARA ADC conjugates, respectively, in a high (MM.1S) and low (U266) CD38-expressing myeloma cell line. Live cell microscopy on MM.1S cells was performed to evaluate binding and internalization kinetics of DARA-IR and DARA-DM1-IR. In vivo fluorescence imaging was performed on fox chase severe combined immunodeficient beige mice bearing MM1.S subcutaneous tumors (n = 3-5/group) transfected with green fluorescence protein and luciferase. 100μg of DARA-IR and DARA-DM1-IR were administered intravenously via tail-vein and daily fluorescence imaging was performed using the IVIS Spectrum CT (IRDye800CW Ex./Em.: 745 nm/820 nm) (Perkin Elmer). Mean fluorescence intensity (MFI), defined as total counts/region of interest, was determined using ImageJ. Tumor-to-background ratio (TBR) was quantified using tumor MFI divided by the MFI of contralateral tissue. Animals were then euthanized and organs were resected and imaged on the IVIS Spectrum CT. Tissue-to-muscle ratio was quantified by using tissue MFI divided by the MFI of the muscle. Tumors from both mouse cohorts were flash frozen, sectioned and stained with Hoechst 33342 (Thermo Fisher). Fluorescent microscopy was performed using an Olympus BX51 epi-fluorescent microscope. Results and Discussion: After conjugation and purification, spectrophotometric analysis showed a degree of labelling of ~1.2 with a 3:1 molar dye to antibody ratio. CD38-dependent myeloma tumor cell killing was observed following incubation of DARA-DM1 (MM.1S IC50: 0.68±0.07 μg/mL; U266 IC50: 2.82±0.14 μg/mL) and conjugation of IRDye800CW to DARA-DM1 did not significantly affect its therapeutic efficacy (MM.1S IC50: 0.55±0.07 μg/mL; U266 IC50: 4.58±0.21 μg/mL).

DARA-IR and DARA-DM1-IR demonstrated similar binding and internalization into CD38+ MM.1S cells within 3 hours post-incubation. Tumor uptake of the fluorescently-labelled DARA conjugates increased with peak TBR achieved 9 days post-contrast (DARA-IR: 4.00±0.73; DARA-DM1-IR: 3.29±0.36) (Fig. 1A,B). Clearance of DARA-IR and DARA-DM1-IR was primarily observed through the liver with no significant difference observed in tumoral uptake (Fig. 1C). Histology of tumor sections following sacrifice demonstrated binding of both conjugates primarily on the tumor cell surface (Fig. 1D). Conclusions: Here, we demonstrated the conjugation of DM1 improved the therapeutic window of DARA. Fluorescently labelling the ADC with IRDye800CW did not affect the biologic activity of the native antibody and allowed for evaluation of the DARA conjugates on a whole-body and cellular level in our mouse models. Future studies will focus on further in vitro and in vivo characterization of other promising anti-CD38 immunotherapies and ADCs in immunocompetent myeloma mouse models with differential CD38 expression.

References: [1] M.C. Minnema, U. Lassen, J. Krejcik, A. Palumbo, N.W.C.J. Van De Donk, N. Brun, P.G. Richardson, Targeting CD38 with Daratumumab Monotherapy in Multiple Myeloma, (2019). doi:10.1056/NEJMoa1506348. [2] M. Pick, V. Vainstein, N. Goldschmidt, D. Lavie, D. Libster, A. Gural, S. Grisariu, B. Avni, D. Ben Yehuda, M.E. Gatt, Daratumumab resistance is frequent in advanced-stage multiple myeloma patients irrespective of CD38 expression and is related to dismal prognosis, Eur. J. Haematol. 100 (2018) 494–501. doi:10.1111/ejh.13046. [3] K. Syed, I.S. Nijhof, J. van Velzen, M.C. Minnema, H.M. Lokhorst, T. Casneuf, A.E. Axel, S. Zweegman, P. Sonneveld, N.W.C.J. van de Donk, B. van Kessel, R.W.J. Groen, A.K. Sasser, M. van Duin, T. Mutis, A.C. Bloem, C. Chiu, CD38 expression and complement inhibitors affect response and resistance to daratumumab therapy in myeloma, Blood. 128 (2016) 959–970. doi:10.1182/blood-2016-03-703439.

Image/Figure:

https://s3.amazonaws.com/amz.xcdsystem.com/1E8A4501-BB41-A02A-1D3B9882B798BFAA_abstract_File10351/GA174_ImageFigure_0512100907.png

Image/Figure Caption: Figure 1. In vivo characterization of DARA-DM1-IR (A) Representative images of DARA-DM1-IR in vivo over 9 days showing uptake in tumor-bearing regions. (B) Calculated tumor-to-background ratios associated with DARA-DM1-IR and DARA-IR. (C) DARA-DM1-IR and DARA-IR biodistribution 2, 7 and 9 days post-administration. (D) Immunohistochemical staining of tumor sections from DARA-IR and DARA-DM1-IR injected mice 9 days post-administration. 40X magnification; scale bar: 20μm

First Name: Nicholas

Last Name: Cho

Email: ncho@wustl.edu

Organization: Washington University in St. Louis School of Medicine

Country: United States

ID: GA176
Optimizing luminescent biosensing of calcium for noninvasive reporting of brain activity

Yichi Su, Stanford University, yichisu@stanford.edu

Category: Neuroscience

Abstract Body : Noninvasive reporting of neuronal activity would be invaluable for revealing how specific brain circuits control animal behaviors. Luminescent calcium biosensors based on luciferase enzymes should enable noninvasive activity reporting from deep locations, as luciferases operate without requiring excitation light and auto-bioluminescence is minimized compared to fluorescence in mammals. To date, a seiries of NanoLuc-based luminescent calcium biosensors have been developed[1-3]. However, the calcium responsivity of these reporters is limited, and NanoLuc substrates that efficiently cross the blood-brain barrier have not yet been identified. Here, we present our efforts to improve CaMBI responsiveness and in vivo brightness in the brain through protein and substrate engineering. We have identified additional sites in NanoLuc where insertion of calcium-binding domains confer calcium sensitivity to light production, and are optimizing the resulting constructs through linker and core mutagenesis. We have also identified a new NanoLuc substrate that produces superior bioluminescence from the brain. Together, these results will advance the future use of luminescent biosensors for calcium and other analytes in the brain.

References: [1] J. Yang, et. al., Coupling optogenetic stimulation with NanoLuc-based luminescence (BRET) Ca++ sensing, Nat. Comm., 2016, 7, 13268. [2] K. Suzuki, et. al., Five colour variants of bright luminescent protein for real-time multicolour bioimaging, Nat. Comm., 2016, 7, 13718. [3] Y. Oh., et. al., An orange calcium-modulated bioluminescent indicator for non-invasive activity imaging, Nat. Chem. Biol., 2019, 15, 433.

First Name: Yichi

Last Name: Su

Email: yichisu@stanford.edu

Organization: Stanford University

Country: United States

ID: GA179

PET mapping of neurofunctional changes after young blood plasma treatment in aged mice under conscious state

Kai Zhang, Laboratory for Pathophysiological and Health Science, RIKEN Center for Biosystems Dynamics Research, Kobe, Japan; Department of Nuclear Medicine and PET center, The Second Affiliated Hospital of Zhejiang University School of Medicine, 914487026@qq.com

---

Category: Neuroscience

Abstract Body : Background: Exposure to young blood or young blood plasma (YBP) has been increasingly documented to be beneficial for alleviating age-related cognitive decline1-5, however, the neurofunctional change after treatment with YBP has not been well characterized in vivo. Positron emission tomography (PET) is an advanced molecular imaging modality and can noninvasively visualize molecular and functional changes involved in biological processes6. PET imaging with radiolabeled glucose analogue 2-[18F]-fluoro-2-deoxy-D-glucose (18F-FDG) has been extensively used to characterize the neural activity by measuring cerebral glucose metabolism7. In vivo PET imaging requires strict restriction of body movement and generally, is conducted under the anesthetized state by using anesthetic agents in animal studies. However, anesthetics are known to reduce neural activity and cerebral metabolism, thereby interfering with the interpretations of in vivo cerebral metabolic imaging data8. In addition, isoflurane which is an extensively used anesthetic during animal PET imaging has been reported to block synaptic plasticity in the hippocampus of mouse9. Objective: The purpose of the present study is to investigate the in vivo neurofunctional changes after YBP treatment in aged mice under conscious state, as well as to explore the mechanisms underlying the effects of YBP treatment on cognitive function in aged mice. Methods: Natural aging mice (aged 56 weeks) were systemically administered with YBP (extracted from 8-week mice) or PBS for 4 weeks via tail vein. One week prior to the PET imaging, the aged mice were trained twice to adapt to the PET imaging under conscious state, according to the previous method8. In vivo 18F-FDG PET imaging was performed in aged mice under conscious state after systemic treatment with YBP and the image data were analyzed using the SPM software. Novel object-location recognition test, novel partner recognition test, and spontaneous Y-maze test were performed to test the short-term recognition memory, long-term recognition memory, and spatial working memory of the aged mice, respectively. Western blot and immunofluorescent staining were conducted to assess the expression levels of brain-derived neurotrophic factor (BDNF), insulin-like growth factor-1 (IGF-1), IGF-1 receptor (IGF-1R), synapsin 1 (SYN1), postsynaptic density-95 (PSD95), or the alterations of AKT and ERK signaling pathways in brain tissues and in vitro cells. Results: YBP treatment exhibited positive effects on the short- and long-term recognition memory, but not on the spatial working memory of the aged mice. Compared with the PBS control group, YBP treatment group demonstrated higher glucose metabolism in the right hippocampus and the bilateral somatosensory cortex, and lower higher glucose metabolism in the left cerebrum and the right bed nucleus of the stria terminalis (both $P < 0$ .05, uncorrected). Ex vivo studies demonstrated that YBP treatment increased the activation of AKT signaling

pathway (P < 0 .05 in both in the hippocampus and somatosensory cortex) and decreased the activation of the EKT signaling pathway (P < 0 .05, and P < 0 .01 in the hippocampus and somatosensory cortex, respectively). Moreover, YBP treatment significantly increased the expressions of BDNF, IGF-1, IGF-1R, and SYN1 in the hippocampus and somatosensory cortex (P < 0 .01, P < 0 .05, P < 0 .05, and P < 0 .05, respectively). This was further supported by the in vitro cell studies which demonstrated that young but not aged blood plasma upregulated the expressions of BDNF, IGF-1, IGF-1R, and SYN1 (P < 0 .01, P < 0 .01, P < 0 .05, and P < 0 .05, respectively). Conclusion: Our results indicate that YBP treatment triggers positive effects on short- and long-term recognition memory in aged mice, which is likely linked to the increased neuronal activity, upregulated cognition-related protein expression, and alterations of key neuronal signaling pathways in the hippocampus and somatosensory cortex. 18F-FDG PET imaging provides a new avenue for exploring the mechanisms underlying YBP treatment.

References: References 1. Katsimpardi L, Litterman NK, Schein PA, et al. Vascular and neurogenic rejuvenation of the aging mouse brain by young systemic factors. Science. 2014;344(6184):630-634. 2. Villeda SA, Luo J, Mosher KI, et al. The ageing systemic milieu negatively regulates neurogenesis and cognitive function. Nature. 2011;477(7362):90-94. 3. Villeda SA, Plambeck KE, Middeldorp J, et al. Young blood reverses age-related impairments in cognitive function and synaptic plasticity in mice. Nature medicine. 2014;20(6):659-663. 4. Castellano JM, Kirby ED, Wyss-Coray T. Blood-Borne Revitalization of the Aged Brain. JAMA neurology. 2015;72(10):1191-1194. 5. Gan KJ, Sudhof TC. Specific factors in blood from young but not old mice directly promote synapse formation and NMDA-receptor recruitment. Proc Natl Acad Sci U S A. 2019;116(25):12524-12533. 6. Tian M, He X, Jin C, et al. Transpathology: molecular imaging-based pathology. Eur J Nucl Med Mol Imaging. 2021. 7. Zhang K, Mizuma H, Zhang X, et al. PET imaging of neural activity, beta-amyloid, and tau in normal brain aging. Eur J Nucl Med Mol Imaging. 2021. 8. Mizuma H, Shukuri M, Hayashi T, Watanabe Y, Onoe H. Establishment of in vivo brain imaging method in conscious mice. J Nucl Med. 2010;51(7):1068-1075. 9. Simon W, Hapfelmeier G, Kochs E, Zieglgänsberger W, Rammes G. Isoflurane blocks synaptic plasticity in the mouse hippocampus. Anesthesiology. 2001;94(6):1058-1065.

Image/Figure:

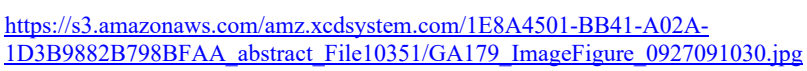
https://s3.amazonaws.com/amz.xcdsystem.com/1E8A4501-BB41-A02A-1D3B9882B798BFAA_abstract_File10351/GA179_ImageFigure_0927091030.jpg

Image/Figure Caption: Figure 1. (A) Schematic of in vivo experimental protocol. (B-D) Effects of YBP treatment on rCGM regional cerebral glucose metabolism in aged mice. YBP treatment group (n = 7) showed higher rCGM in the bilateral somatosensory cortices (B) and right hippocampus (C), but lower in the right bed nucleus of the stria terminalis (D, upper) and left cerebellum (D, lower) than PBS control group (n = 8) (P 2-[18F]-Fluoro-2-deoxy-D-glucose; PET, positron emission tomography. rCGM, regional cerebral glucose metabolism; YBP, young blood plasma; A, anterior; P, posterior; L, left; R, right; x, left (-) to right (+) direction; y, dorsal to ventral direction; z, anterior (+) to posterior (-) direction; z = 0 indicates the position of bregma according to the Mouse Brain Atlas. (E) Schematic illustrating the paradigm of the short-term novel object-location recognition test. (G) YBP treatment group (n=7) demonstrate higher novel object-location preference ratio compared with PBS control group (n=8). (F) Schematic

illustrating the paradigm of long-term novel partner recognition test. (G) YBP treatment group (n=7) demonstrate higher novel partner preference ratio compared with PBS control group (n=8). Data are presented as the mean ± SEM. *P < 0 .05; n.s., no significance; YBP, young blood plasma.

Full Name of Abstract's 1st Author : Kai Zhang

First Name: Kai

Last Name: Zhang

Email: 914487026@qq.com

Organization: Laboratory for Pathophysiological and Health Science, RIKEN Center for Biosystems Dynamics Research, Kobe, Japan; Department of Nuclear Medicine and PET center, The Second Affiliated Hospital of Zhejiang University School of Medicine

Country: China

ID: GA180

Development of a novel hydroxyl dendrimer SPECT tracer, 111In-D6-B483, for selective imaging of brain tumors

Jeffrey Cleland, Ashvattha Therapeutics, jeff@avttx.com

Category: Oncology

Abstract Body : Background: Previous studies of hydroxyl dendrimers (HDs) have demonstrated uptake in tumor associated macrophages and microglia (TAMs) with selectivity superior to antibodies in animal models of orthotopic glioblastoma multiforme (GBM) [1,2]. The initial efforts to develop 111In-D6-B483, a HD with covalently linked DOTA attached to the surface hydroxyl groups, indicated the potential for targeting orthotopic GBM in a mouse model but required further optimization for clinical use [3]. Current approaches for imaging of GBM rely on magnetic resonance imaging (MRI) to diagnose and grade the glioma status. 111In-D6-B483 has the potential to quantify the degree of TAM involvement that may correlate to the severity of the glioma. In addition, D6-B483 may be used for radiotherapy using 90Y in place of 111In. HDs have been observed to be retained in TAMs for up to one month after a single administration providing a local reservoir of radiation with limited systemic exposure (systemic clearance within 2 days). Methods: The synthesis of D6-B483 was achieved in 2 reaction steps. During the first synthetic step, partial propargylation of the dendrimer was achieved using sodium hydride and propargyl bromide. In the second step, azide-terminated DOTA was attached to propargyl dendrimer to yield D6-B483. For the synthesis of Cy5 labeled dendrimer, 1-2 propargyl functional groups on dendrimer were reacted with Cy5 azide to achieve Cy5-D6-B483. Cy5 labelled D6-B483 with either 2-3 or 8-10 DOTA (10 mg/kg) was administered IV to mice. Mice (3/timepoint) were sacrificed at 15 min, 4, 24, 48, and 96 h post-dose. Amount of Cy5-D6-B483 was measured in kidney and liver after tissue homogenization and extraction [1]. D6-B483 was mixed with 111InCl3 heated to 85oC to yield a labeling efficiency of 73%. Using centrifuge membrane system (3kDa cut off), the product was buffer exchanged to remove free 111In and formulated for injection in PBS. The final product had a radiochemical purity of 96%. Twenty female mice were implanted with 106 GL-261-luc2 cells by stereotactic intracranial (IC) surgery. Brain tumor size and location was measured by bioluminescence (BLI) to confirm tumors were between 15 to 60 mm3 prior to dosing. A separate group of 8 mice were implanted subcutaneous (SC) with 106 GL-261-luc2 cells and dosed once tumors were between 125 to 350 mm3 (caliper measurements). All mice received a single IV dose of 111In-D6-B483 (~230 μCi, 45 μg) and SPECT/CT images were obtained at 3-6, 24, 48, 72 and 96 h post-dose. Within 24 h after terminal sacrifice, gamma counting of tissues was performed. Results: HDs have previously been demonstrated in animals and humans to be renally secreted with minimal liver uptake [4]. D6-B483 with 2-3 DOTA had less exposure to the liver than D6-B483 with 8-10 DOTA with comparable kidney exposure. Stability of the 111In-D6-B483 in mouse serum out to 4 days was greater than 90%. Bioluminescence imaging was used to enroll 12 IC tumor and 4 SC tumor mice into the study. SPECT/CT imaging showed relatively high uptake of 111In-D6-B483 in the IC and SC tumors (approximately 15%ID/g and 8% ID/g respectively) compared with approximately 1%ID/g in contralateral brain. 111In-D6-

B483 persisted in the tumors for at least 96 h consistent with the previous study [3]. Conclusion: 111In-D6-B483 is a targeted and highly selective SPECT tracer for non-invasive imaging of brain tumors enabling precise quantitation of HD uptake and corresponding TAM involvement. 111In-D6-B483 is currently being developed for a Phase 1 study in GBM and metastatic brain cancer patients.

References: 1. Liaw et al, Bioeng Transl Med 2020; 5(2): 1-12 2. Cleland et al, Cancer Res 2020; 80(16 Suppl): Abstract 679 3. Cleland et al, Clin Cancer Res 2021; 27(8Suppl): Abstract PO-097 4. Lesniak et al, Mol. Pharmaceutics 1013; 10: 4560-4571

Image/Figure: https://s3.amazonaws.com/amz.xcdsystem.com/1E8A4501-BB41-A02A-1D3B9882B798BFAA_abstract_File10351/GA180_ImageFigure_0513035030.pdf

Image/Figure Caption: (A) Percent injected dose of Cy5-D6-B483 2 DOTA per gram (% ID/g) in kidney and liver after single IV injection (mean ± SD); (B) SPECT image of IC tumor (Arrow) at 24 hr after single IV 111In-D6-B483 injection; (C) SPECT image of SC tumor (Arrow) at 24 hr after 111In-D6-B483 injection; (D) Percent injected dose of 111In-D6-B483 per gram (%ID/g) in IC tumor, contralateral brain in mice with IC tumor or SC tumors over time (mean ± SEM).

First Name: Jeffrey

Last Name: Cleland

Email: jeff@avttx.com

Organization: Ashvattha Therapeutics

Country: United States

ID: GA181
Automatic Design of Quantitative and Rapid Molecular MRI Protocols using an AI-Based Approach

Or Perlman, Massachusetts General Hospital and Harvard Medical School, operlman@mgh.harvard.edu

---

Category: Computational & Data Science

Abstract Body : Introduction: Chemical exchange saturation transfer (CEST) is a molecular MRI technique, capable of amplifying and detecting the signals associated with millimolar concentrations of various biological compounds and metabolites (1). The potential benefit of using this contrast mechanism was demonstrated in a variety of applications, including cancer detection and grading (2), stroke characterization, muscle metabolism imaging, and kidney disease monitoring (3). However, the qualitative nature of the typical CEST analysis metric, and the long acquisition times required, constitute a barrier for clinical translation. Moreover, the unique biophysical characteristics of each metabolite/compound of interest, mandate a careful and exhaustive design of the CEST-MRI acquisition protocols, which is further challenged by the large number of imaging parameters involved (4). Objective: The goal of this work was to develop an AI-based automatic method for designing rapid CEST-MRI acquisition protocols and simultaneously providing the associated quantitative reconstruction means. Methods: The CEST-MRI acquisition protocol was represented as a computational graph, allowing its optimization using auto-differentiation. The saturation block was realized using the analytical solution of the Bloch-McConnell equations (5) and the spin dynamics were calculated during excitation and relaxation, using the Bloch equations with a discrete-time state-space model (6). Finally, the resulting MR signals were mapped into CEST quantitative parameters using a fully connected deep reconstruction network. The resulting method, termed here as AutoCEST, was used for inventing quantitative bio-marker imaging protocols, each suitable for a particular clinically relevant compound/metabolite. Specifically, rapid acquisition protocols were automatically generated for amide, amine, aliphatic relayed nuclear Overhauser enhancement (rNOE), phosphocreatine, and Iohexol. The resulting protocols were initially validated in-vitro at 9.4T, using a variety of imaging phantoms assembled from the above-mentioned compounds, and also compared to an unoptimized CEST MR-fingerprinting protocol (7) of similar length. Next, AutoCEST was used for inventing two in-vivo oriented acquisition protocols, aimed for obtaining quantitative biomarker maps of protein and lipid (via the rNOE compound) and semisolid macromolecule concentrations (via the MT pool). A healthy mouse and a tumor-bearing mouse were then imaged at 7T and 9.4T using the automatically designed acquisition schedules. Results: The acquisition times required for the protocols generated by AutoCEST were 35s (Iohexol, amine, amide, MT), 49s (rNOE), and 71s (phosphocreatine). The quantitative reconstruction time for a 64x64 image slice was 15 ms, using a laptop equipped with 8 CPU cores. The output phantom compound concentration maps were in good agreement with the known solute concentration (RMSE for Iohexol and phosphocreatine: 2.63 mM, Pearson's correlation $r>0.97$ between amide, amine, and rNOE with BSA concentrations). The resulting exchange rates were in agreement with known literature values and pH. The comparative MR-

fingerprinting protocol demonstrated a poor quantification ability, highlighting the importance of automatic optimization. The reconstructed in-vivo semisolid lipid/macromolecule MT volume fractions were lower in the cortex compared to a white-matter region of interest (ROI), as expected. The in-vivo rNOE volume fraction was significantly lower at the tumor compared to the contralateral ROI (two-tailed t-test, p Conclusions: AutoCEST can automatically generate rapid CEST/MT acquisition protocols that can be rapidly reconstructed into quantitative parameter maps, potentially serving as a clinically useful molecular imaging technique.

References: 1. Van Zijl et al., Neuroimage 168 (2018): 222-241. 2. Zhou et al., Journal of Magnetic Resonance in Imaging, 50.2 (2019): 347-364. 3. Pavuluri et al., Science advances 5.8 (2019): eaaw8357. 4. Perlman et al., Magnetic resonance in medicine 83.2 (2020): 462-478. 5. Zaiss M, et al., NMR in Biomedicine 28.2 (2015): 217-230. 6. Zhu et al., ISMRM (2018). 7. Cohen et al., Magnetic resonance in medicine 80.6 (2018): 2449-2463. 8. Zaiss M, et al. Neuroimage 112 (2015) 180-188.

First Name: Or

Last Name: Perlman

Email: operlman@mgh.harvard.edu

Organization: Massachusetts General Hospital and Harvard Medical School

Country: United States

ID: GA182

Acute exposure to e-cigarette vapor promotes neutrophil-platelet aggregation in murine pulmonary microvasculature

Hunter Snoderly, West Virginia University, htsnoderly@mix.wvu.edu

---

Category: Cardiovascular & Pulmonary

Abstract Body : Background & Rationale: Nearly 1 in 5 high school students and 1 in 20 middle school students reported using e-cigarettes (ECs) in the United States in 2020. It is well known that smoking can cause cardiovascular disease and thrombosis; however, few studies have investigated the adverse effects of EC use on the cardiovascular system, especially in the lungs. The public perception of ECs as a "safe" alternative to smoking and high rates of use, particularly amongst youth, demand that EC safety be rigorously studied in order to inform appropriate regulations. EC use has been linked to hypercoagulation and a persistent pro-inflammatory state. Neutrophils and platelets are known to undergo activation and proinflammatory phenotypic changes when exposed to EC vapor, and their aggregation promotes vascular occlusion and further inflammation. Thus, we hypothesize that platelet and neutrophil recruitment will be increased in mice exposed to EC vapor, and that higher rates of aggregate formation will be observed in the pulmonary vasculature of these subjects. Methods: To investigate lung vascular pathology following EC use, we have applied an innovative spinning disk confocal microscopy approach to visualize real-time interactions of blood cells in the lungs of live mice. Identifying neutrophil-platelet aggregates in the lung following EC vapor exposure would suggest that EC users may be at higher risk of atherosclerotic and thrombotic complications that could cause respiratory disease with chronic use. Mice (n=2) were subjected to 3 consecutive days of EC vapor inhalation using a Juul device with Virginia Classic Tobacco e-liquid (5% nicotine) for 3 hours each day for each topographical profile. 3 profiles were investigated: Profile 1- 1 puff/min imaged 6 hours later; Profile 2- 1 puff/2min imaged 1 day later; and Profile 3- 1 puff/min imaged 1 day later. Mice subjected to saline injection via tail vein constituted the control group. Mice were anesthetized to facilitate microsurgery enabling fluorescence microscopy of the living lung 24 hours after completion of the inhalation course. Neutrophils and platelets were labeled with fluorescently tagged antibodies to compare overall presence and aggregation within the lung microvasculature (Fig. 1). At least 15 fields of view (FOVs) were collected for each mouse and quantified using Nikon General Analysis. Results & Conclusions: Preliminary data suggest significant increases in platelet (Profile 2 only; 2.22-fold), neutrophil (up to 2.35-fold), and neutrophil-platelet aggregates (Profile 1 and 2; up to 1.88-fold) presence in mice exposed to EC vapor compared to untreated mice. Collectively, this illustrates that EC vapor induces a pro-inflammatory state in the pulmonary vasculature in as little as one day after short term exposure. These findings will prove useful in future studies seeking to model the consequences of long-term EC use, which will ultimately enhance both clinician monitoring of patients at risk of such complications and public awareness of the potential consequences of EC use. Future work will investigate EC effects on platelet clotting pathways using platelet aggregometry and will make use of in vitro assays to explore constitutive phenotypical changes to platelets and neutrophil isolated from mice exposed to EC vapor.

Image/Figure:

https://s3.amazonaws.com/amz.xcdsystem.com/1E8A4501-BB41-A02A-1D3B9882B798BFAA_abstract_File10351/GA182_ImageFigure_0512110719.png

Image/Figure Caption: Figure 1) Representative fields of view of living lung in A) sham and B) EC vapor exposed mice. Vasculature is labeled in green, neutrophils in blue, and platelets in pink. Arrows indicate blood flow relative to capillaries. Scale bars 20μm.

Full Name of Abstract's 1st Author : Hunter Snoderly

First Name: Hunter

Last Name: Snoderly

Email: htsnoderly@mix.wvu.edu

Organization: West Virginia University

Country: United States

ID: GA183
18F-FDG PET demonstrates altered metabolic brain networks in pediatric frontal lobe epilepsy patients: a graph theoretical analysis

Le Xue, Zhejiang University, 11918441@zju.edu.cn

Category: Neuroscience

Abstract Body : Background: Frontal lobe epilepsy (FLE) is considered to be the second most common type of focal epilepsies of childhood. Focal cortical dysplasias (FCD), highly associated with medication resistant epilepsy, are the most common cause of focal epilepsy in children. In recent years, focal epilepsy is increasingly considered as a disorder of abnormal brain network organization and function that affects large-scale brain networks beyond the epileptic zone. However, to the best of our knowledge, no study has investigated the metabolic brain networks of FLE patients. Objective: The goal of this study was to investigate topological alterations of metabolic brain networks based on 18F-FDG PET in pediatric FLE patients with and without FCD using graph theoretical analysis. Methods: Thirty-three pediatric FLE patients were retrospectively enrolled and divided into the FCD group (n = 15) and the non-FCD group (n = 18). Twenty-five age-matched controls were also enrolled. PET brain images were acquired on a PET/CT scanner, using 3D whole-head acquisition. First, all PET images were preprocessed using SPM12, and the intensity of images was further globally normalized. Afterwards, the mean intensity values of 90 regions were extracted using an AAL90-based atlas for each subject. Metabolic connectivity matrix (90×90) for each group was constructed by calculating Pearson's correlation coefficient of the mean intensity values between pair of regions across subjects. From the connectivity matrix, graph theoretical measures were calculated to investigate topological alterations of metabolic brain networks. Global network measures included small-worldness, global efficiency, local efficiency, clustering coefficient and modularity, while regional network measures included nodal degree, nodal efficiency and betweenness centrality. Betweenness centrality was calculated to identify hubs of the networks. Non-parametric permutation test was performed to compare the statistical differences of the network measures between groups. Results: Compared with controls, both FCD and non-FCD groups showed reduced connections across the whole networks, but the FCD group was much more pronounced. Regarding global network measures, both the networks in patients and controls showed a small-world property. Relative to the non-FCD group, the FCD group showed significantly decreased average degree, global efficiency, local efficiency, clustering coefficient and modularity than controls ($p < 0.05$). In terms of modular structures, there were two modules in controls, less than three modules in the FCD and non-FCD groups. Regarding regional network measures, compared with controls, the FCD group showed a large number of regions with decreased nodal degree mainly in the frontal and temporal lobes, and a large number of regions with decreased nodal efficiency and increased betweenness centrality mainly in the frontal lobe and subcortical structures. In contrast, the non-FCD group showed a few regions with decreased nodal degree mainly in the frontal lobe, and a few regions with decreased nodal efficiency and increased betweenness centrality mainly in the frontal lobe. Besides, hubs with high betweenness centrality gradually decreased from controls (n = 18) to non-FCD (n = 14) group and finally to FCD (n = 11) group. Hubs in

controls were mostly cerebral association regions and distributed over all four lobes. In the non-FCD group, hubs were also distributed over four lobes, but hubs in the frontal lobe were altered. In contrast, in the FCD group, the pattern of distribution of hubs was visibly disrupted, as the hubs were mainly concentrated in the frontal and temporal lobes. Conclusions: Pediatric FLE patients with FCD showed marked topological alterations in metabolic brain networks with network reconfiguration. These findings provide first evidence of altered topological organization of metabolic brain networks in pediatric FLE patients, with disruption of the coordination of cortical and subcortical structures.

Image/Figure:

https://s3.amazonaws.com/amz.xcdsystem.com/1E8A4501-BB41-A02A-1D3B9882B798BFAA_abstract_File10351/GA183_ImageFigure_0513060232.PNG

Image/Figure Caption: Figure 1. A: The weighted undirected metabolic connectivity matrices and visualized brain graphs of FCD group (left), controls (middle) and non-FCD group (right). The size of the node represented the relative nodal degree, and the shade of the edge represented the strength of the connection. B: Average degree, global efficiency, local efficiency, clustering coefficient, modularity and small-worldness in FCD group (red), and non-FCD group (yellow) and controls (green) at thresholds from 0.00 to 0.60. C: Modularity in FCD group (left), controls (middle) and non-FCD group (right). Nodes of the same color belong to the same module. D: Distribution of hub nodes with high betweenness centrality in FCD group (left), controls (middle) and non-FCD group (right). The size of the node represented the relative betweenness centrality. Nodes of the same color belong to the same module. Labels are the node abbreviations.

Full Name of Abstract's 1st Author : Le Xue

First Name: Le

Last Name: Xue

Email: 11918441@zju.edu.cn

Organization: Zhejiang University

Country: China

ID: GA184
A new generation of activatable MRI probe to detect myeloperoxidase activity and inflammation

Cuihua Wang, Massachusetts General Hospital, Wang.Cuihua@mgh.harvard.edu

---

Category: Immunology: Inflammation & Infection

Abstract Body : Background. Myeloperoxidase (MPO) is a highly oxidative and pro-inflammatory enzyme that can generate reactive oxygen/nitrogen species and cause tissue damage if overexpressed. MPO is implicated in multiple inflammatory diseases, and its activity can be noninvasively detected by MPO-Gd, an activatable MRI probe. However, the linear chelate used in MPO-Gd raised safety concerns and its relatively small increase in relaxivity after activation limited its translational potential. In this study, we aimed to develop a more stable and efficient MRI probe to detect MPO activity. Methods. We designed and synthesized a highly efficient myeloperoxidase activatable MRI probe (heMAMP) that contains the macrocyclic DOTA as chelating moiety and two MPO-activatable 5-hydroxyindole moieties linked through a rigid amide bond (Fig. 1). We validated the specificity and efficacy of heMAMP both in vitro and in vivo in rodent models of subcutaneous inflammation with wildtype and MPO-KO mice and unstable carotid atherosclerosis (tandem stenosis) with and without MPO inhibition (AZM198). We compared heMAMP with MPO-Gd and the conventional MRI agent DOTA-Gd. We also performed a molecular docking study to explore the mechanism underlying heMAMP's increased efficiency over MPO-Gd. Results. heMAMP demonstrated markedly higher Gd stability and greater relaxivity change after activation by MPO (Fig. 2). In a mouse model of subcutaneous inflammation, heMAMP demonstrated a 2-3-fold increased contrast-to-noise ratio (CNR) compared to MPO-Gd, and 4-10 times higher CNR compared to conventional DOTA-Gd. When the dose of heMAMP was reduced from 0.3 mmol/kg to 0.1 mmol/kg, the signal increase was comparable to that of MPO-Gd at 0.3 mmol/kg while little CNR increase was observed in MPO-KO mice, confirming the in vivo specificity of heMAMP (Fig. 3). The increased efficacy of heMAMP was further confirmed in vivo in a model of unstable atherosclerotic plaque where heMAMP showed a comparable signal change and responsiveness to MPO inhibition at 3-fold lower dosage compared to MPO-Gd. Molecular docking experiments revealed that a hydrogen bond formed intramolecularly between the two amide bonds which increases the rigidity of heMAMP and improved binding affinity of heMAMP to the active site of MPO compared to MPO-Gd. Conclusion: heMAMP is a potential translational candidate with superior stability and efficacy compared to MPO-Gd and other activatable analogues to detect MPO activity and inflammation.

References: C Wang, D Cheng, N Jalali Motlagh, EG Kuellenberg, GR Wojtkiewicz, SP Schmit, R Stocker, JW Chen. Highly efficient activatable MRI probe to sense myeloperoxidase activity. J. Med. Chem., ASAP, May 4. Doi: 10.1021/acs.jmedchem.1c00038.

Image/Figure:

https://s3.amazonaws.com/amz.xcdsystem.com/1E8A4501-BB41-A02A-1D3B9882B798BFAA_abstract_File10351/GA184_ImageFigure_0512105949.png

Image/Figure Caption: Figure 1. Chemical structures of heMAMP and MPO-Gd. heMAMP contains the macrocyclic DOTA as chelating moiety which confers it more thermodynamically stable and two MPO-activatable 5-hydroxyindole moieties linked through a rigid amide bond. Figure 2. The dynamic R1 ratios of heMAMP and MPO-Gd after activation by MPO. heMAMP demonstrated more efficient activation with >3 times higher R1 ratio compared with MPO-Gd when incubated with MPO, GOX and glucose over 180 min at 40 ℃ (n = 3, * p = 0.033, Kolmogorov-Smirnov test). Figure 3. MR imaging from pre-contrast and at ~60 min for heMAMP, DOTA-Gd, MPO-Gd in wild type mice and heMAMP in MPO-KO mice in a mouse model of subcutaneous inflammation. heMAMP demonstrated a 2-3-fold increased contrast-to-noise ratio (CNR) compared to MPO-Gd, and 4-10 times higher CNR compared to conventional DOTA-Gd. Little CNR increase was observed in MPO-KO mice, confirming the in vivo specificity of heMAMP (n = 3 for each group).

First Name: Cuihua

Last Name: Wang

Email: Wang.Cuihua@mgh.harvard.edu

Organization: Massachusetts General Hospital

Country: United States

ID: GA185
Molecular Imaging of PD-L1 expression using Fluorescence Labeled BMS1166 Probe at Multiscale level

YANG DU, CAS Key Laboratory of Molecular Imaging, Institute of Automation, Chinese Academy of Sciences, duyang@fingerpass.net.cn

---

Category: Oncology

Abstract Body : Nowadays, anti-PD-1/PD-L1 therapy has applied on lung cancer, melanoma, and breast cancer, and achieved certain breakthrough. However, the overall response rate is relatively low. To gain optimum curative effects and avoid serious side effects, it is important to evaluate the in vivo dynamic PD-L1 expression level before immunotherapy. Currently, the PET Imaging of PD-L1 are successfully tried but with certain limitations as radiotoxicity and short half-life. To promote the imaging tracers targeting PD-L1, the anti-PD-L1 antibodies, engineered proteins to nanobodies have been tried, but with longer blood circulation and clearance time, and hence they could not give an exact evaluation in a relatively short time. Thus small molecule targeted PD-L1 imaging are potential candidate for further study. Small molecule chemical entity of unlabeled precursors have many advantages, such as defined chemical structure, deeper tumor penetration, controllable pharmacokinetics and non-immunogenicity etc. In this study, we developed a BMS1166 targeted fluorescence molecular imaging probe BMS1166-Cy5.5 for the in vivo dynamic monitoring of PD-L1 expressing tumors and PD-L1 expression changes with different treatments. The in vitro flow cytometry and confocal imaging data showed that BMS1166-Cy5.5 can realize targeted binding of PD-L1 expressing 4T1, CT26 and B16F10 tumor cells. Moreover, the in vivo targeted fluorescence imaging was also tried on mouse 4T1, CT26 and B16F10 tumor xenografts, which also showed the targeted imaging of PD-L1 expressing tumors with different PD-L1 expressing levels. The ex vivo light sheet fluorescence microscopy also validated the in vivo observation and also input more detailed binding information between BMS1166-Cy5.5 to PD-L1 expressing tumor cells and stromal cells in tumor microenvironment. Moreover, we found that this imaging probe can be metabolized fast from the body with no obvious toxicity and also will not interfere the PD-L1 immunotherapy. Moreover, we can also evaluate the changes of PD-L1 expression level after anti-PD-L1 antibody treatment, which provide guidance for the immunotherapy.

Full Name of Abstract's 1st Author : Yang Du

First Name: YANG

Last Name: DU

Email: duyang@fingerpass.net.cn

Organization: CAS Key Laboratory of Molecular Imaging, Institute of Automation, Chinese Academy of Sciences

Country: China

ID: GA186
Unraveling the crosstalk between neutrophils, platelets, and EVs in breast-to-lung metastasis

Hunter Snoderly, West Virginia University, htsnoderly@mix.wvu.edu

---

Category: Oncology

Abstract Body : Background & Rationale: Breast cancer (BC) is the most diagnosed cancer amongst women, and metastasis drives the majority of deaths in these patients. The lung is a common metastatic site in all BC subtypes; thus, understanding how the pulmonary microenvironment fosters metastasis is of utmost importance. Crosstalk between neutrophils, platelets, neutrophil extracellular traps (NETs), and BC-associated extracellular vesicles (EVs) promotes the formation of the pre-metastatic niche. However, the exact cellular and molecular mechanisms mediating these interactions are not well understood. NETs form when neutrophils extrude their nuclei as web-like structures decorated with pro-inflammatory granular proteins. In cancer, NETs act as a scaffold allowing circulating tumor cells to escape the shear stresses of the vasculature and extravasate. NETs also enhance thrombosis, which itself facilitates metastasis. Increased platelet activation may also lead to enhanced NET formation as a positive feedback loop forms in which NETs activate platelets which then promote further neutrophil activation. A recent study found tumor EVs to be able to generate NET release; however, it was limited by examining EV-induced NETosis in an in vitro setting solely between neutrophils and cell-culture derived EVs. We hypothesize that platelets will be driven towards a prothrombotic state in the presence of tumor EVs, and that platelets and neutrophils will act synergistically to generate higher rates of NET formation through interaction with tumor EVs. Preliminary data show for the first time that these BC-associated EVs not only modulate NET formation but do so in a tumor progression-specific manner. BC-associated EVs isolated from tumorous mice with early metastases provoked the most NET formation. To investigate whether BC-associated EVs also modulate platelet phenotype, and if they can also indirectly modulate neutrophil behavior via platelet-dependent mechanisms, we will coculture isolated neutrophils and platelet rich plasma with or without BC-associated EVs. Methods: In this study, EVs were isolated via sequential centrifugation from the plasma of mice bearing orthotopic 4T1 murine mammary carcinomas 1, 2, 3, or 4 weeks post-tumor establishment. Neutrophils with or without platelets will be isolated from healthy mice and stimulated with BC-associated EVs ex vivo. EVs isolated from healthy mice will serve as controls. The potential of BC-associated plasma EVs to induce NETosis and/or platelet activation will be compared to 4T1 EVs derived from conditioned cell culture medium. The stimulatory effects of BC-associated EVs on platelets and neutrophils will be compared to our preliminary data in which neutrophils alone were stimulated with BC-associated EVs (Media alone or classical NET stimuli will serve as negative and positive controls, respectively. Confocal fluorescent microscopy will evaluate overall levels of NETosis and platelet/neutrophil association. Observed NETosis will be confirmed via ELISA assay detecting citrullinated histone 3 (a highly specific marker of NETosis) or via assays detecting DNA. Coagulation pathways by which EVs promote platelet activation will be revealed via platelet aggregometry. Finally, EV cargo and size characteristics will be determined using mass

spectrometry and nanotracking analysis, respectively. Results & Conclusions: Preliminary results indicate that plasma EVs isolated from week 3 of tumor progression enhance NET formation significantly more than unstimulated neutrophils (media alone) or healthy plasma EV-stimulated neutrophils. All other tumor plasma EVs had higher rates of NET formation than unstimulated neutrophils or those stimulated with healthy EVs; however, this was not significant. We expect the addition of platelets will further enhance NETosis in the presence of BC-associated EVs in general. This research will enable the development of new treatments targeting the mechanisms by which tumors communicate with the rest of the body.

Full Name of Abstract's 1st Author : Hunter Snoderly

First Name: Hunter

Last Name: Snoderly

Email: htsnoderly@mix.wvu.edu

Organization: West Virginia University

Country: United States

ID: GA187
In Vivo Spatial and 3D Monitoring of Specimens Using Content-Aware Neural Networks

Hossein Najafiaghdam, University of California Berkeley, hossein_najafi@berkeley.edu

---

Category: Computational & Data Science

Abstract Body : Introduction: Identification of tumor cell depth with simplistic 2D imagers has tremendous applications for intraoperative imaging and in vivo imaging. For example, in vivo monitoring of the dynamics of immune response within tumors is of key therapeutic importance in cancer therapy. While novel fluorescence imaging instruments and advanced optical techniques such as light-sheet microscopy have been effective tools for extracting 3D information from ex vivo specimens, they are not practical for in vivo imaging. On the other hand, smaller compact devices such as silicon-based electronic microchip imagers [1, 2], are able to achieve virtually seamless integration with surgical settings while still being minimally-invasive. However, due to their smaller form-factor, they exhibit a poorer performance compared to their cumbersome counterparts. While there are some tradeoffs that allow improving the performance of these small sensors, many are significantly costly and some are often not surgically compatible or practical. The tradeoff between miniaturization and image quality, as well as the ability to derive depth information from 2D images, can be partially overcome with computational methods that compensate for non-idealities such as the impact of point-spread-function using various optimization techniques such as deconvolution. However, these techniques are, at their core, only linear methods and are blind and indifferent to the content of the images beyond the raw data. Machine learning and neural networks can incorporate and embed knowledge of the cells and perform content-aware optimization and thus have the potential to outperform conventional optimization algorithms. In this work, we present a module that leverages the processing power of neural networks to extract spatial information and resolve the 3D distribution of cells in 3D specimens, providing location maps of cell clusters at any given depth. We also introduce a second micro-imager to the system on the other side of the specimen (fixed to be 1 mm thick) and quantitatively demonstrate how adding an additional micro-imager for a more uniform coverage of the space contributes to the accuracy of the module. Methods: The module is a 3-layer convolutional neural network that was trained on a dataset of randomly generated cell images. The dataset was generated using perlin noise, thresholding and resizing to replicate real-life images obtained with the micro-imager[3]. Upon training, the network is then able to extract the spatial position of every cell cluster in the 3D specimen from the single or pair of input images (depending on the number of micro-imagers being utilized). We evaluate the module in both conditions and report the improvement in prediction accuracy with the additional sensor. The output cell cluster maps are provided in the form of layers, one for each discretized layer of the 3D specimen, where every pixel in the layer is classified as either “cell” (1) or “no cell” (0). Results: Using only one sensor, the module is able to achieve a detection accuracy of 70% in the nearest layer, decreasing to 60% in the farthest layer from the sensor. When using two sensors, the module achieved an 88% accuracy in the nearest layers which decreased to only 82% when moving to the middle layers (farthest from

either sensor). A detection accuracy beyond 80% is practically high enough to make clinical assessments on changes in cell distribution. Conclusion: Here we presented a module that enables extraction of 3D information from 2D images obtained with miniaturized micro-imagers that can be seamlessly integrated with surgical instruments. The module performs content-aware extraction of cell cluster locations from 2D images and reconstructs the spatial distribution with minimal amount of data required, while achieving a detection accuracy of at least 82%, enough for clinical purposes.

References: [1] E. P. Papageorgiou, B. E. Boser and M. Anwar, “Chip-Scale Angle-Selective Imager for In Vivo Microscopic Cancer Detection,” IEEE Transactions on Biomedical Circuits and Systems, vol. 14, no. 1, pp. 91-103, 2020. [2] E. P. Papageorgiou, B. E. Boser and M. Anwar, “Chip-scale fluorescence imager for in vivo microscopic cancer detection,” 2017 Symposium on VLSI Circuits, 2017, pp. C106-C107. [3] K. Perlin, “An image synthesizer,” In Proceedings of the 12th annual conference on Computer graphics and interactive techniques (SIGGRAPH '85). Association for Computing Machinery, vol. 19, no. 3, pp. 287–296.

First Name: Hossein

Last Name: Najafiaghdam

Email: hossein_najafi@berkeley.edu

Organization: University of California Berkeley

Country: United States

ID: GA188
Real-Time Monitoring of Immune Response with an Implantable Fluorescence Image Sensor

Rozhan Rabbani, University of California, Berkeley, rozhan_rabbani@berkeley.edu

---

Category: Oncology

Abstract Body : Introduction: Fluorescence microscopy is critical in obtaining cellular-level information from targets inside the body. One key application is visualizing the tumor response to therapeutic procedures to help assess effectiveness of the therapy during the course of the oncological treatments. Real-time monitoring of multicellular-level changes provides key information regarding disease progression and immune response, which is of great importance in immunotherapy, a game-changing therapeutic unleashing the immune system to attack cancer [1]. While immunotherapy results in durable responses for patients who respond to the treatment, detailed cellular-level information from the immune response and tumor progression is essential to quickly pivot and personalize the therapy. Due to the low resolution (centimeter-scale) of the current oncological imaging modalities, the curative window for cancer is lost before a critical change in the tumor size is detected [2]. Moreover, invasive methods such as biopsies are impractical on a repeated basis. While state-of-the-art chip-scale image sensors provide high resolution microscopy, they can't be utilized in an implantable fashion or they require wiring and hence not practical for chronic real-time in vivo monitoring [3]. To address this problem, we propose a prototype for an implantable fluorescence microscope-on-chip detecting small clusters of fluorescence-labeled cells (via systemic injection of a fluorophore-labeled antibody) in real-time and wirelessly transmitting the data back to an external interrogator through an ultrasonic link. Miniaturization of the system is achieved by: (1) a fiber optic plate coupled with integrated angle selective gratings to eliminate bulky optical filters [4], (2) a single mm-sized piezoceramic for wireless power and data transfer obviating the need for external wiring and batteries and (3) a mm-sized laser diode replacing optical fibers to provide illumination inside the patient's body. Methods: The fluorescence signal from a cell labeled with fluorophores is proportional to the optical properties of the fluorophores and the excitation power [5]. To obtain a detectable signal from close to 200 cells (~200 fW) with typical optical properties of the fluorophore, Cyanine5.5-NHS Dye (Cy5.5), a mm-sized laser diode with a 30 mW/cm2 excitation power at 635 nm is chosen and is controlled by the imager. 8 distinct illumination intervals ranging from 16 ms to 128 ms can be hardcoded into the implant. To supply the nominal electrical power (36.3 mW) of the excitation source from the ultrasound waves, the implant operates with a 0.5% duty-cycled illumination. The implant takes 20 s to power-up and store enough energy for a subsequent imaging cycle with the optical source turned on. Once a single image is captured, the data is quantized and streamed out for all of the 1440 pixels (36x40 pixel array). The implant will be tested for wireless backscattering using the piezoceramic transceiver in future experiments. We evaluate the resolution of the system with a USAF resolution test target. Results: To verify the performance of the device, a fluorescent Cyanine5.5-NHS dye, distributed over a resolution test target with a fine spatial structure, is imaged and the corresponding image data (11.5 kbits/frame) is steamed out. Interrogated with an AC signal, the imager captures the selected structures with

single pixel resolution (~55 um) after a 20 s charge-up and a 64 ms integration making it possible to visualize comparable sizes of cell foci in real-time. Conclusion: This work presents a fully-contained implantable image sensor enabling real-time monitoring of the immune response at early stages of cancer in immunotherapy. We demonstrate, to the best of our knowledge, an unprecedented proof-of-concept wireless fluorescence microscope-on-chip with frame times close to 20-25 s capturing minute-scale cell movements without focusing lenses, fiber optics, batteries or any external wiring [6].

References: [1] S. A. Rosenberg, “Shedding Light on Immunotherapy for Cancer,” New England Journal of Medicine, vol. 350, no. 14, pp. 1461-1463, 2004. [2] J. V. Frangioni, “New technologies for human cancer imaging,” Journal of Clinical Oncology, vol. 26, no. 24, pp. 4012-21, 2008. [3] Y. Sunaga et al., “Implantable imaging device for brain functional imaging system using flavoprotein fluorescence” Japanese Journal of Applied Physics, vol. 55, no. 3S2, 2016. [4] E. P. Papageorgiou, B. E. Boser and M. Anwar, “Chip-Scale Angle-Selective Imager for In Vivo Microscopic Cancer Detection,” IEEE Transactions on Biomedical Circuits and Systems, vol. 14, no. 1, pp. 91-103, 2020. [5] M. A. Albota, C. Xu, and W. W. Webb “Two-Photon Fluorescence Excitation Cross Sections of Biomolecular Probes from 690 to 960 nm,” Applied Optics, vol. 37, pp. 7352-7356, 1998. [6] S. Qi et al., “Long-term intravital imaging of the multicolor-coded tumor microenvironment during combination immunotherapy,” eLife, vol. 5, pp. e14756, Nov. 2016.

First Name: Rozhan

Last Name: Rabbani

Email: rozhan_rabbani@berkeley.edu

Organization: University of California, Berkeley

Country: United States

ID: GA189
Quantitative chemical sensing of drug in scattering media with Bessel beam Raman spectroscopy

Nan Wang, Xidian University, nwang018@163.com

Category: Instrumentation

Abstract Body : The tissue scattering is a significant challenge for in vivo application of Raman spectroscopy, because it seriously affects the highly-sensitive detection and quantitative analysis of chemical substances in the scattering medium. We here presented a proof of concept for Raman spectroscopic sensing of chemicals in the scattering medium with a self-reconstructing Bessel beam. We first built the Bessel beam Raman spectroscope (BRS) and then compared its performance with the traditional Gaussian beam Raman spectroscope (GRS). We demonstrated the feasibility of this technique by detecting the Raman spectra of the standard samples and medicines. The results demonstrated that the homebuilt BRS had a superior capability in detecting the Raman spectra and quantitating the concentration of chemicals buried in the scattering medium. Compared with the traditional GRS, the BRS system had a superiority in terms of Raman spectrum detection and Raman peak recognition. Subsequently, this new technology was proved its application in the detection and quantification of chemical substances in scattering tissues by detecting acetaminophen buried in the scattering medium. Greater detection depth and better linear quantification capability were achieved than the conventional GRS. In summary, this study demonstrated a significant development towards the label free evaluation of drug in vivo.

Full Name of Abstract's 1st Author : Nan Wang

First Name: Nan

Last Name: Wang

Email: nwang018@163.com

Organization: Xidian University

Country: China

ID: GA190

A Novel Deep Learning Model for PET Image Synthesis Using Low-Dose 18F-FDG PET

Yu Fu, Zhejiang University, 12031066@zju.edu.cn

Category: Computational & Data Science

Abstract Body : Background: 18F-FDG, as the most widely used PET imaging tracer, enables the visualization of detailed metabolic processes in human bodies due to its ability to capture both the biochemical and physiological processes. In practice, the PET imaging needs a full dose radioactive tracer to obtain satisfactory diagnostic accuracy, which raises concerns about the potential over dose radiation exposure especially for those pediatric patients. Hence, researchers have tried to reduce the tracer dose as much as possible for the PET scans to mitigate this negative effect. The quality of low-dose PET (L-PET) images, containing more noises and artifacts, is inevitably lower than that of full-dose PET (F-PET) images, which hardly meet the requirements to conduct successful diagnosis. In order to tackle these problems, deep learning models (DLMs) have been developed to synthesis high-quality F-PET images using low dose ones, but how the inner frameworks and image radiation doses affect the performances of DLMs have yet to be fully investigated. Methods: Totally 32 pediatric epilepsy subjects were included. All 3D brain PET images were acquired on a whole-body hybrid PET/MR system. All of the L-PET images were reconstructed by list-mode, which included doses ranged from 5% to 40%. A novel DLM, which consists of a spatial deformable aggregation module (SDAM) and an enhanced generative adversarial network (E-GAN), was proposed in this study to synthesize high-quality F-PET images from the corresponding L-PET images. This DLM can take full advantage of spatial information among the consecutive L-PET slices and preserve various semantic details, encouraging less blurring and more realistic synthesized results. For a better comparison, we also reproduced three recent state-of-the-art image synthesis models, include Pixel2Pixel, CycleGAN and pGAN. Objective: The aim of this study was to quantitatively and qualitatively show if our model has a better synthesis performance on commonly used metrics (peak signal-to-noise ratio (PSNR), structural similarity index measurement (SSIM) and difference maps) over these image synthesis models (Pixel2Pixel, CycleGAN and pGAN). Results: Qualitatively, the synthesized F-PET images showed marked improvement in image quality compared with the L-PET images and visually resemble the ground truth image (true F-PET). From 5% dose to 40% dose, the PSNR and SSIM of synthesized F-PET images were gradually increased from 38.5 to 41.9 and 0.987 to 0.994, respectively. Leveraging the powerful SDAM and E-GAN, all the synthesized F-PET images derived from only 5% dose displayed delicate and precise textures. No matter for PSNR or SSIM, it’s easy to note that our model significantly outperformed than other three models in all levels of low doses. When considering the whole dose range of 5% to 40%, the Pixel2Pixel, which with the PNSR of 28.6 to 31.4 and SSIM of 0.893 to 0.939, performed worst in all the four models. CycleGAN had the comparable performances with Pixel2Pixel on PSNR at the dose range of 5% to 15% (from 28.4 to 30.8) but showed stronger ability in the dose range of 20% to 40% in both PSNR (from 32.0 to 35.1) and SSIM (from 0.949 to 0.971). The pGAN, with the PSNR of 36.2 to 39.1 and SSIM of 0.979 to

0.989, was the model with best performance other than our model. Besides, synthesized F-PET images based on our model also showed the lowest mean differences relative to the true F-PET images. Conclusions: The proposed DLM can boost the synthesis performance of F-PET from corresponding L-PET images. Our model outperformed three recent state-of-the-art DLMs (Pixel2Pixel, CycleGAN and pGAN) with the highest PSNR and SSIM, and the lowest values in pixel-scale difference maps. Due to its high accuracy, the proposed DLM may show excellent prospects in future clinical applications.

Image/Figure:

https://s3.amazonaws.com/amz.xcdsystem.com/1E8A4501-BB41-A02A-1D3B9882B798BFAA_abstract_File10351/GA190_ImageFigure_0512115906.png

Image/Figure Caption: Figure 1. A: Our proposed DLM, which consists of a spatial deformable aggregation module (SDAM) and an enhanced generative adversarial network (E-GAN). These 2-D FDG PET slices, along with their corresponding adjacent L-PET slices, are first feed to the (a) Offset Prediction Network to generate deformable offset fields. These offset fields are then used as the kernels of the (b) Spatial Deformable Convolution to generate the fused feature maps, leading to the enhanced target L-PET slice. Based on the (c) Process of Discrimination and Generation, the final synthetic F-PET images are generated. B: The ground truth F-PET image and the corresponding synthesized F-PET images using Pixel2Pixel, CycleGAN, pGAN and our model based on 5% dose L-PET images. As shown in the enlarged drawing, it's easy to find that synthesized F-PET image of our model is the closest to the ground truth F-PET image and it retains more semantic details (metabolic information) than other models. C: The pixel-scale difference maps of these synthesized F-PET images relative to corresponding ground truth F-PET images across the dose range of 5% to 40%. Relative to other three synthesis models, our synthesized F-PET images have the smallest difference maps. D: The mean SSIM and PSNR of synthesized F-PET images based on our model. The SSIM and PSNR of synthesized F-PET images were gradually increased from 0.987 to 0.994 and from 38.5 to 41.9, respectively.

Full Name of Abstract's 1st Author : Yu Fu

First Name: Yu

Last Name: Fu

Email: 12031066@zju.edu.cn

Organization: Zhejiang University

Country: China

ID: GA191

Towards Real-Time Dual-modal Photoacoustic Imaging and Ultrasound Localization Microscopy using Deep Learning

Shensheng Zhao, Electrical and Computer Engineering, University of Illinois, Urbana-Champaign, sz35@illinois.edu

---

Category: Instrumentation

Abstract Body : Ultrasound localization microscopy (ULM) breaks the acoustic diffraction limit, allowing super-resolved imaging with a deep penetration1. It relies on locating the fluctuated microbubbles in blood vessels over time to 'paint' the image. Once combined with photoacoustic imaging (PAI), it expands the imaging capability to map not only the fine micro vasculatures and blood flow from ULM, but also the expression of biomarkers from PAI. However, the long data acquisition time restricts ULM in clinical applications. Although much effort has been made to accelerate ULM, such as compressed sensing-based ULM2 and deep learning-based ULM3, all these prior methods cannot allow data acquisition shorter than one second even without considering processing time, which insufficient for real-time clinical applications. In this research, we aim to develop an accelerated ULM (termed A-ULM) using deep neural networks (termed A-net) towards real-time applications beyond one second. With A-ULM, we aim to demonstrate a real-time dual-mode photoacoustic/ULM for in vivo mouse imaging. Our approach starts with A-net, which is trained to reconstruct subwavelength ultrasound images from power doppler images and sparse localization images. Then, randomized singular value-based clutter filtering4 and cross correlation-based localization method5 are integrated with A-net to enable real-time ULM imaging. Finally, simultaneous A-ULM and PAI are implemented on a dual ultrasound/photoacoustic imaging system. We first evaluated the performance of A-net in simulated blood vessels using a series of sparse localization data reconstructed from different numbers of frames. The simulation results reveal that A-net can indeed extract the detailed blood vessel information from power doppler images and sparse localization images. It can reconstruct super-resolved vascular images with high quality (i.e., the similarity index with the real super-resolved image is higher than 0.9) by using only 5% of the total localization points. In other words, it can reduce the data acquisition time by 95%. For example, it will take 500 milliseconds to acquire a ULM image compared to 10 seconds without A-net. To demonstrate the in vivo imaging capability, we constructed a dual-modal imaging system that accommodates the data acquisition, image processing, and co-registration of both A-ULM and PAI. Our imaging system allows a frame rate up to 0.67 Hz to display a reconstructed ULM image from A-net when imaging a mouse kidney. During this process, only 0.5 seconds of data acquisition and 1.5 seconds of data processing are needed for A-net to reconstruct the ULM image. In contrast, the conventional ULM using the localization method requires 4.5 seconds in data acquisition and around 5 minutes for processing to build the same kidney micro-vasculature map. This drastic reduction in both acquisition and data processing provided by A-ULM and fast pre-ULM data processing allows the implementation of towards real-time super-resolution imaging in vivo.

References: 1 Errico, C. et al. Nature 527, 499–502 (2015) 2 Shu, Y. et al. IEEE Access 6, 39298–39306 (2018) 3 van Sloun, R. J. et al. in ICASSP 2019 - 2019 IEEE International Conference on Acoustics, Speech and Signal Processing (ICASSP) 1055–1059 (IEEE, 2019) 4 Song, P. et al. IEEE Transactions on Ultrasonics, Ferroelectrics, and Frequency Control 64, 706–716 (2017) 5 Song, P. et al. IEEE Trans. Ultrason., Ferroelect., Freq. Contr. 65, 149–167 (2018)

Image/Figure:

https://s3.amazonaws.com/amz.xcdsystem.com/1E8A4501-BB41-A02A-1D3B9882B798BFAA_abstract_File10351/GA191_ImageFigure_0513125038.png

Image/Figure Caption: Fig 1: The implementation of towards real-time ULM/PA imaging using random singular value-based clutter filtering (Doppler processing) , cross correlation-based localization and A-net. (a) The demonstration of data acquisition and data processing. Each frame includes data acquisition for ultrasound (Doppler and ULM) and photoacoustic in hardware. Simultaneously, software experiences the data transfer of last frame, beamforming, doppler and localization processing, the inference of A-net and the image display. In in vivo mice kidney experiment, the data acquisition time for each frame is 0.5s, and the processing time is 1.5 s, indicating the frame rate is determined by computation time due to the synchronization of the hardware and software, which is around 0.67 Hz. (b) A-ULM vascular image from a mouse kidney. A-ULM can be obtained from the input of the power doppler image and the sparse ULM. Fusion of A-ULM and the ground truth shows A-ULM (red) has a high similarity with ULM (green). (c) the improvement of image quality with increasing data acquisition time.

First Name: Shensheng

Last Name: Zhao

Email: sz35@illinois.edu

Organization: Electrical and Computer Engineering, University of Illinois, Urbana-Champaign

Country: United States

ID: GA192
A fluorescence endoscope for synchronizing imaging and spectrum collection

Tianyu Yan, Xidian University, yantianyu128@163.com

Category: Instrumentation

Abstract Body : Because of the advantages in specificity, sensitivity, high throughput, and cost-effectiveness, fluorescence imaging has been regarded as a powerful tool for biology and medicine. Combining with endoscopic technology, it can solve the problem of insufficient penetration depth of fluorescence imaging, and has been successfully applied to the clinical diagnosis of cancer, tissue hyperplasia and inflammation. However, most existing fluorescence imaging endoscopes can only obtain intensity information of specific wavelengths through filters, which leads to a high false positive and missed diagnosis rate in clinical applications. An effective solution for this problem is to collect complete spectral information in addition to the intensity information in the field of view. Therefore, we designed a fluorescence spectrum endoscope, which uses a beamsplitter to separate the collected signal light into the camera and the spectrometer to obtain complete spectrum information while performing fluorescence imaging. For endogenous fluorescence, we constructed mice tumor model, used autofluorescence imaging to quickly screen suspicious areas, and used autofluorescence spectrum to achieve qualitative analysis of lesions. In addition, for the exogenous fluorescence generated by the probe, we detected the spectrum shift due to changes in concentration, volume, and pH through the endoscope. The spectrum shift is short (With the in vitro experiments, our endoscope detected a good mathematical mapping relationship between the spectrum shift and the variables(concentration, volume, and pH). In general, our fluorescence spectrum endoscope can simultaneously acquire the fluorescence images and continuous spectrum with high spectral resolution, and is expected to achieve qualitative and quantitative analysis in clinical diagnosis.

Full Name of Abstract's 1st Author : Tianyu Yan

First Name: Tianyu

Last Name: Yan

Email: yantianyu128@163.com

Organization: Xidian University

Country: China

ID: GA193
Genetically Encoded Calcium Indicators for Ultrasound Imaging

Zhiyang Jin, California Institute of Technology, zyjin@caltech.edu

---

Category: Bioengineering, Synthetic Biology and Basic Biology

Abstract Body : Background: Imaging technologies enabling whole-brain observation of specific neural signals represent a “holy grail” of molecular imaging for neuroscience. While the most widely used neuroimaging approaches with fluorescent genetically encoded calcium indicators (GECIs) have enabled major neuroscience discoveries1, they fall far short of providing simultaneous whole-brain imaging of neural signals due to the physical limitation of light scattering2. Alternatively, ultrasound has unique advantages as a modality for neural imaging due to its ability to penetrate much deeper than light (several cm) while providing relatively high spatial and temporal resolution (3,4, a unique class of air-filled protein nanostructures derived from buoyant microbes, have been developed as reporter genes for bacteria and mammalian cells5,6, and most recently as the first acoustic biosensors for enzymatic activity7. Building upon the design of the first GV-based biosensors, we engineered GVs as the first ultrasonic genetically encoded calcium indicators (UGECIs), enabling calcium imaging in mammalian cells with ultrasound in vitro, and potentially brain-wide calcium imaging in the future. Innovation: The key innovation of this abstract is the development of the first genetically encoded calcium indicators for ultrasound. These sensors are reversible and sensitive in physiological conditions. In addition, this work describes the first user of ultrasound to dynamically sense molecular signals inside mammalian cells. Method: Our basic design of UGECIs relies on the fact that GVs with a softer protein shell undergo larger “buckling” deformations in response to ultrasound pulses8–10 ((persuasive data, Fig. S1a), resulting in the production of non-linear ultrasound signals, which can be selectively imaged with conventional ultrasound devices8,11. An alpha-helical protein called GvpC, bound to the GV shell surface, acts as a mechanical stiffener, controlling the extent of GV buckling and non-linear contrast9,11(persuasive data, Fig. S1b). The GvpC was modified to incorporate a peptide domain recognized by a calcium-dependent binding protein (persuasive data, Fig. S1c). Our hypothesis is that upon Ca2+-dependent binding between these two molecular elements, the engineered GvpC wound undergo an allosteric conformational change resulting in reduced GV shell stiffness, increased buckling, and the appearance of non-linear signal (persuasive data, Fig. S1d). UGECIs were characterized for their dynamic range, reversibility, sensitivity and kinetics in purified form, and also expressed in HEK293T cells, where the intracellular calcium sensing was tested. Results: UGECIs, in the purified format, showed significant enhancement in non-linear contrast in response to Ca2+ in 37˚C, and the contrast was reversed by addition of calcium chelator EGTA (persuasive data, Fig. S1e-g). This construct showed a half-maximal contrast at sub-micromolar concentration of Ca2+ in 37˚C in vitro (persuasive data, Fig. S1f). Furthermore, UGECIs were expressed transiently in HEK293T cells and these cells showed calcium-dependent ultrasound contrast. Control cells expressing UGECIs with disabled calcium binding domains did not respond to Ca2++ (persuasive data, Fig. S1h). Impact: These results provided

the first demonstration of genetically encoded calcium indicators for ultrasound, making it possible to conduct ultrasound calcium imaging on mammalian cells.

References: 1. Weisenburger, S. & Vaziri, A. A Guide to Emerging Technologies for Large-Scale and Whole-Brain Optical Imaging of Neuronal Activity. Annual Review of Neuroscience 41, 431–452 (2018). 2. Girven, K. S. & Sparta, D. R. Probing Deep Brain Circuitry: New Advances in in Vivo Calcium Measurement Strategies. ACS Chemical Neuroscience 8, 243–251 (2017). 3. Shapiro, M. G. et al. Biogenic gas nanostructures as ultrasonic molecular reporters. Nat. Nanotechnol. 9, 311–316 (2014). 4. Lakshmanan, A. et al. Molecular Engineering of Acoustic Protein Nanostructures. ACS Nano 10, 7314–7322 (2016). 5. Bourdeau, R. W. et al. Acoustic reporter genes for noninvasive imaging of microorganisms in mammalian hosts. Nature 553, 86–90 (2018). 6. Farhadi, A., Ho, G. H., Sawyer, D. P., Bourdeau, R. W. & Shapiro, M. G. Ultrasound imaging of gene expression in mammalian cells. Science 365, 1469 (2019). 7. Lakshmanan, A. et al. Acoustic biosensors for ultrasound imaging of enzyme activity. Nat Chem Biol 16, 988–996 (2020). 8. Maresca, D. et al. Nonlinear ultrasound imaging of nanoscale acoustic biomolecules. Applied Physics Letters 110, 073704 (2017). 9. Cherin, M. et al. Acoustic behavior of Halobacterium salinarum gas vesicles in the high frequency range: experiments and modeling. Ultrasound in Medicine and Biology 43, 1016–1030 (2017). 10. Zhang, S. et al. The Vibration Behavior of Sub-Micrometer Gas Vesicles in Response to Acoustic Excitation Determined via Laser Doppler Vibrometry. Advanced Functional Materials n/a, 2000239. 11. Maresca, D., Sawyer, D. P., Renaud, G., Lee-Gosselin, A. & Shapiro, M. G. Nonlinear X-Wave Ultrasound Imaging of Acoustic Biomolecules. Physical Review X 8, 041002 (2018).

Full Name of Abstract's 1st Author : Zhiyang Jin

First Name: Zhiyang

Last Name: Jin

Email: zyjin@caltech.edu

Organization: California Institute of Technology

Country: United States

ID: GA194

Hyperpolarized 13C magnetic resonance spectroscopic imaging detects metabolic alterations following mild repetitive traumatic brain injury

Caroline Guglielmetti, University of California San Francisco, caroline.guglielmetti@ucsf.edu

---

Category: Neuroscience

Abstract Body : Background Repetitive mild traumatic brain injury (rTBI) is being steadily recognized to increase the risk of neurodegenerative diseases. However, the mechanisms underlying the adverse effects of rTBI are largely unknown. Preclinical studies in mice have shown alterations in prefrontal cortex-dependent functions and hippocampal-dependent learning impairments following rTBI1-3. In the majority of cases, structural damage following rTBI is not seen on T2-weighted MRI1, hampering diagnosis and clinical care. There is thus a need for more sensitive noninvasive techniques to detect rTBI-induced brain changes thereby potentially predicting long-term cognitive outcomes. Hyperpolarized 13C magnetic resonance spectroscopic imaging (HP 13C MRSI) is a recent imaging method that enables detection of metabolic changes in moderate TBI models4,5. Objective/Hypothesis We investigated whether 13C MRSI of HP [1-13C]pyruvate and [13C]urea could detect metabolic impairment in vivo in a rTBI model. Methods Animals and mild rTBI induction: Eight weeks old male C57BL/6J mice were assigned to a Sham (n=10) or rTBI (n=10) group. rTBI was induced as previously described using the Closed-Head Impact Model of Engineered Rotational Acceleration (CHIMERA) device1,6. Timeline is shown in Suppl.Figure1A. Behavior: Risk-taking behavior was evaluated using the Elevated Plus Maze (EPM). MRI: A 14.1T MR scanner was used to acquire T2-w MRI and HP 2D 13C CSI (parameters shown in Suppl.Table.1). [1-13C]pyruvate and [13C]urea were co-polarized for ~1h. 13C data were acquired 16 seconds post-intravenous injection. MR analysis: Brain volumes were calculated using T2-w data. The area-under-the-curve of HP [1-13C]pyruvate, [1-13C]lactate and [13C]urea, and lactate/pyruvate ratios were calculated for cortex, subcortex and blood. Spectrophotometric assays: Pyruvate dehydrogenase (PDH) activity was measured in cortex and subcortex. Statistical analyses: Statistical significance was evaluated using unpaired Student t-test. *p 7. Syndromic plots were performed using the R syndRomics package8 and PC naming using loadings >|0.45|. Results Mild rTBI increased risk-taking behavior, reflected by longer time spent in open arms and center of the EPM (Figure1.A, p=0.0102). However, no differences in brain volumes were found between Sham and rTBI (Figure1.B). In cortical voxels, no changes in HP [1-13C]lactate production was observed. In contrast, HP [1-13C]pyruvate and [1-13C]urea were increased in rTBI (Figure1.C, p=0.0101; p=0.006, respectively). The subsequent HP [1-13C]lactate/pyruvate ratio was lower in rTBI (p=0.001), as visualized on the corresponding heatmaps. PDH, the enzyme that converts pyruvate into acetyl-coA, was decreased in prefrontal cortex (p=0.0044) and cortex (p=0.0375) of rTBI (Figure1.D). Given the multidimensional nature of risk-taking behaviors, MRI, and enzymatic assays, we examined the relationships between the measured variables using linear PCA to identify sets of covariance that self-organized into functionally related groups based on their cross-correlations, which yielded PC1 (33.8% variance, Figure1.E). PC1 suggests the

predictive nature of MRI for rTBI-induced chronic changes: decreases in lactate/pyruvate ratio correlates with increased risk-taking behavior. In subcortical voxels, HP metabolites were increased in rTBI, but the lactate/pyruvate ratio and PDH activity remained unchanged (Suppl.Figure1.B-C). Despite lack of group differences in subcortex, MRI's potential for predicting rTBI-induced changes were observed in this region (Figure1.E-yellow highlights). HP [13C]urea was increased in rTBI's blood and relationships with brain, enzymatic, and behavioral changes were also revealed in PC1. Conclusions rTBI induced long-lasting behavioral deficits invisible on T2w MRI. HP 13C MRSI detected cortical metabolic alterations characterized by decreased HP lactate/pyruvate ratios and PDH activity. Interestingly, HP pyruvate and urea were higher in rTBI, suggesting vascular, and/or blood-brain-barrier alterations9-11. Furthermore, PCA demonstrated the potential of HP 13C MRSI in predicting long-term rTBI-induced behavioral outcomes. Altogether, our results demonstrate that HP 13C MRSI can detect metabolic impairment following injury, and thus offer new possibilities for the detection of rTBI-induced damages in the clinical setting.

References: 1 Nolan, A. et al. Repeated Mild Head Injury Leads to Wide-Ranging Deficits in Higher-Order Cognitive Functions Associated with the Prefrontal Cortex. J Neurotrauma 35, 2425-2434, doi:10.1089/neu.2018.5731 (2018). 2 Krukowski, K. et al. Integrated Stress Response Inhibitor Reverses Sex-Dependent Behavioral and Cell-Specific Deficits after Mild Repetitive Head Trauma. J Neurotrauma 37, 1370-1380, doi:10.1089/neu.2019.6827 (2020). 3 Chen, H., Desai, A. & Kim, H. Y. Repetitive Closed-Head Impact Model of Engineered Rotational Acceleration Induces Long-Term Cognitive Impairments with Persistent Astrogliosis and Microgliosis in Mice. J Neurotrauma 34, 2291-2302, doi:10.1089/neu.2016.4870 (2017). 4 Guglielmetti, C. et al. In vivo metabolic imaging of Traumatic Brain Injury. Sci Rep 7, 17525, doi:10.1038/s41598-017-17758-4 (2017). 5 DeVience, S. J. et al. Metabolic imaging of energy metabolism in traumatic brain injury using hyperpolarized [1-(13)C]pyruvate. Sci Rep 7, 1907, doi:10.1038/s41598-017-01736-x (2017). 6 Namjoshi, D. R. et al. Merging pathology with biomechanics using CHIMERA (Closed-Head Impact Model of Engineered Rotational Acceleration): a novel, surgery-free model of traumatic brain injury. Mol Neurodegener 9, 55, doi:10.1186/1750-1326-9-55 (2014). 7 Haefeli, J. et al. A data-driven approach for evaluating multi-modal therapy in traumatic brain injury. Sci Rep 7, 42474, doi:10.1038/srep42474 (2017). 8 Torres-Espin, A. et al. Reproducible analysis of disease space via principal components using the novel R package syndRomics. Elife 10, doi:10.7554/eLife.61812 (2021). 9 Tagge, C. A. et al. Concussion, microvascular injury, and early tauopathy in young athletes after impact head injury and an impact concussion mouse model. Brain 141, 422-458, doi:10.1093/brain/awx350 (2018). 10 Bashir, A. et al. Increased severity of the CHIMERA model induces acute vascular injury, sub-acute deficits in memory recall, and chronic white matter gliosis. Exp Neurol 324, 113116, doi:10.1016/j.expneurol.2019.113116 (2020). 11 Abrahamson, E. E. & Ikonomovic, M. D. Brain injury-induced dysfunction of the blood brain barrier as a risk for dementia. Exp Neurol 328, 113257, doi:10.1016/j.expneurol.2020.113257 (2020).

Image/Figure: https://s3.amazonaws.com/amz.xcdsystem.com/1E8A4501-BB41-A02A-1D3B9882B798BFAA_abstract_File10351/GA194_ImageFigure_0513013816.pdf

Image/Figure Caption: (A) Schematic illustration of the EPM. Quantitative analyses revealed longer time spent in open arms and center of the EPM, reflecting increased risk-taking behavior

following rTBI. (B) Representative manual brain masking of T2-weighted MRI data (yellow: cortex, pink: hippocampus; green: ventricles; blue: subcortex) and corresponding volume sizes for Sham and rTBI. (C) T2 image and overlaid grid used for HP 13C MRSI analyses, red voxels indicate cortical areas and their corresponding HP 13C spectra for Sham and rTBI. Quantitative analyses of HP 13C (B) lactate, (C) pyruvate, (D) urea and (E) lactate/pyruvate for cortical areas. Representative HP metabolites heatmaps from a Sham and a rTBI mouse showing higher HP [1-13C]pyruvate and HP 13C urea levels in the entire brain of rTBI compared to Sham. Heatmaps of HP [1-13C]lactate/pyruvate ratio show lower values in cortical areas in rTBI. (D) PDH activity was decreased in cortical areas, including the prefrontal cortex and cortex, of rTBI compared to Sham. (E) Multidimensional analysis of risk-taking behaviors, MRI, and enzymatic alterations due to rTBI were examined using linear principal component (PC) analysis. PC1 accounts for 33.8% of the total variance and denotes relationships between risk-taking behaviors, MRI (brain and blood), and post-mortem enzymatic changes. Positive and negative correlations between the variables listed in PC1 are indicated by the arrows and corresponding numbers. As an example, decreases in lactate/pyruvate ratio correlates with increased risk-taking behavior. On a larger scale, we also observe that several HP 13C MRSI variables are predictive of behavioral outcomes (not just a single variable).

Full Name of Abstract's 1st Author : Caroline Guglielmetti

First Name: Caroline

Last Name: Guglielmetti

Email: caroline.guglielmetti@ucsf.edu

Organization: University of California San Francisco

Country: United States

ID: GA195
Identification of metastatic lymph nodes using indocyanine green fluorescent images

Kyungsu Kim, Korea University, k_gangter@korea.ac.kr

Category: Oncology

Abstract Body : Background: The complete resection of tumor and metastatic lymph node (MLN) is important to reduce the recurrence rate of cancer and improve the quality of life in patients with solid malignancies. Recently, near-infrared (NIR) fluorescence imaging technology with indocyanine green (ICG) has been promoted to visualize of the tumor and its resection margins in clinical practice intraoperatively. Objective: Since there are no studies evaluating the ability of intravenous ICG to detect MLN, we aim to use preclinical and clinical studies to explore the feasibility of intravenous ICG to detect MLN and tumor. Patients: A total of 15 patients (13 with lung cancer and 2 with esophageal cancer) were enrolled this study. The patients were 7 males and 8 females, and the average age was 66 ± 10 years (49-84 years). In lung cancer, 11 cases were adenocarcinoma and 2 cases were squamous cell carcinoma, and the tumor diameter was 2.2 ± 1.0 cm (range 0.9-3.9 cm). According to the 8th edition of the TNM staging system, 5 cases were stage IA, 3 cases were stage IB, and 4 cases were stage IIB. In esophageal cancer, all patients were squamous cell carcinoma with stage IIIB, and the tumor diameters was 10 cm and 3.7 cm, respectively. Methods: To evaluate the ability of ICG to detect MLNs, we established four C57BL/6 mouse footpad tumor models using Lewis lung carcinoma-green fluorescent protein (LLC-GFP) cell line. ICG (5 mg/kg) was injected into the tail vein, and the distribution in tumor and lymph nodes (LNs) was detected by NIR fluorescence imaging system at 12 hours. In clinical studies, patients were administered with ICG (2 mg/kg) intravenously 12 hours before surgery, and the tumor and LNs were detected with the NIR fluorescence imaging system. The fluorescence signal intensities of the target region were measured using the fluorescent signal of tumor-to-normal ratio (TNR). Results: We evaluated the ability of ICG to detect MLN by comparing the TNR of MLN and normal lymph nodes (NLN). The TNR of tumor and MLNs was significantly higher than normal NLN in mice ($p=0.0015$ and $p=0.038$, respectively). In the fluorescence microscopy image, ICG is distributed in the metastatic site with GFP signal. In patients, a total of 268 LNs, ICG fluorescence signals in LNs have investigated 52 LNs which were selected based on preoperative CT and PET/CT LNs with suspected metastasis, as well as hilar and lobe-specific LNs. Within those 52 LNs, there were 33 LNs with no fluorescent signal confirmed no metastasis. 10 of the rest 19 LNs had metastases, 5 of which were not detected by CT or PET/CT. 9 of 19 LNs showed false positives which were consistent with the results of CT and PET/CT. The TNR of primary cancer and MLN was significantly higher than NLN ($p=0.0001$ hand $p=0.0002$, respectively), and there was no significant difference between PC and MLN. Conclusion: Intravenous injection of ICG can not only successfully detect tumors, but also MLN. This research can provide accurate information for tumors and MLN by fluorescence signals during surgery to achieve minimal resection. These findings offer the potential to prevent unnecessary resection by accurately identification from NLN and precisely resect the MLNs without missing them.

Image/Figure:

https://s3.amazonaws.com/amz.xcdsystem.com/1E8A4501-BB41-A02A-1D3B9882B798BFAA_abstract_File10351/GA195_ImageFigure_0513022633.png

Image/Figure Caption: Figure 1. Detection of metastatic lymph node by NIR fluorescence imaging system with ICG, and the ex vivo study. Figure 2. CT, PET, NIR fluorescence, and pathological images for each patient group. Figure 3. Representative NIR fluorescence image & fluorescent signal of tumor-to-normal ratio (TNR).

Full Name of Abstract's 1st Author : Kyungsu Kim

First Name: Kyungsu

Last Name: Kim

Email: k_gangter@korea.ac.kr

Organization: Korea University

Country: South Korea

ID: GA196
Monitoring macrophage burden using an apoA-1 based PET tracer

Geoffrey Prévot, Icahn School of Medicine at Mount Sinai, geoffrey.prevot@gmail.com

---

Category: Immunology: Inflammation & Infection

Abstract Body : Lipoproteins are natural nanostructures with essential roles in cell function, metabolism, and disease1,2. High-density lipoproteins (HDL), predominantly composed of phospholipids and apolipoprotein A1 (apoA-I), play a crucial role in regulating the immune system. For example, HDL mediates cholesterol efflux from macrophages3,4. Previous work has shown that radiolabeled reconstructed HDL can be used to noninvasively study macrophage-rich inflammatory lesions, such as tumors and atherosclerotic plaques5–7. Here, a radiolabeled apoA-I fragment was developed to monitor macrophage burden by PET imaging. The terminal cysteine of this apoA-I mimetic was functionalized with the chelator deferoxamine (DFO) and subsequently radiolabeled with 89Zr (89Zr-apoA-I mimetic, Fig 1A). This compound's avidity for HDL was assessed in vitro by size exclusion chromatography (SEC) (Fig 1B). Pharmacokinetics and biodistribution of the 89Zr-apoA-I mimetic were evaluated by PET imaging and ex vivo gamma counting in wild-type mice (Figs 1C-D). Results revealed a half-life of 2.8 min (Fig 1C) and high uptake in liver, kidney, spleen, and bone marrow (Figs 1D and E). We then evaluated 89Zr-apoA-I mimetic's properties in two different mouse models of inflammatory diseases: myocardial infarction (MI), and melanoma. (Figs 1F-M). PET imaging 24 hours after 89Zr-apoA-I mimetic injection showed heterogeneous accumulation in the tumor (Fig 1F). The mean maximum standardized uptake value (SUVmax) of the tumor was 2.57 ± 0.66, while the reference (muscle) had a SUVmax of 0.61 ± 0.04 (Fig 1G). Imaging results were validated by ex vivo gamma counting (Fig 1H). PET imaging at 24 hours on MI mice revealed an infarct accumulation of 89Zr-apoA-I mimetic, SUVmax of 2.66 ± 0.42 compared to 0.54 ± 0.04 in the reference (Figs 1I and J). This specific infarct uptake was confirmed by gamma counting compared to the remote myocardium and the non-infarcted control mice (Fig 1K). To investigate cellular avidity of the apoA-I mimetic, a non-radioactive apoA-I mimetic (90Zr-apoA-I mimetic) was injected to MI and melanoma mice and cytometry time of flight (CyTOF) was then performed on the tumor and infarcted myocardium, respectively. (Figs 1L and M). We employed an extensive multicolor CyTOF panel that combined myeloid cell markers, including CD11b, Ly6G, and F4/80, as well as neutrophil marker Ly6G. The resulting high-dimensional dataset was visualized using the viSNE algorithm and indicated a Zr signal colocalized with F4/80 and CD11b positive cells, suggesting macrophage uptake. Combined, our results demonstrate 89Zr-apoA-I mimetic's applicability as an HDL-avid PET tracer that allows noninvasively monitoring macrophage burden in inflammatory disease.

References: 1. Mulder, W. J. M. et al. High-Density Lipoprotein Nanobiologics for Precision Medicine. Acc. Chem. Res. 51, 127–137 (2018). 2. Tulenko, T. N. & Sumner, A. E. The physiology of lipoproteins. J. Nucl. Cardiol. 9, 638–649 (2002). 3. Kaji, H. High-density lipoproteins and the immune system. J. Lipids 2013, 684903 (2013). 4. Catapano, A. L., Pirillo, A., Bonacina, F. & Norata, G. D. HDL in innate and adaptive immunity. Cardiovasc. Res. 103,

372–383 (2014). 5. Mulder, W. J. M., Strijkers, G. J., van Tilborg, G. A. F., Griffioen, A. W. & Nicolay, K. Lipid-based nanoparticles for contrast-enhanced MRI and molecular imaging. NMR Biomed. 19, 142–164 (2006). 6. Pérez-Medina, C. et al. PET imaging of tumor-associated macrophages with 89Zr-labeled high-density lipoprotein nanoparticles. J. Nucl. Med. 56, 1272–1277 (2015). 7. Mason, C. A. et al. An 89Zr-HDL PET Tracer Monitors Response to a CSF1R Inhibitor. J. Nucl. Med. 61, 433–436 (2020).

Image/Figure:

https://s3.amazonaws.com/amz.xcdsystem.com/1E8A4501-BB41-A02A-1D3B9882B798BFAA_abstract_File10351/GA196_ImageFigure_0513030103.jpg

Image/Figure Caption: Fig. 1 (A) DFO-functionalization and radiolabeling of the apoA-I mimetic (B) In vitro SEC spectrum of (from top to bottom) HDL only (UV detector), 89Zr only, HDL + 89Zr, 89Zr-apoA-I mimetic only, and HDL + 89Zr-apoA-I mimetic (radio detector). (C) 89Zr-apoA-I mimetic's blood half-life fitted with a biexponential decay function injected to C57BL/6 mice n = 5. (D-E) PET imaging (D) and (E) gamma counting quantification of 89Zr-apoA-I mimetic uptake in various organs 24 hours after injection in to C57BL/6 mice; n = 5. BM: bone marrow. %ID/g: Injected dose per gram of tissue. (F-H) PET imaging (F), mean maximum standardized uptake value (SUVmax) (G), and gamma counting quantification (H) of 89Zr-apoA-I mimetic on mice bearing melanoma tumor, 24 hours after injection; n = 5. (I-K) PET imaging (I), SUVmax (J), and gamma counting quantification (K) of 89Zr-apoA-I mimetic on MI mice, 24 hours after injection. (L-M) viSNE plots of viable leukocytes within the infarcted myocardium (L) or the tumor (M), based on CyTOF analysis 24 hours after intravenous 90Zr-apoA-I mimetic injection. Plots are color-coded for 90Zr and surface markers.

First Name: Geoffrey

Last Name: Prévot

Email: geoffrey.prevot@gmail.com

Organization: Icahn School of Medicine at Mount Sinai

Country: United States

ID: GA197
Reproducibility of 18F-FDG PET imaging in healthy and tumor-bearing mice

Kel Tan, University of Hong Kong, kelvintan.kvt@gmail.com

Category: Oncology

Abstract Body : Introduction: Preclinical PET imaging has become an important tool to non-invasively study the onset and progression of human diseases in small animals. Specifically, 18F-FDG is the most commonly used radiotracer to monitor tumor progression and transformation, and serves as a benchmark for evaluation of other imaging agents in mice. While clear, standardized protocols such as RECIST or EANM guidelines for tumor imaging have been created for clinical practice, protocols for preclinical imaging tend to vary widely, resulting in poor translatability of preclinical data (1). It is well recognized that dietary state, ambient temperature and mode of anesthesia will affect glucose metabolism in the background organs of mice, hence affecting the reproducibility across subjects (2). This study investigates the impact of the standardized imaging protocols on 18F-FDG biodistribution in healthy and tumor-bearing mice. In particular, the effect of fasting status on 18F-FDG tumor uptake is being explored. Methods: Six healthy and three MDA-MB-213-bearing mice (same strain, age and sex) underwent dynamic 18F-FDG PET at 40 min post-injection, before and after 16 h fasting. Mice were kept warmed and under isoflurane before 18F-FDG administration until the end of PET scans. Blood glucose was measured before and after PET. Images of 50 and 60 min post-injection were compared. Results: Using a standardized animal handling procedure throughout the PET scans i.e. warmed and asleep uptake under isoflurane), no distinct uptake differences were seen in the background organs (liver, lung and muscle) before and after 16 h fasting in healthy mice. When applying the same imaging protocol on tumor xenografts, the tumor demonstrated reasonably good uptake (2.46 ± 0.36 and 2.71 ± 0.42 %ID/g, respectively) at 60 min post-injection before and after 16 h fasting, with good tumor-to-muscle ratio observed regardless of dietary status (2.96 and 3.33, respectively) (Figure 1). No significant differences in tumor uptake at 50 and 60 min post-injection after fasting, although a lower uptake on muscle was seen at later timepoint (0.92 ± 0.10 and 0.81 ± 0.21 %ID/g, respectively), giving rise to a slightly higher the tumor-to-muscle ratio (2.77 and 3.33, respectively). Glucose levels were found to be varied widely across each mice although not significantly lower after fasting. Conclusions: A standardized PET imaging protocol is important to ensure reproducibility of tumor uptake and background organs across small animals.

References: 1. Mannheim JG, Mamach M, Reder S, Trxl A, Mucha N et. al., J Nucl Med. 2019;60:1483-1491. 2. Fueger BJ, Czernin J, Hilderbrandt I, Tran C, Halpern BS et. al., J Nucl Med. 2006;47:999-1006.

Image/Figure:

https://s3.amazonaws.com/amz.xcdsystem.com/1E8A4501-BB41-A02A-1D3B9882B798BFAA_abstract_File10351/GA197_ImageFigure_0513035624.png

Image/Figure Caption: Figure 1. (A) Representative PET/MRI images of 18F-FDG in athymic nude mice bearing subcutaneous MDA-MB-231 tumors at 50 minutes and 60 minutes post-injection. Blue arrows indicate the tumors. %ID/g of tumor and background organs in (B) healthy mice and (C) tumor xenografts before and after 16 h fasting. %ID/g, percentage of injected dose per gram.

First Name: Kel

Last Name: Tan

Email: kelvintan.kvt@gmail.com

Organization: University of Hong Kong

Country: Hong Kong

ID: GA198
In vivo SPECT imaging of steatohepatitis in NAFLD preclinical models using an anti-VCAM-1 nanobody

Pascale Perret, LRB INSERM U1039, pascale.perret@univ-grenoble-alpes.fr

---

Category: Systemic Diseases (Kidney, Liver and Pancreas)

Abstract Body : Introduction. The prevalence of non-alcoholic fatty liver diseases (NAFLD) is increasing worldwide and is estimated to be ~25%. NAFLD include a large spectrum of liver injuries from simple steatosis to non-alcoholic steatohepatitis (NASH) which affects around one-third of those patients. Whereas simple steatosis has a good prognosis, NASH is associated with worse long-term outcome, with progressive fibrosis as well as higher risk of cardiovascular disease. Liver biopsy remains the only diagnostic tool that can distinguish steatosis from NASH and grade disease severity [1]. So, NASH is categorized histologically, by the presence of steatosis, inflammation with hepatocytes injury (eg. ballooning), with or without fibrosis. Hepatic steatosis can be easily diagnosed noninvasively using ultrasound imaging, and the advanced progression of NAFLD can be evaluated using ultrasound elastography by quantifying liver fibrosis. However, despite the fact that advanced fibrosis imaging in NASH has been shown to be a relevant prognostic marker of liver failure and HCC, current imaging tools, are inadequate for early detection of steatohepatitis [1]. In particular, liver inflammation which is an early event in the process cannot be currently evaluated noninvasively; new imaging tools are then greatly needed. Vascular cell adhesion molecule-1 (VCAM-1) contributes to in situ recruitment of inflammatory cells in response to cytokines. Moreover, VCAM-1 was recently deemed to be a top upregulated gene and a key pathophysiological player in NASH [2]. In this study, we evaluated the expression of VCAM-1 in the liver of several NAFLD mouse models and the potential of SPECT imaging, using an anti-VCAM-1 nanobody - 99mTc-cAbVCAM1-5 - [3], to diagnose preclinical liver inflammation. Methods. First, C57BL6/J mice fed a choline deficient (MCD) or a standard diet (STD) were imaged with 99mTc-cAbVCAM1-5 (V-MCD) or with an irrelevant control nanobody (C-MCD) as a proof-of-concept. Then, models with metabolic NAFLD were employed: wild type fed a normal (Ctl) or high fat diet (WH), FOZ fed a high fat diet (FH) and C57BL6/J fed a choline-deficient (CDH) or -supplemented (CSH) high fat diet. NAFLD activity score (NAS) was obtained from liver histology analysis. The hepatic expression of VCAM-1 and proinflammatory markers was measured using RT-qPCR and VCAM-1 protein content using ELISA. 99mTc-cAbVCAM1-5 liver uptake was expressed as a concentration (SUV) or as a total uptake (%ID: % of injected dose). Results. In MCD mice, 99mTc-cAbVCAM1-5 specifically accumulated in V-MCD liver in comparison to C-MCD and STD (SUV: 0.48±0.11 vs 0.28±0.04 and 0.26±0.03, respectively, p WH and CSH were characterized by moderate steatosis score (1.2±0.7 and 0.8±0.4) and mild inflammation score (1.0±0.6 and 0.7±0.5), while FH and CDH exhibited severe steatosis (score of 3) and inflammation (score 2.7±0.5 and 3.0±0.0). VCAM-1 expression was higher in mice with NAFLD than in Ctl (WH: 1.40±0.70, FH: 7.61±2.28, CSH: 2.74±0.38 and CDH: 8.29±4.52 fold increase over Ctl) and correlated with the expression of MCP1 (r=0.77, p 99mTc-cAbVCAM1-5 total liver uptake was 3-fold and 6-fold higher in CDH and FH livers respectively than in

controls, strongly correlated with histological inflammation score (r=0.86, p steatohepatitis from simple steatosis with high performance (AUROC=0.89, p=0.035). Conclusions. 99mTc-cAbVCAM1-5 detects liver inflammation and identifies steatohepatitis in vivo noninvasively in NAFLD mouse models. Given that 99mTc-cAbVCAM1-5 is already in phase 1 clinical trial (NCT04483167) for atherosclerotic lesion imaging, these data have the potential for rapid translation and pave the way toward using 99mTc-cAbVCAM1-5 as a novel way to evaluate liver inflammation in the ever growing NAFLD population, a current unmet medical need.

References: [1] Castera L, et al. Gastroenterology. 2019, 156(5):1264-1281.e4. [2] Furuta K, et al. J Clin Invest. 2021, 131(6). [3] Broisat A, et al. Circ Res. 2012;110(7):927-937.

Image/Figure:

https://s3.amazonaws.com/amz.xcdsystem.com/1E8A4501-BB41-A02A-1D3B9882B798BFAA_abstract_File10351/GA198_ImageFigure_0513041832.jpg

Image/Figure Caption: Left: Total liver uptake (%ID) of 99mTc-cAbVCAM1-5 determined in vivo by SPECT imaging quantification (one-way ANOVA, n=6-8 mice/group). Right: Representative SPECT sagittal, coronal and transversal images of mice fed a high fat diet supplemented (CSH) or deficient (CDH) in choline. All Mean ± SD.

First Name: Pascale

Last Name: Perret

Email: pascale.perret@univ-grenoble-alpes.fr

Organization: LRB INSERM U1039

Country: France

ID: GA199
Can We Transform a Bioluminescent Reporter Gene into a Reporter for Radionuclide-based Imaging?

Natasa Gaspar, Erasmus MC, n.gaspar@erasmusmc.nl

Category: Bioengineering, Synthetic Biology and Basic Biology

Abstract Body : Background: Even though a combination of multiple reporter genes is a feasible approach for indirect cell labeling, therapeutic cells are often engineered using constructs that do not allow insertion of multiple reporter genes for imaging purposes. In this study we offer a solution to this unmet need by developing a small reporter gene that allows multimodality imaging. Our reporter gene system, derived from the 'NanoBiT' split-system [1, 2], enables bioluminescence (BLI) with radionuclide imaging using PET or SPECT. The LgBiT subunit, one of the split pieces of NanoLuc luciferase, was expressed and anchored in the membrane of cancer cells. Upon administration of small part of the 'NanoBiT' split-system, the HiBiT peptide tag (11 AA) [3], full NanoLuc luciferase will be reconstituted, upon co-localization with LgBiT subunit. Experimental design: We constructed a chimeric transmembrane reporter gene (TM-LgBiT) by fusion of LgBiT to a C-terminal transmembrane anchoring domain of platelet-derived growth factor receptor (PDGFR) and HA tag for membrane expression on cancer cells. Furthermore, we conjugated the HiBiT peptide to DOTA chelator via a 6-aminohexanoic acid (Ahx) linker and radiolabeled it for single-photon emission-computed tomography (SPECT), yielding [111In] In-DOTA-6-Ahx-HiBiT. In vitro characterization of reporter probes was followed by in vivo evaluation. We determined the characteristics of our reporter system using bioluminescence and radioactivity as detection techniques in mice bearing PC-3 tumors. Results: We established a reliable procedure for labelling HiBiT peptide with indium-111, using the [111In] In-DOTA-6-Ahx-HiBiT tracer we synthesized. Specific uptake of DOTA-6-Ahx-HiBiT was detected using bioluminescence imaging in vitro in cells, and in vivo from PC-3 tumors expressing TM-LgBiT reporter. After a SPECT/CT scan, we found specific [111In] In-DOTA-6-Ahx-HiBiT tracer uptake in mice implanted with target PC-3 positive cells (TM-LgBiT), which we confirmed using ex vivo biodistribution studies. Additionally, and importantly, uptake by tumours expressing TM-LgBiT was shown to be specific by blocking the interaction with excess of unlabeled peptide. Conclusion: We have generated and validated a novel multi-modality gene reporter system that has the potential to be applied in many fields of life sciences and we will further investigate its specificity for therapeutic cells tracking.

References: 1. Dixon, A.S., et al., NanoLuc Complementation Reporter Optimized for Accurate Measurement of Protein Interactions in Cells. ACS Chemical Biology, 2016. 11(2): p. 400-408. 2. Hall, M.P., et al., Engineered Luciferase Reporter from a Deep Sea Shrimp Utilizing a Novel 3. Schwinn, M.K., et al., CRISPR-Mediated Tagging of Endogenous Proteins with a Luminescent Peptide. ACS Chemical Biology, 2018. 13(2): p. 467-474.

Image/Figure:

https://s3.amazonaws.com/amz.xcdsystem.com/1E8A4501-BB41-A02A-1D3B9882B798BFAA_abstract_File10351/GA199_ImageFigure_0513042828.jpg

Image/Figure Caption: Figure legend: (A) In vitro evaluation of TM-LgBiT expression and HiBiT probe affinity. Luminescence signals were detected at the IVIS, validating the expression of reporter (TM-LgBiT) when expressed on the membrane or within the cytosol of PC-3 cells, upon administration of different concentrations of HiBiT probe. (B) Specific binding after 1h of incubation with 10-9 M of [111In] In-DOTA-6-Ahx-HiBiT in cells expressing TM-LgBiT in comparison to control cells. Shown results were performed in triplicates and values are indicated as means ± SD. (C) Longitudinal bioluminescence (BLI) imaging of HiBiT probe distribution in mice xenografts implanted with target (TM-LgBiT) positive tumors (left) versus control TM-LgBiT xenografts without HiBiT probe administration (right). (D) A strong and specific bioluminescent signal was detected at the tumour site, 30 min post peptide (DOTA-6-Ahx-HiBiT), and 1 minute upon substrate administration. (E) [111In]In-DOTA-6-Ahx-HiBiT SPECT/CT imaging and ex vivo biodistribution in PC-3 tumor xenografts. [111In] In-DOTA-6-Ahx-HiBiT showed higher uptake in the TM-LgBiT positive tumor (left flank, +) compared with the TM-LgBiT negative tumor (right flank, -) at 1h post i.v. administration of [111In] In-DOTA-6-Ahx-HiBiT tracer. (F) Ex vivo biodistribution study confirmed the [111In] In-DOTA-6-Ahx-HiBiT specificity.

Full Name of Abstract's 1st Author : Natasa Gaspar

First Name: Natasa

Last Name: Gaspar

Email: n.gaspar@erasmusmc.nl

Organization: Erasmus MC

Country: Netherlands

ID: GA200

Novel NODAGA-Based Gallium-68 Chelates for Mitochondrial Dysfunction: Synthesis and Biological Evaluation

Bradley Osborne, Imperial College London, b.osborne18@imperial.ac.uk

---

Category: New Chemistry, Materials & Probes

Abstract Body : Background: Changes in mitochondrial membrane potential (ΔΨm) can be directly linked to mitochondrial dysfunction in various disease states, such as cardiotoxicity and cancer.1 Clinically, myocardial perfusion imaging is routinely performed by means of Single Photon Emission Computed Tomography (SPECT), with lipophilic cations such as [99mTc]Tc-sestaMIBI and [99mTc]Tc-tetrofosmin being used.2,3 While these imaging agents delivery in tissues is perfusion-dependent, as cationic species, their retention within mitochondria is determined by ΔΨm-dependent trapping according to the Nernst equation.4 If the retention of such lipophilic cations could be corrected for perfusion, either by pharmacokinetic modelling or parallel injection of non-mitochondrially dependent perfusion imaging agents, these radiotracers could be repurposed to provide a non-invasive imaging index on mitochondrial dysfunction in evolving diseases such as cancer and cardiovascular diseases, as we have recently proposed.5 Positron Emission Tomography (PET) offers significant advantages over SPECT in terms of spatial resolution, sensitivity, and primarily, the capacity for dynamic imaging to allow for such pharmacokinetic perfusion correction modelling. Previous work in our group focussed on the development of fluorine-18 and gallium-68 lipophilic cations provided the foundation for this promising approach.6–9 Aims: (i) To develop a series of PET-compatible ligands for mitochondrial dysfunction, with differing alkyl-functionalisation motifs to provide opportunities for tuneable lipophilicity, as a means of optimising their pharmacokinetic profiles. (ii) Assess their capacity to report on ΔΨm by assessing their pharmacokinetic profiles in isolated perfused rat hearts. Results: We have synthesised and radiolabelled a series NODAGA-based radiotracers, with triarylphosphonium-functionalisation, with gallium-68 to form lipophilic cations. The tracers radiolabel with over 97 % RCY in significantly mild conditions, and exhibiting log D values of between -2.43 and -0.37. The candidate tracer exhibited less than 3 % retention in healthy hearts, which was not significantly diminished by mitochondrial depolarisation with CCCP. This work suggests that while this approach is promising, the lipophilicity of this class of tracers must be increased in order for them to exhibit more favourable cardiac uptake and retention.

References: 1 B. Kadenbach, R. Ramzan, R. Moosdorf and S. Vogt, Mitochondrion, 2011, 11, 700–706. 2 J. Maddahi, H. Kiat, K. F. Van Train, F. Prigent, J. Friedman, E. V Garcia, N. Alazraki, E. G. DePuey, K. Nichols and D. S. Berman, Am. J. Cardiol., 1990, 66, E55–E62. 3 J. D. Kelly, A. M. Forster, B. Higley, C. M. Archer, F. S. Booker, L. R. Canning, K. W. Chiu, B. Edwards, H. K. Gill and M. McPartlin, J. Nucl. Med., 1993, 34, 222–7. 4 M. P. Murphy, Biochim. Biophys. Acta - Bioenerg., 2008, 1777, 1028–1031. 5 Z. M. Safee, F. Baark, E. C. T. Waters, M. Veronese, V. R. Pell, J. E. Clark, F. Mota, L. Livieratos, T. R. Eykyn, P. J. Blower and R. Southworth, Sci. Rep., 2019, 9, 216. 6 A. Haslop, L. Wells, A. Gee, C. Plisson and N.

Long, Mol. Pharm., 2014, 11, 3818–3822. 7 S. P. McCluskey, A. Haslop, C. Coello, R. N. Gunn, E. W. Tate, R. Southworth, C. Plisson, N. J. Long and L. A. Wells, J. Nucl. Med., 2019, 60, 1750–1756. 8 A. J. Smith, P. J. Gawne, M. T. Ma, P. J. Blower, R. Southworth and N. J. Long, Dalt. Trans., 2018, 47, 15448–15457. 9 A. J. Smith, B. E. Osborne, G. P. Keeling, P. J. Blower, R. Southworth and N. J. Long, Dalt. Trans., 2020, 49, 1097–1106. 10 E. Mariotti, M. Veronese, J. T. Dunn, R. A. Medina, P. J. Blower, R. Southworth and T. R. Eykyn, EJNMMI Res., 2013, 3, 74.

Image/Figure: https://s3.amazonaws.com/amz.xcdsystem.com/1E8A4501-BB41-A02A-1D3B9882B798BFAA_abstract_File10351/GA200_ImageFigure_0513052448.pdf

Image/Figure Caption: Lipophilic and cationic NODAGA-based chelators for gallium-68 (top left), a photo of the Langendorff isolated perfused heart model, showing the unique setup of the triple gamma-detector system (top right),10 and representative time-activity curves demonstrating [68Ga]Ga-NODAGA-xy-TXP injection, uptake and washout in arterial inflow, heart and venous outflow (bottom). The first injection is into a healthy heart, the second into a heart infused with 600 nM CCCP.

Full Name of Abstract's 1st Author : Bradley Edward Osborne

First Name: Bradley

Last Name: Osborne

Email: b.osborne18@imperial.ac.uk

Organization: Imperial College London

Country: United Kingdom

ID: GA201
A longitudinal study evaluating treatment response to CAM intervention in ischemic stroke patients using MRI

Rama Jayasundar, Department of NMR, All India Institute of Medical Sciences, New Delhi, India, ramajayasundar@gmail.com

---

Category: Neuroscience

Abstract Body : Introduction Recent times have seen an alarming increase in the incidence of stroke1, a major cause of disability worldwide. With increasing interest in Complementary and Alternative Medicine (CAM), the current study has evaluated the effect of a CAM modality, namely ayurveda, in ischemic stroke patients using MRI and clinical assessment scores. Materials and methods The study was carried out with approval from the Institute Ethics Committee. Twelve first-ever stroke patients (18-60 years) were enrolled after obtaining written informed consent. The patients were assessed using MRI and clinical assessment scores such as The National Institutes of Health Stroke Scale (NIHSS), Modified Rankin Score (mRS) and Barthel Index at pre- and 6 months post-ayurveda intervention. 3D-T1 images were obtained at 3T using the following parameters: echo time 4.8 ms, repetition time 10 ms, slice thickness 1mm, voxel size- 0.75x0.75x0.75 mm3, acquisition matrix - 320x318x240, flip angle-80. FLAIR images were also obtained using the following parameters: voxel size-1x1x1mm3, acquisition matrix-22x19x380, TR/TE(ms)-4800/302.Standard FreeSurfer (v6.0) software was used for segmentation and measurement of cortical thickness and volume. Results Figure 1 (persuasive data) shows a representative MR segmentation data obtained before treatment (Fig. 1a) and 6 months post-ayurveda intervention (Fig. 1b) and the difference image (Fig. 1c). The latter shows the areas (outlined by circle)which have registered an increase in cortical thickness, indicating a positive response to the treatment. Figure 2 shows the corresponding clinical scores (NIHSS, mRS and Barthel Index) between pre- and post-intervention, reflecting the clinical improvement in the patient. Conclusion With increasing interest in the use of CAM2, there is a need for rigorous scientific evaluation of the same. This study has evaluated using MRI, the structural changes effected by ayurveda in ischemic stroke patients. The preliminary results have shown an increase in cortical grey matter thickness effected by ayurveda intervention in ischemic stroke patients. Although further in-depth analysis and studies are underway, the study has shown that MRI has a definite role to play in the scientific evaluation and validation of the effect of CAM.

References: References (1) Putaala J. Ischemic Stroke in Young Adults. Continuum (Minneap Minn), 26, 386-414, 2020. (2) Harini JA, et al. Ayurvedic Treatment of Acute Ischemic Stroke: A Prospective Observational Study. Glob Adv Health Med, 8, 2019.

Image/Figure:

https://s3.amazonaws.com/amz.xcdsystem.com/1E8A4501-BB41-A02A-1D3B9882B798BFAA_abstract_File10351/GA201_ImageFigure_0513054948.jpg

Image/Figure Caption: Figure 2: Percentage improvement in clinical assessment scores of the ischemic stroke patient whose MR segmentation data results are presented

First Name: Rama

Last Name: Jayasundar

Email: ramajayasundar@gmail.com

Organization: Department of NMR, All India Institute of Medical Sciences, New Delhi, India

Country: India

ID: GA202
Disrupted local and long-range resting-state functional connectivity in a rat model of ADHD revealed by functional ultrasound imaging

Benjamin Vidal, Theranexus, benjamin.vidal@theranexus.com

Category: Neuroscience

Abstract Body : Neuroimaging has been widely used to map physiopathological underpinnings in attention deficit hyperactivity disorder (ADHD). In particular, functional magnetic resonance imaging studies have suggested disruption of the resting-state functional connectivity in ADHD patients1. Besides, animal models remain a valuable tool to study the pathological mechanisms involved in ADHD and guide towards the development of new treatments2. Here we investigated the resting-state functional connectivity of the spontaneously hypertensive rat (SHR) as compared to the similar genetic background control strain (Wistar-Kyoto), using functional ultrasound imaging (fUS). This new technique, enabling fast measurement of cerebral blood volume changes (CBV), has been shown as promising to study brain functional connectivity in rodents with high spatiotemporal resolution and sensitivity3. One day after a thinned-skull surgery, SHR (n=8) and Wistar-Kyoto (n=7) rats were anesthetized using isoflurane and kept in a stereotaxic frame. Body temperature was maintained using a heated blanket and cardiac and breathing rates were continuously monitored during the imaging session. Doppler images were acquired every 2.8 seconds for 20 minutes with a small animal fUS system (Iconeus, France) over two brain slices (bregma +2.2 and -4.8mm), using a motorized displacement of the ultrasonic probe, to follow spontaneous CBV changes in the prefrontal cortex and the visual areas. After spatial coregistration and frequency filtering, functional long-range connectivity was estimated between pairs of regions from an anatomical atlas. The local connectivity was also investigated using regional homogeneity analysis, with temporal coherence measurement between each pixel and its neighbors4. As compared with the control strain, SHR rats displayed altered long-range functional connectivity between spatially distinct regions, with increases between the primary and the secondary cingulate cortex, and between the primary cingulate and the mediolateral secondary visual cortex. Conversely, the connectivity between the pretectal area and the brainstem was decreased. Additionally, SHR also displayed altered local connectivity, with significant increases of regional homogeneity in the secondary motor cortex and the mediomedial secondary visual cortex, along with significant decreases in the secondary cingulate cortex, the superior colliculus and the pretectal area. As a conclusion, we show that SHR rats display various functional connectivity alterations in different scales, with signs of hyperconnectivity among different cortical regions and especially the visual cortex, and signs of hypoconnectivity in subcortical regions of the visual system such as the pretectal area and the superior colliculus. These findings are consistent with previous clinical studies that showed similar alterations of functional connectivity in ADHD1 and demonstrate the potential of fUS for investigating animal models of CNS disorders for both local and long-range connectivity.

References: 1. Konrad K, Eickhoff SB. Is the ADHD brain wired differently? A review on structural and functional connectivity in attention deficit hyperactivity disorder. Hum Brain

Mapp. 2010 Jun;31(6):904-16. 2. Russell VA. Overview of animal models of attention deficit hyperactivity disorder (ADHD). Curr Protoc Neurosci. 2011 Jan;Chapter 9:Unit9.35. 3. Osmanski BF, et al. Functional ultrasound imaging of intrinsic connectivity in the living rat brain with high spatiotemporal resolution. Nat Commun. 2014 Oct 3;5:5023. 4. Zang Y, et al. Regional homogeneity approach to fMRI data analysis. Neuroimage. 2004 May;22(1):394-400.

Image/Figure:

https://s3.amazonaws.com/amz.xcdsystem.com/1E8A4501-BB41-A02A-1D3B9882B798BFAA_abstract_File10351/GA202_ImageFigure_0513060254.jpg

Image/Figure Caption: On the left: long-range functional connectivity between the regions of interest as defined by the SIGMA rat brain atlas. The bottom left corner shows the mean connectivity matrix for the Wistar-Kyoto strain; the top right corner shows the mean connectivity matrix for the SHR strain. For statistical comparisons, a Fisher Z-transformation was applied to the correlation coefficients before two-way ANOVA followed by multiple comparisons with a false discovery rate of 0.1 (*q-value < 0.1). On the right: regional homogeneity maps, showing the local functional connectivity (mean for each group). The maps were obtained by estimating the temporal coherence between each pixel and its neighbors. For normalization purposes, each individual map was converted into Z-score.

First Name: Benjamin

Last Name: Vidal

Email: benjamin.vidal@theranexus.com

Organization: Theranexus

Country: France

ID: GA203
Ultrasound Imaging of Tumor-Homing and Intestinal Bacteria Using Acoustic Reporter Genes

Marjorie Buss, California Institute of Technology, mbuss@caltech.edu

---

Category: Bioengineering, Synthetic Biology and Basic Biology

Abstract Body : Genetically engineered bacteria have the potential to outperform traditional diagnostics and therapeutics due to their ability to sense and respond to unique signals, access hard-to-reach areas of the body, and deliver therapeutics directly to these areas [1-2]. However, current tools to non-invasively monitor their activity and spatial distribution in vivo are limited. Optical imaging methods that use fluorescent and luminescent reporter genes suffer from the poor penetration depth of light in tissue [3], while nuclear imaging methods rely on radioactive tracers that have relatively low spatial resolution and require a complex synthesis pipeline [4-5]. Ultrasound imaging has the potential to address these limitations because it is a widely available technique that does not use ionizing radiation and has tissue penetration depth of several centimeters and spatial resolution below 100 microns [6]. Recently, the first genetically encoded ultrasound contrast agents based on gas vesicles, which are air-filled protein nanostructures that are naturally used by aquatic microbes to regulate their buoyancy, were developed to link ultrasound to gene expression in bacteria [7]. However, these first-generation acoustic reporter genes (ARGs) expressed too poorly under in vivo conditions to enable ultrasound imaging of bacteria in therapeutically relevant contexts. Here, we present a new and improved ARG construct that results in high levels of robust gas vesicle expression in the probiotic bacterium E. coli Nissle, and enables ultrasound imaging of these cells with high sensitivity using non-destructive pulse sequences. This second-generation ARG construct – bARGSer – uses genes derived from a different bacterial species and was incorporated into optimized gene circuits for gene expression monitoring. We demonstrate that with bARGSer, we can visualize the spatial distribution of engineered E. coli Nissle after they home to and colonize tumors upon systemic administration [8]. We also demonstrate that the engineered E. coli Nissle can be imaged with ultrasound when colonizing the gastrointestinal (GI) tract of mice. By enabling monitoring of the precise spatial location of engineered probiotic bacteria inside the body, this technology could greatly improve the development and eventual clinical use of this emerging class of microbial cell-based theranostics.

References: [1] Charbonneau, M.R., Isabella, V.M., Li, N. et al. Developing a new class of engineered live bacterial therapeutics to treat human diseases. Nat Commun 11, 1738 (2020). [2] Riglar, D., Silver, P. Engineering bacteria for diagnostic and therapeutic applications. Nat Rev Microbiol 16, 214–225 (2018). [3] Piraner, D.I., Farhadi, A., Davis, H.C. et al. Going Deeper: Biomolecular Tools for Acoustic and Magnetic Imaging and Control of Cellular Function. Biochem 56, 5202–5209(2017). [4] Kang, SR., Min, JJ. Recent Progress in the Molecular Imaging of Tumor-Treating Bacteria. Nucl Med Mol Imaging 55, 7–14 (2021). [5] James, M. L. & Gambhir, S. S. A Molecular Imaging Primer: Modalities, Imaging Agents, and Applications. Physiological Reviews 92, 897–965 (2012). [6] Maresca, D., Lakshmanan, A., Abedi, A., et al.

Biomolecular Ultrasound and Sonogenetics. Annu Rev Chem Biomol Eng 9, 229–252(2018). [7] Bourdeau, R., Lee-Gosselin, A., Lakshmanan, A. et al. Acoustic reporter genes for noninvasive imaging of microorganisms in mammalian hosts. Nature 553, 86–90 (2018). [8] Hurt, R. C.#, Buss, M.T.#, Wong, K., et al. Genomically Mined Acoustic Reporter Genes Enable On-Demand In Vivo Monitoring of Tumor-Homing Bacteria. bioRxiv 2021.04.26.441537 (2021) doi:10.1101/2021.04.26.441537. # Equal contribution.

Image/Figure:

https://s3.amazonaws.com/amz.xcdsystem.com/1E8A4501-BB41-A02A-1D3B9882B798BFAA_abstract_File10351/GA203_ImageFigure_0513060900.png

Image/Figure Caption: After homing to the necrotic core of tumors, engineered probiotic bacteria (E. coli Nissle) were induced to express optimized acoustic reporter genes (ARGs). Expression of these ARGs results in high levels of gas vesicle production (shown by the TEM images in the bottom right) that enable the bacteria to be imaged with ultrasound with high sensitivity and specificity (bottom left). Ultrasound images of bacteria correspond well with anti-E. coli staining of tissue sections (center left).

Full Name of Abstract's 1st Author : Marjorie T. Buss

First Name: Marjorie

Last Name: Buss

Email: mbuss@caltech.edu

Organization: California Institute of Technology

Country: United States

ID: GA204
Biofunctionalization of goat milk exosomes with folic acid by exosome engineering for oncological diagnosis

Desiré Herreros Pérez, Fundación para la Investigación Biomédica del Hospital Gregorio Marañón, Madrid, dherreros@hggm.es

---

Category: New Chemistry, Materials & Probes

Abstract Body : Introduction: Exosomes are described as nanometric extracellular vesicle (EV) with a key role in cell-cell communication and tumor-niche formation. Due to their nanosized and liposome-like structure, exosomes are explored as nanodevices for the development of new theragnostic applications.1,2 Among the ideal characteristics that make natural exosomes a promised nanoplatforms is the heterogeneity in their composition, which allow us to chemically modify their surface. This is known as "engineering of exosomes" and the aim is to improve the uptake of the nanovesicles in the targeted tissue, such as a tumor.2-6 The objective of this study is the enrichment of these natural nanoparticles with folic acid by the covalent functionalization of their surface and the in vitro and in vivo evaluation as diagnostic tool in oncology by optical imaging. Methods: Milk exosomes were isolated by ultracentrifugation and conjugated by two synthesis steps; an initial biological functionalization and further fluorescent labeling. For the initial bioconjugation, folic acid (0.1 mg) was activated in presence of EDC (0.06 mg) and sulfo-NHS (0.2 mg) at RT for 35 min and then, mixed with exosomes (30 μg) over night, at 4ºC. Further optical labeling of the folate-exosomes was performed in presence of Sulfo-Cyanine5 NHS ester (SCy5) in mild conditions (pH 8.5, 4ºC, 90 min). The purification of fluorescent Fol-Exo-SCy5 exosomes was performed using by Exo-spinTM columns. Biofunctionalized exosomes were characterized by TEM, NTA, Z-potential (ZP), MALDI-TOF MS and Fluorospectrometer. In vitro assays were performed in murine macrophages (RAW 264.7) and human cervical cancer (HeLa) cells by flow cytometry and confocal microscopy. Blocking assays were performed in presence of enriched medium folic acid (1 mg/mL). In vivo and ex vivo validation of nanoprobes by optical imaging was performed in nude HeLa xenograft tumor model (2x106 HeLa cells, 250 μL matrigel:DMEM). Imaging studies performed at 1h, 3h, 6h and 24h after i.v injection of the nanoconjugate (30 μg, 200μL PBS). Histological evaluation of tumor tissue was performed by immunohistochemistry (IHC). Results: TEM confirmed that Fol-Exo-SCy5 conserved their morphology, NTA revealed a slight increase of their size (149.8+/-1nm) and ZP a surface modification (-8.2+/-1mV). MS spectrum confirmed the incorporation of folic acid and SCy5 into the nanoparticles and fluorescence was confirmed by fluorimetry. In vitro studies revealed a fast uptake of the probe in RAW 264.7 while HeLa requires longer times for the probe uptake. Both cell lines confirmed the uptake reduction of the nanoprobe in presence of free folic acid (Fig 1). In vivo optical imaging in a HeLa xenographic model showed signals of Fol-Exo-SCy5 in tumor tissue even at short timepoints,1h. Ex vivo biodistribution at 24h revealed main accumulation in liver, tumor, lungs, uterus and kidneys. The tumor cells populations with overexpression of folate receptors (macrophages and tumor cells) were characterized by histology/IHC and correlated with the Fol-Exo-SCy5 signal (Fig 2). Conclusion: We have optimized a covalent method for bioengineering of natural exosomes with

folic acid. The full characterization of the nanoparticles confirmed the successful bioconjugation in the surface of the nanovesicles without modifying their morphology or size. In vitro results showed a selective uptake of Fol-Exo-SCy5 via folate receptors and preliminary in vivo and ex vivo results confirmed the ability of the nanoparticles to reach tumor tissue. Acknowledgement: This work was partially supported by Comunidad de Madrid (Y2018/NMT-4949 (NanoLiver – CM and S2017/BMD-3867 RENIM-CM, co-financed by European Structural and Investment Funds), A. Santos-Coquillat is grateful for financial support from Ministerio de Ciencia e Innovación, Instituto de Salud Carlos III Sara Borrell Fellowship grant CD19/00136.

References: 1. Luan X., et al. Engineering exosomes as refined biological nanoplatforms for drug delivery. Acta Pharmacol Sin. 2017; 38(6): 754-763.1 2. Munagala, R., et al. Bovine milk-derived exosomes for drug delivery. Can. Letters. 2016; 371(1): 48-61 3. Fernandez M., et al. Advances in targeting the folate receptor in the treatment/imaging of cancers. Chem. Sci. 2018, 9: 790 4. Poh S., et al. Selective liposome targeting of folate receptor positive immune cells in inflammatory diseases. Nanomedicine. 2018; 14: 1033-1043 5. Siwowska K., et al. Folate Receptor-Positive Gynecological Cancer Cells: In Vitro and In Vivo Characterization. Pharmaceuticals (Basel). 2017; 10(3): 72 6. Thommey P., et al. Folate-targeted nanoparticles show efficacy in the treatment of inflammatory arthritis. Arthritis Rheum. 2011; 63(9): 2671–2680.

Image/Figure:

https://s3.amazonaws.com/amz.xcdsystem.com/1E8A4501-BB41-A02A-1D3B9882B798BFAA_abstract_File10351/GA204_ImageFigure_0513061128.jpg

Image/Figure Caption: Figure 1. Physicochemical characterization of Fol-Exo-SCy5 and their uptake evaluation in vitro. Figure 2. In vivo and ex vivo Fol-Exo-SCy5 biodistribution in nude mice by optical imaging.

First Name: Desiré

Last Name: Herreros Pérez

Email: dherreros@hggm.es

Organization: Fundación para la Investigación Biomédica del Hospital Gregorio Marañón, Madrid

Country: Spain

ID: GA205

Silver-coated iron oxide nanoroses as a potential multi-functional theranostic nanomaterial for thrombosis

Karla Ximena Vazquez Prada, The University of Queensland, k.vazquezprada@uqconnect.edu.au

---

Category: Cardiovascular & Pulmonary

Abstract Body : Cardiovascular disease (CVD) is the leading cause of death worldwide. Thrombosis and its complications are responsible for 30% of deaths annually1. The limitations of current methods for diagnosing and treating thrombosis highlight the need to improve diagnosis and treatment strategies2. In this study, we designed and successfully synthesized a novel theranostic nanomaterial based on an iron core and an outer layer of silver with strong absorbance at the near-infrared wavelength. Elemental silver was grown on the surface of small iron oxide nanoparticles. The silver-coated iron oxide nanoparticles (AgIONPs) were stabilized with polyethylene glycol (PEG). For targeting purposes, the nanoparticles were conjugated with RGD, fibrin-binding peptide (FibPeps) and a single chain antibody (ScFv) targeting activated platelets. In vitro human clot binding assays showed that from the three binding ligands tested, ScFv has more specific binding to the clots. The nanoparticles exhibited good r2 relaxivity (30.1 mM-1s-1) at 9.4T and demonstrated its ability to darken T2-weighted signal of in vitro thrombus. In vitro and ex vivo PAI studies showed that AgIONPs enhanced the signal of in vitro thrombus in photoacoustic imaging, especially for excitation wavelengths in the near-infrared region. Laser-enhanced thrombolysis in vitro with human blood clots indicated that an enhanced effect of thrombolysis was observed with the nanoparticles in a dose-dependent manner. Furthermore, hemocompatibility assay on red blood cells and Presto Blue Viability assay on CHO cells suggested good biocompatibility of the nanosystem. Altogether, these results suggest that the nanosystem could potentially act as a multi-imaging theranostic nanomaterial for diagnosis and treatment of thrombosis.

References: 1.WHO. Cardiovascular diseases (CVDs). 2017. 2.Varna M, Juenet M, Bayles R, Mazighi M, Chauvierre C, Letourneur D. Nanomedicine as a strategy to fight thrombotic diseases. Future science OA 2015;1:Fso46.

Image/Figure:

https://s3.amazonaws.com/amz.xcdsystem.com/1E8A4501-BB41-A02A-1D3B9882B798BFAA_abstract_File10351/GA205_ImageFigure_0513063122.jpg

Image/Figure Caption: A,B,C) Characterization of the nanosystem showing TEM image of AgIONPs with irregular nanorose-like shape, absorbance in the near-infrared wavelength and EDS spectra illustrating the percentage of both metals in a AgIONP, resectively. D) T2 weighted images of phantom tubes and D) PA images of polyethylene tubes with AgIONPs showing an enhancement in the contrast signal with each increasing concentration. F) AgIONPs promotes

thrombolysis when exposed to 808 nm laser. G) Thermal images showing the increase in temperature and the AgIONPs-induced thermolysis of clot in a dose dependent manner.

First Name: Karla Ximena

Last Name: Vazquez Prada

Email: k.vazquezprada@uqconnect.edu.au

Organization: The University of Queensland

Country: Australia

ID: GA206
Single fluorinated agent for multiplexed 19F-MRI with micromolar detectability based on dynamic exchange

Nishanth D Tirukoti, Weizmann Institute of Science, deva-nishanth.tirukoti@weizmann.ac.il

---

Category: New Chemistry, Materials & Probes

Abstract Body : Introduction: The weak thermal polarization of nuclear spins limits the sensitivity of MRI, even for MR-sensitive nuclei as fluorine-19. This leads to the inability to map very low concentrations of targets using 19F-MRI, which thus raises the need to further enhance this platform's capabilities. Here, we employ the principles of CEST-MRI in 19F-MRI to obtain a 900-fold signal amplification of a biocompatible fluorinated agent, which can be presented in a "multicolor" fashion1. Capitalizing on the dynamic interactions in host-guest supramolecular assemblies in an approach termed GEST (guest exchange saturation transfer), we demonstrate that an inhalable fluorinated anesthetic can be used as a single 19F-probe for the concurrent detection of micromolar levels of two targets, with potential in-vivo translatability. Method: 19F-GEST NMR data were acquired on 9.4 T NMR with a pre-saturation pulse B1 (2.5μT/ 3s) applied prior to the 90o RF pulse with its frequency swept from Δω= +6.1ppm to Δω=-6.1ppm. 19F-GEST MRI of phantoms was performed using a CEST-RAREst sequence with the following parameters: B1 = 2.5μT/ 3000 ms, TR/TE=10000/2.93ms, RARE factor=18, 10mm slice, FOV=3.2×3.2cm2, matrix size=32×32, NA=120. 19F-GEST spectra were obtained after B0 correction and 19F-GEST maps were calculated using MTRasym analysis. In vivo experiments were performed on a horizontal 15.2 T scanner followed bilaterally injections of either H1 or H2 into the mouse brain striatum. Then a Low-Flow anesthesia system was used to deliver fluroxene to the mouse brain while placed inside the scanner through inhalation. Localized 19F-GEST experiments were performed on a 2.5×2.5×2.5 mm3 voxel using Image-Selected In-vivo Spectroscopy (ISIS) protocol with a pre-saturation pulse B1=2.5μT/ 2000ms in a total scan time of 16min. Results: Studying 24 different pairs composed of fluorinated anesthetic and macrocycle hosts the fluorinated anesthetic fluroxene (light blue sphere, Fig. 1a) showed the ability to generate a significant 19F-GEST contrast in the presence of two different molecular hosts (H1 and H2, Fig. 1a) with two opposite Δω values, either downfield or upfield relative to the chemical shift of unbound fluroxene. While the effect of H2-fluroxene was at Δω=–2.2 ppm (green, Fig. 1b) that of H1-fluroxene was obtained at Δω= +1.6 ppm (magenta, Fig. 1b). Then, 19F-GEST experiments conducted with a fixed concentration of fluroxene and reduced concentrations of either H1 or H2 demonstrating the ability to detect extremely low concentrations of both H1 (500 nM) and H2 (1 μM), respectively. 19F-GEST MRI experiments were then performed and presented as pseudo-multicolor imaging maps showing the ability to spatially map multiplexed systems even at the same ROI (Fig. 1c). Using a fluorinated anesthetic as an inhalable 19F-agent (i.e., fluroxene), the potential use of the proposed platform for in-vivo studies was demonstrated. For that purpose, solutions of either of the examined hosts were injected intracranially to the two hemispheres of a live mouse (Fig. 1d), after which the mouse was placed in a 15.2 T MRI scanner and anesthetized with fluroxene (schematics in Fig. 1d,

bottom). After confirming successful delivery of the guest to the brain (Fig. 1e), in-vivo localized 19F-GEST spectroscopy (Fig. 1f) was performed to show the in-vivo applicability of 19F-GEST. Conclusion: We reported here on the design, development, characterization and implementation of an approach that combines the principles of supramolecular chemistry with CEST and 19F-MRI for multiplexed MRI that can detect micromolar concentrations of targets. Based on the CEST principles, which allow signal amplification, and relying on 19F-MRI, low concentrations of multiple targets could be detected. By using fluorinated anesthetic, which is delivered at a mM concentration to a rodent brain the applicability of in vivo GEST-MRS was demonstrated2 and should be further developed.

References: 1. Aime, S.; Carrera, C.; Delli Castelli, D.; Geninatti Crich, S.; Terreno, E., Tunable Imaging of Cells Labeled with MRI-PARACEST Agents. Angewandte Chemie International Edition 2005, 44 (12), 1813-1815. 2. Shusterman-Krush, R.; Tirukoti, N. D.; Bandela, A. K.; Avram, L.; Allouche- Arnon, H.; Cai, X.; Gibb, B. C.; Bar-Shir, A., Single fluorinated agent for multiplexed 19F-MRI with micromolar detectability based on dynamic exchange. Angewandte Chemie International Edition (Just accepted).

Image/Figure:

https://s3.amazonaws.com/amz.xcdsystem.com/1E8A4501-BB41-A02A-1D3B9882B798BFAA_abstract_File10351/GA206_ImageFigure_0513074535.png

Image/Figure Caption: Figure 1. (a) Schematic representation of the dynamic exchange process between free fluroxene (light-blue sphere) and its complex with either H1 (Fluroxene@H1) or H2 (Fluroxene@H2). (b) Corresponding GEST z-spectrum obtained from a tube containing a mixture of fluroxene and 10 μM of each of H1 and H2. (c) 19F-GEST maps at $\Delta\omega = +1.6$ ppm (magenta), at $\Delta\omega = -2.2$ ppm (green) of different aqueous solutions containing fluroxene and either of the hosts H1 or H2 or their mixture. (d) Schematic illustration of the in-vivo experimental setup. (e) In vivo 1H-MRI (showing the voxels used for 19F-GEST MRS) and 19F-MRI of a mouse injected with H1 and H2 and anesthetized with fluroxene. (f) In-vivo 19F-ISIS-GEST data of two voxels acquired from the regions injected with H1 (magenta) and H2 (green). The 19F-GEST spectra represent the subtraction of the 19F-NMR spectra obtained when the saturation pulse was applied “on-resonance” from the 19F-NMR spectra generated when the saturation pulse was applied “off-resonance” as noted with arrows.

Full Name of Abstract's 1st Author : Ronit Shusterman-Krush

First Name: Nishanth D

Last Name: Tirukoti

Email: deva-nishanth.tirukoti@weizmann.ac.il

Organization: Weizmann Institute of Science

Country: Israel

ID: GA207
MRS metabolomics screening of human lung cancer using blood serum prior to disease diagnosis

Leo Cheng, MGH/Harvard Medical School, lcheng@mgh.harvard.edu

---

Category: Oncology

Abstract Body : Lung cancer (LuCa), the leading cause of cancer deaths, is often diagnosed late. Low-dose spiral CT can detect small and early stage LuCa lesions, but cannot be used widely as an annual LuCa screening tool. Metabolomics detects global metabolite variations under physiology and pathology. We hypothesize that metabolomic profiles measured from blood may reveal LuCa at early stages as a screening tool to triage suspicious patients to CT tests. To test this hypothesis, we designed our innovative study of using paired blood sera samples obtained from LuCa patients both prior to and at the time of their LuCa diagnosis to establish LuCa screening metabolomic profiles. Samples. Sera from non-small cell LuCa (NSCLC) patients and their age, gender and smoking habit matched healthy controls were grouped according to the design of training-testing-validation cohorts in this study. The training cohort included 25 NSCLC sera from patients at the time of diagnosis (TOD) and controls (Ctrl); the testing cohort consisted 25 sera collected 0.5 to 5 yrs prior to diagnosis (PTD) from the 25 NSCLC patients in the training cohort; and the validation cohort recruited sera collected less than 2 yrs PTD from additional 54 NSCLC patients and controls. MR Spectroscopy. High resolution magic angle spinning (HRMAS) MRS analysis of serum samples are performed at 4°C by a 600MHz Bruker spectrometer at 3,600Hz spinning rate. Spectra are analyzed with a MatLab-based curve fitting program. Data Analysis. 57 spectral regions were selected based on the training and testing cohorts. Following selections of these regions, all data analytical procedures, including principal component and canonical analyses, were performed on the training cohort and followed by the testing and validation cohorts. Analyses of native sera HRMAS MRS of the training cohort selected 57 spectral regions for statistical analyses, and PCA and canonical analysis were conducted to differentiate TOD from Ctrl groups, with the testing and validation cohorts passively followed the calculations to produce scores within each case. Using the mean plus one standard error (M+SE) as the threshold, calculated from the canonical score differences between TOD and PTD for each case, i.e. the difference of the two scores for each patient, a Kaplan-Meier survival analysis indicates better survival rate from their time of NSCLC diagnoses for patients with score differences higher than the threshold ($p=0.031$). Furthermore, for Stage I and IIA patients, survivals can be predicted ($p=0.027$) from their PTD samples, if their score values are higher than the M+SE threshold. Since neither testing nor validation cohorts were involved in the determination of values of the canonical score, by collectively examining all Stage I and IIA in both cohorts, the resulting Kaplan-Meier survival predicting capability by the threshold (established by the testing cohort) was enhanced significantly ($p=0.0044$). For 5-year survival, our data showed Sen=0.63, Spe=1.00, PPV=1.00, NPV=0.21, ACC=0.67, and F1=0.78. Thus, serum metabolomics may be a screening candidate for early detections with the potential to further probe into all the related metabolic pathways for better understanding of disease.

First Name: Leo

Last Name: Cheng

Email: lcheng@mgh.harvard.edu

Organization: MGH/Harvard Medical School

Country: United States

ID: GA208
Multimodality Imaging of Plectin-1 Targeted Nanoparticles for the Precision Detection of Pancreatic Ductal Adenocarcinoma In Vivo

Wenjia Zhang, Peking Union Medical College Hospital, Chinese Academy of Medical Sciences, zwj_medimaging@163.com

---

Category: Oncology

Abstract Body : Purpose Pancreatic ductal adenocarcinoma (PDAC) is currently the fourth highest cause of cancer-related death in the world, which showed the lowest 5-year relative survival rate of 9%[1]. Early and precision detection is particularly important for PDAC patients[2]. Therefore,accurate imaging for aiding diagnosis and subsequent treatment are indispensable for improving the therapeutic efficacy and patients' survival rate[3]. The aim of this study was to perform multimodality imaging as fluorescence molecular imaging (FMI), magnetic particle imaging (MPI) and magnetic resonance imaging (MRI) for the precision detection of both orthotopic and subcutaneous PDAC xenografts. Methods Plectin-1 targeted superparamagnetic iron oxide nanoparticles (SPIONs) conjugated with IRDye800CW (PTP-Fe3O4-IRDye800CW) were synthesized for targeted imaging probe. Subcutaneous and orthotopic PDAC mouse models were established. A multi-modality imaging method, including FMI, MPI and MRI, was conducted for quantitative evaluation of tumor. Histology and immunohistochemical analysis were used as references for validation. Results We successfully developed the PTP-Fe3O4-IRDye800CW nanoparticles with outstanding targeting specificity of PDAC xenografts. The probe showed good imaging performance for FMI, MPI and MRI in vitro. In both subcutaneous and orthotopic PDAC xenograft models, the PTP-Fe3O4-IRDye800CW nanoparticles showed better targeting specificity, uniform distribution, distinct periphery of tumors and longer retention effects for 7 days compared with CON-Fe3O4-IRDye800CW nanoparticles. In the orthotopic model, multi-modality imaging had the best observations at 48 h post-injection. For FMI imaging, PTP-Fe3O4-IRDye800CW group showed significantly higher normalized FMI intensities than CON-Fe3O4-IRDye800CW group (64.49% ± 7.03% vs. 41.99% ± 0.12%, P MPI imaging, PTP-Fe3O4-IRDye800CW group showed significantly higher normalized MPI signals than CON-Fe3O4-IRDye800CW group (85.72% ± 1.54% vs. 74.41% ± 1.91%, P PTP-Fe3O4-IRDye800CW nanoparticles distributed throughout the tumor and drew distinct periphery of tumors instead of confined to the injection site as CON-Fe3O4-IRDye800CW nanoparticles. Histology and immunohistochemical observations were in accordance with the multi-modality imaging. Conclusion Integration of the individual imaging advantages of FMI, MPI and MRI could allow more comprehensive and precision detection of PDAC with high sensitivity and resolution for better diagnosis at anatomical and molecular levels, which may potentially benefit patients with PDAC for early and sensitive diagnosis. Moreover, the utilization of novel MPI is more suitable for imaging tumors in deep organ due to its special imaging properties. The nanoparticles also possess intraoperative imaging and hyperthermia properties with potential for the guidance of subsequent precision therapy.

References: 1. Siegel, R.L., K.D. Miller, and A. Jemal, Cancer statistics, 2020. CA Cancer J Clin, 2020. 70(1): p. 7-30. 2. Willett, C.G., et al., Locally advanced pancreatic cancer. J Clin Oncol, 2005. 23(20): p. 4538-44. 3. Eser, S., et al., In vivo diagnosis of murine pancreatic intraepithelial neoplasia and early-stage pancreatic cancer by molecular imaging. Proc Natl Acad Sci U S A, 2011. 108(24): p. 9945-50.

Full Name of Abstract's 1st Author : Wenjia Zhang

First Name: Wenjia

Last Name: Zhang

Email: zwj_medimaging@163.com

Organization: Peking Union Medical College Hospital, Chinese Academy of Medical Sciences

Country: China

ID: GA209
MRI Evaluation of Physiotherapy Induced Corticospinal Tract Changes in Ischemic Stroke Patients

Rama Jayasundar, Department of NMR, All India Institute of Medical Sciences, New Delhi, India, ramajayasundar@gmail.com

---

Category: Neuroscience

Abstract Body : Introduction Stroke is a leading cause of disability worldwide and affects the economy and work productivity of countries.1 Physiotherapy is the conventional rehabilitation technique. The present study evaluates the effect of physiotherapy in post-stroke rehabilitation by Magnetic Resonance imaging (MRI). Materials and methods Eleven first-ever stroke patients (18-60 years) with ischemia in left hemisphere were enrolled for the study after obtaining approval from Institute Ethics Committee and written informed consents. Qualified physiotherapists gave standard physiotherapy to all patients, one hour every day for six consecutive months. National Institutes of Health Stroke Scale was determined at 0, three and six months post-intervention. Diffusion Tensor Imaging (DTI) was carried out at 3T (Ingenia, Philips MR scanner), using the following parameters: repetition time 12210 ms, echo time 83 ms, acquisition matrix 112 X 110, flip angle 900, number of slices 66, gradient direction 32. DTI images were acquired and processed with FSL 5.0.9. Color coding of tractography pathways was based on a standard red-green-blue (RGB) code that was applied to the vector in each brain area (red for right to left, blue for dorsal to ventral, and green for anterior to posterior). Comparisons between groups (pre- and post-physiotherapy) for longitudinal changes were carried out. Results Percentage improvement in NIHSS score was observed for all the patients after three (71.5%) and six (80%) months of physiotherapy. Representative images of processed DTI data shown in Figure-1 shows the physiotherapy induced mean changes in fractional anisotropy of corticospinal tract for left and right hemisphere separately. The fractional anisotropy of left corticospinal tract decreased between on 3 and 6 months, whereas increased in the right corticospinal tract. This shows that the contralateral region has taken the activity and resulted in increase in CST tract volume. Conclusion Physiotherapy plays a major role in post stroke rehabilitation. Although there are reports on physiotherapy induced changes in physiological functions,2 to the best of our knowledge there are no studies to assess the white matter changes effected by physiotherapy in post-stroke recovery. The current study has evaluated for the first time physiotherapy induced corticospinal tract changes in post-stroke recovery using DTI. The results have shown that DTI can play a crucial role in understanding the effects of physiotherapy in post-stroke recovery.

References: 1. World Health Organization, Global Strategy for the Prevention and Control of Noncommunicable Diseases. Report by the Director General. A 53/14 Fifty-third World Health Assembly, May 2000. 2. Carvalho R, Azevedo E, Marques P, Dias N, Cerqueira JJ. Physiotherapy based on problem-solving in upper limb function and neuroplasticity in chronic stroke patients: A case series. J Eval Clin Pract. 2018; 3: 552-560.

Image/Figure:

https://s3.amazonaws.com/amz.xcdsystem.com/1E8A4501-BB41-A02A-1D3B9882B798BFAA_abstract_File10351/GA209_ImageFigure_0513081214.jpg

Image/Figure Caption: Figure 1. Mean percentage of physiotherapy induced changes in fractional anisotropy of corticospinal tract

First Name: Rama

Last Name: Jayasundar

Email: ramajayasundar@gmail.com

Organization: Department of NMR, All India Institute of Medical Sciences, New Delhi, India

Country: India

ID: GA211
MR detection of gas microbubbles via hyperCEST: a path toward a dual modality contrast agent

Christian McHugh, The University of North Carolina at Chapel Hill, ctmchugh@live.unc.edu

---

Category: New Chemistry, Materials & Probes

Abstract Body : Introduction Gaseous microbubbles (MB) are an established clinical ultrasound (US) contrast agent. They consist of a heavy gas core stabilized by a lipid shell, which can be easily functionalized with adhesion ligands to allow for targeted molecular imaging1–3. MB can also provide MRI contrast, which originates primarily from the susceptibility difference between their gas core and the liquid environment in which they reside4. However, the susceptibility contrast produced by bare MB is too weak, requiring the use of MB doses in excess of what is typically used for clinical US4 or the doping of the lipid shell with superparamagnetic iron oxide nanoparticles for MR detection6. HyperCEST is an indirect MR detection scheme capable of revealing signals from very dilute molecules whose concentration fails below the typical MR sensitivity. HyperCEST has been used for molecular MRI applications both in vitro5,7–10 and in vivo11. The scope of this work was to assess whether bare MB could be detected by using hyperCEST at the fM in-blood concentrations used in clinical US studies to enable their use as a dual-modality molecular imaging agent. Methods First, HyperCEST contrast was simulated using quantitative hyperCEST (qHyperCEST)18 with the Full HyperCEST (FHC) solution19. Simulations were performed for MB with different diameters and concentrations, and for different saturation pulse strengths. In vitro hyperCEST studies were performed on a high resolution 500 MHz NMR spectrometer. Small-sized (0.9 ± 0.4 μm) and medium-sized (2 ± 1 μm) perfluorocarbon MB were prepared in-house as previously described20. The size distributions and concentrations were determined via single particle optical sizing. Large-sized (3.2 ± 0.7 μm), commercially-available MB were purchased directly from Advanced Microbubbles Inc (Newark, CA, USA). Each sample was diluted to reflect standard in blood concentrations used for contrast US (10 μL/kg at 1010 MB per mL for humans17). Before NMR signal acquisition, MB samples were equilibrated to 37 °C to replicate in vivo conditions. Fresh HP 129Xe was periodically bubbled directly into the sample, followed by a continuous-wave presaturation pulse (B1), a 90° excitation pulse, and signal acquisition. The resulting Z-spectra were fit according to the FHC solution19. Results The results showed that MB produced a strong hyperCEST contrast in agreement with the simulation results. Specifically, we found that hyperCEST contrast increases with gas-volume concentration as well as with B1 strength. In addition, an optimal MB size exists that provides an exchange rate that is neither too fast (where the occupation time of 129Xe inside the MB is too short to be appreciably saturated) nor too slow (where the amount of saturated 129Xe exchanging into solution is insufficient on the timescale of an experiment). Exceptional gas turnover rates provided substantial contrast even at low B1 strengths. Efficacy diminishes once the MB diameter exceeds 2 μm. No hyperCEST effect was observed in the absence of MB. Most importantly, MB produced hyperCEST contrast at concentrations as low as 10s of fM, which is at the clinical in-blood concentration used in

humans. Conclusions MB are efficient and are capable of accommodating millions of 129Xe atoms at a time. Therefore, they are detectable at concentrations much lower than carriers that maintain a 1:1 stoichiometry. Compared to nanoemulsions21 and gas vesicles7,22, MB are kinetically and magnetically superior; they can be detected at a much lower concentrations, while their narrower gas-phase peak characteristic of their spherical geometry leads to more efficient saturation, lessening concerns about SAR limitations for in vivo translation. As such, hyperCEST detection of gas MB is expected to enable the use of MB as a dual-modality contrast agent for combined US and MRI molecular imaging applications.

References: [1] R. Gessner, P. A. Dayton, Mol. Imaging 2010, 9, 117–127. [2] J. Wischhusen, F. Padilla, IRBM 2019, 40, 3–9. [3] A. L. Klibanov, in Bioconjug. Chem., 2005. [4] J. S. Cheung, A. M. Chow, H. Guo, E. X. Wu, Neuroimage 2009, 46, 658–664. [5] F. Yang, Y. Li, Z. Chen, Y. Zhang, J. Wu, N. Gu, Biomaterials 2009, 30, 3882–3890. [6] L. Schröder, T. J. Lowery, C. Hilty, D. E. Wemmer, A. Pines, Science (80-.). 2006, 314, 446–449. [7] M. G. Shapiro, R. M. Ramirez, L. J. Sperling, G. Sun, J. Sun, A. Pines, D. V. Schaffer, V. S. Bajaj, Nat. Chem. 2014, 6, 629–634. [8] A. Farhadi, G. Ho, M. Kunth, B. Ling, A. Lakshmanan, G. J. Lu, R. W. Bourdeau, L. Schröder, M. G. Shapiro, AIChE J. 2018, 64, 2927–2933. [9] G. J. Lu, A. Farhadi, J. O. Szablowski, A. Lee-Gosselin, S. R. Barnes, A. Lakshmanan, R. W. Bourdeau, M. G. Shapiro, Nat. Mater. 2018, 17, 456–463. [10] S. Klippel, C. Freund, L. Schröder, Nano Lett. 2014, 14, 5721–5726. [11] F. T. Hane, T. Li, P. Smylie, R. M. Pellizzari, J. A. Plata, B. Deboef, M. S. Albert, Sci. Rep. 2017, 7, 1–7. [12] M. Kunth, C. Witte, L. Schröder, J. Chem. Phys. 2014, 141, 194202(1–9). [13] M. Zaiss, M. Schnurr, P. Bachert, J. Chem. Phys. 2012, 136, 144106(1–10). [14] S. M. Fix, A. G. Nyankima, M. D. McSweeney, J. K. Tsuruta, S. K. Lai, P. A. Dayton, Ultrasound Med. Biol. 2018, 44, 1266–1280. [15] “Full Prescribing Information for DEFINITY®,” can be found under https://www.definityimaging.com/prescribing-information.html, 2020. [16] T. K. Stevens, R. M. Ramirez, A. Pines, J. Am. Chem. Soc. 2013, 135, 9576–9579. [17] M. Kunth, G. J. Lu, C. Witte, M. G. Shapiro, L. Schröder, ACS Nano 2018, 12, 10939–10948.

Image/Figure: https://s3.amazonaws.com/amz.xcdsystem.com/1E8A4501-BB41-A02A-1D3B9882B798BFAA_abstract_File10351/GA211_ImageFigure_0513090425.pdf

Image/Figure Caption: Effect of on-resonance saturation on 129Xe NMR spectrum. (A) Sketch of the experimental NMR setup (not on scale). A suspension of MB was placed in an NMR tube. Fresh HP 129Xe gas was bubbled directly into the suspension through a long narrow PEEK tube, connected to an HP-compatible ventilator on one end, and immersed in the NMR tube on the other end. 129Xe exchanges into and out of the MB according to kAB and kBA, respectively. (B) 129Xe NMR spectra from a suspension of MB, with on-resonance (-194.6 ppm) and off-resonance RF saturation. Peaks at 0 ppm and -192 ppm correspond to 129Xe dissolved in the solvent, and residual 129Xe gas inside of the PEEK tubing, respectively. At the low MB concentrations used here, the gas-phase signal originating from 129Xe inside of the MB core, and located 2.6 ppm upfield from the gas-phase peak inside of the PEEK tubing, cannot be observed directly. But, when B1 is on-resonance the MB, a significant attenuation of the dissolved-phase signal is observed. (C) NMR 129Xe spectra of a solvent sample without MB, acquired with on- and off-resonance RF saturation. Peaks at 0 ppm and -192 ppm are still visible. However, no solvent signal reduction is observed after RF saturation at -194.6 ppm. (D) Z-

spectrum showing a ~40% signal loss for a saturation frequency of -194.6 ppm is observed only in presence of MB.

First Name: Christian

Last Name: McHugh

Email: ctmchugh@live.unc.edu

Organization: The University of North Carolina at Chapel Hill

Country: United States

ID: GA212
Vascular network segmentation in photoacoustic mesoscopy

Emma Brown, University of Cambridge, emma.brown@cruk.cam.ac.uk

---

Category: Computational & Data Science

Abstract Body : Introduction: Photoacoustic mesoscopy is an emerging modality that can non-invasively visualise vascular networks at high resolution, yielding insight into their role in tumour development and therapy response1. Quantification of these vascular networks remains limited, as it requires accurate vessel segmentation, which is challenging to validate. Using a combination of in silico, in vitro and in vivo photoacoustic images, we assessed the accuracy and performance of two vessel segmentation methods, with and without vesselness filtering, to establish how these methods influence tumour vessel segmentation. Methods: To generate in silico ground-truth (GT) vascular networks, we utilised Lindenmayer systems2 (referred to as L-nets, n=30). We simulated photoacoustic imaging of the L-nets using SIMPA3 (v0.1.1) at 532nm and the k-Wave MATLAB toolbox (v1.3, MATLAB v2020b), assuming a speed of sound of 1500 ms-1. Red-coloured string agar phantoms provided in vitro GT (n=7). Strings were embedded at three different depths from the agar surface (0.5, 1 and 2mm). For in vivo analysis, breast patient-derived xenografts (PDXs) were implanted (n=14). Photoacoustic mesoscopy imaging of string phantoms and PDXs was conducted at 532nm. Excised PDXs underwent ex vivo immunohistochemistry to stain for CD31 (normalised area measures vessel density). We tested a moment preserving thresholding method (included in Fiji v2.1.0, referred to as Auto-Thresholding (AT)) and a learning-based segmentation method using random forest classifiers4 (ilastik v1.3.325, referred to as Random Forest (RF)). Between pre-processing and segmentation, feature enhancement was tested as a variable using Sato filtering (α=0.25) to produce vesselness filtered images (VF). Therefore, 4 segmentation pipelines were tested on all datasets: AT, RF, AT+VF and RF+VF. Results: Using L-nets as in silico GT, we found learning-based RF segmentation methods provide the most accurate segmentation, with lower mean squared errors (MSE) compared to the GT for segmented blood volume (MSE: AT=0.046±0.0005, AT+VF=0.058±0.0008, RF=0.023±0.0002, RF+VF=0.016±0.0002). We observed that RF methods are able to segment vessels distant from the simulated illumination source, where the signal-to-noise ratio (SNR) decreases, whereas AT methods fail to do so. Supporting this, in vitro in string phantoms, with strings placed at different depths, RF methods were able to cope with the depth-dependent decrease in SNR. AT methods failed to accurately segment the full extent of the strings at depth. Visual inspection of the in vivo tumour networks subjected to our processing pipelines suggests that VF increases vessel diameters in vivo, which quantitatively resulted in increased normalised blood volume. All methods resulted in segmented blood volumes that correlated with vessel density measured ex vivo, except AT (Pearson's correlation coefficient r with p-value: AT r=0.22 p=0.45; AT+VF r=0.64 p=0.01; RF r=0.61 p=0.02; RF+VF r=0.55 p=0.04). Discussion: In silico and in vitro GT datasets both highlighted that a learning-based RF methods can better segment vessels at depth, where SNR decreases because of the decrease in light fluence. The performance of RF methods is explained by the inclusion of features other than just intensity, as with AT methods, but also vessel edges and texture, resulting

in more accurate segmentations. VF visually increases vessel diameters and ultimately blood volume in vivo, which can be associated with acoustic reverberations observed surrounding vessels in vivo, spreading the apparent extent of vessels and ultimately increased blood volume. Correlations with vessel density measured ex vivo, support our in vivo measured blood volumes in all methods except AT. Conclusion: Using a combination of in silico, in vitro and in vivo photoacoustic mesoscopy datasets, we have compared and validated the performance of two vessel segmentation methods, with or without the application of vesselness filtering, for use in photoacoustic data segmentation and quantification, finding that learning-based methods yield the best performance.

References: 1. Omar, M., Aguirre, J. & Ntziachristos, V. Optoacoustic mesoscopy for biomedicine. Nature Biomedical Engineering vol. 3 354–370 (2019) 2. Galarreta-Valverde, M. A., Macedo, M. M. G., Mekkaoui, C. & Jackowski, M. P. Three-dimensional synthetic blood vessel generation using stochastic L-systems. in Medical Imaging 2013: Image Processing 86691I (2013). doi:10.1117/12.2007532. 3. Gröhl, J., Dreher, K. K., Schellenberg, M., Seitel, A. & Maier-Hein, L. SIMPA: an open source toolkit for simulation and processing of photoacoustic images. Photons Plus Ultrasound Imaging Sens. (2021). 4. Berg, S. et al. ilastik: interactive machine learning for (bio)image analysis. Nat. Methods 16, 1226–1232 (2019)

First Name: Emma

Last Name: Brown

Email: emma.brown@cruk.cam.ac.uk

Organization: University of Cambridge

Country: United Kingdom

ID: GA213
MR imaging of oxidative stress during drug induced liver injury using the oxidatively activated MR imaging probe Fe-PyC3A

Eric Gale, Massachusetts General Hospital and Harvard Medical School, emgale@mgh.harvard.edu

---

Category: New Chemistry, Materials & Probes

Abstract Body : Study objectives and hypothesis: The goal of this study is to evaluate whether the reactive oxygen species (ROS) activated magnetic resonance imaging (MRI) probe Fe-PyC3A can be used to non-invasively image an increase in intrahepatic neutrophil content in a mouse model of acetaminophen overdose. Fe-PyC3A is a low molecular weight iron complex that is oxidized from a low-relaxivity Fe2+ (r1 = 0.18 mM-1s-1, 4.7T, RT) to a high-relaxivity (r1 = 2.4 mM-1s-1, 4.7T, RT) complex by ROS.1 In normal liver ROS levels are low, but the metabolic and inflammatory changes (e.g. infiltration of activated neutrophils) associated with drug induced liver injury results in increased ROS levels and an aberrant oxidizing liver microenvironment.2-4 We hypothesize that ROS imaging using Fe-PyC3A represents a biomarker to detect, quantify, and monitor changes in liver oxidative stress associated with acute liver inflammation. Innovation and Significance. Liver toxicity is the most frequent form of drug related adverse event and is responsible for an estimated 1/5th of post-approval drug withdrawals.5-7 Liver toxicity is also a major reason for discontinuation of drug development programs.7 Drug hepatotoxicity is often linked to an increase in intrahepatic ROS levels related to altered hepatocellular metabolism or acute liver inflammation.8 The results of this preliminary study demonstrate how Fe-PyC3A generates liver signal increase that correlates with pathologic neutrophil infiltration following acute drug related liver injury. Our preliminary results suggest that liver ROS imaging with Fe-PyC3A represents a potentially powerful biomarker to noninvasively diagnose and monitor inflammation and/ or oxidative stress related to drug hepatotoxicity. Experiment design. We used Fe-PyC3A to image liver inflammation following a hepatotoxic dose of acetaminophen (formulated at 15 mg/mL and administered i.p.). Male C57BL/6 mice (5 weeks of age) were imaged 16 - 22 hours after receiving an intraperitoneal dose of 300 mg/kg acetaminophen (N = 9), 450 mg/kg acetaminophen (N = 20), or saline vehicle (N = 12). Each mouse was euthanized after imaging and the right and left liver lobes were harvested for analysis of inflammatory infiltrate by flow cytometry. A total of 41 mice were used in this experiment. The mice were imaged with a 4.7 T small-bore scanner (Bruker Biospec) with a custom-built volume coil. 2D T1-weighted coronal gradient echo images of the abdomen were acquired prior to and 2 minutes after injection of 0.2 mmol/kg Fe-PyC3A via the tail vein. The (post-pre) injection change in liver vs. muscle contrast-to-noise ratio (DCNR) was quantified separately in the left and right lobes of the liver. After imaging, the left and right lobes of the liver were harvested and assayed for neutrophil content by flow cytometry. Flow cytometry data was reported as percentage of live leukocytes. A portion of the right and left lobes of N=11 mice receiving a 450 mg/kg dose of acetaminophen were also assayed for myeloperoxidase positive (MPO+) cell content by immunohistochemistry (IHC). Comparisons in DCNR and intrahepatic leukocyte levels between groups of mice were made using one-way ANOVA followed by

Tukey's post-hoc test for multiple comparisons. We tested for correlations between DCNR and percentage intrahepatic neutrophils using the entire set of 82 liver samples analyzed by calculating the Pearson's product-moment correlation coefficient. Results. Figure 1A compares coronal T1-weighted images of mice 18 hours after i.p. injection of either saline or 450 mg/kg acetaminophen acquired prior to and 2 min after Fe-PyC3A injection. DCNR correlated positively and significantly with intrahepatic neutrophil content determined by flow cytometry (P Conclusions. Our data indicate that Fe-PyC3A represents a potentially useful technology for precision imaging of ROS-generating inflammatory cells in the liver.

References: 1. Wang, H.; Clavijo Jordan, V.; Ramsay, I. A.; Sojoodi, M.; Fuchs, B. C.; Tanabe, K. K.; Caravan, P.; Gale, E. M., Molecular Magnetic Resonance Imaging Using a Redox-Active Iron Complex. J. Am. Chem. Soc. 2019, 141 (14), 5916-5925. 2. Mossanen, J. C.; Tacke, F., Acetaminophen-induced acute liver injury in mice. Lab Anim 2015, 49 (1 Suppl), 30-6. 3. Williams, C. D.; Bajt, M. L.; Farhood, A.; Jaeschke, H., Acetaminophen-induced hepatic neutrophil accumulation and inflammatory liver injury in CD18-deficient mice. Liver Int 2010, 30 (9), 1280-92. 4. James, L. P.; McCullough, S. S.; Knight, T. R.; Jaeschke, H.; Hinson, J. A., Acetaminophen toxicity in mice lacking NADPH oxidase activity: role of peroxynitrite formation and mitochondrial oxidant stress. Free Radic Res 2003, 37 (12), 1289-97. 5. Alempijevic, T.; Zec, S.; Milosavljevic, T., Drug-induced liver injury: Do we know everything? World J Hepatol 2017, 9 (10), 491-502. 6. Haque, T.; Sasatomi, E.; Hayashi, P. H., Drug-Induced Liver Injury: Pattern Recognition and Future Directions. Gut Liver 2016, 10 (1), 27-36. 7. Siramshetty, V. B.; Nickel, J.; Omieczynski, C.; Gohlke, B. O.; Drwal, M. N.; Preissner, R., WITHDRAWN--a resource for withdrawn and discontinued drugs. Nucleic Acids Res 2016, 44 (D1), D1080-6. 8. Shuhendler, A. J.; Pu, K.; Cui, L.; Uetrecht, J. P.; Rao, J., Real-time imaging of oxidative and nitrosative stress in the liver of live animals for drug-toxicity testing. Nat Biotechnol 2014, 32 (4), 373-80.

Image/Figure:

https://s3.amazonaws.com/amz.xcdsystem.com/1E8A4501-BB41-A02A-1D3B9882B798BFAA_abstract_File10351/GA213_ImageFigure_0513092820.png

Image/Figure Caption: Figure 1. (A) Coronal 2D T1W gradient echo MR images of mice 18h after receiving an i.p. dose of saline or 450 mg/kg acetaminophen recorded 2 min after Fe-PyC3A injection, and quantitation of DCNR 2 min after injection. Robust liver enhancement is observed 2 minutes after injection in the acetaminophen-treated mouse. Imaging parameters: TE/TR = 2.9/190.4, flip-angle = 60°, Averages = 4. (B) Correlation of DCNR recorded 2 min after injection with intrahepatic neutrophil content for mice imaged 16 - 22 h after receiving i.p. doses of saline, 300, or 450 mg/kg of acetaminophen. (C). DCNR recorded 2 min after injection also correlates with intrahepatic myeloperoxidase positive cell content determined by IHC assay.

First Name: Eric

Last Name: Gale

Email: emgale@mgh.harvard.edu

Organization: Massachusetts General Hospital and Harvard Medical School

Country: United States

ID: GA214
Translational ImmunoPET of B cell lymphoma using radiolabelled CD19-targeting antibodies

Simone Blaess, University of Tuebingen, Werner Siemens Imaging Center, simone.blaess@med.uni-tuebingen.de

---

Category: Oncology

Abstract Body : Introduction: CD19 proved to be an excellent therapeutic target in B cell malignancies. With CD19-directed chimeric antigen receptor (CAR) T cells, bispecific T cell engagers (BiTE), and Fc-optimized monoclonal antibodies (mAbs), three auspicious treatment approaches have been developed for relapsed/refractory B cell lymphoma; however, all suffering from limited response rates and/or considerable toxicities [1, 2]. In clinical routine, therapy decisions are solely based on histological CD19 staining at initial diagnosis, disregarding tumor heterogeneity and altered temporal CD19 expression levels during treatment. In this work, we report on the development of radiolabeled αCD19-mAbs for positron emission tomography (CD19-ImmunoPET) aiming to visualize CD19 expression on B cell lymphomas non-invasively, thus facilitating both personalized patient stratification and therapy guidance. Methods: The anti-human CD19 mAb 4G7 (αhCD19), the GMP-grade Fc optimized anti-human CD19 mAb 4G7SDIE (αhCD19-Fcopt), and the anti-mouse CD19 mAb 1D3 (αmCD19) were conjugated by the metal chelator NODAGA for radiolabeling with copper-64 (64Cu). The radiolabeling efficiency was assessed by HPLC and TLC. Antigen excess cell binding and blocking studies were performed to determine the immunoreactive fraction, specific binding, and internalization of the mAbs. Human Daudi lymphoma cells or CD19KO Daudi cells were injected subcutaneously in CD1 nude mice. The syngeneic A20 lymphoma cells were engrafted in BALB/c mice for imaging studies of the αmCD19. Mice receiving either unrelated 64Cu-control mAb, blocking of CD19 binding sites or a B cell depleting anti-CD20 mAb (syngeneic mouse model) served as control groups. ImmunoPET was performed 6 h, 24 h, and 48 h after 64Cu-αCD19 injection. For ex vivo cross-validation, the organ uptake was measured by γ-counting after the last imaging time point. Most importantly, 64Cu-αhCD19-Fcopt was administered to four B cell lymphoma patients based on compassionate use to evaluate the eligibility for CD19-directed therapy. Results: Constantly high radiolabeling efficiency of >90% was achieved for all three 64Cu-αCD19. We revealed immunoreactive fractions of 62% (64Cu-αhCD19), 72% (64Cu-αhCD19-Fcopt), and 67% (64Cu-αmCD19), respectively. The three radioimmunoconjugates bound specifically to CD19 expressing cells and an internalization capacity of 56% after 24 h was assessed for 64Cu-αhCD19-Fcopt. ImmunoPET confirmed in vivo targeting of 64Cu-αhCD19-Fcopt to CD19-positive lymphoma lesions with a significantly higher accumulation in Daudi tumors (6.2 %ID/cc) compared to CD19KO tumors (4.4 %ID/cc, p 50% higher in the target group compared to the control groups. Ex vivo biodistribution analyses confirmed the obtained in vivo results. Furthermore, neither the binding to physiological B cells in the syngeneic A20 lymphoma model nor the enhanced Fc-γ mediated spleen uptake of the 64Cu-αhCD19-Fcopt affected distinct detection of CD19-positive lymphoma sites by CD19-ImmunoPET. Thus, the GMP-grade αhCD19-Fcopt, which was already clinically applied to treat

minimal residual disease of childhood leukemia [3], was radiolabeled for investigations in humans. In four Non-Hodgkin-Lymphoma patients with histologically confirmed CD19 expression 64Cu-αhCD19-Fcopt was able to detect cervical, mediastinal, and abdominal CD19-positive lymphoma sites as well as bone marrow infiltration. Conclusion: CD19-ImmunoPET enables the non-invasive in vivo identification of CD19-positive lymphoma sites in different lymphoma mouse models and patients. These results emphasize the potential application of 64Cu-CD19-mAbs as a novel imaging tool to guide emerging CD19-targeting therapies.

References: 1. Brudno, J.N., et al., Safety and feasibility of anti-CD19 CAR T cells with fully human binding domains in patients with B-cell lymphoma. Nat Med, 2020. 26(2): p. 270-280. 2. Velasquez, M.P., et al., T cells expressing CD19-specific Engager Molecules for the Immunotherapy of CD19-positive Malignancies. Sci Rep, 2016. 6: p. 27130. 3. Seidel, U.J., et al., Reduction of Minimal Residual Disease in Pediatric B-lineage Acute Lymphoblastic Leukemia by an Fc-optimized CD19 Antibody. Mol Ther, 2016. 24(9): p. 1634-43.

Full Name of Abstract's 1st Author : Simone Blaess

First Name: Simone

Last Name: Blaess

Email: simone.blaess@med.uni-tuebingen.de

Organization: University of Tuebingen, Werner Siemens Imaging Center

Country: Germany

ID: GA215
In vivo mapping of the spatio-temporal invasion of immune cells into bioscaffold using 19F magnetic resonance imaging.

Michel Modo, University of Pittsburgh, mmm154@pitt.edu

Category: Neuroscience

Abstract Body : Bioscaffolds consisting of extracellular matrix (ECM) based hydrogel have the potential to promote tissue restoration after a stroke. Infiltration of immune cells, especially macrophages, is a pivotal event to drive hydrogel biodegradation that leads to the invasion of neural cells. However, the spatio-temporal dynamics of the infiltration of immune cells into peri-infarct tissue and the ECM hydrogel remain poorly understood. The tagging of immune cells using perfluorcarbon (PFC) nanoemulsions afford their in vivo visualization using 19F magnetic resonance imaging (MRI). Rats with middle cerebral artery occlusion, a model of ischemic stroke, were implanted with ECM hydrogel 14 days after infarction using MRI-guidance to define the site and volume of injection. One day prior to the ECM implantation, animals were injected with PFC through the tail vein and baseline 19F MR image was acquired to verify the injection and potential passive influx to the stroke-damage brain. No PFC influx to the brain was evident at this time point. Longitudinal "time lapse" imaging over 24 hours indicated that no immune cells invaded the brain for 6 hours after ECM implantation, although a major infiltration in the scalp incision wound was evident within 1 hour after surgery. Infiltration of immune cells was first evident in the peri-infarct area at 9 hours post-implantation with subsequent invasion into the ECM hydrogel. By 24 hours a robust invasion of immune cells into the ECM hydrogel was evident, as verified by immunohistochemistry in post-mortem tissue. Histologic analyses revealed that almost all invading macrophages were labeled with PFC indicating that these were peripheral macrophages rather than brain-derived microglia. ECM hydrogel implantation therefore induces a briefly delayed invasion of macrophages into the stroke-damaged brain through the peri-infarct area that is governed by peripheral macrophage effecting the initial biodegradation events that lead to brain tissue restoration.

Image/Figure:

https://s3.amazonaws.com/amz.xcdsystem.com/1E8A4501-BB41-A02A-1D3B9882B798BFAA_abstract_File10351/GA215_ImageFigure_0513100902.jpg

Image/Figure Caption: Immune cells, such as macrophages, were tagged systemically by injecting PFCs through the tail vein. This afforded their in vivo detection using 19F MRI and localization to the peri-infarct area during the infiltration process as well as their invasion into the ECM bioscaffold. A 19F MRI and histology overlay provided confirmation of immune cells corresponding to the PFC signal on 19F MRI.

First Name: Michel

Last Name: Modo

Email: mmm154@pitt.edu

Organization: University of Pittsburgh

Country: United States

ID: GA216
Molecular MR imaging of intestinal fibrosis using a type I collagen targeting probe

Mariane Le Fur, Massachusetts General Hospital / Harvard medical school, mlefur@mgh.harvard.edu

---

Category: New Chemistry, Materials & Probes

Abstract Body : Introduction. Intestinal fibrosis is a common complication of inflammatory bowel disease (IBD) and is characterized by an excessive deposition of extracellular matrix (ECM) proteins.1 Current medical therapies used in IBD are directed at treating inflammation and do not prevent or reverse the formation of fibrosis. Surgical resection of fibrotic strictures remains the only treatment option.2 Identifying markers of intestinal fibrosis would contribute to the development of new diagnostic and therapeutic approaches to help evaluate the risk of patients developing fibrosis and detect early stages of fibrosis to minimize symptoms occurrence. Type I collagen is a major component of fibrotic tissue present in the extracellular space at a concentration above 10 μM, thus making it an acceptable target for MRI. Here we investigated a novel MRI collagen targeting contrast agent as a potential intestinal fibrosis biomarker in a mouse model of IBD. Materials and methods. To induce colitis, 7-week-old male C57BL/6 mice received 2.0% dextran sulfate sodium (DSS) in the drinking water for 5 days followed by 16 days of normal water. To evaluate disease progression, this 3-week cycle was repeated 2, 3 or 4 times (Fig. 1A). Age-matched mice receiving normal drinking water were used as controls. MR imaging was conducted after 2, 3 and 4 cycles using EP-3533, a type I collagen-targeting MR probe. To minimize bowel peristalsis during scanning, mice received an anti-peristaltic agent (N-Butylscopolamine, 5 mg/kg) via i.p. injection. MR imaging was performed on a 4.7T (Bruker Biospec) scanner. Axial T1-weighted 2D FLASH images, covering the descending colon and the small intestine, were acquired prior to and 15, 30, 40 and 50 minutes after i.v. injection of 5 μmol/kg EP-3533. To demonstrate specific binding to type I collagen, another group of DSS mice were imaged at 12 weeks using EP-3612, an isomeric non-binding control probe. These same mice were imaged again 24h later using EP-3533. Mice were euthanized after each scanning session and the colons collected for histology. Additionally, a tissue section from a mouse that received EP-3533 was used for elemental mapping of Gd by laser ablation inductively coupled plasma mass spectrometry (LA-ICP-MS) to evaluate the probe distribution within the bowel wall. For MR image analysis, signal intensity (SI) of the bowel wall was measured pre and post probe injection and the % increase calculated (%SI); the slope obtained from %SI vs time post injection was used as an indicator of probe washout rate. Results. As demonstrated by histology, the 3 DSS-treated groups developed intestinal fibrosis with an increased collagen deposition compared to the control groups (Fig. 1B). After EP-3533 administration to DSS injured mice, the initial %SI in the bowel wall was lower than in control mice, but the signal intensity persisted over the course of the study while in control mice the %SI decreased rapidly (Fig. 1C). The washout rate was highly significant for distinguishing fibrosis from normal intestine. The washout rate of EP-3533 in DSS-treated mice was similar regardless of treatment cycles with DSS, and this correlates with histological analysis where no major

difference in disease severity was observed after 2, 3 or 4 cycles of DSS (Fig 1D). EP-3533 showed significantly higher signal enhancement in DSS injured mice compared to non-binding isomer EP-3612 demonstrating specificity for collagen (Fig. 1E, 1F). Elemental imaging of a colon section from a mouse that received EP-3533 clearly indicates that the probe distribution correlates with the collagen layer (Fig 1G). Conclusion. The type I collagen targeting probe EP-3533 is specific for intestinal fibrosis in the DSS mouse model of colitis. Our results lend evidence to the use of EP-3533 as a potentially translatable biomarker of intestinal fibrosis.

References: 1- Le Fur, M., Zhou, I. Y., Catalano, O., & Caravan, P. (2020). Toward molecular imaging of intestinal pathology. Inflammatory Bowel Diseases, 26(10), 1470–1484. 2- Rieder, F., Fiocchi, C., & Rogler, G. (2017). Mechanisms, Management, and Treatment of Fibrosis in Patients With Inflammatory Bowel Diseases. Gastroenterology, 152(2), 340-350.e6.

Image/Figure:

https://s3.amazonaws.com/amz.xcdsystem.com/1E8A4501-BB41-A02A-1D3B9882B798BFAA_abstract_File10351/GA216_ImageFigure_0513101700.png

Image/Figure Caption: Figure 1 A) Protocol for colitis induction using 2.0% dextran sulfate sodium water. B) Representative images of colon tissue stained with trichrome for control mice and mice with colitis exposed to 4 cycles of DSS/normal water showing deposition of collagen (blue stain). Yellow arrows point to the collagen layer. C) Time – signal intensity curves for DSS-injured mice (4 cycles) compared to age-matched control mice after injection of 5 µmol/kg collagen targeting MR probe EP-3533. D) Slope of %SI vs time curves showing significant differences in probe washout between the control and DSS-injured mice after 2, 3 and 4 cycles; no significant difference in slopes was observed between the 3 DSS groups. E) Axial T1-weighted MR images of a DSS-treated mouse prior to and 50 minutes post injection of the isomeric non-binding control probe EP-3612 (top), and the same mouse imaged 24h later with EP-3533 (bottom). Signal enhancement of the bowel wall was observed only after EP-3533 administration. Arrows point to the bowel wall. F) Change in signal intensity in the bowel wall of DSS-treated mice after injection of EP-3533 or EP-3612. The significant difference indicates the specificity of EP-3533 for detecting intestinal fibrosis. G) EP-3533 distribution in a colon section obtained from a mouse with colitis analyzed by LA-ICP-MS (detection of gadolinium m/z 157). An adjacent section was stained with trichrome. The probe distribution correlates with the collagen layer stained in blue with Masson's trichrome stain, validating the specific detection of intestinal fibrosis.

Full Name of Abstract's 1st Author : Mariane Le Fur

First Name: Mariane

Last Name: Le Fur

Email: mlefur@mgh.harvard.edu

Organization: Massachusetts General Hospital / Harvard medical school

Country: United States

ID: GA217

Inorganic-Organic Theranostic Nanoparticles (IOH-NPs) for Monitored Delivery of Gemcitabine to Pancreatic Ductal Adenocarcinoma Cells

Myrto Ischyropoulou, University Medical Center of Goettingen (UMG), Max Planck institute Exp. Medicine (MPI), myrto7@gmail.com

---

Category: Oncology

Abstract Body : Introduction Pancreatic ductal adenocarcinoma (PDAC) is one of the most lethal cancers. Gemcitabine is currently the most effective chemotherapy. However, severe side effects and the development of chemoresistance often occur1. Since epidermal growth factor receptor (EGFR) is over-expressed by approximately 80% of PDAC tumours2 resulting in increased EGFR activity, tumorigenicity and therapy resistance the chimeric monoclonal antibody Cetuximab targeting human EGFR has been applied not only for therapy but also to enhance drug delivery to tumours. Herein, new therapeutic agents and delivery strategies are crucial3 such as inorganic-organic hybrid nanoparticles (IOH-NPs)4,5 that consist of one or multiple chemotherapeutic drugs, and fluorescent dyes, and can be coated with various components (e.g. monoclonal antibodies). The aim of the study was to evaluate the in vitro delivery of Gemcitabine via IOH-NPs and to study their efficacy in PDAC cells by imaging approaches. Methods Three types of NPs were investigated: 1) Zirconium-based IOH-NPs composed of Gemcitabine and the fluorescent dye DUT549 (Gem-NPs), 2) Gem-NPs overcoated with glucose (Gem-Glu-NPs) aiming at higher uptake due to elevated glucose metabolism6 and 3) Gem-NPs functionalised with Cetuximab specifically targeting human but not binding to mouse EGFR, for improved targeting (Gem-CTX-NPs) (Fig. 1A). Drug-free reference NPs, composed of gemcitabine non-active analogue (Cytidine) and the fluorescent dye DUT549 (Ref-NPs) or additionally coated with glucose or Cetuximab (Ref-Glu-NPs and Ref-CTX-NPs), as well as the clinically applied Gemcitabine were used as controls. Murine KPC- and Panc02-, and human Capan1 PDAC cells, as well as MHS mouse macrophages, were applied for in vitro studies. Cell uptake over time was studied using Ref-NPs, Ref-Glu-NPs and Ref-CTX-NPs in combination with confocal microscopy. Concentration-dependent efficacy of Gem-, Gem-Glu- and Gem-CTX-NPs on cell viability of PDAC cells was assessed over time with a live-cell imaging system (Incucyte) and compared to the efficacy of Gemcitabine. Cell Uptake and drug efficacy were investigated for Gem-NPs over time with the Evorion Cell City microfluidic chip system7 after encapsulating PDAC cells in hydrogel beads. Results Ref-, Ref-Glu-NPs and Ref-CTX-NPs derived fluorescence was detectable in all tested PDAC cells as early as 5h after incubation with intensity increased over time, resulting in a high cell load after 48 h, thus demonstrating that IOH-NPs are effective vehicles for drug delivery into PDAC cells (Fig. 1B). KPC cells were more responsive to Gemcitabine and NPs based treatment than Panc02 cells. While incubation of KPC cells with 100nM Gem-NPs led to no cell survival, Panc02 cells still partly survived the NP based treatment, requiring up to 500nM Gem-NPs to obtain a similar effect. The clinical drug Gemcitabine was effective at 10nM. Although, as expected, we did not observe any specific binding of Gem-CTX-NPs to mouse tumour cells, those NPs were still effectively internalized by the mouse cells and lead to toxicity comparable with non-

functionalised Gem-NPs (200nM for KPC and 400nM for Panc02). For human Capan1 cells, expressing a relatively low amount of EGFR, an improved binding or internalization of Gem-CTX-NPs was not observed. In accordance with the uptake experiments, Gem-Glu-NPs were five times less effective than the non-coated Gem-NPs in murine cells. 3D live cell microchip imaging confirmed early uptake and high efficacy of the Gem-NPs already within the first 10h of incubation. Conclusion All tested NPs were taken up by PDAC cells over time, with the non-coated NPs having the fastest and highest uptake. Coating of Gem-NPs with glucose did not improve the in vitro efficacy. Next, IOH-NPs will be assessed in vitro in different human cell lines for improved cetuximab binding and efficacy and in vivo in mouse models of PDAC.

References: 1. Saif MW, Lee Y, Kim R. Harnessing gemcitabine metabolism: a step towards personalized medicine for pancreatic cancer. Ther Adv Med Oncol. 2012;4(6):341-346. doi:10.1177/175883401245375 5 2. Oliveira-Cunha M, Newman WG, Siriwardena AK. Epidermal growth factor receptor in pancreatic cancer. Cancers (Basel) 2011;3:1513–26. 3. Adiseshaiah PP, Crist RM, Hook SS, McNeil SE. Nanomedicine strategies to overcome the pathophysiological barriers of pancreatic cancer. Nat Rev Clin Oncol. 2016;13(12):750-765. doi:10.1038/nrclinonc.2016.119 4. Napp J, Markus MA, Heck JG, et al. Therapeutic Fluorescent Hybrid Nanoparticles for Traceable Delivery of Glucocorticoids to Inflammatory Sites. Theranostics. 2018;8(22):6367-6383. doi:10.7150/thno.28324 5. Neumeier BL, Khorenko M, Alves F, et al. Fluorescent Inorganic-Organic Hybrid Nanoparticles. ChemNanoMat. 2019;5(1):24-45. doi:https://doi.org/10.1002/cnma.201800310 6. Kawada K, Iwamoto M, Sakai Y. Mechanisms underlying 18 F-fluorodeoxyglucose accumulation in colorectal cancer. World J Radiol. 2016;8(11):880. doi:10.4329/wjr.v8.i11.880 7. Rezaei M, Martins Cavaco AC, Stehling M, et al. Extracellular Vesicle Transfer from Endothelial Cells Drives VE-Cadherin Expression in Breast Cancer Cells, Thereby Causing Heterotypic Cell Contacts. Cancers. 2020;12(8):2138. doi:10.3390/cancers12082138

Image/Figure:

https://s3.amazonaws.com/amz.xcdsystem.com/1E8A4501-BB41-A02A-1D3B9882B798BFAA_abstract_File10351/GA217_ImageFigure_0610073351.jpg

Image/Figure Caption: Fig. 1 In vitro studies of efficacy and cell uptake of IOH NPs. A) Overview of the IOH-NPs used in the project. B) Fluorescence microscopy showing uptake of: Ref-Glu-NPs, Ref-NPs and Ref-CTX-NPs are taken up by Panc02 cells over time. Blue: DAPI nuclei staining, red: Nanoparticles (due to the incorporated DUT549 NPs fluorescent dye), green: autofluorescence C) Uptake and Efficacy studies Gem-NPs analyzed using KPC cells and live-cell imaging performed with Evorion's Cell City system in combination with fluorescence microscopy. Red-arrow: fluorescent NPs, yellow circle: KPC cells which died after NPs internalisation

Full Name of Abstract's 1st Author : Myrto Ischyropoulou

First Name: Myrto

Last Name: Ischyropoulou

Email: myrto7@gmail.com

Organization: University Medical Center of Goettingen (UMG), Max Planck institute Exp. Medicine (MPI)

Country: Germany

ID: GA218

High-precision neural-network analysis of 1H MR spectra from human plasma samples to detect pancreatic cancer using a specialized data-augmentation technique

Meiyappan Solaiyappan, The Johns Hopkins University School of Medicine, msolaiy@jhmi.edu

---

Category: Oncology

Abstract Body : Introduction: The poor prognosis of pancreatic ductal adenocarcinoma (PDAC) is mainly due to late-stage diagnosis [1]. Only ~20% of pancreatic cancers are resectable by the time they are detected. With a five-year survival of 9%, early detection of pancreatic cancer through routine screening is a major unmet clinical need. Here we have applied neural-network analysis to 1H magnetic resonance spectra obtained from human plasma samples to differentiate between healthy subjects (control), subjects with benign lesions, and subjects with pancreatic ductal adenocarcinoma (PDAC). Our data support developing a neural-network approach to identify PDAC from 1H MRS of plasma samples. Methods: Plasma samples from healthy subjects (control, n=56), from subjects with benign pancreatic lesions (benign, n=49), and from subjects with PDAC (PDAC/malignant, n=53) were analyzed with 1H MRS. 1H MR spectra were acquired on a Bruker Avance III 750 MHz (17.6 T) MR spectrometer equipped with a 5 mm probe. Plasma (250µL) was diluted with D2O buffer (350µL) and spectra with water suppression were achieved using pre-saturation and were acquired using a single pulse sequence. All spectral acquisition, processing and quantification were performed using TOPSPIN 3.5 software. Area under peaks were integrated and normalized with respect to reference signal. Representative spectra from the three groups are presented in Figure 1(a). After the initial processing of the spectral data to calibrate against the reference peak signal and the plasma volume quantity, mean spectra for each classification group and the differences of the mean spectra of benign and malignant from the control group were calculated to identify segments of the spectra that exhibit significant differences to provide a set of key target locations in the spectra. The spectral differences with respect to the mean of the control spectra at each of these target locations were computed to construct a feature vector. This feature vector was used as the input variable for the neural network analysis to discriminate the three classes. To enhance the accuracy and robustness, a specialized data augmentation technique based on the Variational Auto-Encoder (VAE) neural network approach was used to double the original data-size of 158 feature-vector samples to 316. This made the data size more suitable for meeting the demands of a neural-network technique that otherwise may result in overfitting. To further reduce overfitting and biases, a minimalist neural network design was used and data samples were randomly divided in to training, validation and testing purposes. All the artificial neural-network functions were developed in MATLAB 2020b (MathWorks, Inc). Results: Representative 1H MR spectra from each group are displayed in Fig. 1a. The results and the performance of the neural network to successfully discriminate the three classes are illustrated in Fig. 1(b-d). The scatter plot in Fig. 1(b) illustrates the neural network's ability to successfully encode the feature vectors into well-separated clusters of the classes with minimal overlap. The classification approach provided the

basis for the high sensitivity, specificity, and precision accuracy presented in the receiver operating characteristics (ROC) curves in Fig. 1(c). The confusion matrix plot in Fig. 1(d) shows the prediction accuracies within each class and as well as between all classes. Discussion: A combination of spectral features extraction and neural network processing of 1H MRS data of plasma samples can successfully discriminate between control, benign and malignant PDAC. Acknowledgement: This work was supported by NIH R35CA209960, R01CA193365, and U01CA210170. We thank Dr. Karen Horton for her support.

References: 1. Blackford AL, Canto MI, Klein AP, Hruban RH, Goggins M: Recent trends in the incidence and survival of Stage 1A Pancreatic Cancer: A Surveillance, Epidemiology, and End Results analysis. J Natl Cancer Inst., 2020, 112:1162-9

Image/Figure:

https://s3.amazonaws.com/amz.xcdsystem.com/1E8A4501-BB41-A02A-1D3B9882B798BFAA_abstract_File10351/GA218_ImageFigure_0513103015.PNG

Image/Figure Caption: Figure 1. (a) Representative 1H MRS spectra obtained from plasma of healthy subjects (control/normal), patients with benign disease and PDAC patients. Expansion of the spectra from 2.2 ppm to 2.5ppm are 4X vertically zoomed highlighting changes in metabolic patterns. (BHB; betahydroxybutyrate, BCA; branch chain amino acid, PUFA; Polyunsaturated fatty acid). (b) The scatter-plot shows the 2D embedding of the neural-network's classification variables to illustrate the efficient separation of control, benign, and malignant (PDAC) samples with minimal misclassification. (c) The Receiver Operating Characteristics (ROC) curves show the sensitivity and specificity performance of the neural-network, with the area under the curve (AUC) for all three classifications above 0.99. (d) The confusion-matrix plot shows the result of cancer plasma prediction. The green diagonal boxes show the correct predictions in each class and red boxes indicate misclassifications. The numbers in each box correspond to the number of samples (and their percentage of the total data). The column at the far right shows the precision value (positive predictive value) for each predicted class (in green). The bottom-row shows the prediction accuracy value for each class (in green) and the bottom-right corner box shows the overall accuracy value (in green) and error rate (in red). Cancer plasma classification resulted in a 98.1% correct prediction.

First Name: Meiyappan

Last Name: Solaiyappan

Email: msolaiy@jhmi.edu

Organization: The Johns Hopkins University School of Medicine

Country: United States

ID: GA219
Genetically Encoded Acoustic Detonators for Image-guided Mechanotherapy

Avinoam Bar-Zion, California Institute of Technology, barz@caltech.edu

---

Category: Bioengineering, Synthetic Biology and Basic Biology

Abstract Body : Recent advances in cell-based and biomolecular therapies provide unprecedented treatment specificity based on the recognition of unique molecular signatures. However, the mechanisms for spatiotemporal control of such therapies remain limited, increasing the risk of off-target side effects. In addition, the range of effects these therapeutic approaches can apply to the target tissue is restricted and does not include the production of local mechanical forces. The ability to combine cellular homing and molecular targeting with image-guided actuation of mechanical force would provide powerful new capabilities for precise therapeutics. Here we demonstrate this combination using ultrasound-detonated biomolecules. Recently, we introduced genetically encoded air-filled proteins called gas vesicles (GVs) as acoustic reporter genes based on their ability to scatter sound waves1,2. Subsequently, we showed that at lower ultrasound (US) frequencies, GVs can nucleate the formation of oscillating and imploding bubbles, a phenomenon known as ultrasound cavitation3. Here, we show that the vibrating bubbles seeded by ultrasound-detonated GVs can produce various bio-effects such as selective cell lysis and drug delivery. We propose a mechanism for GV-seeded cavitation in which ultrasound pulses, with sufficient positive pressure, collapse the GVs, releasing nanoscale air bubbles. Under strong ultrasound pulses, these nanobubbles coalesce into micron-scale bubbles over several cycles, enabling them to undergo violent inertial cavitation. The proposed mechanism for GV cavitation was validated and studied using two different approaches: spectral analysis of the acoustic emissions from GVs upon insonation and high frame rate microscopy at 5 million frames per second. Following this proof of concept, we investigated two applications of GV cavitation. First, we showed that genetically modified GVs, targeted to over-expressed integrins in U87 (glioblastoma) tumor cells, can seed cavitation activity and selectively open their membranes. Furthermore, GV cavitation was shown to propel the flow and spatial dispersion of molecular payloads, as demonstrated with tissue-mimicking phantoms. We then looked at GV-expressing tumor-homing cells. When focused ultrasound was used to detonate GV-expressing bacteria, this led to their lysis and a 16-fold increase in the released concentration of a co-expressed luciferase payload. Similarly, we showed that ultrasound can trigger the lysis of GV-expressing mammalian HEK cells. In our in vivo experiments, GVs taken up by tissues were acoustically triggered to produce local hemorrhage and necrosis, and GVs administered to subcutaneous MC26 tumors produced robust cavitation, which is detectable by its acoustic signature. Finally, systemically injected tumor-homing bacteria were shown to colonize deep-tumor regions and produce GVs inside the tumor core, an area that is inaccessible using traditional microbubble cavitation nuclei (Fig. 1). When exposed to focused ultrasound, GV expressing cells were shown to improve the results of checkpoint inhibitor immunotherapy, resulting in slower A20 tumor growth and extended median survival time. Expression of GVs in tumor-homing bacteria can allow these cells to open a range of new theranostic possibilities, including precise drug delivery and selective mechanical and thermal ultrasound therapy.

Furthermore, the recent expression of GVs in mammalian cells has the potential to enable novel image-guided cell-based immunotherapy approaches.

References: 1. Bourdeau, R. W. et al. Acoustic reporter genes for noninvasive imaging of microorganisms in mammalian hosts. Nature 553, 86–90 (2018). 2. Farhadi, A., Ho, G. H., Sawyer, D. P., Bourdeau, R. W. & Shapiro, M. G. Ultrasound imaging of gene expression in mammalian cells. Science (80-.). 365, 1469–1475 (2019). 3. Bar-Zion, A. et al. Acoustically Detonated Biomolecules for Genetically Encodable Inertial Cavitation. bioRxiv 620567 (2019) doi:10.1101/620567.

Image/Figure:

https://s3.amazonaws.com/amz.xcdsystem.com/1E8A4501-BB41-A02A-1D3B9882B798BFAA_abstract_File10351/GA219_ImageFigure_0513103335.jpg

Image/Figure Caption: Tumor-homing cells colonize deep tumor regions (green, xAM non-linear imaging), distinct from highly perfused regions observed using intravascular microbubble ultrasound contrast agents (red, ultrasound super-localization).

First Name: Avinoam

Last Name: Bar-Zion

Email: barz@caltech.edu

Organization: California Institute of Technology

Country: United States

ID: GA220
PD-L1 Photoimmunotherapy of Ovarian Cancer

Marie-France Penet, Johns Hopkins University, mpenet2@jhmi.edu

---

Category: Oncology

Abstract Body : Ovarian cancer is one of the leading causes of cancer-related deaths in women in the United States. It has been estimated that 1 in 6 women die within the first 3 months of diagnosis, demonstrating the high morbidity and mortality caused by advanced stage disease presentation and challenges of effective therapy (1). Improvements in the treatment of patients with advanced stage disease have extended median survival, but overall survival has not significantly changed (2). Most patients with advanced stage ovarian cancer ultimately suffer recurrence and eventually develop drug-resistant tumors. The lack of curative treatment and the high rate of relapse for women with advanced stage ovarian cancer highlight a clear need for new therapeutic strategies. Photoimmunotherapy (PIT), using a near infrared (NIR) dye conjugated to an antibody, provides an effective theranostic strategy to detect and selectively eliminate cell populations (3). NIR-PIT induces specific cell death of targeted cells with minimal adverse effects in normal tissue (3). Programmed death-1 (PD-1) signaling pathway, consisting of the PD-1 receptor expressed on T cells and its ligand programmed death ligand-1 (PD-L1) is being extensively studied for immune checkpoint blockade. PD-L1 expression is prevalent across all major histological subtypes of ovarian cancer and is commonly expressed by cancer cells and by tumor associated macrophages (TAMs) (4). Here, we used PIT to eliminate PD-L1 expressing TAMs and cancer cells in ovarian cancer xenografts. IR700-conjugated antibodies were synthesized as previously described (5). PIT was performed to quantify cell death induced by PD-L1-IR700 associated with NIR light in two murine ovarian cancer cells, ID8-Defb29-VEGF, MOSE (murine ovarian surface epithelial), and in murine macrophages RAW264.7, with and without IFN-g. IgG-IR700 was used as control. A light emitting diode provided NIR photoirradiation to the cells with irradiation doses of 16, 32, or 64 J/cm2. Dose-dependent efficacy of PDL1-IR700-mediated cell death in ID8-Defb29-VEGF and MOSE was shown. Increased cytotoxicity was observed with increased photoirradiation. A stronger effect was measured in cells treated with IFN-g. Irradiation did not alter viability of ovarian cancer cells incubated with IgG-IR700, or with PDL1-IR700 in the absence of irradiation. RAW264 cells with or without IFN-g treatment were highly sensitive to PDL1-IR700 combined with photoirradiation. In vivo, we observed a higher level of PDL1 in ID8-Defb29-VEGF orthotopic tumors as compared to subcutaneous tumors. We also observed a slightly higher level of CD11b, but no difference in F4/80, a macrophage marker. Efficacy of NIR-PIT was then assessed in orthotopic ID8-Defb29-VEGF tumors implanted in C57BL/6-albino mice. MRI was used to follow the tumor progression over a 3 week period. Mice received an i.v. injection of PBS, IgG-IR700 or PDL1-IR700, and light was applied 24h post injection. Tumor growth reduction was observed when PDL1-IR700 was combined with photoirradiation (Figure 1). While efficacy was observed in some mice treated with the combination PDL1-IR700 and light, we also observed toxicity in some mice with death occurring within 24h of photoirradiation. This was not observed with PDL1-IR700 alone, or with any of the other treatments. Studies to better understand this

toxicity are ongoing. Acknowledgement: This work was supported by NIH R35 CA209960 and the Emerson Collective.

References: (1) Lheureux et al, Lancet 2019, (2) Riester, JNCI 2014, (3) Kobayashi and Choyke, Acc Chem Res 2019, (4) Nowak, Cell, 2020, (5) Jin et al, Sci Rep. 2016;6:2787

Image/Figure:

https://s3.amazonaws.com/amz.xcdsystem.com/1E8A4501-BB41-A02A-1D3B9882B798BFAA_abstract_File10351/GA220_ImageFigure_0513103412.png

Image/Figure Caption: Figure1: NIR images of 2 representative ID8-Defb29-VEGF orthotopic tumor bearing mice 24h post injection of IgG-IR700 (left column) or PDL1-IR700 (right column), before (A) and right after (B) photoirradiation. Normalized tumor growth of ID8-Defb29-VEGF orthotopic tumor bearing mice treated with PBS (n=5), IgG-IR700 (n=3), IgG-IR700+light (n=8), PDL1-IR700 (n=5), PDL1-IR700+light (n=8).

First Name: Marie-France

Last Name: Penet

Email: mpenet2@jhmi.edu

Organization: Johns Hopkins University

Country: United States

ID: GA221

SELECTION OF A POTENT PEPTIDE BINGDING TO NUCLEOLAR DDX24 FROM A BACTERIA-DISPLAYED SYSTEM

红军 金, 中山大学附属第五医院, **jinhj3@mail.sysu.edu.cn**

Category: Oncology

Abstract Body : Background DDX24 is an important nucleolar protein, which was recently identified to be an important oncogen, and also associated to vascular malformations disease named Multi-organ Venous and Lymphatic Defect Syndrome (MOVLD). The purpose of this research is to develop a highly potent peptide probe that could be used for DDX24-related disease detection via binding to nucleolar DDX24 protein. Materials and Methods Screening of binding peptide candidates to DDX24 from a random bacterial surface display library coupled with magnetic cell sorting (MACS) and fluorescence-activated cell sorting (FACS) respectively (Figure 1A). Then the binding potency of selected peptides were docked with homology modeling of DDX24 to further identify specific peptide probes. To validate the chosen peptide probe, the peptides were labeled with FITC and tested the binding ability for DDX24 in cell line stably expressed DDX24, via immunofluorescence (IF) and flow cytometry (FCM) experiments in vitro. Moreover, the tumor-bearing mice models were established and tested with CY7-labeled optimal peptide via intratumoral injection to evaluated the specificity and affinity targeting DDX24 in vivo. Results Several potent and selective peptides targeting DDX24 have been successfully screened via bacteria-displayed peptide method. The ATP-binding domain of DDX24 was docked with peptides using homology modeling by Schrodinger software, revealing a peptide2/DDX24 interaction with geometrical and energy match (-10.785 kcal/mol) (Figure 1B). IF, FCM and cell saturation binding fluorescence experiments were performed to identify that the peptide 2 was the most highly selective peptide (Figure 1C). NIRF imaging revealed that CY7-labeled peptide 2 showed a higher uptake in DDX24-positive tumor than DDX24-negative tumor in live animals (Figure 1D, E). Conclusions Peptide 2, bound to DDX24 specifically and sensitively. It may be a potential candidate for molecular imaging detection and targeting therapy of DDX24-related diseases.

Image/Figure Caption: Figure 1. Selection of potent peptide probe for DDX24 (A) Schematic representation of DDX24-targeted peptides selection procedure, and list of screened peptides sequences. (B) Docked structure of peptide 2 on ATP-domain of DDX24. (C) Binding of FITC-peptide 2 to DDX24-positive CHO cell. Scale bar 10μm. (D) In vivo NIRF imaging of DDX24+ and DDX24- tumor-bearing mice after intratumoral injection of cy7-labeled peptide 2. (E) Antibody staining on DDX24+ tumor and DDX24- tumor sections of DDX24, respectively. Scale bar 100μm.

Full Name of Abstract's 1st Author : Zhijun Li

First Name: 红军

Last Name: 金

Email: jinhj3@mail.sysu.edu.cn

Organization: 中山大学附属第五医院

Country: China

ID: GA222

Non-invasive photoacoustic imaging of the breast cancer vascular microenvironment correlates with the underlying biological phenotype and genotype

Emma Brown, University of Cambridge, emma.brown@cruk.cam.ac.uk

---

Category: Oncology

Abstract Body : Introduction: Vascular phenotypes in breast cancer are diverse and influence tumour biology and therapy response1. Photoacoustic imaging (PAI) is an emerging modality that allows non-invasive visualisation of tumour vascular features through the endogenous contrast of deoxy- and oxy-haemoglobin (Hb and HbO2)2. We hypothesised that PAI could provide a non-invasive tool to monitor vascular phenotypes in breast patient-derived xenografts (PDXs). Methods: Two luminal B (lumB) PDXs (AB580, STG143) and two basal PDXs (STG139, STG321) were implanted in NSG mice (nAB580(LumB) = 17, nSTG143(LumB) = 6; nSTG139(Basal) = 26, nSTG321(Basal) = 12). In vivo PAI was performed at the mesoscopy (RSOM) and macroscopy (MSOT) levels. RSOM was conducted weekly once tumours were palpable to yield longitudinal data on tumour blood volume (BVRSOM). MSOT was conducted when tumours reached ~0.4cm. Total haemoglobin (THbMSOT = Hb+HbO2) and blood oxygen saturation images (SO2MSOT = HbO2/THbMSOT) were captured3. Once excised, tumours underwent immunohistochemistry (IHC) to stain CD31 (endothelial cells), CAIX (hypoxia), VEGF (angiogenic factor) and ASMA (%ASMA coverage of CD31+ vessels, indicating vessel maturity). Total RNA was extracted from flash frozen tumour tissue. Libraries for RNA-seq were prepared with Illumina TruSeq and sequenced. Transcript levels were quantified with Salmon and further analysis was conducted in R. Scores for expression of a breast hypoxia gene signature4 were generated using GSVA5. Results: Longitudinal data analyses showed that BVRSOM increased linearly with tumour volume in all models and at a significantly higher rate in basal PDXs compared to lumB PDXs (p=0.03). Supporting this, THbMSOT was significantly higher in basal PDXs (2958±195.8a.u. vs. 1391±254.8a.u., p Vessel maturity was higher in the basal STG321 model (%ASMA coverage:STG321 36.75±1.27% vs. STG139 20.08±1.15%, AB580 28.76±1.35%, STG143 25.64±0.75%, p Discussion: We have examined breast PDXs from basal and lumB subtypes, finding markedly different vascular phenotypes between subtypes as well as between individual models. Our results suggest that while both lumB PDXs (AB580 and STG143) contain relatively few blood vessels, they are mature and perfuse the tumour, leading to high SO2MSOT and low hypoxia. Despite low CAIX expression, GSVA scores of hypoxic gene signature expression were relatively high in AB580 and the hypoxic pathways involved need further investigation. Both basal PDXs (STG139 and STG321) have high blood vessel content however, differences in vessel maturity appear to govern the perfusion, oxygenation and ultimately lead to discordance in their overall levels of hypoxia. This was supported by GSVA scores, which were higher in STG139 than STG321, giving a molecular basis to the phenotypic variation observed non-invasively using PAI. Conclusion: PAI is sensitive to different vascular phenotypes in breast PDXs across scales, providing a non-invasive visualisation of these phenotypes observed using IHC and reflecting underlying gene expression.

Importantly, our results suggest that some vascular features are model dependent, whereas others are subtype dependent potentiating further exploration in additional mouse models and in future, in patients.

References: 1. Junttila, M. R. and de Sauvage, F. J. (2013). Influence of tumour micro-environment heterogeneity on therapeutic response. Nature 501, 346. 2. Wang, L. V and Hu, S. (2012). Photoacoustic Tomography: In Vivo Imaging from Organelles to Organs. Science (80-.). 335, 1458–1462. 3. Tomaszewski, M. R., Gonzalez, I. Q., O'Connor, J. P., Abeyakoon, O., Parker, G. J., Williams, K. J., Gilbert, F. J. and Bohndiek, S. E. (2017). Oxygen Enhanced Optoacoustic Tomography (OE-OT) Reveals Vascular Dynamics in Murine Models of Prostate Cancer. Theranostics 7, 29 4. I. Chae Ye, Elana J. Fertig, Josh W. DiGiacomo, Michael Considine, Inês Godet and Daniele M. Gilkes (2018) Molecular Portrait of Hypoxia in Breast Cancer: A Prognostic Signature and Novel HIF-Regulated Genes. Molecular Cancer Research 16, 12. 5. Hänzelmann, S., Castelo, R. & Guinney, J. (2013) GSVA: gene set variation analysis for microarray and RNA-Seq data. BMC Bioinformatics 14, 7.

Image/Figure:

https://s3.amazonaws.com/amz.xcdsystem.com/1E8A4501-BB41-A02A-1D3B9882B798BFAA_abstract_File10351/GA222_ImageFigure_0513110855.png

Image/Figure Caption: Raster-scanning optoacoustic mesoscopy (RSOM) exemplar image of a breast PDX tumour blood vessel network. Image split into low (11-33MHz, red) and high (33-99MHz, blue) ultrasound frequency bands to highlight large and small vessels respectively. Scale bar = 1mm.

Full Name of Abstract's 1st Author : Emma Louise Brown

First Name: Emma

Last Name: Brown

Email: emma.brown@cruk.cam.ac.uk

Organization: University of Cambridge

Country: United Kingdom

ID: GA223

Young Fecal Microbiota Transplants Improve Cognition of Natural Aged Mice via Affecting Neuroinflammation, Microglia Activation and Glucose Metabolism

Rui Zhou, Zhejiang University, zhourui196@zju.edu.cn

Category: Neuroscience

Abstract Body : Background: The gut-brain axis has been recognized to play a critical role in health and disease. Gut microbiota dysbiosis during aging affects multiple systems including digestive system, circulated system and central nervous system. Fecal microbiota transplants have been applied to treat intestinal disease. However, whether fecal transplants from young donors could improve cognition decline induced by aging is still unclear. In this study, we investigated the effect of young fecal microbiota transplants in cognition of natural aged mice. Methods: Young fecal microbiota was collected from young donors (3 months, n = 10). Aged mice (14 months, n = 40) were randomly assigned into two groups, 14M control (14M WT, n = 20) and 14M Trans (n = 20). All the group received antibiotic treatment for two weeks, followed by young fecal microbiota transplantation twice a week for two weeks in 14M Trans group. After this two-week period, 14M Trans group received microbiota transplantation once a week for five months. Open field assay and passive avoidance assay were used to evaluate the motor function and memory of aged mice, respectively. 18F-fluorodeoxyglucose (18F-FDG) scanning was performed to estimate the glucose metabolism of brain. Western blot, reverse transcription-polymerase chain reaction (RT-qPCR), and immunofluorescence were performed to depict the changes of neuroinflammation and microglia activation in the brain. Results: Open field assay showed that aged mice received young fecal microbiota transplants had no difference in motor function compared with 14M WT group (A-D). However, 14M Trans group performed better in passive avoidance assay, which indicated that the cognition of 14M Trans group was improved (E). 18F-FDG scanning showed that the glucose uptake in hippocampus (p Conclusion: Our results showed that young fecal microbiota transplants could attenuate the cognition decline in natural aged mice. Glucose metabolism was improved in natural aged mice, especially in hippocampus and striatum. TNF-α and activated microglia were decreased after young fecal microbiota transplantation. These results suggested that young fecal microbiota transplantation might improve cognition of natural aged mice via affecting neuroinflammation, microglia activation and glucose metabolism.

Image/Figure: https://s3.amazonaws.com/amz.xcdsystem.com/1E8A4501-BB41-A02A-1D3B9882B798BFAA_abstract_File10351/GA223_ImageFigure_0513111123.pdf

Image/Figure Caption: (A-C) The distance (A), line crossings (B) and time immobile (C) in natural aged mice after 5 months treatment of young fecal microbiota transplants (14M WT, n = 9; 14M Trans, n = 7); (D) Represented image of mice trajectory in open field; (E) Mouse in 14M Trans (n = 8) had a longer latency to step into the dark compartment compared with mouse in 14M WT (n = 9); (F) TNF-α expression level in 14M Trans (n = 3) was significantly lower than 14M WT (n = 3); (G) Represented image of 18F-FDG scanning; (H-K) Statistic analysis of

cortex (H), hippocampus (I), striatum (J) and amygdala (K) in 14M Trans (n = 6) and 14M WT (n = 7); (L) Western blot results showed the expression level of ZO-1 and occludin in 14M Trans (n = 3) and 14M WT (n = 3); (M and N) Represented immunofluorescence images of activated microglia (Iba1+/CD68+) in 14M Trans and 14M WT.

Full Name of Abstract's 1st Author : Rui ZHOU

First Name: Rui

Last Name: Zhou

Email: zhourui196@zju.edu.cn

Organization: Zhejiang University

Country: China

ID: GA224

Metastatic status of lymph nodes in nasopharyngeal carcinoma detected by ultrasound-guided photoacoustic imaging using Carbonic Anhydrases IX targeted probe

Wenhui Huang, College of Medicine and Biological Information Engineering, Northeastern University, 18027110926@163.com

---

Category: Oncology

Abstract Body : Background and purpose Nasopharyngeal carcinoma (NPC) is most likely to occur with metastatic lymph nodes (mLN) in head and neck tumors owing to the extensive extravascular lymphatic capillary network under the mucosa1. The presence of mLN is a significant predictor of distant metastasis, especially when extranodal extension (ENE), described as tumor cells perforating the capsule into perinodal tissue, is diagnosed2,3. Yet significant advances in magnetic resonance imaging and positron emission tomography/computed tomography have increased the diagnosed accuracy of mLN, there has insufficient sensitivity and specificity to detect occult mLN with axial diameters smaller than 10 mm, and inadequate spatial resolution to confirm ENE for current imaging methods4,5. The purpose in our study is to evaluate the potential of Carbonic Anhydrases IX targeted probe (CAIX-800) for in vivo detection of occult mLN with higher sensitivity and specificity, and identification of ENE with sufficient spatial resolution using ultrasound guided spectroscopic photoacoustic imaging. Method Cell surface marker CAIX was validated for protein expression by western blot and confocal microscopy in seven human NPC cells. A peptide probe CAIX-800, containing IRDye 800CW and a moiety with high affinity to CAIX was synthetized based on our previous study6. The mLN models were generated by footpad injection of two human NPC cell lines (S18 and 5-8F) with high metastatic potential, respectively (n=10 per group, nude mice). Each mouse was received intravenous injection of 15 μM CAIX-800 and imaged with a closed-field near-infrared fluorescence imager to detect the occult mLN after 3 weeks of footpad injection. The feasibility of ENE identification was further in vivo imaged by a preclinical Vevo 2100 LAZR Imaging system. Harvested LNs were histologically examined ex vivo by the pathologist to confirm their metastatic status. Results Analysis of western blot revealed high-to-moderate levels of CAIX expression in seven NPC cell lines. Confocal microscopy demonstrated the satisfying cell targeting ability of CAIX-800 in vitro. In vivo optical imaging showed a significantly higher mean fluorescence intensity (MFI) in metastatic LNs vs. benign LNs, 3.646 ± 1.609 vs. 1.292 ± 0.737, respectively (mean ± standard deviation; Mann–Whitney U-test, p High area under the curve (AUC) were obtained for MFI (AUC = 0.9225, 95% confidence interval (CI), 0.8449–1.000) in receiver operating characteristic curve (ROC). The optimal threshold value for MFI was 1.960 at which a 80% sensitivity and a 80% specificity was reached (likelihood ratio 4.0). Notably, CAIX-800 clearly visualized most mLN(16/20) with excellent image quality, even if the axial diameter is as small as 1.6 mm(Figure.1B). Photoacoustic signal in the LNs corresponding to accumulated CAIX-800 were spectrally unmixed using a linear least square algorithm. Metastatic LNs had a third-fold increase in photoacoustic signal compared to benign LNs at 8 hour time point (Fig. 1E, p Conclusion Our findings offer an effective and

accurate tool to non-invasively identify occult mLN and extranodal extension, which have a strong potential for the diagnosis of early stage of metastatic NPC .

References: 1.Chen YP, Chan ATC, Le QT, Blanchard P, Sun Y, Ma J. Nasopharyngeal carcinoma. Lancet. 2019;394:64-80. 2.Mao Y, Wang S, Lydiatt W, et al. Unambiguous advanced radiologic extranodal extension determined by MRI predicts worse outcomes in nasopharyngeal carcinoma: Potential improvement for future editions of N category systems. Radiother Oncol. 2021;157:114-121. 3.Zhang Y, Zhang ZC, Li WF, Liu X, Liu Q, Ma J. Prognosis and staging of parotid lymph node metastasis in nasopharyngeal carcinoma: an analysis in 10,126 patients. Oral Oncol. 2019;95:150-156. 4.D'Cruz, AK, Vaish R, Kapre N, et al. Elective versus therapeutic neck dissection in node-negative oral cancer. N Engl J Med. 2015;373(6):521–529. 5.Prabhu RS, Magliocca KR, Hanasoge S, et al. Accuracy of computed tomography for predicting pathologic nodal extracapsular extension in patients with head-and-neck cancer undergoing initial surgical resection. Int J Radiat Oncol Biol Phys 2014;88:122–129. 6.Huang W, Wang K, An Y, et al. In vivo three-dimensional evaluation of tumor hypoxia in nasopharyngeal carcinoma using FMT-CT and MSOT. Eur J Nucl Med Mol Imaging. 2020;47(5):1027-1038.

Image/Figure:

https://s3.amazonaws.com/amz.xcdsystem.com/1E8A4501-BB41-A02A-1D3B9882B798BFAA_abstract_File10351/GA224_ImageFigure_0513111352.png

Image/Figure Caption: In vivo imaging of occult metastatic lymph nodes and extranodal extension. (A) Schematic illustrates normal nodal architecture and the growth of mLN. Metastatic cancer cells originally enter subcapsular sinus via afferent lymphatics. The growing metastases eventually perforate the capsule into perinodal tissue, resulting in ENE. (B) In vivo fluorescence image of a representative S18 mLN model at 12 hours after injection of CAIX-800. The mLN (orange arrow) is successfully visualized, with a minimum axial diameter of 1.6 mm. (C) Quantitative analysis of MFI between metastatic LNs and benign LNs ($p < 0.001$). (D) Representative fusion of ultrasound and photoacoustic images within mLN at 2 hour and 8 hour after injection of CAIX-800. Spectroscopic photoacoustic signal is displayed using red color. Metastatic lymph node is outlined in orange dashed line. Note the strong signal between subcapsular sinus and perinodal tissue. White arrows represent suspicious ENE. (E) Quantitative analysis of photoacoustic signal using average signal intensity in the highest 10% of pixels at different time points. The metastatic lymph nodes exhibit a statistically significant increase in the signal intensity ($p < 0.05$). (F) H&E and CAIX staining of lymph nodes from mice with positive signal in lymph nodes validate the presence of the metastases and extranodal invasion. Metastases are outlined in red dashed line. The white arrows represent ENE. P-values were determined via a two-tailed Mann–Whitney U test. mLN, metastatic lymph node. ENE, extranodal extension. MFI, mean fluorescence intensity. ROC, receiver operating characteristic curve. AUC, areas under the curve. CAIX, carbonic anhydrases IX.

Full Name of Abstract's 1st Author : Wenhui Huang

First Name: Wenhui

Last Name: Huang

Email: 18027110926@163.com

Organization: College of Medicine and Biological Information Engineering, Northeastern University

Country: China

ID: GA225
Biosynthesis of an Activatable Fluorescent MRI Contrast Agent

Harvey Lee, Michigan State University, leedohyu@msu.edu

Category: Bioengineering, Synthetic Biology and Basic Biology

Abstract Body : Objective: Studies involving the binding of proteins and rare earth elements (REE) are attractive to many researchers due to the versatility of proteins and unique attributes of rare earths. Among REEs, gadolinium is the most commonly used element for molecular imaging in the clinic with more than 30 million injections a year1. Several protein-based MRI contrast agents have been reported with attributes such as enhanced relaxivity, stability, and targeting capabilities2. Synthesis of these contrast agents can be simply achieved via bioreactors, allowing mass production at an affordable price while eliminating several steps and byproducts from chemical reactions. It is ideal to assess the presence of free ions left in the solution after initiating a binding to avoid reaction with other molecules in-vivo, and an excess amount of protein/chelate may be added to ensure safety. The answer to the question of how much more should be added above the theoretical ratio could differ with unique binding kinetics and adding too much would decrease performance. A current method of evaluating the existence of free rare earths involves the use of Arsenazo III, which is a calcium sensing dye that reacts with REEs as well as uranium, thorium, and zirconium. Here, we sought out to create a biosynthetically producible recombinant protein that directly indicates binding with high specificity for REEs, which can be utilized downstream as an MRI and optical imaging agent upon binding gadolinium. We have developed such a probe and have termed this new construct GLamouR (Green Lanmodulin-based Reporter, Figure 1). Methods: Protein was expressed in E. coli and isolated with HIS-tag purification and size exclusion. Western blot against the V5 tag (fused to the C terminus of the protein) was used to cross-confirm purification. Samples were dialyzed with TRIS buffer to remove residual imidazole in the solution. Fluorescence was acquired every 11 seconds, and REEs were added after the initial two readings. MRI measurements were performed under a field strength of 7T with samples in 1.5 mL centrifuge tubes. T1 relaxation times were acquired in six 1mm slices with 12 TR experiments ranging from 800ms to 17500ms, averaged 3 times. T2 relaxation times were acquired in the same geometry, with 75 echo images from 7.5ms to 562.5ms averaged 7 times. Results: Emission at 510nm (Figure 1 of Persuasive Data, n=5 wells with 10 averages, confirmed with separately purified GLamouR from 3 independent colonies) were observed to change +170.3% (±17.2) for Gd3+ and +169.2% (±21) for La3+, when compared to the first read. Negative controls were -9.5% for Ca2+ (±4.1) and -14.5% (±0.4) for TRIS buffer. Decrease in the controls are thought to be attributed to dilution upon adding REEs. MRI data (Figure 2 of Persuasive Data, confirmed for 2 independent batches) show the T1 relaxation time was shortened by approximately 50% from 3316 (± 9) ms for TRIS buffer to 1698 (±16) ms for TRIS solution containing the GLamouR-Gd complex. T2 relaxation time was shortened from 288.1 (±2.7) ms to 224.5 (±1.3) ms, resulting in a decrease of about 22%. Conclusion: Biosynthesis of contrast agents such as the GLamouR have the potential to be utilized as a contrast agent for MRI and optical imaging as well as a probe for residual gadolinium reported through an increase of fluorescence. This system can eliminate several steps

needed for quality control and synthesis, dramatically simplifying the process. Scaling up production while lowering costs via biosynthesis is being used in the pharmaceutical industry for therapeutics but has yet to be explored with molecular imaging probes.

References: 1. Guo, B.J. et al. Front Mol Neurosci 11, 335 (2018). 2. Salarian, M. et al. Nat Commun 10, 4777 (2019).

Image/Figure:

https://s3.amazonaws.com/amz.xcdsystem.com/1E8A4501-BB41-A02A-1D3B9882B798BFAA_abstract_File10351/GA225_ImageFigure_0513112240.png

Image/Figure Caption: Figure 1: A schematic illustration of GLamouR undergoing conformational change upon binding with gadolinium, resulting in increased light emission detectable at 510nm upon excitation at 488nm.

Full Name of Abstract's 1st Author : Harvey D. Lee

First Name: Harvey

Last Name: Lee

Email: leedohyu@msu.edu

Organization: Michigan State University

Country: United States

ID: GA226

In vivo monitoring of atherosclerosis by visualization of sr39tk expressing smooth muscle cells with [18F]FHBG positron emission tomography/magnetic resonance imaging (PET/MRI)

Dimitri Stowbur, Eberhard Karls University of Tuebingen, dimitri.stowbur@med.uni-tuebingen.de

---

Category: Cardiovascular & Pulmonary

Abstract Body : Introduction Cardiovascular diseases such as stroke, coronary and peripheral artery diseases are the leading cause for morbidities and mortalities in the western world. Life threatening clinical manifestations are based on the formation of an arterial plaque as a consequence of atherosclerosis. This process is initiated by endothelial lesions, followed by immune cell infiltration and intracellular accumulation of lipid molecules finally forming a core of extracellular lipids called atherosclerotic plaques. Herein, vascular smooth muscle cells (VSMCs), which are characterized by their enormous plasticity, are present at all stages and thus play a dominant role in disease progression but also in protection of the pathogenesis (1). Consequently, non-invasive in vivo visualization and tracking of VSMCs in atherosclerosis might represent a novel powerful tool to monitor atherosclerotic plaque formation and to uncover the dedicated role of VSMCs in atherosclerosis. Methods First, we generated experimental mice which express the PET reporter gene sr39tk exclusively in VSMCs (sr39tk/VSMCs) after Cre-mediated recombination enabling their non-invasive in vivo visualization. Furthermore, to enable visualization of the temporal dynamics of atherosclerotic plaque formation, sr39tk/VSMCs mice were crossed with apolipoprotein-deficient (ApoE-/-) mice which develop atherosclerosis. Thus, the radiotracer [18F]FHBG exclusively accumulates in sr39tk expressing VSMCs after sr39tk-mediated phosphorylation enabling non-invasive in vivo detection of VSMCs by PET/MRI. In our experimental setup MRI was used for anatomical co-registration. In addition we performed biodistribution analysis, autoradiography, histopathology (H&E) and immunohistochemistry for ex vivo cross validation of the in vivo [18F]FHBG. Results Non-invasive in vivo [18F]FHBG PET/MRI of transgenic sr39tk/VSMCs mice revealed a significantly increased [18F]FHBG uptake in sr39tk expressing VSMCs in the aorta and its branched vessels but not in wild-type control mice without sr39tk expressing VSMCs (PET signal equals background signal). In line with our expectations we determined an even more profound [18F]FHBG uptake in atherosclerotic plaques of atherosclerosis developing sr39tk/VSMCs x ApoE-/- mice. In these mice [18F]FHBG PET/MRI allowed the precise visualization of arteries as well as the site of aortic atherosclerotic plaque formation. Quantitative analysis of the increased [18F]FHBG uptake within the aortic atherosclerotic plaques of sr39tk/VSMCs x ApoE-/- mice revealed significantly elevated [18F]FHBG uptake values (1.075 %ID/ml ± 0.188 %ID/ml SEM; n = 5) when compared to the unaffected aortic arch of sr39tk/VSMCs mice (0.6112 %ID/ml ± 0.058 %ID/ml SEM; n = 5). Ex vivo [18F]FHBG biodistribution and autoradiography analysis verified our in vivo [18F]FHBG PET/MRI examinations. Conclusion/Discussion We are the first group monitoring atherosclerotic plaque formation with [18F]FHBG PET/MRI via direct targeting of sr39tk expressing VSMCs. In conclusion, sr39tk reporter mice are a powerful tool to track

defined cells of interest and hence, even tiny structures like atherosclerotic plaques, in experimental disease models using [18F]FHBG PET/MRI and facilitate deeper insights into the pathogenesis of specific diseases.

References: 1. Basatemur GL, Jørgensen HF, Clarke MCH, Bennett MR, Mallat Z. Vascular smooth muscle cells in atherosclerosis. Nature Reviews Cardiology. 2019;16(12):727-44.

Full Name of Abstract's 1st Author : Dimitri Stowbur

First Name: Dimitri

Last Name: Stowbur

Email: dimitri.stowbur@med.uni-tuebingen.de

Organization: Eberhard Karls University of Tuebingen

Country: Germany

ID: GA227

Molecular imaging and mechanism of CXCL12/CXCR4 axis in liver metastasis by Precision MRI (pMRI)

zongxiang gui, Georgia State University, ZGUI1@STUDENT.GSU.EDU

Category: New Chemistry, Materials & Probes

Abstract Body : The Chemokine CXCL12 /stromal cell-derived factor 1 alpha and its receptor CXCR4 play important roles in various biological and pathological processes, including growth, migration, adhesion, invasion and infiltration of multiple cancer and organ specific metastasis. There is a pressing unmet need to develop non-invasive molecular imaging, with the additional quantification capability to monitor the CXCL12/CXCR4 axis at different stages of liver metastasis promoted by the high-fat diet at the cell, tissue, and body levels. Here we report the recent development of our pioneered novel class of protein-based MRI contrast agents focusing on humanized Gd3+ based CXCR4 and CXCL12 targeted MRI contrast agents (hProCA32.CXCR4 and hProCA32.CXCL12). Both hProCA32.CXCR4 and hProCA32.CXCL12 exhibits high dual relaxivities that are 5-10 folds of Eovist and Multihance at both 1.4T and 7.0T. They also exhibit much stronger serum stability and metal selectivity for Gd over physiological metal ions than clinically approved agents. Importantly CXCR4 targeted contrast agent has a strong binding capability to expressed CXCR4 on cancer cells (Kd: 0.4 ± 0.05 μM) while not perturbing downstream signaling. This important feature enables us to apply ProCA32.CXCR4 as an excellent companion diagnostic agent for monitoring treatment effects and drug development. We have demonstrated that ProCA32.CXCR4 has enabled early detection and stage of liver metastasis of cancers (including uveal melanoma, ovarian cancer) with much-improved sensitivity and specificity compared with non-targeted agents and Eovist. The CXCL12 targeted MRI contrast agent (hProCA32.CXCL12) is able to provide the first delineation of the micro-vessel (sinusoid space) structure of the liver using pMRI. We discovered that high fat largely alters liver sinusoid structure with a microenvironment pro-metastasis. Large production and application of these developed contrast agents will have a major impact on tumor diagnosis and treatment stratification.

References: Chatterjee, Samit, Babak Behnam Azad, and Sridhar Nimmagadda. "The intricate role of CXCR4 in cancer." Advances in cancer research 124 (2014): 31-82. Bakalian, Silvin, et al. "Molecular pathways mediating liver metastasis in patients with uveal melanoma." Clinical Cancer Research 14.4 (2008): 951-956. Xue, S. et al. Protein MRI contrast agent with unprecedented metal selectivity and sensitivity for liver cancer imaging. Proceedings of the National Academy of Sciences 112, 6607-6612 (2015). Yang, Jenny J., et al. "Rational design of protein-based MRI contrast agents." Journal of the American Chemical Society 130.29 (2008): 9260-9267. Tan, S. et al. Chemokine receptor 4 targeted protein MRI contrast agent for early detection of liver metastases. Science Advances 6, eaav7504 (2020). Ohashi, Koichiro, et al. "NOD-like receptor C4 inflammasome regulates the growth of colon cancer liver metastasis in NAFLD." Hepatology 70.5 (2019): 1582-1599.

Image/Figure:

https://s3.amazonaws.com/amz.xcdsystem.com/1E8A4501-BB41-A02A-1D3B9882B798BFAA_abstract_File10351/GA227_ImageFigure_0513113240.png

Image/Figure Caption: CXCR4-targeted protein MRI contrast agent (hProCA32.CXCR4) (A) Show high relaxivities. (B) Post-injection ProCA32.CXCR4, MR image of the OCM1 mouse exhibits the liver metastases which are invisible in the pre-injection MR image. Metastases in the H&E staining are well-correlated with the ones recognized in the MR image. (C) MR image of ovarian cancer mouse model (SK-OV-3) shows the enhancement of liver metastatic lesions with hProCA32.CXCR4 administration. Metastases in the MR image were identified in the H&E staining (red-circle regions). CXCL12-targeted protein MRI contrast agent (hProCA32.CXCL12) (D) Show high relaxivities. (E) Intrahepatic vessels show in the MRI imaging of colon cancer liver metastasis after application of hProCA32.CXCL12.

Full Name of Abstract's 1st Author : Zongxiang Gui

First Name: zongxiang

Last Name: gui

Email: ZGUI1@STUDENT.GSU.EDU

Organization: Georgia State University

Country: United States

ID: GA228
Neuroinflammation Following Sport Concussion in Collegiate Athletes

Kiel Neumann, University of Virginia, kdn2e@virginia.edu

Category: Neuroscience

Abstract Body : Since 1997, a multidimensional approach has been recommended to diagnose and manage athletes suspected of having a sport-related concussion (SRC).1, 2 The recommended assessment protocol consists of clinic-based measures of balance, neurocognitive function, and concussion-related symptomology which has been demonstrated to have a sensitivity of up to 100% within 24 hours of a diagnosed SRC in collegiate athletes.3, 4 Despite the clinical utility of this multifaceted approach, a growing body of evidence suggests that physiological recovery from a SRC may persist well beyond apparent clinical recovery based on this accepted multi-faceted clinical evaluation. Microglia function to serve and protect the brain, and are wholly dedicated to maintaining homeostasis. Microglia phagocytose apoptotic neurons and secrete inflammatory factors to attract other immune cells to the site of injury. The resolution of this series of events is a tightly regulated process that occurs when injury has been resolved.5,6 However, if left unresolved, such as the case of chronic or pathologic inflammation, neuronal damage and loss of brain function can occur and impede recovery. More recent human-based studies have investigated central inflammation using positron emission tomography (PET) and single-photon emission computerized tomography (SPECT) following a SRC7-9 targeting the translocator protein (TSPO), which is an 18 kDa transmembrane protein overexpressed in mitochondria of microglia as a result of neuronal insult. For example, Coughlin et al studied [11C]DPA-713 in active and retired NFL athletes and demonstrated increased distribution volume (Vt), as measured by PET, in the hippocampus, amygdala, supramarginal gyrus, and temporal pole compared to healthy age-matched controls. These studies present evidence that chronic neuroinflammation may be a consequence of individuals engaged in career contact sport. The purpose of this pilot study was to determine the presence of neuroinflammation beyond clinical recovery in active, collegiate athletes following a diagnosed SRC using [18F]DPA-714, a radiopharmaceutical specific for TSPO10. We hypothesized that collegiate athletes who were diagnosed with a SRC, but have been permitted to return to play, would show significantly higher Vt compared to healthy age-matched controls. We enrolled 10 athletes and 10 healthy age-matched controls (5 male and 5 female in each category). All subjects completed a standard clinical battery of concussion tests to achieve “return-to-play” status. Before returning to sport, subjects consented to T1-weighted MP-RAGE MRI and a 90 minute dynamic PET scan. Total distribution volume was derived and corrected for metabolites by blood sampling. Regional CNS comparisons between groups showed >75% differences in Vt across 11/12 brain regions. These data suggest neuroinflammation persists in collegiate athletes who have sustained a concussion, despite being cleared to return-to-play using the current clinical gold standard workup. Further studies confirming these findings in an expanded cohort are ongoing.

References: 1. (1997). Practice parameter: the management of concussion in sports (summary statement). Report of the Quality Standards Subcommittee. Neurology 48, 581-585. 2. McCrory,

P., Meeuwisse, W., et al. (2017). Consensus statement on concussion in sport-the 5(th) international conference on concussion in sport held in Berlin, October 2016. Br J Sports Med 51, 838-847. 3. Broglio, S.P., Harezlak, J., et al(2019). Acute Sport Concussion Assessment Optimization: A Prospective Assessment from the CARE Consortium. Sports Med 49, 1977-1987. 4. Resch, J.E., Brown, C.N., et al. (2016). The sensitivity and specificity of clinical measures of sport concussion: three tests are better than one. BMJ Open Sport & Exercise Medicine 2, 1-10. 5. Tronel, C., Largeau, B., et al. (2017). Molecular Targets for PET Imaging of Activated Microglia: The Current Situation and Future Expectations. Int J Mol Sci 18. 6. Graeber, M.B. and Streit, W.J. (2010). Microglia: biology and pathology. Acta Neuropathol 119, 89-105. 7. Coughlin, J.M., Wang, Y. et al (2017). Imaging of Glial Cell Activation and White Matter Integrity in Brains of Active and Recently Retired National Football League Players. JAMA Neurol 74, 67-74. 8. Coughlin, J.M., Wang, Y., et al (2015). Neuroinflammation and brain atrophy in former NFL players: An in vivo multimodal imaging pilot study. Neurobiol Dis 74, 58-65. 9. Ebert, S.E., Jensen, P., et al (2019). Molecular imaging of neuroinflammation in patients after mild traumatic brain injury: a longitudinal (123) I-CLINDE single photon emission computed tomography study. Eur J Neurol 26, 1426-1432. 10. Doorduin, J., Klein, H.C., et al. (2009) [11C]-DPA-713 and [18F]-DPA-714 as New PET Tracers for TSPO: A Comparison with [11C]-(R)-PK11195 in a Rat Model of Herpes Encephalitis. Mol Imaging Biol 11, 386.

Image/Figure Caption:

First Name: Kiel

Last Name: Neumann

Email: kdn2e@virginia.edu

Organization: University of Virginia

Country: United States

ID: GA229

Synthesis and preclinical evaluation of a novel dual PET/NIRF probe for the targeting of urokinase receptor

Ivan Hawala, Università degli Studi di Torino, ivan.hawala@gmail.com

---

Category: New Chemistry, Materials & Probes

Abstract Body : The combination of two different imaging modalities overcomes certain limitations related to each technique. Here, a dual probe for imaging urokinase receptor (uPAR) by molecular positron emission tomography (PET) and Near InfraRed Fluorescence (NIRF) imaging has been designed to assess the biomarker expression in a pre-operative setting, by 68Ga (or 44Sc)-PET and, in case of positive response, exploiting the NIRF moiety to aid surgeons intra-operatively to discriminate between tumor and healthy tissues during tumor resection. The synthetic pathway (2 steps) relied on an innovative synthesis approach based on the native chemical ligation. The first step consisted in the condensation between chelator, pre-activated as thioester, and peptide, functionalized with an N-terminal cysteine, in buffer at pH around 7. Afterwards, a solution containing S-Cy5.5, pre-activated as maleimide, was added to the reaction mixture (step 2). Final purification was performed by semi-preparative reverse phase liquid chromatography, to obtain AAZTA-C4-CO-Cys(Sulfo Cy 5.5)-AE105 (1) with 99% of purity and an overall yield of 27%. Metal complexation with natural gallium isotope was easily carried out in 10 minutes using equimolar amounts of 1 and gallium chloride at room temperature in acetate buffer at pH 3.8. The uPAR affinity of Ga-AAZTA-C4-CO-Cys(Sulfo Cy 5.5)-AE105 (2) was evaluated by flow cytometry, showing a highest affinity for the U-87 MG glioblastoma cell line with respect to the control MCF-7. The behavior of the control cell line MCF-7 with probe 2 depicted lower fluorescence values, thus confirming the difference in the urokinase receptor expression of the two cell populations. The demonstration that the binding of probe 2 is driven by the targeting vector is provided by the observation that S-Cy 5.5 dye alone showed no affinity for U-87 MG glioblastoma cell line, with values below 5% in all concentrations range. A further confirmation of uPAR targeting was gained by performing blocking experiments with a 100 fold excess concentration of the AE105 peptide that highlighted a significant decrease in the number of cells that bind probe 2. Overall, these results underline that probe 2 recognize uPAR on the surface of U-87 MG glioblastoma cell line with a dose-dependent behavior in the tested concentration range. A preliminary preclinical validation of the dual probe 2, aimed at assessing its ability to be taken up by uPAR expressing tumors, was carried out on mice grafted with U-87 MG cells. The animals were intravenously administered with 5 nmol of probe 2. NIRF images were acquired from 30 min up to 24 h post administration. The images provided a clear indication about the predominant renal elimination of the probe. The tumor-to-background ratio, using muscles as reference, was comprised between 2 and 3 in the entire time window investigated, with a maximum tumor signal detected 2h post injection. After the last in vivo imaging acquisition, mice were sacrificed and ex vivo imaging of harvested organs showed that 24h post-injection probe 2 accumulated mainly in kidneys and tumors, and slightly less in liver and intestine. The almost null brain uptake is a relevant important finding if considering the use of this probe in surgical treatments of glioblastoma. In summary, a new

potential dual PET/NIRF peptide-based imaging probe for the targeting of urokinase receptor, has been efficiently synthesized. The in vitro results confirmed the good affinity and specificity of the probe (complexed with “cold” Ga(III)), whose cell binding was proportional to the expression levels of uPAR. The preliminary in vivo evaluation of probe 2 was performed by NIRF imaging on a mouse model of glioblastoma (U87-MG) showing a good tumor uptake up to 24 h post injection, with a maximum tumor fluorescence signal detected 2h post injection.

References: Baart, V. M., Houvast, R. D., de Geus-Oei, L. F., Quax, P. H. A., Kuppen, P. J. K., Vahrmeijer, A. L., and Sier, C. F. M. (2020) Molecular imaging of the urokinase plasminogen activator receptor: opportunities beyond cancer. EJNMMI Res 10, 87. Seibold, U., Wängler, B., Schirrmacher, R., and Wängler, C. (2014) Bimodal imaging probes for combined PET and OI: recent developments and future directions for hybrid agent development. Biomed Res Int 2014, 153741. Ploug, M., Østergaard, S., Gårdsvoll, H., Kovalski, K., Holst-Hansen, C., Holm, A., Ossowski, L., and Danø, K. (2001) Peptide-derived antagonists of the urokinase receptor. affinity maturation by combinatorial chemistry, identification of functional epitopes, and inhibitory effect on cancer cell intravasation. Biochemistry 40, 12157-68. Manzoni, L., Belvisi, L., Arosio, D., Bartolomeo, M. P., Bianchi, A., Brioschi, C., Buonsanti, F., Cabella, C., Casagrande, C., Civera, M., De Matteo, M., Fugazza, L., Lattuada, L., Maisano, F., Miragoli, L., Neira, C., Pilkington-Miksa, M., and Scolastico, C. (2012) Synthesis of Gd and (68)Ga complexes in conjugation with a conformationally optimized RGD sequence as potential MRI and PET tumor-imaging probes. ChemMedChem 7, 1084-93. Ghiani, S., Hawala, I., Szikra, D., Trencsényi, G., Baranyai, Z., Nagy, G., Vágner, A., Stefania, R., Pandey, S., and Maiocchi, A. (2021) Synthesis, radiolabeling, and pre-clinical evaluation of [Eur J Nucl Med Mol Imaging. Hawala, I., De Rosa, L., Aime, S., and D'Andrea, L. D. (2020) An innovative approach for the synthesis of dual modality peptide imaging probes based on the native chemical ligation approach. Chem Commun (Camb) 56, 3500-3503.

Image/Figure:

https://s3.amazonaws.com/amz.xcdsystem.com/1E8A4501-BB41-A02A-1D3B9882B798BFAA_abstract_File10351/GA229_ImageFigure_0513113931.png

Image/Figure Caption: In vivo dynamic images and profiles acquired after injection of 5 nmol of probe 2 and ex vivo ROI (Region of Interest) evaluation in the organs 24h post injection. Time points: 0.5h, 1h, 2h, 4h, 6h, 8h, and 24h. Organs: 1. Blood, 2. Heart, 3. Lung, 4. Testis, 5. Bladder, 6. Prostate, 7. Intestine, 8. Skin, 9. Liver, 10. Spleen, 11. Muscle, 12. Tumor, 13. Salivary glands, 14. Brain, 15. Kidneys.

Full Name of Abstract's 1st Author : Ivan Hawala

First Name: Ivan

Last Name: Hawala

Email: ivan.hawala@gmail.com

Organization: Università degli Studi di Torino

Country: Italy

ID: GA230

Validation of the Intramuscular Route as an Appropriate Alternative to Intravenous Injection for Hamster 18F-FDG PET/CT Studies in a BSL-4 Setting

Hui Wang, Integrated Research Facility, National Institute of Allergy and Infectious Disease, National Institutes of Health, hui.wang3@nih.gov

---

Category: Immunology: Inflammation & Infection

Abstract Body : Background: Infectious diseases remain one of the biggest challenges for human health. To understand the pathogenesis of infectious diseases and develop effective diagnostic tools, therapeutics, and vaccines, finding a suitable animal model is essential. The golden hamster (Mesocricetus auratus) has been used as a small animal model to study emerging and acute human viral diseases caused by highly pathogenic viruses, such as Nipah, Ebola, and Marburg viruses, as well as SARS-CoV-2. 18F-FDG-PET imaging has been used to diagnose and monitor longitudinally inflammatory responses because 18F-FDG accumulates in activated inflammatory cells. However, the quantitative capability of 18F-FDG-PET is based on precise bolus intravenous (IV) administration of 18F-FDG, which is particularly difficult in high-containment laboratory settings, required for highly pathogenic animal studies, because of the lack of easily accessible veins in hamsters and also multiple layers of the personal protective equipment required for personnel safety in biosafety level 4 (BSL-4) laboratories. With an increasing need to use 18F-FDG on numerous imaging studies within short time periods, it is essential to search for alternate administration routes that are technically easier, faster, and reproducible without complications. Objectives: Intramuscular (IM) and intraperitoneal (IP) routes were compared with the IV route for 18F-FDG administration in healthy hamsters. Materials and Methods: The study used a total of 16 age- and gender-matched hamsters, including 10 surgically implanted with vascular access ports (VAPs) for IV administration of 18F-FDG in BSL-4 settings. Serial PET scans were performed with the IM, IP, or IV routes to assess the technical feasibility; spatial and temporal distributions of 18F-FDG were compared by serial PET scans at different time points after administration. Additional dynamic PET scans were performed to further compare the characteristics of the IM and IV routes. The injected dose for SUV calculation was corrected for residual 18F-FDG activity at the injection sites for IM and within the catheters for IV route. Two-way ANOVA was used for the comparison of repeated measurements. Results and Discussion: In IM route hamsters, 18F-FDG retained at the injection site accounted for 9.73 ± 3.48% of the whole-body radioactivity at 60 min post-injection (p.i.). The IV route via VAP was successful initially; however, significant leakage occurred during 18F-FDG administration, which may have resulted from shifting of the catheter in these rapidly growing animals, indicating limited application in longitudinal PET studies. At 60 min p.i., the IM and IP groups had comparable 18F-FDG uptake in the brain, heart, kidney, liver, lungs, and muscles. However, a significantly higher abdominal 18F-FDG retention (p At 60 min p.i., the IM and IV groups had comparable 18F-FDG uptake in the liver, lungs, muscles, and blood, with the IM group showing higher uptake in the brain, heart, and kidney (p 18F-FDG accumulation changes at 7–55 min after administration, the area under the curve (AUC) of the time-activity curve from the IM and IV groups were calculated and compared. The AUC of the IM group was

greater than that of the IV group in the brain, liver, and blood (p This is likely due to slow release of the tracer from the IM injection depot. Conclusion and Significance: To conduct hamster 18F-FDG PET imaging in BSL-4 laboratories, IM injection could serve as an alternative to the IV route because it's technically easy, highly reproducible, and safe. However, the injection route, PET acquisition time, and other experimental settings should be determined before the study start and kept consistent throughout the longitudinal studies.

References: Kim, C., I. H. Kim, S. I. Kim, Y. S. Kim, S. H. Kang, S. H. Moon, T. S. Kim, and S. K. Kim. "Comparison of the Intraperitoneal, Retroorbital and Per Oral Routes for F-18 Fdg Administration as Effective Alternatives to Intravenous Administration in Mouse Tumor Models Using Small Animal Pet/Ct Studies." Nucl Med Mol Imaging 45, no. 3 (Sep 2011): 169-76. https://dx.doi.org/10.1007/s13139-011-0087-7. Koski, A., H. Ahtinen, H. Liljenback, A. Roivainen, A. Koskela, M. Oksanen, K. Partanen, L. Laasonen, K. Kairemo, T. Joensuu, and A. Hemminki. "[(18)F]-Fluorodeoxyglucose Positron Emission Tomography and Computed Tomography in Response Evaluation of Oncolytic Adenovirus Treatments of Patients with Advanced Cancer." Hum Gene Ther 24, no. 12 (Dec 2013): 1029-41. https://dx.doi.org/10.1089/hum.2013.123. Mahakian, L. M., D. G. Farwell, H. Zhang, J. W. Seo, B. Poirier, S. P. Tinling, A. M. Afify, E. M. Haynam, D. Shaye, and K. W. Ferrara. "Comparison of Pet Imaging with 64cu-Liposomes and 18f-Fdg in the 7,12-Dimethylbenz[a]Anthracene (Dmba)-Induced Hamster Buccal Pouch Model of Oral Dysplasia and Squamous Cell Carcinoma." Mol Imaging Biol 16, no. 2 (Apr 2014): 284-92. https://dx.doi.org/10.1007/s11307-013-0676-1.

Image/Figure:

https://s3.amazonaws.com/amz.xcdsystem.com/1E8A4501-BB41-A02A-1D3B9882B798BFAA_abstract_File10351/GA230_ImageFigure_0513114037.JPG

Image/Figure Caption: Figure 1. Representative PET images from one hamster that received 18F-FDG via intramuscular (IM) and intravenous (IV) administration 4 d apart. The sagittal views showed higher brain uptake of 18F-FDG with IM (A) administration as compared to IV (C) administration, while coronal views showed that comparable 18F-FDG uptake in liver, lungs, and muscle (B vs. D). PET imaging was performed at 60 min post-injection (p.i.). The scale bar indicates SUV values.

First Name: Hui

Last Name: Wang

Email: hui.wang3@nih.gov

Organization: Integrated Research Facility, National Institute of Allergy and Infectious Disease, National Institutes of Health

Country: United States

ID: GA232
Synthesis, in vitro and in vivo evaluation of a novel SPECT and Auger electron-emitting radionuclide thallium-201

Alex Rigby, King's College London, alex.rigby@kcl.ac.uk

Category: New Chemistry, Materials & Probes

Abstract Body : Introduction 201Tl (t1/2 = 73 hours, ~37 Auger electrons/decay) can be tracked in vivo via its gamma emissions (imaged using SPECT scanners) whilst delivering a therapeutic dose to tumours via its Auger emissions. Auger electron therapy uses low energy electrons emitted during radioactive decay which travel very short distances (typically Methods Following a recently published method using iodobeads, [201Tl]Tl(III) was generated from commercially available [201Tl]Tl(I) in a quick, simple and biomolecule-friendly way.[1] We evaluated a wide range of chelating agents for [201Tl]Tl(III), of which H4pypa (Fig 1B), previously established as an excellent chelator for [111In]In(III), showed the most promising properties.[2] The serum stability of the radiolabelled [201Tl]Tl(III)-pypa complex was then investigated via incubation in human serum (37 °C) at various time points (1, 24 and 48 h) with monitoring by RP-TLC. A PSMA targeting bioconjugate (Fig 1C) of H4pypa was synthesised and radiolabelled. We used SPECT imaging to probe the in vivo biodistribution and stability of [201Tl]Tl(III)-pypa-PSMA bioconjugate in healthy SCID beige mice, and compared it to [201Tl]Tl(I)Cl and [201Tl]Tl(III)Cl3 as controls. Results [201Tl]TlCl3 was prepared from [201Tl]TlCl using iodobeads under mild conditions within 15 minutes at room temperature.[1] [201Tl]Tl(III) generated was chelated by H4pypa in high yields (98 ± 2 %) at room temperature within 15 minutes, as shown by the HPLC in Fig 1A. The complex remained largely intact in serum for an hour, but integrity dropped to 61 % after 24 h and 44 % after 48 h (Fig 1B). A PSMA bioconjugate of pypa was synthesised using a lipophilic linker, based on PSMA-617 (Fig 1C).[3] [201Tl]Tl(III)-pypa-PSMA showed excretion through the kidneys and bladder with little heart uptake observed, suggesting adequate in vivo stability for delivery to tumours. In contrast, [201Tl]Tl(I)Cl and [201Tl]Tl(III)Cl3 both showed high heart uptake at 15 minutes, and renal excretion over the following hour. Compared to [201Tl]Tl(III)-pypa-PSMA, [201Tl]Tl(I)Cl and [201Tl]Tl(III)Cl3 showed significantly less radioactivity in the bladder (Fig 1D). Conclusions [201Tl]Tl(III) can be chelated at room temperature within 15 minutes using H4pypa. The complex showed good serum stability in human serum. A PSMA bioconjugate was radiolabelled and in vivo biodistribution studies revealed fast renal clearance with no evidence of [201Tl]Tl(III) release. This, combined with promising radiobiologial evaluation of the cellular toxicity of internalised 201Tl, highlights the potential use of 201Tl for use as a theragnostic agent to deliver a therapeutic dose, while being tracked within the body using SPECT imaging.

References: [1] Rigby A, Blower JE, Blower PJ, Terry SYA, Abbate V. Targeted auger electron-emitter therapy: Radiochemical approaches for thallium-201 radiopharmaceuticals. Nucl Med Biol 2021;98–99:1–7. https://doi.org/10.1016/j.nucmedbio.2021.03.012. [2] Li L, Jaraquemada-Peláez MDG, Kuo HT, Merkens H, Choudhary N, Gitschtaler K, et al. Functionally Versatile and Highly Stable Chelator for 111In and 177Lu: Proof-of-Principle

Prostate-Specific Membrane Antigen Targeting. Bioconjug Chem 2019;30:1539–53. https://doi.org/10.1021/acs.bioconjchem.9b00225. [3] Li L, de Guadalupe Jaraquemada-Peláez M, Aluicio-Sarduy E, Wang X, Barnhart TE, Cai W, et al. Coordination chemistry of [Y(pypa)]- and comparison immuno-PET imaging of [44Sc]Sc- And [86Y]Y-pypa-phenyl-TRC105. Dalt Trans 2020;49:5547–62. https://doi.org/10.1039/d0dt00437e.

Image/Figure:

https://s3.amazonaws.com/amz.xcdsystem.com/1E8A4501-BB41-A02A-1D3B9882B798BFAA_abstract_File10351/GA232_ImageFigure_0513114716.png

Image/Figure Caption: Figure 1 – (A) HPLC trace for [201Tl]Tl(III)-pypa, orange = counts per second (CPS), blue = UV (mAU). (B) The structure of pypa-PSMA. (C) The structure of H4pypa and the serum stability of [201Tl]Tl(III)-pypa after incubation with human serum at 37 °C at 1, 24 and 48 h. Solid phase = reverse phase TLC, mobile phase = MeCN (30 %)/H2O. (D) In vivo images of [201Tl]Tl(I)Cl, [201Tl]Tl(III)Cl3 and [201Tl]Tl(III)-pypa-PSMA at 15, 30, 45 and 60 minutes post injection.

Full Name of Abstract's 1st Author : Alex Rigby

First Name: Alex

Last Name: Rigby

Email: alex.rigby@kcl.ac.uk

Organization: King's College London

Country: United Kingdom

ID: GA233

Precision MR imaging of intrahepatic reactive oxygen species in a mouse model of nonalcoholic steatohepatitis

Eric Gale, Massachusetts General Hospital and Harvard Medical School, emgale@mgh.harvard.edu

---

Category: New Chemistry, Materials & Probes

Abstract Body : Study objectives and hypothesis. Inflammation plays a key pathogenic role in NASH but there is a paucity of radiologic tools to image, quantify, and monitor liver inflammation. The goal of this study is to evaluate whether the reactive oxygen species (ROS) activated magnetic resonance imaging (MRI) probe Fe-PyC3A can be used to non-invasively image pathologic increases in intrahepatic ROS in a dietary mouse model of nonalcoholic steatohepatitis (NASH). Fe-PyC3A is a first in class ROS-responsive MR imaging probe that generates virtually zero signal in normal tissue but strong signal enhancement in the presence of ROS. In normal liver ROS levels are low, but the metabolic and inflammatory changes associated with NASH result in increased ROS levels and an aberrant oxidizing liver microenvironment.1-3 We hypothesize that ROS imaging using Fe-PyC3A represents a noninvasive biomarker to detect, quantify, and monitor changes in liver ROS levels associated with NASH. Innovation and Significance. Inflammation play a key pathogenic role in NASH and in this study we demonstrate how MR imaging of reactive oxygen species using the novel MR imaging probe Fe-PyC3A represents a potential biomarker for pathologic inflammatory changes associated with NASH. Experiment design. For this study, three groups of male C57BL/6 mice (5 weeks at start of study) were fed either L-amino acid defined, choline deficient, and high fat diet (CDHAFD) or normal diet (ND) for 4, 6, or 8 weeks and then imaged. N=6 CDAHFD and N=4 ND mice were imaged for each dietary treatment. The mice were imaged with a 4.7 T small-bore scanner (Bruker Biospec) with a custom-built volume coil. 2D T1-weighted coronal gradient echo images of the abdomen were acquired prior to and 2 minutes after injection of 0.2 mmol/kg Fe-PyC3A via the tail vein. The (post-pre) injection change in liver vs. muscle contrast-to-noise ratio (DCNR) were quantified separately in the left and right lobes of the liver. After imaging, the left and right lobes of the liver were harvested and assayed for myeloid leukocyte content (neutrophils and CCR2, M1 and M2 macrophages) by flow cytometry. Flow cytometry data was reported as percentage of live leukocytes. Comparisons in DCNR and intrahepatic leukocyte levels between CDAHFD and ND mice were made separately for each group using a two-sided t-test with a Bonferroni-Dunn correction for multiple comparisons. We tested for correlations between DCNR and percentage intrahepatic neutrophils using the entire set of 60 liver samples (30 mice x 2 liver lobes) using Pearson's product moment correlation coefficient. Results. Figure 1A compares T1-weighted coronal images of mice fed a 6-week regimen of ND and CDAHFD diet recorded 2 min after Fe-PyC3A injection. At the 6-week time point, DCNR was significantly elevated in CDAHFD mice compared to ND mice (1.9±0.65 vs. -1.5±1.8, P DCNR and neutrophils (P = 0.015) and M1 macrophages (P = 0.034), Figure 1C. Conclusions. Fe-PyC3A provides greater liver vs. muscle DCNR in mice fed a 6-week regimen of CDAHFD compared to control mice fed ND. Intrahepatic levels of ROS-generating myeloid leukocytes are

also increased in CDAHFD mice at 6 weeks. Across all liver samples analyzed DCNR correlated positively and significantly with liver neutrophil and M1 macrophage infiltration. Taken together, our data indicates that MR imaging using Fe-PyC3A may represent a non-invasive biomarker to monitor pathologic hepatic inflammatory changes that accompany NASH.

References: 1. Wang, H.; Clavijo Jordan, V.; Ramsay, I. A.; Sojoodi, M.; Fuchs, B. C.; Tanabe, K. K.; Caravan, P.; Gale, E. M., Molecular Magnetic Resonance Imaging Using a Redox-Active Iron Complex. J. Am. Chem. Soc. 2019, 141 (14), 5916-5925. 2. Browning, J. D.; Horton, J. D., Molecular mediators of hepatic steatosis and liver injury. J Clin Invest 2004, 114 (2), 147-52. 3. Tosello-Trampont, A. C.; Landes, S. G.; Nguyen, V.; Novobrantseva, T. I.; Hahn, Y. S., Kuppfer cells trigger nonalcoholic steatohepatitis development in diet-induced mouse model through tumor necrosis factor-alpha production. J Biol Chem 2012, 287 (48), 40161-72. 4. Pulli, B.; Wojtkiewicz, G.; Iwamoto, Y.; Ali, M.; Zeller, M. W.; Bure, L.; Wang, C. H.; Choi, Y.; Masia, R.; Guimaraes, A. R.; Corey, K. E.; Chen, J. W., Molecular MR Imaging of Myeloperoxidase Distinguishes Steatosis from Steatohepatitis in Nonalcoholic Fatty Liver Disease. Radiology 2017, 284 (2), 390-400.

Image/Figure:

https://s3.amazonaws.com/amz.xcdsystem.com/1E8A4501-BB41-A02A-1D3B9882B798BFAA_abstract_File10351/GA233_ImageFigure_0513114916.png

Image/Figure Caption: Figure 1. (A) Coronal 2D T1W gradient echo MR images (TE/TR = 2.9/190.4, flip-angle = 60°, Averages = 4) of the abdomen of mice fed a 6-week regimen of CDAHFD or ND acquired 2 min after Fe-PyC3A injection. Quantification of (post-pre)injection liver vs. muscle contrast to noise ratio shown in false color scale. (B) Comparison of (post-pre)injection liver vs. muscle contrast to noise ratio acquired 2 min after Fe-PyC3A injection and intrahepatic levels of neutrophils, CCR2, M1, and M2 macrophages in mice fed ND (white) or CDAHFD (grey) for 4, 6, or 8 weeks. (C) Across all the liver specimens analyzed, DCNR correlates positively and significantly with the percentage of intrahepatic neutrophil and M1 macrophage cell levels relative to live leukocytes determined by flow cytometry.

First Name: Eric

Last Name: Gale

Email: emgale@mgh.harvard.edu

Organization: Massachusetts General Hospital and Harvard Medical School

Country: United States

ID: GA234
iMPI - human-sized interventional Magnetic Particle Imaging

Patrick Vogel, University of Würzburg, patrick.vogel@physik.uni-wuerzburg.de

---

Category: Instrumentation

Abstract Body : Introduction Over the past decade, Magnetic Particle Imaging (MPI) has become a promising tomographic method for multiple applications in biology, chemistry, medicine and physics [1]. For cardiovascular medicine in particular, MPI could become an applicable radiation-free option for endovascular interventions supporting the common x-ray standard (digital subtraction angiography – DSA) [2, 3]. As next step on the path of MPI into clinical practice, MPI hardware needs to be scaled up for human-sized applications [4, 5], which is associated with several issues related to SAR (specific absorption rate) and PNS (peripheral nerve stimulation) limitations [6]. In this abstract, a first dedicated concept for a human-sized MPI scanner based on the Traveling Wave approach is presented [7], which is specifically designed to meet the requirements for cardiovascular interventions such as percutaneous transluminal angioplasty (PTA) and stenting. Materials & Methods The aim of the interventional MPI scanner (iMPI) is to provide a radiation-free system comparable to the clinical gold-standard DSA (digital subtraction angiography). This requires spatial resolution in the range of millimeters, high temporal resolution below 100 ms per image, near real-time visualization with low latency, and an open design that provides a comfortable and flexible environment for patients and medical staff, as well as sufficient space for interventional instrumentation and its operation. Additionally, the open design allows for simultaneous conventional DSA, which is especially important in the trial and testing phase [8]. To provide a sufficient magnetic field gradient, which is required for a high spatial resolution in MPI, a novel hardware approach is used to generate a FFL dynamically within a specific region of interest (ROI) (see Fig. 1 top left). By rapidly moving the FFL along specific trajectories through the ROI using additional coils, the nonlinear response signal of the tracer (superparamagnetic iron-oxide nanoparticles – SPION) is used to determine their spatial distribution [9]. The result is projection display comparable to DSA, e.g., of vascular structures and stent positioning. Results To guarantee a strong magnetic field gradient of about 0.7 T/m, currents of about 200 Ampere driving the main electromagnets (N=50) are required. This results in a power dissipation of about 50-60 Kilowatts in continuous mode, which requires a sophisticated cooling management. An alternative approach is a pulsed measurement mode, where a short sequence (< 1 ms) is generated to scan the ROI sequentially. In Fig. 1 bottom the results of a simulated dataset of a femoral artery model with the proposed scanner design is indicated. Conclusion A first human-sized projection MPI scanner for interventional treatment of human-sized legs has been designed and built providing promising results to pave the way to clinical routine.

References: [1] Gleich B & Weizenecker J. Tomographic Imaging using the nonlinear response of magnetic particles. Nature. 2005; 435:1214-7. [2] Herz S et al. Magnetic Particle Imaging Guided Real-Time Percutaneous Transluminal Angioplasty in a Phantom Model. Cardiovasc Intervent Radiol. 2018; 41(7):1100-5. [3] Herz S et al. Magnetic Particle Imaging-Guided

Stenting. J Endovasc Ther. 2019; 26(4):512-9. [4] Graeser M et al. Human-sized magnetic particle imaging for brain applications. Nature Comm. 2019; 10:1936. [5] Mason E E et al. Design analysis of an MPI human functional brain scanner. Int J Magn Part Imaging. 2017; 3(1):1703008. [6] Saritas E U. Magnetostimulation Limits in Magnetic Particle Imaging. IEEE TMI. 2013; 32(9):1600-10. [7] Vogel P et al. Traveling Wave Magnetic Particle Imaging. IEEE TMI. 2014; 33(2):400-7. [8] Vogel P et al. Magnetic Particle Imaging meets Computed Tomography: first simultaneous imaging. Nature Sci Rep. 2019; 9:12627. [9] Vogel P et al. Flexible and Dynamic Patch Reconstruction for Traveling Wave Magnetic Particle Imaging. Int J Magn Part Imaging. 2016; 2(2):1611001.

Image/Figure:

https://s3.amazonaws.com/amz.xcdsystem.com/1E8A4501-BB41-A02A-1D3B9882B798BFAA_abstract_File10351/GA234_ImageFigure_0513120120.png

Image/Figure Caption: Figure 1: top: left: basic hardware concept for the generation of the field free line (FFL) encoding scheme. Right: picture of the first iMPI prototype. Bottom: Simulation example of a projection image of a femoral artery.

First Name: Patrick

Last Name: Vogel

Email: patrick.vogel@physik.uni-wuerzburg.de

Organization: University of Würzburg

Country: Germany

ID: GA235
Genetically engineered SARS-CoV-2 mimetics as a molecular imaging tool to study viral-induced pathologies

Andrea Galisova, Weizmann Institute of Science, a.galisova@gmail.com

---

Category: Immunology: Inflammation & Infection

Abstract Body : Introduction: Understanding viral-induced pathologies is of great interest both scientifically and therapeutically, particularly due to the current COVID19 pandemic. In this regard, extracellular vesicles (EVs) offer a unique platform for studying viral infection paths and mechanisms due to similar properties (size and bio-membrane properties) and possibility of visualization by imaging methods [1]. Here, we show the development of genetically engineered EVs displaying the receptor-binding domain (RBD) of SARS-CoV-2 on their surface as corona-virus-like mimetics that can be labeled both magnetically or fluorescently. The labeled corona-like mimetics shown here as non-infectious formulation for multimodal imaging can be further applied for studying SARS-CoV-2 manifestation in the body. Methods: HEK293 cells were genetically modified to express the RBD of SARS-CoV-2 on their surface (Fig. 1A). Then, these cells were incubated with SPIO nanoparticles (BioPal, 2.5-40 μg/mL) and the secreted labeled EVs (EVsRBD as corona-mimetics or EVsno-RBD as controls) were isolated by differential centrifugation and characterized by several methods (MRI, NanoSight, Western blot and flow cytometry, see Fig. 1A, Persuasive Data). Two types of subcutaneous tumors were induced in nude mice (HEK293T as control or HEK293T overexpressing ACE2, HEKACE2) to study in vivo targeting of EVsRBD to the ACE2 receptor, t. Genetically engineered EVs (3x1011), either presenting the RBD (EVsRBD) or control (EVsnoRBD) labeled with SPIONs for MRI or with DiR for fluorescence were intravenously injected in mice followed by in vivo MRI (15.2T MR scanner) and ex vivo fluorescence imaging (IVIS Lumina XR). T2-/T2*-weighted MR images of mice bearing two tumors (HEK or HEKACE2) were acquired before and after intravenous administration of the SPIONs-labeled EVs. Results: Following incubation of the HEK293 cells with SPIONs, the secreted genetically engineered EVs (EVsRBD or EVsno-RBD) showed typical EVs size (~100 nm) and expression of RBD (for EVsRBD). Binding to the ACE2 receptors was proved by higher uptake of EVsRBD in ACE2-expressing cells compared to control EVsnoRBD (Persuasive Data). MRI of isolated EVs showed concentration-dependent accumulation of SPIONs as depicted from the lower MRI signal on T2-weighted images (Figure A) confirming successful labeling of the engineered EVs. In vivo targetability of EVsRBD was proved by MRI and fluorescence imaging of mice with injected EVs. The higher accumulation of the EVsRBD in HEKACE2 tumor as compared to control (HEK) was confirmed by the lower T2/T2* MRI signal (Figure B). Ex vivo fluorescence imaging of tumors showed higher accumulation of EVsRBD in the ACE2 tumors compared to EVsno-RBD (Figure C). Conclusion: Here, we show a multimodal imaging platform for mapping the binding of coronavirus mimetics to the ACE2 receptors both in vivo and in vitro by genetically engineered EVs expressing the RBD of SARS-CoV-2. The principles described could be further extended to better understand the mechanism and development of SARS-CoV-2 infection. The proposed

platform can be implemented to study other viruses by engineering a tailored peptide on the EVs surface and thus to explore the role of receptors in a wide spectrum of viral-induced pathologies.

References: [1] Han Z, et al. Highly efficient magnetic labelling allows MRI tracking of the homing of stem cell-derived extracellular vesicles following systemic delivery. Journal of Extracellular vesicles 2021, 10(3): e12054

Image/Figure:

https://s3.amazonaws.com/amz.xcdsystem.com/1E8A4501-BB41-A02A-1D3B9882B798BFAA_abstract_File10351/GA235_ImageFigure_0513120339.png

Image/Figure Caption: Figure. Production of magnetically labeled genetically engineered SARS-CoV-2 mimetics (A): HEK293 cells are transfected with a plasmid expressing the SARS-CoV-2-RBD peptide on the membrane surface. After labeling of parental cells with SPIO nanoparticles, the released extracellular vesicles (EVs) can be detected by MRI in a concentration-dependent manner (A). In vivo targetability of SARS-CoV-2 mimetics to ACE2 receptors (B, C). In vivo MRI imaging of tumor-bearing mice showed preferential accumulation of EVsRBD in the ACE2-expressing tumors compared to the control tumors. T2*-weighted images of mice show lower MR signal in the HEKACE tumors after injection of EVsRBD (B). Ex vivo fluorescence imaging of tumors confirmed higher accumulation of EVsRBD in ACE2 tumors compared to the control vesicles (EVsno-RBD) (C).

Full Name of Abstract's 1st Author : Andrea Galisova

First Name: Andrea

Last Name: Galisova

Email: a.galisova@gmail.com

Organization: Weizmann Institute of Science

Country: Israel

ID: GA236

A Web-Based Image Data Storage and Analysis Workflow for Multi-Modality Preclinical Imaging

Rahul Pemmaraju, Rutgers University, prahul1025@gmail.com

Category: Computational & Data Science

Abstract Body : Purpose: Preclinical multimodality imaging is a powerful tool in biomedical research [1]. In the context of cancer early detection, in vivo and ex vivo imaging techniques can be used to better understand cancer biology, assist in the development of novel biomarkers, and aid in the creation and testing of therapeutic drugs [2]. There are several dedicated preclinical modalities including miniaturized counterparts to clinical PET/CT, CT, and MRI scanners and optical imaging techniques, which are specifically designed for ex-vivo and in-vitro experimentation. The availability and access to this broad spectrum of preclinical imaging modalities in the form of a centralized shared core facility play a key role for biomedical researchers to be able to integrate imaging into their routine experimental setups. With the increased usage of such facilities, however, the requirements for data storage, management, and quantitative analysis become important and challenging issues. Unlike clinical modalities, where each modality is managed separately with a basic data management system, preclinical image data management is lagging mainly due to non-standardized image file format and proprietary issues. This also hinders the fast-growing data science and machine learning application development specific for preclinical imaging [5]. In this study, we are developing a web-based image storage and analysis workflow model that facilitates and streamlines the preclinical imaging process starting from image acquisition to final analysis. Methods: The prototype software system design consists of a database for data storage and integration with a user interface for easy access. The integrated application was built using Django, a Python-based framework for creating web applications. By using Django, we were able to easily include analysis tools written in Python into the application. HTML and JavaScript were also used to create the website. Django was used to develop the database architecture (currently an SQLite database) and HTML and JavaScript were used primarily to create the user interface. Image processing and analysis tools were written using a mixture of third-party Python packages. NumPy was the primary package used for scientific computing and OpenCV for image analysis. Results: The data storage model was structured in a manner that best reflects the routine preclinical imaging process. Specific metadata that would be stored and prompted by the user can easily be uploaded and linked to the associated image data. Data is structured using project objects, where each project represents a study or series of related experiments including non-imaging data. Within a project, a user can create different animal objects for storing information for each animal in the study. Within a project, users can upload single images, stacks of 3D images, or folders representing images taken from different imaging modalities. Stored image files can be quickly viewed by the image viewer built into the application. The client or the user interface was designed to allow for easy navigation and viewing of the different components of the application. Conclusion: The prototype application was designed with an emphasis on more structured image data storage and on detailed metadata recordkeeping in order to help facilitate

research efforts. The overall project structure integrates an animal manager that makes keeping notes on specific study animals and files generated easy and efficient. Although the application in its current form is fully implemented, it is currently being tested by some advanced users to ensure that it robust, user friendly and includes important key features.

References: 1. Cunha L, Horvath I, Ferreira S, et al. Preclinical imaging: an essential ally in modern biosciences. Mol Diagn Ther. 2014;18(2):153-173. doi:10.1007/s40291-013-0062-3 2. Fass L. Imaging and cancer: a review. Mol Oncol. 2008;2(2):115-152. doi:10.1016/j.molonc.2008.04.001 3. Lauber DT, Fülöp A, Kovács T, Szigeti K, Máthé D, Szijártó A. State of the art in vivo imaging techniques for laboratory animals. Lab Anim. 2017;51(5):465-478. doi:10.1177/0023677217695852 4. Laraway S, Snycerski S, Pradhan S, Huitema BE. An Overview of Scientific Reproducibility: Consideration of Relevant Issues for Behavior Science/Analysis. Perspect Behav Sci. 2019;42(1):33-57. Published 2019 Mar 22. doi:10.1007/s40614-019-00193-3 5. Davenport T, Kalakota R. The potential for artificial intelligence in healthcare. Future Healthc J. 2019;6(2):94-98. doi:10.7861/futurehosp.6-2-94 6. Lee, Jasper & Liu, Yue & Liu, Brent. (2011). A Solution for Archiving and Retrieving Preclinical Molecular Imaging Data in PACS Using a DICOM Gateway. Proc. of SPIE. 7967. 796710-1. 10.1117/12.877739.

Image/Figure:

https://s3.amazonaws.com/amz.xcdsystem.com/1E8A4501-BB41-A02A-1D3B9882B798BFAA_abstract_File10351/GA236_ImageFigure_0513120455.png

Image/Figure Caption: Figure 1: A prototype web-based data storage application designed to structure all data in projects in a matter that best parallels actual experimentation procedure (Basic Workflow on Top Left and Top Right). Users can document information about each imaging study before the experiment and upload either single images or stacks of 3D images acquired from imaging instruments. These files can be viewed and processed in the application. The user can upload, download, update, delete, and search on their uploaded files (Screenshot of application on Bottom Left). Users can also navigate to other features, such as the study manager and an Image Viewer (Screenshot of image viewer on Bottom Right). Image processing modules can also be easily added and implemented for further image analysis applications.

Full Name of Abstract's 1st Author : Rahul Pemmaraju

First Name: Rahul

Last Name: Pemmaraju

Email: prahul1025@gmail.com

Organization: Rutgers University

Country: United States

ID: GA237

Glutamine transporter downregulation mediates metabolic reprogramming in pancreatic tumors

Raj Kumar Sharma, The Johns Hopkins University, School of Medicine, rsharm40@jhmi.edu

---

Category: Oncology

Abstract Body : Pancreatic ductal adenocarcinoma (PDAC) is the fourth leading cause of cancer related death in the United States with a five-year survival of 9%. Identifying novel targets for PDAC treatment is a major need for effective treatment strategies since PDAC exhibit limited response to chemo- and radiation therapy. Because pancreatic cancer cells are 'glutamine avid' [1], targeting glutamine metabolic pathways can provide novel options for treatment. The glutamine transporter, SLC1A5, is being actively investigated as a pharmacological target in cancer [2]. Here we have engineered human pancreatic cells expressing shRNA to downregulate the glutamine transporter SLC1A5. We performed high-resolution 1H magnetic resonance spectroscopy (MRS) to understand the metabolic reprograming that occurs with SLC1A5 downregulation. Patient derived pancreatic cancer cells (Pa04C) were genetically engineered to express shRNA against SLC1A5 (Pa04C_SLC1A5) using lentiviral transduction. Downregulation of SLC1A5 was verified with q-RT-PCR and immunoblotting. Pa04C cells genetically engineered to express an empty vector (Pa04C_EV) using lentiviral transduction were used as controls. Tumors were derived by injecting 2x106 EV or Pa04C_SLC1A5 cells in the flank of 4 to 6-week-old male SCID mice. Tumor growth was monitored, and tumors excised and snap frozen at the end of the experiment. Dual phase extraction was performed on cells (EV n= 4, Pa04C_SLC1A5 n= 4) and tumors (EV n= 7, Pa04C_SLC1A5 n= 9), as previously described [3]. High-resolution 1H MR spectra were obtained from the aqueous phase extracts on a 750 MHz spectrometer. All data acquisition, processing and quantification was performed with TOPSPIN 3.5 software. We verified significant downregulation of SLC1A5 in Pa04C_SLC1A5 cells and tumors compared to EV cells and tumors. Downregulation of SLC1A5 also resulted in a significantly growth delay of Pa04C_SLC1A5 tumors compared to EV tumors. Metabolic heat maps generated from quantitative 1H MRS, of cell and tumor aqueous extracts, identified significant downregulation of the glutamine/glutamate ratio in cells with SLC1A5 downregulated (Figure 1 A). Other than the significant decrease of glutamine/glutamate in the Pa04C_SLC1A5 cells, no other significant metabolic differences were detected in these cells. In tumors, however, SLC1A5 downregulation resulted in a significant decrease of branched chain amino acids (BCAA), valine, alanine, glutamate, acetate, aspartate, glutathione, choline, phosphocholine, glycine, tyrosine, phenylalanine and histidine (Figure 1 B). SLC1A5 downregulation clearly resulted in significant tumor growth delay, supporting its importance as a therapeutic target. Our data expand the understanding of the diverse metabolic reprogramming that occurs following SLC1A5 downregulation in tumors in vivo that may lead to the development of additional metabolic targets. These data also identify the role of the tumor microenvironment in the metabolic reprogramming identified in tumors. Supported by NIH R01CA193365 and R35CA209960.

References: 1 Son J, Lyssiotis CA, Ying H, Wang X, Hua S, Ligorio M et al. Glutamine supports pancreatic cancer growth through a KRAS-regulated metabolic pathway. Nature 2013; 496: 101-105. 2 Bhutia YD, Ganapathy V. Glutamine transporters in mammalian cells and their functions in physiology and cancer. Biochim Biophys Acta 2016; 1863: 2531-2539. 3 Winnard PT, Jr., Bharti SK, Sharma RK, Krishnamachary B, Mironchik Y, Penet MF et al. Brain metabolites in cholinergic and glutamatergic pathways are altered by pancreatic cancer cachexia. Journal of cachexia, sarcopenia and muscle 2020.

Image/Figure:

https://s3.amazonaws.com/amz.xcdsystem.com/1E8A4501-BB41-A02A-1D3B9882B798BFAA_abstract_File10351/GA237_ImageFigure_0513120744.jpg

Image/Figure Caption: Figure 1. Quantitative analyses of metabolites are displayed in the metabolic heat maps to summarize differences in Pa04C_EV and Pa04C_SLC1A5 cells (A) and tumors (B). *represents significant (p-values .

First Name: Raj Kumar

Last Name: Sharma

Email: rsharm40@jhmi.edu

Organization: The Johns Hopkins University, School of Medicine

Country: United States

ID: GA238
D-[11C]methionine PET/MRI in humans - an innovative approach for imaging bacterial infection

Ilona Polvoy, University of California, San Francisco, Ilona.Polvoy@ucsf.edu

---

Category: Immunology: Inflammation & Infection

Abstract Body : PURPOSE This ongoing trial investigates the biodistribution, dosimetry and diagnostic performance of D-[11C]methionine ([11C]D-Met), a novel bacteria-specific PET radiotracer. Current clinical imaging of infection is not specific, unable to distinguish infection from mimics such as tumors or inflammation1. [11C]D-Met, based on a 'mirror-image' amino acid, is rapidly incorporated into peptidoglycan, part of the bacterial cell wall2. We recently developed a reliable radiosynthesis that was successfully tested in animal infection models3. Now, we report human dosimetry as well as initial results in patients with suspected prosthetic joint infection (PJI). METHODS AND MATERIALS 370-740 MBq [11C]D-Met was synthesized by automated in-loop radiosynthesis3 followed by injection of asingle bolus into 6 HVs (3 males, 3 female) and 3 patients with suspected PJI. HVs underwent 6 whole-body PET/MRI scans for purposes of dosimetry. Time-activity curves were used to calculate residence time for each source organ. Absorbed doses to each organ and body effective dose were calculated using OLINDA/EXM 1.1 with ICRP60 tissue weighting factors. Patients with suspected PJI received dynamic PET for 30 minutes targeted at the site of infection followed by a whole body PET/MRI. RESULTS Effective dose was estimated at 0.0040 mSv/MBq with highest activity in the urinary and hepatobiliary systems. [11C]D-Met showed clearance from both hepatobiliary (slow) and urinary (rapid) pathways. Early background uptake was observed in the liver, pancreas and kidneys with minimal background uptake in other organs. Importantly, minimal uptake was observed in the GI tract or lungs, despite potential concerns regarding the uptake within the human microbiomes. Additionally, minimal background uptake was observed in the spine, CNS or musculoskeletal system. In 2/3 patients with suspected PJI, [11C]D-Met showed increased focal uptake in the area of interest in both early focused scans and delayed whole-body scans. CONCLUSION [11C]D-Met PET/MR imaging is a novel imaging technique with modest radiation dose, minimal background, and no observed adverse effects. Moreover, the agent showed increased focal uptake in an area of suspected chronic infection, making this a promising agent for targeted imaging of bacteria that could have an important impact on the diagnosis and management of infections.

References: 1. Signore, A., Glaudemans, A. W. J. M., Galli, F. & Rouzet, F. Imaging infection and inflammation. (2015). 2. Neumann, K. D. et al. Imaging active infection in vivo using d-amino acid derived pet radiotracers. Sci. Rep. 7, 7903 (2017). 3. Stewart, M. N. et al. High Enantiomeric Excess In-Loop Synthesis of d-[methyl-11C]Methionine for Use as a Diagnostic Positron Emission Tomography Radiotracer in Bacterial Infection. ACS Infect. Dis. 6, 43–49 (2020). 4. Deloar, H. M. et al. Estimation of internal absorbed dose of L-[methyl-11 C] methionine using whole-body positron emission tomography. Eur. J. Nucl. Med. 25, 629–633 (1998).

Image/Figure: https://s3.amazonaws.com/amz.xcdsystem.com/1E8A4501-BB41-A02A-1D3B9882B798BFAA_abstract_File10351/GA238_ImageFigure_0513120749.pdf

Image/Figure Caption: Figure: (A) Healthy volunteer dosimetry shows tracers clearance from urinary (rapid) and hepatobiliary (slow) pathways with minimal background; (B) to (D) shows [11C]D-Met focal uptake in suspected infected prosthetic knee joint; (B) PET whole body scan, blue outlines the area of the suspected infection (C) MIP PET image of the left knee (D) trans-axial PET image; (E) PET/MR fused image; red arrows indicates increased uptake of [11C]D-Met (C)-(D).

First Name: Ilona

Last Name: Polvoy

Email: Ilona.Polvoy@ucsf.edu

Organization: University of California, San Francisco

Country: United States

ID: GA239
In Vivo Tracking of Iron Labeled Extracellular Vesicles by Magnetic Particle Imaging

Victoria Toomajian, Michigan State University, toomaji2@msu.edu

---

Category: Oncology

Abstract Body : Introduction: Breast cancer remains a common cancer worldwide. When breast cancer results in brain metastases, it is typically fatal [1]. While treatments such as surgery and radiation therapy have been used, the life span of patients remains low, with a median overall survival of 7 months [2]. Targeted therapeutics may be excluded by the blood brain barrier (BBB), resulting in reduced efficacy in the treatment of brain metastases [3]. Therefore, there is a clinical need to develop therapeutic delivery vehicles that cross the BBB. Delivery tools based on extracellular vesicles (EVs) may address this need. EVs are small particles released from cells, and are a natural means of cell-to-cell communication that have been implicated in driving a number of biological processes, including metastasis [4]. EVs can be exploited to deliver therapeutic agents to recipient cells, and have been investigated as a delivery tool for treating cancer [5]. EVs are capable of crossing the BBB, which would allow them to deliver a therapeutic to brain metastases [5][6]. The development of EVs as delivery tools to treat brain metastasis requires an understanding of the timing of EV accumulation, and their localization relative to metastatic progression. Magnetic particle imaging (MPI) is an emerging sensitive, quantitative imaging method that detects superparamagnetic iron, which allows for characterization of EV biodistribution in metastatic disease after labeling EVs with superparamagnetic iron oxide nanoparticles (SPION). Methods: Murine breast cancer cells expressing firefly luciferase (4T1-fLuc2) or brain metastatic cells expressing firefly luciferase and green fluorescent protein (4T1BR5-fLuc/GFP) were labeled with fluorescent SPIONs, using protamine-sulfate and heparin to enhance uptake. Following 24h labeling, the cells were washed to eliminate any extracellular iron and incubated in EV-depleted medium. EVs from these cells were collected as iron-labeled EVs (FeEVs) at 24h after loading, and concentrated via differential ultracentrifugation. Nanoparticle tracking analysis was performed to characterize the size and concentration of FeEVs. For in vivo experiments, Balb/C mice received either 4T1-fLuc2 cells via mammary fat pad injections (n=8) or 4T1BR5-fLuc/GFP cells via intracardiac (IC) injection (n=3). Reporter genes enabled assessment of tumor progression via in vivo bioluminescence imaging (BLI). At times correlating to late-stage disease, FeEVs derived from 4T1-fLuc2 or 4T1BR5-fLuc/GFP cells were delivered via intratumoral (IT) or IC injections, respectively, into mice with mammary tumors (3wk post injection: PI) or brain metastasis (9d PI). SPIONs were used as a control. Mice were imaged at multiple time points using MPI and micro-CT to assess either retention in the mammary tumors or rate of accumulation and loss in metastasis. Iron content of FeEV pellets and the amount of iron remaining in tumors were quantified by comparison to a calibration curve of known iron concentrations. Further early and late time point brain metastasis experiments are in progress. Results: Primary tumors: Post-IT injection of FeEVs (A) or SPIONs (B), mammary 4T1-fLuc2 tumors retained more iron when injected with FeEVs relative to uncoated SPIONs, correlating to increased retention

(C). Preliminary microscopy of tumor sections showed little or no remaining iron when SPIONs were injected. In tumors of mice injected with FeEVs, iron was identified in CD11b+ macrophages and CD47+ tumor cells (D, E). Brain metastases: 4T1BR5-fLuc/GFP cells were monitored over 9 days by BLI (F). 1-2h following IC injection (preliminary results) of either FeEVs or SPIONs, 14X more signal was found in heads of mice injected with FeEVs compared to SPIONs (G, H). Conclusions: Multi-modal imaging of FeEVs suggested that EVs can cross the BBB and accumulate in metastatic sites, and are preferentially retained in primary tumors. These findings will allow for further study of EVs for use as a therapeutic delivery vehicle to treat brain metastasis.

References: [1] Aversa C, Rossi V, Geuna E, Martinello R, Milani A, Redana S, et al. Metastatic breast cancer subtypes and central nervous system metastases. Breast. 2014;23:623–8. [2] Witzel I, Laakmann E, Weide R, Neunhöffer T, Park-Simon TJ, Schmidt M, et al. Treatment and outcomes of patients in the Brain Metastases in Breast Cancer Network Registry. Eur J Cancer. 2018;102:1–9. [3] Bendell JC, Domchek SM, Burstein HJ, Harris L, Younger J, Kuter I, et al. Central nervous system metastases in women who receive trastuzumab-based therapy for metastatic breast carcinoma. Cancer. 2003;97:2972–7. [4] Harris DA, Patel SH, Gucek M, Hendrix A, Westbroek W, Taraska JW. Exosomes released from breast cancer carcinomas stimulate cell movement. PLoS One. 2015;10:e0117495–e0117495. [5] Jia G, Han Y, An Y, Ding Y, He C, Wang X, et al. NRP-1 targeted and cargo-loaded exosomes facilitate simultaneous imaging and therapy of glioma in vitro and in vivo. Biomaterials. 2018;178:302–16. [6] Yang T, Martin P, Fogarty B, Brown A, Schurman K, Phipps R, et al. Exosome delivered anticancer drugs across the blood-brain barrier for brain cancer therapy in Danio rerio. Pharm Res. 2015;32:2003–14. [7] Gutova M, Frank JA, D'Apuzzo M, et al. Magnetic resonance imaging tracking of ferumoxytol-labeled human neural stem cells: studies leading to clinical use. Stem Cells Transl Med. 2013;2(10):766-775. doi:10.5966/sctm.2013-0049 [8] Mondal A, Ashiq KA, Phulpagar P, Singh DK, Shiras A. Effective Visualization and Easy Tracking of Extracellular Vesicles in Glioma Cells. Biol Proced Online. 2019;21:4. Published 2019 Mar 15. doi:10.1186/s12575-019-0092-2

Image/Figure:

https://s3.amazonaws.com/amz.xcdsystem.com/1E8A4501-BB41-A02A-1D3B9882B798BFAA_abstract_File10351/GA239_ImageFigure_0513120804.png

Image/Figure Caption: Figure 1: Localization of iron loaded EVs and SPIONs in mice. Overlay images of micro-CT and MPI scans of primary tumor-burdened mice injected with FeEVs (A) or SPIONs (B), 24 h post injection. More signal is retained in the tumor over 72h when FeEVs are injected (arrows indicate location of tumor signal) (C). Staining of tumor sections showed little to no iron when SPIONs were injected. Fluorescently labeled SPION (magenta) is identified in CD11b+ macrophages (green) (D) and in CD47+ tumor cells (yellow) (E). Zoomed insets identify iron-labeled cells (arrowheads). Intracardiac (IC) injection of 4T1-BR5 cells, which stably express firefly luciferase resulted in metastasis in the brain, visualized using BLI (F, 7 days post injection). IC injection of SPIONs (G) or FeEVs (H) 9 days PI showed increased MPI signal in excised heads post-mortem (I). Scale bars: 50 mm, *p < 0 .05.

First Name: Victoria

Last Name: Toomajian

Email: toomaji2@msu.edu

Organization: Michigan State University

Country: United States

ID: GA240
Investigation of Pulmonary N-Glycomics in COVID-19 Patients

Caitlin Tressler, The Johns Hopkins University School of Medicine, ctressl3@jhmi.edu

---

Category: Immunology: Inflammation & Infection

Abstract Body : Introduction: In the wake of the SARS-CoV-2 pandemic which has infected millions of people worldwide, post-acute COVID-19 syndrome (PCS) has been identified in at least 10% of cases [1-3]. In many cases of PCS, baseline organ function, including lung, kidney, and heart do not return to normal for multiple weeks to months after the infection resolves[4]. One possible explanation for this observed decline in organ function is tissue damage sustained during the acute phase of the infection. Development of prevention and treatment strategies for PCS require a greater understanding of the molecular mechanisms that drive the observed pathology in COVID-19, which could lead to persistent diminished organ function in PCS. Methods: Post-mortem COVID-19 patient lung samples (n = 10) and post-mortem controls without any major lung involving illness (n = 10) were selected for study with one COVID-19 patient and one control per slide. Tissues were digested with PNGase F and sprayed with 5 mg/mL CHCA matrix prior to imaging. All tissues were imaged on a Bruker RapifleX MALDI TOF/TOF instrument in reflectron positive mode with 200 laser shots per pixel with 50-micron spot size and 50-micron raster. A mass range of m/z 600 to 3200 was collected. N-glycans were identified using tandem MS experiments. Adjacent sections were H&E stained for co-registration. Data was analyzed in FlexImaging and SCiLS Lab software. Results: Marked differences were observed by both H&E and MALDI imaging. COVID-19 lungs showed diffuse alveolar damage, chronic inflammatory cell infiltrates, and hemorrhage. Using IHC, a subset of COVID-19 lungs was probed for SARS-CoV-2 spike protein and nucleocapsid, which were not detected. MALDI imaging of COVID-19 lungs showed heterogenous increases of high mannose and complex N-glycans across each section.While all COVID-19 patient lungs showed increases in high mannose and complex N-glycans, profiles among affected cases were not identical. Discussion: Glycoproteins play key roles in infection and response. H&E stains show immune cells of various types in COVID-19 patient lungs, as well as various characteristic tissue responses to severe lung damage. Observed increases of N-glycans are most likely a result of increased immune cells within patient lungs. Inflammatory proteins are also often N-glycosylated which may also result in the increase in observed N-glycans. Conclusions: Histopathology and MALDI imaging revealed increased inflammatory and immune response in COVID-19 patient lungs. Profiling of the N-glycans demonstrated an increase in complex and high mannose glycans associated with this response. We are currently performing further statistical analysis to determine if other factors (age, sex, pre-existing conditions, among others) played a role in elevating complex and high mannose N-glycans. We are also in the process of identifying more N-glycans and more rigorously analyzing the histopathology results for more detailed spatial correlation with MALDI imaging results.

References: 1. Banda, J.M., et al., Long-term patient-reported symptoms of COVID-19: an analysis of social media data. medRxiv, 2020: p. 2020.07.29.20164418. 2. Moreno-Pérez, O., et

al., Post-acute COVID-19 Syndrome. Incidence and risk factors: a Mediterranean cohort study. The Journal of infection, 2021: p. S0163-4453(21)00009-8. 3. Halpin, S.J., et al., Postdischarge symptoms and rehabilitation needs in survivors of COVID-19 infection: A cross-sectional evaluation. Journal of Medical Virology, 2021. 93(2): p. 1013-1022. 4. Jain, U., Effect of COVID-19 on the Organs. Cureus, 2020. 12(8): p. e9540-e9540.

Image/Figure:

https://s3.amazonaws.com/amz.xcdsystem.com/1E8A4501-BB41-A02A-1D3B9882B798BFAA_abstract_File10351/GA240_ImageFigure_0513121036.png

Image/Figure Caption: Preliminary analysis of two sets of N-glycan images of Hex5HexNAc4 (m/z 1664.3), a high mannose glycan, as identified by tandem MS. This N-glycan is significantly increased in COVID-19 lungs as compared to normal control lungs. Data are displayed with an intensity scale where purple equals zero and yellow equals the highest detected intensity. In both COVID-19 lungs, a significant increase in this N-glycan is observed when compared to both controls. The area under the curve for this analysis was 0.885 (where 1 equals zero false positive rate, 0.5 equals false positive).

First Name: Caitlin

Last Name: Tressler

Email: ctressl3@jhmi.edu

Organization: The Johns Hopkins University School of Medicine

Country: United States

ID: GA241
Tracking dendritic cell migration in vivo with magnetic particle imaging

Julia Gevaert, University of Western Ontario, jgevaert@uwo.ca

---

Category: Immunology: Inflammation & Infection

Abstract Body : Introduction: Dendritic cell (DC)-based immunotherapies rely on migration to secondary lymphoid organs to deliver treatment, and the magnitude of the ensuing anti-tumour T cell response is proportional to the number of lymph node-migrated DC1. Despite advancements, in vivo fate of these therapeutic cells remains largely unknown and quantification of cells is vital for predicting immune responses. We have successfully detected DC migration to lymph nodes using superparamagnetic iron oxide nanoparticles (SPION)-based MRI, however, this method is semi-quantitative at best, and limited by specificity2. Magnetic Particle Imaging (MPI) is an emerging modality capable of overcoming these limitations. MPI directly detects SPION response to a magnetic field and produces signal that is linearly correlated with iron, allowing unambiguous imaging and quantification. In this study, we describe Magnetic Particle Imaging (MPI) as a novel technique for tracking and quantifying DC migration.
Methods: C57BL/6 mouse bone marrow-derived immature DC were labeled for 24 hours (200ug/mL) with Synomag-D™ and transfection agents3. Cells were matured for the final 24 hours of culture with a defined maturation cocktail4. Iron loading efficiency, phenotype and viability was conducted alongside imaging studies. Following magnetic column enrichment of Synomag-D+ DC, 3x105 cells were injected into each hind footpad of a C57BL/6 mouse. MPI was immediately conducted (Day 0) with 3D (35 projections, 30 min) parameters using a Momentum™ scanner (Magnetic Insight, Inc.). MPI was repeated 48 hours later (Day 2) to identify DC that migrated to the draining popliteal lymph nodes (pLN). MRI was acquired on Day 3 using a 3T clinical scanner to confirm DC migration. After, pLNs were excised and imaged with MPI. Iron was quantified using calibration lines made from a 1:1 dilution series of Synomag-D. Iron per cell was estimated by imaging a known number of cells and dividing by the amount of iron. Cell numbers were then calculated using measured MPI iron content and known iron per cell content. Results: Signal from Synomag-D+ DC in both the left and right hind footpad was detected on Day 0 MPI, as expected. Day 2 MPI showed signal in the left and right pLNs, with approximately 1.03x104 (0.045µg Fe) and 7.77x103 (0.034 µg Fe) cells in the left and right pLN, suggesting a 4% and 2.5% migration rate (respectively). Window leveling was required to visualize pLN signal compared to the stronger gastrointestinal and lingering footpad signals. Day 3 MRI displayed signal voids in both the left and right pLNs, confirming DC migration. Ex vivo MPI of lymph nodes excised on Day 3 showed clear signal in both pLNs, with lower iron and cell numbers (left = 3.50x103 cells, 0.015 µg Fe, right = 1.80x103 cells, 0.008 µg Fe). Conclusion: Here we describe the first study using MPI to track and quantify the in vivo fate of migrating Synomag-D labeled DC. As DC migrate from the site of injection to the lymph nodes we measured a decrease in signal in the footpads and an increase in signal at the pLNs. By also measuring the iron mass per cell after DC labeling we are able to provide a good estimate of cell number for each source of signal. The presence of iron in nodes was validated by ex vivo MPI on Day 3; lower signal was measured due to the later timepoint and possibly from

cells lost during excision. MPI results agree with MRI, DC were detected as signal voids in pLNs. This study demonstrates the clear advantage of MPI to detect and quantify cells in vivo, bridging the gap left by cellular MRI, and all other in vivo imaging modalities, and opening the door for quantitative imaging of cellular immunotherapies.

References: 1. Osada, T., Clay, T. M., Woo, C. Y., Morse, M. A. & Lyerly, H. K. Dendritic Cell-Based Immunotherapy. International Reviews of Immunology 25, 377–413 (2006). 2. Dekaban, G. A. et al. Tracking and evaluation of dendritic cell migration by cellular magnetic resonance imaging. WIREs Nanomedicine and Nanobiotechnology 5, 469–483 (2013). 3. Thu, M. S. et al. Self-assembling nanocomplexes by combining ferumoxytol, heparin and protamine for cell tracking by magnetic resonance imaging. Nature Medicine 18, 463–467 (2012). 4. Fink, C. et al. Fluorine-19 Cellular MRI Detection of In Vivo Dendritic Cell Migration and Subsequent Induction of Tumor Antigen-Specific Immunotherapeutic Response. Mol Imaging Biol 22, 549–561 (2020).

Image/Figure:

https://s3.amazonaws.com/amz.xcdsystem.com/1E8A4501-BB41-A02A-1D3B9882B798BFAA_abstract_File10351/GA241_ImageFigure_0513121059.png

Image/Figure Caption: Figure 1: MPI and MRI of C57BL/6 mouse depicting DC migration following injection of 3x105 Synomag-D+ DC into the hind left (L) and right (R) footpads. All images are representative slices selected from 3D image sets. Day 0 MPI (A) displays two regions of signal in the hind left (orange brackets) and right (orange dashed brackets) footpads after injection of 3x105 Synomag-D+ DC, with iron quantification and the estimate of cell number in corresponding brackets below. Day 2 MPI (B) shows DC migration to the left (blue brackets) and right (blue dashed brackets) pLNs, image is window leveled to the min/max signal of the lymph nodes and oversaturates gut (red arrow) and footpad signals. Day 3 MRI (C) displays regions of signal loss in both the left (white box) and right (white dashed box) pLNs. Day 3 ex vivo MPI validation in (D) shows clear signal in excised left (blue brackets) and right (blue dashed brackets) pLNs.

Full Name of Abstract's 1st Author : Julia J. Gevaert

First Name: Julia

Last Name: Gevaert

Email: jgevaert@uwo.ca

Organization: University of Western Ontario

Country: Canada

ID: GA242

The Synthesis and In Vivo Evaluation of Variants of 89Zr-DFO-Pertuzumab Synthesized Using Random and Site-Specific Lysine Modification Strategies

Cindy Rodriguez, CUNY Hunter College, cindy.rodriguez54@myhunter.cuny.edu

---

Category: Oncology

Abstract Body : Introduction: The synthesis of radioimmunoconjugates via the random attachment of bifunctional chelators to lysine residues yields heterogeneous products that can display suboptimal in vitro and in vivo behavior. In light of this, several site-specific and site-selective approaches to bioconjugation have been developed, including strategies based on unnatural amino acids, chemoenzymatic transformations, the manipulation of the heavy chain glycans, and the reduction and modification of interchain disulfides.[1] Yet each of these approaches comes with attendant drawbacks, for example the expense and complexity of incorporation unnatural amino acids into mAb. In this work, we describe the attachment of the chelator desferrioxamine (DFO) to the HER2-binding antibody pertuzumab via a novel, lysine-targeted approach to site-specific bioconjugation as well as its labeling with [89Zr]Zr4+ to create [89Zr]Zr-SSKDFO-pertuzumab. Subsequently, we compared the performance of [89Zr]Zr-SSKDFO-pertuzumab to traditionally synthesized [89Zr]Zr-DFO-pertuzumab via surface plasmon resonance (SPR) analysis, bead-based binding assays, and PET imaging experiments. Methods: Randomly modified DFO-pertuzumab was synthesized via the sequential modification of the antibody with an NHS-bearing, linear azide and a dibenzocyclooctyne-bearing variant of DFO (DBCO-DFO). In contrast, SSKDFO-pertuzumab was synthesized via the site-selective acyl-transfer of a branched bis-azide moiety onto the light chain of the antibody followed by the addition of DBCO-DFO. Both immunoconjugates were labeled with [89Zr]Zr4+ using standard protocols and purified via size exclusion chromatography to yield [89Zr]Zr-DFO-pertuzumab and [89Zr]Zr-SSKDFO-pertuzumab. The immunoreactivity of the radioimmunoconjugates was determined using Ni-NTA beads coated with purified HER2, and the kinetic binding parameters for each construct were determined via SPR. Finally, both [89Zr]Zr-SSKDFO-pertuzumab and [89Zr]Zr-DFO-pertuzumab were administered to mice bearing subcutaneous HER2-positive BT474 human breast cancer xenografts, and PET images were collected 6, 24, 48, 72, 96, 120, and 144 h after administration. Results: The site-specific bioconjugation of SSKDFO-pertuzumab was validated by ESI mass spectrometric analysis. [89Zr]Zr-SSKDFO-pertuzumab and [89Zr]Zr-DFO-pertuzumab were synthesized in >99% radiochemical yield, >99% radiochemical purity, and specific activities of ~2 mCi/mg. The immunoreactivities of both radioimmunoconjugates were >90%, and the binding constants of SSKDFO-pertuzumab and DFO-pertuzumab were found via SPR to be 0.8 x 10-9 M and 1.65 x 10-9 M, respectively. Finally ¾ and most importantly ¾ both [89Zr]Zr-SSKDFO-pertuzumab and [89Zr]Zr-DFO-pertuzumab produced high contrast PET images in mice bearing BT474 xenografts. In each case, the tumor could clear be visualized as early as 24 h post-injection, and the accretion of the radioimmunoconjugates continued over the course of the experiment reaching maxima of ~75% ID/g at 120 h. Conclusion: Our lysine-mediated site-specific bioconjugation technology produced a radioimmunoconjugate, [89Zr]Zr-SSKDFO-pertuzumab, that is better defined and

better characterized than a traditionally synthesized analog and exhibits excellent in vitro and in vivo behavior. We are currently working to validate [89Zr]Zr-SSKDFO-pertuzumab in other murine models of HER2-positive cancer.

References: 1. Vivier D, Fung K, Rodriguez C, Adumeau P, Ulaner GA, Lewis JS, Sharma SK, Zeglis BM. The Influence of Glycans-Specific Bioconjugation on the FcγRI Binding and In vivo Performance of 89Zr-DFO-Pertuzumab. Theranostics 2020; 10(4):1746-1757. doi:10.7150/thno.39089

Image/Figure:

https://s3.amazonaws.com/amz.xcdsystem.com/1E8A4501-BB41-A02A-1D3B9882B798BFAA_abstract_File10351/GA242_ImageFigure_0513121157.png

Image/Figure Caption: Fig 1. (A) Schematic for the synthesis of [89Zr]Zr-DFO-pertuzumab and [89Zr]Zr-SSKDFO-pertuzumab. (B) Surface plasmon resonance data for native pertuzumab, DFO-pertuzumab, or SSKDFO-pertuzumab with recombinant HER2 protein; (C) Immunoreactivity measurements of [89Zr]Zr-DFO-pertuzumab and [89Zr]Zr-SSKDFO-pertuzumab determined through a bead-based assay with HER2-coated Ni-NTA beads for 1 h; (D) Representative PET images acquired 24, 72, and 120 h p.i. after the administration of [89Zr]Zr-DFO-pertuzumab or [89Zr]Zr-SSKDFO-pertuzumab (~200 μCi, ~115 μg) to athymic nude mice bearing subcutaneous HER2(+) BT474 xenografts (n = 5 for each cohort). Images on the left are coronal slices; images on the right are maximum intensity projections (MIPs).

Full Name of Abstract's 1st Author : Cindy Rodriguez

First Name: Cindy

Last Name: Rodriguez

Email: cindy.rodriguez54@myhunter.cuny.edu

Organization: CUNY Hunter College

Country: United States

ID: GA243
Evaluation of α3β1-targeted 68Ga-labeled HEVNPs in human colorectal cancer xenografts

ELISAVET LAMBIDIS, University of Helsinki, eliza.lambidis@helsinki.fi

---

Category: Oncology

Abstract Body : Objectives: The Hepatitis E virus-like nanoparticles (HEVNPs) are small and safe protein capsids (≈ 30 d.nm). All the physical characteristics of the HEV are retained by the HEVNPs while the genome is lacking. The self-assembling ability of the HEVNPs enables them to act as cargo vehicles1,2. LXY30 is a peptide targeting to α3β1 integrin. Previously, LXY30 has been successfully used for targeting HEVNPs in breast cancer2. In order to evaluate LXY30-HEVNP for targeted drug delivery and theranostics of colorectal cancer, the NPs were first radiolabeled with 68Ga and their stability was evaluated. Subsequently, the uptake of [68Ga]Ga-DOTA-HEVNP-LXY30 in HCT 116 tumor cells was determined, and their ex vivo biodistribution was investigated in mice bearing human colorectal xenograft tumors. Methods: Conjugation of DOTA chelator to the LXY30-HEVNP lysine amino acids: DOTA-NHS ester (21.3 mg, 33.66 μmol) was dissolved in 0.01 M phosphate buffer (PB) pH 7.4 and added to LXY30-HEVNPs dispersed in 0.01 M PB pH 7.48 (1.05 mg/ml, 28.05 nmol). The final reaction volume was 1430 μl (adjusted pH to 7.3). The reaction was run overnight at 4oC, followed by a purification with two consecutive PD-10 columns. Gallium-68 radiolabeling: DOTA-HEVNP-LXY30 was dispersed in metal-free 0.25 M ammonium acetate buffer pH 7 (800 μl) and 68GaCl3 in 0.1 M HCl was added (80-140 MBq in 1 ml). The reaction mixture (pH 4.5) was incubated for 30 min at 60oC after which the radiolabeled HEVNPs were purified with a PD-10 column. Stability assay: The purified targeted NPs, [68Ga]Ga-DOTA-HEVNP-LXY30, were incubated in 0.01 M PBS, 50% human plasma, FeCl3 (10 mg/ml), or CO2-independent cell culture medium (Gibco) at 37oC for 1 h. Cell uptake: The HCT 116 (ATCC® CCL247™) cells (2.2 million cells/ml/well) were incubated at 37oC for 3 h with either the targeted 68Ga-HEVNP-LXY30, the non-targeted 68Ga-HEVNP, or 68GaCl3 (0.2 MBq/well). Ex vivo biodistribution: The evaluation of [68Ga]Ga-DOTA-HEVNP-LXY30 was performed in HCT 116 colon tumor-bearing female nude NMRI mice (n = 13, 7-8 weeks, 17-20 g). [68Ga]Ga-DOTA-HEVNP-LXY30 were injected into the tail vein in 200 μl of PB pH 7.4 (0.2-0.5 MBq). The mice were euthanized at 15, 30 and 60 min after the administration, and the organs were harvested, weighed and their radioactivity was counted on a gamma-counter. Results: The RCY of [68Ga]Ga-DOTA-HEVNP-LXY30 was 67.87 ± 3.31% (n = 3), the Am was 104 GBq/μmol and the RCP was 98.43 ± 0.38%, n = 3 (radio-TLC). [68Ga]Ga-DOTA-HEVNP-LXY30 remained intact (≥ 90%) after 1 h of incubation under all the tested conditions (Fig.1A). The in vitro cellular uptake of the targeted HEVNPs in HCT 116 colorectal carcinoma cells was confirmed by the cell study which revealed 13.27 ± 0.68% (n = 3) internalized NPs in 2 h and 21.04 ± 0.73% (n = 3) in 3 h (Fig.1B). The internalization of the targeted HEVNPs was double the one of the non-targeted HEVNPs in all time points. Evaluation of the ex vivo biodistribution of [68Ga]Ga-DOTA-HEVNP-LXY30 (n = 4) revealed that only the 0.83 ± 0.39%ID/g of [68Ga]Ga-DOTA-HEVNP-LXY30 accumulated in the subcutaneous HCT 116 xenografts in

vivo. At the last time point (1 h), some [68Ga]Ga-DOTA-HEVNP-LXY30 were still circulating in the blood (1.83 ± 0.55%ID/g), and they were distributed mainly in the liver (39.82 ± 12.97%ID/g). Conclusions: LXY30-HEVNPs were successfully radiolabeled with 68Ga for imaging of the drug delivery carrier distribution. The labeled NPs have high in vitro stability and sufficient in vitro cell internalization capability in HCT 116 cells. Nevertheless, the tumor uptake of [68Ga]Ga-DOTA-HEVNP-LXY30 in vivo was low most likely due to the rapid sequestration of the HEVNPs to the liver. Acknowledgements: Academy of Finland (decision numbers: 298481, 320102 and 318422).

References: 1. P. Steppert et al., Quantification and characterization of virus-like particles by size-exclusion chromatography and nanoparticle tracking analysis, J. Chromatogr. A, 2017, 1487, 89–99. 2. C.-C. Chen et al., Chemically activatable viral capsid functionalized for cancer targeting, Nanomed., 2016, 11, 377–390.

Image/Figure:

https://s3.amazonaws.com/amz.xcdsystem.com/1E8A4501-BB41-A02A-1D3B9882B798BFAA_abstract_File10351/GA243_ImageFigure_0513121803.png

Image/Figure Caption: Fig.1: Chemical and enzymatic stability of [68Ga]Ga-DOTA-HEVNP-LXY30 (A), and HCT 116 colorectal carcinoma-cell internalization of [68Ga]Ga-DOTA-HEVNP-LXY30 and controls (non-targeted [68Ga]Ga-DOTA-HEVNP and [68Ga]GaCl3) (B). The data points and columns represent the average ± SD (n = 3 in both A and B).

Full Name of Abstract's 1st Author : Elisavet Lambidis

First Name: ELISAVET

Last Name: LAMBIDIS

Email: eliza.lambidis@helsinki.fi

Organization: University of Helsinki

Country: Finland

ID: GA244

Second-Generation Mammalian Acoustic Reporter Genes Enable Enhanced, Continuous Nonlinear Imaging of Gene Expression in Orthotopic Tumors

Mengtong Duan, Caltech, mduan@caltech.edu

Category: Bioengineering, Synthetic Biology and Basic Biology

Abstract Body : Ultrasound is an established technology for noninvasive deep-tissue imaging that overcomes the low penetration depth of optical methods. However, until recently it was impossible to couple ultrasound contrast to gene expression or cellular function. Gas vesicles (GVs) were recently introduced as the first genetically encoded ultrasound contrast agents expressed from acoustic reporter genes (ARGs) in bacteria [1] and mammalian cells [2]. However, the first-generation mammalian acoustic reporter genes (mARGs), based on 9 essential GV genes from a soil bacterium B. megaterium, suffer from a number of limitations: linking individual GV genes into compact mammalian polycistronic expression cassettes severely attenuates GV expression and ultrasound contrast compared to the cotransfection of individual genes, both transient and stably transduced mARGs require coexpression of three separate polycistronic cassettes for GV production, and the acoustic properties of B. megaterium GVs only allow imaging using a destructive ultrasound modality, limiting their use to endpoint measurements. Here we present a new generation of mARGs that overcome the above-mentioned limitations. We demonstrate that mARGs2.0 provide strong expression from only two polycistronic expression cassettes with optimized cassette ratio, nonlinear acoustic properties that allow for nondestructive continuous imaging using amplitude modulation pulse sequences [3,4], and the ability to modulate acoustic properties based on gene composition. We extensively characterize mARGs2.0 in vitro and demonstrate their utility in vivo by imaging gene expression in an orthotopic cancer model. For this purpose, we stably integrated these reporter genes into the genomes of human breast cancer cells and imaged them nondestructively in vivo after tumor formation in mouse mammary fat pads and chemically induced expression.

References: [1] Bourdeau, R., Lee-Gosselin, A., Lakshmanan, A. et al. Acoustic reporter genes for noninvasive imaging of microorganisms in mammalian hosts. Nature 553, 86–90 (2018). [2] Farhadi, A., Ho, G., Sawyer, D. et al. Ultrasound imaging of gene expression in mammalian cells. Science 365, 1469-1475 (2019). [3] Maresca, D., Lakshmanan, A., Lee-Gosselin, A. et al. Nonlinear ultrasound imaging of nanoscale acoustic biomolecules. Applied Physics Letters 110, 073704 (2017) [4] Maresca, D., Sawyer, D. et al. Nonlinear X-wave ultrasound imaging of acoustic biomolecules. Physical Review X 8, 041002 (2018).

Full Name of Abstract's 1st Author : Mengtong Duan

First Name: Mengtong

Last Name: Duan

Email: mduan@caltech.edu

Organization: Caltech

Country: United States

ID: GA245

In vivo tracking of cancer cells in the mouse brain with magnetic particle imaging (MPI) and nanoflower multicore superparamagnetic iron oxide nanoparticles

Natasha Knier, Western University, nknier@uwo.ca

Category: Instrumentation

Abstract Body : Introduction: Magnetic resonance imaging (MRI) techniques have been developed for tracking the fate of metastatic breast cancer cells labeled with superparamagnetic iron-oxide nanoparticles (SPIONs) with high sensitivity1–5. However, MRI cell tracking with SPIONs has some limitations. First, quantification of iron-induced signal loss is challenging. Second, other regions of signal void lead to low specificity. Magnetic particle imaging (MPI) cell tracking has the potential to overcome these challenges. MPI detects the response of SPIONs to an applied magnetic field. The MPI signal appears as a hot spot with no background, providing high specificity. MPI signal is proportional to iron content and directly quantifiable, providing measures of iron mass and cell number. Sensitivity and resolution in MPI depend heavily on the magnetic properties of the SPION. In this study, we evaluate a SPION called Synomag-D™, a nanoflower-shaped multi-core particle, for the detection and quantification of metastatic cancer cells by MPI. To the best of our knowledge, Synomag-D has not yet been used to label breast cancer cells for imaging with MPI. Objective: To utilize Synomag-D for quantitative MPI of breast cancer cells disseminated in the mouse brain and compare to our previous work where breast cancer cells were labeled with micron sized iron particles (MPIO) and imaged by MRI. Methods: Human brain metastatic breast cancer cells (231BR) were labeled with Synomag-D (MicroMod GmbH). Synomag-D has a core size of 25-30 nm (individual cores are 8-9 nm) which is considered ideal for MPI based on relaxometry and simulations6. Labeling was validated with a Perl's Prussian Blue (PPB) stain for iron and MPI of cell pellets. MPI relaxometry was acquired for triplicate samples of 1uL of Synomag-D, 10uL of MPIO, and 5.0x105 231BR cells labeled with Synomag-D or MPIO. NOD/SCID/ILIIrg−/− mice (n=6) were injected with 2.5x105 cells intracardially (IC). MPI was performed on a MOMENTUM scanner (Magnetic Insight Inc., Almeda, CA, USA) on Day 0 and 7 (n=6) using the 3D high sensitivity isotropic (multichannel) scan mode. MPI data was compared to MRI from a prior study using mice injected IC with 2.5x105 MPIO-labeled 231BR cells. Results: Synomag-D labeled cells with an efficiency of 98.0±0.40% (Fig. A) and 98% viability. Mean iron/cell was 5 pg. There was a linear relationship between iron content and MPI signal (R2 = 0.96, p On Day 0, MPI signal was detected in 3/6 mouse brains (Fig. D); the mean iron content was 0.08 ug, which is ~16,000 cells in the mouse brain. MPI signal was also visible in the lung/liver region since cells injected IC are distributed throughout the body. Strong MPI signal may impede detection of low signal in nearby regions; and may result in no signal being detected in 3/6 mice on Day 0. On Day 7 lung/liver signal was diminished and brain signal was detected in 5/6 mice. The signal decreased from Day 0; mean iron content was 0.012ug (~2,400 cells) (Fig. F). This is expected, as cancer cells die and clear by Day 7 in this model1. In Day 0 MRI, MPIO-labeled cells appear as discrete signal voids (Fig. E). Quantification of these images is challenging; voids are counted

or the percentage of black pixels calculated, however, this does not allow for determination of cell number. Conclusions: This is the first study to demonstrate that brain metastatic breast cancer cells can be labeled with Synomag-D and quantified in vivo with MPI. Employing MPI for experimental cancer cell tracking allows for the detection and quantification of the arrest, clearance, and retention of cancer cells in vivo.

References: 1. Parkins, K. M. et al. A multimodality imaging model to track viable breast cancer cells from single arrest to metastasis in the mouse brain. Scientific reports 6, 1–9 (2016). 2. Heyn, C. et al. In vivo magnetic resonance imaging of single cells in mouse brain with optical validation. Magn Reson Med 55, 23–29 (2006). 3. Heyn, C. et al. In vivo MRI of cancer cell fate at the single-cell level in a mouse model of breast cancer metastasis to the brain. Magnetic Resonance in Medicine: An Official Journal of the International Society for Magnetic Resonance in Medicine 56, 1001–1010 (2006). 4. Knier, N. N., Hamilton, A. M. & Foster, P. J. Comparing the fate of brain metastatic breast cancer cells in different immune compromised mice with cellular magnetic resonance imaging. Clin Exp Metastasis 37, 465–475 (2020). 5. Murrell, D. H. et al. MRI surveillance of cancer cell fate in a brain metastasis model after early radiotherapy. Magnetic resonance in medicine 78, 1506–1512 (2017). 6. Tay, Z. W., Hensley, D. W., Vreeland, E. C., Zheng, B. & Conolly, S. M. The Relaxation Wall: Experimental Limits to Improving MPI Spatial Resolution by Increasing Nanoparticle Core size. Biomed Phys Eng Express 3, (2017).

Image/Figure: https://s3.amazonaws.com/amz.xcdsystem.com/1E8A4501-BB41-A02A-1D3B9882B798BFAA_abstract_File10351/GA245_ImageFigure_0513122027.pdf

Image/Figure Caption: Figure A: Perls Prussian Blue stain showing successful labeling of 231BR cells (shown in red) with Synomag-D (blue), resulting in a labeling efficiency of 98.0 ± 0.40 %. Figure B: The relationship between iron content and MPI signal is linear at both high and low concentrations of iron, with the equation to quantify iron content shown below. Figure C: Relaxometry of triplicate samples of Synomag-D, MPIO, and 5.0x105 231BR cells labeled with Synomag-D or MPIO. Figure D: Representative MPI of mouse brains injected with 2.5x105 Synomag-D labeled 231BR cells at day 0. Figure E: Representative MRI of mouse brains injected with 2.5x105 MPIO labeled 231BR cells at day 0. Discrete signal voids representing iron labeled cancer cells appear throughout the brain (white arrows). Figure F: MPI and iron quantification of mouse brains injected with 2.5x105 Synomag-D labeled 231BR cells at day 0 and Day 7, overlayed onto MRI (bottom). MPI of the mouse body is shown at Day 0 for mouse without detectable brain signal and with strong signal visible in the lung/liver region.

Full Name of Abstract's 1st Author : Natasha N. Knier

First Name: Natasha

Last Name: Knier

Email: nknier@uwo.ca

Organization: Western University

Country: Canada

ID: GA246

Light LisNR: A novel liposomal nanosensor architecture for noninvasive mapping of optical illumination profiles in deep tissue with MRI

Jacob Simon, MIT, jcsimon@mit.edu

Category: New Chemistry, Materials & Probes

Abstract Body : Optical technologies are increasingly important in modern biological research, but identifying sources and targets of optical illumination is challenging in living tissue. Here we introduce liposomal nanoparticle reporters (LisNRs), a novel nanoprobe design that addresses this limitation permitting noninvasive volumetric mapping of illumination profiles in vivo using magnetic resonance imaging (MRI). The LisNR mechanism leverages reversible light-dependent changes in the water permeability of a liposomal membrane encapsulating a large reservoir of paramagnetic contrast agent. This system permits T1 contrast from a large number of encapsulated contrast agents to be modulated simultaneously by a relatively small number of photoisomerizable molecules, enabling amplified light detection. We implement this general MRI contrast mechanism for light detection through the incorporation AzoPC, an azobenzene-containing phospholipid that promotes high bilayer permeability in its ultraviolet light-favored cis conformation but low permeability in its blue light-favored trans state. We screen a number of lipid compositions to determine optimal performance for in vitro light sensing in MRI. The resulting light LisNR displays maximal T1 relaxivity changes up to 200% with sensitivity to total incident photon counts of approximately 1016. We apply the nanosensor in vivo to measure three-dimensional illumination profiles characteristic of widely used optogenetics and photometry applications in the rat brain. Light exposure as short as 2 minutes, with fiber tip power of 0.3 mW corresponding to < 1 017 total incident photons, generated mean signal changes of approximately 10% and all observed responses were completely reversible over multiple light cycles. Our results reveal previously undescribed spatial profiles of light propagation arising in the presence of physiological tissue microstructure. This work introduces a general basis for mapping light in opaque environments, as well as a potent and adaptable sensor architecture for MRI.

Image/Figure: https://s3.amazonaws.com/amz.xcdsystem.com/1E8A4501-BB41-A02A-1D3B9882B798BFAA_abstract_File10351/GA246_ImageFigure_0513043351.pdf

Image/Figure Caption: Light-responsive nanosensors for light mapping in opaque tissue with magnetic resonance imaging (MRI). A) Representation of the effect of azoPC photoisomerization on liposome bilayer water permeability and longitudinal relaxation rate (R1) in light-sensitive liposomal nanoparticle reporter (light LisNR). B) Response of light LisNR in vitro over 3 cycles of saturating UV (365 nm) and blue (460 nm) light. Data acquired at 9.4T (Bruker). Inset shows raw longitudinal (T1-weighted) MRI signal. Colored bars indicate UV/blue light exposure. Experiments were performed with a gadolinium contrast agent concentration of 2.2 mM. C) T1-weighted signal change maps (% SC) of light LisNR responses to UV light (+1.5 to - 0.5 mm from bregma) applied using an implanted optical fiber (diameter of

200 μM, total power of 0.3 mW). Data acquired at 9.4T (Bruker). Inset shows close-ups of area marked by the white box. LisNR was delivered by acute intracranial injection (15 μL at [Gd] = 4.4 mM, injected over 2 hours). D) Same as C) but in response to blue light. E) Light responses were completely reversible in vivo over multiple cycles, colored shading represents light exposure. No light response was observed ipsilateral to fiber implantation. No light response was observed in control liposomes lacking AzoPC (data not shown). F) Mean signal change following blue or UV light exposures of different duration. Error bars show SEM. All responses ipsilateral to the light fiber (purple) were significant ($p < 0$ .05) compared to light LisNR contralateral to the fiber (red).

First Name: Jacob

Last Name: Simon

Email: jcsimon@mit.edu

Organization: MIT

Country: United States

ID: GA247

Development of 18F-OP-801: a novel hydroxyl dendrimer PET tracer for imaging maladaptive inflammation in the whole body and brain

Mackenzie Carlson, Stanford University, mlc18@stanford.edu

Category: Neuroscience

Abstract Body : Background: Mounting evidence indicates that innate immune dysfunction, involving chronic activation of macrophages and microglia, plays a critical role in the onset and progression of many neurological diseases. While PET imaging provides a potential non-invasive method to visualize and quantify innate immune activation in the brain and periphery, most available PET tracers are not specific for macrophages/microglia. We identified OP-801, a new synthetic PAMAM hydroxyl dendrimer that crosses the blood-brain barrier in the presence of inflammation and is selectively (>95%) taken up by reactive macrophages/microglia, as a candidate agent to radiolabel. Here we aim to 1) develop the first hydroxyl dendrimer PET tracer targeting reactive macrophages/microglia and 2) evaluate its ability to detect inflammation in the brain and periphery of mice following lipopolysaccharide (LPS)-induced sepsis. Methods: OP-801 was radiolabeled using a 2-step azide fluorination and copper-catalyzed click reaction.Formulated tracer (150-250 μCi, 0.04 ng/μCi in saline and 10% ethanol) was injected into female C57BL/6 mice by tail vein, 24 hours after intraperitoneal administration of LPS (10 mg/kg, n=14) or saline (n=6), and 60 minute dynamic PET/CT images were acquired. Brain PET images were quantified by co-registering PET and CT images followed by fitting a standard brain atlas within the skull of each mouse. Symptoms were assessed using the murine sepsis score (MSS) [1] and three LPS mice with negligible symptoms excluded from subsequent analysis. After imaging, all mice underwent cardiac puncture followed by perfusion with saline. Organs were dissected, weighed, and placed into a gamma counter to measure radioactivity. Tracer distribution within the brain was further evaluated using high resolution autoradiography. Brain slices used for autoradiography were subsequently stained with cresyl violet to enable quantification of 18F-OP-801 uptake in specific brain regions; one saline and one LPS animal were excluded from biodistribution analysis due to poor perfusion. Ex vivo plasma stability of 18F-OP-801 was evaluated at 60- and 150-minutes post-injection (n=4/group). Results: 18F-OP-801 was afforded in >4.7±2.66% yield (n=4 syntheses, decay-corrected) with >95% radiochemical purity. Brain PET/CT images (summed 50-60 minutes) revealed linearly increasing 18F-OP-801 uptake, corelating with MSS [1] (R=0.82, p=0.001). Quantitation of whole brain time activity curves demonstrated significantly elevated signal in LPS- versus saline-injected mice (p 18F-OP-801. Brain atlas analysis of 50-60 min summed PET images showed that uptake differed significantly (p x vivo biodistribution data confirmed PET findings for LPS (n=6) vs. saline (n=5) mice, showing significant differences in organs expected to have elevated reactive macrophages, including liver (2.7±2.20 saline vs. 27.0±30.11 LPS %ID/g, p=0.009), lung (2.9±4.34 vs. 26.2±26.47 %ID/g, p=0.030), and spleen (2.0±1.60 vs. 21.4±18.24 %ID/g, p=0.004). Importantly, ex vivo plasma stability of 18F-OP-801 was >95%, on average, after 150 minutes. Conclusion: 18F-OP-801 is a new PET tracer with extraordinary potential for highly sensitive and specific detection of activated macrophages/microglia in the

whole body and brain. Based on our promising proof-of-concept data, we plan to evaluate the utility of 18F-OP-801 for imaging innate immune activation in mouse models of Alzheimer's disease and multiple sclerosis. In parallel, we are working toward clinical translation of 18F-OP-801 to use for patient stratification and monitoring responses to novel immunomodulatory therapies.

References: Shrum, B., et al. BMC Res Notes. 2014, 7(233).

Image/Figure:

https://s3.amazonaws.com/amz.xcdsystem.com/1E8A4501-BB41-A02A-1D3B9882B798BFAA_abstract_File10351/GA247_ImageFigure_0513122457.jpg

Image/Figure Caption: Figure 1: A. Representative summed brain PET/CT images 50-60 minutes after tracer administration and 24 hours after injection of saline or LPS (10 mg/kg). Mice injected with LPS displayed varying murine sepsis scores indicative of their symptom severity – here we show PET images of mice with low and high sepsis scores and demonstrate the ability of 18F-OP-801 to detect increasing levels of inflammation in a manner that corelates with symptom severity. B. Whole body PET/CT images revealed markedly higher uptake of 18F-OP-801 in LPS-injected mice compared to those given saline alone.

Full Name of Abstract's 1st Author : Mackenzie Carlson

First Name: Mackenzie

Last Name: Carlson

Email: mlc18@stanford.edu

Organization: Stanford University

Country: United States

ID: GA248

Early Detection and Staging of Lung Fibrosis enabled precision MRI (pMRI) by collagen-targeted Protein Contrast Agents

Oluwatosin Ibhagui, Georgia State Uuniversity, oodubade1@student.gsu.edu

---

Category: Systemic Diseases (Kidney, Liver and Pancreas)

Abstract Body : Acute and chronic lung diseases including COVID-19, idiopathic pulmonary fibrosis (IPF), and chronic obstructive pulmonary disease (COPD) characterized by diffuse, progressive remodeling of the lung parenchyma with increased extracellular matrix (ECM) deposition, including collagen within the lung with the worst prognosis is a major health crisis affecting over half a billion patients globally. Early and noninvasive detection and staging of these lung diseases are pressing unmet medical needs limiting the potential for treatment monitoring and possible reversal of disease progression. Here we used magnetic resonance imaging with a new human collagen-targeted protein MRI contrast agent (hProCA32.collagen) to progressively detect and quantify fibrosis using both idiopathic pulmonary fibrosis and COPD animal models. hProCA32.collagen exhibits very strong collagen I binding affinity and is able to specifically bind to collagen 1 overexpressed in lung fibrosis of human patient. hProCA32.collagen possesses high relaxivities per particle (r1 and r2) at both 1.4 and 7.0 T enabling early detection by multiple imaging techniques of IPF using our established progressive bleomycin-induced IPF mice model closely mimicking key human morphological features of IPF including reticular opacities, traction bronchiectasis, and honeycombing-like cystic clustering. Both conventional (RARE and T2 weighted MRI) and ultra-short 3D (3D-UTE) MRI pulse sequences were able to detect overexpressed collagen in lung fibrosis with strong sensitivity and specificity. SNR values obtained by molecular MRI correlates well with the amount of histological lung collagen and hydroxyproline content in fibrotic mice. Furthermore, the enhancement pattern of hProCA32.collagen closely resemble the histological morphology of collagen overexpression in mice. The observed MR image enhancement was progressive with 60 % and 139 % SNR increase in early-stage IPF mice (n=4) and late-stage IPF mice (n=6) respectively. Signal retention up to 80.5% was also observed in the more fibrotic late-stage mice compared to healthy mice indicative of selective collagen binding of hProCA32.collagen. This observation was absent in the MR image obtained after injection of clinical contrast agent Gadovist® and our developed non collagen targeted contrast agent hProCA32. This enhancement specificity was further demonstrated in a second mouse model of chronic obstructive pulmonary disease (COPD) with nicotine-induced bronchial collagen accumulation with lung MRI enhancement in the bronchi structure of mice in contrast to alveolar distribution observed in IPF mice model. The low dose attribute of hProCA32.collagen helps mitigates metal toxicity and is expected to overcome the major clinical barriers in early diagnosis, noninvasive detection and staging of lung diseases with have strong translational potential in facilitating effective treatment to halt further chronic lung disease progression.

References: Yang JJ, Yang J, Wei L, Zurkiya O, Yang W, Li S, Zou J, Zhou Y, Maniccia AL, Mao H, Zhao F, Malchow R, Zhao S, Johnson J, Hu X, Krogstad E, Liu ZR. Rational design of

protein-based MRI contrast agents. J Am Chem Soc. 2008;130(29):9260-7. Epub 2008/06/26. doi: 10.1021/ja800736h. PubMed PMID: 18576649; PMCID: PMC2692035. Salarian M, Ibhagui, O., Yang, J. Molecular Imaging of Extracellular Matrix Proteins with Targeted Probes using MRI. WIREs Nanomedicine & Nanobiotechnology. 2019. Xue S, Qiao J, Pu F, Cameron M, Yang JJ. Design of a novel class of protein-based magnetic resonance imaging contrast agents for the molecular imaging of cancer biomarkers. Wiley Interdiscip Rev Nanomed Nanobiotechnol. 2013;5(2):163-79. Epub 2013/01/22. doi: 10.1002/wnan.1205. PubMed PMID: 23335551; PMCID: PMC4011496. Salarian M, Turaga RC, Xue S, Nezafati M, Hekmatyar K, Qiao J, Zhang Y, Tan S, Ibhagui OY, Hai Y, Li J, Mukkavilli R, Sharma M, Mittal P, Min X, Keilholz S, Yu L, Qin G, Farris AB, Liu ZR, Yang JJ. Early detection and staging of chronic liver diseases with a protein MRI contrast agent. Nat Commun. 2019;10(1):4777. Epub 2019/10/31. doi: 10.1038/s41467-019-11984-2. PubMed PMID: 31664017; PMCID: PMC6820552.

Image/Figure: https://s3.amazonaws.com/amz.xcdsystem.com/1E8A4501-BB41-A02A-1D3B9882B798BFAA_abstract_File10351/GA248_ImageFigure_0513122901.pdf

Image/Figure Caption: Detection of early and late stage IPF. A. Ultrashort echo time (UTE)-MRI of the lungs of normal, early stage and late stage bleomycin (BM) treated mice. Coronal T1-weighted Ultrashort echo time (UTE)-MR images of mice from various groups of mice (A) Healthy mice before, 1 h, 3 h and 24 h after injection of hProCA32.collagen; (B) mice treated with bleomycin for 3 weeks (early stage) pre, 1h, 3h and 24 h after injection of hProCA32.collagen with heterogeneous enhancement of collagenous honeycombing at the sub plueral and paraseptal areas of the lung (black arrows) (C) 6 weeks BM treatment (late stage) pre, 1h, 3h and 24 h after injection of hProCA32.collagen with heterogeneous enhancement of collagenous honeycombing at the sub plueral and paraseptal areas of the lung (black arrows) with traction bronchiectasis (arrow heads) (D) 6 weeks BM treatment (late stage) pre, 1h, 3h and 24 h after injection of non-targeted hProCA32 with homogenous and rapid enhancement of collagenous honeycombing at the sub plueral and paraseptal areas of the lung at the 1 h time point (black arrows), at the 3 h time point, a noticeable wash out of hProCA32.collagen was observed. (E) 6 weeks BM treatment (late stage) pre, 30 mins, 3h and 24 h after injection of Gadovist® with no significant enhancement in the lung F. Lung SNR plot of healthy, early stage and late stage IPF mice before and after injection of the MRI contrast agents. H, I Scatter-plots of lung collagen area and modified Ashcroft score against AUC_0–24 respectively showed a linear correlation in BM-induced IPF model. I., Histogram pixel analysis of normal mice before and at peak enhancement (1 h) after injection of hProCA32.collagen, J. 6 weeks BM-treated mice before and at peak enhancement (1 h) after injection of gadovist, K. 3 weeks BM-treated mice before and at peak enhancement (3 h) after injection of hProCA32.collagen with heterogeneous lung SNR distribution compared to the pre time point, the heterogeneity was also observed for 6 weeks treated mice injected with hProCA32.collagen (L).

Full Name of Abstract's 1st Author : Oluwatosin Y. Ibhagui

First Name: Oluwatosin

Last Name: Ibhagui

Email: oodubade1@student.gsu.edu

Organization: Georgia State Uuniversity

Country: United States

ID: GA249
[68Ga]Ga-THP-Pam: A PET radiotracer for imaging vascular calcification in rats

George Keeling, King's College London, george.keeling@kcl.ac.uk

---

Category: Cardiovascular & Pulmonary

Abstract Body : [68Ga]Ga-THP-Pam was previously demonstrated to have high affinity towards a number of calcium salts while [18F]NaF, the most used PET radiotracer for bone imaging has high affinity only for hydroxyapatite (the main component of bone mineral).1 It was hypothesised that the broad calcium mineral affinity of [68Ga]Ga-THP-Pam may be advantageous in detection of vascular calcification (VC), where the composition of solid calcium mineral may be more varied than the composition of bone.2 A direct comparison of [68Ga]Ga-THP-Pam and [18F]NaF in a rat model of VC was performed to test this hypothesis. A model of VC was used in which rats were fed a diet containing warfarin and vitamin K1 along with subcutaneous administration of vitamin D3 to induce severe VC.3 Anaesthetised rats were injected with [68Ga]Ga-THP-Pam and scanned using preclinical PET/CT 60–120 min post-injection. The rats were imaged using the same protocol with [18F]NaF the following day. As a control study, animals fed a healthy diet were imaged using the same procedure. Organs were harvested and their radioactivity was measured for ex vivo biodistribution. Organs of interest were fixed in formalin and embedded in paraffin. Paraffin-embedded organs were scanned using μCT. Imaging (Figure 1A) showed high uptake of [68Ga]Ga-THP-Pam and [18F]NaF (3.44 ± 0.69 and 0.91 ± 0.24 %ID respectively, $p = 0.002$, Figure 1B) in a region of tissue around the stomach, with severe calcification as identified by CT. Additionally, [68Ga]Ga-THP-Pam demonstrated increased uptake in the VC group vs. the healthy group across several major organs, most notably in the kidneys (2.21 ± 0.76 vs. 0.25 ± 0.13 %ID, $p = 0.002$, Figure 1B). Ex vivo biodistribution data confirmed the increased uptake of [68Ga]Ga-THP-Pam observed in the imaging data. The presence of calcification in the kidneys, stomach and other organs of interest was confirmed by microCT-based 3D X-ray histology (XRH) and conventional histology (Figure 1C). To visualise small areas of interest such as the aorta, a prototype post-reconstruction method to improve the spatial resolution of preclinical PET with gallium-68 was used. Analysis of the mineral composition of the calcifications is ongoing. These results demonstrate that [68Ga]Ga-THP-Pam may offer improved detection of VC in comparison to [18F]NaF, including microcalcifications undetectable by preclinical CT.

References: 1. G. P. Keeling, B. Sherin, J. Kim, B. San Juan, T. Grus, T. R. Eykyn, F. Rösch, G. E. Smith, P. J. Blower, S. Y. A. Terry and R. T. M. de Rosales, Bioconjugate Chem., DOI: 10.1021/acs.bioconjchem.0c00401, 2020. 2. E. Tsolaki and S. Bertazzo, Materials, 2019, 12, 3126. 3. J. Bordoloi, PhD Thesis, King's College London, 2015.

Image/Figure:

https://s3.amazonaws.com/amz.xcdsystem.com/1E8A4501-BB41-A02A-1D3B9882B798BFAA_abstract_File10351/GA249_ImageFigure_0513123107.png

Image/Figure Caption: Figure 1. (A) PET-CT MIP images of rats with vascular calcification and control rats with both [68Ga]Ga-THP-Pam and [18F]NaF 60–120 min post-injection. The images of calcified rats are both of the same rat, and the control images are also data from the same rat. Each PET image shows a standard uptake value (SUV) scale of 0.3–10. S = stomach. K = kidneys. (B) Quantification from PET images of [68Ga]Ga-THP-Pam and [18F]NaF in %ID in rats fed a diet to induce VC and rats fed a healthy diet. (C) Ex vivo detection of calcification in kidneys by μCT XRH (top panel, colour scales matched) and conventional histology with Alizarin Red staining (bottom panel) in kidneys from rats from the VC group and the healthy group.

Full Name of Abstract's 1st Author : George Patrick Keeling

First Name: George

Last Name: Keeling

Email: george.keeling@kcl.ac.uk

Organization: King's College London

Country: United Kingdom

ID: GA250

In vitro and in vivo assessment of cellular sensitivity for magnetic particle imaging and fluorine-19 MRI in mesenchymal stem cells

Olivia Sehl, Robarts Research Institute, osehl@uwo.ca

Category: Instrumentation

Abstract Body : Introduction: Therapeutic mesenchymal stem cells (MSC) have great potential for regenerative medicine. After administration, many MSC die due to a hostile, pro-inflammatory environment and unfortunately, cases of graft failure are only detected after several months based on lack of tissue repair1. Early detection and intervention for failed MSC therapies could be made possible with sensitive and quantitative imaging. Magnetic particle imaging (MPI) with superparamagnetic iron oxide nanoparticles and fluorine-19 (19F) magnetic resonance imaging (MRI) with perfluorocarbon nanoemulsions both produce images which allow for quantification of cells2. MPI is an emerging instrument for cell tracking which is expected to have superior cellular sensitivity compared to 19F MRI, however, this has not been carefully compared. The objective of this study is to assess the cellular sensitivity of MPI and 19F MRI for detection of MSC. Methods: Cell Preparation: MSC were labeled by overnight co-incubation with 55µg Fe/mL ferucarbotran and transfection agents3 or 2.5mg/mL perfluoropolyether (PFPE). Cell pellets were produced by serial dilution from 1.024x106 to 1000 cells (n=9 per cell number). Ferucarbotran-labeled MSCs (1x105) or PFPE-labeled MSCs (2x106) were injected to immunocompromised mice by subcutaneous or intraperitoneal administration (n=4 total). Imaging protocol: Ferucarbotran-labeled cells (pellets and in vivo) were imaged with a preclinical Momentum MPI scanner using weak (3T/m) gradients in 2D (1.5 min) and 3D (22.8 min). 19F MRI of PFPE-labeled MSC were acquired on a 3T clinical MRI using a 4.3cm dual-tuned surface coil and a 3D balanced steady state free precession sequence. Cell pellets were imaged in 1.5 minutes (same as MPI) and 4.5 minutes, and in vivo 19F MRI was 35 minutes. MPI and 19F MRI in vitro cell detection limits were defined as the minimum number of MSC detected with signal-to-noise ratio (SNR) >5. Quantification of MPI and 19F signal was calculated as mean signal intensity times the area of the region of interest. Validation: Ferucarbotran labeling was validated with Perl's Prussian blue stain and by measuring iron mass per cell by MPI2. PFPE labeling was validated by microscopy and by measuring 19F atoms per cell by NMR4. Results: Cell number was correlated with MPI signal (R2 = 0.9988) and 19F signal (R2 = 0.9865). For MPI, MSC labeled with 19.09±2.50pg Fe/cell and as few as 4000 MSC could be reliably detected in 2D (SNR=5.5, 8/9 replicates). Improved sesitivity was seen in 3D; 2000 MSC were detected (SNR=6.6, 9/9 replicates) and as few as 1000 MSC could be visualized (SNR 1.55 x1011 19F/cell and the range of 256-1024 x103 MSC were detectable in short scans (SNR=7.12, 1.5 min/pellet). Fewer cells (128x103) were detected with longer imaging times (4.5 min/pellet, SNR=5.9, 2/9 replicates). In vivo MPI showed a reduction in MPI signal measured from cells injected subcutaneously (53%) and intraperitoneal (49%) compared to signal from a pellet of 1x105 MSC. With 19F MRI, the same amount of signal was detected from 2x106 cells in pellets (1.1x1018 19F spins) and after subcutaneous (9.3x1018 19F spins) and intraperitoneal (1.1x1018 19F spins) injections. Conclusions: While

impossible to make a direct comparison between these cellular imaging modalities, we detected fewer MSC with MPI than with 19F MRI, using the same scan time. There is no doubt that cellular sensitivity will continue to improve with cellular uptake strategies and optimized versions of cell labels. We also found differences in sensitivity in vivo compared to in vitro. The dispersion of cells in vivo can result in some cells to fall below the intravoxel detection limits. Additional factors in vivo that influence cell detection include motion, effects of Brownian relaxation (MPI), and the coil filling factor (19F MRI). To advance imaging of cellular therapeutics, it is essential to continue to understand and improve cellular sensitivity.

References: [1] Nejadnik, H et al. Wires Nanomed Nanobi 11 (2019). [2] Sehl, OC et al. Tomography 6 (2020). [3] Thu, M.S et al. Nat Med 18 (2012). [4] Fink, C. Sci Rep 8:590 (2018).

Image/Figure:

https://s3.amazonaws.com/amz.xcdsystem.com/1E8A4501-BB41-A02A-1D3B9882B798BFAA_abstract_File10351/GA250_ImageFigure_0513123633.png

Image/Figure Caption: (A) In vitro detection of ferucarbotran-labeled MSC with MPI. Detection of as few as 4,000-16,000 MSC in 2D (1.5 min) and 1,000-2,000 MSC in 3D (22.5 min) are shown. Perl's Prussian blue stain shows efficient iron labeling of cells. (B) In vitro detection of PFPE-labeled MSC with 19F MRI. In shorter scans (1.5 minutes/pellet), 256,000 – 1,024,000 MSC are detected. With longer scan times, the SNR is improved and the detection of 128,000 cells is enabled. PFPE-labelling can be visualized in microscopy as lipid nanodroplets (black arrows). (C) MPI signal from 100,000 ferucarbotran-labeled cells is diminished after subcutaneous and intraperitoneal injection. (D) Sagittal 1H/19F overlay showing PFPE-labeled cells that are administered by subcutaneous or intraperitoneal injection. M = million, k = thousand.

Full Name of Abstract's 1st Author : Olivia C. Sehl

First Name: Olivia

Last Name: Sehl

Email: osehl@uwo.ca

Organization: Robarts Research Institute

Country: Canada

ID: GA251

In-vivo CRISPR/Cas9-induced VMAT2 knockdown evokes local molecular and network-level functional changes in the rat brain

Tudor Mihai Ionescu, Werner Siemens Imaging Center, Department of Preclinical Imaging and Radiopharmacy, Eberhard Karls University Tuebingen, Tuebingen, Germany, Tudor.Ionescu@med.uni-tuebingen.de

---

Category: Neuroscience

Abstract Body : Introduction Recent advances in CRISPR/Cas9 technology have enabled its use as a powerful tool for in-vivo gene editing. Previously, we have validated this technique in-vivo by assessing vesicular monoamine transporter 2 (VMAT2) knockdown (KD) effects using [11C]DTBZ and [11C]raclopride PET, behavioral experiments and ex-vivo analyses [1]. However, the effects of targeted gene editing using CRISPR/Cas9 on whole-brain function have not been studied to date. Here, we targeted the Slc18a2 gene, encoding the VMAT2, using Cas9 from Staphylococcus aureus (SaCas9) in rats. We performed simultaneous PET/fMRI scans to elucidate the effects of gene editing on both local molecular and network-level functional connectivity (FC) changes. Methods Baseline [11C]raclopride PET/fMRI scans were acquired in adult rats (n=23) under medetomidine (0.05mg/kg bolus+0.1 mg/kg/h infusion) and 0.5% isoflurane in air over 60 min using a 7T small-animal MRI with a PET insert. The tracer was applied as a bolus and fMRI was acquired using an EPI-BOLD sequence (TR=2500ms, TE=18ms). AAV-SaCas9 and AAV-sgRNA-Slc18a2 were next injected into the right substantia nigra pars compacta (SNc) and DPBS into the left SNc. The rats were rescanned 8-14 weeks after using the same PET/fMRI protocol and additional PET scans were performed using [11C]DTBZ and [18F]FMZ. Following standard preprocessing, the PET data were assessed for molecular changes and fMRI was used to evaluate effects in default-mode (DMN) and sensorimotor (SMN) network FC. Results and Discussion Based on the [11C]DTBZ scans we split the rats into low knockdown (KD 20%, n=10) groups (Figure 1A). On a molecular level, we found correlations between VMAT2 KD and D2R expressions (R2 = 0.52, p Conclusion Our study is the first to assess CRISPR/Cas9 gene editing as an in-vivo method for the investigation of not only local, but also network-level brain function. While we detected functional changes at both low and high KD, we could robustly separate the two cohorts, thus recommending the used multimodal study design for future research of both early and advanced disease phenotypes. Therefore, we demonstrated the tremendous potential the combination of CRISPR/Cas9 and PET/fMRI imaging has to bridge the gap in understanding the link between targeted gene alterations and whole-brain functional changes.

References: [1] Marciano S et al, Imaging In Vivo CRISPR/Cas9 Neuronal Gene Editing in the Adult Rat Brain, World Molecular Imaging Meeting 2020, peer-reviewed talk.

First Name: Tudor Mihai

Last Name: Ionescu

Email: Tudor.Ionescu@med.uni-tuebingen.de

Organization: Werner Siemens Imaging Center, Department of Preclinical Imaging and Radiopharmacy, Eberhard Karls University Tuebingen, Tuebingen, Germany

Country: Germany

ID: GA252
Liposomes Encapsulating Co(II) Complex-based Shift Agents as MRI probes

Md Saiful Chowdhury, State University of New York at Buffalo, mdsaiful@buffalo.edu

---

Category: New Chemistry, Materials & Probes

Abstract Body : Co(II) shift agents loaded into liposomes produce lipoCEST effects comparable to that of liposomes containing Tm(III) and Dy(III) shift agents. [1,2] These paramagnetic complexes shift the intraliposomal water proton resonance, thereby producing lipoCEST (liposomal CEST) agents due to the exchange of intra and extra liposomal water molecules through the bilayer membrane. Shift agents were encapsulated in the intraliposomal interior or as amphiphilic complexes in the liposomal bilayer. In order to prepare improved lipoCEST agents, new Co(II) complexes that are highly soluble with an overall neutral or cationic charge complexes have been employed. These agents are Co(II) octahedral coordination complexes of the 14-membered tetraaza cyclam macrocycle with bisbenzyl and bisamide/bis-N-glycinamide pendants appended to the cyclam amines as shown in figure 1. Neutral shift agents have lower tonicity than charged analogues imparting higher osmotic shrinkage of the shift agent loaded liposomes when placed in aqueous solutions of similar osmolarity. This yielded a lipoCEST peak 5 ppm away from bulk water at a relatively low saturation power of 6 uT in isotonic 300 mOsm solution for a neutral Co(II) complex loaded into 100 nm liposomes. Being saturation power dependent, the lipoCEST peak was found to shift further with an increase in saturation power. Asymmetry of Z-spectra was plotted to calculate the position of LipoCEST peak against bulk water peak. Moreover, larger shrinking and a corresponding shift in the position of the lipoCEST peak were observed with hypertonic solutions due to an increased bulk magnetic susceptibility (BMS) effect from the more shrunken liposomes. Integration of a freeze-thaw step during the liposome formulation after the extrusion enhanced the core loading efficiency of the liposomes and so the concentration of the intraliposomal shift agent was higher than the liposomes made without freeze-thawing. The encapsulation efficiency of the shift agent inside the liposomes increased from 4.0% to 37.8% with 5 cycles of freezing in liquid nitrogen and thawing at 55 °C. The lipoCEST peak from one such formulation was shifted 9 ppm away from bulk water at 6 uT saturation power under similar isotonic condition. The position of the lipoCEST peak further shifted from 9 ppm to 12 ppm with an increase in saturation power (15.4 uT). Additionally, two amphiphilic Co(II) complexes containing charged or neutral Co(II) complexes are being investigated with the expectation of producing larger shifts and a greater magnitude of the CEST peak. These two contrast agents both have two stearyl long chain pendants alkylated to the macrocycle amines. These complexes will be integrated into the liposomal membrane for liposomes core loaded with hydrophilic shift agents. Both relaxivity and lipoCEST data from these liposomes are employed to image phantoms or animals with these MRI probes.

References: 1. Abozeid, S. M.; Asik, D.; Sokolow, G. E.; Lovell, J. F.; Nazarenko, A. Y.; Morrow, J. R., Co(II) Complexes as Liposomal CEST Agents. Angew Chem Int Ed . 2020, 59 (29), 12093-12097. 2. Maruyama, S.; Ueda, J.; Kimura, A.; Murase, K., Development and

Characterization of Novel LipoCEST Agents Based on Thermosensitive Liposomes. Magn. Reson. Med. Sci. 2016, 15 (3), 324-34.

Image/Figure:

https://s3.amazonaws.com/amz.xcdsystem.com/1E8A4501-BB41-A02A-1D3B9882B798BFAA_abstract_File10351/GA252_ImageFigure_0513124859.png

Image/Figure Caption: Figure 1 - Co(II) shift agents

Full Name of Abstract's 1st Author : Md Saiful Islam Chowdhury

First Name: Md Saiful

Last Name: Chowdhury

Email: mdsaiful@buffalo.edu

Organization: State University of New York at Buffalo

Country: United States

ID: GA253

Simultaneous PET/MR Imaging based tracking of the migration and homing dynamics of CD8+ T cells and phagocytes in acute and chronic contact hypersensitivity reaction

Julia Stahl, Werner Siemens Imaging Center, julia.carolin.stahl@med.uni-tuebingen.de

---

Category: Immunology: Inflammation & Infection

Abstract Body : Introduction: Non-invasive in vivo tracking of T cells enables to follow their migration and homing dynamics in cancer and autoimmune diseases. We aimed to establish simultaneous 89Zr-DFO-CD8-minibody and 19F-Perfluorocarbon (PFC) PET/MR imaging in T cell driven acute and chronic contact hypersensitivity reaction (CHSR). CHSRs are orchestrated by CD8+ and CD4+ T cells and are accompanied by immigration and activation of phagocytic cells. The aim of our study was to distinguish the differential impact of CD8+ T cells and phagocytes in acute and chronic CHSRs by 89Zr-DFO-CD8-minibody/19F-PFC PET/MR imaging of NF-κB.p52-/- mice, which are unable to develop chronic CHSR, and in wild-type mice. Methods: Acute and chronic CHSR was induced by one (acute CHSR) or five (chronic CHSR) repetitive trinitrochlorobenzene (TNCB) challenges of the right ear of TNCB-sensitized C57BL/6J and C57BL/6-NF-κB.p52-/- mice. The left ear served as healthy control. For in vivo PET/MR investigations we used a 89Zr-DFO-murine CD8-specific minibody (IAB42, ImaginAb, USA) and 19F-PFC to track CD8+ T cells and phagocytes namely neutrophils, macrophages, and monocytes non-invasively in vivo with simultaneous PET/MR. Imaging studies were performed before, 12h and 24h after the 1st and 5th TNCB-ear-challenge (n = 5). For ex vivo cross-validation we conducted 89Zr-DFO-CD8-biodistribution, immunohistochemistry (IHC) and flow-cytometry analysis (FACS). Results/Discussion: Our in vivo PET/MRI studies in wild-type mice revealed a strongly, up to 14-fold increased 89Zr-DFO-murine-CD8-minibody uptake in ears with chronic CHSR (2.73 %ID/cc, 24h) and no increase in ears with acute CHSR (0.19 %ID/cc, 24h) when compared to the healthy left ears (acute CHSR: 0.19 %ID/cc, 24h; chronic CHSR: 0.37 %ID/cc, 24h). In the draining cervical lymph nodes (dLNs) of mice with chronic CHSR the 89Zr-DFO-murine-CD8-minibody uptake (8.20 %ID/cc, 24h) was 3-fold enhanced compared to mice with acute CHSR (2.61 %ID/cc, 24h). In inflamed ears of NF-κB.p52-/- mice with chronic CHSR we determined an approximately 50% reduced 89Zr-DFO-CD8-minibody uptake (1.47 %ID/cc, 24h) when compared to wild-type mice (2.73 %ID/cc) and only a moderate reduction in the dLNs of NF-κB.p52-/- mice (5.98 %ID/cc, 24h) when compared to wild-type mice. Focusing on phagocyte tracking, we identified a strongly enhanced 19F-PFC-uptake exclusively in inflamed ears of wild-type mice with chronic CHSR (7.51% PFC uptake normalized to standard, 24h) but not in ears with acute CHSR (3.59%). Interestingly, we identified hardly any differences in the 19F-PFC-uptake in inflamed ears of NF-κB.p52-/- mice (7.11%) when compared to wild-type mice (7.51%). In the dLNs of NF-κB.p52-/- mice (11.67%) with chronic CHSR we detected an even higher PFC uptake when compared to wild-type mice (8.48%). Most importantly, extensive ex vivo biodistribution and FACS analysis as well as IHC confirmed our in vivo PET/MRI data. Conclusions: Highly innovative simultaneous non-invasive in vivo 89Zr-DFO-CD8-minibody- and 19F PFC PET/MR

imaging enables differential tracking of CD8+ T cells and phagocytes in secondary lymphatic organs and the sites of acute and chronic CHSR. Thus, this imaging approach is applicable to gain more profound knowledge about the dynamics of cellular processes during disease progression and facilitates dual monitoring of novel anti-inflammatory treatment approaches.
Acknowledgement: This work was supported by the Horizon2020 Programme under grant agreement n° 675417 (PET3D) and the EU/EFPIA/Innovative Medicines Initiative 2 Joint Undertaking under grant agreement n° 831514 (Immune-Image).

Full Name of Abstract's 1st Author : Julia Carolin Stahl

First Name: Julia

Last Name: Stahl

Email: julia.carolin.stahl@med.uni-tuebingen.de

Organization: Werner Siemens Imaging Center

Country: Germany

ID: GA254

MRI-guided low intensity ultrasound stimulation to improve chemotherapy with liposomal doxorubicin in human ovarian cancer xenograft mouse model

Deyssy Patrucco, Department of Molecular Biotechnology and Health Sciences, University of Turin, deyssy.patrucco@unito.it

---

Category: Oncology

Abstract Body : The ovarian cancer is one of the gynaecological tumor with the highest mortality rate1. The aim of this study is to improve the therapeutic effect of the chemotherapy based on theranostic PEGylated liposomes co-loaded with doxorubicin (Doxo) and Gadoteridol using low intensity pulsed ultrasound (LIUS) on ovarian cancer xenograft mouse model. MRI is a technique of election to monitor the tumor progression and visualize the Gd-based agent that can report on the US-triggered drug release and predict the long-term therapeutic outcome. Sonosensitive theranostic liposomes (Gd-Doxo-Lipo) were prepared by using the film hydration method (lipid composition: DPPC/DSPC/ Chol /DSPE-PEG2000, molar ratio 10/5/4/1) and loaded with doxorubicin 1 mg/mL and Gadoteridol 300 mM.2 Female athymic nude mice Foxn1-/ Foxn1- were purchased by Envigo (Milano, Italy) and were inoculated with human ovarian cancer cells (A2780). Tumor volume were evaluated by T2w-MR images acquired at 7 T. Mice were divided in three groups i) not treated group ii) group treated with Gd- Doxo-Lipo, and iii) group treated with Gd-Doxo-Lipo and US local application, T1w MR images were acquired before and after the treatment. The US treatment was performed using US waves generated by a piezoelectric transducer (1 MHz, intensity < 5 W/cm2) purchased by Precision Acoustics (Dorset, UK). The amount of Doxo and Gadoteridol in the tumour was assessed spectrofluorimetrically and by ICP-MS, respectively. After the individuation of the best the US setup conditions for the maximal release of the drug and the Gd-based agent from liposomes, the most appropriate US parameters to obtain the internalization in the tumour cell membrane were optimized in vitro and in vivo. Gadoteridol and Doxo showed a similar ability to be released from the liposomes and be internalized by sonoporation. The tumour US stimulation resulted in a T1-contrast enhancement in the tumour and in the kidney calix and bladder, thus indicating the effective intratumor release of gadoteridol and drug from the liposomes. The tumour uptake of the Gd-agent and the drug was confirmed by confocal images and quantification (Fig. 1). Notably, the group of mice treated with Gd-Lipo-Doxo and US-stimulated showed an arrest in the tumor progression, and in some cases the lesion completely remitted. Interestingly, the tumour T1 contrast enhancement measured just after the US treatment showed a positive correlation with the therapeutic outcome after three weeks. Low intensity US stimulation seems to be a very appealing method to improve the chemotherapy efficacy of a liposomal formulation of doxorubicin in a mouse model of ovarian carcinoma. The three components of the theranostic agents (liposomes, Doxo, and Gadoteridol) are already used in clinic, making this approach suitable for clinical translation. Moreover, MRI confirms to be an excellent imaging technique to monitor and predict the therapeutic effect.

References: 1. Momenimovahed, Z., Tiznobaik, A., Taheri, S. & Salehiniya, H. Ovarian cancer in the world: Epidemiology and risk factors. International Journal of Women's Health vol. 11 287–299 (2019). 2. S. Rizzitelli, P. Giustetto, J.C. Cutrin, D. Delli Castelli, C. Boffa, M. Ruzza, V. Menchise, F. Molinari, S. Aime, E. Terreno, Sonosensitive theranostic liposomes for preclinical in vivo MRI-guided visualization of doxorubicin release stimulated by pulsed low intensity non-focused ultrasound, J. Control. Release 202 (2015) 21–30.

Image/Figure:

https://s3.amazonaws.com/amz.xcdsystem.com/1E8A4501-BB41-A02A-1D3B9882B798BFAA_abstract_File10351/GA254_ImageFigure_0513125041.jpg

Image/Figure Caption: Left top: T1w MR images of kidneys and tumor (white arrows) pre and after the injection of Gd-Doxo Lipo with and without the US application. Left bottom: confocal microscopy image of slice tumor after the Gd-Doxo Lipo injection with and without the US application (blue: DAPI-stained nuclei, green:CD31-stained vascular endothelium, red: doxorubicin) Right: Tumor growth of ovarian cancer in xenograft mouse model after the treatment with Gd-Doxo Lipo and after the treatment with Gd Doxo Lipo and US application

Full Name of Abstract's 1st Author : Deyssy Patrucco

First Name: Deyssy

Last Name: Patrucco

Email: deyssy.patrucco@unito.it

Organization: Department of Molecular Biotechnology and Health Sciences, University of Turin

Country: Italy

ID: GA255
[125I]IAZA: A New Imaging Agent for Human Alzheimer's Disease Brain

Thrisha Reddy, University of California Irvine, ttreddy@uci.edu

---

Category: Neuroscience

Abstract Body : Objective: Imaging studies of amyloid b (Ab) accumulation in Alzheimer's disease (AD) have shown clinical utility. We have previously shown the high affinity Ab plaque binding properties of [11C]TAZA and [18F]Flotaza in postmortem human brain (AD and cognitively normal CN; Pan et al., 2016; Kaur et al., 2021). The aim of this study was to develop and evaluate the effectiveness of a new iodine-125 analog, [125I]IAZA (4-[125I]iodo-4'-N,N-dimethylaminoazobenzene), as a potential Ab human plaque imaging agent for autoradiographic studies. Methods: 4-Tributyltin-4'-N,N-dimethylaminoazobenzene precursor was synthesized using commercially available starting materials. The radiosynthesis of [125I]IAZA was carried out using electrophilic substitution by sodium [125I]iodide (Matsumura et al., 2011). To sodium [125I]iodide (0.23 mCi in 40 mL 0.1N NaOH; ARC, St Louis, USA), 0.8 mg of precursor in 100 mL ethanol was added, followed by 100 mL 1N HCl and 100 mL of 3% H2O2. After 15 mins at room temperature reaction was quenched with 100 mL NaHSO3. The reaction mixture was extracted with dichloromethane and purified by chromatography. Human AD post-mortem brain slices (10 μm thick cut using Leica 1850 cryotome) consisting of anterior cingulate (AC) and corpus callosum CC as well as temporal cortex were used for in vitro binding studies. Brain slices were incubated with [125I]IAZA in 50% ethanol PBS buffer pH 7.4 (60 mL;0.02 μCi/mL) at 25 oC for 1.25 hr. Nonspecific binding was measured in the presence of 5-OH-BTA-0. The slices were then washed with cold PBS buffer, 50% ethanolic PBS buffer, 90% ethanolic PBS buffer, PBS buffer and cold water. Brain sections were dried, exposed overnight on phosphor film, and placed on the phosphor films and analyzed using Optiquant software and extent of binding of [125I]IAZA was measured in DLU/mm2. Results: The single step radiosynthesis of [125I]IAZA was very efficient. Product was purified on preparative thin layer chromatography, extracted and the final product taken up in absolute ethanol. Radiochemical yields (>50%) were obtained with a radiochemical purity of >95%. Specific activity based on [125I]iodide was >15 Ci/mmol. For Ab plaques, slices from subjects were positively immunostained with anti-Ab Biolegend 803015 (Biolegend, CA, USA) which is reactive to amino acid residue 1-16 of b-amyloid. Selective binding of [125I]IAZA was observed in grey matter regions shown to contain the Ab plaques. The ratio of anterior cingulate to corpus callosum was >20. Similarly, temporal cortex exhibited significant binding of [125I]IAZA. Very little white matter binding was seen when 90% alcohol was used in the washing of the slices. Washing with PBS buffer or even with 50% alcohol was insufficient to remove the nonspecific white matter binding. Incubation with 5-OH-BTA-0 did not reduce [125I]IAZA binding. Conclusion: [125I]IAZA exhibited high binding in postmortem human AD brains. It is therefore potentially a suitable iodinated radioligand for human Ab plaques. Further studies are underway to confirm if binding of [125I]IAZA is on Ab plaques site different from 5-OH-BTA-0 or on neurofibrillary tangles. Along with our recently developed [125I]IPPI for Tau (Mukherjee et al., 2021), it offers a useful tool for the study of

postmortem AD brains. Studies are underway to evaluate the utility of [125I]IAZA in transgenic AD mice models and evaluate dual targeting drugs as therapeutics for AD (Samra et al., 2018).

References: Mukherjee J, Liang C, Patel KK, Lam PQ, Mondal, R.; Development and evaluation [125I]IPPI for tau imaging in post-mortem human Alzheimer's disease brain. Synapse, 74: e22183, 2021. Pan ML, Mukherjee MT, Patel HH, Patel B, Constantinescu CC, Mirbolooki MR, Liang C, Mukherjee J.; Evaluation of [11C]TAZA for amyloid Aβ plaque imaging in postmortem Alzheimer's disease brain region and whole body distribution in rodent PET/CT. Synapse, 70: 163-176, 2016. Samra GK, Dang K, Ho H, Baranwal A, Mukherjee J.; Dual targeting agents for Aβ plaque/P-glycoprotein and Aβ plaque/nicotinic acetylcholine α4β2* receptors - Potential approaches to facilitate Aβ Plaque removal in Alzheimer's disease brain. Medicinal Chemistry Research, 27: 1634-1646, 2018. Matsumura K, Ono M, Hayashi S, Kimura H, Okamotoa Y, Ihara M, Takahashi R, Mori H. Saji H.; Phenyldiazenyl benzothiazole derivatives as probes for in vivo imaging of neurofibrillary tangles in Alzheimer's disease brains. Med. Chem. Commun. 2: 596-600, 2011. Kaur, H., Felix, M.R., Liang, C., Mukherjee J. Development and evaluation [18F]Flotaza for Aβ plaque imaging in post-mortem Alzheimer's disease brain. Bioorg. Med. Chem. Lett., under review, May 2021 (Presented at the World Molecular Imaging Congress 2020, October 7-10, 2020).

Image/Figure:

https://s3.amazonaws.com/amz.xcdsystem.com/1E8A4501-BB41-A02A-1D3B9882B798BFAA_abstract_File10351/GA255_ImageFigure_0513125102.png

Image/Figure Caption: Figure Legend AD Human [125I]IAZA. (A). AD brain section, 10 micron thick consisting of grey matter (GM) anterior cingulate (AC) and white matter (WM) corpus callosum (CC); (B). Anti-Ab IHC showing Ab plaques; (C). [125I]IAZA binding in adjacent section, with low nonspecific binding in WM with GM to WM ratios >20.

Full Name of Abstract's 1st Author : Thrisha Thriveashley Reddy

First Name: Thrisha

Last Name: Reddy

Email: ttreddy@uci.edu

Organization: University of California Irvine

Country: United States

ID: GA256

Activity-based Sensing By CEST-MRI Enabled by The Transient Uncaging of Radicals In A Magnetic Field

Adam Shuhendler, University of Ottawa, Adam.Shuhendler@uottawa.ca

---

Category: New Chemistry, Materials & Probes

Abstract Body : Introduction: Quenched fluorescent probes provide a multi-colour tool box of agents that can be designed to selectively 'turn on' when acted upon by biomolecular targets of interest[1]. Optical techniques are restricted in vivo by limited tissue imaging depths on millimeter scales[2]. While this "quenching" approach has been applied to gadolinium-based contrast agents[3,4], multiplexed evaluation of biochemical targets akin to that afforded by fluorophores has been elusive to MRI. CEST-MRI is capable of multiplexed imaging, and the ability to "quench" PARACEST signal production via T1-shortening effects of nitroxyl radicals has been demonstrated[5]. Herein we introduce a non-radical moiety, N-hydroxy piperidine (N-OH Pip), that can be induced to have radical properties when placed in a magnetic field. N-OH Pip-mediated diaCEST suppression may enable multiplexed, whole subject interrogation of biomolecular targets by CEST-MRI. Methods: Known diaCEST beacons were coupled to 4-carboxyTEMPO, 4-carboxy-N-OH Pip, or analogs thereof (Fig. 1C). The FAP substrate Gly-Pro was converted to a CEST-MRI probe through coupling to N-OH-Pip and barbiturate. Z-spectra were acquired on a 300 MHz NMR for in vitro samples, and on an MR Solutions 3T MRI for enzyme assay and in vivo evaluations using a single-shot FSE sequence. Magnetospectroelectrochemical evaluation of radical uncaging was performed on a custom setup where two neodymium magnets generated a Bo = 1 T at the midpoint of the electrochemical cell. Results: The conjugation of 5-methylaminosalicylic acid to 4-carboxyTEMPO resulted in a suppression of diaCEST signal (Fig. 1A). While reduction of TEMPO to N-OH Pip was expected to restore the CEST signal, maintained signal suppression (~ 1% MTRasym) was observed (Fig. 1B). This suppression was maintained across various diaCEST classes (Fig. 2), and required the direct conjugation to the N-OH Pip group to maintain signal suppression (i.e. suppression was not observed in a physical mixture of diaCEST beacon and N-OH Pip) (Fig. 3). The mechanism of quenching was investigated by taking advantage of the photochromic and redox properties inherent to N-OH Pip, permitting spectral differentiation of the redox species (i.e. N-O• vs. N-OH) with and without the application of a 1T magnetic field (Fig. 4a). From this analysis it was observed that, upon application of the magnetic field, a radical character of the N-OH was uncaged, which was corroborated by T1-shortening observed in the MRI (Fig. 4b), and which is known to contribute to CEST suppression[5]. In applying this design strategy to an enzyme substrate, a diaCEST contrast agent was made to map the activity of Fibroblast Activating Protein-a (FAP) in vivo (Fig. 5) in FAP-high and -low cancers. Only in FAP-high tumors was diaCEST signal observed to evolve over time (Fig. 5B), supporting the application of this CEST beacon-suppressor pair for MRI-based activity-based sensor generation. Discussion: Efforts to expand the capabilities for activity-based sensing by molecular MRI are presented herein with the discovery of N-OH Pip as a broadly-acting non-radical quencher of diaCEST signal. Importantly, the through-space signal suppression provided by N-OH Pip may be shorter range

than that induced by TEMPO. In addition to the limited stability of TEMPO in vivo (t1/2 = 10-20 min) through nitroxy reduction[7], which is not an issue for N-OH-based moieties, the requirement for direct conjugation of N-OH Pip to the CEST beacon may provide higher fidelity reporting of a broad range of biomolecular activities in living subjects. Conclusion: The uncaging of radical character of N-OH Pip in the presence of a magnetic field has been applied to develop activity-based contrast agents for diaCEST MRI. The ability of N-OH Pip to broadly suppress signals across a range of diaCEST classes may enable multiplexed molecular MRI of biomolecule interactions, signaling or metabolic pathways.

References: [1] Kolanowski JL, et al. Chem Soc Rev 2018, 47:195-208. [2] James ML, Gambhir SS. Physiol Rev 2012, 92:897-965. [3] Lux J, Sherry AD. Curr Opin Chem Biol 2018, 45:121-130. [4] Choi JS et al., Nat Materials 2017, 16:537-542. [5] Ratnakar JS, et al. JACS 2013, 135:14904-14907. [6] Shindo M et al. Yakugaku Zasshi 1971, 91:590-593; Davidson D et al. J Org Chem 1936, 1:305-314. [7] Paletta J et al. Org Lett 2012, 14:5322-5325.

Image/Figure:

https://s3.amazonaws.com/amz.xcdsystem.com/1E8A4501-BB41-A02A-1D3B9882B798BFAA_abstract_File10351/GA256_ImageFigure_0513125217.png

First Name: Adam

Last Name: Shuhendler

Email: Adam.Shuhendler@uottawa.ca

Organization: University of Ottawa

Country: Canada

ID: GA257
In-vivo MRI mapping of labile Zn2+ in the brain based on fast ion-chelate exchange dynamics

Nishanth D Tirukoti, Weizmann Institute of Science, deva-nishanth.tirukoti@weizmann.ac.il

---

Category: New Chemistry, Materials & Probes

Abstract Body : Introduction Large pools of labile Zn2+ can be found in specific tissues and mapping Zn2+ distribution is crucial to understand its cellular function and its role in disease development1-3. Here, we show the design of MRI-sensor for Zn2+ that possess reversible ion-binding properties with a rapid dissociation rate allowing the detection of a wide range of biologically relevant concentrations of the cation. By combining CEST and 19F-MRI, in an approach termed 19F-iCEST,4-7 the designed 19F-probe was found to be applicable for a wide range of biological-relevant Zn2+ concentrations and was used for in-vivo mapping of Zn2+ pools in the brain of live mice with high specificity. Method 19F-sensors NIS-1, NIS-2 were synthesized using reductive amination and NIS-3 by using the N-alkylation procedure. 19F-NMR and 19F-iCEST (B1 = 2.3 μT/2 s) experiments were performed on 9.4 T NMR at 37 oC and the obtained data were fitted using the Bloch-McConnell equations8-10 to quantify the the ion-chelate dissociation rate, kex (Fig. 1a). Phantom was prepared with 7 mM NIS-3 and 100 μM of cation's as noted in (Fig. 1b) and 19F-iCEST was performed on 9.4 T MRI with B1 = 2.3 μT/2 s. In-vivo 19F-iCEST was performed on 15.2 T scanner by continuous delivery of NIS-3 to the location of interest (hippocampal region CA3 or the thalamus (TH) via implanted cannula. 19F-CEST-RAREst sequence was used to acquire the in-vivo data with: TR/TE=3000/10.93 ms, RARE factor=16, FOV=22x22 mm2 (32x32 matrix). B1 = 2μT/1.5s was applied "on-resonance", Δω=+3.2 ppm (NIS-3:Zn2+ bound peak) or "off-resonance", Δω=-3.2 ppm and the obtained data were used to generate the Zn2+map, similar experiments were performed on Δω=18 ppm as another control (Fig, S1g). Results The fluorinated sensors NIS-1, NIS-2 and NIS-3 were synthesized, purified and characterized. Then, their Zn2+ binding properties, 19F-NMR characteristic, 19F-iCEST performance and binding conformation were studied (Fig. 1a, S1a). Although all examined chelates showed well-resolved downfield peak of NIS-bound Zn2+ in the 19F-NMR spectrum (Δω>3 ppm), NIS-3 showed the highest 19F-iCEST effect. This large iCEST effect is attributed to the fast exchange rate between Zn2+-bound and free NIS-3 (kex = 845 s-1) and thus allow the detection of very low concentrations of Zn2+ (500 nM, Fig. S1f) . It's specificity as compared to other cations was studied and clearly shows the ability to use NIS-3 to map Zn2+ with no background signal from other competitive cations (Fig. 1b, S1d-e). After validation that NIS-3 does not possess any toxicity effect on cells (Fig, S1b), in-vivo 19F-iCEST MRI experiments were performed to obtain Zn2+ map in the CA3 region of the hippocampus of live mice. To this end, NIS-3 was delivered to either the CA3 (Zn2+-rich ROI) or to the thalamus (TH, Zn2+-poor ROI) via cannula following by in-vivo 19F-iCEST experiments. Clearly, a significant (29±5%, N=7/group, ***p-value was observed only in Zn2+-rich ROI (CA3, Fig. 1c-d) and only when the saturation pulse was applied at (Δω=+3.2 ppm) showing the specificity of the designed approach to map labile Zn2+ in-vivo. Conclusion We showed here an approach for

in-vivo mapping of labile Zn2+ with the use of fluorinated-chelate (NIS-3) that reversibly binds the cation at very low affinity to obtain a relatively fast dissociation rate (kex = 845 s-1) of bound-Zn2+. These properties are not just ideal for the cation mapping but also maintain its basal levels in the tissue. This proposed 19F-iCEST chelate can and should be further applied to map labile Zn2+ in other tissues (Pancreas and prostate) and the iCEST principle outlined in this work should be further extended to rationalize the design of new 19F-iCEST probes to map other metal ions with biological importance.

References: 1. Lubag, A. J. M. et.al, Noninvasive MRI of β-cell function using a Zn(2+)-responsive contrast agent. Proceedings of the National Academy of Sciences of the United States of America 2011, 108 (45), 18400-18405. 2. Clavijo Jordan, M. V. et.al , Zinc-sensitive MRI contrast agent detects differential release of Zn(II) ions from the healthy vs. malignant mouse prostate. Proc Natl Acad Sci U S A 2016, 113 (37), E5464-71. 3. Martins, A. F. et.al, Imaging Insulin Secretion from Mouse Pancreas by MRI Is Improved by Use of a Zinc-Responsive MRI Sensor with Lower Affinity for Zn2+ Ions. Journal of the American Chemical Society 2018, 140 (50), 17456-17464. 4. Allouche-Arnon, H et.al, MRI-based Sensors for In Vivo Imaging of Metal Ions in Biology. Israel Journal of Chemistry 2017, 57 (9), 843-853. 5. Bar-Shir, A. et.al, Journal of the American Chemical Society 2013, 135 (33), 12164-12167. 6. Bar-Shir, A. et,al, Molecular Engineering of Nonmetallic Biosensors for CEST MRI. ACS Chemical Biology 2015, 10 (5), 1160-1170. 7. Yuan, Y. et,al, Development of Zinc-Specific iCEST MRI as an Imaging Biomarker for Prostate Cancer. Angewandte Chemie International Edition 2019, 58 (43), 15512-15517. 8. Zaiss, M. et.al, Exchange-dependent relaxation in the rotating frame for slow and intermediate exchange – modeling off-resonant spin-lock and chemical exchange saturation transfer. NMR in Biomedicine 2013, 26 (5), 507-518. 9. Zaiss, M. et.al, A combined analytical solution for chemical exchange saturation transfer and semi-solid magnetization transfer. NMR in Biomedicine 2015, 28 (2), 217-230. 10. Zaiss, M. et.al, QUESP and QUEST revisited – fast and accurate quantitative CEST experiments. Magnetic Resonance in Medicine 2018, 79 (3), 1708-1721.

Image/Figure:

https://s3.amazonaws.com/amz.xcdsystem.com/1E8A4501-BB41-A02A-1D3B9882B798BFAA_abstract_File10351/GA257_ImageFigure_0513125606.png

Image/Figure Caption: Figure 1: a) 19F-NMR and 19F-iCEST spectra of fluorinated chelates NIS-1,2,3 in presence of 30 μM Zn2+. b) (I) schematic representation of MRI phantom containing 7 tubes of NIS-3 and different metal ions ((#1) Ca2+, (#2) Cu2+, (#3) Mg2+, (#4) Na+, (#5) K+, (#6) no metal, (#7) Zn2+), (II) 1H MRI, (III) 19F-iCEST MRI at saturation pulse Δω=+3.2 ppm, (IV) 19F-iCEST MRI at saturation pulse Δω=-3.2 ppm, (V) 19F-iCEST contrast obtained by subtracting (III) form (IV), (VI) overlay of 19F-iCEST contrast on 1H MRI. c) From left to right: schematic illustration of the region to which NIS-3 was delivered (CA3 or TH), 1H MRI, 19F-iCEST MRI SΔω=+3.2 ppm, 19F-iCEST MRI SΔω=-3.2 ppm, 19F-iCEST contrast (Zn2+ map) obtained from subtraction of 19F-iCEST MRI SΔω=+3.2 ppm from 19F-iCEST MRI SΔω=+3.2 ppm. d) Averaged 19F-iCEST contrast obtained from CA3 (N=7) and TH (N=7). Error bars denotes SEM, ***p-value < 0 .001, unpaired Student's t-Test.

Full Name of Abstract's 1st Author : Deva Nishanth Tirukoti

First Name: Nishanth D

Last Name: Tirukoti

Email: deva-nishanth.tirukoti@weizmann.ac.il

Organization: Weizmann Institute of Science

Country: Israel

ID: GA258
Economical enclosure for PET/CT study of mice under BSL2 or greater conditions

Jai Woong Seo, Stanford University, jaiwseo@stanford.edu

Category: Instrumentation

Abstract Body : Preclinical small animal imaging involving agents rated biosafety level-2 (BSL-2) or greater is important for studying infectious diseases and particularly timely due to the SARS-CoV-2 global pandemic. We are investigating the pharmacokinetics of SARS-CoV-2 and subsequent gene transduction in an hACE2 mouse model1. This project requires imaging of mice after administration of spike protein-coated pseudotyped lentivirus in a preclinical PET/CT scanner. Several BSL-3 compliant imaging chambers are commercially available; however, these enclosure systems are expensive, developed for the specific PET/CT scanner, and can accommodate at most two mice simultaneously. Here, we constructed developed a generalizable enclosure system adaptable to many preclinical PET/CT, PET and CT systems for in vivo multi-animal imaging of biohazardous agents. Materials and system assembly. Materials were primarily purchased from McMASTER-CARR and include polycarbonate cylinder (4" OD, 8585K55, Figure 1A), clear polycarbonate disks (8508K78), snap-in pipe and tubing grommets (63595K54), barrel-style DC connector receptacles (8320N128) and push-in plugs (8320N111), plastic barbed tube fittings (5463K709), plastic barbed tubing fittings for thru-wall finishing (5463K81), Wye connectors (2974K391), tubing, plastic quick-turn tube coupling sockets (51525K212) and plugs (51525K122). The enclosure system was designed to easily snap a polycarbonate disk (Figure 1B) to the clear polycarbonate cylinder (Figure 1A) and connected to a HEPA filter. For the clear polycarbonate cylinder, one side of an impact-resistant polycarbonate clear cylinder was closed with a polycarbonate disc. For the snap-in disk part (Figure 1B), a second clear polycarbonate disk was glued to the snap-in pipe and tubing grommet, and airtight fittings with airflow channels. DC connectors (Figure 1C) were inserted in the middle of the polycarbonate disk to connect to heating strip plugs on the 3D-printed four-mice imaging bed (Sofie Biosciences). Wires and tubings were connected and sealed (Figure 1D). The total cost for one enclosure system was approximately $300. Demonstration of enclosure system for PET/CT imaging with BSL2 procedures. All experiments were performed under protocols approved by the Administrative Panel on Biosafety (APB) and Administrative Panel on Laboratory Animal Care (APLAC) at Stanford University. All work was conducted under a biosafety cabinet except when in transit to and imaging on the PET/CT scanner. Four hACE2-expressing mice were transferred from their cage to an induction chamber. Anesthesia, vacuum exhaust and heating lines were connected between the four-mice bed and the polycarbonate disk. The anesthesia gas entry line and outlet of the vacuum line were fitted with HEPA filters. Mice were anesthetized with 1.5% isoflurane in oxygen and placed on the bed, and the bed was slid into the polycarbonate cylinder. The polycarbonate disk was snapped into the polycarbonate cylinder to seal the system. The surface of the enclosure system was sanitized with 70% ethanol gauze or spray prior to transfer out of the biosafety cabinet and onto the PET/CT scanner sled (Figure 1D). The unit with mice remained on the PET/CT for 90 min at

room temperature and then returned to the biosafety cabinet to return mice to their cages. Mice respiration and temperatures were monitored visually and using a thermal gun, respectively. Results and conclusion. All hACE2 mice remained stable throughout the handling and 90min scanner procedures. Respiration was within normal ranges while under anesthesia within the enclosure system and their body temperatures remained stable. The sealed enclosure and HEPA filtration system ensured no potential release of infectious particles. The enclosure system was economical compared to the commercially available units and could be easily adapted to most PET/CT systems.

References: 1. McCray, P. B. et al. Lethal Infection of K18-hACE2 Mice Infected with Severe Acute Respiratory Syndrome Coronavirus. J. Virol. 81, 813–821 (2007).

Image/Figure:

https://s3.amazonaws.com/amz.xcdsystem.com/1E8A4501-BB41-A02A-1D3B9882B798BFAA_abstract_File10351/GA258_ImageFigure_0513125902.png

Image/Figure Caption: Figure 1. A. Polycarbonate cylinder unit. B. Polycarbonate disk with two gas passages and electrical unit for thermal beds. C. Polycarbonate disk snaped into the polycarbonate cylinder. D. Enclosure system on PET/CT scanner, inserted 3D printed stackable mice bad.

First Name: Jai Woong

Last Name: Seo

Email: jaiwseo@stanford.edu

Organization: Stanford University

Country: United States

ID: GA259
Novel NIR Fluorescent ChoKα inhibitor for intraoperative tumor imaging in a veterinary clinical trial

Sofya Osharovich, University of Pennsylvania, sofyaosharo@gmail.com

---

Category: Oncology

Abstract Body : Choline Kinase α (ChoKα) is an enzyme overexpressed in 60% of human lung tumors. It is associated with an aggressive phenotype, high histological tumor grade, and poor clinical outcome1-3. ChoKα catalyzes the phosphorylation of choline to generate phosphocholine, a precursor of the cell membrane phospholipid, phosphatidylcholine (PtdCho)4. A novel near-infrared (NIR) fluorescent ChoKα inhibitor, JAS239, has been developed in our lab (excitation: 745 nm, emission: 775 nm)5. JAS239 binds to the active site of ChoKα, competitively inhibiting phosphocholine production, and thus can be used as a targeted NIR imaging agent for tumor resection guidance in ChoKα-overexpressing tumors. Previously, we have utilized JAS239 to image ChoKα-overexpressing breast5,6and lung tumor xeno- and allografts in mice, as well as lung metastases. Here, we translate JAS239 into the veterinary clinic for intraoperative and back-bench imaging in client-owned dogs with spontaneous lung adenocarcinomas. An initial toxicology study was performed using five experimental dogs that received a single dose of JAS239 at five times the imaging dose of 1 mg/kg (5 mg/kg total). The dogs were observed for overt signs of toxicity, including lethargy, vomiting, and anorexia. Blood was collected at baseline, 0, 6, 12, 24, 48 hours, and 5 days post injection for pharmacokinetics, complete blood count-brief (CBC-brief) and blood chemistry. The dogs were adopted out at the end of the study. To date, three canine patients with operable lung adenocarcinomas have been recruited into an owner informed consent clinical trial. Patients received either 0.5 or 1 mg/kg JAS239 24 hours prior to intraoperative imaging. The VisionSense Imaging System was used to image the lung tumors in situand ex vivo. After tumor resection, all sides of the tumor were imaged, sections of tumor and normal tissue were excised for back table imaging, and the fluorescent borders were marked with sutures for pathology. Cut pieces of the tumors were imaged on the LI-COR Pearl and the IVIS Lumina and submitted to the School of Veterinary Medicine Comparative Pathology Core (CPC) for H&E and ChoKαimmunohistochemistry (IHC) (results pending). The experimental dogs showed no overt signs of toxicity and CBC-brief and blood chemistry results were within normal limits. Pharmacokinetics showed rapid probe elimination from the serum, with 80% eliminated by 6 hours, further indicating low toxicity. Intraoperative tumor imaging showed clear margin delineation with higher fluorescence in the tumor than in the normal lung. Initial pathology results found no malignancies at the fluorescent border indicating clear margins. The purpose of these preliminary clinical cases is to establish the optimal dosing and timing for imaging JAS239 fluorescence in canine lung tumors. The clinical trial will recruit up to 30 patient with the goal of determining the efficacy of JAS239 for detecting ChoKα levels in tumor margins, identifying residual tumor lesions, lymph node involvement, and detection of micrometastases from primary lung or other cancers. The ultimate goal of this study is the translation of ChoKα sensors for fluorescence guidance during human lung tumor resections.

References: 1. Cuadrado, A., et. al. “Phosphorylcholine: a novel second messenger essential for mitogenic activity of growth factors.” Oncogene 8.11 (1993): 2959-2968. PMID: 8414498. 2. Molina, A., et. al. "Expression of Choline Kinase Alpha to Predict Outcome in Patients with Early-stage Non-small-cell Lung Cancer: A Retrospective Study." The Lancet Oncology 8.10 (2007): 889-97. PMID: 17851129. 3. Molina, A., et. al. "Overexpression of Choline Kinase Is a Frequent Feature in Human Tumor-derived Cell Lines and in Lung, Prostate, and Colorectal Human Cancers." Biochemical and Biophysical Research Communications 296.3 (2002): 580-83. PMID: 12176020. 4. Arlauckas, S., et al. “Choline Kinase Alpha—Putting the ChoK-Hold on Tumor Metabolism.” Progress in Lipid Research, vol. 63, 2016, pp. 28–40. PMID: 27073147. 5. Arlauckas, S., et al. “Direct Inhibition of Choline Kinase by a Near-Infrared Fluorescent Carbocyanine.” Molecular Cancer Therapeutics, vol. 13, no. 9, 2014, pp. 2149–2158. PMID: 25028471. 6. Arlauckas, Sean P., et al. “Near Infrared Fluorescent Imaging of Choline Kinase Alpha Expression and Inhibition in Breast Tumors.” Oncotarget, vol. 8, no. 10, 2017, pp. 16518–16530. PMID: 28157707

Full Name of Abstract's 1st Author : Sofya Osharovich

First Name: Sofya

Last Name: Osharovich

Email: sofyaosharo@gmail.com

Organization: University of Pennsylvania

Country: United States

ID: GA260
Photodynamic Therapy of Prostate Cancer: Active Targeted Nanoparticles versus Small Molecules

Dong Luo, Case Western Reserve University, dxl576@case.edu

Category: New Chemistry, Materials & Probes

Abstract Body : Prostate cancer is the third most common non-skin cancer in the United States[1]. Men diagnosed with the disease typically undergo radical prostatectomy. Recurrence of the disease often occurs in patients when tumor tissue remains after surgery[2]. Currently, identification of incomplete surgery can only be identified post-operatively by pathological assessment of excised prostate gland margins. Photodynamic therapy (PDT) agents are used as a minimally invasive therapy clinically but are not selectively taken up by tumors[3]. A major concern with PDT is off-target tissue accumulation and activation of photosensitizer leading to cell death in normal tissue. Nanoparticles offer great opportunities for precision medicine. Prostate-specific membrane antigen (PSMA) is a unique membrane-bound biomarker which is overexpressed in prostate cancer and neovasculature of many solid tumors[4]. The objective of the study is to develop a nanoparticle agent that could target prostate cancer, provide sustained photodynamic therapy (PDT) agent release based on cathepsin activity, enable fluorescence imaging and multiple PDT irradiation to achieve the best therapeutic outcomes. PSMA-targeted gold nanoparticles (AuNPs) were synthesized and loaded with photosensitizer, Pc158, via a cathepsin-cleavable linker (GFLGC) (Fig. 1a). PSMA-targeted small molecular PDT agent, PSMA-Pc413 was synthesized as a control. In vitro binding affinity, cell targeting, programmed intracellular release, and phototoxicity were tested using PC3pip cells (PSMA+) and PC3flu cells (PSMA-). In vivo tumor targeting, local Pc158 release and multiple PDT irradiation were monitored by a Maestro Imaging System. Tumor damage was confirmed by H&E and immunochemistry staining and PDT therapy was evaluated by monitoring tumor growth over 24 days. In vitro cellular uptake demonstrated significantly higher AuNPs uptake in PC3pip cells than in PC3flu cells. AuNPs-Pc158 was cleaved by cathepsin in lysosomes and Pc158 was released to mitochondria over 24 h, but could be accelerated by light irradiation. The un-cleaved Pc158 was inactivate and showed no phototoxicity until complete release from AuNPs and migration to the mitochondria. In vivo fluorescence results demonstrated higher AuNPs accumulation and local Pc158 release in PC3pip tumors than in PC3flu tumors. Sustained Pc158 release from AuNPs also enabled sequential PDT, which greatly enhanced AuNPs uptake and therapeutic efficacy, whereas the PSMA-Pc413 was photo-bleached at the first irradiation (Fig. 1b-d). Tumor tissue damages were confirmed by H&E and immunochemistry staining. The nanoparticle system provided high selectivity with sustained targeted sensitizer accumulation and a strongly improved PDT efficacy, which was superior over the small molecular counterpart for PDT of prostate cancer.

References: [1] Siegel, R. L.; Miller, K. D.; Fuchs, H. E.; Jemal, A. Cancer Statistics, 2021. , Ca-Cancer J. Clin. 2021, 71, 7-33. [2] Wang, X.; Huang, S. S.; Heston, W. D.; Guo, H.; Wang, B. C.; Basilion, J. P. Development of Targeted Near-Infrared Imaging Agents for Prostate

Cancer. Mol. Cancer Ther. 2014, 13, 2595-2606. [3] Van Straten, D.; Mashayekhi, V.; de Bruijn, H. S.; Oliveira, S.; Robinson, D. J. Oncologic Photodynamic Therapy: Basic Principles, Current Clinical Status and Future Directions. Cancers 2017, 9, 19. [4] Wang, X.; Ramamurthy, G.; Shirke, A. A.; Walker, E.; Mangadlao, J.; Wang, Z.; Wang, Y.; Shan, L.; Schluchter, M. D.; Dong, Z.; Brady-Kalnay, S. M.; Walker, N. K.; Gargesha, M.; MacLennan, G.; Luo, D.; Sun, R.; Scott, B.; Roy, D.; Li, J.; Basilion, J. P. Photodynamic Therapy Is an Effective Adjuvant Therapy for Image-Guided Surgery in Prostate Cancer. Cancer Res. 2020, 80, 156-162.

Image/Figure:

https://s3.amazonaws.com/amz.xcdsystem.com/1E8A4501-BB41-A02A-1D3B9882B798BFAA_abstract_File10351/GA260_ImageFigure_0513010009.png

Image/Figure Caption: Figure 1. a) Schematic illustration of PSMA-targeted AuNPs and small molecular PSMA-Pc413 for photodynamic therapy of prostate cancer. Photosensitizer, Pc 158 was conjugated to AuNPs via a bio-cleavable linker, GFLGC, to control its release in vitro and in vivo. Pc413, an analogue of Pc158, was conjugated directly to targeting ligands, PSMA-1. b) Scheme shows the timeline of the repeated PDT treatments in mice with 500 mm3 tumors. c) Maestro fluorescence images of mice injected with AuNP-Pc158 and PSMA-Pc413 conjugates before and after each PDT treatment (150 J/cm2) with a single injection of PDT agents. d) AuNPs enhances the multiple photodynamic therapy outcome for the eradication of large tumors (around 500 mm3) compared to the small molecular PSMA-Pc413.

First Name: Dong

Last Name: Luo

Email: dxl576@case.edu

Organization: Case Western Reserve University

Country: United States

ID: GA261
"Ferronostics": Applying a first in class radiotracer to identify diseases susceptible to therapies targeting the labile iron pool

Michael Evans, UCSF, michael.evans@ucsf.edu

Category: New Chemistry, Materials & Probes

Abstract Body : Background: Although cancer has been known for decades to harbor an insatiable appetite for iron, only recently has the chemistry emerged to exploit this altered state therapeutically, by targeting the expanded cytosolic 'labile' iron pool (LIP), of the cancer cell. The state of the art includes therapies that react with the LIP to produce cytotoxic radical species (in some cases also releasing drug payloads), and molecules that exacerbate LIP-induced oxidative stress to trigger "ferroptosis". Effectively implementing LIP targeted therapies in patients will require biomarkers to identify those tumors with the most elevated LIP, and thus most likely to succumb to LIP targeted interventions. Toward this goal, we tested herein whether tumor uptake of the novel LIP sensing radiotracer 18F-TRX aligns with tumor sensitivity to LIP targeted therapies. Methods: 18F-TRX uptake was assessed in vivo among ten subcutaneous and orthotopic human xenograft models. Glioma and renal cell carcinoma were prioritized as these tumors have the highest relative expression levels of STEAP3, the oxidoreductase that reduces ferric iron to the ferrous oxidation state, in the Cancer Cell Line Encyclopedia. The antitumor effects of the LIP activated prodrug TRX-CBI, which releases the DNA alkylator cyclopropylbenzindoline (CBI), were compared in mice bearing U251 or PC3 xenografts, tumors with high and intermediate levels of 18F-TRX uptake, respectively. Results: 18F-TRX showed a wide range of tumor accumulation. An antitumor assessment study showed that the growth of U251 xenografts, the model with the highest 18F-TRX uptake, was potently inhibited by TRX-CBI. Moreover, the antitumor effects against U251 were significantly greater than those observed for PC3 tumors, consistent with the relative 18F-TRX determined LIP levels in tumors prior to therapy. Lastly, a dosimetry study showed that the estimated effective human doses for adult males and females were comparable to those of other 18F-based imaging probes. Conclusions: We report the first evidence that tumor sensitivity to a LIP targeted therapy can be predicted with a molecular imaging tool. More generally, these data bring a new dimension to the nuclear theranostic model by showing a requirement for imaging to quantify in situ the concentration of a metastable bioanalyte toward predicting tumor drug sensitivity.

First Name: Michael

Last Name: Evans

Email: michael.evans@ucsf.edu

Organization: UCSF

Country: United States

ID: GA262
Evaluation of new allysine-targeting 68Ga-PIF7 probe in preclinical model of pulmonary fibrosis

Sergey Shuvaev, Martinos Center for Biomedical Imaging/Harvard Medical School, sshuvaev@mgh.harvard.edu

---

Category: New Chemistry, Materials & Probes

Abstract Body : Introduction Idiopathic pulmonary fibrosis (IPF) is a chronic and progressive lung disease resulting in scarring that impedes oxygen transport, and is ultimately fatal. Measuring disease activity in IPF would improve prognostication and assess whether drug treatment is effective. Allysine, an amino acid residue formed on extracellular proteins during active fibrosis, has been proposed as a disease activity marker.[1] The goal of this work was to develop an allysine-targeted PET probe with high specific uptake in fibrotic lungs and low background signal in adjacent tissues of heart, liver, muscle, and blood. Materials and Methods Probe 68Ga-PIF7 (Fig 1a) was synthesized in 5 steps. Male C57BL/6 mice were intratracheally instilled with bleomycin (1.2 U/kg) and imaged after 14 days when allysine levels peak in the lung.[2] Bleomycin injured mice or age-matched controls were placed in a micro-PET/MRI scanner and administered 68Ga-PIF7 as a bolus via the lateral tail vein and dynamically imaged for 60 min. At 90 min p.i. animals were euthanized, and their organs were harvested for gamma counting. After gamma counting, lungs were flash-frozen and later analyzed for hydroxyproline (total collagen, fibrosis measure) and allysine content. Results 68Ga-PIF7 (Fig 1a) was selected from a library of PET tracers screened to select for high specificity towards aldehydes, rapid renal clearance and low non-specific uptake. 68Ga-PIF7 showed rapid blood clearance (Fig 1b) with elimination exclusively through the kidneys (Fig 1d). Very low signal is observed in the liver, heart, muscle, bone, or healthy lungs (Fig 1c, 1d). Significantly higher probe uptake was observed in the lungs of bleomycin-injured animals than in naïve controls, and lung to background (e.g. heart) ratios were also significantly higher in bleomycin injured mice (Fig 1d, 1e, 1f). Conclusion 68Ga-PIF7 is a hydrophilic, aldehyde-reactive PET probe with extracellular distribution and rapid renal clearance. Compared to the previously reported 68Ga-NODAGA-indole which employed an indole oxyamine moiety for Pictet-Spengler ligation to aldehydes,[1] 68Ga-PIF7 showed twice the uptake in bleomycin injured lung and no hepatobiliary clearance resulting in greater lung-to-background contrast, important for delineating disease activity in the lower lung where injury is more prevalent in IPF.

References: [1] J. Wahsner, P. Desogere, E. Abston, K. A. Graham-O'Regan, J. Wang, N. J. Rotile, M. D. Schirmer, D. D. Santos Ferreira, J. Sui, B. C. Fuchs, M. Lanuti and P. Caravan, J Am Chem Soc 2019, 141, 5593-5596. [2] H. H. Chen, P. A. Waghorn, L. Wei, L. F. Tapias, D. T. Schuhle, N. J. Rotile, C. M. Jones, R. J. Looby, G. Zhao, J. M. Elliott, C. K. Probst, M. Mino-Kenudson, G. Y. Lauwers, A. M. Tager, K. K. Tanabe, M. Lanuti, B. C. Fuchs and P. Caravan, JCI Insight 2017, 2, e91506.

Image/Figure:

https://s3.amazonaws.com/amz.xcdsystem.com/1E8A4501-BB41-A02A-1D3B9882B798BFAA_abstract_File10351/GA262_ImageFigure_0513011159.png

Image/Figure Caption: Fig.1 Molecular structure of 68Ga-PIF7 (a). Blood clearance of 68Ga-PIF7 in a naïve animal with distribution and elimination half-lives (b). Biodistribution of 68Ga-PIF7 in lung, heart, liver and kidney 90 min p.i. (c). PET maximum intensity projection images of bleomycin-injured and naïve mice 55 min p.i. (d). Axial (top) and sagittal (bottom) PET/MR images showing much higher lung signal in bleomycin-treated mice at 55 min p.i. (e) PET lung signal (55 min p.i.) and lung-to-heart ratio (90 min p.i.) showing significant differences between bleomycin-treated and naïve animals (f).

Full Name of Abstract's 1st Author : Sergey Shuvaev

First Name: Sergey

Last Name: Shuvaev

Email: sshuvaev@mgh.harvard.edu

Organization: Martinos Center for Biomedical Imaging/Harvard Medical School

Country: United States

ID: GA263

Assessment of [64Cu]Cu-labeled adeno-associated virus9 (AAV9) on AAVR mice models

Jai Woong Seo, Stanford University, jaiwseo@stanford.edu

Category: New Chemistry, Materials & Probes

Abstract Body : Adeno-associated virus (AAVs) encapsulates single-stranded deoxyribonucleic acid (ssDNA) within a 25-nm capsid. Currently, thirteen naturally occurring AAV serotypes have been identified. The cellular binding and entry of most serotype AAVs are associated with the AAV receptor (AAVR) as the critical host factor1,2. Previously, we reported a [64Cu]Cu-AAV labeling method using inverse electron demand Diels-Alder reaction (IEDDA) and assessed the pharmacokinetics of AAVs in mice3. Here, we labeled a few lysines on the surface of AAV9 with copper-64 and evaluated the pharmacokinetics and biodistribution of AAV9 in AAVR overexpressing (OE), knock-out (KO), and wild-type (WT) mice. AAV9 labeling of [64Cu]Cu via IEDDA reaction. Surface lysines on AAV9:CMV-eGFP reacted with tetrazine-NHS ester (Tz-NHS) for 30 min at room temperature. After overnight dialysis of the mixture, Tz-AAVs were reacted with [64Cu]Cu pre-labeled multichelators ((NOTA)8-TCO) for 30 minutes. The mixture was diluted to 15 mL PBS (0.01% Pluronic F-68), concentrated with an Amicon spin filter (MWCO, 100 kDa,) and repeated twice. IEDDA reaction afforded [64Cu]Cu-AAV9 (0.74-1.1 MBq) with radiochemical purity of >98% on instant thin-layer chromatography (ITLC). The purity of AAV9, Tz-AAV9, and [64Cu]Cu-AAV9 capsids on SDS-PAGE displayed three intact viral protein bands without extraneous additional bands. The recovery yield of [64Cu]Cu-AAV9 calculated by qPCR was 63±22% (n=4) PET/CT imaging analysis and biodistribution of [64Cu]Cu-AAV9 in AAVR OE, KO, and WT mice. For PK and biodistribution of AAV9, [64Cu]Cu-AAV9 (118±14 KBq) was systemically administered to AAVR OE (n=4), KO (n=4), and WT mice (n=3). PET/CT images (Figure 1A) were acquired at 0, 4, and 21 hours, and biodistribution was performed at 22 hours. Time activity curves (TACs) demonstrated that the circulation time and liver uptake of [64Cu]Cu-AAV9 were closely related to the AAVR expression in the corresponding mouse model (Figure 1B, C). Circulating radioactivity at 22 h (Figure 1D) was greater for the KO mice (14±3.1 %ID/g) as compared to the OE mice (1.6±0.3 %ID/g. p=0.0096) and WT mice (6.7±1.3 %ID/g, p=0.0375). The liver uptake of AAV9 in OE (34.5±2.3 %ID/g) mice at 22 hours was significantly greater than those in WT (20.0±1.4 %ID/g, p=0.004) and KO (12.5±4.0 %ID/g, p=0.005) mice (Figure 1E). Transduction of the eGFP gene in the liver at 3 weeks was correlated with [64Cu]Cu-AAV9 uptake. In conclusion. [64Cu]Cu-AAV9 PET imaging displayed specific binding in AAVR OE, KO, and WT mice. Organ-specific AAVR expression in the liver and brain were differentiated amongst those cohorts. PET imaging of AAV9 mapped early AAVR-mediated binding and longitudinal accumulation over 21 hours.

References: 1. Pillay, S. et al. An essential receptor for adeno-associated virus infection. Nature 530, 108–112 (2016). 2. Pillay, S. & Carette, J. E. Host determinants of adeno-associated viral vector entry. Curr. Opin. Virol. 24, 124–131 (2017). 3. Seo, J. W. et al. Positron emission

tomography imaging of novel AAV capsids maps rapid brain accumulation. Nat. Commun. 11, 2102 (2020).

Image/Figure:

https://s3.amazonaws.com/amz.xcdsystem.com/1E8A4501-BB41-A02A-1D3B9882B798BFAA_abstract_File10351/GA263_ImageFigure_0513011303.png

Image/Figure Caption: Figure 1. A. PET/CT images of AAVR OE, KO, and WT mice acquired at 0, 4, and 21 hours after intravenous administration of [64Cu]Cu-AAV9. B. Blood and C. liver time activity curve generated from the ROI analysis in AAVR OE, KO, and WT mice. D. Circulating blood activity and E. the liver uptake of [64Cu]Cu-AAV9 from biodistribution study at 22 hours after the tail vein injection

First Name: Jai Woong

Last Name: Seo

Email: jaiwseo@stanford.edu

Organization: Stanford University

Country: United States

ID: GA264
Transcompartmental In Vivo Sodium Magnetic Resonance Spectroscopic Imaging in Brain Cancer

Muhammad Khan, Yale University, muhammad.khan@yale.edu

Category: Oncology

Abstract Body : Cancer is the second-leading cause of death in the United States, next to cardiovascular disease. Glioblastoma multiforme (GBM) is the most common and lethal primary central nervous system (CNS) tumor. Despite increased attention, GBM treatment regimens prolong median survival rate by only several months, and long-term patient prognosis remains poor. While the majority of research has gravitated toward profiling/targeting tumor-specific molecules, altered metabolism in tumors is implicated heavily in oncologic survival and progression. Healthy maintain strong ion gradients across the cell membrane. Sodium (Na+) and chloride (Cl-) are high (~150 mM) in blood and extracellular spaces, and low (~15 mM) in intracellular milieu; potassium (K+) concentrations are reversed. These balances are responsible for critical functions like nerve signaling and osmoregulation. Na+ levels in blood (Na+b), extracellular (Na+e), and intracellular (Na+i) spaces specifically engender weak transendothelial (ΔNa+end = Na+b – Na+e) and strong transmembrane (ΔNa+mem = Na+e – Na+i) gradients. These are involved, respectively, in the integrity of the blood-brain barrier (BBB) and maintenance of the cell membrane potential (Vm). Cancer cells, however, exhibit altered metabolism resulting in inefficient energetics and disturbed gradients, particularly ΔNa+end and ΔNa+mem. Current methods to determine specific compartmental Na+ concentrations are undesirable, requiring biopsies, insertion of voltammetric microelectrodes, and other invasive techniques which preclude human translation. Nuclear magnetic resonance (NMR) has been shown to non-invasively detect the 100%-abundant isotope sodium-23 (23Na), but cannot resolve the degenerate signals from different physiological compartments. Traditional 23Na magnetic resonance imaging (MRI) attempted to isolate specific Na+compartments by exploiting relaxation differences, but these methods lacked complete compartmental specificity. 23Na magnetic resonance spectroscopic imaging (MRSI), following administration of a paramagnetic lanthanide-based contrast agent consisting of a lanthanide(III) ion (Ln3+) complexed with a macrocyclic chelate, was shown to induce compartmental chemical shift differences and resolve the 23Na-NMR signal into separate peaks which could be quantified individually with greater specificity. This 23Na-MRSI technique was applied in vivo in several rat GBM models (RG2, U87, and U251) using the thulium(III) (Tm3+) salt of the chelate 1,4,7,10-tetraazacyclododecane-1,4,7,10-tetrakis(methylenephosphonate) (DOTP8-), or TmDOTP5-. The sensitivity of 23Na chemical shift to TmDOTP5-concentration was found to be ~2.1 ppm/mM in vitro, which manifested in three separated peaks in vivo upon intravenous infusion. The shifting was more pronounced in tumor tissue, where a compromised BBB permitted greater TmDOTP5- extravasation, compared to healthy tissue, but was evident throughout the whole brain at various depths. Integration of the separated peaks permitted non-invasive quantification of spatial heterogeneity in compartmental Na+ levels. Na+b concentrations were found to be elevated within all three tumors relative to healthy tissue, and significantly so (p This 3D 23Na-

MRSI method is the first to compartmentalize Na+ levels within the tumor microenvironment with minimal invasiveness, and explore spatial heterogeneity in ΔNa+end and ΔNa+mem. It has potential to be used to monitor chemotherapeutic and anti-angiogenic drugs, and also to be used with other agents based on gadolinium (Gd3+) which are already approved for clinical use in GBM patients.

References: Khan, M.H., Walsh, J.J., Mihailović, J.M. et al. Imaging the transmembrane and transendothelial sodium gradients in gliomas. Sci Rep 11, 6710 (2021).

Image/Figure: https://s3.amazonaws.com/amz.xcdsystem.com/1E8A4501-BB41-A02A-1D3B9882B798BFAA_abstract_File10351/GA264_ImageFigure_0513011557.pdf

Image/Figure Caption: (a) Demonstration of 23Na peak separation in vivo following TmDOTP5− administration into a rat brain bearing a U251 tumor. 1H-MRI of an axial slice displaying the anatomical tumor boundary (white outline). The 23Na-MRSI is overlaid on top of the 1H-MRI. Candidate voxels (b) inside and (c) outside the tumor are indicated (yellow boxes). Before TmDOTP5− delivery, a single 23Na peak was observed at 0 ppm, both inside and outside the tumor (black spectra). Following TmDOTP5−delivery, compartmental peak separation was achieved to varying extents throughout the brain (blue spectra). (b) Within the tumor, this separation was most pronounced due to a compromised blood-brain barrier (BBB), which permits substantial accumulation of TmDOTP5− in the extracellular space. (c) Outside of the tumor (bottom spectra), such a high degree of extravasation would not be possible, but some shifting is still observed. The TmDOTP5− distribution in the brain warrants labeling the most shifted peak as blood sodium (Na+b), which occurred consistently around 2 ppm. The unshifted peak, which has no access to TmDOTP5−, is intracellular sodium (Na+i). The intermediate peak, therefore, is extracellular sodium (Na+e), which is shifted more inside the tumor than outside in healthy tissue. (d) Spatial distributions of compartmentalized 23Na signals (Na+b, Na+e, Na+i) as well as transendothelial (ΔNa+end) and transmembrane (ΔNa+mem) gradients in an RG2 tumor. The high-resolution 1H-MRI data are shown in the left four columns, whereas the lower resolution 23Na-MRSI data are shown in the next five columns on the right. The left column shows the tumor location (white outline) on the anatomical 1H-MRI (left), whereas the next two columns show the T2 maps (range shown: 0-100 ms) before and after TmDOTP5− injection, and the subsequent column depicts the ΔR2 map (i.e., difference between 1/T2 maps before and after, range shown: 0 – 30 s-1), which is proportional to [TmDOTP5-] in healthy and tumor tissues. Since the integral of each 23Na peak represents the [Na+], the respective three columns show the integral maps of Na+b, Na+e, and Na+i from left to right (i.e., ∫Na+b, ∫Na+e, ∫Na+i). The last two columns on the right show ΔNa+end = ∫Na+b-∫Na+e and ΔNa+mem = ∫Na+e-∫Na+i. The ∫Na+b map reveals low values in healthy tissue compared to tumor tissue, and within the tumor boundary a high degree of heterogeneity. The ∫Na+e map reveals low values in tumor and normal tissues, but within the tumor boundary a small degree of heterogeneity is visible while ventricular voxels show very high values. The ∫Na+i map reveals low values ubiquitously except some ventricular voxels. The ΔNa+end map reveals dramatically high values within the tumor only. The ΔNa+end was driven primarily by an increase of ∫Na+b inside the tumor and which was more pronounced in superficial regions of the brain compared to deeper slices. The ΔNa+mem map shows low values in tumor tissue compared to normal tissue, although ventricular voxels show very high values.

The ΔNa+mem is driven primarily by decreased ∫Na+e and thus shows similar level of heterogeneity as the ∫Na+e map. All maps use the same color scale and are relative.

First Name: Muhammad

Last Name: Khan

Email: muhammad.khan@yale.edu

Organization: Yale University

ID: GA265
PET-MRI for Spatio-Temporal Tracking of the Myocardial Growth Hormone Secretagogue Receptor After Myocardial Infarct with a Novel 18F-Labelled Ligand

Savita Dhanvantari, Lawson Health Research Institute, sdhanvan@lawsonimaging.ca

---

Category: Cardiovascular & Pulmonary

Abstract Body : Introduction: Early detection of heart disease is critical in its prognosis, treatment and management. The current paradigm of anatomic imaging and measurement of circulating biomarkers detect heart disease after significant structural and functional changes have occurred. Therefore, there is a need for the use of in vivo molecular imaging techniques that can target a biomarker localized to cardiac tissue that is altered before functional derangements are evident. The hormone ghrelin and its receptor, the growth hormone secretagogue receptor (GHSR) are expressed in the myocardium, and are associated with cardioprotection through promotion of contractility and growth, and inhibition of inflammation and apoptosis. We have previously shown that the dynamics of ghrelin and GHSR are abnormally up-regulated in human heart failure and heart disease, thereby indicating that GHSR is a clinically relevant target for molecular imaging of heart disease. We therefore used a quantitative PET-MRI approach in a preclinical canine model of myocardial infarction to determine the in vivo specificity and sensitivity of a radiolabelled GHSR ligand, [18F]LCE470. Methods: Myocardial infarction (MI) was surgically induced in 11 month-old female hounds (n=4) by 2h ligation of the left anterior descending coronary artery. PET-MR imaging was conducted 3 days prior to surgery, and at multiple time points over a period of 1.5 years. All hounds were first administered 7 MBq/kg body weight of 13N-NH3 i.v. for measurement of cardiac perfusion, with a dynamic list-mode PET acquisition and simultaneous MR cine for heart function, and T1 and 3D T1w for anatomical images. 50 min later, 7 MBq/kg [18F]LCE470 was injected for determination of GHSR using the same PET-MR acquisition parameters. Compartmental modelling of both tracers was done through Carimas (turkupetcentre.fi/carimas/) on segmented polar maps delineating 3 regions of interest: infarct, left circumflex (LCX) and remote myocardium. Net uptake rate (Ki) for 13N-NH3 uptake and distribution volumes (VD) for [18F]LCE470 were calculated for each of these 3 regions for all time points. At the end of the study, animals were euthanized and endomyocardial tissue samples from each region were obtained for analysis of GHSR by confocal microscopy using a fluorescent GHSR ligand, Cy5-cyclo-ghrelin(1-20). Fluorescence intensities were determined using the Percentile algorithm in Image J FIJI. Results: The VD for [18F]LCE470 decreased significantly (p Conclusion and Significance: We have characterized the specificity and sensitivity of [18F]LCE470 in detecting myocardial GHSR in a preclinical large animal model. Using this unique PET tracer, we show that regional GHSR distribution is altered after MI independently of changes in perfusion. Therefore, molecular PET imaging of myocardial GHSR may indicate subclinical changes that precede some functional changes associated with heart disease.

First Name: Savita

Last Name: Dhanvantari

Email: sdhanvan@lawsonimaging.ca

Organization: Lawson Health Research Institute

Country: Canada

ID: GA266
Tumor vasculature on-a-chip for studying Prostate-Specific Membrane Antigen biology

Magdalena Skubal, Memorial Sloan Kettering Cancer Center, skubalm@mskcc.org

---

Category: Instrumentation

Abstract Body : Prostate-Specific Membrane Antigen (PSMA) overexpression is a characteristic of prostate cancer and is associated with cancer progression, metastasis, and poor prognosis in patients. Interestingly, increased expression levels of PSMA are also found on the vasculature of a variety solid tumors. Using cutting-edge microfluidic organ on a chip technology and patient derived cell line, we have established an innovative approach to investigate PSMA-dependent mechanisms promoting tumor vascularization. Vascularized tumor on a microfluidic chip allows us to mimic a tumor with its microenvironment in vitro. Cells are migrating, coordinating and organizing themselves into three-dimensional structures similar to those found in a human body. We are able to design an extracellular microenvironment, monitor real time changes in vessels microarchitecture and interactions of tumor and endothelial cells. Our preliminary data confirmed that endothelial cells can be activated to sprout and further driven by secreted cytokines from tumor cells. Endothelial cells with elevated PSMA expression levels are more likely to form vessel-like structures in comparison to endothelial cells lacking PSMA. We can alter some of these interactions using angiogenic inhibitors that successfully impact endothelial cell activation. We hope to gain more understanding of this complex system that reliably bridges the gap between in vitro and in vivo models and allows precise studies of cellular and molecular mechanisms driving PSMA-dependent tumorigenesis.

First Name: Magdalena

Last Name: Skubal

Email: skubalm@mskcc.org

Organization: Memorial Sloan Kettering Cancer Center

Country: United States

ID: GA267

Concurrent Chemotherapy-Radiotherapy of Prostate Cancer with Multifunctional Gold Nanoclusters

Dong Luo, Case Western Reserve University, dxl576@case.edu

Category: Oncology

Abstract Body : Prostate cancer is the most frequently diagnosed cancer among men in the United States[1]. Nearly 91% of prostate cancers first detected in men are estimated to be clinically localized, qualifying these patients as potential candidates for radical prostatectomy [2]. Clinical radiation therapy is a noninvasive means of killing cancer cells and effectively reducing tumor burden. This method of treatment is prescribed for more than 50% of cancer patients [3]. Although radiation therapy is highly effective for the majority of cancer patients, the nonspecificity of irradiation can result in toxicity for surrounding tissues. Radiosensitizers have been developed to amplify the effects of radiation within tumor cells. Nanoparticles with high-atomic-number, such as gold nanoparticles, have been proposed as next-generation radiosensitizers, due to their excellent absorptivity over soft tissue and the generation of secondary electrons, producing biological damage [4-5]. Adjuvant radiation has been shown to mitigate disease progression, however, there is a big proportion of patients with lethal prostate cancer that do poorly even with post-operation radiotherapy, and they may receive systemic therapy, including androgen deprivation therapy (ADT) and chemotherapy [6-7]. In randomized clinical trials, concurrent chemotherapy-radiotherapy has demonstrated improved local tumor control and overall survival [8]. A principal rationale for using concurrent chemotherapy with radiotherapy is the ability of chemotherapy drugs to radiosensitize. The objective of this study is to develop theranostic gold nanoclusters for prostate cancer targeted radiotherapy and chemotherapy to improve the therapy efficacy and survival rate. CY-PSMA-1 ligands were synthesized and conjugated with monomethyl auristatin E (MMAE), and then reacted with $HAuCl_4$ via an one-step reaction[9] to produce PSMA-targeted AuNCs-MMAE conjugates (Fig. 1a). PSMA-targeted AuNCs without MMAE were synthesized as a control. In vitro binding affinity, cell targeting, MMAE release, cytotoxicity and radiotherapy were tested using PC3pip cells (PSMA+) and PC3flu cells (PSMA-). In vivo tumor targeting, biodistribution and clearance of AuNCs were monitored by an IVIS Spectrum Imaging System and ICP-OES. Tumor damage was confirmed by H&E and immunochemistry staining, and radiotherapy and chemotherapy were evaluated by monitoring tumor growth over 24 days. AuNCs-MMAE conjugates with size around 2.5 nm showed strong fluorescence with ex/em at 490nm/670nm, and in vitro cellular uptake demonstrated significantly higher AuNPs uptake in PC3pip cells than in PC3flu cells. MMAE was cleaved from AuNCs by cathepsin and released intracellularly, leading to cell apoptosis, but could be inhibited by the addition of cathepsin inhibitor. Synergetic radiotherapy by MMAE and AuNCs was confirmed with a colony formation assay, showing the best therapy outcome for the AuNCs-MMAE conjugates. In vivo fluorescence results demonstrated higher AuNCs accumulation in PC3pip tumors than in PC3flu tumors, and fast urinal clearance of AuNCs. In vivo therapeutic studies showed that a single injection of AuNCs-MMAE conjugates significantly inhibited PC3pip tumor growth compared to small molecular PSMA-MMAE, and a

6 Gy of radiation further enhanced the therapeutic efficacy by a synergetic effect of MMAE and AuNCs (Fig. 1b-c). Tumor tissue damage were also confirmed by H&E and immunochemistry staining. The nanocluster system with a high selectivity showed the potential for fluorescence imaging and the integrating of gold and MMAE demonstrated excellent concurrent chemotherapy-radiotherapy efficacy, which was superior over the small molecular counterpart for prostate cancer therapy.

References: [1] Siegel, R. L.; Miller, K. D.; Fuchs, H. E.; Jemal, A. Cancer Statistics, 2021. , Ca-Cancer J. Clin. 2021, 71, 7-33. [2] Wang, X.; Huang, S. S.; Heston, W. D.; Guo, H.; Wang, B. C.; Basilion, J. P. Development of Targeted Near-Infrared Imaging Agents for Prostate Cancer. Mol. Cancer Ther. 2014, 13, 2595-2606. [3] Luo, D.; Wang, X.; Zeng, S.; Ramamurthy, G.; Burda, C.; Basilion, J. P. Prostate-Specific Membrane Antigen Targeted Gold Nanoparticles for Prostate Cancer Radiotherapy: Does Size Matter for Targeted Particles? Chem. Sci. 2019, 10, 8119−8128. [4] Song, G.; Cheng, L.; Chao, Y.; Yang, K.; Liu, Z. Emerging nanotechnology and advanced materials for cancer radiation therapy. Adv. Mater. 2017, 29, 1700996. [5] Goswami, N.; Luo, Z.; Yuan, X.; Leong, D. T.; Xie, J. Engineering gold-based radiosensitizers for cancer radiotherapy. Mater. Horiz. 2017, 4, 817-31. [6] Thompson, I. M.; Tangen, C. M.; Paradelo, J.; Lucia, M. S.; Miller, G.; Troyer, D.; Messing, E.; Forman, J.; Chin, J.; Swanson, G.; Canby-Hagino, E.; Crawford, E. D. Adjuvant radiotherapy for pathologic T3N0M0 prostate cancer significantly reduces risk of metastases and improves survival: long-term followup of a randomized clinical trial. J Urol. 2009, 181, 956-62. [7] Hurwitz, M. D. Chemotherapy and radiation for prostate cancer. Transl. Androl. Erol 2018, 7, 390-98. [8] Buckel, L.; Savariar, E. N.; Crisp, J. L.; Jones, K. A.; Hicks, A. M.; Scanderbeg, D. J.; Nguyen, Q. T.; Sicklick, J. K.; Lowy, A. M.; Tsien, R. Y.; Advani, S. J. Tumor radiosensitization by monomethyl auristatin E: mechanism of action and targeted delivery. Cancer Res 2015, 75, 1376-87. [9] Luo, D.; Wang, X.; Zeng, S.; Ramamurthy, G.; Burda, C.; Basilion, J. P. Targeted Gold Nanocluster-Enhanced Radiotherapy of Prostate Cancer. Small 2019, 15, 1900968.

Image/Figure:

https://s3.amazonaws.com/amz.xcdsystem.com/1E8A4501-BB41-A02A-1D3B9882B798BFAA_abstract_File10351/GA267_ImageFigure_0513012049.png

Image/Figure Caption: Figure 1. a) Schematic illustration of PSMA-targeted AuNCs-MMAE conjugates and the molecular structure of CY-MMAE-PSMA-1 ligands used for the AuNCs synthesis. b) Spectrum fluorescence images show the in vivo PC3pip tumor accumulation of PSMA-targeted AuNCs. c) In vivo antitumor activity of mice injected with PBS, AuNCs, PSMA-MMAE, AuNCs-MMAE conjugates, and mixture of PSMA-MMAE and AuNCs, without radiotherapy (no RT) and with radiotherapy (RT, 6 Gy). Data are presented as mean ± SD (n = 5).

First Name: Dong

Last Name: Luo

Email: dxl576@case.edu

Organization: Case Western Reserve University

Country: United States

ID: GA268
Assessment of NK Cell Trafficking in Whole Mice for HIV Therapy using Cryo-imaging

Madhusudhana Gargesha, BioInVision, madhu.gargesha@bioinvision.com

---

Category: Immunology: Inflammation & Infection

Abstract Body : Aim: Developing a functional cure for HIV is a major goal of the HIV/AIDS research field. Recently, it has been found that natural killer (NK) cells are effective at killing HIV-infected cells. To validate this in a preclinical setting, we assessed the whole-mouse 3D biodistribution of natural killer (NK) cells to gain a better understanding of NK cell homing to potential latent HIV reservoirs. For accurate whole-body assessment of cell trafficking, we used the CryoVizTM cryo-imaging system which acquires 3D microscopic anatomical color and molecular fluorescence volumes with single-cell sensitivity spanning a whole mouse by serially sectioning and imaging the block-face at ultra-high resolution. Methods: Approximately 10M Qtracker-625 (red) labeled human NK cells were injected into NCr nu/nu mice (n=2). In one of the mice, we injected cells intravenously (IV) while in the other, NK cells were administered intraperitoneally (IP). 48 hours after injection, both mice were euthanized, embedded in a medium, and flash frozen in liquid nitrogen for imaging. Mice were imaged with an in-plane (xy) resolution of 10.2µm and a z-section thickness of 40µm. We used an eGFP long pass (>510nm) fluorescence filter which was optimal for detection of Qtracker-625 (red) NK cells. The imaging system created 2D color anatomical and fluorescence block-face images from the whole mouse samples and automatically processed them to obtain 3D volumes. We semi-automatically segmented in 3D the following organs of interest - lung, liver, and spleen - from the color anatomical volumetric data. Using the machine-learning-based algorithm of the system, we automatically detected NK cells from the fluorescence volumetric data. After a careful manual review and editing of automated cell detection results, we obtained refined cell count estimates globally and locally within the segmented organs. Results: With the IV injection (Figure 1A), we observed immune cell homing to the lungs, liver, spleen, lymph nodes, bone marrow and the gastrointestinal tract mucosa. Some cells were also found to be retained in the tail (injection site). With the IP injection, we observed cell clumping at the site of injection (in and around abdominal region) and local cell retention with no evidence of migration (Figure 1B). Conclusions: This study has uniquely revealed whole-body trafficking of fluorescently labeled NK cells, which will be of significant value in strategies to develop a functional cure for HIV, a major goal of the HIV/AIDS research field. Accurate whole-body assessment of NK cell trafficking and 3D biodistribution analyses were obtained using CryoVizTM cryo-imaging. In future studies, we will employ this technique to assess the efficacy of strategies to engineer NK cells to improve their homing to sites harboring latent HIV, the primary obstacle to achieving a functional cure for HIV.

Image/Figure:

https://s3.amazonaws.com/amz.xcdsystem.com/1E8A4501-BB41-A02A-1D3B9882B798BFAA_abstract_File10351/GA268_ImageFigure_0513013411.png

Image/Figure Caption: Figure 1. 3D biodistribution of NK cells for (A) IV injected mouse and (B) IP injected mouse. In (A-B), a 3D volume rendering of true-color anatomy is shown fused with detected NK cells rendered in yellow and segmented organs rendered in pseudo-colors (lung-RED, liver-GREEN, spleen-BLUE). With IV injection (A), we observed NK cell homing mainly to the lungs, liver, spleen, femoral and vertebral bone marrow, with some cells retained in the tail (injection site, magenta arrow in A). With IP injection (B), we observed cell clumping at the injection site in and around the abdominal region (blue arrow in B). We found the IV administration method to be more efficacious than the IP route in terms of immune cell trafficking.

First Name: Madhusudhana

Last Name: Gargesha

Email: madhu.gargesha@bioinvision.com

Organization: BioInVision

Country: United States

ID: GA269

A novel vascular disrupting agent (NOV202) increases the anticancer efficacy of the PARP inhibitor olaparib in prostate cancer cells with BRCA1/2 mutations

Evangelia Sereti, Lund University, evangelia.sereti@med.lu.se

---

Category: Oncology

Abstract Body : Introduction and Objectives: Despite substantial progress in prostate cancer therapeutic landscape, metastatic castration-resistant prostate cancer (mCRPC) remains a lethal disease with poor clinical outcome. DNA damage repair (DDR) defects are present in 20-25% of mCRPC patients, with BRCA1/2 mutations representing the most frequent events [1]. Recent clinical trials have shown that mCRPC patients harboring DDR defects responded well to poly (ADP-ribose) polymerase inhibitors (PARPi). The PARPi olaparib was found to significantly improve survival in patients with BRCA1/2 mutated mCRPC. Although robust data exist for PARPi as monotherapy in selected patients, there is a clinical need for combinational therapeutic approaches to improve the efficacy of PARPi and overcome or prevent PARPi resistance [2]. NOV202 is a novel vascular disrupting agent (VDA) with strong anti-proliferative effects in a large panel of cancer cells. This study aimed to evaluate if NOV202 could improve the efficacy of olaparib in prostate cancer cells with BRCA1/2 mutations in vivo. Materials and Methods: Prostate cancer-based xenografts were developed from human DU145 (BRCA1/2 mutated) cell line. Luciferase-transfected DU145 cells were inoculated subcutaneously in male NMRI nude mice. Animals were treated with olaparib (100 mg/kg), NOV202 (30 mg/kg), or their combination for 21 days, followed by either 1 or 2 weeks of no treatment. Tumor growth and response to therapy were monitored by non-invasive bioluminescence optical imaging (BLI) and tumor size was also measured by caliper. During the experiment, a 25-parameter blood analysis, including hemoglobin concentration, red and white blood cells, and neutrophil granulocytes was performed weekly. Results: Olaparib and NOV202, as single drug treatments, induced tumor growth inhibition in BRCA1/2 mutated xenografts. Compared to monotherapy, the combination of olaparib and NOV202 exerted significant synergistic effect. The combinational effect continued for 2 weeks post-treatment period. Changes in the mean values of hematological parameters were not statistically significant in combinational versus monotherapy groups. Conclusions: Single agent treatment with the VDA agent NOV202 and interestingly also with olaparib reduced tumor growth in prostate cancer xenografts with BRCA1/2 mutations in vivo. The anticancer efficacy of olaparib was significantly increased when combined with NOV202 in BRCA1/2 mutated xenografts. A clinical trial of this combination is planned.

References: 1. Lozano R, Castro E, Aragón IM, et al. Genetic aberrations in DNA repair pathways: a cornerstone of precision oncology in prostate cancer. Br J Cancer. 2021;124(3):552-563. doi:10.1038/s41416-020-01114-x 2. Nizialek E, Antonarakis ES. PARP Inhibitors in Metastatic Prostate Cancer: Evidence to Date. Cancer Manag Res. 2020 Sep 7;12:8105-8114. doi: 10.2147/CMAR.S227033. PMID: 32982407; PMCID: PMC7489946.

Full Name of Abstract's 1st Author : Evangelia Sereti

First Name: Evangelia

Last Name: Sereti

Email: evangelia.sereti@med.lu.se

Organization: Lund University

Country: Sweden

ID: GA270

MRI responsive probe for Zn2+ based on supramolecular self-assembly for prolonged in-vivo imaging

Nishanth D Tirukoti, Weizmann Institute of Science, deva-nishanth.tirukoti@weizmann.ac.il

---

Category: New Chemistry, Materials & Probes

Abstract Body : Introduction: Small molecular imaging probes for MRI applications are an important set of sensors that were developed for mapping a variety of analytes ranging from neurotransmitters to metal ion's. Nevertheless, their fast clearance from tissues frequently limits their detectability but also prevents the performance of longitudinal studies. Prolonged infusion strategies were found to be a solution for rapidly cleared responsive probes in in-vivo studues1, 2 but other strategies for extending the tissue retention time of designed probes are still of need for desired applications. Here, we show the design of an MRI responsive probe for Zn2+, which undergoes spontaneous self-assembly into a supramolecular hydrogel under physiological conditions. The fluorinated probe shown was developed to detect Zn2+ based on the combination of CEST and 19F-MRI (19F-iCEST)3-5 and found to be detectable in-vivo even 24 hours after its injection allowing longitudinal in-vivo MRI studies. Method: A fluorinated-chelate that is based on a dipicolylamine motif, which specifically binds Zn2+, was synthesized followed by its coupling to a BTA (benzene-1,3,5-tricarboxamide) backbone to obtain the tripod NIS-4. 19F-NMR and19F-iCEST (B1 = 2.3 μT/2 s) were performed on 9.4 T NMR at 25 oC and 37 oC. Hydrogel formation was evaluated by dynamic light scattering (DLS), diffusion NMR studies, and photography at 25 oC and 37 oC. In-vivo experiments were performed on a 9.4 T MRI scanner after intracranial injection of 2 μL of NIS-4 (0.25M in DMSO) to the CA3 region of the hippocampus. In-vivo 19F-NMR experiments were performed to study the sensor clearance rate from the live animal brain. For 19F-MRI experiment, 19F-RAREst sequence was used with the following parameters: TR/TE=4000/10.8 ms, RARE factor=16, FOV=22X22 mm2 (32x32 matrix). Results: The Zn2+ responsive probe NIS-4 (Fig. 1a) with its 19F-dipicolylamine motifs as Zn2+ binding moieties was synthesized and characterized based on the hypothesis that tripods of this type tend to self-assemble to large architectures at elevated temperatures6. The effect of the addition of Zn2+ to an aqueous solution of NIS-4 resulted in an additional peak of the Zn2+-NIS-4 complex in 19F-NMR spectrum (Δω=+5 ppm, Fig. 1b). At 37 oC an additional peak of the formed self-assembly of NIS-4 was obtained upfield. A characteristic 19F-iCEST spectrum showed a high CEST effect (Fig. 1e) from NIS-4 in presence of labile Zn2+ at 37 oC revealing its potentiality to map the ion with MRI. The transformation of NIS-4 to a hydrogel at 37 oC was observed by a naked-eye (Fig. 1c, inset) and confirmed by both diffusion NMR (Fig. 1c) and DLS measurements (Fig. 1d). Intracranially injection of NIS-4 to a mouse brain was followed by in-vivo 19F-MRS and 19F-MRI. The long retention time (>20 hours) of the injected probe was clearly evident by longitudinal in-vivo 19F-MRS (Fig. 1f). In-vivo 19F-MRI show the spatial distribution of NIS-4 21 hours after its injection (Fig. 1g) confirming its prolonged retention time in the delivered region. Conclusion: We showed the design of an MRI-responsive probe for Zn2+ sensing that is self-assembled to a hydrogel upon its injection to a live animal. We have

demonstrated that the formed supramolecular hydrogel is capable to detect Zn2+ when implementing the CEST principles in 19F-MRI (an approach termed 19F-iCEST). Moreover, we showed that upon its delivery, the 19F-MRI signal is preserved for more than 20 h after its injection. While the proposed approach was demonstrated here for a Zn2+ responsive probe that was designed for 19F-iCEST it can be generalized for the design of additional MRI responsive probes for applications that require long tissue-retention times for longitudinal in-vivo studies.

References: 1. Savić, T.; Gambino, G.; Bokharaie, V. S.; Noori, H. R.; Logothetis, N. K.; Angelovski, G., Early detection and monitoring of cerebral ischemia using calcium-responsive MRI probes. Proceedings of the National Academy of Sciences 2019, 116 (41), 20666-20671. 2. Barandov, A.; Bartelle, B. B.; Williamson, C. G.; Loucks, E. S.; Lippard, S. J.; Jasanoff, A., Sensing intracellular calcium ions using a manganese-based MRI contrast agent. Nature Communications 2019, 10 (1), 897. 3. Allouche-Arnon, H.; Tirukoti, N. D.; Bar-Shir, A., MRI-based Sensors for In Vivo Imaging of Metal Ions in Biology. Israel Journal of Chemistry 2017, 57 (9), 843-853. 4. Bar-Shir, A.; Gilad, A. A.; Chan, K. W. Y.; Liu, G.; van Zijl, P. C. M.; Bulte, J. W. M.; McMahon, M. T., Metal Ion Sensing Using Ion Chemical Exchange Saturation Transfer 19F Magnetic Resonance Imaging. Journal of the American Chemical Society 2013, 135 (33), 12164-12167. 5. Yuan, Y.; Wei, Z.; Chu, C.; Zhang, J.; Song, X.; Walczak, P.; Bulte, J. W. M., Development of Zinc-Specific iCEST MRI as an Imaging Biomarker for Prostate Cancer. Angewandte Chemie International Edition 2019, 58 (43), 15512-15517. 6. Hendrikse, S. I. S.; Su, L.; Hogervorst, T. P.; Lafleur, R. P. M.; Lou, X.; van der Marel, G. A.; Codee, J. D. C.; Meijer, E. W., Elucidating the Ordering in Self-Assembled Glycocalyx Mimicking Supramolecular Copolymers in Water. Journal of the American Chemical Society 2019, 141 (35), 13877-13886.

Image/Figure:

https://s3.amazonaws.com/amz.xcdsystem.com/1E8A4501-BB41-A02A-1D3B9882B798BFAA_abstract_File10351/GA270_ImageFigure_0513012950.png

Image/Figure Caption: Figure 1: a) Cartoon for Hydrogel formation of NIS-4 at 37 ºC. b) 19F-NMR of 2 mM NIS-4 and 1.2 mM of Zn2+ at 25 oC and 37 oC. c) Diffusion NMR experiment of NIS-4 at 25 oC and 37 oC. d) DLS measurements of NIS-4 at 25 oC and 37 oC. e) 19F-iCEST effect plot obtained from a solution of 2 mM of NIS-4 and 80 µM of Zn2+. f) 19F-NMR spectra of a mouse brain following intracranial injection of NIS-4 at different time points. g) 1H MRI and 19F-MRI.

Full Name of Abstract's 1st Author : Deva Nishanth Tirukoti

First Name: Nishanth D

Last Name: Tirukoti

Email: deva-nishanth.tirukoti@weizmann.ac.il

Organization: Weizmann Institute of Science

Country: Israel

ID: GA273

Systematic Determination of the Highest Quality Reconstruction Methods for Preclinical Pet Imaging

Elise Wang, University of Rochester School of Medicine, elise.wang@macaulay.cuny.edu

---

Category: Computational & Data Science

Abstract Body : Purpose: Molecular imaging using positron emission tomography (PET) is an essential tool in preclinical and clinical research. It is extensively used for various studies involving cancer biology, assessment of therapeutic drugs, and implementation of novel biomarkers and development of imaging agents. The wide popularity and application of PET are due to its ability to quantitatively measure the molecular bio-distribution of radiopharmaceuticals injected into a patient or subject. Despite its widespread use, however, there is no standardized image acquisition and analysis procedure for every type of PET scan. A single PET imaging study follows several steps including pre-scan preparation, raw data acquisition, image reconstruction and analysis. In each of these steps, several parameters are often involved, which some may be selected and tuned to optimize for specific purposes and applications. As PET is a highly quantitative instrument, it is important to maintain its quantitative accuracy with less variability between and across similar studies as much as possible. For this study, we evaluated several 2D and 3D reconstruction variants provided with the Inveon PET/CT (Siemens) instrument to investigate whether there were any significant differences between the reconstruction variants relative to vendor-recommended methods. Methods: We evaluated over 20 reconstruction variants that can be selected from the Inveon PET/CT image acquisition software system. The reconstruction algorithms were grouped into 6 categories based on simple type similarity. A cylindrical phantom with four fillable spheres of different sizes filled with Cu64 was scanned three times at different radioactivity decay time points. Another cylinder tube filled with known radioactivity was also scanned to compute the calibration factor ratio for each reconstruction method. The study was also replicated with F18. The phantom scans were reconstructed by the selected reconstruction methods compared for computed %ID/g, Percentage Coefficient of Variation, Signal to Noise ratio and Contrast to Noise Ratio using overlayed Regions of Interests (ROIs). For validation, the reconstruction methods were also tested on previously acquired PET image data from an imaging study using a live mouse model of neuroinflammation using TSPO (translocator protein 18 kDa) or TREM1 (Triggering receptor expressed on myeloid cells-1) radiotracers, labeled with F18 and Cu64 respectively. Phantom images were analyzed using the vendor analysis software (Siemens Inveon Research Workplace) and a semi-automatic brain atlas segmentation software package in VivoQuant (InvicroCRO, MA) was employed to segment and analyze the mouse PET images, quantifying the mean and max values of the cerebellum, cortex, and hippocampus ROIs. Results: The result of the Cu-64 phantom study showed that 2D and 3D iterative algorithms with proper calibration provide uniform quantitative accuracy with consistent variability of less than 3% (for bigger size ROI). For small size ROI or low uptake values, the 3D OSEM (Ordered Subset Expectation Maximization) performed better compared to all other variants with less variability Conclusion: Overall, our findings indicate that the 3D OSEM iterative algorithm alone may be

able to generate robust image quality with less variability and a slightly better contrast to noise ratio. Further analysis is being conducted to evaluate the superiority of 3D OSEM with respect to different radioactive tracer distribution patterns, high and low uptake regions, and radiotracer type.

References: 1. McDougald, W., Vanhove, C., Lehnert, A., Lewellen, B., Wright, J., Mingarelli, M., Corral, C. A., Schneider, J. E., Plein, S., Newby, D. E., Welch, A., Miyaoka, R., Vandenberghe, S., & Tavares, A. A. S. (2019). Standardization of Preclinical PET/CT Imaging to Improve Quantitative Accuracy, Precision, and Reproducibility: A Multicenter Study. Journal of Nuclear Medicine, 61(3), 461–468. https://doi.org/10.2967/jnumed.119.231308 2. Ketabi, A., Ghafarian, P., Mosleh-Shirazi, M. A., Mahdavi, S. R., Rahmim, A., & Ay, M. R. (2018). Impact of image reconstruction methods on quantitative accuracy and variability of FDG-PET volumetric and textural measures in solid tumors. European Radiology, 29(4), 2146–2156. https://doi.org/10.1007/s00330-018-5754-y 3. Yan, J., Schaefferkoetter, J., Conti, M., & Townsend, D. (2016). A method to assess image quality for Low-dose PET: analysis of SNR, CNR, bias and image noise. Cancer Imaging, 16(1), 26. https://doi.org/10.1186/s40644-016-0086-0

Image/Figure:

https://s3.amazonaws.com/amz.xcdsystem.com/1E8A4501-BB41-A02A-1D3B9882B798BFAA_abstract_File10351/GA273_ImageFigure_0513013423.png

Image/Figure Caption: Figure 1: Comparison of selected 2D and 3D image reconstruction variants available on the Inveon PET/CT acquisition software. Left, Phantom scan using a cylindrical phantom with fillable spheres. Spheres were filled with a solution of slight CT contrast and about 5 times higher radioactive tracer relative to the background signal. Right, Top, show the result of mean region of interest (ROIs) after applying calibration correction to each reconstruction method, Right, Middle, show the percentage variability between three phantom scans at different radioactive decays, and Right, bottom, show the time each reconstruction takes to generate images.

Full Name of Abstract's 1st Author : Elise Wang

First Name: Elise

Last Name: Wang

Email: elise.wang@macaulay.cuny.edu

Organization: University of Rochester School of Medicine

Country: United States

ID: GA274

Effects of TOF and non-TOF reconstruction algorithms on SUV of different brain volumes in 11C-PIB PET/MRI

Dilani Wimalarathne, Department of Nuclear Medicine, Union Hospital, Tongji Medical College, Huazhong University of Science and Technology, dilanineranjana@gmail.com

---

Category: Computational & Data Science

Abstract Body : Objective: To compare the effect of Time-of-flight (TOF) and non-Time-of-Flight (non-TOF) reconstruction algorithms on standard uptake value (SUV) of different brain volume of interest (VOI) of 11C-PIB positron emission tomography magnetic resonance imaging (PET/MRI) brain images. Methods: 11C-PIB PET/MRIs, performed for diagnosing and prognosis evaluation of Alzheimer's and Parkinson's patients (AD/PD) were retrospectively reconstructed using TOF and non-TOF algorithms of reconstruction. Maximum of SUV (SUVmax), Mean of SUV (SUVmean), Minimum of SUV (SUVmin) and Standard deviation of SUV (SUVsd) of 17 different segmented brain VOIs i.e. FL: Frontal Lobe; TL: Temporal Lobe; PL: Parietal Lobe; OL: Occipital Lobe; CN Caudate Nuclei; NA: Nucleus Accumbens; PU: Putamen; Th: Thalamus; PA: Palladium; CoC: Corpus callosum; SN: Substantia Nigra; IN: Insulla; ACC: Anterior cingular cortex; PCC: Posterior cingulate cortex; CC: Cerebellar cortex; BS: Brainstem; C_WM: Cerebellar white matter were collected by using the 3.906 PNEURO module. Paired t-test was performed to compare SUVs between two reconstruction methods among segmented brain VOIs. Relative average difference (%RAD) of SUVs were calculated and brain VOIs were divided into two groups by its volume of 40ccm. Spearman correlation coefficient was used to analyze the correlation between the %RAD of SUV and the segmented brain VOI groups. Correlation graphs were made for identifying the correlation between two reconstruction methods among different SUVs. Distributions of SUVmax, SUVmean, SUVmin and SUVsd for all the brain VOIs under two reconstruction algorithms are shown in Figure 2. Results: Total 34 (n=34), 11C-PIB PET/MRI patients were included with the median age (years) and Body Mass Index (BMI-kg/m2) of 62.2±6.8 y and 24.7±2.9 kg/m2. SUVmax, SUVmean, SUVmin and SUVsd showed significant difference (p 40ccm (r-value: 0.900; p Conclusions: Among the two reconstruction algorithms, TOF can significantly improve the SUVmax SUVmean, SUVmin and SUVsd in different brain VOIs.

Image/Figure: https://s3.amazonaws.com/amz.xcdsystem.com/1E8A4501-BB41-A02A-1D3B9882B798BFAA_abstract_File10351/GA274_ImageFigure_0516030745.docx

Image/Figure Caption: Figure 1. Comparison of paired average TOF and non-TOF values of segmented brain regions among SUVmax, SUVmean, SUVmin and SUVsd; FL: Frontal Lobe; TL: Temporal Lobe; PL: Parietal Lobe; OL: Occipital Lobe; CN Caudate Nuclei; NA: Nucleus Accumbens; PU: Putamen; Th: Thalamus; PA: Palladium; CoC: Corpus callosum; SN: Substantia Nigra; IN: Insula; ACC: Anterior cingular cortex; PCC: Posterior cingulate cortex; CC: Cerebellar cortex; BS: Brainstem; C_WM: Cerebellar white matter Figure 2.Distribution of SUVmax, SUVmean, SUVmin and SUVsd for all the segmented brain VOIs under two

reconstruction algorithms (non-TOF and TOF). Figure 3.Correlation graphs of TOF SUVs versus non-TOF SUVs, among segmented brain VOIs; all the four SUVs, SUVmax, SUVmean, SUVmin and SUVsd shows strong positive correlation in TOF Vs. non-TOF reconstructions.

Full Name of Abstract's 1st Author : Dewalage Dilani Neranjana Wimalarathne

First Name: Dilani

Last Name: Wimalarathne

Email: dilanineranjana@gmail.com

Organization: Department of Nuclear Medicine, Union Hospital, Tongji Medical College, Huazhong University of Science and Technology

Country: China

ID: GA275
Feasibility of high-resolution MR imaging of HP 13C[DHA] and 13C[Vitamin C]

Kofi Deh, Memorial Sloan Kettering Cancer Center, kofi.deh@gmail.com

---

Category: Computational & Data Science

Abstract Body : INTRODUCTION: Dissolution dynamic nuclear hyperpolarization (dDNP) provides an increase of up to four orders of magnitude in SNR for MRI, enabling the study of metabolism at unprecedented spatio-temporal resolutions(1). It was recently proposed to use multi-shot multi-echo echo planar imaging (EPI) to more efficiently utilize the transient magnetization. In this work, this approach is extended to a challenging low SNR HP probe, [1-13C]dehydroascorbate(DHA) (Fig. 1a) where high spatial resolution is not readily acquired with standard imaging sequences. Using simulations and phantoms, it is shown that it is possible to reconstruct high spatial resolution HP images of both DHA and its product Vitamin C, if the acquired data is post-processed to increase SNR (2). METHODS: All experiments were performed on a preclinical Bruker BioSpec 3T scanner, using a dual-tuned transmit/receive 1H/13C 42-mm diameter birdcage coil and a multi-shot multi-echo GRE EPI sequence. A number of signal averages (NSA) simulation (3) was performed to determine the optimum ΔTE values for a least-squares (IDEAL) reconstruction of the acquired multi-echo EPI data. Two plastic syringes, filled with approximately 1 mL of 4M [1-13C]acetate (pH adjusted for chemical shift of 182 ppm) and 1 mL of 2 M [1-13C]acetate (pH adjusted for chemical shift of 178 ppm) respectively were used as a phantom (Fig. 1a). The acquisition parameters for 4 EPI scans were TR = 1 second, matrix size=32×32, 40x 40, 50 x 50 and 64 x 64, FOV=50×50×50 mm, excitation=90°, receiver bandwidth = 150 kHz, 6 echoes and 1 slice. An EPSI and a T1-weighted image were acquired to verify the identity of the chemicals and the location of each tube. For improved performance of IDEAL, the SNR of the EPI images was increased by averaging neighboring pixels or by denoising with a median filter. RESULTS: Four optimum ΔTE values for IDEAL reconstruction were determined from the NSA simulation to be 2.59, 2.62 and 3.156 and 3.084 ms (Fig. 1b). These ΔTE values could be achieved on the Bruker BioSpec 3T MRI scanner using 6, 6, 8 and 12 interleaved EPI shots for the desired matrix sizes of 32×32, 40x40, 50x50 and 64x64. The two chemical species were accurately reconstructed both spatially and quantitatively by IDEAL for the lowest spatial resolution of 1.5625 mm (Fig. 1c). Increasing the resolution of the acquired EPI data from 1.25 to 0.78 mm resulted in increasingly worse SNR and the failure of IDEAL to recover the images of the chemical species. (Fig.1d – IDEAL reconstruction without denoising). Improving image SNR by median filtering resulted in complete recovery of both chemical species at 1.25 mm and partial recovery at 1 mm (Fig.1d – IDEAL reconstruction of median filtered EPI data). Improving image SNR by binning neighboring pixels resulted in over 98% of the chemical species signal being assigned to the correct map (Fig.1d – IDEAL reconstruction with downsampled EPI data). Although, improving the SNR of the EPI data with a post-processing method results in a qualitative improvement in IDEAL separation of the chemical species, it also results in a decrease in its quantitative accuracy as can be seen in the increasing discrepancy between the gold standard spectroscopy quantitation and the ROI means quantitation of the species from 39% at a resolution of 1.56 mm

to 117% at a resolution of 0.78 mm(Fig. 1e). CONCLUSION: Multi-shot, multi-echo EPI with IDEAL enables high resolution imaging of low SNR 13C chemicals; however, there is loss of quantitation accuracy with increasing spatial resolution. Clinical applications of this technique will help to better visualize small lesions that may occur in cancer metastasis.
Acknowledgements: Starr Cancer Consortium (SCC-I12-0031), Thompson Family Foundation and NIH R01 CA252037.

References: 1. Keshari KR, Wilson DM. Chemistry and biochemistry of 13C hyperpolarized magnetic resonance using dynamic nuclear polarization. Chem Soc Rev 2014;43(5):1627-1659. 2. Keshari KR, Kurhanewicz J, Bok R, Larson PE, Vigneron DB, Wilson DM. Hyperpolarized 13C dehydroascorbate as an endogenous redox sensor for in vivo metabolic imaging. Proc Natl Acad Sci U S A 2011;108(46):18606-18611. 3. Reeder SB, Brittain JH, Grist TM, Yen YF. Least-squares chemical shift separation for (13)C metabolic imaging. J Magn Reson Imaging 2007;26(4):1145-1152. 4. Deh K, Granlund KL, Eskandari R, Kim N, Mamakhanyan A, Keshari KR. Dynamic volumetric hyperpolarized. Magnetic resonance in medicine : official journal of the Society of Magnetic Resonance in Medicine / Society of Magnetic Resonance in Medicine 2021;85(2):978-986.

Image/Figure:

https://s3.amazonaws.com/amz.xcdsystem.com/1E8A4501-BB41-A02A-1D3B9882B798BFAA_abstract_File10351/GA275_ImageFigure_0513013647.png

Image/Figure Caption: a)Non-localized spectroscopy of phantom used in this study for simulating 4 ppm shift resulting from reduction of [1-13C]DHA to [1-13C] Vitamin C in-vivo. Chemical diagram reproduced with permission from Keshari et al. PNAS 2011. b)Number of signal averages (or equivalently) condition number simulation for determining optimal ΔTE for IDEAL separation of DHA and Vitamin C. Shorter ΔTE with high NSA result in better performance of IDEAL. c) T1-weighted of phantom setup showing syringes filled with DHA and Vitamin C separated by a 15 mL falcon tube for loading the coil. An EPSI image was acquired for verifying the location and quantity of the chemicals by spectroscopy. The magnitude of the EPI image acquired at 1.563 mm resolution and the IDEAL decomposition into Vitamin C and DHA maps are shown. d) The IDEAL decomposition of EPI images acquired at 3 spatial resolutions with and without denoising are shown. Downsampling is performed using bilinear interpolation, after which the results of IDEAL are resampled back to the acquired spatial resolution. f) The quantitative accuracy of IDEAL is assessed by measurement of the mean intensity of a region of interest (ROI) drawn on each chemical species map . The spectroscopic quantitation is determined by peak integration .

Full Name of Abstract's 1st Author : Kofi Deh

First Name: Kofi

Last Name: Deh

Email: kofi.deh@gmail.com

Organization: Memorial Sloan Kettering Cancer Center

Country: United States

ID: GA276

Directed evolution and phylogenetic discovery of acoustic reporter genes for in vivo imaging of gene expression in mice

Robert Hurt, Caltech, rchurt@caltech.edu

Category: Bioengineering, Synthetic Biology and Basic Biology

Abstract Body : A major outstanding challenge in the fields of biological research, synthetic biology, and cell-based medicine is a lack of methods to noninvasively image the functions of natural and engineered cells inside opaque organisms. A promising imaging modality for this purpose is ultrasound (US), with its penetration depth of several cm and spatial resolution of tens of μm. Recently, the first genetically encoded US contrast agents—gas vesicles (GVs)—were shown to link cellular function to an US readout via heterologous expression in both commensal bacteria1 and mammalian cells2. GVs are air-filled protein nanostructures derived from buoyant photosynthetic microbes, in which they serve as cellular flotation devices. GVs are encoded by operons of 8-14 genes, and most of their molecular makeup comprises the structural protein GvpA. The air inside GVs allows them to scatter US. GVs can be imaged nondestructively with high specificity by taking advantage of their nonlinear US scattering properties.3 Just as the discovery of the first fluorescent proteins was followed by the engineering and evolution of their properties, we are working to engineer the properties of GVs as acoustic reporters. In this work, we sought to 1) increase the amount of nonlinear signal produced by bacterially-expressed GV gene clusters under mammalian physiological conditions, 2) identify GV clusters capable of producing nonlinear GVs when expressed in mammalian cells with small genetic footprints to facilitate gene delivery, and 3) engineer GV types compatible with nondestructive multiplexed imaging. We accomplished these goals using two complementary approaches: homolog screening and directed evolution. Critical for both approaches was the development of a high-throughput assay for various US phenotypes of interest in bacterially-expressed GVs. To enable this screening, we developed the first “acoustic plate reader,” which enabled the automated screening of >1000 bacterially-expressed GV gene cluster variants in a matter of hours. We used this system to screen GV gene cluster homologs from 11 unique species, and thousands of mutants of the primary GV structural protein GvpA/GvpB. In our homolog screen, we tested candidate gas vesicle gene clusters from several diverse species of bacteria and archaea. We identified two GV clusters with improved properties over existing ones: one with greatly enhanced nonlinear contrast and stability in bacteria,4 and another that enables nonlinear detection of mammalian cells and has a more compact genetic footprint than GV clusters previously used for mammalian expression. The former GV gene cluster allowed us to noninvasively image the spatial distribution of tumor colonization by engineered tumor-homing bacteria in situ in living mice, and the latter enabled noninvasive nonlinear imaging of tumor cells themselves. In our directed evolution screen, we generated scanning site saturation libraries for two homologs of GvpA and screened them in E. coli using our custom-built robotic US plate scanner. Custom imaging pulse sequences were used to assess the acoustic phenotypes of each bacterial patch, including total backscattering, nonlinear scattering, and collapse pressure. Using this technique, we identified mutants of GvpA with >150x higher acoustic signal than their

parents, enabling both their specific detection in bacteria and nondestructive multiplexed imaging of two GV types. Here, we report the discovery of novel GV gene clusters that enable nonlinear imaging of bacterial and mammalian cells in situ, as well as clusters that enable multiplexed GV imaging. These results suggest that high-throughput protein engineering could play as large a role in engineering acoustic biomolecules as it has in the development of their fluorescent counterparts.

References: 1. Bourdeau, R. W. et al. Acoustic reporter genes for noninvasive imaging of microorganisms in mammalian hosts. Nature 553, 86–90 (2018). 2. Farhadi, A., Ho, G. H., Sawyer, D. P., Bourdeau, R. W. & Shapiro, M. G. Ultrasound imaging of gene expression in mammalian cells. Science 365, 1469–1475 (2019). 3. Maresca, D., Sawyer, D. P., Renaud, G., Lee-Gosselin, A. & Shapiro, M. G. Nonlinear X-Wave Ultrasound Imaging of Acoustic Biomolecules. Phys. Rev. X 8, 041002 (2018). 4. Hurt, R. C., Buss M.T. et al. Genomically Mined Acoustic Reporter Genes Enable On-Demand In Vivo Monitoring of Tumor-Homing Bacteria. http://biorxiv.org/lookup/doi/10.1101/2021.04.26.441537 (2021) doi:10.1101/2021.04.26.441537.

Full Name of Abstract's 1st Author : Robert C. Hurt

First Name: Robert

Last Name: Hurt

Email: rchurt@caltech.edu

Organization: Caltech

Country: United States

ID: GA277

Quantitative radionuclide imaging study for enhanced drug delivery induced by near-infrared photoimmunotherapy

Winnaung Kuribayashi, National Institutes for Quantum and Radiological Science and Technology, winn.aung@qst.go.jp

---

Category: Oncology

Abstract Body : Objective: Photoimmunotherapy (PIT) is an upcoming potential cancer treatment modality. Meanwhile, due to the limited therapeutic effect of PIT alone, the combination of anticancer agents with PIT is an option to improve the therapeutic outcome. PIT causes a super-enhanced permeability and retention (SUPR) effect. The selection of drug molecule sizes that are suitable for enhanced permeability is also important for optimizing therapeutic efficacy. Thus, a method that supports to investigate the drug delivery of varying molecular weights coupled with PIT is desirable. Here, we evaluated the SUPR effect using radiolabeled drugs of varying molecular weights (18F-5FU, 111In-DTPA, 99mTc-HSA-D, and 111In-IgG) to determine the appropriate drug size. Methods: PIT was conducted with an indocyanine green-labeled anti-HER2 antibody and an 808-nm laser irradiation. Mice were subcutaneously inoculated with HER2-positive cells in both legs. The tumor on one side was treated with PIT, and the contralateral side was not treated. The differences between tumor accumulations were quantitatively evaluated using positron emission tomography (PET) or single-photon emission computed tomography (SPECT). In this study, we used the four radionuclide imaging probes: 18F-5FU, a low-molecular-weight (148 Da) PET probe; 111In-DTPA, a low-molecular-weight (504 Da) SPECT probe, 99mT- HSA-D, a medium-molecular-weight (66492 Da) SPECT probe, and 111In-IgG, a high-molecular-weight (147111 Da) SPECT probe to quantify the SUPR effect induced by PIT. Results: PIT-treated tumors showed significantly increased uptake of 18F-5FU (P Conclusion: The radionuclide imaging approach is elucidated for the PIT-mediated SUPR effect and can help in optimizing therapeutic measures by means of the feasibility of selecting a drug size and monitoring its distribution. Our findings encourage further preclinical and clinical studies to develop a combination therapy of PIT with conventional anticancer drugs.

First Name: Winnaung

Last Name: Kuribayashi

Email: winn.aung@qst.go.jp

Organization: National Institutes for Quantum and Radiological Science and Technology

Country: Japan

ID: GA278
203Pb-DOTA-based pretargeting for theranostic 203Pb/212Pb therapy

Sarah Cheal, Memorial Sloan Kettering Cancer Center, cheals@mskcc.org

---

Category: Oncology

Abstract Body : 203Pb/212Pb is a very promising theranostic pair for molecularly targeted radionuclide therapy. The gamma-emitting radionuclide 203Pb (t1/2 = 52.1 h) can be used for image-guided treatment with the elementally identical therapeutic nuclide 212Pb. 212Pb, produced via 224Ra/212Pb generator, is a beta (β)-emitter (t1/2 = 10.6 h) that decays to 212Bi, which is an α-emitter (t1/2 = 1.06 h), i.e., 212Pb functions as an in vivo generator of 212Bi. A pretargeted radioimmunotherapy (PRIT) approach that utilizes anti-tumor antigen/anti-DOTA bispecific antibodies (BsAb) in combination with rapidly clearing low-molecular weight DOTA-radiohaptens (DOTA-PRIT) have been developed against a variety of human tumor types for high-therapeutic index (TI) treatment with β- or α-emitting radioisotopes. Herein we tested the hypothesis that high-TI targeting of 203Pb-DOTA-radiohaptens would be feasible with the modular DOTA-PRIT approach. TCMC (1,4,7,10-tetrakis (carbamoylmethyl)-1,4,7,10-tetraazacyclododecane) has been used successfully to form conjugates for labeling with 203Pb/212Pb [1]. A novel TCMC-based DOTA-hapten was synthesized consisting of bifunctional p-isothiocyanate-TCMC chelate coupled to a non-radioactive DOTA-Lu3+-PEG4 (TCMC-PEG4-LuDOTA) for BsAb binding. For addition of 203Pb, 203PbCl2 (39.2 MBq / 1.06 mCi) in 15 µL of 0.5 M HCl (Lantheus Medical Imaging, Billerica, MA) was transferred to a metal-free 1.5 mL microcentrifuge tube and diluted with 200 µL of chelexed aqueous 0.5 M NH4OAc (pH 5.3). To this was added 10 µL of 1 mM TCMC-PEG4-LuDOTA (10 nmol) and mixed gently. After 30 min at 40 °C, the reaction was cooled briefly, then purified with a 30 mg Strata-X SPE cartridge. The product was eluted with 200 µL ethanol and diluted with 2.0 mL normal saline and sterile filtered to obtain [203Pb]TCMC-PEG4-LuDOTA (36.1 MBq (975 µCi), 92% yield, AM = 3.9 MBq/nmol (106 µCi/nmol)). RadioHPLC confirmed that no free radiometal remained (98.1% radiochemical purity; major isomer tR = 10.8 min). Assay of in vitro stability of [203Pb]TCMC-PEG4-LuDOTA in human serum revealed no detectable degradation (i.e., no [203Pb]EDTA tR = 2.2 min) when incubated at 37 °C for 24 h. The in vivo clearance of [203Pb]TCMC-PEG4-LuDOTA was evaluated in non-tumored nude mice and proof-of-concept studies of DOTA-PRIT + [203Pb]TCMC-PEG4-LuDOTA were performed in a model DOTA-PRIT system (i.e., targeting subcutaneous GPA33-expressing SW1222 human colorectal cancer (CRC) xenografts in mice). SW1222 tumor-bearing nude mice (n = 5) were injected intravenously in the tail vein: 250 µg (1.19 nmol) of anti-GPA33/anti-DOTA BsAb huA33-C825 [2], followed 24 h later with 25 µg (2.76 nmol) of dendrimer-clearing agent [3], and after an additional 4 h, [203Pb]TCMC-PEG4-LuDOTA was administered (~30 µCi/280 pmol). Ex vivo biodistribution studies were performed with gamma counting of 203Pb activity in tissue, and data is presented as %injected activity per gram of tissue (%IA/g; average ± SD). [203Pb]TCMC-PEG4-LuDOTA cleared very rapidly from blood (t1/2 = 15.47 min; R2 = 0.974), and > 97% cleared the plasma after 1 h. For pretargeted [203Pb]TCMC-PEG4-LuDOTA, the blood, SW1222 tumor, and kidney uptakes at 24 h p.i. were 0.27 ± 0.14 %IA/g, 8.04 ± 2.94

%IA/g, and 0.88 ± 0.14 %ID/g, respectively, corresponding to tumor-to-organ activity ratios (T:NT) of 30 ± 9 and 9.2 ± 1.6 for blood and kidney, respectively. Using serial biodistribution data from 2–168 h p.i., prospective 212Pb-dosimetry was estimated based on local absorption of progeny alphas only. The preliminary absorbed doses to tumor, blood, and kidney were 8713 mGy/MBq, 219.5 mGy/MBq (TI = 40), and 753 mGy/MBq (TI = 11.6), respectively. Experiments are planned to refine dosimetry. We conclude that TCMC-PEG4-LuDOTA is a promising radiohapten precursor for theranostic 203Pb/212Pb therapy with DOTA-PRIT, especially for GPA33-expressing human CRC.

References: [1] Nucl Med Biol. 2000 Jan;27(1):93-100. [2] J Nucl Med. 2017 Nov;58(11):1735-1742. [3] Bioconjug Chem. 2020 Mar 18;31(3):501-506.

Image/Figure:

https://s3.amazonaws.com/amz.xcdsystem.com/1E8A4501-BB41-A02A-1D3B9882B798BFAA_abstract_File10351/GA278_ImageFigure_0513014559.jpg

Image/Figure Caption: 203Pb-DOTA-based pretargeting with [203Pb]TCMC-PEG4-LuDOTA. The 175Lu-DOTA-benzene portion of the molecule (yellow circle) is recognized with picomolar affinity by the anti-DOTA C825 scFv domains of the anti-tumor antigen/anti-DOTA bispecific antibodies (BsAb). The TCMC (green triangle) can be efficiently loaded with 203Pb.

First Name: Sarah

Last Name: Cheal

Email: cheals@mskcc.org

Organization: Memorial Sloan Kettering Cancer Center

Country: United States

ID: GA279

Monitoring intralesional antimicrobial exposure in pulmonary and central nervous system tuberculosis with 18F-pretomanid PET

Filipa Mota, Johns Hopkins University School of Medicine, fdamota2@jhmi.edu

---

Category: Immunology: Inflammation & Infection

Abstract Body : Background: Tuberculosis (TB) remains a global health threat causing over 1 million deaths yearly. Standard of care for pulmonary TB includes multidrug treatment for 6-30 months and poses a risk of low compliance and development of drug resistance. Shorter and more effective treatments are needed for multidrug resistant (MDR)-TB. MDR TB meningitis (TBM) has a nearly 100% fatality rate, and new regimens are urgently required. Pretomanid was approved in 2019 for use in combination with bedaquiline and linezolid (BPaL regimen) in the treatment of pulmonary MDR-TB. However, its potential efficacy for cavitary TB and TBM remains unknown. While antimicrobial pharmacokinetic (PK) parameters are traditionally derived from biological samples such as blood and cerebrospinal fluid, these do not accurately represent the intralesional drug PK in tissues, which is affected by drug properties, tissue blood supply, blood-brain-barrier (BBB) permeability, and the inflammatory microenvironment of TB lesions. We developed 18F-pretomanid for in vivo multi-compartment analysis and quantified the penetration of 18F-pretomanid into privileged sites, including infected lung lesions, cavitary walls, and infected brains in preclinical models of TB. Methods: Radiochemistry: We developed a new synthetic route to obtain 18F-pretomanid through halogen exchange nucleophilic 18F-fluorination of an aryl-OCF2Br precursor, in the presence of silver(I) triflate. In vitro: Stability and protein binding of 18F-pretomanid were tested in mouse, rabbit, and human serum for three hours at 37° C. Ex vivo gamma counting: Post-mortem biodistribution in Mycobacterium tuberculosis-infected mice was performed 1, 2, and 4 hours after intravenous injection of 18F-pretomanid (40 ± 10 μCi, n=4/group). Imaging: Dynamic 18F-pretomanid PET/CT imaging was performed in mouse and rabbit models of pulmonary TB (mice: 103 ± 27 μCi, n=7; rabbits: 290 ± 52 μCi, n=3) and TBM (mice: 100 ± 12 μCi, n=4; rabbits: 126 ± 17 μCi, n=4). A subset of animals underwent PET/CT imaging with 18F-py-albumin and 18F-FDG to assess vascular supply and inflammation. 18F-pretomanid high-resolution autoradiography was performed in infected tissues. Results: 18F-petomanid was synthesized with 5 ± 2 % non-decay corrected yield (>98% radiochemical purity) and was stable in serum, with protein binding ranging from 74-84% across species. 18F-pretomanid PET/CT shows heterogeneous drug distribution in Mycobacterium tuberculosis-infected lung tissues, in mice and rabbits. In the rabbit model of pulmonary and cavitary TB, 18F-pretomanid shows overall high lung penetration (AUC ratio to plasma > 1) but heterogenous distribution with reduced uptake in lung lesions and cavitary walls (P 1) but decreased penetration in the brain lesions, which can be identified by 18F-FDG PET/CT and are characterized by BBB disruption observed by increased 18F-py-albumin signal. Comparatively, 76Br-bedaquiline1 and 18F-linezolid2 show low brain penetration, with AUC ratios to plasma of 0.15 and 0.3, respectively. 18F-pretomanid autoradiography corroborates findings of heterogenous drug distribution in TBM lesions. Conclusions: We developed and validated 18F-pretomanid as a molecular imaging tool to derive in vivo intralesional drug

exposure levels. 18F-pretomanid PET/CT shows high penetration is achieved in infected lungs, with decreased penetration into lung lesions and cavitary walls being attributed to reduced vascular supply. We also observed high penetration of 18F-pretomanid into infected brains. Since the penetration of 76Br-bedaquiline and 18F-linezolid into the brain parenchyma is low, we propose new pretomanid-containing regimens should be tested for the treatment of TBM. The heterogeneous profile of 18F-pretomanid tissue penetration highlights the value added by radiolabeled antimicrobials in the optimization of drug regimens for TB.

References: 1. Ordonez, A.A. et al, Radiosynthesis and PET bioimaging of 76Br-Bedaquiline in a Murine Model of Tuberculosis, ACS Infectious Diseases, 2019, 5(12), 1996-2002 2. Mota, F. et al., Radiosynthesis and biodistribution of 18F-linezolid in Mycobacterium tuberculosis-infected mice using positron emission tomography, ACS Infectious Diseases, 2020, 6(5), 916-921.

Image/Figure:

https://s3.amazonaws.com/amz.xcdsystem.com/1E8A4501-BB41-A02A-1D3B9882B798BFAA_abstract_File10351/GA279_ImageFigure_0513015104.jpg

Image/Figure Caption: Figure 1. Radiosynthesis and PET/CT imaging of 18F-pretomanid in preclinical models of tuberculosis. A. 18F-pretomanid was synthesized by 18F-fluorination of an aryl-OCF2Br precursor in the presence of silver(I) triflate, in dichloroethane at 60 °C for 20 min. B. PET/CT derived time-activity curves of 18F-pretomanid distribution in the lungs of mice with pulmonary TB (n=7 mice, n=26 ROIs of infected lung, n=16 ROIs of unaffected lung). C. Area under the curve (AUC 0-60 min) tissue/plasma ratios show heterogeneity in the distribution of 18F-pretomanid in lung lesions, cavitary walls, and areas of unaffected lung in a rabbit model of pulmonary and cavitary TB (n=3 rabbits, n=9 ROIs of cavitary wall, n=8 ROIs of lesions, n=9 ROIs of unaffected lung). D. AUC (0-60 min) tissue/plasma rations of 18F-pretomanid distribution in brain lesions and areas of unaffected brain in a mouse model of tuberculous meningitis (n=4 mice, n=7 ROIs of brain lesions, n=7 ROIs of unaffected brain). Representative MIP and brain axial slide of 18F-pretomanid in a mouse with tuberculous meningitis. E. High resolution autoradiography of 18F-pretomanid in Mycobacterium tuberculosis-infected rabbit brain shows decreased penetration in brain lesions, identifiable by hematoxylin & eosin staining.

Full Name of Abstract's 1st Author : Filipa Mota

First Name: Filipa

Last Name: Mota

Email: fdamota2@jhmi.edu

Organization: Johns Hopkins University School of Medicine

Country: United States

ID: GA281

Solution Relaxivity and Biodistribution Studies in Mice of Closed Coordination Fe(III) Complexes for Use as T1 MRI Contrast Agents

Elizabeth Kras, SUNY, University at Buffalo, ekras@buffalo.edu

---

Category: New Chemistry, Materials & Probes

Abstract Body : Macrocyclic complexes of Fe(III) typically have greater kinetic inertness towards dissociation than linear chelates, making them a good choice for designing new contrast agents. Phosphonate pendants offer a way to introduce negatively charged groups to the coordination sphere of MRI contrast agents and, when used in Gd(III) and Mn(II) contrast agents, have been shown to increase proton relaxivity of the agents.1, 2 Using multiple phosphonate pendants on a single macrocyclic-based ligand allows for additional negative charges in the coordination sphere, to produce an anionic complex. High spin iron(III) has a moderately long electronic relaxation time and can be used as an alternative to Gd(III) for the development of MRI contrast agents.3, 4 Using these principles, a series of Fe(III) complexes have been synthesized using 1, 4, 7-triazacyclononane (TACN), containing one, two, or three phosphonate pendants resulting in closed coordination complexes with a varying degree of anionic charge. For the non-phosphonates in this series, hydroxypropyl donor groups have been used. The three phosphonate pendant TACN complex (Fe-NOTP) shows similar r1 relaxivity values (0.98 mM-1 s-1, 1.4 T) compared to the hydroxypropyl derivative (1.0 mM-1 s-1, 1.4 T) and both show slightly higher r1 relaxivity values compared to the tris-carboxylate TACN complex (Fe-NOTA, 0.63 mM-1 s-1, 1.4 T). However, Fe-NOTP showed a 58% increase in relaxivity in the presence of HSA, whereas the hydroxypropyl derivative5 and Fe-NOTA show a 23% and Fe-NOTP showed higher kinetic inertness in the presence of acid (100 mM HCl) than the hydroxypropyl derivative, with no dissociation of Fe-NOTP observed after three days at 37 °C. The phosphonate and hydroxypropyl derivatives both show high kinetic inertness towards dissociation in the presence of HEPES buffer and biologically relevant anions (carbonate and phosphate). The two also showed similar reduction potentials (near -330 mV vs. NHE), suggesting both phosphonates and hydroxypropyl donor groups stabilize iron (III) well. Mouse MR imaging studies with Fe-NOTP show kidney and vena cava T1 contrast enhancement similar to DOTAREM when twice as much Fe-NOTP is injected (100 μmol/kg vs. 200 μmol/kg). However, Fe-NOTP shows slightly prolonged kidney elimination compared to DOTAREM. The hydroxypropyl derivative has been reported to show kidney and vena cava enhancement similar to that of DOTAREM at equal injection concentrations (50 μmol/kg), however, higher doses of the hydroxypropyl derivative were not reported due to lower solubility.5 This data suggested that phosphonate pendants can increase kinetic inertness of the iron complexes in acid, HSA binding, and aqueous solubility. However, the hydroxypropyl donor groups show faster clearance in vivo and slightly higher relaxivity values. Future studies with the mixed phosphonate-hydroxypropyl donor pendants could produce a complex that has increased solubility and inertness as well as in vivo enhancement comparable or better than DOTAREM at equal injection concentrations.

References: 1. Drahoš, B.; Pniok, M.; Havlíčková, J.; Kotek, J.; Císařová, I.; Hermann, P.; Lukeš, I.; Tóth, É., Mn2+ complexes of 1-oxa-4,7-diazacyclononane based ligands with acetic, phosphonic and phosphinic acid pendant arms: Stability and relaxation studies. Dalton Transactions 2011, 40 (39), 10131-10146. 2. Vitha, T.; Kubíček, V.; Kotek, J.; Hermann, P.; Vander Elst, L.; Muller, R. N.; Lukeš, I.; Peters, J. A., Gd(iii) complex of a monophosphinate-bis(phosphonate) DOTA analogue with a high relaxivity; Lanthanide(iii) complexes for imaging and radiotherapy of calcified tissues. Dalton Transactions 2009, (17), 3204-3214. 3. Tweedle, M. F., Science to Practice: Will Gadolinium Chelates Be Replaced by Iron Chelates in MR Imaging? 2018, 286 (2), 409-411. 4. Bertini, I.; Turano, P.; Vila, A. J., Nuclear magnetic resonance of paramagnetic metalloproteins. Chemical Reviews 1993, 93 (8), 2833-2932. 5. Asik, D.; Smolinski, R.; Abozeid, S. M.; Mitchell, T. B.; Turowski, S. G.; Spernyak, J. A.; Morrow, J. R., Modulating the Properties of Fe(III) Macrocyclic MRI Contrast Agents by Appending Sulfonate or Hydroxyl Groups. Molecules 2020, 25 (10), 2291.

Full Name of Abstract's 1st Author : Elizabeth A Kras

First Name: Elizabeth

Last Name: Kras

Email: ekras@buffalo.edu

Organization: SUNY, University at Buffalo

Country: United States

ID: GA282

Mn(II)-based MR probes for imaging hepatic fibrogenesis

Hua Ma, Harvard Medical School, HMA11@mgh.harvard.edu

Category: New Chemistry, Materials & Probes

Abstract Body : Introduction Hepatic fibrogenesis, the active process of liver fibrosis, is a hallmark of many chronic liver diseases, which if left untreated results in cirrhosis, primary liver cancer, and/or organ failure. Molecular MR imaging of fibrogenesis has the potential for early diagnosis of liver fibrosis and to monitor disease progression and treatment response. Oxidized collagen with aldehyde containing allysine residues is a marker of fibrogenesis. Here we describe novel macrocyclic Mn(II) chelates containing hydrazine moieties for targeting aldehydes. Rational design results in MR probes that are stable in vivo, have low signal enhancement in normal liver, but are highly reactive toward aldehydes resulting in a marked turn-on in relaxivity upon binding and enhancement of fibrotic liver. Materials and Methods The novel Mn-PC2A derivatives (Fig 1A) were synthesized in 6 steps from the pyclen macrocycle. Hydrazone formation kinetics with butyraldehyde as a model compound were measured by UV spectroscopy at 220 nm, 25 °C, pH 7.4, PBS. Hydrazone hydrolysis kinetics were measured by HPLC with UV detection at 220 nm using excess formaldehyde to trap the liberated hydrazine and prevent the reverse reaction. Allysine-modified BSA (BSA-Ald, 17.4 mg/mL, 260 μM aldehyde) as a soluble model protein or BSA (17.3 mg/mL, 16.8 μM aldehyde) and MnL1 or MnL2 (50-200 μM) were incubated at 37 °C for 3 h, and 1/T1 was measured at 1.4 T, 37 °C, and plotted vs concentration to obtain relaxivity. The protein-bound probe was isolated by ultrafiltration and the relaxivity of the protein-bound fraction measured. All Mn concentrations were measured by ICP-MS. Liver fibrosis was induced in male C57BL/6 mice by oral gavage with CCl4 for 12 weeks, 2-3 times per week, while control mice received vehicle (olive oil). 3D FLASH images (TR/TE/FA =15ms/2ms/30°, 0.25 mm3 spatial resolution) were acquired on a 4.7 T Bruker Biospec prior too and dynamically for 40 min p.i. of 100 μmol/kg MnL1. Liver to muscle contrast to noise was calculated as CNR = (SILiver-SIMuscle)/SDAir where SI = signal intensity and SD = standard deviation in SI. Results We synthesized two macrocyclic Mn(II) chelates with pendant hydrazine moieties for aldehyde targeting (Figure 1A). The a-carboxylate moiety in MnL1 results in a 3-fold higher rate constant for hydrazone formation (Fig. 1B) compared to MnL2, and is one of the highest rate constants reported to date.1 However, the a-carboxylate also catalyzes hydrolysis with the half-life of MnL1-hydrazone about half that of the MnL2-hydrazone (Fig. 1C). Relaxivities (Fig. 1D) of MnL1 and MnL2 were similar in PBS (3 mM-1s-1) consistent with the presence of one coordinated water ligand. Relaxivity was not enhanced in BSA solution indicating little nonspecific protein binding, but relaxivity is increased 90% in the presence of allysine modified BSA. The relaxivity of the protein-bound form of MnL1 and MnL2 was almost 3 times higher than the unbound form. MnL1 administration produced significant liver signal enhancement in CCl4 injured mice but not in controls (Fig. 1E). DCNR showed persistent liver signal enhancement in CCl4 treated mice, while the liver only transiently enhanced in mice treated with vehicle (Fig. 1F). DCNR was 3-fold higher at 20 minutes post injection, and the area under the ΔCNR curve was significantly larger in CCl4 treated mice than

in vehicle treated mice, demonstrating the potential for imaging liver fibrogenesis. Conclusion MnL1 is a novel macrocyclic Mn(II) MR probe with a pendant hydrazine carboxylate moiety that enables rapid reaction with aldehydes, a 270% turn on in relaxivity at 1.4T, low nonspecific liver enhancement in healthy mice, but markedly higher liver signal enhancement in mice with ongoing liver fibrosis, and shows potential for noninvasive imaging of liver fibrosis.

References: (1) Akam, E. A.; Abston, E.; Rotile, N. J.; Slattery, H. R.; Zhou, I. Y.; Lanuti, M.; Caravan, P. Improving the reactivity of hydrazine-bearing MRI probes for in vivo imaging of lung fibrogenesis. Chemical science 2020, 11 (1), 224

Image/Figure:

https://s3.amazonaws.com/amz.xcdsystem.com/1E8A4501-BB41-A02A-1D3B9882B798BFAA_abstract_File10351/GA282_ImageFigure_0513020742.jpg

Image/Figure Caption: Figure 1. (A) Structures of MnL1 and MnL2; (B) Second order rate constant (kon) for reaction of MnL1 and MnL2 with butyraldehyde; (C) Half-life (t1/2) for hydrolysis of condensation product of MnL1 and MnL2 with butyraldehyde; (D) Relaxivity values of MnL1 and MnL2 in PBS, in BSA solution, in allysine modified BSA-Ald, and bound to BSA-Ald; (E) Axial T1-weighted MR images of CCl4 mice imaged at pre- and 20 min post-injection of MnL1 (100 μmol/kg, i.v., liver labeled with yellow dash line); (F) Liver-to-muscle contrast to noise ratio (DCNR) of vehicle (n=3) and CCl4 (n=3) mice as a function of time following injection of MnL1(0.1 mmol/kg, i.v.) (F) Significant difference (P=0.02) in area under the ΔCNR curve (AUC0-40) between vehicle (n=3) and CCl4 (n=3) mice.

Full Name of Abstract's 1st Author : Hua Ma

First Name: Hua

Last Name: Ma

Email: HMA11@mgh.harvard.edu

Organization: Harvard Medical School

Country: United States

ID: GA283

Targeted co-delivery of stroma-penetrating and immunomodulating theranostic nanoparticles for image-guided drug delivery and immunotherapy of pancreatic cancer

Lily Yang, Emory University School of Medicine, lyang02@emory.edu

---

Category: Oncology

Abstract Body : Despite recent successes in immune checkpoint blockade therapy of several types of human cancers, pancreatic cancer has a poor response to immunotherapy1-3. Increasing evidence shows that a dense stromal barrier in pancreatic cancer blocks drug delivery and intratumoral distribution4,5. Stromal physical and immunosuppressive biological barriers further limit the number and function of infiltrating effector T cells3,6. It is clear that the presence of a pro-immune tumor microenvironment is required for a good therapeutic response to immune checkpoint therapy6-9. Pancreatic cancer is an immunologically cold tumor that has a low level of neoantigens, lacks infiltration of immune effector cells, and contains massive immunosuppressive cells1,3,5. To improve therapeutic responses to immune checkpoint therapy in pancreatic cancer, an MRI capable and ultra-small magnetic iron oxide nanoparticle(IONP)-based immune checkpoint PD-L1 inhibitor (Nano-iPD-L1) has been developed by conjugating high-affinity PD-L1 binding and blocking peptides (PD1Y) to the polymer coating of 5 nm core size IONPs. Systemic delivery of near-infrared dye-labeled Nano-iPD-L1 led to the selective accumulation of the IONPs in pancreatic tumors of the Kras-driven transgenic mice for optical and MR imaging of intratumoral delivery of the nanoparticle PD-L1 inhibitor. Importantly, IONP mediated delivery of PD-L1 blocking peptides increased intratumoral infiltration of antigen-presenting dendritic cells and CD8+ cytotoxic T cells. To further improve the delivery of Nano-iPD-L1 and activation of tumor-specific immune responses, a receptor-targeted and stroma breaking theranostic IONP has been developed by conjugating a recombinant ligand containing the amino-terminal fragment (ATF) of uPA and the catalytic domain of matrix metalloproteinase-14 (ATFmmp14-IONP), which confers the ability to target uPAR expressing tumor and stromal cells and promotes nanoparticle/drugs to migrate through the stromal cell and extracellular matrix barriers to reach tumor cells. Results showed that co-delivery of Nano-iPD-L1 with ATFmmp14-IONP could overcome stromal barriers and enhance intratumoral delivery and penetration of both IONPs in mouse pancreatic tumors. Furthermore, the combination therapy using ATFmmp14-IONP encapsulated with a chemotherapy drug, Doxorubicin (DOX), and Nano-iPD-L1 significantly inhibited tumor growth in the KPC mouse pancreatic cancer model. However, inhibition of PD-L1 alone using Nano-iPD-L1did not show an anti-tumor effect in this tumor model. Histological analysis showed that targeted co-delivery of these theranostic IONPs into tumors further increased infiltration of dendritic cells and effector T cells and decreased immunosuppressive cells, converting an immune “cold” pancreatic tumor into a “hot” tumor. Flow cytometry analysis revealed a higher level of activated CD8+ cytotoxic T cells in the tumor-infiltrating lymphocytes obtained from the tumors of the mice that received Nano-iPD-L1, ATFmmp14-IONP, or the combination treatment than those in tumors from the no treatment control. Immunofluorescence analysis of tumor tissues revealed that conventional

DOX treatment markedly increased the levels of expression of immune checkpoint proteins, PD-L1 and Siglec 1510, which are strong inhibitors of cytotoxic CD8+ T cells. However, treatment with ATFmmp14-IONP/DOX or the combination of ATFmmp14-IONP/DOX and Nano-iPD-L1 inhibited DOX-induced upregulation of PD-L1 and Siglec 15 in tumors. Results of this study suggest that improved drug delivery in tumors by co-administrations of a stroma penetrating ATFmmp14-IONP/DOX and a Nano-iPD-L1 leads to a strong therapeutic response through improved intratumoral delivery and stromal penetration, enhanced direct tumor cell killing and tumor antigen presentation, activating tumor immune responses, and blocking PD-L1 function to enhance the cytotoxicity of CD8+ T cells. Therefore, these targeted theranostic and immunotherapy IONPs and the combination therapy have the potential for further translational development of a new image-guided and targeted cancer immunotherapy for advanced pancreatic cancer.

References: 1) Andersson R, Pereira CF, Bauden M, Ansari D. Is immunotherapy the holy grail for pancreatic cancer? Immunotherapy, 2019, 11(17):1435–1438. 2) Beatty GL, Eghbali S, Kim R. Deploying immunotherapy in pancreatic cancer: defining mechanisms of response and resistance. American Society of Clinical Oncology Educational Book. 2017, 37:267-78. 3) Balachandran VP, Beatty GL, Dougan SK. Broadening the impact of immunotherapy to pancreatic cancer: Challenges and opportunities. Gastroenterology. 2019,156(7):2056-2072. 4) M. Schober, R. Jesenofsky, R. Faissner, C. Weidenauer, W. Hagmann, P. Michl, R.L. Heuchel, S.L. Haas, J.M. Lohr. Desmoplasia and chemoresistance in pancreatic cancer, Cancers (Basel) 6(4) (2014) 2137-54. 5) Lafaro KJ, Melstrom LG. The Paradoxical Web of Pancreatic Cancer Tumor Microenvironment. Am J Pathol. 2019, 189(1):44-57. 6) Pitt JM, Vétizou M, Daillère R, Roberti MP, Yamazaki T, Routy B, Lepage P, Boneca IG, Chamaillard M, Kroemer G, Zitvogel L. Resistance mechanisms to immune-checkpoint blockade in cancer: tumor-intrinsic and-extrinsic factors. Immunity. 2016, 21;44(6):1255-69. 7) Zhang J, Endres S, Kobold S. Enhancing tumor T cell infiltration to enable cancer immunotherapy. Immunotherapy. 2019,16;11(3):201-13. 8) Tang H, Wang Y, Chlewicki LK, Zhang Y, Guo J, Liang W, Wang J, Wang X, Fu YX. Facilitating T cell infiltration in tumor microenvironment overcomes resistance to PD-L1 blockade. Cancer cell. 2016, 14;29(3):285-96. 9) Mariathasan S, Turley SJ, Nickles D, Castiglioni A, Yuen K, Wang Y, Kadel III EE, Koeppen H, Astarita JL, Cubas R, Jhunjhunwala S. TGFβ attenuates tumour response to PD-L1 blockade by contributing to exclusion of T cells. Nature. 2018, 554(7693):544. 10) Wang J, Sun J, Liu LN, Flies DB, Nie X, Toki M, Zhang J, Song C, Zarr M, Zhou X, Han X. Siglec-15 as an immune suppressor and potential target for normalization cancer immunotherapy. Nature medicine. 2019, 25(4):656-66.

Image/Figure: https://s3.amazonaws.com/amz.xcdsystem.com/1E8A4501-BB41-A02A-1D3B9882B798BFAA_abstract_File10351/GA283_ImageFigure_0513021352.pdf

Image/Figure Caption: Development of targeted theranostic magnetic iron oxide nanoparticles (IONP) for image-guided drug delivery and immunotherapy A PD-L1 targeting and blocking IONP (Nano-iPD-L1, 5 nm core) is produced by conjugating an engineered inhibiting peptide with two PD-L1 binding domains. A uPAR targeted stroma-penetrating theranostic IONP has stroma breaking targeting ligand consisting of an amino-terminal fragment of uPA fused with the catalytic domain of MMP14 and encapsulated Doxorubicin. NanoiPD-L1 targets PD-L1 that is highly expressed in tumor and stromal cells for targeted delivery of the immune checkpoint

inhibiting peptides. ATFmmp14 conjugated theranostic IONP allows targeting uPAR expressing endothelial cells, stromal fibroblast and macrophages, and tumor cells. Optical imaging shows co-delivery of two theranostic IONPs into the KPC pancreatic tumor cell-derived tumors. Five systemic co-administration of both IONPs results in significant inhibition of tumor growth in the KPC mouse pancreatic tumor model. Targeted delivery of theranostic IONPs in pancreatic tumors induces increased infiltration of cytotoxic CD8+ T cells.

First Name: Lily

Last Name: Yang

Email: lyang02@emory.edu

Organization: Emory University School of Medicine

Country: United States

ID: GA286
Ultrafast amplitude modulation for molecular and hemodynamic ultrasound imaging

Claire Rabut, California Institut of Technology, crabut@caltech.edu

---

Category: Instrumentation

Abstract Body : Motivation Ultrasound is playing an emerging role in molecular imaging thanks to new nanoscale contrast agents and reporter genes. Acoustic methods for the selective detection of these agents are needed to maximize their impact in biology. Existing ultrasound pulse sequences use the nonlinearity in contrast agents' response to distinguish them from linear tissue scattering [1,2,3]. However, such pulse sequences typically scan the sample using focused transmissions, resulting in a limited frame rate and restricted field of view. Meanwhile, existing wide-field scanning techniques based on plane wave transmissions suffer from limited sensitivity or nonlinear artifacts [4,5,6]. To overcome these limitations, we introduce ultrafast amplitude-modulated imaging (uAM): a nonlinear modality combining amplitude-modulated pulses, multiplane wave transmissions and selective coherent compounding. Methods Bursts of N successive tilted plane waves are repeated three times with modulated amplitudes: +1/2, +1/2 and +1 (Fig.A). After reception, the subtraction of the two half-amplitude bursts from the full amplitude burst allows the elimination of linear signal and the capture of specifically nonlinear responses. Modulated multiplane waves (MPW) bursts are then repeated N times, and for each repetition the polarities of the successive plane waves are given by the column of the Hadamard matrix of order N (Fig.B). In conventional MPW imaging, the contribution of all the Hadamard RFi data is summed to produce a coherent recombination of compounded plane wave signals [7]. We however found that the first Hadamard summation systematically leads to a pulse-inversion like summation of polarized pulses and therefore carries inappropriately time-delayed echoes in the recombined signals (Fig.C). We therefore introduced selective coherent compounding of all Hadamard RF data except the first one H1. The resulting image, for which harmonic residues at inappropriate time have been eliminated, is expected to contain (N-1) times the signal obtained with a single plane wave. We demonstrate the performance of uAM by imaging gas vesicles (GVs), an emerging class of genetically encodable biomolecular contrast agents. In vitro results We first evaluated in vitro the performance of uAM in comparison to slower gold-standard amplitude modulation sequence parabolic-AM (pAM)[2] and xAM[3] (Fig.D.E) in a tissue-mimicking phantom containing two rows of 2mm diameter wells filled with GVs. uAM achieves contrast imaging sensitivity (Fig.E) comparable to pAM or xAM (250kHz imaging framerate) but allows the recording of a significantly larger and deeper field of view (Fig.D) and at a much faster imaging framerate of 3.2 kHz. In vivo results These exceptional spatio-temporal performances enable simultaneous nonlinear and linear image formation and allow concurrent monitoring of ultrafast phenomena, such as acoustic reporter gene dynamic and blood volume variations. We therefore demonstrated in vivo the performance of uAM technique by imaging the circulation and phagolysosomal absorption of GVs. We monitored in real-time both the blood flow dynamic and the phagolysosomal function of a mouse liver after intravenous injection of GVs (Fig.F). Leveraging the ability of uAM processing to extract simultaneously both linear and

nonlinear information from the same pulse sequence, we processed two complementary sets of data (Fig.G): by applying a clutter filter to the linearly-processed uAM images, we obtained Power Doppler (PD) images of the liver, tracking the vascular enhancement due to circulating GVs (Fig.H); while the nonlinear-processed images from the same plane tracked the contrast of GVs only. AM images therefore express the population of circulating GVs, but also GVs taken up by liver tissue (Fig.I). This in vivo application highlights the capacity of uAM to provide simultaneous access to nonlinear contrast and ultrafast phenomena such as blood flow. Conclusion uAM's exceptional combination of speed, sensitivity and spatial coverage will give this pulse sequence a bright future in contrast ultrasound.

References: [1]: Shen and Li, Pulse-Inversion-Based Fundamental Imaging for Contrast Detection. IEEE Trans Ultrason Ferroelectr Freq Control (2003) [2]: Maresca et al., Nonlinear Ultrasound Imaging of Nanoscale Acoustic Biomolecules. Appl. Phys. Lett. (2017) [3]: Maresca et al., Nonlinear X-Wave Ultrasound Imaging of Acoustic Biomolecules. Phys. Rev. X (2018) [4]: Gong et al., Improved Contrast-Enhanced Ultrasound Imaging with Multiplane Wave Imaging. IEEE Trans Ultrason Ferroelectr Freq Control (2018) [5]: Gong et al., S. Delay-Encoded Harmonic Imaging (DE-HI) in Multiplane-Wave Compounding. IEEE Transactions on Medical Imaging (2017) [6]:Shen and Yan. High-Order Hadamard-Encoded Transmission for Tissue Background Suppression in Ultrasound Contrast Imaging: Memory Effect and Decoding Schemes. IEEE Transactions on Ultrasonics, Ferroelectrics, and Frequency Control (2019) [7]: Tiran et al., Multiplane Wave Imaging Increases Signal-to-Noise Ratio in Ultrafast Ultrasound Imaging. Phys. Med. Biol. (2015)

Image/Figure:

https://s3.amazonaws.com/amz.xcdsystem.com/1E8A4501-BB41-A02A-1D3B9882B798BFAA_abstract_File10351/GA286_ImageFigure_0513024810.jpg

Image/Figure Caption: Figure: A. Schematic representation of the uAM pulse sequence for N=4 angles: amplitude-modulated (AM) pulses are combined with multiplane wave transmissions and repeated four times with different polarizations (given by the columns of the Hadamard matrix of order 4). B. Raw-Frequency (RF) Data received after uAM (4 angles) transmission in an agarose phantom with a point source inclusion of GVs. C. After Hadamard summing, individual plane waves are retrieved with amplitude N, except for H1, which contains additional nonlinear echoes. Selective compounding omitting H1 enables the reconstruction of a nonlinear image sans artifact. D. In vitro evaluation of uAM-8angles performance in comparison with parabolic-AM and xAM [2,3] (2mm diameter GVs-inclusions are embedded in a tissue-mimicking phantom): we immediately observe that uAM offers the widest and deepest field of view compared to pAM and xAM. E. Contrast-to-Tissue Ratio (CTR) and Contrast-to-Artifact Ratio (CAR) for each pulse sequence. CTR=upper inclusions/upper background. CAR=upper inclusions/artifact region underneath. Err.b.± SEM (N=3) F. Schematic of the in-vivo experiment: purified GVs were intravenously injected in an anesthetized mouse, and the liver was continuously monitored with uAM. G. uAM imaging of simultaneous nonlinear and blood flow imaging to visualize mouse liver function. H. After injection, the vascular signal quickly reaches a maximum within 60 s, then decreases back to a baseline. I. Meanwhile, the AM signal progressively increases to a maximum around 600 s after the injection, corresponding to the

largest concentration of intact GVs in the liver. Macrophages then degrade the GVs, resulting in a gradual decrease towards baseline. Scale bars: 1 mm.

First Name: Claire

Last Name: Rabut

Email: crabut@caltech.edu

Organization: California Institut of Technology

Country: United States

ID: GA287

Membrane nanoarchitecture of NIR theranostic photonanomedicines dictates optics, photochemistry and tumor selective delivery in orthotopic head and neck cancer

Chanda Bhandari, University of Texas at Dallas, chanda.bhandari@utdallas.edu

---

Category: Oncology

Abstract Body : Lipid based photonanomedicines activated by NIR light are an emerging platform technology for tumor imaging and therapy as they provide advantages of tunability, high payloads of drugs and fluorophores, in addition to nanotechnology-facilitated tumor selectivity. The membranes of such NIR photonanomedicines contain lipidated photosensitizer molecules which serve as both optical imaging contrast agents and photodynamic agents. The impact that the conformation of these lipidated photosensitizer molecules has on their functionality as NIR activable theranostic nanoconstructs has not been explored to date. In this study, we modulate the membrane nanoarcitecture of these NIR photonanomedicines by engineering lipid conjugates of the clinically used photosensitizers; Benzoporphyrin Derivative (BPD) and IRDye700DX. NIR photonanomedicines containing lipid conjugated BPD are membrane-inserting and NIR photonanomedicines containing lipid conjugated IRDye700DX are membrane-protruding. Our results demonstrate that the membrane-protruding nanoarchitecture allows for 15.3-fold higher optical brightness of the NIR photonanomedicines than the membrane-inserting nanoarchitecture, provides allows up to 5-fold greater production of reactive oxygen species and allows for a 10-fold faster rate of NIR triggered drug release. On the other hand, the membrane-inserting nanoarchitecture is more potent at photodynamic destruction of head and neck cancer cells, and provides 6.3-fold greater uptake in orthotopic FaDu head and neck tumors than the membrane-protruding nanoarchitecture. Interestingly, tumor penetration was identical for both nanoarchitectures. Hence, this study provides important insights on tailoring the lipidated NIR activable photonanomedicines nanoarchitecture based on the required tumor imaging and theranostic modality.

References: 1. G. Obaid et al., "Impacting Pancreatic Cancer Therapy in Heterotypic in Vitro Organoids and in Vivo Tumors with Specificity-Tuned, NIR-Activable Photoimmunonanoconjugates: Towards Conquering Desmoplasia?," Nano Lett 19(11), 7573-7587 (2019). 2. I. Rizvi et al., "Photodynamic therapy: Promoting in vitro efficacy of photodynamic therapy by liposomal formulations of a photosensitizing agent," Lasers Surg Med 50(5), 499-505 (2018).

Image/Figure:

https://s3.amazonaws.com/amz.xcdsystem.com/1E8A4501-BB41-A02A-1D3B9882B798BFAA_abstract_File10351/GA287_ImageFigure_0513024921.png

Image/Figure Caption: Figure1: Representative FLI/uCT images of orthotopic FaDu tumors after 24hours if intravenous injection in mice.

Full Name of Abstract's 1st Author : Chanda Bhandari

First Name: Chanda

Last Name: Bhandari

Email: chanda.bhandari@utdallas.edu

Organization: University of Texas at Dallas

Country: United States

ID: GA288

In vivo Characterization of a Hybrid Hydrogel-Nanoparticle Delivery System for Cervical Cancer Therapy by Multimodal PET/CT/MRI Imaging

Mariia Kiseleva, Laval University, mariia.kiseleva.1@ulaval.ca

---

Category: New Chemistry, Materials & Probes

Abstract Body : Introduction, hypothesis, and objectives: Hydrogels are widely used in a variety of biomedical applications as localized delivery systems.[1] Gold nanoparticles (AuNPs) are being increasingly integrated into radiotherapy applications, and in this perspective, their delivery by hydrogels applied topically is gaining a lot of interest e.g. for cervical cancer therapy. [1,2] The kinetics of gel degradation is a crucial parameter since it can govern not only the release of encapsulated nanoparticles, but also the schedule of the following medical procedures. In fact, it is essential to track the biological behavior of the released AuNPs to ensure that their transit in the treatment site matches the time window for radiotherapy, followed by their rapid clearance by the renal route. In this study, these parameters were investigated quantitatively by multimodal PET/CT/MRI imaging. Therefore, the applicability of the developed hydrogel-nanoparticle formulation for localized delivery on cervical cancer was demonstrated by studying: 1) in vivo hydrogel degradation by MRI; 2) in vivo release of AuNPs and their biodistribution by PET/CT. Materials & Methods: Hydrogel: Pluronic F127 (PF127) and alginate were used as the two main components for the hydrogel preparation. AuNPs synthesis and radiolabeling: AuNPs coated with PEG and deferoxamine B (DFO) were synthesized by the adapted Brust method previosly developed in our group and characterized by TEM, DLS, and FTIR. The synthesized AuNPs were radiolabeled with zirconium-89 (t1/2 = 3.3 days) via chelator DFO by incubation with neutralized [89Zr]ZrCl4 for 1h, and purified by size-exclusion chromatography (NAP-5 columns). Purified [89Zr]Zr-AuNPs were mixed with the PF127-alginate polymer solution. Imaging: Two groups of Balb/c female mice (n=6 each) were subcutaneously injected with the PF127-alginate gel +/- AuNPs (0.1 mg/ml) and imaged by acquiring MRI scans right after injections and at 3-, 10-, and 14-days post-injection (p.i., T1-weighted spin-echo sequence, echo time/repetition time: 13.5/704.2 ms). The third group of mice (n=6) was subcutaneously injected with the same gel containing [89Zr]Zr-AuNPs (0.1 mg/ml, 3-4 MBq) and PET/CT-imaged for 30 min (t=0) or 1 hour (t=24, 48h). An ex-vivo biodistribution study was also performed (t=48h). Results: Ultra-small AuNPs were successfully synthesized with a core size -1, 1539 cm-1; amine peak: 3328 cm-1). Radiolabeling efficiency was found to be >95%, and radiochemical yield after purification was equal to 85% (decay-corrected). Upon s.c.injection in mice, the formed gels were clearly observed on MRI scans (Figure 1). The gels' volume declined rapidly in the first 3 days because of the dissolution of the PF127 component and as expected for this hydrogel system. Then, the volume continued to decrease at a slower rate until the end of the experiment. Overall, ~26% of the initial gels' volume remained at day 14 p.i. for the group injected with PF127-alginate alone, and ~20% for the group injected with the gel containing AuNPs. The PET/CT study demonstrated that [89Zr]Zr-AuNPs were rapidly released from the gel and then excreted via renal clearance ((Figure 1). Conclusion: In this study, the performance of a localized delivery system made of a PF127-alginate hydrogel and tuned to optimize the

release of AuNPs prior to radiotherapy treatments, was quantitatively evaluated in vivo in a small animal model by multimodal PET/CT/MRI imaging. The gels degraded in the first days after injection in vivo, thus releasing [89Zr]Zr-AuNPs in the vicinity of the administration site. These results confirm the potential of the hydrogel system to release radiosensitizing AuNPs on the site of cervix cancer, prior to administration of a radiotherapeutic dose, while avoiding the uptake of AuNPs to other organs (e.g. liver and spleen).

References: References: [1] F Ordikhani et al., Pharmaceutics 8 (3) (2016). [2] M Laprise-Pelletier et al., Adv. Healthc. Mater. 7 (16), 27 (2018). [3] M. B. Brust M., J. Chem. Soc., Chem. Commun., (1994)

Image/Figure:

https://s3.amazonaws.com/amz.xcdsystem.com/1E8A4501-BB41-A02A-1D3B9882B798BFAA_abstract_File10351/GA288_ImageFigure_0513025439.png

Image/Figure Caption: a) MRI scans of the mouse injected with PF127-alginate formulation right after administration and at 14-days post administration; b) PET/CT scans of the mouse injected with Pluronic F127-alginate gel containing [89Zr]Zr-AuNPs right after administration and at 2-days post administration, the gels are pointed with red arrows

Full Name of Abstract's 1st Author : Mariia Kiseleva

First Name: Mariia

Last Name: Kiseleva

Email: mariia.kiseleva.1@ulaval.ca

Organization: Laval University

Country: Canada

ID: GA289
Quantitative ex vivo 3D imaging of the human pancreas with micrometre resolution

Max Hahn, Umeå University, Sweden, max.hahn@umu.se

Category: Systemic Diseases (Kidney, Liver and Pancreas)

Abstract Body : The opportunity to quantitatively study specific cellular phenomenon of a complete human pancreas with preserved spatial 3D context would have extensive significance for pre-clinical and clinical research. For studies of human pathophysiology and underlying anatomy, a method that could selectively label full human organs would be highly desirable. A variety of mesoscopic imaging approaches are currently available for deep tissue imaging of biological samples, including optical projection tomography (OPT)1 and light sheet fluorescence microscopy (LSFM)2-4. Whereas optical 3D imaging techniques have powerfully progressed, they have remained limited due to insufficient antibody labelling within large tissue volumes. In research fields incorporating cell-loss or cell exhaustion studies, like the fate of beta cells in the pancreas in settings of diabetes, a better understanding of disease pathogenesis for the recovery of beta-cell mass is lacking. In this study, we describe a ex vivo concept that enables 3D imaging of the full human pancreas with micrometre resolution. In analogy to a 3D jig saw puzzle, entire human pancreata were sliced in a 3D printed matrix for high-throughput tissue-preparations of cm3-sized tissue cuboids, immunolabelled (against insulin), optically cleared (in BABB), 3D imaged and the resultant image data sets were computationally stitched back in 3D space. The method enabled quantification of antibody labelled cells with preserved organ context. Analysed pancreatic tissues from healthy and type 2 diabetic (T2D) donors encompassing over 200.000 islets of Langerhans provided information about normal and abnormal islet compositions, including the localization of regions with densely packed islets and, in T2D, islets with internal haemorrhaging and loss of sphericity of larger islets. The study provides 3D evidence that human islet mass may exhibit significant heterogeneities in its distribution, and it confirms stereological5 indications of the appearance of islet clusters in the periphery of the organ, be it from non-diabetic or T2D donors. Taking advantage of the autofluorescent properties of tissues as a source of contrast to outline cellular compositions or processes6,7, more specific of red blood cells, thousands of hyperaemic islets within or in colocalization with the antibody labelled regions were identified. However, the impact of these lesions on human islet physiology and whether they are specifically formed in connection with T2D remains to be elucidated. In summary, the presented method provides a mean to characterize previously unrecognized features in larger tissue volumes of the human pancreas with micrometre resolution and maintained spatial context. Further, it may be directly translated to assessments of other markers and organ systems.

References: 1. Sharpe, J. et al. Optical projection tomography as a tool for 3D microscopy 668 and gene expression studies. Science 296, 541-545, 669 doi:10.1126/science.1068206 (2002). 2. Dodt, H. U. et al. Ultramicroscopy: three-dimensional visualization of neuronal networks in the whole mouse brain. Nat Methods 4, 331-336, doi:10.1038/nmeth1036 (2007). 3. Huisken, J.,

Swoger, J., Del Bene, F., Wittbrodt, J. & Stelzer, E. H. Optical sectioning deep inside live embryos by selective plane illumination microscopy. Science 305, 1007-1009, 4. Keller, P. J., Schmidt, A. D., Wittbrodt, J. & Stelzer, E. H. Reconstruction of zebrafish early embryonic development by scanned light sheet microscopy. Science 322, 1065-1069, doi:10.1126/science.1162493 680 (2008). 5. Ionescu-Tirgoviste, C. et al. A 3D map of the islet routes throughout the healthy human pancreas. Sci Rep 5, 14634, doi:10.1038/srep14634 694 (2015). 6. onici, M. Cell and tissue autofluorescence research and diagnostic applications. Biotechnol Annu Rev 11, 227-256, doi:10.1016/S1387- 2656(05)11007-2 (2005). 7. Hahn, M. et al. Mesoscopic 3D imaging of pancreatic cancer and Langerhans islets based on tissue autofluorescence. Sci Rep 10, 18246, doi:10.1038/s41598-020-74616-6 (2020). 8. Hahn, M., van Krieken, P.P., Nord, C. et al. Topologically selective islet vulnerability and self-sustained downregulation of markers for β-cell maturity in streptozotocin-induced diabetes. Commun Biol 3, 541 (2020). https://doi.org/10.1038/s42003-020-01243-2

Image/Figure:

https://s3.amazonaws.com/amz.xcdsystem.com/1E8A4501-BB41-A02A-1D3B9882B798BFAA_abstract_File10351/GA289_ImageFigure_0922090032.jpg

Image/Figure Caption: A method for high resolution quantitative ex vivo 3D imaging of human pancreata reveals high islet density regions and intra-islet haemorrhaging. The process of tissue processing and 3D rendering as applied to the human pancreas (a). Intact fixed pancreata from diseased donors are embedded in agarose, sliced into cm3-sized tissue cuboids using a 3D printed matrix and subjected to whole mount immunolabelling and tissue clearing. The tissue cuboids are scanned individually by optical projection tomography (OPT)1. Using the autofluorescence of the tissue (grey), the resultant reconstructed tomographic data are then stitched back in 3D space to their original orientation. An example of 10 cuboids with preserved micrometre resolution display blood vessels, the main pancreatic duct and antibody labelled islets of Langerhans. Hereby, statistical analysis, islet classification and analysis on islet compositions can be performed, including 3D coordinates, volumes, and shapes of the islets in context of the entire pancreas (b). By computational image processing, islets located within 300µm from their nearest neighbour reveal the appearance of islet clusters located towards the organ's periphery. In comparison to the mean islet density, these regions display a close to threefold increase in islet density. Complementary high-resolution analysis performed by light sheet fluorescence microscopy (LSFM)2-4 confirm the presence of intra-islet haemorrhages. These islet lesions are scattered by the hundreds throughout the gland from a type 2 diabetic donor. The intra-islet autofluorescence signal was characterized by stereological post-3D imaging assessments of the exact same islets demonstrating the preservation of the tissue and verifying the signal as red blood cells.

First Name: Max

Last Name: Hahn

Email: max.hahn@umu.se

Organization: Umeå University, Sweden

Country: Sweden

ID: GA290

Optimization of Gd(III) probes for quantitative imaging of liver fibrogenesis: Impact of dual targeting groups on relaxivity, on-rate, and off-rate

Yingying Ning, Harvard Medical School, Mass General Hospital, YNING2@mgh.harvard.edu

---

Category: New Chemistry, Materials & Probes

Abstract Body : Introduction. Fibrosis is an outcome of aberrant tissue repair which can result in organ dysfunction and failure.1 Fibrogenesis is accompanied by upregulation of lysyl oxidase enzymes which catalyze oxidation of lysine e-amino groups on extracellular matrix proteins to form the aldehyde containing amino acid allysine which then undergoes cross-linking reactions. Prototype gadolinium probes functionalized with a hydrazine moiety can target allysine in vivo to quantify fibrogenesis.2-4 To optimize the sensitivity of these probes, two hydrazine groups were introduced in one molecule to increase the reaction on-rate with allysine, increase the relaxivity of the protein-bound product, and lower its off rate, and thereby increasing the sensitivity and dynamic range for noninvasive imaging of liver fibrogenesis. Results and discussions. Cis-1,4-Gd(CHyd)2 (Gd-1,4) and trans-1,7-Gd(CHyd)2 (Gd-1,7) are Gd-DOTA derivatives with two hydrazine arms but different orientation (Fig 1a). Compared to Gd-CHyd which only has one hydrazine moiety, Gd-1,4 and Gd-1,7 showed 6- and 3-fold higher initial on-rate for binding to allysine-modified BSA (BSA-Ald, Fig 1b). Relaxivity (mM-1s-1) in the presence of BSA-Ald increased from 5.0 for Gd-CHyd to 11.7 for Gd-1,4 and 9.0 for Gd-1,7 (Fig 1c). Dual binding complexes also show slower off-rate with BSA-Ald (Fig 1d). Interestingly, the cis-isomer Gd-1,4 shows a significantly higher on rate and relaxivity than the trans-isomer Gd-1,7 in the presence of BSA-Ald, revealing the importance of the orientation of targeting groups in designing dual binding probes. The difference in reactivity between these two isomers was attributed to the different binding rate of the second hydrazine arm. To support this hypothesis, Gd-1,4C which has only one hydrazine was synthesized. Gd-1,4C shows similar protein-bound relaxivity and on-rate to the monohydrazine Gd-CHyd in BSA-Ald, indicating that the improved properties of Gd-1,4 stem from both hydrazine moieties binding to allysine residues. This is further supported by the higher protein bound relaxivity for Gd-1,4 (17.7) and Gd-1,7 (18.7) compared to Gd-CHyd (11.8) and Gd-1,4C (13.7), which results from restricted internal rotation of the dual binders which promotes high relaxivity. Next, Gd-CHyd, Gd-1,4 and Gd-1,7 were tested in mice treated with CCl4 or olive oil vehicle for 12 weeks to induce liver fibrosis. Ex vivo analyses of liver hydroxyproline (collagen marker) and Sirius Red staining indicated consistent fibrosis in the CCl4 group (Fig 2a-c). Both Gd-1,4 and Gd-1,7 enhanced MRI show significantly higher liver-to-muscle contrast to noise ratio (ΔCNR) in CCl4 injured mice than Gd-CHyd, and Gd-1,4 shows significantly higher ΔCNR than Gd-1,7 (Fig 1e-f). We also compared Gd-1,4 and Gd-1,7 in the same mice, imaged 24 hours apart, and Gd-1,4 gives consistently higher ΔCNR than Gd-1,7 (Fig 2d-e). To further demonstrate the specificity of Gd-1,4 for liver fibrogenesis, a blocking study was performed using Yb-1,4 (Gd3+ ion is replaced by Yb3+, Fig 2f). Figure 1g shows ΔCNR for CCl4 injured mice imaged first with Gd-1,4 and then the next day imaged 15 minutes after a 10-fold higher blocking dose of Yb-1,4, showing a

complete block and demonstrating the specificity of Gd-1,4 for fibrotic liver. Conclusion. Rationally introducing dual binding hydrazine groups in aldehyde-reactive gadolinium probes boosts on-rate, allysine protein bound relaxivity, and lowers off-rate. Structural optimization on the orientation of targeting moieties gives Gd-1,4 as the highest sensitive probe. Gd-1,4 shows 6-fold higher reactivity, 2.3-fold higher relaxivity and 1.5-fold slower off-rate than previously published Gd-CHyd and this translates to 10-fold higher ΔCNR in vivo. This study reveals the efficiency of dual binding and the importance of orientation modulation in designing targeted MRI probes in vivo.

References: 1. Henderson, N. C., Rieder, F., & Wynn, T. A. Nature. 2020, 587, 555-566; 2. Chen, H. H., Waghorn, P. A., Wei, L., et al. JCI insight, 2017, 2, e91506; 3. Waghorn, P. A., Jones, C. M. et al. Angew. Chem. Int. Ed. 2017, 56, 9825-9828; 4. Akam, E. A., Abston, E., Rotile, N. J., Slattery, H. R., Zhou, I. Y., Lanuti, M., & Caravan, P. Chem. Sci. 2020, 11, 224-231.

Image/Figure:

https://s3.amazonaws.com/amz.xcdsystem.com/1E8A4501-BB41-A02A-1D3B9882B798BFAA_abstract_File10351/GA290_ImageFigure_0513030403.png

Image/Figure Caption: Figure 1. a) Chemical structures of Gd complexes studied in this work; b) Percentage r1 change of Gd complexes over time following incubation allysine modified bovine serum albumin, BSA-Ald; c) Relaxivity values at 60 MHz (PBS, pH 7.40, 24 h, 37°C) in the presence or absence of BSA and BSA-Ald; d) Hydrolysis of BSA-Ald bound Gd-CHyd and Gd-1,4 monitored by longitude relaxation at 60 MHz (PBS, pH 7.40, 37°C); e) Axial liver (outlined in yellow) images of CCl4 mouse imaged at pre- and 45 mins post-injection of Gd-CHyd, Gd-1,7 and Gd-1,4 (0.1 mmol/kg i.v.); f) Liver to muscle contrast to noise ratio (ΔCNR) of vehicle and CCl4 mice at 45 mins post-injection of Gd-CHyd, Gd-1,7 and Gd-1,4 (n = 6/group); g) Gd-1,4 ΔCNR in CCl4 mice before and after pretreatment with 10-fold dose of MR-silent Yb-1,4 (n = 3). *P < 0 .05, **P < 0 .01, ***P < 0 .001, ***P < 0 .001.

Full Name of Abstract's 1st Author : Yingying Ning

First Name: Yingying

Last Name: Ning

Email: YNING2@mgh.harvard.edu

Organization: Harvard Medical School, Mass General Hospital

Country: United States

ID: GA291
Quantification of biodistribution and tumor accumulation of 18F-siPSMA-14 using PET imaging in the HET-CAM model.

Jessica Loeffler, Ulm University Medical Center, jessica.loeffler@uni-ulm.de

---

Category: Oncology

Abstract Body : Objective For the evaluation of newly developed radiopharmaceuticals, the assessment of biodistribution is pivotal and usually requires animal experiments, primarily in rodents. The demand for alternative methods in compliance with the 3Rs-principles is steadily increasing. The HET-CAM (hen's egg test- chorioallantoic membrane) model might be such an alternative to the use of animal testing in initial biodistribution studies in the process of radiopharmaceutical development, thus reducing the number of required animal experiments. The aim of this study was to evaluate the quantifiability and reproducibility of HET-CAM PET data using molecular imaging of PSMA-expression as a model system. Material/Methods Tumor xenografts of a PSMA-positive (LNCaP C4-2) and a PSMA-negative cell line (PC-3) were established on the CAM. MRI and PET measurements were performed within embryonic development days 12 to 15 in n=8. MRI (BioSpec 117/16, Bruker) involved an overview scan (Flash3D) of the total egg and a high-resolution scan (RARE) of the tumor region. After i.v. application of the PSMA-specific radiotracer 18F-siPSMA-14 into a blood vessel of the CAM, dynamic PET measurements were done over 60 min (Focus 120, Siemens Medical Solutions, Inc.). MRI and PET data were superimposed and analyzed using Pmod (ver. 4.105, PMOD Technologies Ltd.). Based on the MRI data, VOIs were placed to derive the time-activity curves of the tumors and organs-of-interest. Following the PET scan, tumor xenografts were excised, and radioactivity was quantified using a γ-counter (Cobra II, PerkinElmer). The PSMA expression was verified by western blots (WB) and by additional immunohistochemical (IHC) staining. Results PSMA expression was verified by WB and IHC for LNCaP C4-2 (PSMA+) while no PSMA was detected for PC-3 (PSMA-). Based on MRI data, tumor volumes were similar for LNCaP C4-2 (29.2±9.3) mm^3 and PC-3 tumors (23.4±11.3) mm^3 (n=8). After fusion of the PET and MRI data, significantly higher accumulation of 18F-siPSMA-14 was detected in the PSMA+ LNCaP C4-2 xenografts (2.6±1.1) %IA/mL, compared to the PSMA- PC-3 (1.5±1.0) %IA/mL (p=0.01) with a ratio of PSMA+/PSMA- = 2.5±1.3. In concordance, γ-counter measurements revealed significantly higher values for LNCaP C4-2 (13.0±6.9) %IA/mL compared to PC-3 (7.5±3.0) %IA/mL (p=0.04), with a ratio of PSMA+/PSMA- = 1.7±0.8. Conclusion PET and γ-counter measurements of the HET-CAM model resulted in concordant data, successfully demonstrating a PSMA-specific accumulation of 18F-siPSMA-14. Furthermore, PET is excellently complemented by MRI for tumor volume determination and precise definition of VOIs. Thus, quantification of radiolabeled peptide accumulation with PET is possible in the HET-CAM model and the presented platform can be used for initial evaluation of new radiopharmaceuticals. The use of the HET-CAM model for the pre-selection of new radiopharmaceuticals will allow a reduction of animal experiments in accordance with the 3Rs-principles of animal welfare.

First Name: Jessica

Last Name: Loeffler

Email: jessica.loeffler@uni-ulm.de

Organization: Ulm University Medical Center

Country: Germany

ID: GA292

Uncovering the migration and homing dynamics of CD4+ T cells and phagocytes in T cell driven immune mediated inflammatory diseases by simultaneous non-invasive in vivo PET/MRI

Nannina Most, Werner Siemens Imaging Center Department of Preclinical Imaging and Radiopharmacy Eberhard Karls University of Tübingen, Germany, n.most@outlook.de

---

Category: Immunology: Inflammation & Infection

Abstract Body : Introduction: Immune mediated inflammatory diseases (IMIDs) such as rheumatoid arthritis, psoriasis, and contact hypersensitivity reactions (CHSR). are driven by interferon-y-producing CD4+ (Th1) autoantigen specific T cells. These Th1-mediated processes are classified as delayed-type hypersensitivity reaction (DTHR) and often accompanied by infiltrating neutrophils. In our studies we aimed to track the in vivo migration and homing dynamics of CD4+ T cells with Zirconium-89-desferrioxamine (89Zr-DFO) labelled CD4-minibody (IAB46; ImaginAb, USA) and of phagocytic cells (such as neutrophils) with 19F-perflurocarbon emulsion (PFC) using simultaneous Positron Emission Tomography (PET) and Magnetic Resonance Imaging (MRI) in two experimental DTHR models. Methods: We investigated K/BxN-mice which spontaneously develop polyarthritis beginning at 3-4 wks of age. In addition, C57BL/6J mice were sensitized with trinitrochlorobenzene (TNCB) at the abdomen and challenged once at the right ear to induce acute CHSR. Chronic CHRS was elicited by five repetitive TNCB-ear challenges every two days. We clinically assessed the severity of inflammation by determination of ankle- or ear-swelling. 89Zr-DFO-CD4-minibody was injected i.v. 48h and 19F-PFC 24h before examination of diseased mice. Simultaneous PET/MRI was performed in 4, 8 and 12 wks old arthritic K/BxN-mice and in TNCB-sensitized mice before, 12 and 24h after the 1st or 5th TNCB-ear-challenge. Finally, we isolated organs of interest for ex vivo biodistribution analysis, histopathology (H&E staining), immunohistochemistry (CD4, phagocytes) and flow cytometry analysis (immune cell composition and activation state). Results/Discussion: Simultaneous PET/MRI revealed an enhanced 89Zr-CD4-DFO-minibody-uptake in the inflamed front paws and ankles of K/BxN-mice peaking at the early disease stage of 4 weeks of age (n = 6). Histopathological analysis of the front paws and ankle revealed acute inflammation with an acute inflammatory infiltrate (composed mainly of neutrophils) at 4 wks and chronic inflammation at 12 wks of age composed mainly of mononuclear cells together with bone and cartilage destruction. The hind paws served as unaffected healthy control as we observed no histopathological signs of inflammation at all investigated timepoints. In contrast, we observed no 89Zr-CD4-DFO-minibody uptake in the inflamed right ears with acute CHSR but a strongly enhanced uptake in inflamed ears with chronic CHSR (n = 5). No uptake was detected in the healthy contralateral ear. Corresponding to our in vivo 89Zr-CD4-DFO-minibody-PET results, we identified strongly enriched 19F-PFC levels in inflamed joints at the early state of arthritic joint disease indicating a pronounced phagocyte infiltration. In line with our 89Zr-CD4-DFO-minibody-PET/MRI results we determined the most pronounced elevation in 19F-PFC levels in inflamed ears with chronic CHSR but not in the healthy control ears. Most importantly, our ex vivo analysis including biodistribution and CD4/phagocyte

immunohistochemistry of inflamed ears and joints confirmed our in vivo PET/MRI imaging data. Conclusion: Simultaneous tracking of the temporal dynamics of the accumulation and homing sites of CD4+ T cell and phagocytes by non-invasive in vivo PET/MRI might help to improve the evaluation of novel immunotherapeutic compounds as well as the monitoring of IMIDs. Thus, this dual 89Zr-CD4-DFO-minibody and 19F-PFC PET/MRI-based imaging approach might help to elucidate the pathogenesis experimental autoimmune diseases such rheumatoid arthritis or psoriasis. Acknowledgment: This work was supported by the Horizon2020 Programme under grant agreement n° 675417 (PET3D) and the EU/EFPIA/Innovative Medicines Initiative 2 Joint Undertaking under grant agreement n° 831514 (Immune-Image).

Full Name of Abstract's 1st Author : Nannina Most

First Name: Nannina

Last Name: Most

Email: n.most@outlook.de

Organization: Werner Siemens Imaging Center Department of Preclinical Imaging and Radiopharmacy Eberhard Karls University of Tübingen, Germany

Country: Germany

ID: GA293
Protein engineering using machine learning: evolving and optimizing reporter genes for magnetic resonance imaging

Alexander Bricco, Michigan State University, briccoal@msu.edu

---

Category: New Chemistry, Materials & Probes

Abstract Body : INTRODUCTION The development of further techniques in synthetic biology is dependent on reporter genes to generate a quantifiable response on whether the base circuit is set up correctly. Reporter genes for Magnetic Resonance Imaging (MRI) would allow genes to be measured in a non-invasive and safe manner, paving the way for translational use in human subjects. One of the best mechanisms for generating such a reporter gene is Chemical Exchange Saturation Transfer (CEST), which generates contrast without addition of outside metals and allows for the contrast mechanism to be controlled. Previous CEST reporter genes[1, 2] can be further optimized via protein evolution but have proven difficult to improve using typical protein optimization engineering methods. We hypothesized that these limitations could be overcome via application of machine learning. INNOVATION We developed the Protein Optimization Evolving Tool (POET). POET uses Genetic Programing, a method of machine learning, to identify motifs within peptides that allows them to produce MRI contrast. From these motifs POET then produces a list of peptides that are predicted to have high contrast. We then ordered the predicted peptides and evaluated them via MRI to determine how much contrast they generate. This in turn becomes new training data for POET to use to predict a new generation of peptides. This method is not only a new way of designing peptides, but due to the nature of the program, a far wider search space of peptides is analyzed, leading to the exploration of novel mechanisms to optimize the production of CEST contrast. METHODS Twelve amino acid long peptides were synthesized by Genscript (NJ) and were tested on a preclinical 7T Bruker scanner in a phantom designed specifically for this purpose. The scans used a modified RARE sequence with a TR of 10000 ms and a TE of 4.74 ms. Saturation was performed with 4.7 μT pulse for 4000 ms. In these experiments POET was used to optimize for contrast at 3.6 ppm, but could be used to optimize for any given frequency. RESULTS & DISCUSSION This process has been used over the course of eight generations and has produced peptides with MRI contrast up to four times higher than previously Poly-L-Lysine (PLL; Figure, top panel, Red line) which is the gold standard for peptide based contrast at 3.6ppm [3]. Further, this mechanism has shown the ability to discover new peptides that have challenged the current understanding about what chemical properties allow MRI contrast to be generated. Although the training data, and prior research was focused on peptides that were both positively charged and basic, POET had led to the discovery of CEST agents that are neutral in charge and pI, but produce more contrast than PLL (Figure, bottom panel). CONCLUSION This process allows for a wider search space of peptides to be analyzed than via directed evolution and for developing proteins that challenge current theories about how CEST contrast works. This will aid future research into peptides used to generate CEST contrast as well as developing short peptides to fill a variety of other functions. This study demonstrates how protein engineering using machine learning can be leveraged to develop new molecular imaging probes

References: ACKNOWLEDGMENTS: 1. Gilad, A.A., et al., Artificial reporter gene providing MRI contrast based on proton exchange. Nat Biotechnol, 2007. 25(2): p. 217-219. 2. Perlman, O., et al., Redesigned reporter gene for improved proton exchange-based molecular MRI contrast. Scientific Reports, 2020. 10(1): p. 20664. 3. Goffeney, N., et al., Sensitive NMR detection of cationic-polymer-based gene delivery systems using saturation transfer via proton exchange. J Am Chem Soc, 2001. 123(35): p. 8628-9.

Image/Figure:

https://s3.amazonaws.com/amz.xcdsystem.com/1E8A4501-BB41-A02A-1D3B9882B798BFAA_abstract_File10351/GA293_ImageFigure_0513031644.png

Image/Figure Caption: Top: CEST MRI contrast (MTRasym) is plotted by generation for peptides developed by using POET. Bottom: the MTRasym is plotted as a function of the isoelectric point (pI) if each peptide. The black circles represent the training data, and demonstrate CEST contrast produced by peptides. The red squares represent peptides generated by POET. These reveal a new class of peptides that provide superior CEST contrast but have neutral pI. This is in contrasts to the accepted dogma that only positively charged peptides are good CEST agents. In both graphs the MTRasym is normalized against the contrast generated by K12 (PLL) in the same experiment to provide a consistent comparison across experiments.

Full Name of Abstract's 1st Author : Alexander Bricco

First Name: Alexander

Last Name: Bricco

Email: briccoal@msu.edu

Organization: Michigan State University

Country: United States

ID: GA294
89Zr-Anti-IgM radiotracer for the early detection of infectious processes by immunoPET imaging

Mario González-Arjona, Fundación para la Investigación Biomédica del Hospital Gregorio Marañón, mgarjona@hggm.es

---

Category: Immunology: Inflammation & Infection

Abstract Body : Introduction: Nowadays bacterial infections represent a major threat globally, especially in healthcare facilities [1]. Current diagnostic tools require invasive biopsy samples from the patient and, in some cases they are not able to localize the infective foci. Imaging techniques, especially nuclear imaging, offer the advantages of being non-invasive techniques with high sensitivity and specificity. However, the gold standard PET radiotracer 18F-FDG struggles to distinguish between infected and inflamed tissue, due to non-specific uptake of macrophages and neutrophils in inflamed regions [2-5]. To overcome these limitations, we have focused our work on the development of a novel radiotracer selective to IgM, the first class of antibody that appears as a primary infection response and the most abundant during early stages of the disease [6]. This works presents a radiolabeled anti-IgM immunoconjugate for the non-invasive and early detection of infectious processes by immunoPET imaging. Methods: Anti-IgM antibody was conjugated with ten-fold molar excess of p-SCN-Bz-DFO (30min, 37ºC, PD-10 column), radiolabeled with 2-3 mCi of 89Zr-oxalic acid (1h, RT) and filtered using 100kDa-Amicon [7] (figure 1A). Purity and specific activity were assessed by iTLC and Bradford-Coomassie. In vitro stability in PBS was measured by iTLC. Blood circulation half-life was carried out in SD rats by blood extraction (2 weeks). Infected/non-infected animal model was performed by injection of active and heat-killed S. aureus intramuscularly into the left and right paw, respectively. In vivo PET/CT imaging was performed in animal models at 1h, 24h, 48h and 72h post-injection (p.i.). As control study, 18F-FDG PET/CT imaging was performed 96h post-infection (1 mCi, 200 µL 1X PBS). Ex vivo biodistribution study was performed after imaging, 72h post-injection of the radiotracer. Finally, autoradiography and immunohistochemistry were performed to confirm PET/CT results. Results/Discussion: 89Zr-DFO-anti-IgM was successfully synthetized with a maximum radio-chemical yield of 83%, 94% of purity level and a specific activity of 12.55 ± 4.16 mCi/mg. Stability studies in PBS showed a 7.8 ± 4.3% degradation of the tracer after 48h and 19.6 ± 0.5% after 72h. Pharmacokinetic evaluation confirmed an hepatobiliary metabolism of the antibody, as expected of molecules Conclusion: We have synthesized and fully characterized the specific immunoPET tracer 89Zr-DFO-anti-IgM for infection detection based on radiolabeled anti-IgM antibody. In vivo PET/CT assessment of the probe and further ex vivo studies have confirmed its ability to selective detect the active infectious processes and avoid false positives by inflammatory uptake, improving the diagnostic capacity in comparison to the commercial 18F-FDG in an infected/non-infected model.

References: 1. Widmer, E.; Que, Y.-A.; Entenza, J.M.; Moreillon, P. New concepts in the pathophysiology of infective endocarditis. Current infectious disease reports 2006, 8, 271-279. 2.

Brøndserud, M.B.; Rosenvinge, F.S.; Høilund-Carlsen, P.F.; Hess, S. Clinical value of FDG-PET/CT in bacteremia of unknown origin with catalase-negative gram-positive cocci or Staphylococcus aureus. European Journal of Nuclear Medicine and Molecular Imaging 2019, 46, 1351-1358. 3. Giraudo, C.; Evangelista, L.; Fraia, A.S.; Lupi, A.; Quaia, E.; Cecchin, D.; Casali, M. Molecular Imaging of Pulmonary Inflammation and Infection. International Journal of Molecular Sciences 2020, 21, 894. 4. Wei, W.; Rosenkrans, Z.T.; Liu, J.; Huang, G.; Luo, Q.-Y.; Cai, W. ImmunoPET: Concept, Design, and Applications. Chemical Reviews 2020, 120, 3787-3851. 5. Ordonez, A.A.; Sellmyer, M.A.; Gowrishankar, G.; Ruiz-Bedoya, C.A.; Tucker, E.W.; Palestro, C.J.; Hammoud, D.A.; Jain, S.K. Molecular imaging of bacterial infections: Overcoming the barriers to clinical translation. Science translational medicine 2019, 11, eaax8251. 6. Alberts, B.; Johnson, A.; Lewis, J.; Walter, P.; Raff, M.; Roberts, K. The Adaptive Immune System. In Molecular Biology of the Cell 4th ed.; Garland Science: 2002. 7. Vosjan, M.J.; Perk, L.R.; Visser, G.W.; Budde, M.; Jurek, P.; Kiefer, G.E.; Van Dongen, G.A. Conjugation and radiolabeling of monoclonal antibodies with zirconium-89 for PET imaging using the bifunctional chelate p-isothiocyanatobenzyl-desferrioxamine. Nature protocols 2010, 5, 739-743.

Image/Figure:

https://s3.amazonaws.com/amz.xcdsystem.com/1E8A4501-BB41-A02A-1D3B9882B798BFAA_abstract_File10351/GA294_ImageFigure_0513031813.jpg

Image/Figure Caption: Figure 1. A) Conjugation and radiolabeling of 89Zr-DFO-anti-IgM. B) Longitudinal in vivo PET/CT imaging of 89Zr-DFO-Anti-IgM at 1h, 24h, 48h and 72h post-injection, and 18F-FDG at 96h post-infection. C) PET images quantification, expressed as mean SUV. D) Ex vivo biodistribution of animals injected with 89Zr-DFO-Anti-IgM expressed as % ID/g.

Full Name of Abstract's 1st Author : Mario González Arjona

First Name: Mario

Last Name: González-Arjona

Email: mgarjona@hggm.es

Organization: Fundación para la Investigación Biomédica del Hospital Gregorio Marañón

Country: Spain

ID: GA296
DeepNI: A cloud computing system for deep learning-based neural image analysis

Zi-Min Weng, University of Alabama at Birmingham, zimin99@uab.edu

---

Category: Computational & Data Science

Abstract Body : Overview: There is a growing number of deep learning-based methods for the processing, classification, identification, and quantification of neural images. As more and more open-source deep learning models are being shared in the open domain, making such models easily accessible and useable for researchers of all levels of computer skills has been an important task as we aim to promote the usage of such advanced computational methods. We present a software platform, DeepNI, that facilitates an easy and fast deployment of deep learning-based neural image processing and analysis tools. Objective: DeepNI, where NI stands for neuroimaging, is an open-source software based on cloud-computing developed with MATLAB with the following objectives: 1) To establish a cloud computing system equipped with graphical processing units (GPUs) to implement deep learning computation of classification, segmentation, and detection tasks on neural imaging. 2) To build up a MATLAB-based user-friendly graphic user interface (GUI) for easy and intuitive operations for image processing. 3) To deploy a reliable data transmission and communication between cloud computing server and multiple clients. Method: DeepNI[1] is implemented with MATLAB as the client-end and server-end programs. For the client-end programs, a GUI is developed for data import, job submission, job status checking and data retrieval upon completion of the deep learning-based image processing tasks. A view is also included for results verification and evaluation. For the server-end programs, we have implemented the job handling through the MATLAB Job Manager toolbox [2] as the communication component in DeepNI to transmit jobs and results between the server and clients through the Transmission Control Protocol (TCP) and to manage multiple jobs from clients for the computing processes. The server is established on the Google cloud platform with virtual instances that are equipped with GPU resources. Result: DeepNI has been implemented and currently shared on GitHub for free academic use. Multiple deep learning models have been integrated into DeepNI as more new models being added into our system. More advanced functions, such as a web-based user interface, will continue to be added into DeepNI in order to further stimulate the testing and evaluation of deep learning models for neural image processing and analysis.

References: [1] DeepNI: https://github.com/IQMLatUAB/DeepNI [2] MATLAB job manager: https://github.com/bronsonp/matlab-job-manager

Image/Figure:


https://s3.amazonaws.com/amz.xcdsystem.com/1E8A4501-BB41-A02A-1D3B9882B798BFAA_abstract_File10351/GA296_ImageFigure_0513051328.PNG

Image/Figure Caption: DeepNI Viewer GUI of deep learning human brain segmentation result.

Full Name of Abstract's 1st Author : Zi Min Weng

First Name: Zi-Min

Last Name: Weng

Email: zimin99@uab.edu

Organization: University of Alabama at Birmingham

Country: United States

ID: GA297

The chick chorioallantoic membrane tumor model: quantifying therapeutic agent delivery with multispectral paired-agent imaging

Veronica Torres, Dartmouth College, veronica.c.torres@dartmouth.edu

---

Category: Oncology

Abstract Body : Tumor heterogeneity limits the efficacy of population-based cancer therapeutics. Head and neck squamous cell carcinomas (HNSCC) are particularly heterogenous, and as a result, have poor prognosis for patients with locally advanced disease (It has been demonstrated that paired-agent imaging (PAI) is both highly sensitive and specific in quantifying cell-surface receptor concentrations3. Here, we extend the same principles to cell-penetrating agents for quantification of intracellular drug binding – intracellular PAI (iPAI) – in a chick chorioallantoic membrane (CAM) xenograft assay. Fertilized chicken eggs were incubated over a 14-day period, during which time eggshells were windowed and pieces of ~1-mm3 A431 human HNSCC xenografts (grown subcutaneously in athymic nude mice) were implanted on the surface of the CAMs. For imaging, a 100 μL fluorescent cocktail (intracellular targeted agent: 6.8 μM Erl-SiTMR; intracellular control agent: 6.8 μM Erl-TMR; extracellular targeted agent: 3.4 μM ABY-029 – IRDye 800CW conjugated to anti-EGFR Affibody molecule; extracellular control agent: 0.3 μM IRDye 680LT conjugated to Imaging Agent Control Affibody molecule) was intravenously injected. Multispectral images (550-700 nm and 650-850 nm in 5 nm increments) were collected using the Maestro fluorescence imaging system in 10-minute intervals over two hours. Post-acquisition, motion correction and a spectral unmixing routine were employed to isolate the relative contributions of each of the PAI and iPAI agents, and a ratiometric calculation of binding potential (BP) – proportional to EGFR concentration – was performed. Results demonstrated that all four imaging agents could be spectrally unmixed using a linear least squares fitting approach. Figure 1(a) shows a representative fluorescence spectrum from a tumor region collected 1 h post-injection along with the spectral fit and individual unmixed fluorophore signals. Performing this on a pixel-by-pixel basis produced images of each agent's tissue distribution, and permitted calculation of BP maps, i.e., intracellular and extracellular protein receptor availability [Fig. 1(c)]. Interestingly, iPAI and PAI findings had opposite signal intensities in the tumor regions that resulted in an unexpected negative intracellular BP. This may be attributed to necrosis [Fig. 1(b)] in the bulk of the tumor (where most of the iPAI and PAI BP inconsistencies were), whose effects were amplified since the intracellular agents emit in the dominant blood-absorbing region. Therefore, it is likely that autofluorescence was the signal shown in the TMR channel of the tumors because of the lack of blood flow, while surrounding signal was being suppressed by blood. Extracellular BP results on the other hand were more consistent with what was expected where BP was highest in the tumor regions. Further investigation into egg hemodynamics and accounting for blood absorption are currently being investigated (supplementary), but these initial findings support the potential for the CAM model to provide measures of therapeutic agent delivery and ultimately response.

References: 1. C. R. Leemans et al., Nat Rev Cancer 11, 9-22, 2011 2. V. Vigneswara and A. Kong, Ann Oncol, 29(4), 794-796, 2018 3. K. M. Tichauer et al., Mol Imaging Biol, 14(5), 584-92, 2012

Image/Figure:

https://s3.amazonaws.com/amz.xcdsystem.com/1E8A4501-BB41-A02A-1D3B9882B798BFAA_abstract_File10351/GA297_ImageFigure_0513032457.png

Image/Figure Caption: Figure 1. (a) Representative spectral unmixing of fluorescence signal from a tumor region. Left: measured and fitted data. Right: unmixed signal from independent fluorophores. (b) White light image of CAM with tumors indicated with arrows. The dashed box shows the presented H&E and IHC regions. (c) Intracellular (top row) and extracellular (bottom row) spectrally unmixed fluorescent images and corresponding binding potential maps.

First Name: Veronica

Last Name: Torres

Email: veronica.c.torres@dartmouth.edu

Organization: Dartmouth College

Country: United States

ID: GA298

High Efficiency CRISPR Editing of Chimeric Antigen Receptor T (CAR-T) Cells Expressing Human-Derived MRI and PET Reporter Genes

John Kelly, University of Western Ontario, jkell5@uwo.ca

Category: Bioengineering, Synthetic Biology and Basic Biology

Abstract Body : Introduction: Chimeric antigen receptor T (CAR-T) cells have shown remarkable efficacy in treating blood-based cancers1. However, current challenges of these transformative therapies include low effectiveness in many patients, cell accumulation in normal tissues leading to serious side effects, and insufficient migration into and treatment of solid tumours. Translationally relevant imaging technologies that allow one to monitor the fate of CAR-T cells could enable prediction of patient response and side effects, as well as better evaluation of new CAR-T designs. We recently developed our second-generation CRISPR system for editing cancer cells with multimodality imaging reporter genes at the AAVS1 safe harbor2. However, this system was too inefficient for editing primary cells aimed for clinical use. Our objective in this study was to develop a highly efficient CRISPR system for editing human T cells with multiple transgenes at loci known to improve both safety and efficacy, whilst also making them "visible" with clinically relevant modalities. First, as described previously3, to improve CAR-T cell potency and delay exhaustion, we edited T cells at the TRAC locus to knock-in a CAR and simultaneously knock-out the endogenous T cell receptor (TCR). We then incorporated human MRI, PET or preclinical bioluminescent reporter genes into our CRISPR system for molecular-genetic imaging of edited CAR-T cells. Methods: T cells were nucleofected with ribonucleoprotein complexes (RNPs) that cut genomic DNA at the TRAC or AAVS1 loci. Adeno-associated virus (AAV) particles containing CD19CAR and/or the organic anion transporting polypeptide 1B3 (OATP1B3) MRI reporter gene, sodium iodide symporter (NIS) PET reporter gene or Akaluc bioluminescent reporter gene were used as DNA donors. A truncated human LNGFR gene was also included for magnetic bead sorting of edited cells. Editing efficiency was determined by flow cytometry and integration by PCR analysis. CD19+ human B cell lymphoma (NALM6) cells expressing firefly luciferase (FLuc) were engineered for CAR-T targeted kill assays. Uptake of the PET tracer [18F]tetrafluoroborate was measured with a gamma counter. Uptake of the MRI contrast agent Gd-EOB-DTPA was determined using a 3T clinical MRI scanner. Results: Initial experiments showed >85% GFP+/TCR- editing efficiency when targeting CD19CAR-GFP to the TRAC locus (Figure 1A, B). T cells edited at the AAVS1 locus showed pre-sort efficiencies of ~21% for OATP1B3-LNGFR and ~50% for NIS-LNGFR (Figure 2A, B), which increased to 80-95% purity post-magnetic LNGFR sorting. Junction PCR analysis confirmed that the CAR and reporter genes were inserted at the correct loci. NIS- and OATP1B3-edited T cells showed significant uptake of their respective tracer ([18F]tetrafluoroborate) and contrast agent (Gd-EOB-DTPA) (Figure, 2C, D). Multiplexed editing with both CD19CAR and reporter genes together produced TCR-/LNGFR+ cell populations, which effectively killed NALM6 cells (Figure 3). These data indicate that both the CAR and reporter gene components were functional in single and double-edited T cells. To improve efficiency, all-in-one AAV vectors containing CD19CAR-OATP1B3, -NIS or -Akaluc

were constructed and targeted to the TRAC locus (Figure 4A). Correct integration and bioluminescence signal for CD19CAR-Akaluc edited cells was confirmed (Figure 4B). In addition, only TRAC RNP and all-in-one AAV edited T cells killed NALM6 cells, whereas those without the CAR did not (Figure 4C). These data indicate that both the CAR and reporter genes are functional using an all-in-one approach. Conclusion: Our work demonstrates the first CRISPR-Cas system for highly efficient editing of cancer-killing CAR-T cells with clinically relevant human reporter genes. Ongoing efforts are extending these studies to MRI and PET of edited CAR-T cells in preclinical mouse cancer models. These advanced CRISPR tools should have broad utility for co-editing primary cells with therapeutic genes and reporter genes to make trackable therapeutic cells with improved efficacy and safety profiles.

References: 1) Vitale, C. and Strati, P., Frontiers in Oncology, 2020. 2) Kelly J.J. et al., Science Advances, 2021. 3) Eqyuem J. et al., Nature, 2017.

First Name: John

Last Name: Kelly

Email: jkell5@uwo.ca

Organization: University of Western Ontario

Country: Canada

ID: GA299

Exploring sensitivity and resolution for cell tracking with magnetic particle imaging: the effects of cell proliferation and intracellular nanoparticle relaxation

Maryam Berih, Western University, mberih@uwo.ca

Category: Instrumentation

Abstract Body : Introduction: Magnetic resonance imaging (MRI) cell tracking can be used to monitor the fate of cells labeled with superparamagnetic iron oxide (SPIO) nanoparticles. One limitation of this method is the inability to track proliferative cells long-term due to dilution of the SPIO amongst cell progeny1-3. This is particularly concerning for tracking rapidly dividing cells (cancer). Magnetic particle imaging (MPI) is an emerging modality which directly detects SPIOs. In vivo we expect to be able to track proliferation of SPIO labeled cells with MPI as long as the cells and progeny remain in the same field of view. To begin to study this, our first aim is to quantify the dilution of SPIOs in breast cancer cells in vitro using MPI. MPI signal is generated from a combination of Néel (internal rotation of magnetization) and Brownian (physical rotation of nanoparticle) relaxation. Brownian relaxation of SPIO is influenced by the nanoparticle's surroundings and we hypothesize this may have implications for detecting partially immobilized intracellular SPIOs. A second aim is to determine how MPI signal and resolution change when SPIOs are intracellular (live cells) compared to free SPIOs (lysed cells). Methods (Aim 1): 4T1 murine breast cancer cells were labeled in vitro by co-incubation with 55 g Fe/mL ferucarbotran, with heparin and protamine sulfate4. Triplicate samples of 1x106 ferucarbotran-labeled 4T1 cells were collected after 24 hours (day 0), and the remaining cells were returned to culture. After 22 hours (day 1), 1x106 ferucarbotran-labeled cells were collected again, and this was repeated at 41 hours (day 2). MPI of cells was acquired on a Momentum MPI in 2D using dual-channel 5.7T/m gradients and excitation of 20mT (X-channel) and 26mT (Z-channel). Each day, a cytospin of 4T1 cells was performed and cells were stained for iron with Perl's Prussian blue (PPB). Methods (Aim 2): Mesenchymal stem cells (MSC) were labeled using the same protocol. Three samples of 2.5x105 ferucarbotran-labeled MSC were collected. MP relaxometry using rf amplitude 20mT and bandwidth 160mT was conducted for 3 samples of ferucarbotran and ferucarbotran-labeled MSC. MSC were lysed with 70L RIPA buffer then sonicated. Relaxometry was repeated for lysed cells. Sensitivity was evaluated by normalizing curves by sample iron mass and resolution was evaluated by measuring the full-width half maximum (FWHM). Results (Aim 1): MPI signal was reduced and PPB stain revealed less iron content in proliferating cells over two days (Fig A). The iron content in 4T1 cells (measured by MPI) decreased by 68% from day 0 to day 1 ($p < 0.01$) and by 93% on day 2 ($p < 0.0001$) (Fig B). (Aim 2): MP relaxometry revealed a 44% reduction in sensitivity ($p < 0.01$) and increased FWHM by a factor of 2 ($p < 0.001$) as ferucarbotran was incorporated into cells. Following sonication of cells, sensitivity was significantly recovered ($p < 0.01$, Fig C, D). Conclusion: A reduction in MPI signal was measured from SPIO-labeled 4T1 cells following proliferation in vitro. Our measurements of intracellular iron are in close agreement with a theoretical reduction of 66% (day 1) and 87% (day 2). Future work will examine this in vivo. As ferucarbotran was incorporated into MSC, a reduction in MPI sensitivity and resolution

were measured; this is likely related to increased Brownian relaxation times of intracellular SPIO5-7. With cell lysis, the MPI signal is recovered. This indicates a loss in MPI sensitivity is induced by cellular uptake of ferucarbotran. For a standard 5.7T/m gradient, the reduction in resolution is equivalent to 1.6mm (free iron) compared to 3.2mm (intracellular iron). MPI cell tracking is in its infancy and these studies contribute important knowledge towards monitoring proliferative cells in vivo and optimizing resolution and sensitivity for cell detection.

References: 1. Makela et al. Sci. Rep (7). 2017. 2. Arbab AS et al. Radiology. 2003. 3. Foster PJ et al. Neoplasia (10). 2008. 4. Economopoulos V et al. Transl. Oncol. (6). 2013. 5. Zheng et al. Sci Rep. (5). 2015 6. Saritas EU et al. J Magn Reson (229). 2013 7. Suzuka H et al. J Nanosci Nanotechnol (19). 2019. 8. Arami et al. Med Phys (40). 2013.

Image/Figure: https://s3.amazonaws.com/amz.xcdsystem.com/1E8A4501-BB41-A02A-1D3B9882B798BFAA_abstract_File10351/GA299_ImageFigure_0513035741.jpeg

Image/Figure Caption: Figure 1: (A) MPI signal for 1 x 106 ferucarbotran-labeled 4T1 cells is reduced after collection from culture over 3 consecutive days. PPB stain exhibits sufficient labeling of cells with ferucarbotran labeling (day 0), and reduced iron content as cells proliferate in culture (day 1 and 2). (B) Iron mass per cell, measured by MPI, was significantly reduced over time. (C) Relaxometry curves for ferucarbotran and 2.5 x 105 live and lysed ferucarbotran-labeled MSC. (D) The peak MPI signal (sensitivity) was significantly higher for free ferucarbotran and ferucarbotran released from lysed cells, compared to ferucarbotran-labeled cells. The FWHM was increased in live and lysed ferucarbotran-labeled cells, compared to free ferucarbotran. * $p < 0.05$, ** $p < 0.01$, *** $p < 0.001$.

First Name: Maryam

Last Name: Berih

Email: mberih@uwo.ca

Organization: Western University

Country: Canada

ID: GA300

Effect of (2-hydroxypropyl)-β-cyclodextrin on the solubility and in vivo behavior of the myocardial perfusion imaging agent [18F]FRho6G-DEG

James Inkster, Division of Nuclear Medicine & Molecular Imaging, Boston Children's Hospital/Harvard Medical School, James.Inkster@childrens.harvard.edu

---

Category: Cardiovascular & Pulmonary

Abstract Body : Objectives: [18F]FRho6G-DEG is an 18F-labeled analogue of rhodamine 6G that is taken up by mitochondria-rich cells such as cardiomyocytes and as such is being developed as a myocardial perfusion PET imaging agent.[1] In swine, [18F]FRho6G-DEG shows a high first-pass extraction fraction (84%) that is independent of flow. However, human PET studies using 10% EtOH/saline as the vehicle resulted in tracer accumulation in the IV apparatus and vein, along with suboptimal uptake into heart vs. liver. These phenomena might be related to tracer solubility and/or the formation of aggregates. If so, an alternative drug formulation might positively modulate [18F]FRho6G-DEG biodistribution. With this in mind, we chose to assess propylene glycol (PG) as a clinically approved alternative to EtOH in the final formulation. We also investigated the use of (2-hydroxypropyl)-β-cyclodextrin (HPβCD) as an excipient, because rhodamine 6G can form an inclusion complex with HPβCD.[2] Methods: [18F]FRho6G-DEG was obtained from its tosylated precursor via a standard nucleophilic aliphatic 18F-fluorination reaction.[3] The tracer was HPLC-purified, extracted via tC18 solid-phase extraction cartridge, and eluted with EtOH. Fractions of [18F]FRho6G-DEG solution were concentrated under Ar, then resolubilized as reported in Table 1. The extent of aggregation was estimated by filtration of [18F]FRho6G-DEG in various matrices through 0.2 μm microcentrifuge filters (14,000 rcf, 5 min), and protein binding was assessed in the same matrices by ultrafiltration (30,000 MW cutoff, Table 1).[4] Non-specific membrane binding (NSB) was estimated using formulations incubated in PBS and these factors were used to correct % free fractions in serum. Sprague-Dawley rats were injected with [18F]FRho6G-DEG in Matrices B-E and μPET images were acquired over 60 min. Results: The use of 30% HPβCD as excipient and/or 40% PG as solvent caused a marked increase in % activity passing through 0.2 μm filters, indicating enhanced solubility. A small increase in % free fraction of [18F]FRho6G-DEG in serum was observed using solvent matrices containing 30% HPβCD (Matrices C & E) vs. those without HPβCD (Matrices B & D). Dynamic PET images (5-min intervals) of [18F]FRho6G-DEG in rats suggest that when using 10% EtOH/saline as the solvent, the presence of 30% HPβCD has little effect on the ratio of activity concentration (Ac) in the left ventricle (LV) vs. liver at later time points (3.0 vs. 3.1 at 55-60 min). A heart:liver ratio of 2.7 was observed when using 40% PG/saline alone. However, when 30% HPβCD was used in conjunction with 40% PG/saline, the observed ratio increased to 5.1. Matrix Formulation % Activity through filtera % free fraction in serum±SDb Ac(LV)/Ac(liver)c 0-5→55-60 min A PBS (pH 7.4) 7.7 22.9±3.6d - B 10% EtOH/saline 28.5±5.1d 26.4±1.7e 0.53→3.0 C 10% EtOH/saline with 30% HPβCD 79.7±2.5d 40.7±1.6e 0.55→3.1 D 40% PG/saline 91.5±2.1e 30.8±3.8d 0.35→2.7 E 40% PG/saline with 30% HPβCD 92.3±2.8e 40.9±4.7d 0.61→5.1 Table 1. a0.2 μm pore size. bCorrected for NSB. cAcs in kBq/cc. dn = 5. en = 3. Conclusion: The

solubility of [18F]FRho6G-DEG in 10% EtOH in saline was improved by the addition of 30% HPβCD, but greater improvement was observed with the use of 40% PG in saline as solvent, either with or without HPβCD. All three of these alternative formulations also decreased protein binding. As observed in μPET scans, the use of 30% HPβCD in 40% PG/saline results in higher heart:liver ratios from 0-60 min compared with 10% EtOH/saline, 10% EtOH/saline with 30% HPβCD, or 40% PG/saline only. The relationship between solvent matrices, complexing excipients, and the biodistribution of radiopharmaceutical candidates bearing the rhodamine scaffold remains incompletely understood, but additional investigations of this system are ongoing.

References: [1]M.D. Bartholoma et al., Nucl. Med. Biol. 2015, 42, 796. [2]S. Bakkialakshmi and T. Menaka, Spectrochim. Acta A 2011, 81, 8. [3]J.A.H. Inkster et al., MedChemComm 2017, 8, 1891. [4]N. Amini et al. J. Pharm. Biomed. Anal. 2014 98, 140

Image/Figure:

https://s3.amazonaws.com/amz.xcdsystem.com/1E8A4501-BB41-A02A-1D3B9882B798BFAA_abstract_File10351/GA300_ImageFigure_0513033332.jpg

Image/Figure Caption: Figure 1. a) [18F]FRho6GDEG. B) Composite (0-60 min) PET images (rat) of [18F]FRho6GDEG in 40% PG with (b) and without (c) 30% HPβCD. Purple arrow = heart, orange arrow = liver.

Full Name of Abstract's 1st Author : James Andrew Howard Inkster

First Name: James

Last Name: Inkster

Email: James.Inkster@childrens.harvard.edu

Organization: Division of Nuclear Medicine & Molecular Imaging, Boston Children's Hospital/Harvard Medical School

Country: United States

ID: GA301

Prostate Specific Membrane Antigen Targeted Dextran as a PD-L1 siRNA carrier for Prostate Cancer Specific Immunotheranostics

Zhihang Chen, Johns Hopkins University, zchen19@jhu.edu

Category: Oncology

Abstract Body : Immune checkpoint inhibitors are providing novel opportunities for exploiting the immune system to destroy cancer cells. The availability of siRNA as gene-specific silencing agents makes them promising agents in single or multiplexed immune checkpoint blockade, especially if these can be specifically delivered to cancer cells to avoid the autoimmune complications of antibody based checkpoint blockade. Because prostate-specific membrane antigen (PSMA) is abundantly expressed on the surface of castrate-resistant prostate cancer (PCa), here we have developed an ~20 nm diameter PSMA-targeted biodegradable dextran nanoparticle (NP) to deliver PD-L1 siRNA to PSMA expressing PCa cells. A schematic representation of the NP structure is shown in Figure 1A. In the NPs, small molecules containing amine groups were conjugated to the dextran scaffold through acetal bonds that were cleaved in weak acid conditions, meanwhile the small molecular PSMA targeting moieties were conjugated to the dextran through polyethylene glycol (PEG) linker. Imaging and therapy studies with the NP were performed with PC3-PIP cells that overexpress PSMA, and with PC3-PIP cells treated with ZJ-43, which is a PSMA blocking agent. Cell imaging studies indicated that the cellular uptake of siRNA NPs in PC3-PIP cells was much higher than that in PC3-PIP cells treated with ZJ-43 (Figure 1B-left). The measurement of fluorescence by flow cytometry confirmed these results (Figure 1B-right). mRNA and protein analysis indicated that PD-L1 siRNA dextran NPs reduced PD-L1 levels in PC3-PIP cells but not in PC3-PIP cells with PSMA blocked with ZJ-43 (Figure 1C). Our data confirm that PSMA targeted dextran NPs can be used as a safe siRNA carrier to effectively reduce PD-L1 expression specifically in PSMA expressing PCa cells. Supported by P41 EB024495, R01 CA253617, P30 CA006973, R35 CA209960, R01 CA134675

Image/Figure:

https://s3.amazonaws.com/amz.xcdsystem.com/1E8A4501-BB41-A02A-1D3B9882B798BFAA_abstract_File10351/GA301_ImageFigure_0513033525.jpg

Image/Figure Caption: Figure 1A: Schematic representation of the nanoparticle structure. B: Live-cell laser confocal fluorescence microscopy of PC3-PIP cells incubated with siRNA dextran NPs displayed as without or with bright field overlay. C: Relative fluorescence intensity of the siRNA dextran NPs in PC3-PIP cells under different treatment conditions (concentration of siRNA: 100 nM; N/P ratio: 15, incubation time:2h). D: Changes in mRNA levels in PC3-PIP cells following different siRNA treatments. (siRNA concentration: 100 nM; N/P ratio: 15; Incubation time: 24h; Values represent Mean ± SD (n = 3). mRNA levels were normalized to untreated cells. E: Representative immunoblot assays of PD-L1 expression in PC3-PIP cells

under different treatment conditions (1: control; 2. 48 hours PD-L1siRNA Dextran NP treatment; 3. 48 hours PD-L1siRNA Dextran NPs + ZJ-43 treatment).

First Name: Zhihang

Last Name: Chen

Email: zchen19@jhu.edu

Organization: Johns Hopkins University

Country: United States

ID: GA302
Hyperpolarized MR imaging of ascorbate-mediated oxidative stress in cancer

Nathaniel Kim, Memorial Sloan Kettering Cancer Center, kimn1@mskcc.org

---

Category: Oncology

Abstract Body : Introduction Tumor progression and survival is driven by genetic mutations and environmental conditions. Recent work has revealed that redox metabolism is deregulated in pancreatic cancer and may provide new opportunities for diagnosis and targeted treatment. Specifically, a therapeutic strategy for targeting KRAS mutant cancers using high dose ascorbate was introduced to disrupt redox homeostasis.1 While targeted therapeutic strategies have been introduced, methods to monitor the metabolic reprogramming of redox homeostasis are critically needed. We sought to identify hyperpolarized DHA (HP DHA)2 as an imaging agent for monitoring oxidative stress in patient derived xenograft models (PDXs) of cancer. Methods Ascorbate therapy of pancreatic cancer PDXs – KRAS-driven (PC106) and BRCA-driven (HyMad1) PDX models, created from patient samples and verified using targeted IMPACT sequencing,3,4 were subcutaneously xenografted in the right flank of NSG mice. 2 weeks after implantation, mice were randomly divided into two groups. One group was treated with freshly prepared vitamin C in 250 μL of PBS (4 g/kg) twice a day via IP injection (PC106, n = 7; HyMad1, n = 7). Control group mice were treated with PBS using the same twice a day dose (PC106, n = 7; HyMad1 n = 7). T2 images of these mice were acquired weekly to quantify tumor size and evaluate changes in tumor growth over time. HP DHA imaging of pancreatic cancer PDXs – Ascorbate and vehicle-treated mice of both PDX models were injected with 250 μL of 30 mM HP DHA in D2O to investigate the redox status of the implanted tumor over time. 13C HP MRS was performed using an axial 2D CSI acquisition on a 5T small animal MRI spectrometer to measure DHA/ascorbate metabolism. DHA/ascorbate ratios were quantified by taking the area under the curve and compared between ascorbate-treated and vehicle mice to determine changes in tumor redox upon ascorbate therapy. Metabolomics of solid tumors – Tumor samples of ascorbate and vehicle-treated mice of both PDX models were extracted after 1 week and 5 weeks treatment. Tumor samples were analyzed by untargeted metabolomics to quantify differences in key redox and metabolic pathways between treatment and vehicle groups for both PDX models. Results Ascorbate treatment was shown to slow tumor growth in the PC106 model after 3 weeks (36.5% ± 9.3%, p=.0035) while the effect on tumor growth was significant in the HyMad1 PDX model after 7 days (74.0% ± 12.3%, p=.0001, Figure 1A). Interestingly, the observed HP DHA/ascorbate ratio in vivo for PC106 PDXs after 1 week of ascorbate treatment did not change (8.5% ± 21.7%, p=.7105), mirroring the lack of significant response observed in tumor growth after 1 week (Figure 1B). The observed HP DHA/ascorbate ratio in vivo in HyMad1 PDXs after 1 week of ascorbate treatment was found to decrease by 28.0% ± 12.3% (p=.0593), reflecting the increase in oxidative stress upon ascorbate treatment (Figure 1C). Initial metabolomic results for the KRAS-driven PDX model show significant changes in the redox machinery of the tumor after 1 week of ascorbate treatment. NADH levels in tumors treated with ascorbate increased by an average 90% ± 29.8% (p=.0240) while NADP levels increased by an average 100% ± 39.4% (p=.0353) versus tumors treated with vehicle.

Conclusion We demonstrated HP DHA as an imaging agent for probing oxidative stress in PDX models of cancer. HP DHA was then used to characterize the biochemical response of these PDX models to ascorbate therapy. Changes in DHA/ascorbate metabolism were observed in these tumor models after prolonged treatment, demonstrating a new method for assessing ascorbate therapy in pancreatic cancer. Acknowledgements This work was supported by the Starr Cancer Consortium (SCC-I12-0031), Stand Up 2 Cancer, Thompson Family Foundation and NIH R01 CA252037.

References: 1. Yun, J., Mullarky, E., Lu, C., Bosch, K. N., Kavalier, A., Rivera, K., Roper, J., Chio, I. I. C., Giannopoulou, E. G., Rago, C., Muley, A., Asara, J. M., Paik, J., Elemento, O., Chen, Z., Pappin, D. J., Dow, L. E., Papadopoulos, N., Gross, S. S., & Cantley, L. C. (2015). Vitamin C selectively kills KRAS and BRAF mutant colorectal cancer cells by targeting GAPDH. Science, 350(6266), 1391-1396. doi:10.1126/science.aaa5004 2. Keshari, K. R., Kurhanewicz, J., Bok, R., Larson, P. E., Vigneron, D. B., & Wilson, D. M. (2011). Hyperpolarized 13C dehydroascorbate as an endogenous redox sensor for in vivo metabolic imaging. Proceedings of the National Academy of Sciences of the United States of America, 108(46), 18606-18611. Doi:10.1073/pnas.1106920108 3. Cheng, D. T., Mitchell, T. N., Zehir, A., Shah, R. H., Benayed, R., Syed, A., … Berger, M. F. (2015). Memorial Sloan Kettering-Integrated Mutation Profiling of Actionable Cancer Targets (MSK-IMPACT): A Hybridization Capture-Based Next-Generation Sequencing Clinical Assay for Solid Tumor Molecular Oncology. The Journal of Molecular Diagnostics, 17(3), 251–264. doi:10.1016/j.jmoldx.2014.12.006 4. Mattar, M., McCarthy, C. R., Kulick, A. R., Qeriqi, B., Guzman, S., & de Stanchina, E. (2018). Establishing and Maintaining an Extensive Library of Patient-Derived Xenograft Models. Frontiers in Oncology, 8, 19. doi:10.3389/fonc.2018.00019

Image/Figure: https://s3.amazonaws.com/amz.xcdsystem.com/1E8A4501-BB41-A02A-1D3B9882B798BFAA_abstract_File10351/GA302_ImageFigure_0513060214.pdf

Image/Figure Caption: Tumor growth curves for patient derived xenograft models of KRAS and BRCA driven cancer. 2 weeks after tumor implantation, mice were randomly divided into two groups. One group was treated with freshly prepared vitamin C in 400 mL of PBS (4 g/kg) twice a day via IP injection (KRAS, n = 7; BRCA, n = 7). Control group mice were treated with PBS using the same twice a day dose (KRAS, n = 7; BRCA, n = 7). Tumor growth change for the KRAS PDX tumors is significant after 21 days of ascorbate treatment (36.5% ± 9.3%, p=.0035) and significant for the BRCA PDX tumors after 7 days pf ascorbate treatment (74.0% ± 12.3%, p=.0001). Early changes in hyperpolarized ascorbate in KRAS PDX tumors are not observed with 1 week of high dose ascorbate treatment (Ascorbate treatment N = 4, vehicle treatment N = 4, 8.5% ± 21.7%, p=.7105). A representative HP 13C MRS of a vehicle-treated KRAS PDX tumor is given. Early changes in hyperpolarized ascorbate in BRCA PDX tumors are observed with 1 week of high dose ascorbate treatment (Ascorbate treatment N = 4, vehicle treatment N = 4, 28.0% ± 12.3%, p=.0593). A representative HP 13C MRS of a vehicle-treated BRCA PDX tumor is given.

Full Name of Abstract's 1st Author : Nathaniel Kim

First Name: Nathaniel

Last Name: Kim

Email: kimn1@mskcc.org

Organization: Memorial Sloan Kettering Cancer Center

Country: United States

ID: GA303

Temperature Sensitive State Switches For Genetic Control of Macrophage Immunotherapy

Abdullah Farooq, California Institute of Technology, afarooq@caltech.edu

---

Category: Bioengineering, Synthetic Biology and Basic Biology

Abstract Body : Cell therapy has tremendous potential to transform the treatment of many diseases such as cancer and autoimmune disorders. Despite recent advances in synthetic genetic control systems, there is a current lack of technological ability to secrete therapeutic agents from engineered cells with precise spatiotemporal control. The ability to induce a localized modulation would prevent the development of potentially lethal side effects associated with systemic release of therapeutic proteins, such as autoimmune disorders. Here, we are developing temperature-sensitive recombinase circuits to remotely control immune cells deep within the body using high-precision non-invasive techniques such as focused ultrasound hyperthermia. A permanent gene expression transition can be achieved by coupling a short pulse of thermal activation with recombinase expression. We have verified the activity of these circuits in a panel of immune cells demonstrating its broad applicability. Remarkably, these circuits display extremely low baseline activity in the absence of the thermal stimulus, and high induction after stimulation. This tool was used to control CD19 bispecific T-cell engager (BiTE) production and release by macrophages in vitro. Engineered macrophages were shown to traffic into CD19+ Raji tumors in an immunocompromised mouse model. Trafficked macrophages harboring the temperature-sensitive recombinase reporter circuit can be activated in vivo using focused ultrasound hyperthermia (FUS). In addition to enhancing cell therapeutics, this tool also has the potential to address fundamental scientific questions, such as cell migration and multicellular development.

First Name: Abdullah

Last Name: Farooq

Email: afarooq@caltech.edu

Organization: California Institute of Technology

Country: United States

ID: GA304

Evaluation of [18F]ROStrace as Radiotracer for Imaging Oxidative Stress in a Murine Model of Alzheimer's Disease

JI YOUN LEE, University of Pennsylvania, JiYoun.Lee@Pennmedicine.upenn.edu

---

Category: Neuroscience

Abstract Body : Evaluation of [18F]ROStrace as Radiotracer for Imaging Oxidative Stress in a Murine Model of Alzheimer's Disease Ji Youn Lee, Catherine Hou, Chia-Ju Hsieh, Kuiying Xu, Hsiaoju Lee, Shihong Li, and Robert H. Mach* Department of Radiology, Perelman School of Medicine, University of Pennsylvania, Philadelphia, Pennsylvania 19104, United State Introduction Alzheimer's disease (AD) is a progressive neurodegenerative disease that is characterized by memory loss and cognitive dysfunction. Oxidative stress has been highlighted as a key player in the neurodegeneration associated with this disease. In this study, we measured elevated levels of reactive oxygen species (ROS) in a transgenic mouse model of AD using [18F]ROStrace, a radiotracer that measures ROS. A series of PET imaging studies were conducted in wild type and APPSWE/PS1dE9 female and male mice at 5, 10 and 16 months of age, and the results were compared with histological measures of Aβ burden. Methods PET studies using [18F]ROStrace were conducted using a total of 91 mice. Radiotracer (~ 0.25 mCi) was injected through the tail vein and dynamic images were obtained for 60 min and analyzed using Pmod. The cortex, thalamus, cerebellum, hypothalamus, brain stem, central gray, striatum, hippocampus, amygdala, and midbrain from the Mirrione atlas were included for volume of interest (VOI) quantification. To confirm specific uptake regions of [18F]ROStrace, ex vivo autoradiography was performed and compared with the PET data. Antibody staining to measure Aβ plaque density was conducted in the same mice after PET to assess the correlation between [18F]ROStrace and Aβ burden. Results An increase in brain uptake of [18F]ROStrace was observed from 5 months to 16 months, with the APP/PS1 mice showing higher brain uptake than the wild type mice. We observed higher [18F]ROStrace uptake in cortex and hippocampus by SPM analysis. This was confirmed by two-way ANOVA test, we demonstrated a significant difference in cortex (p Conclusion PET studies of [18F]ROStrace were conducted to measure superoxide levels in a murine model of AD. We observed that [18F]ROStrace brain uptake in APP/PS1 mice was higher than in wild type mice, and specific uptake corresponded to regions with a high Aβ burden. We also observed higher uptake of [18F]ROStrace in female AD mice than male AD mice. Based on these results, we conclude that [18F]ROStrace is a useful radiotracer for imaging the increase in levels of oxidative stress thought to occur in AD. Funding sources: AG055142

Image/Figure: https://s3.amazonaws.com/amz.xcdsystem.com/1E8A4501-BB41-A02A-1D3B9882B798BFAA_abstract_File10351/GA304_ImageFigure_0513034306.pdf

Image/Figure Caption:

Full Name of Abstract's 1st Author : JI YOUN LEE

First Name: JI YOUN

Last Name: LEE

Email: JiYoun.Lee@Pennmedicine.upenn.edu

Organization: University of Pennsylvania

Country: United States

ID: GA305
Hydrazine equipped turn-on manganese-based MRI probes for imaging liver fibrogenesis

Yingying Ning, Harvard Medical School, Mass General Hospital, YNING2@mgh.harvard.edu

---

Category: Systemic Diseases (Kidney, Liver and Pancreas)

Abstract Body : Introduction. Liver fibrosis can occur in most chronic liver diseases, and can lead to cirrhosis, liver failure, primary liver cancer, and/or organ failure.1 Fibrogenesis is accompanied by upregulation of lysyl oxidase enzymes which catalyze oxidation of lysine e-amino groups on extracellular matrix proteins to form the aldehyde containing amino acid allysine which then undergoes cross-linking. MRI probes functionalized with a hydrazine moiety can bind to allysine in vivo to detect fibrogenesis, 2-4 but these are all gadolinium-based and there is growing concern about the long term safety of Gd-based probes.5 Here, we describe the design and synthesis of novel manganese-based MRI probes with high signal amplification for imaging liver fibrogenesis. Results and discussions: The design of hydrazine equipped manganese probes for imaging liver fibrogenesis must meet several requirements: 1) chemically stable Mn2+ complex that does not release free Mn2+ or undergo redox chemistry; 2) limited hepatobiliary elimination to minimize liver background signal; 3) contain coordinated water co-ligand to promote high relaxivity; 4) achieve higher relaxivity when bound to fibrotic tissue to increase signal at site of fibrosis. To meet these requirements, we designed the probes Mn-2Hyd, Mn-2CHyd and Mn-1CHyd based on the stable Mn-1,4-DO2A chelate (Fig 1a).6 In model reactions with butyraldehyde, Mn-2CHyd showed the highest on-rate and conversion yield (Fig 1b). Temperature dependence of the H217O tranverse relaxivity showed that the inner-sphere number of water molecule decreases from 0.90 in Mn-1,4-DO2A to 0.44 in Mn-2CHyd (Fig 2a), resulting in a lower relaxivity of Mn-2CHyd in PBS (1.6 mM-1s-1). However, Mn-2CHyd exhibits an almost 5-fold turn-on relaxivity when bound to allysine modified BSA protein (7.7 mM-1s-1, Fig 1c), indicating high affinity towards allysine residues and increased relaxivity upon binding. Mn-2CHyd is more inert to Mn2+ release than Mn-1,4-DO2A (Fig 2b). Unlike Mn-1CHyd which showed high Mn liver levels in healthy mice at 60 mins post-injection, Mn-2CHyd showed little accumulation in the healthy liver (Fig 2c). This combination of stability, turn-on relaxivity, and low uptake in healthy liver indicate that Mn-2CHyd is quite promising as a novel probe for liver fibrogenesis detection. Mn-2CHyd was tested in mice treated with CCl4 or olive oil vehicle for 12 weeks to induce liver fibrosis. Ex vivo analyses of liver hydroxyproline and Sirius red staining indicated consistent fibrosis in the CCl4 group (Fig 2e-g). Gd-DOTA was used as a comparison to demonstrate the specificity of Mn-2CHyd towards fibrosis. At 45 mins post-injection, there is no liver enhancement with Gd-DOTA in CCl4 mice, but strong signal enhancement and high liver-to-muscle contrast to noise ratio (ΔCNR) in mice injected with Mn-2CHyd (Fig 1d-e). The vehicle group imaged with Mn-2CHyd showed significantly lower liver enhancement (Fig 2d). These data indicated that Mn-2CHyd shows high sensitivity and is specific for in vivo detection of liver fibrogenesis. Conclusion. A series of hydrazine equipped manganese MRI probes were designed and synthesized. Mn-2CHyd shows

the highest affinity and turn-on relaxivity in allysine containing protein solution, and low liver uptake in normal mice. The ability of this probe to detect liver fibrogenesis was demonstrated in vivo using a CCl4 mouse model, where it shows significantly enhanced liver signal in CCl4 injured mice than in control mice. This study opens the door to study manganese-based hydrazine equipped probes for imaging fibrogenesis.

References: 1. Bataller, R., & Brenner, D. A. J. Clin. Invest. 2005, 115, 209-218; 2. Chen, H. H., Waghorn, P. A., Wei, L., et al. JCI insight, 2017, 2, e91506; 3. Waghorn, P. A., Jones, C. M. et al. Angew. Chem. Int. Ed. 2017, 56, 9825-9828; 4. Akam, E. A., Abston, E., Rotile, N. J., Slattery, H. R., Zhou, I. Y., Lanuti, M., & Caravan, P. Chem. Sci. 2020, 11, 224-231; 5. Grobner, T. Nephrol. Dial. Transplant. 2006, 21, 1104−1108; 6. Garda, Z., Forgács, A., Do, Q. N., Kálmán, F. K., et al. J. Inorg. Biochem. 2016, 163, 206-213.

Image/Figure:

https://s3.amazonaws.com/amz.xcdsystem.com/1E8A4501-BB41-A02A-1D3B9882B798BFAA_abstract_File10351/GA305_ImageFigure_0513034728.png

Image/Figure Caption: Figure 1. a) Chemical structures of Mn complexes studied in this work; b) Conversion yield of Mn complexes (25 μM) over time in the reaction with butyraldehyde (100 μM), characterized by LC-ICP; c) Relaxivity values at 60 MHz (PBS, pH 7.40, 2h, 37°C) in the presence or absence of BSA and BSA-Ald; d) Axial liver (outlined in yellow) images of CCl4 and vehicle mouse imaged in pre- and 45 mins post-injection of GdDOTA or Mn-2CHyd (0.1 mmol/kg i.v.); e) Change in liver to muscle contrast to noise ratio (ΔCNR) post probe injection of vehicle treated (n = 4) and CCl4 mice (n = 6) at 45 mins post-injection of GdDOTA and Mn-2CHyd. *P < 0 .05, **P < 0 .01.

Full Name of Abstract's 1st Author : Yingying Ning

First Name: Yingying

Last Name: Ning

Email: YNING2@mgh.harvard.edu

Organization: Harvard Medical School, Mass General Hospital

Country: United States

ID: GA307

In vivo quantitative assessment of therapeutic response to bortezomib therapy in disseminated animal models of multiple myeloma with 18F-FDG and 64Cu-LLP2A PET

Anchal Ghai, washington university school of medicine, a.ghai@wustl.edu

---

Category: Oncology

Abstract Body : Background: Multiple myeloma (MM) is the second most common hematological cancer attributed to abnormal plasma cells originating from the bone marrow. While still incurable, conventional therapies have improved the survival rates in MM patients. Optimization and timely determination of therapeutic response is critical for improving outcomes in MM patients. The activated form of the α4β1 integrin (very late antigen-4, VLA-4) is overexpressed in MM, and plays an important role in ensuring myeloma cell adhesion and survival within the bone marrow. Here, we compared the efficacy of the gold standard 18F-FDG PET with VLA-4 targeted 64Cu-LLP2A PET for quantitative longitudinal imaging of bortezomib (proteasome inhibitor) therapy response in disseminated MM models of human myeloma, using two cell lines bearing by variable (high and low) VLA-4 expression. Methods: MM.1S-GFP-luc (3e6 cells/mouse) and U266-GFP-luc (10e6 cells/mouse) human MM cells with variable expression of VLA-4 were injected via tail vein in NOD SCID Gamma (NSG) mice. Tumor burden and progression were monitored by weekly bioluminescence imaging (BLI) in mice treated with bortezomib. Mice with established disseminated disease were randomly grouped into untreated and treated cohorts, along with an additional cohort of age and strain matched healthy control cohort. The treated group received bortezomib (1mg/kg) intraperitoneally, twice a week. Small PET imaging was performed with 18FDG and 64Cu-LLP2A at baseline (prior to start of treatment) and then sequentially (one day apart) every week for upto six weeks. Whole body PET/CT images were acquired on the small animal INVEON PET/CT scanner and images were coregistered using Inveon Research Workplace (IRW) software. Regions of interest (ROI) were drawn and selected from PET images using CT anatomical guidelines and the activity associated with the ROI was measured with IRW software. When feasible, tissues were extracted for ex vivo flow cytometry. Results: Flow cytometry studies confirmed high expression of CD49d (α4 subunit of VLA-4) in U266-luc myeloma cells (>99%) compared to MM.1S-luc cells with ~52% cells showing CD49d expression. Bortezomib therapy response was monitored by longitudinal small imaging PET and BLI in MM.1S-luc and U266-luc disseminated tumor bearing mice. BLI data in mice from the untreated cohort showed 4-fold increased total body luciferase activity as compared to the mice from the treated cohort at week 3 in both the mouse models. In MM.1S-luc myeloma mouse model, compared to the treated cohort of mice (where treatment was started at week 0), 64Cu-LLP2A localized with a significantly higher SUVmean in bone marrow rich skeletal sites such as spine (0.58 versus 0.31) and femur (0.72 versus 0.39) at week 4. Similarly, in U266-luc tumor bearing untreated mice, the percent increase in the 64Cu-LLP2A uptake in spine was 4 times higher than the treated mice at week 4.64Cu-LLP2A PET/CT imaging at 4 h post injection of the radiotracer showed significant differences in the uptake among the treated and untreated cohort

demonstrating better monitoring of therapy response with this tracer as compared to 18FDG (1 h post injection) in both the myeloma tumor models. Conclusion: We observed qualitative and quantitative differences in the uptake of standard-of-care 18F-FDG and VLA4 targeted 64Cu-LLP2A tracers in human models of MM. Based on the in vitro and in vivo data, we posit that the accuracy of MM detection and treatment monitoring can be significantly improved by the complementary use of the metabolic and plasma cell receptor targeted tracers.

First Name: Anchal

Last Name: Ghai

Email: a.ghai@wustl.edu

Organization: washington university school of medicine

Country: United States

ID: GA308
Comparative Evaluation of PET Imaging Agents in Neuroendocrine Prostate Cancer

Joshua Korsen, Weill Cornell Medicine, jak2058@med.cornell.edu

---

Category: Oncology

Abstract Body : Objective: Neuroendocrine Prostate Cancer (NEPC) is an aggressive subtype of prostate cancer (PC) that is resistant to current standard of care treatments including androgen receptor signaling inhibition (ARSI) [1]. The patients have aggressive disease with visceral metastasis and have short survival time (7-10 months) [2]. Genomic and proteomic characterization of biopsy samples of NEPC lesions indicates loss of androgen receptor (AR) signaling [3]. In the current clinical scenario, PC patients are routinely screened with [68Ga]-PSMA11 or other PSMA targeting agents. [68Ga]-DOTATATE that targets somatostatin receptors has been postulated as a potential imaging agent for NEPC. Recently, we have shown that Delta-like ligand 3 (DLL3) is exclusively expressed in NEPC and can be targeted with our imaging agent [89Zr]-SC16. The goal of our study was to evaluate the diagnostic performance of PET imaging agents [68Ga]-PSMA11, [68Ga]-DOTATATE and [89Zr]-SC16 in imaging NEPC lesions. Methods: We have used well characterized NCI-H660 cell line as representative NEPC model and compared it with prostate adenocarcinoma LNCaP cell line and androgen independent PC cell line DU145. qPCR was used to measure relatively levels of AR-regulated gene transcripts (AR, PSMA, PSA), NEPC marker DLL3, and SSTR2 and normalized to b-actin in the cell lines. Protein levels were determined by immunohistochemistry analysis on cell pellets. In vitro radioactive ligand binding assays were performed on NCI-H660, DU145, and LNCaP cells using [89Zr]-SC16. For in vivo PET imaging, a dual tumor model using NCI-H660 and LNCaP xenografts or single tumor model using NCI-H660 or DU145 xenografts were established in 6-8 week old male athymic nude mice. The mice were administered with [89Zr]-SC16 and/or [68Ga]-PSMA11 and/or [68Ga]-DOTATATE and PET imaging was performed either at 1 h (for Ga-68 agents) or 48 h (for Zr-89 agent). Results: In vitro studies indicated that NCI-H660 cell line had elevated levels of DLL3 expression in comparison to LNCaP cells and were negative for AR, PSA, and PSMA at the transcriptional level. Further, no differences in SSTR2 mRNA expression was observed between NCI-H660 and LNCaP cells. In vitro cell binding assay indicates that [89Zr]-SC16 binds only to NCI-H660 cells with minimal binding in LNCaP and DU145 cells. In vivo PET imaging with [89Zr]-SC16, [68Ga]-PSMA11, and [68Ga]-DOTATATE show that detection of NCI-H660 cells are only detectable upon administration of DLL3-targeting [89Zr]-SC16, demonstrating the inability to non-invasively detect NEPC lesions with AR-targeted and SSTR2-targeted agents. Conclusion: Our findings demonstrate that NEPC tumors are detectable only using DLL3 targeted imaging agent [89Zr]-SC16. AR-targeted and SSTR2-targeted agents do not accumulate in NEPC lesions and therefore are unsuitable to detect these lesions. Acknowledgement: Partial funding for these studies was provided by 2019 Geoffrey Beene Cancer Research Center Grant.

References: 1. Watson, P.A., V.K. Arora, and C.L. Sawyers, Emerging mechanisms of resistance to androgen receptor inhibitors in prostate cancer. Nat Rev Cancer, 2015. 15(12): p. 701-11. 2. Apostolidis, L., Nientiedt, C., Winkler, E.C., et al., Clinical characteristics, treatment outcomes and potential novel therapeutic options for patients with neuroendocrine carcinoma of the prostate. Oncotarget, 2018. 10: p. 17-29. 3. Puca, L., Gavyert, K., Sailer, V., et al., Delta-like protein 3 expression and therapeutic targeting in neuroendocrine prostate cancer. Sci Transl Med, 2019. 11(484).

Full Name of Abstract's 1st Author : Joshua Korsen

First Name: Joshua

Last Name: Korsen

Email: jak2058@med.cornell.edu

Organization: Weill Cornell Medicine

Country: United States

ID: GA309
Fluorescence-guided debridement of devitalized and infected bone in the context of orthopaedic trauma

Jonathan Elliott, Dartmouth-Hitchcock, jonathan.t.elliott@dartmouth.edu

---

Category: Immunology: Inflammation & Infection

Abstract Body : Fluorescence-guided surgery has emerged as an important tool in a number of different disciplines such as cancer resection [1], plastics and reconstructive surgery [2] and gastric surgery [3]. However, it has not appreciably impacted the field of orthopaedic trauma. One of the dominant challenges in orthopaedic trauma surgery is the management and treatment of infection, which can result in repeated procedures, prolonged morbidity and huge economic cost. To properly address infection, both infected and devitalized (i.e., hypoperfused) bone and soft tissue must be cleared in a thorough debridement. However, no current approach exists to precisely identify these tissues. Our team has established intraoperative methods to quantify perfusion [4-6] and are now developing infection-sensitive contrast. As a corollary to the Dartmouth-Hitchcock initiated multicenter clinical study funded by NIH/NIAMS, our group is advancing fluorescence-guided debridement (FGD), the use of two contrast agents—one sensitive to perfusion, the other sensitive to infection/inflammation—to guide removal of infected and devitalized bone and tissue. Approval was obtained from the IRB to administer indocyanine green (ICG) and/or 5-aminoluvulinic acid (5-ALA) to patients undergoing re-debridement and re-fixation under suspicion of osteomyelitis, and acquire a time-series of fluorescent images using the SPY Elite (Stryker Corp.). Hardware from patients suspected of having implant-associated infection was also removed and analyzed for bacteria. Depth-resolved bacterial biofilms on the surface of tibiotalocalcaneal fusion nails were imaged with 3 μm axial resolution using Ganymede optical coherence tomography (OCT) system (Thorlabs, USA). Functional OCT speckle variance technique applied in 25ms increments over four seconds for each depth slice was used to detect individual bacteria through their temporal motility rates. Nails, screws and rods were soaked in a solution of 10 mM of 5-ALA for 2 hours, and then imaged using a wide-field fluorescence microscope under 405 nm excitation. In a wide spectrum of gram-positive and gram-negative bacteria, 5-ALA induces porphyrin synthesis (e.g., protoporphyrin IX, but others as well), which are photosensitizers and emit red light (635 nm) when excited with blue (405 nm). A 630±30 nm bandpass filter was mounted to a sCMOS camera (PCO, Germany) and imaged at a 1 Hz framerate. Figure 1A-H shows the results of Patient 1 who sustained a Gustilo Type IIIA distal tibia fracture that was complicated by infection. The patient was administered ICG just prior to re-debridement, re-fixation and Masquelet bone grafting. The signal void in on the right side of the field-of-view is suggestive of devitalization. The ingress slope (wash-in rate) shows reduced values and the time-to-peak at the peripheral regions of the compromised region (ROI2) show extremely slow and disrupted kinetics. Two weeks following this surgery, persistent nonunion was confirmed and the patient underwent transtibial amputation. Figure 1I-O shows fluorescence and OCT analysis of a tibiotalocalcaneal fusion nail removed from Patient 2, who sustained a pilon fracture leading to MRSA-positive osteomyelitis. The nail was half-submerged in a 10 mM solution of 5-ALA, and

imaged. Figure 1I shows the 635 nm PpIX intensity as a function of position, and J-L show the fluorescence intensity maps corresponding to three positions indicated. Fig. 1M and N show the functional and structural OCT 3-D maps, respectively, and Fig 1O shows the ST at a depth of 18. Hardware will undergo quantitative microbiology and NGS 16s rRNA microbiome analysis to determine the presence of viable and dead microbes. Ongoing clinical studies will investigate association between in vivo ICG and 5-ALA images, ex vivo analysis of hardware and microbiome diversity to determine performance of fluorescence for detecting devitalized and/or infectious tissue.

References: 1. J. T. Alander, et al. International Journal of Biomedical Imaging 2012, 2012. 2. A. Losken, et al. Plastic and reconstructive surgery 129(4), 2012. 3. M. Diana, et al. British Journal of Surgery 102(2), 2015. 4. J. T. Elliott et al., Journal of biophotonics 12(8), 2019. 5. Gitajn IL et al., Journal of biomedical optics. 25(8), 2020. 6. Elliott JT et al., Journal of biomedical optics. 25(6), 2020.

Image/Figure:

https://s3.amazonaws.com/amz.xcdsystem.com/1E8A4501-BB41-A02A-1D3B9882B798BFAA_abstract_File10351/GA309_ImageFigure_0513035723.png

Image/Figure Caption: Figure 1. (A) Maximum intensity, (B) ingress slope (C) time-to-peak of ICG following bolus injection in Patient 1 with an infected non-union; (E-G) violin plots of the regions-of-interest in D and (H) the time-fluorescence curves of the same regions. Hardware removed from Patient 2 was (I) illuminated with 405 nm light after soaking in 10mM of 5-ALA for 120 minutes; (J-L) the fluorescence intensity at different positions along the rod, (M) the functional and (N) morphological 3D scans of OCT and (O) a slice in the z-direction showing the surface of the cement nail, which is presumed to be positive for MRSA.

First Name: Jonathan

Last Name: Elliott

Email: jonathan.t.elliott@dartmouth.edu

Organization: Dartmouth-Hitchcock

Country: United States

ID: GA310
Dynamic Perfusion PET/CT Imaging in Esophageal Cancer Patients Receiving Radiation Therapy

Katherine Binzel, Wright Center of Innovation in Biomedical Imaging, binzel@wcibmi.org

---

Category: Oncology

Abstract Body : Aim: To assess the feasibility and value of performing dynamic perfusion PET imaging for the evaluation of esophageal tumors over the course of radiation therapy. Methods: Fifteen patients with esophageal tumors were imaged prior to radiation therapy, at the midway point of therapy, and post-therapy, an average of 12 weeks after baseline imaging. Dynamic perfusion imaging was acquired over a single bed position at the site of the primary tumor for 15 minutes immediately following injection of 185 MBq 18F-FDG. Imaging was performed on a digital photon counting system (Philips Vereos). Patients spent the remaining uptake period in the injection suite followed by whole body imaging at 75 minutes post-injection as standard imaging. Listmode data from the dynamic acquisition were reconstructed with 1 minute per frame. Regions of interest were placed over the primary tumor, aorta/blood pool, paraspinal muscle, and a portion of healthy liver. Results: Excellent image quality and quantifiably robust data were produced for all acquisitions. Physiologic motion could readily be corrected for, however very little motion was observed. Differences in perfusion and dynamic uptake patterns in the individual tumors were identifiable. From baseline to post-treatment, patients with Grade 1-2 (well and moderately differentiated) tumors had greater decreases in the initial rate of FDG uptake than did those with Grade 3 (poorly differentiated) tumors, on average an 86% decrease in the slope of the dynamic uptake curve for Grades 1-2 versus only a 56% decrease in slope for Grade 3 tumors. Patients who responded well to radiation therapy also had tumors which tended to show a greater initial perfusion peak on the uptake curve than did those which did not respond well to therapy. Conclusion: We have demonstrated that dynamic perfusion FDG PET/CT is robustly achievable. Quantification of tumor features, including initial tumor perfusion and uptake rates, is robust as well as the assessment of changes in perfusion and uptake in response to therapy. This PET-based methodology can be applied to assess changes in the rates of tumor perfusion and radiotracer uptake over the course of therapy, adding additional insight beyond delayed, static measures of SUV.

Image/Figure:

https://s3.amazonaws.com/amz.xcdsystem.com/1E8A4501-BB41-A02A-1D3B9882B798BFAA_abstract_File10351/GA310_ImageFigure_0513035812.jpg

First Name: Katherine

Last Name: Binzel

Email: binzel@wcibmi.org

Organization: Wright Center of Innovation in Biomedical Imaging

Country: United States

ID: GA312

Quantitative and noninvasive detection of treatment response in a mouse model of pulmonary fibrosis by molecular MRI

Yingying Ning, Harvard Medical School, Mass General Hospital, YNING2@mgh.harvard.edu

---

Category: Cardiovascular & Pulmonary

Abstract Body : Introduction: Pulmonary fibrosis results in thickening of the lung interstitium, abolition of alveolar spaces and eventual respiratory failure.1 It is accompanied by upregulation of lysyl oxidase and Lox-like enzymes which catalyze oxidation of lysine e-amino groups on extracellular matrix proteins (chiefly collagens) to form the aldehyde containing amino acid allysine which then undergoes cross-linking reactions with other proteins to stabilize the matrix. Hydrazine derivatized gadolinium probes can bind to allysine in vivo to stage and quantify fibrogenesis.2-4 Here, we designed a new probe, Gd-1,4, with two hydrazine moieties where dual binding to allysine may enhance on-rate and slow the off-rate relative to the previous reported probe Gd-CHyd,4 and assessed whether Gd-1,4 can be used to monitor treatment response in a model of pulmonary fibrosis with a promising natural product EGCG being developed clinically.5 Methods: Cis-1,4-Gd(CHyd)2 (Gd-1,4) is a Gd-DOTA derivative with two hydrazine arms synthesized by amide coupling of two tBu-piperazin-1-ylcarbamate groups to to 1,4,7,10-tetraazacyclododecane-1,4-bis(tBu-acetate)-4,10-bis(glutaric acid 1-tBu ester), followed by acid deprotection and gadolinium complexation. C57Bl/6 adult male mice at 8 weeks of age received a single intratracheal dose of bleomycin, 1 U/kg body weight (50 μL total volume) as previously described.6 A pair-wise imaging study of Gd-CHyd and Gd-1,4 was carried out in mice at day 14 post bleomycin injury on a 4.7 T Bruker Biospec MRI with a dose of 100 μmol/kg of each probe. For the treatment study, mice were imaged first at day 10 post bleomycin injury, then treated daily with oral gavage of either epigallocatechin gallate (EGCG, 100 mg/kg) or PBS (vehicle) for 11 days. At day 21 post bleomycin injury, the animals were imaged again. MRI consisted of T1-weighted UTE (TR/TE/flip angle = 4 ms/0.011ms/15°) images acquired prior to and up to 30 minutes following intravenous administration of Gd-1,4 (100 μmol/kg). Following the second imaging session, animals were euthanized (60 minutes post injection), and lung tissues were removed for further analysis. Results and discussions: We first compared the dual hydrazine probe Gd-1,4 to Gd-CHyd in a head-to head comparison in vivo. We imaged mice 14 days after bleomycin injury first with Gd-CHyd and then 4 h later with Gd-1,4. This pairwise study showed that the signal generated by Gd-1,4 in fibrotic lung is 3-fold higher (P Conclusion. A novel allysine targeting dual binder MR probe Gd-1,4 was developed and it shows higher sensitivity towards pulmonary fibrogenesis detection than the state of the art. Importantly, Gd-1,4 can noninvasively and sensitively monitor treatment response with an antifibrotic drug currently in clinical development for IPF treatment.

References: 1. C. Kuhn, J. Boldt, T. E. King, E. Crouch, T. Vartio and J. A. McDonald, Am. Rev. Respir. Dis., 1989, 140, 1693–1703; 2. Chen, H. H., Waghorn, P. A., Wei, L., et al. JCI insight, 2017, 2, e91506; 3. Waghorn, P. A., Jones, C. M. et al. Angew. Chem. Int. Ed. 2017, 56,

9825-9828; 4. Akam, E. A., Abston, E., Rotile, N. J., Slattery, H. R., Zhou, I. Y., Lanuti, M., & Caravan, P. Chem. Sci. 2020, 11, 224-231; 5. Chapman, Harold A., et al. N. Engl. J. Med. 2020, 382, 1068-1070; 6. Desogere, P., et al. J Nuc Med 2017, 58, 1991-1996.

Image/Figure:

https://s3.amazonaws.com/amz.xcdsystem.com/1E8A4501-BB41-A02A-1D3B9882B798BFAA_abstract_File10351/GA312_ImageFigure_0513040116.png

Image/Figure Caption: Figure 1. a) Axial T1-weighted UTE MR images of lung in pair-wise study at pre- and 25 mins post-injection of Gd-CHyd or Gd-1,4; b) Quantification of MR signal in the lungs in a) with paired t test (n= 4); c) Quantification of the gadolinium content in the left lungs of BM or naïve animals at 60 mins post injection of Gd-1,4; d) Schematic illustration of the MR imaging and treatment timeline; e) Axial T1-weighted UTE MR images of lung at 25 mins post-injection of Gd-1,4 in aged matched naïve mice (Naive), in mice challenged with bleomycin intratracheally 10 days prior (Bleo(D10)), in mice that received 11 days of PBS treatment (Vehicle(D21)) and in mice that received 11days of EGCG treatment starting 10 days after bleomycin injury; f) Quantification of lung to muscle contrast to noise ratio (ΔCNR) of different groups in e) (n=6).*P < 0 .05.

Full Name of Abstract's 1st Author : Yingying Ning

First Name: Yingying

Last Name: Ning

Email: YNING2@mgh.harvard.edu

Organization: Harvard Medical School, Mass General Hospital

Country: United States

ID: GA313

Paired-agent imaging is comparative with gold standard hematoxylin and eosin (H&E) staining but more time-efficient in frozen section of head and neck cancer

Cheng Wang, Dartmouth College, cheng.wang.th@dartmouth.edu

Category: Oncology

Abstract Body : Head and neck squamous cell carcinoma (HNSCC) is the sixth most common cancer worldwide and accounts for about 4% of all cancers in the United States. In the treatment of HNSCC the single most important prognostic factor for patient survival is tumor free, or "negative margins", after surgical excision. During tumor excision surgery, it is common practice for surgeons to collect multiple biopsy samples from the tumor wound bed to be prepared as "frozen sections". In real time, a pathologist assesses the frozen sections for residual tumor cells using gold standard hematoxylin and eosin (H&E) staining. This process is time-consuming (typically 20-30 minutes per sample), disruptive to pathological work-flow, expensive, and only approaches 90% accuracy compared to the final diagnosis. Additionally, the vast majority of frozen sections are negative for tumor. Therefore, a high through-put, time-efficient, labor-saving method is needed to screen HNSCC and detect positive margins intra-operatively. Over 90% of HNSCC express epidermal growth factor receptor (EGFR), and cancer cell proliferation is positively correlated with expression of EGFR. Several fluorescent EGFR-targeting agents are in clinical trials for use in fluorescent guided surgery. However, non-specific binding and uptake in normal tissues of single fluorescent agents confounds detection of microscopic tumor burden in thick (several millimeters) tissue sections. Here, we propose using paired-agent imaging (PAI) to quantify microscopic tumor burden in tissue samples using "back-table" imaging during surgery. PAI is a true molecular imaging method that uses a control agent to separate the non-specific signal from the targeted signal. This method has been successfully applied in quantifying tumor cells in lymph node, sarcoma and tongue bulk tumor. In order to develop a fast method to confirm a tumor-free margin intra-operatively, here we investigate PAI for cancer detection in a murine model of tongue HNSCC tumors in frozen section. Meanwhile, the performance of clinically prevalent hematoxylin-eosin (H&E), gold standard IHC, PAI frozen section are compared in parallel. As a result, PAI frozen section provides comparative tumor-detection ability with gold standard IHC and H&E frozen section. Moreover, the image of PAI frozen section only takes 5 minutes to acquire and 5 minutes to process, which provides quick and precise information about either confirming tumor-free margins or identifying residual tumor cells. As a time-efficient, and labor-saving method, it may open up a new chapter for biopsy screening and intra-operative margin detection.

First Name: Cheng

Last Name: Wang

Email: cheng.wang.th@dartmouth.edu

Organization: Dartmouth College

Country: United States

ID: GA314

Development of an extension framework to enable deep learning-based image processing and analysis with cloud computing for open-source imaging software

Sheng-Chieh Chiu, The University of Alabama at Birmingham, leon1215@uab.edu

---

Category: Computational & Data Science

Abstract Body : Overview: A novel framework that is designed as extensions for open-source image software is proposed that facilitates deep learning-based image processing and analysis over cloud computing servers, and to demonstrate the feasibility we present our extension for brain parcellation with deep learning in the widely used 3D Slicer [1]. With the rapid growth of deep learning technologies and their application over medical imaging, more and more openly shared models have been made available and possess a strong potential for advanced image processing. However, for inexperienced users, setting up and testing such open-source models remains to be a challenging task. To address these challenges, we propose to develop computational tools that require minimal effort for users to set up while maintaining the same computational performances. Our framework is based on the open-source image viewer, 3D Slicer, by implementing its extension that utilizes the MatlabBridge Extension [2] in 3D Slicer, the MATLAB Job Manager [3], and deep learning models configured and executed on the Google Cloud. Objective: We aim to create a versatile and user-friendly software environment for users of all experience levels to perform deep learning-based image processing by eliminating the barrier of the demanding hardware and software requirements. Methodology: The proposed project was divided into three components of implementation. 1) The cloud server environment establishment: The server was established in the Google cloud platform with GPU support. Docker images were used within the server for executing the deep learning models to avoid software conflicts and inconsistencies. 2) Deep learning model implementation: The deep learning model, FastSurfer [4], was used as a proof of concept as the deep learning-based brain segmentation model in the cloud server. We package FastSurfer and its required libraries into a single Docker image for easy deployment and isolated environment setups. 3) Bridging between 3D Slicer and the cloud server: With the aim to transmit data to the server, MATLAB Job Manager was deployed under MatlabBridge Extension. This job manager packages the data and commands into jobs, submits jobs from the local computer, distributes and executes them on the cloud, and returns the completed results back to the client. The user will only be required to install 3D Slicer and our extension without any specific settings for FastSurfer or other libraries. Result: We have successfully implemented the framework as a 3D Slicer extension. Brain parcellation was greatly accelerated by the 3D Slicer FastSurfer extension while the user does not need local GPU resources. By demonstrating the feasibility and performance improvements with deep learning-based image processing methods through our work, such computational frameworks can be generalized to other deep learning-based image processing and analysis models to stimulate novel and advanced imaging research in the future.

References: 1. Fedorov, A.; Beichel, R.; Kalpathy-Cramer, J.; Finet, J.; Fillion-Robin, J.C.; Pujol, S.; Bauer, C.; Jennings, D.; Fennessy, F.; Sonka, M.; et al. 3D Slicer as an image

computing platform for the Quantitative Imaging Network. Magn. Reson. Imaging 2012, 30, 1323–1341. 2. MatlabBridge, https://www.slicer.org/wiki/Documentation/Nightly/Extensions/MatlabBridge, Accessed March 25th, 2021. 3. Matlab Job Manager. https://github.com/bronsonp/matlab-job-manager. Accessed January 28th, 2021. 4. Henschel L, Conjeti S, Estrada S, Diers K, Fischl B, Reuter M. FastSurfer-A fast and accurate deep learning based neuroimaging pipeline. NeuroImage. 2020:117012.

Image/Figure:

https://s3.amazonaws.com/amz.xcdsystem.com/1E8A4501-BB41-A02A-1D3B9882B798BFAA_abstract_File10351/GA314_ImageFigure_0513040253.png

Image/Figure Caption: The figure shows the segmentation result by loading the pre-segmentation DICOM file and The segmentation DICOM RT file. The DICOM RT file will be stored in the default path on the local PC.

Full Name of Abstract's 1st Author : Sheng-Chieh Chiu

First Name: Sheng-Chieh

Last Name: Chiu

Email: leon1215@uab.edu

Organization: The University of Alabama at Birmingham

Country: United States

ID: GA315
Using microfluidics to prepare heat-denatured macroaggregated albumin microparticles for SPECT/CT imaging

Marta Bergamo, University of British Columbia, marta.bergamo@alumni.ubc.ca

---

Category: Cardiovascular & Pulmonary

Abstract Body : Due to its high versatility and availability, albumin has always been an attractive molecule for biomedical and pharmaceutical applications. A wide range of albumin-based systems, such as drug conjugates and nanoparticles, have been reported over the years as diagnostic imaging agents as well as to improve a drugs' pharmacokinetic, safety and efficacy profile [1-3]. Besides their long-standing use as a lung perfusion imaging agent, significantly less attention has been given to macroaggregated albumin (MAA) microparticles. One of the hurdles holding back the development of MAA is how the microparticles are prepared, i.e., by heating a bulk solution of albumin, which results in an undesirably large size distribution and batch-to-batch variability [4, 5]. The aim of our study was to develop a method to prepare MAA microparticles in a more defined, tunable and reproducible manner. To do this, a microfluidic chip was prepared using thiol-ene chemistry that had an integrated flow focusing droplet generator and curing network [Figure 1A]. Aqueous droplets containing albumin were formed within a continuous oil phase, which then travelled through a 1.2 m long channel heated to 85°C to denature and aggregate the protein into stable MAA microparticles. By carefully adjusting the flow rates into the chip, microparticles between 70 to 300 μm with a polydispersity index of Overall, this study shows that microfluidics is a viable alternative to prepare MAA in a more controlled fashion. Although it was not possible to obtain microparticles smaller than 70 μm with our current set up, changes in the geometry of the flow focusing region or refinement of the continuous oil phase may solve this problem. Current studies are also undergoing to evaluate how drugs can be incorporated within the MAA microparticle matrix for passive lung-targeting delivery.

References: 1. Bhushan, B., et al., Impact of albumin based approaches in nanomedicine: Imaging, targeting and drug delivery. Advances in Colloid and Interface Science, 2017. 246: p. 13-39. 2. Wang, J. and B. Zhang, Bovine Serum Albumin as a Versatile Platform for Cancer Imaging and Therapy. Curr Med Chem, 2018. 25(25): p. 2938-2953. 3. Spada, A., et al., The Uniqueness of Albumin as a Carrier in Nanodrug Delivery. Molecular Pharmaceutics, 2021. 18(5): p. 1862-1894. 4. Hung, J.C., et al., Evaluation of Macroaggregated Albumin Particle Sizes for Use in Pulmonary Shunt Patient Studies. Journal of the American Pharmaceutical Association (1996), 2000. 40(1): p. 46-51. 5. Arshady, R., Albumin microspheres and microcapsules: Methodology of manufacturing techniques. Journal of Controlled Release, 1990. 14(2): p. 111-131.

Image/Figure:

https://s3.amazonaws.com/amz.xcdsystem.com/1E8A4501-BB41-A02A-1D3B9882B798BFAA_abstract_File10351/GA315_ImageFigure_0513040341.jpg

Image/Figure Caption: Fig.1: (A) Design of the microfluidic device used for the preparation of MAA microparticles showing the inlets for the acqueous albumin solution and continuous oil phase; in the dashed box is an enlargement of the flow-focusing region of the device. (B) Size distribution of the microfluidic MAA microparticles obtained by using different flow rates compared to clinical grade 99mTc-MAA. (C) Representative SPECT/CT images of intravenously administered 111In-labeled microfluidic MAA into mice over 24 h. B, bladder; L, lungs; Li, liver; Sp, spleen.

First Name: Marta

Last Name: Bergamo

Email: marta.bergamo@alumni.ubc.ca

Organization: University of British Columbia

Country: Canada

ID: GA316
High Throughput Preclinical Digital PET/CT – A Multi-rodent Approach and Demonstration

Katherine Binzel, Wright Center of Innovation in Biomedical Imaging, binzel@wcibmi.org

---

Category: Instrumentation

Abstract Body : Aim: Micro-CT systems traditionally used for preclinical imaging of small animals is limited in terms of throughput. New digital photon counting PET technology provides improved count statistics and higher definition image reconstruction such that a clinical system can now deliver adequate image quality for rodents and other small preclinical imaging. We have fabricated a 'mouse hotel' for high throughput imaging, testing the feasibility, image quality, and quantitative robustness of imaging multiple animals in a single imaging session under anesthesia. Methods: Animal subjects from several ongoing preclinical studies underwent imaging on a next-generation digital PET/CT system (Philips Vereos). The animals were injected with 18F-FDG via tail vein injection. Approximately 40-60 minutes post-injection, the animals were anesthetized and placed, up to 6 at a time, in the mouse hotel. The hotel is comprised of numerous clear resin blocks with columns bored through the centers, large enough to accommodate a single mouse per block. The blocks are slid into a Plexiglas grid and placed inside an induction chamber connected to the anesthesia machine. This way each animal is positioned separately and stably for the duration of imaging. Following a high resolution CT scan, a single 10 min PET acquisition was performed, covering all 6 rodents at once. Retrospective image reconstruction is then performed, one reconstructed image set per rodent, to correct for each animal's weight, injection dose, and injection time. An ultra-high definition 1x1x1 mm voxel image reconstruction can be performed retrospectively as well. Results: Imaging was performed in a robust manner, 18 mice were imaged on two separate days as part of the larger experiment being conducted. The average injected dose was 168 mCi, and the 10 min PET acquisition provided more than sufficient counts for excellent image quality upon reconstruction. Visual and quantitative assessments of the images were aided by use of a separate reconstructed image set per animal, and correlation of the images from the two days was readily achieved. The mouse hotel enabled high quality, high throughput imaging with all 18 animals completed from injection to acquisition in about 2 hours' time, each day. The use of resin cubes for animal placement within the hotel allowed for easy substitution with another cube in cases of urine or other radioactive contamination during imaging, causing no delays in beginning imaging for the next batch of animals. Conclusion: High throughput preclinical imaging on a clinical PET/CT system is accurate and robust, as enabled by the next generation digital photon counting technology and the development of a system for imaging multiple animals simultaneously. This approach can help facilitate translational research, cutting back on cost and time, as well as stress on the animal subjects. Improved utilization of radiotracers via batch injection and imaging is valuable in all scenarios, particularly those involving short lived radionuclides.

Image/Figure:

https://s3.amazonaws.com/amz.xcdsystem.com/1E8A4501-BB41-A02A-1D3B9882B798BFAA_abstract_File10351/GA316_ImageFigure_0513040729.jpg

First Name: Katherine

Last Name: Binzel

Email: binzel@wcibmi.org

Organization: Wright Center of Innovation in Biomedical Imaging

Country: United States

ID: GA317
Quantitative Detection of Gemcitabine Delivery and Resulting Metabolic Implications

Caitlin Tressler, The Johns Hopkins University School of Medicine, ctressl3@jhmi.edu

---

Category: Oncology

Abstract Body : Introduction: Gemcitabine is a first line chemotherapy agent used to treat pancreatic cancer and metastatic disease [1]. While gemcitabine metabolism has been well studied by LC-MS and pharmacokinetics, little has been done to determine the spatial distribution of drug delivery and metabolism [1-3]. This is particularly important as pancreatic tumors are prone to high rates of reoccurrence, which may result from non-uniform distribution and response to treatment across the tumor. Furthermore, the metabolic response to gemcitabine treatment in tumor tissue is unknown. Methods: Athymic nude mice were inoculated in their flanks with Panc1 tumors which were grown to 500 cm3. Prior to euthanasia, animals were injected with 200 mg/kg gemcitabine via tail vein at 0.5, 1.0, and 2.0 hours. Animals were euthanized with CO2, and tumors, pancreases, livers, and kidneys were collected for analysis. Tissue mimetic model was prepared from homogenized untreated mouse liver. All tissues were cryo-sectioned at 10-micron thickness onto pre-chilled indium tin oxide slides. MALDI imaging was performed on a Bruker RapifleX MALDI TOF/TOF instrument. Tissues were imaged at 50-micron pixel size in reflectron positive mode with 200 laser shots per pixel. Mass spectral range was m/z 150 to 2,000. Data was normalized to total ion count and analyzed in FlexImaging and SCiLS Lab. Results: Gemcitabine was detected in tumors and quantified using the tissue mimetic model. Concentrations of gemcitabine peaked at 0.5 hours post-injection at around 230 μg per mg tissue in the tumor tissue. In addition, gemcitabine triphosphate was detected in treated tissues. Tumor tissue images were imported into SCiLS lab for unsupervised analysis of the lipid region (m/z 400 to 1,200). Segmentation analysis revealed significant differences between the 1 and 2 hour-time points. These differences in segmentation were also observed in the pancreas but not in liver and kidney. Discussion: Our data demonstrate that gemcitabine was metabolized to the active drug metabolite gemcitabine triphosphate in tumor and pancreas and peaked at 1 hour of post-injection. MALDI images of [Gem+H+] at m/z 264 revealed that gemcitabine and gemcitabine triphosphate were not evenly distributed throughout the tumor. Profound overall metabolite and lipid profile changes were observed in tumor and pancreas as shown by segmentation analysis, likely resulting from a metabolic response to gemcitabine treatment. Conclusions: Gemcitabine is delivered and metabolized unevenly across Panc1 flank tumor models. Furthermore, gemcitabine has a profound effect on metabolites and lipids within tumor tissue. We are currently completing measurements of additional biological repeats, histopathology stains (H&E, trichrome) and identifying metabolite and lipid markers of response to gemcitabine treatment.

References: 1. de Sousa Cavalcante, L. and G. Monteiro, Gemcitabine: metabolism and molecular mechanisms of action, sensitivity and chemoresistance in pancreatic cancer. Eur J Pharmacol, 2014. 741: p. 8-16. 2. Bapiro, T.E., et al., Gemcitabine diphosphate choline is a

major metabolite linked to the Kennedy pathway in pancreatic cancer models in vivo. Br J Cancer, 2014. 111(2): p. 318-25. 3. Bapiro, T.E., et al., A novel method for quantification of gemcitabine and its metabolites 2',2'-difluorodeoxyuridine and gemcitabine triphosphate in tumour tissue by LC-MS/MS: comparison with (19)F NMR spectroscopy. Cancer Chemother Pharmacol, 2011. 68(5): p. 1243-53.

Image/Figure:

https://s3.amazonaws.com/amz.xcdsystem.com/1E8A4501-BB41-A02A-1D3B9882B798BFAA_abstract_File10351/GA317_ImageFigure_0513040751.png

Image/Figure Caption: MALDI imaging of gemcitabine (Gem) and gemcitabine triphosphate (GemTP) in Panc1 tumor xenografts. (A) Simultaneous Gem (red, m/z 264) and GemTP (green, m/z 504) imaging in Panc1 tumor xenograft sections in the PBS control and at the three post-injection time points of Gem treatment in our mouse study was possible with DHB matrix. (B) On tissue quantification of both Gem and GemTP. (C) Unsupervised segmentation analysis of Panc1 tumor xenografts demonstrating global changes as a result of Gem treatment and metabolism.

First Name: Caitlin

Last Name: Tressler

Email: ctressl3@jhmi.edu

Organization: The Johns Hopkins University School of Medicine

Country: United States

ID: GA318
Identification of a suitable untargeted agent for the clinical translation of ABY-029 paired-agent imaging in fluorescence guided surgery

Cheng Wang, Dartmouth College, cheng.wang.th@dartmouth.edu

Category: Oncology

Abstract Body : Non-specific uptake and retention of molecular targeted agents and heterogeneous tissue optical properties diminish the ability to differentiate between tumor and normal tissues using molecular targeted fluorescent agents. Paired-agent imaging (PAI) can increase the diagnostic ability to detect tumor tissue by mitigating these non-specific effects and providing true molecular contrast by co-administration of an untargeted control imaging agent with a targeted agent. This study evaluates the suitability of available clinically translatable untargeted agents for the translation of PAI in fluorescence guided surgery using an affibody-based targeted imaging agent (ABY-029). Three untargeted agents that fluoresce near 700 nm and exhibit good clinical safety profiles (methylene blue, IRDye 700DX and IRDye 680LT) were tested in combination with the clinically tested IRDye 800CW labeled anti-epidermal growth factor receptor (EGFR) Affibody molecule, ABY-029 (eIND 122681). Properties of the untargeted agent important for human use and integrity of PAI were tested: 1) plasma protein binding; 2) fluorescence signal linearity in in vitro whole blood dilution; 3) in vivo pharmacokinetic matching to targeted agent in negative control tissue; and 4) in vivo diagnostic accuracy of PAI vs single agent imaging (SAI) of ABY-029 alone in orthotopic oral head and neck squamous cell carcinomas. Results: Overall, IRDye 680LT outperformed IRDye 700DX and methylene blue with the highest signal linearity ($R2 = 0.9998 \pm 0.0002$, 0.9995 ± 0.0004, 0.91 ± 0.02, respectively), the highest fluorescence yield in whole blood at 1 μM (104.42 ± 0.05, 103.68 ± 0.09, 101.9 ± 0.2, respectively), and the most closely matched ABY-029 pharmacokinetics in EGFR-negative tissues (Binding Potential error percentage = $0.31\% \pm 0.37\%$, $10.25\% \pm 1.30\%$, and $8.10\% \pm 5.37\%$, respectively). The diagnostic ability of PAI with ABY-029 and IRDye 680LT outperformed conventional SAI with an area-under-the-receiver-operating-characteristic curve (AUC) value of 0.964 vs. 0.854, and 0.978 vs. 0.925 in the Odyssey scanning system and Pearl wide field imaging system, respectively. Conclusion: PAI is a highly promising methodology for increasing detection of tumors in fluorescence guided surgery. Although not yet clinically approved, IRDye 680LT demonstrates promise as an untargeted agent when paired with ABY-029. The clinical translation of PAI to maximize tumor excision, while minimizing normal tissue removal could improve both patient survival and life quality.

Full Name of Abstract's 1st Author : Cheng Wang

First Name: Cheng

Last Name: Wang

Email: cheng.wang.th@dartmouth.edu

Organization: Dartmouth College

Country: United States

ID: GA319

Comparison of different routes of administration and in vivo biodistribution of the vaccine adjuvant P60 using SPECT/CT imaging

Marta Bergamo, University of British Columbia, marta.bergamo@alumni.ubc.ca

---

Category: Immunology: Inflammation & Infection

Abstract Body : Vaccines commonly include adjuvants in order to increase the immune response against the antigen that is contained within the formulation [1]. In order to elicit the desired immune response, different adjuvant strategies can be employed, such as depletion in the lymphatic tissues of T-regulatory cells (T-regs), an immunosuppressive subset of CD4+ cells [2]. It was reported that the cell-penetrating peptide P60 could selectively impair T-regs by binding to FOXP3, a nuclear transcription factor found in the T-regs' nucleus [3]. P60 showed some efficacy in murine models, but its pharmacokinetics remains unknown. With this study, we aimed to evaluate the in vivo biodistribution of a radioactive version of P60 by using SPECT/CT imaging. P60 c-terminal cysteine was modified site-specifically with the chelator maleimide-DTPA, in order to stably radiolabel it with the gamma-emitter 111In, obtaining the final product 111In-DTPA-P60. The latter was characterized in vitro, by assessing its toxicity, cellular uptake and proteolytic stability in mouse serum. 111In-DTPA-P60 was then administered to healthy mice intravenously (IV), subcutaneously (SQ) and intraperitoneally (IP). Afterwards, the mice underwent serial SPECT/CT scans over 24 h. Quantitative analysis on the imaging data allowed to evaluate organ accumulation over time, and ex vivo biodistribution was performed following the terminal scan. Maximum cellular uptake was observed within two hours and 111In-DTPA-P60 showed good stability in mouse serum. The peptide did not show toxicity, both in vitro and in vivo. From the pharmacokinetics analysis, 111In-DTPA-P60 was rapidly cleared via the renal pathway for all the routes of administration tested. Negligible uptake was observed in the target tissues, such as the lymph nodes, at all time points following IV, IP and SQ injections of the radiolabeled peptide. Overall, 111In-DTPA-P60 showed to be quickly eliminated by the kidneys, thus not allowing the peptide to be retained in target lymphatic tissues long enough to translocate into T-regs' nucleus and inhibit their function. Our data shows that to optimally utilize P60 as a vaccine adjuvant and increase its efficacy, new peptide modifications and/or formulations should be investigated.

References: 1. Petrovsky, N. and J.C. Aguilar, Vaccine adjuvants: Current state and future trends. Immunology And Cell Biology, 2004. 82: p. 488. 2. Nair, S., et al., Vaccination against the forkhead family transcription factor Foxp3 enhances tumor immunity. Cancer Res, 2007. 67(1): p. 371-80. 3. Casares, N., et al., A peptide inhibitor of FOXP3 impairs regulatory T cell activity and improves vaccine efficacy in mice. J Immunol, 2010. 185(9): p. 5150-9.

Image/Figure:

https://s3.amazonaws.com/amz.xcdsystem.com/1E8A4501-BB41-A02A-1D3B9882B798BFAA_abstract_File10351/GA319_ImageFigure_0513042404.jpg

Image/Figure Caption: At the top, structure of 111In-DTPA-P60. The radiolabeled peptide was administered to healthy mice subcutaneously (blue), intravenously (red) and intraperitoneally (green). At the bottom, representative SPECT/CT images at 0 h, showing activity located at the injection site (IS), and its retaintion over time (graph in dashed box), bladder (Bl) and in the intraperitoneal space (IP).

First Name: Marta

Last Name: Bergamo

Email: marta.bergamo@alumni.ubc.ca

Organization: University of British Columbia

Country: Canada

ID: GA320
Optimized Coil Design for Direct Feedthrough Suppression in Magnetic Particle Imaging

Quincy Huynh, University of California, Berkeley, quincy.huynh@berkeley.edu

---

Category: Instrumentation

Abstract Body : The arbitrary waveform relaxometer (AWR) is an indispensable platform for developing magnetic nanoparticle tracers for magnetic particle imaging (MPI) applications. By characterizing the point spread function (PSF) of a specific magnetic nanoparticle, the AWR can evaluate the performance (e.g. SNR and spatial resolution) of the magnetic nanoparticle for MPI [1]. The design of wideband (DC-400 kHz) and arbitrary waveforms enables rapid optimization of pulse sequence design. Currently, the AWR serves as a complementary tool for MPI as well as a sensor for many applications [2-4]. One of the biggest challenges in arbitrary waveform excitation is direct feedthrough interference, which is usually six orders of magnitude larger than the signal from magnetic nanoparticles. In MPI and conventional magnetic particle spectrometers (MPS), a high-pass filter and tuned filter are applied to filter out the single tone interference, which cannot be done for arbitrary waveform excitation. The AWR uses a very fine shimming system, which employs a cantilever and duplicated gradiometer receive coil. This mechanism currently achieves over six orders of magnitude of direct feedthrough attenuation [1]. A challenge in mechanical coil shimming is that it is highly sensitive to spatial variations, which often occur as the shimming process is done before each scan to ensure the highest possible feedthrough rejection. This abstract will show results for a design of a solenoidal gradiometric coil that is less sensitive to spatial variations and still provides adequate direct feedthrough rejection. The main approaches used are that varying the winding pitch at the ends of the transmit (TX) solenoid coil reduces the spatial variation of the magnetic field produced when driven by a current; and varying the winding pitch at the ends of the receive (RX) solenoid coil reduces the spatial variation of the total flux through the loops of the coil. Preliminary results show a factor of 2 reduction in spatial variation with just one varied pitch extra turn on the ends of the TX and RX coils.

References: [1] Tay ZW, et. al, Sci rep. 2016; [2] Orlov AV, et. al, Analytical chem. 2013; [3] Khurshid H, et. al, Med phys. 2018; [4] Wu K, et. al, J of Physics D: Applied Phys. 2019; [5] Pantke D, et. al, Med phys. 2019; [6] Huang W, et. al, J of EM Eng Sci, 2018. [7] Ütkür M, et. al, IWMPI 2015; [8] Cagil AR, et. al, IJMPI 2020

Image/Figure:

https://s3.amazonaws.com/amz.xcdsystem.com/1E8A4501-BB41-A02A-1D3B9882B798BFAA_abstract_File10351/GA320_ImageFigure_0513042534.png

Image/Figure Caption: Top plot is the normalized received flux (or mutual inductance) versus distance from coil center of two concentric TX and RX gradiometric coils. The blue line is the

magnetic flux for a tightly wound coil, the orange line is the flux for a coil with an extra turn that is 10 mm away. Mutual inductance can be used to quantify the direct feedthrough. The bottom plot is the slope of the mutual inductance.

First Name: Quincy

Last Name: Huynh

Email: quincy.huynh@berkeley.edu

Organization: University of California, Berkeley

Country: United States

ID: GA323

Evaluation of [18F]4-fluorogabapentin in healthy rats, healthy non-human primates, and a rat model of neuropathic pain

Yu-Peng Zhou, Massachusetts general hospital, yzhou40@mgh.harvard.edu

---

Category: Neuroscience

Abstract Body : Introduction: Current assessment of neuropathic pain relies on self-reported pain and the physiological/behavioral response to evoking stimuli, which do not provide information of changes at the cellular or molecular level.1 PET imaging is a noninvasive molecular imaging technique that can quantify biochemical processes underlying pain mechanisms. Increased expression of the α2δ-1 subunit of voltage-dependent calcium channels has been observed in the spinal cord and nerves in many different animal models of neuropathic pain2. Additionally, gabapentinoids, which bind to the α2δ-1 protein, reverse the increase in α2δ-1 expression and reduce the neuropathic pain phenotype in animal models.2 Therefore, the expression level of α2δ-1 appears to be a robust biomarker of neuropathic pain. Gabapentin, a highly selective α2δ-1 ligand with nanomolar affinity, is a first line treatment for neuropathic pain3. Based on this knowledge, we hypothesized that radiolabeled gabapentin could serve as a new PET tracer and offer objective measures of neuropathic pain. Two novel fluorinated derivatives of gabapentin (cis- and trans- 4-fluorogabapentin) and their 18F-labeled versions have been developed recently.4 Here, we describe the evaluation of these novel radiotracers in healthy non-human primates, healthy rats, and rats post spinal nerve ligation (SNL), a model of neuropathic pain. Methods: Radiotracers trans-[18F]4-fluorogabapentin ([18F]tGBP4F) and cis-[18F]4-fluorogabapentin ([18F]cGBP4F) were synthesized according to recently developed method.4 SNL rats were acquired from Charles River ~7 days post-surgery. The specific binding of the tracer was confirmed using in vitro autoradiography on rat spinal cord sections. The binding affinity (IC50) was measured by competitive radioligand binding to spinal cord sections using quantitative autoradiography. Rats were euthanized at 75 min after tracer injection and the critical tissues were dissected and counted using a gamma-counter. Following gamma-counting, the spinal nerves were imaged using ex vivo autoradiography. Dynamic PET imaging and arterial blood sampling were performed on two rhesus monkeys at baseline and after pre-injection of gabapentin (5 mg/kg). Blood samples were analyzed by gamma counting and HPLC to determine the radioactivity concentrations in whole blood and plasma as well as radiometabolites. Time activity curves were extracted from brain regions of interest and kinetic analysis was applied to estimate volume of distribution and receptor occupancy. Results: Autoradiography on rat spinal cord sections showed binding of both radiotracers to the dorsal horn region consistent with the reported expression of α2δ-1 protein by immunohistochemistry5. [18F]tGBP4F showed slightly higher binding affinity than gabapentin whereas [18F]cGBP4F showed lower binding affinity (IC50: tGBP4F = 23 ± 11 nM, n = 4; GBP = 35 ± 12 nM, n = 4; cGBP4F > 500 nM, n = 2). Analysis of monkey blood showed that both radiotracers undergo minimal metabolism in vivo (>95% parent fraction 90 min post injection) and that the tracer has low plasma protein binding (free fraction >90%). Monkey dynamic PET imaging showed modest brain penetration and differences between the tracers (brain SUV120-180min: [18F]tGBP4F =

~0.3, [18F]cGBP4F = ~0.6). Logan and Lassen graphical analyses indicated 60.1 ± 6.3% specific displacement of [18F]cGBP4F by gabapentin at 5.0 mg/kg. In rats, the brain penetration was consistent with that in monkeys. Gamma counting and ex vivo autoradiography studies in SNL rats showed significant increase in tracer accumulation in ligated nerves compared with non-ligated nerves (tGBP4F: 205 ± 51%, n = 5; cGBP4F: 166 ± 22 %, n = 4). Conclusion: α2δ-1 PET radiotracers trans-4-fluorogabapentin ([18F]tGBP4F) and cis-4-fluorogabapentin ([18F]cGBP4F) were synthesized and evaluated in vitro, in vivo, and ex vivo. [18F]tGBP4F showed >20-fold higher in vitro binding affinity towards α2σ-1 and [18F]cGBP4F showed higher CNS permeability. Both tracers showed significant increase of tracer accumulation at the ligated nerves, which indicate their potential application in PET imaging of neuropathic pain.

References: [1] PAIN 135, 7-10 (2008); [2] Neuroscience 338, 183-206 (2016). [3] Nat. Rev. Neurosci. 13, 542-555 (2012); [4] J. Nucl. Med. 61 (supplement 1), 68 (2020); [5] Neuroscience 155, 510-521 (2008).

First Name: Yu-Peng

Last Name: Zhou

Email: yzhou40@mgh.harvard.edu

Organization: Massachusetts general hospital

Country: United States

ID: GA324
Optimizing and functionalizing a radiolabeled dendrimer nanosystem for PET imaging of glioblastoma

Béatrice Louis, AIX-MARSEILLE UNIVERSITE, beatrice.louis@etu.univ-amu.fr

---

Category: Oncology

Abstract Body : Nanometric size promotes the penetration of chemicals into solid tumors via the enhanced permeability and retention effect (EPR effect) that is not constantly found. Late diagnosis and variability of drug penetration in tumors are both regularly associated with poor prognosis. To these concerns, supramolecular radiolabelable dendrimers self-assembling into "dendrimersomes" were designed to assess EPR effect heterogeneity (see References). Aiming at lowering healthy organ exposure and increasing tumor uptake, dendrimers underwent chemical modifications for optimization. To improve targeting efficiency and specificity, functionalization of the dendrimers with a specific RGD moiety was considered to target the αvβ3 integrin, widely overexpressed in many tumors including glioblastoma. This study aimed at 1) evaluating the impact of chemical modifications on dendrimer biodistribution to select the best formulation and 2) evaluating the impact of the functionalization on the in vitro binding specificity of dendrimersomes and on their in vivo biodistribution and tumor targeting. Methods: Five different dendrimer formulations (A,B,C,D,E) were radiolabeled with gallium-68. Healthy Swiss mice (n=6 per formulation) were injected intravenously and dynamically imaged using microPET/CT. Activities were quantified at 5, 10, 15, 20, 30, 45, 60, 75, 90, and 120min post-injection in the organs of interest. Six mice per formulation were injected intravenously with gallium-68 dendrimersome, 20µL-blood samples were withdrawn at PET time points, and quantified using a calibrated gamma counter. Mice were euthanized at 120min and organs were harvested and counted using gamma-counter. Quantifications were expressed as %ID/g. Non-compartmental analysis (NCA) and compartmental analysis (CA) were achieved with PKanalix and Monolix softwares respectively. Different ratios of the optimal radiolabelled dendrimer / RGD moiety (6:1, 3:1, 1:0, 1:3, 1:6, 1:9) were evaluated by cell-based receptor binding assay on U87 human glioblastoma cells (n=3). MicroPET/CT studies were performed in athymic nude mice (n=4) bearing orthotopic U87 glioblastoma xenografts with the best-functionalized dendrimersome identified in vitro, compared to the non-functionalized dendrimersome. Results: Radiochemical purity was superior to 95% and stable at least up to 4h in 37°C serum. Amongst the 5 formulations, microPET results with formulation E showed significantly lower retention in the liver and increased urinary elimination compared to the others with significantly higher activity in the bladder at 2h (Fig.1a, Table 1). These results were confirmed by gamma-counting (Table 2). Dendrimersome E also displayed the lowest systemic exposure with an AUC of 0.038 %ID/mm3.h, the highest clearance (2.656 mL/h), and a short blood terminal half-life (2.21 h), which could be ascribed to a more efficient renal elimination as suggested by bladder data (Table 3). The volume of distribution was higher than for other dendrimers (8.002mL versus 4.031-5.954mL), suggesting a wider distribution in the organism, in line with the higher concentrations observed at the first time points in the main organs. AUCs in the main organs were contrarily lower for dendrimersome E, due to a short half-life. The semi-mechanistic model confirmed

other dendrimersomes were retained longer in the liver, with lower transfer rates from the liver to blood. The 6:1, 3:1, and 1:3 ratios showed a significantly improved dendrimersome binding on U87 cells compared to the 1:0 control ratio (Table 4). The 1:3 ratio was selected for in vivo studies. A significant increase of microPET/CT quantifications in tumors was observed with the 1:3 ratio functionalized dendrimersome compared with the non-functionalized dendrimersome (brain-to-cerebellum activity ratios respectively: 1.80± 0.65 and 1.47±0.62; *P =0.0382, Fig.1b). Conclusion: Formulation E appeared as the optimal dendrimer with an optimized biodistribution profile. Functionalisation of radiolabelled dendrimersomes provides a new perspective for adding molecular targeting to passive EPR targeting, illustrating the high versatility of this type of nanosystem for molecular imaging and offering novel outlooks for theranostics applications.

References: (1) https://doi.org/10.1073/pnas.1812938115 ; (2) https://doi.org/10.1039/C9CC07750B ; (3) https://doi.org/10.1002/smll.202003290 ;

Image/Figure:

https://s3.amazonaws.com/amz.xcdsystem.com/1E8A4501-BB41-A02A-1D3B9882B798BFAA_abstract_File10351/GA324_ImageFigure_0513043623.png

Image/Figure Caption: Fig. 1a : Representative images from microPET/CT of healthy mice injected with each formulation of dendrimer. Fig. 1b: Representative images from microPET/CT of orthotopic U87 glioblastoma mice injected with dendrimer A, E or E+RGD (1:3).

Full Name of Abstract's 1st Author : Béatrice LOUIS

First Name: Béatrice

Last Name: Louis

Email: beatrice.louis@etu.univ-amu.fr

Organization: AIX-MARSEILLE UNIVERSITE

Country: France

ID: GA325

Clinical Translation of Near Infrared Nerve-Specific Fluorophores for Fluorescence-Guided Nerve Sparing Surgical Procedures

Connor Barth, Oregon Health & Science University, connorwbarth@gmail.com

---

Category: New Chemistry, Materials & Probes

Abstract Body : Nerve damage plagues surgical outcomes, significantly affecting post-surgical quality of life. Nerve damage occurs in ~8% of all surgeries and intraoperative nerve injuries affect 25 million patients annually worldwide, incurring undue pain, loss of function, and high costs to the healthcare system. Intraoperative nerve detection is completed using anatomical knowledge and conventional white light visualization when possible. However, nerves can be difficult or impossible to identify by white light visualization and neuroanatomy is often varied between patients. Fluorescence-guided surgery (FGS) offers a potential means for enhanced intraoperative nerve identification and preservation. To date, a variety of nerve specific fluorophores have been tested in preclinical models, however a clinically approved nerve-specific contrast agent does not yet exist. Synthesis and functional validation of a nerve-specific library has resulted in development of the first-in-class near infrared (NIR) nerve-specific small molecule fluorophores for translation to first-in-human clinical studies using existing clinical infrastructure of FGS systems. Further synthetic tuning of the most promising fluorophores has generated improved brightness, solubility, and safety. Increased brightness levels have resulted in 2-3x increase in nerve signal-to-background ratio (SBR). Improved solubility has enable water-soluble nerve-specific fluorophores with improved toxicity. Single-dose toxicity testing including blood chemistry and 14-day monitoring has facilitated definition of the no observable adverse effect level (NOAEL), informing plans for upcoming investigational new drug (IND) enabling studies. Pharmacodynamics studies have been completed to identify the optimal imaging time point and dose, where nerve contrast is generated within 15 minutes and remains present for up to four hours following systemic administration. Clinically relevant formulation strategies have been explored to enable solubilization of these promising fluorophores for systemic administration when necessary. Micelle based formulations have been identified that provide equivalent performance to the previously utilized co-solvent formulation while possessing clinically relevant safety and stability profiles. Additional work is underway to identify the biomolecular target of these structure-inherent targeting small molecule fluorophores to enable a mechanistic understanding for nerve-specificity. Clinically relevant, minimally invasive surgical procedures guided by NIR nerve-specific fluorescence have been completed in large animal models using the da Vinci surgical robot, demonstrating efficacy in surgically relevant models using existing clinical FGS system intrastructure. Given the interplay between recent synthetic tuning efforts and safety and pharmacology testing, we anticipate translation to the clinic within the next two years. We believe that the continued development and use of these fluorophores in humans will improve nerve identification during surgery and reduce nerve injury, improving outcomes across all surgical specialties.

First Name: Connor

Last Name: Barth

Email: connorwbarth@gmail.com

Organization: Oregon Health & Science University

Country: United States

ID: GA326

Myelin content is decreased in the brain of Down syndrome animal model compared to its littermate wild type during aging process: an in vivo PET 11C-PIB imaging study

Larissa Estessi de Souza, University of Sao Paulo Medical School, larissa.estessi@gmail.com

---

Category: Neuroscience

Abstract Body : Introduction: There is evidence that with normal aging, defects in myelin occur, which are an early pathological mark that occurs in oligodendrocytes before other brain cells show signs of degeneration(1). Molecular neuroimaging allows in vivo and noninvasive studies of cellular and molecular processes, and therefore, is an important tool to understand the cells changing over time. Positron Emission Tomography (PET) imaging using Pittsburgh Compound B labelled with carbon-11 (11C-PIB) is traditionally used for β-amyloid plaque quantification, however, in the last decade has also been used for myelin quantification (2-4). Objective: The objective of this study was to evaluate the myelin content changes over the life of an animal model of Down syndrome (Ts65Dn) and its wild type, by 11C-PIB PET imaging. This in vivo evaluation has not been previously performed in the literature. Methods: Transgenic mice (TS65Dn) and its littermate wild type (WT), were evaluated with 11C-PIB PET imaging in 3 different ages: 2, 5 and 14-month-old (WT=6 and Ts65Dn=6 animals). 11C-PIB (±18 MBq) was injected intravenously and 30 min after tracer injection a static PET image of 20 min was acquired in a PET scanner for small animals (β-cube, Molecubes) with the animal anesthetized with isoflurane 2-3% in oxygen. Images were quantified by PMOD™ software using T1-MRI as brain template and the data was expressed in SUV (Standardized Uptake Value) mean±standard deviation in different brain regions: striatum, cortex, hippocampus, thalamus, cerebellum, brainstem and midbrain. Comparisons were made by 2-way ANOVA (SPSS). Statistical differences were considered significant when $P \leq 0.05$. Results: 11C-PIB uptake profile is similar in the transgenic and WT animals, showing increased uptake at 5 months of age, compared to 2 months, indicating ongoing myelination process. At 14 months, the 11C-PIB uptake is significantly lower in the Ts65Dn compared to the WT animals indicating that the Down syndrome animals are more affected by myelin loss caused by aging process. The 11C-PIB uptake (SUV) was, WT 2-month-old group: striatum 0.042±0.007, cortex 0.049±0.006, hippocampus 0.043±0.008, thalamus 0.041±0.007, cerebellum 0.044±0.007, brainstem 0.052±0.009 and midbrain 0.051±0.012; WT 5-month-old (compared to 2-months-old): 0.095±0.018 (p=0.001), 0.107±0.0220(p= 0.001), 0.104±0.027 (p=0.001), 0.095±0.026 (p=0.001), 0.109±0.024 (p=0.001), 0.118±0.035 (p=0.002) and 0.117±0.051 (p=0.001) in the respective brain regions; WT 14-month-old (compared to 2-months-old): 0.086±0.031 (p=0.005), 0.105±0.034 (p= 0.001), 0.093±0.032 (p=0.002), 0.089±0.033 (p=0.002), 0.100±0.022 (p=0.001), 0.105±0.037 (p=0.001) and 0.085±0.038 (p=0.004) in the respective brain regions. For the Ts65Dn 2-month-old, the 11C-PIB SUV was: striatum 0.038±0.013, cortex 0.037±0.012, hippocampus 0.033±0.013, thalamus 0.034±0.013, cerebellum 0.038±0.015, brainstem 0.044±0.015 and midbrain 0.039±0.015; Ts65Dn 5-month-age was (compared to 2-months-old)

0.091±0.020 (p=0.001), 0.094±0.015 (p=0.001), 0.096±0.020 (p=0.001), 0.082±0.019 (p=0.001), 0.094±0.010 (p=0.001), 0.103±0.020 (p=0.001) and 0.094±0.023 (p=0.004) in the respective brain regions; Ts65Dn 14-month-old (compared to 2-months-old) 0.073±0.023 (p=0.015), 0.085±0.029 (p= 0.004), 0.076±0.020 (p=0.006), 0.068±0.020 (p=0.013), 0.078±0.024 (p=0.002), 0.083±0.020 (p=0.013) and 0.063±0.020 (p=0.066) in the respective brain regions. At 14-months-old there was uptake difference between WT and Ts65Dn in hippocampus (p=0.031), thalamus (p=0.030), brainstem (p=0.015) and midbrain (p=0.010). Conclusion: 11C-PIB PET imaging showed similar myelination process in the brain of WT and Ts65Dn animals and showed that in older animals (14 months) the myelin content in the Down syndrome animal model is significantly lower than in its littermate wild type indicating that these animals are more affected by the aging process regarding myelin content.

References: 1. Chapman TW, Hill RA. Neuroscience Letters. 2020;715. 2. Stankoff B, et al. Ann Neurol. 2011;69(4):673-80. 3. Faria Dde P, et al. Eur J Nucl Med Mol Imaging. 2014;41(5):995-1003. 4. Carvalho RHF, et al. Multiple Sclerosis and Related Disorders. 2019;35:108-15.

Full Name of Abstract's 1st Author : Larissa Estessi de Souza

First Name: Larissa

Last Name: Estessi de Souza

Email: larissa.estessi@gmail.com

Organization: University of Sao Paulo Medical School

Country: Brazil

ID: GA327
Super-resolution of HP 13C images through high frequency transfer

Kofi Deh, Memorial Sloan Kettering Cancer Center, kofi.deh@gmail.com

---

Category: Computational & Data Science

Abstract Body : INTRODUCTION: Despite an unprecedented increase in spatio-temporal resolution of 13C metabolic imaging afforded by dissolution dynamic nuclear polarization (dDNP), the currently achievable spatial resolution is unsatisfactory. Even the application of compressed sensing and variable-resolution imaging (1,2) may not be sufficient to obtain satisfactory spatial resolution for metabolic products produced in low concentrations or for probes with low polarization rates (e.g. [1-13C]dehydoxyascorbate, [2-13C]pyruvate, [6-13C]arginine, [1-13C]glutamine) (3). Researchers have proposed super-resolution (SR) of the acquired 13C image using a corresponding anatomic proton image as a reference (4,5). However, this method depends on accurate registration and similarity of contrast between the proton and carbon images as well as accurate segmentation of the proton image, which may not be reasonable with complicated anatomy. This abstract shows that it is possible to generate high resolution 13C metabolic maps by transferring high spatial frequencies from a single high-resolution image of a thermal 13C phantom to a low-resolution 13C metabolite map, thus potentially realizing high spatial resolution HP MRI from existing data. METHOD: SR of 13C images via high-frequency transfer was demonstrated using multi-echo EPI data of phantoms and live mice on a preclinical Bruker Biospec 3T with a 1H/13C 42 mm diameter birdcage coil. The thermal phantom for constructing the SR database consisted of syringes and spheres containing 13C-Urea. Hyperpolarized 13C images of a mouse injected with 13C-pyruvate were acquired and separated into metabolite maps using a least-squares algorithm (IDEAL)(6). Theory: A MATLAB implementation of the example-based super-resolution algorithm (7) was used for this experiment. It extracts and stores overlapping patches from the feature maps of an input high resolution image and its blurred, downsampled version. By ensuring that the candidate patch for adding high-frequency content to the low-resolution image being upsampled matches not only the low-resolution patch being replaced but also the overlapping pixels, an image with a consistent appearance is generated. Fig. 1a describes the extension of this approach to hyperpolarized 13C data.RESULTS: Fig. 1b presents a scheme for generating high-resolution 13C maps by separating chemical species present in multi-echo EPI data with IDEAL and then upsampling the individual maps using SR. Figure 1c shows both the proton and the carbon EPI images of syringes and balls filled with 13C-labeled chemicals used for generation of the SR database at varying target resolution. The SR database is created from the first echo magnitude image of the carbon EPI acquisition and used to upsampled the 13C pyruvate map extracted with IDEAL from a multi-echo EPI imaging data of a mouse injected with 13C-pyruvate. Improved detail can be seen in the SR image compared to bicubic interpolation, which is the best performing standard approach (Fig. 1d). Extending this further, a noisy 13C-alanine map is upsampled with bicubic interpolation as well as with SR, and then overlaid on an anatomic image (Fig. 1e). The latter method shows the best visual improvement in visualization of 13C-alanine distribution in the heart and kidneys, including spatial resolution of the heart chambers

which is expected at higher spatial resolutions. Discussion:It has been shown that detail in low resolution 13C metabolite maps can be enhanced using transfer of high spatial frequencies from the scan of a thermal phantom, resulting in better visualization of anatomy such as the heart chambers and kidneys. Unlike the use of deep learning techniques, which require the use of large amounts of data, this approach only requires a single image. In future work, we will perform a quantitative comparison of superresolution algorithms for high-frequency transfer and apply these approaches to reconstruct higher spatial resolution human metabolic images which can not be readily acquired. Acknowledgements: NIH R01CA237466 and R01CA252037.

References: 1. Milshteyn E, von Morze C, Reed GD, Shang H, Shin PJ, Zhu Z, Chen HY, Bok R, Goga A, Kurhanewicz J, Larson PE, Vigneron DB. Development of high resolution 3D hyperpolarized carbon-13 MR molecular imaging techniques. Magnetic resonance imaging 2017;38:152-162. 2. Gordon JW, Autry AW, Tang S, Graham JY, Bok RA, Zhu X, Villanueva-Meyer JE, Li Y, Ohilger MA, Abraham MR, Xu D, Vigneron DB, Larson PEZ. A variable resolution approach for improved acquisition of hyperpolarized. Magnetic resonance in medicine : official journal of the Society of Magnetic Resonance in Medicine / Society of Magnetic Resonance in Medicine 2020;84(6):2943-2952. 3. Keshari KR, Kurhanewicz J, Bok R, Larson PE, Vigneron DB, Wilson DM. Hyperpolarized 13C dehydroascorbate as an endogenous redox sensor for in vivo metabolic imaging. Proc Natl Acad Sci U S A 2011;108(46):18606-18611. 4. Ma J, Park JM. Super-Resolution Hyperpolarized (13)C Imaging of Human Brain Using Patch-Based Algorithm. Tomography 2020;6(4):343-355. 5. Dwork N, Gordon JW, Tang S, O'Connor D, Hansen ESS, Laustsen C, Larson PEZ. Di-chromatic interpolation of magnetic resonance metabolic images. MAGMA 2021. 6. Deh K, Granlund KL, Eskandari R, Kim N, Mamakhanyan A, Keshari KR. Dynamic volumetric hyperpolarized. Magnetic resonance in medicine : official journal of the Society of Magnetic Resonance in Medicine / Society of Magnetic Resonance in Medicine 2021;85(2):978-986. 7. Freeman WT, Jones TR, Pasztor EC. Example-based super-resolution.

Image/Figure:

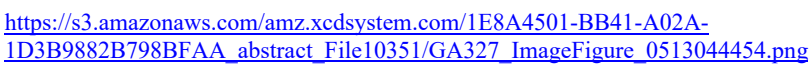
https://s3.amazonaws.com/amz.xcdsystem.com/1E8A4501-BB41-A02A-1D3B9882B798BFAA_abstract_File10351/GA327_ImageFigure_0513044454.png

Image/Figure Caption: a) Schematic of high frequency transfer thermal phantom to HP 13C imaging. b) Demonstration of multi-echo EPI imaging of a phantom of 13C-Urea and 13C-Acetate at a resolution of 1.6 mm with a separation of the image into separate maps by IDEAL. An SR database created from an 0.8 mm image of a 13C-Alanine phantom is used to upsample the 1.6 mm maps. The structural similarity index (SSIM) between the natively acquired high resolution image and the bicubic interpolated image is 0.2,, but increases to 0.5 for the SR image. c) Gradient-echo multi-echo maps of various containers with 13-C labeled chemicals for creating a SR database for in-vivo SR upsampling. d) An in-vivo metabolic map of 13C-pyruvate generated using IDEAL of multi-echo EPI images of a mouse injected with 13C-pyruvate. The images are upsampled 4-fold using bicubic interpolation and SR. White arrows show improved anatomic detail. e) An in-vivo metabolic map of 13C-alanine acquired at 3 mm, and upsampled 4-fold using bicubic and SR interpolation. White arrows show improved anatomic detail.

Full Name of Abstract's 1st Author : Kofi Deh

First Name: Kofi

Last Name: Deh

Email: kofi.deh@gmail.com

Organization: Memorial Sloan Kettering Cancer Center

Country: United States

ID: GA328
Imaging nanobiologic trained immunity therapy in cancer mouse models

Bram Priem, Icahn School of Medicine, bram.priem@gmail.com

Category: Oncology

Abstract Body : Introduction: Nanobiologic therapy can effectively induce trained immunity to inhibit tumor growth by overcoming the immunosuppressive tumor microenvironment. Trained immunity is a functional state of innate immune cells that is metabolically and epigenetically regulated, and can synergize with current clinically relevant checkpoint blockade therapies [1,2]. While the simultaneous targeting of trained immunity and immune checkpoints is very effective in several tumor mouse models, the exact changes in tumor immune microenvironment remain to be elucidated. The current study explores a combination of multi-probe PET imaging and single cell sequencing techniques to acquire a full picture of immune reprogramming as a result of the aforementioned combination immunotherapy. Methods and results: Trained immunity-inducing nanobiologics (TI-nanobiologics) were produced by microfluidics from phospholipids, cholesterol, apolipoprotein A-1 (apoA1) and a muramyl tripeptide functionalized phospholipid. TI-nanobiologics have a mean hydrodynamic diameter of 20 nm ± 2 nm (Đ = 0.3) and a discoidal morphology as shown by cryogenic transmission electron microscopy (Figure 1A). To determine their in vivo characteristics, nanobiologics were radiolabeled with zirconium-89 (89Zr) to allow studying their biodistribution in both mice and non-human primates using PET/CT and PET/MRI respectively. Upon intravenous administration in mice, PET/CT revealed nanobiologic accumulation in the bone marrow and spleen, with a relatively low liver uptake. Dynamic PET/MRI imaging of two non-human primates showed fast bone marrow and spleen accumulation, as well as liver uptake. At 48 hours post injection, uptake was predominantly found in the bone marrow and spleen to relatively favorable levels as compared to the liver (Figure 1B). To locally investigate cell association, live mice were injected with fluorescently labeled TI-nanobiologic as well as green fluorescent dextran and were subjected to intravital microscopy (IVM). The TI-nanobiologic association with myeloid cells was observed throughout the calvarium bone marrow (Figure 1C). Myelopoiesis, the production of myeloid cells from hematopoietic stem and progenitor cells (HSPCs), is an integral part of trained immunity resulting in systemic changes in the immune landscape [3]. This process is accompanied with metabolic changes in the bone marrow which was visualized and quantified by injecting C57BL/6 mice with 18F-fluorodeoxyglucose (18F-FDG) at day five after the first TI-nanobiologic injection followed by PET imaging. Significantly higher 18F-FDG uptake in the bone marrow of TI-nanobiologic treated animals was observed; the mean maximum standardized uptake value (SUVmax) in this treatment group was 1.45 ± 0.31 as compared to a SUVmax of 1.02 ± 0.04 for the control group (P = 0.017) (Figure 1D). Resulting changes in myeloid cell accumulation were investigated using PET imaging following intravenously injected 89Zr labeled CD11b-specific nanobodies [4]. PET/CT revealed a significantly higher SUVmax in the spleen one day post-treatment (SUVmax TI-nanobiologic: 2.9 ± 0.4; PBS: 1.8 ± 0.3, P = 0.0079). Bone marrow image analysis showed a trend towards increased CD11b+ cells at day eight (SUVmax MTP10-HDL: 1.6 ± 0.2; PBS: 1.5 ± 0.2, p = 0.1508) (Figure 1E). Therapeutic studies

in B16F10 bearing mice showed that continuous treatment with TI-nanobiologic in combination with checkpoint inhibitors resulted in a more than eightfold reduction in mean tumor volume, as compared to PBS and checkpoint inhibitors alone, at day nine (p Conclusion: This study demonstrates the value of integrating non-invasive PET imaging with deep profiling to optimize cancer immunotherapy strategies. Specifically in this study, it was found that simultaneously mobilizing the two arms of our immune system i.e. innate and adaptive immunity results in very effective anti-tumor response.

References: [1] Netea, M.G., Joosten, L.A., Latz, E., Mills, K.H., Natoli, G., Stunnenberg, H.G., O'Neill, L.A., and Xavier, R.J. (2016). Trained immunity: A program of innate immune memory in health and disease. Science 352. [2]Netea, M.G., Joosten, L.A.B., and van der Meer, J.W.M. (2017). Hypothesis: stimulation of trained immunity as adjunctive immunotherapy in cancer. J Leukoc Biol 102, 1323-1332. [3] Mitroulis, I., Ruppova, K., Wang, B., Chen, L.S., Grzybek, M., Grinenko, T., Eugster, A., Troullinaki, M., Palladini, A., Kourtzelis, I., et al. (2018). Modulation of Myelopoiesis Progenitors Is an Integral Component of Trained Immunity. Cell 172, 147-161. [4] Rashidian, M., Ingram, J.R., Dougan, M., Dongre, A., Whang, K.A., LeGall, C., Cragnolini, J.J., Bierie, B., Gostissa, M., Gorman, J., et al. (2017). Predicting the response to CTLA-4 blockade by longitudinal noninvasive monitoring of CD8 T cells. J Exp Med 214, 2243-2255

Image/Figure:

https://s3.amazonaws.com/amz.xcdsystem.com/1E8A4501-BB41-A02A-1D3B9882B798BFAA_abstract_File10351/GA328_ImageFigure_0513044552.jpg

Image/Figure Caption: 1A. Schematic representation of the TI-nanobiologic. Particle size of as determined by DLS, is 20 nm. CryoTEM reveals a discoidal structure approximately 15 nm in diameter, with a thickness of 5 nm. 1B. Biodistribution mice and non-human primates using PET/CT and PET/MRI respectively. (left) a maximum intensity projection of mouse PET/CT. (middle) Dynamic PET/MRI scans of a non-human primate 1, 30 and 60 minutes after injection of 89Zr labeled TI-nanobiologic. Fast bone marrow and spleen accumulation, as well as liver uptake can be observed. (right) PET/MRI scan of a non-human primate injected with 89Zr labeled nanobiologics displays a favorably high bone marrow and spleen accumulation relative to the liver. 1C. Intravital microscopy image of a live mouse calvarium eight hours post administration of fluorescently labeled TI-nanobiologic. Clear uptake can be seen throughout the bone marrow. FITC-dextran was injected intravenously to display the vasculature. 1D. 18F-FDG-PET of C57BL/6 mice. 18F-FDG was intravenously injected one hour before PET/CT imaging. A higher SUVmax of the bone marrow was observed in mice injected with TI-nanobiologic, indicating increased metabolic activity. 1E. C57BL/6 mice inoculated with 1x105 B16F10 cells treated with either TI-nanobiologic or PBS received an intravenous injection of 89Zr labeled CD11b specific nanobody at day seven. There is a higher SUVmax in the bone marrow and the spleen indicating higher amounts of CD11b-expressing cells present. 1F. Tumor growth curves of mice treated with PBS and TI-nanobiologic (dotted lines), checkpoint inhibitor immunotherapy alone (yellow boxes) versus in combination with TI-nanobiologic. Combining anti-PD-1 + anti-CTLA-4 has no significant effect on tumor growth rate and tumor size. Adding TI-nanobiologic dramatically decreases the tumor growth rate, an effect that is even more pronounced after the TI-nanobiologic regimen rises from three to six injections.

Full Name of Abstract's 1st Author : Bram Priem

First Name: Bram

Last Name: Priem

Email: bram.priem@gmail.com

Organization: Icahn School of Medicine

Country: United States

ID: GA329
Engineered cancer cell-derived vesicles coated nano theranostics for triple-negative breast cancer therapy

Jagathesh Chandra Bose Rajendran, Masonic Medical research institute, rbose@mmri.edu

---

Category: Oncology

Abstract Body : Triple-negative breast cancer (TNBC) is the most aggressive subtype of breast cancer, accounting for the majority of breast cancer-related death. Owing to the lack of specific therapeutic targets, the development of targeted anticancer therapy has been extremely challenging. To overcome this problem, we investigate whether uPAR targeted heterologous miRNA delivery of uPA nano cocktails contain engineered extracellular vesicles (uPA-eEV and Sc-uPA-eEV) coated polymeric nanocarrier (PNCs) separately loaded with antimiR-21 or an antimiR-10b elicits synergistic antitumor responses. To monitor the tumor-specific accumulation of nano cocktails, we conjugated NH2 reactive indocyanine green (ICG) to the 4T1- eEV-PNCs, and then monitored the cocktail accumulation by dual molecular imaging modalities (NIR fluorescence and photoacoustic imaging). The uPA-eEVs coating on PNCs offers a means of enhancing natural tumor targeting affinities and thereby enhancing the antitumor activity of antimiRs -nano cocktails. The systemic administration of the uPA-eEV-PNCs nano cocktail showed a robust tumor tropism in nude and syngeneic mice models (Figure.1), which significantly enhanced the combinational antitumor effect of antimiR-21 and antimiR-10b that leads to complete tumor regression and extension of progression-free survival of syngenic 4T1 tumor-bearing mice. Besides, the uPA-eEV-PNCs-antimiRs nano cocktail with low dose doxorubicin displays a synergistic antitumor effect as evidenced by the inhibition of tumor growth, reduction of lung metastasis, and extension of the survival of 4T1 tumor-bearing mice. Our targeted heterologous miRNA therapy can be easily translated into the clinics by using eEVs isolated from autologous tumor cells that have the flexibility for ex vivo expansion and genetic engineering.

References: JC Bose, Rajendran, Sukumar Uday Kumar, Yitian Zeng, Rayhaneh Afjei, Elise Robinson, Kenneth Lau, Abel Bermudez et al. "Tumor cell-derived extracellular vesicle-coated nanocarriers: an efficient theranostic platform for the cancer-specific delivery of anti-miR-21 and imaging agents." ACS nano 12, no. 11 (2018): 10817-10832. Bose, Rajendran JC, Ramasamy Paulmurugan, James Moon, Soo-Hong Lee, and Hansoo Park. "Cell membrane-coated nanocarriers: the emerging targeted delivery system for cancer theranostics." Drug Discovery Today 23, no. 4 (2018): 891-899. Di Ianni, Tommaso, Rajendran JC Bose, Uday K. Sukumar, Sunitha Bachawal, Huaijun Wang, Arsenii Telichko, Carl Herickhoff et al. "Ultrasound/microbubble-mediated targeted delivery of anticancer microRNA-loaded nanoparticles to deep tissues in pigs." Journal of Controlled Release 309 (2019): 1-10. Bose, Rajendran JC, and Robert F. Mattrey. "Accomplishments and challenges in stem cell imaging in vivo." Drug discovery today 24, no. 2 (2019): 492-504.

Image/Figure:

https://s3.amazonaws.com/amz.xcdsystem.com/1E8A4501-BB41-A02A-1D3B9882B798BFAA_abstract_File10351/GA329_ImageFigure_0513045149.jpg

Image/Figure Caption: Figure. a) Schematic illustration for the preparation strategy of 4T1-engineered extracellular vesicles that display uPAR targeting uPA or scrambled uPA peptide-functionalized PLGA nanocarriers separately loaded with AmiR-21 or AmiR 10b and the transmission electron micrograph shows the PLGA nanocarrier and 4T1-eEVs coated PLGA NPs. Negative-stain electron microscopy was performed to visualize the eEVs on the PLGA NCs. Scale bars, 100 nm. In vivo biodistribution and uPAR targeted 4T1 tumor accumulation in syngeneic subcutaneous Nude mice (nu/nu) tumor model. b) IVIS fluorescence imaging shows the whole-body biodistribution and 4T1 – tumor-specific accumulation of uPA and Sc-uPA nano cocktails formulations ICG labeled Sc-uPA and uPA nano cocktail formulations (150 µL) was administered via tail vein on days 0,6 and 12 and imaged on Days 2,7 and 15 using a Lago (Spectral Imaging system). c) Day 16 (Photoacoustic imaging) for ICG fluorescence and photoacoustic signals. d) Ex-vivo fluorescence imaging shows the uPAR mediated 4T1 tumor-specific accumulation of uPA nano cocktails formulations. The uPA and Sc-uPA nano cocktails formulations injected nude animals were sacrificed on day 17, and the organs (liver, spleen, kidney, heart, lungs, and brain) were collected for ex vivo analysis. e) The biodistribution and tumor-specific accumulation of AmiR-21 and AmiR-10b in uPA and Sc-uPA nano cocktails formulations injected nude mice organs. The Taqman real-time qRT-PCR was used for the organ-specific biodistribution based on the quantification of AmiRs. In vivo biodistribution and uPAR targeted 4T1 tumor accumulation in the syngeneic BALB/CJ animals bearing the 4T1 subcutaneous tumor model. f) IVIS fluorescence imaging shows the whole-body biodistribution and 4T1 – tumor-specific accumulation of uPA and Sc-uPA nano cocktails formulations ICG labeled Sc-uPA and uPA nano cocktail formulations (150 µL) was administered via tail vein on days 0,6 and 12 and imaged on Days 2,7 and 15 using a Lago (Spectral Imaging system) for ICG fluorescence. g) Ex-vivo fluorescence imaging shows the uPAR mediated 4T1 tumor-specific accumulation of uPA nano cocktails formulations in BALB/CJ animals bearing syngeneic 4T1 subcutaneous tumor model. The uPA and Sc-uPA nano cocktails formulations injected nude animals were sacrificed on day 17, and the organs (liver, spleen, kidney, heart, lungs, and brain) were collected for ex vivo analysis. h) The biodistribution and tumor-specific accumulation of AmiR-21 and AmiR-10b delivered using uPA and Sc-uPA nano cocktails formulations injected in BALB/CJ animals bearing 4T1 subcutaneous tumor model. The Taqman real-time qRT-PCR was used for the organ-specific biodistribution based on the quantification of AmiRs.

Full Name of Abstract's 1st Author : Rajendran Jagathesh Chandra Bose

First Name: Jagathesh Chandra Bose

Last Name: Rajendran

Email: rbose@mmri.edu

Organization: Masonic Medical research institute

Country: United States

ID: GA330
Overcoming immunotherapy resistance in cancer with a drug loaded FDA-approved theranostic nanoparticle

Evan Stater, Weill Cornell Graduate School, evs2007@med.cornell.edu

---

Category: Oncology

Abstract Body : An iron oxide nanoparticle, Feraheme (ferumoxytol, FH) is currently in clinical use as an intravenous iron supplement, as well as an off-label T2 contrast agent for MR imaging. In cancer patients, FH is known to passively target tumor-associated macrophages; furthermore, a variety of small molecule pharmaceuticals can be non-covalently captured and retained within the exterior carbohydrate shell of FH. FH therefore has promise as a clinical nano-drug platform to target delivery to tumor-associated macrophages and other tumor-infiltrating immune cells, while simultaneously enabling MR monitoring of nanoparticle uptake efficiency and response of the tumor to therapy. We have shown that FH can stably capture a clinically-approved immunostimulatory drug, allowing the nanoparticle-drug complex ("FH-drug") to function as an immunostimulatory agent and polarize macrophages toward an anti-tumorigenic phenotype in cancer. The B16 mouse model of melanoma produces rapidly expanding tumors that are poorly responsive to immunotherapeutic antibodies. Here, we show that FH-drug improves the therapeutic response of B16 to anti-CD40 agonist monoclonal antibodies. Mice with subcutaneous B16 xenografts receiving anti-CD40 in combination with FH-drug exhibited slower tumor growth, increased tumor inhibition, lengthened tumor latency time, and improved survival compared to mice receiving only the antibody therapy. This regimen also was more therapeutically efficacious than anti-CD40 combination therapy with an equivalent dose of free drug. FH-drug, composed of FDA-approved materials, is therefore promising as adjunctive agent to anti-CD40 therapy, and perhaps as an adjunct to other immunotherapeutic regimens in the clinic. The theranostic nature of this particle could allow simultaneous treatment and monitoring of therapeutic response, as well as noninvasive estimation of nanoparticle uptake by the tumor.

References: PMID 24594970

Image/Figure:

https://s3.amazonaws.com/amz.xcdsystem.com/1E8A4501-BB41-A02A-1D3B9882B798BFAA_abstract_File10351/GA330_ImageFigure_0513045227.png

Image/Figure Caption: A) Tumor growth plots of C57BL6 mice implanted with subcutaneous B16F10 tumors (n=10 per cohort). Treatment of animals with FH-drug (10 μg Fe/kg) in combination with anti-CD40 monoclonal antibodies (100 μg) resulted in reduced tumor growth rates. Animals were treated by IV injection on days 5 and 12. B) Measured tumor volumes of all mice in panel A on day 18 post tumor challenge. Mice receiving combination therapy had significantly smaller tumors ($p<0.05$) than mice receiving only anti-CD40 treatment. C) Area under the curve (AUC) of tumor volume tracks from panel A on day 18 post tumor challenge.

The AUC was significantly reduced in the combination therapy group compared to anti-CD40 alone ($p<0.001$). D) Survival of mice after tumor challenge. Mice receiving combination therapy exhibited the longest survival duration compared to all other groups.

Full Name of Abstract's 1st Author : Evan Paul Stater

First Name: Evan

Last Name: Stater

Email: evs2007@med.cornell.edu

Organization: Weill Cornell Graduate School

Country: United States

ID: GA331
Intravital microscopy of T cell effector function in melanoma during immuno-thermal therapy

Bettina Weigelin, University of Tuebingen, bettina.weigelin@med.uni-tuebingen.de

---

Category: Oncology

Abstract Body : For many cancer types, immunotherapy is an emerging first-line treatment, with the potential to reach complete regression in patient subsets. The main effector cells mediating tumor eradication are cytotoxic T lymphocytes (CTL), which kill cancer cells in a cell-contact and tumor-antigen-specific manner. Adoptive transfer of ex vivo activated tumor-specific CTL (ACT) is, thus, a promising strategy to increase anti-tumor immunity but its capacity to control tumor growth is often insufficient. External application of heat in the fever-range (38 – 40 °C) has been shown to activate and support immune effector functions in tumors. However, the rational design of ACT and hyperthermia combinations is currently hampered by an incomplete understanding how both therapies synergize and which remaining immunosuppressive mechanisms limit their combined efficacy. By using live-cell microscopy and optical reporters, we monitored structural damage induced by OVA-specific CTL to the cellular and nuclear membranes and DNA double-strand breaks in B16F10/OVA melanoma cells. CTL-mediated damage was predominantly sub-lethal and followed by rapid recovery of the tumor cell. Treatment with 39.5 °C, applied either continuously or for 1 – 3 h on 2 consecutive days, significantly increased tumor apoptosis rates and correlated with stabilized CTL-tumor cell contacts and impaired recovery of melanoma cells from CTL-mediated damage. To evaluate the efficacy of ACT and whole-body hyperthermia (WBH) in the context of the melanoma microenvironment, we used intravital multiphoton microscopy combined with an imaging window for longitudinal monitoring of CTL effector function. Following intradermal tumor injection and adoptive CTL transfer, we applied WBH of 39.5 °C for 1 or 2 h and repeated the treatment every other day for one week. Directly following the first treatment, imaging revealed an immediate block of tumor cell proliferation and increased apoptosis rates. Time-lapse microscopy showed enhanced CTL killing activity while CTL-tumor cell interaction dynamics remained unchanged, ranging from stable, long-lasting to highly dynamic contacts. The combination of ACT and WBH further induced the infiltration of phagocytic cells which was absent in tumors of mice treated with either therapy alone. Macrophage infiltration partially resolved or stabilized despite repeated WBH treatments. Subregional analysis of tumor cell viability further revealed a resistance of tissue-invading tumor cells to WBH monotherapy which was overcome by combined ACT/WBH treatment. Thus, kinetic imaging and intravital microscopy were successfully applied to deepen the mechanistic understanding of immune cell function during fever-range WHB which forms the basis for improved, rationale design of combination therapies.

Image/Figure:

https://s3.amazonaws.com/amz.xcdsystem.com/1E8A4501-BB41-A02A-1D3B9882B798BFAA_abstract_File10351/GA331_ImageFigure_0513050203.jpg

Image/Figure Caption: Fever-range thermal therapy to support ACT efficacy. A) Longitudinal monitoring of ACT using imaging windows and intravital multiphoton microscopy (iMPM). Immune cells for transfer were isolated from fluorescent donor mice, in vitro activated and adoptively transferred by i.v. injection in tumor-bearing mice. Using an imaging window, fluorescently labeled tumors and immune cell infiltration were monitored over time (up to 3 weeks). Using iMPM allowed to monitor CTL effector function in tumor subregions at subcellular resolution. B) Repeated 1 h treatments of mice with whole-body hyperthermia at 39.5 °C significantly delayed B16F10/OVA tumor progression during the treatment period. C) Tumor mitosis and apoptosis rates, determined by dynamic iMPM, revealed inhibition of mitotic activity and enhanced tumor apoptosis rates immediately following treatment and (D) enhanced density of macrophages. Error bars, SD.

First Name: Bettina

Last Name: Weigelin

Email: bettina.weigelin@med.uni-tuebingen.de

Organization: University of Tuebingen

Country: Germany

ID: GA332
In Vivo Detection of CAR-T cell Immunotherapy using 3 Tesla Fluorine-19 MRI

Veronica Dubois, Western University, vdubois@uwo.ca

Category: Oncology

Abstract Body : Introduction: Chimeric antigen receptor T (CAR-T) cell therapy is a relatively new cancer treatment in which a patient's own T cells are isolated and engineered to express a CAR. CAR engineering redirects the T cells to bind to a specific cancer antigen and induce cancer cell death. CAR-T cell therapies have shown promising results in patients with hematological malignancies with up to 70% of patients responding to treatment1. Despite this success, CAR-T cell therapies can cause severe off-target toxicities and not all patients respond to this treatment (up to 30%). Currently, CAR-T cell monitoring is limited to blood tests that are invasive and one-dimensional as they only provide information on the total number of circulating CAR-T cells and lack any information about biodistribution, particularly at tumour sites2. An imaging tool for tracking CAR-T cells could provide important patient-specific data on CAR-T cell fate to inform on potential success or failure of treatment as well as off-target toxicities. Fluorine-19 magnetic resonance imaging (19F MRI) allows for the detection of 19F perfluorocarbon (19F PFC) labeled cells non-invasively and in real time to provide information on cell location(s), cell number, and tumour homing ability. Our goal is to track the fate of 19F PFC-labeled CAR-T cells in leukemia bearing mice using 3 Tesla 19F MRI. Methods: T cells were engineered to co-express a CD19 targeting CAR and GFP, expanded, and then labeled with 5 mg/ml PFC overnight. CD19+ B cell leukemia cells (NALM6) were engineered to express the firefly luciferase (FLuc) reporter gene to enable detection of viable cancer cells with bioluminescence imaging (BLI). NSG mice (n=17) received subcutaneous injections of 1 million NALM6-FLuc cells in their left hind flank. Twenty-one days later, each mouse received an intratumoural injection of 10 million PFC labeled CAR-T cells (n=6), unlabeled CAR-T cells (n=3), PFC labeled T cells (n=5), or saline (n=3). 19F MRI was performed on a 3T clinical scanner days 1, 3, and 7 post PFC labeled cell injection. BLI was performed on an IVIS Lumina system days -1, 5, 10, and 14 from injection day in all treatment groups. Results: Flow cytometry revealed that engineered T cell populations were approximately 68.6% GFP/CAR positive. 19F signal was successfully detected in the tumours of all mice that received PFC labeled cells using 19F MRI on days 1, 3, and 7 post-injection. In vivo BLI data revealed that PFC labeled CAR-T cells show no significant difference in cytotoxicity compared to unlabeled CAR-T cells. Mice treated with labeled or unlabeled CAR-T cells have significantly lower tumour burden by day 14 compared to mice treated with labeled T cells (p Conclusions: We have shown for the first time that 19F MRI is able to detect PFC labeled CAR-T cells up to 7 days post injection using a 3T clinical scanner. Importantly, PFC labeling did not significantly affect CAR-T cell cytotoxicity in vivo. These imaging tools may have broad applications for tracking emerging CAR-T cell therapies in preclinical models and may be useful for the evaluation of CAR-T cells in patients.

References: References: [1] Maude (2014) N Engl J Med., [2] Porter (2011) N Eng J Med.

Image/Figure:

https://s3.amazonaws.com/amz.xcdsystem.com/1E8A4501-BB41-A02A-1D3B9882B798BFAA_abstract_File10351/GA332_ImageFigure_0513050915.jpg

Image/Figure Caption: Figure 1: In vivo imaging of PFC labeled CAR-T cells and their treatment response in a leukemia bearing mouse. (A) 19F MRI of 19F PFC labeled CAR-T cells on days 1, 3, and 7 post-intratumoural injection. (B) BLI of firefly luciferase expressing leukemia cells days -1, 5, 10, and 14 post-CAR-T cell treatment.

First Name: Veronica

Last Name: Dubois

Email: vdubois@uwo.ca

Organization: Western University

Country: Canada

ID: GA333
Liposomal delivery to murine brain using Focused Ultrasound and Microbubbles: Rapid Short Pulses (RaSP) Vs Conventional Long Pulses

Aishwarya Mishra, King's College London, aishwarya.mishra@kcl.ac.uk

---

Category: Neuroscience

Abstract Body : Introduction: Focused ultrasound (FUS) in combination with microbubbles has been shown to open the blood-brain barrier (BBB) increasing drug delivery, being effective for small-molecule drugs1. Recently, RaSP FUS has been used to safely deliver fluorescently labelled-dextran (3 kDa) and AuNPs (25 nm)2,3 to the brain. PEGylated liposomal nanomedicines (ca. 100 nm) are clinically available drug delivery systems, but suffer from the inability to cross the BBB. In this study, we examine the ability of RaSP FUS to deliver liposomes safely and efficiently in the brain of mice in vivo, compared to conventional long ultrasound pulse sequences4. Methods: DiD-PEGylated liposomes (DPLs) were synthesized by co-incubation of DiD dye and PEGylated stealth liposomes for 2 hrs/37oC. The DPLs were purified using size exclusion chromatography and characterized using fluorescence/DLS. 36 female wild-type mice underwent FUS after injection of Sonovue® microbubbles and DPLs. The left hippocampus of mice was exposed to either: (i) low-energy short pulses (1 MHz, 5 cycles, MPapk-neg = 0.4 and 0.6 MPa, n = 18 mice) of US emitted at a rapid rate (1.25 kHz) in bursts (0.5 Hz) or (ii) standard long pulses (10 ms, 0.5 Hz, MPapk-neg = 0.4 and 0.6 MPa, n = 18 mice). Mice were sacrificed at 0 hr (n=16) or 2 hr (n=16) after US treatment. The delivered liposome dose was quantified using normalized optical density (NOD) measurements and tissue damage assessed by H&E staining. Staining of neurons, microglia and astrocytes was performed to examine the liposome uptake in these cells. Results: DPLs were synthesized with a dye concentration of 2.1±0.5 μg/mL with no modification to size, zeta potential and PDIs from the original PEG liposomes. DPLs were stable in human serum up to 48 h. The long pulses with 0.6 MPa showed uptake of DPLs with fluorescence signal concentrated around the blood vessels. The delivery with RaSP sequences showed more diffused delivery from vessels. ROIs around the left (US) and right (control) hippocampus were selected. The NOD analysis showed DPL delivery in brains with long pulse and RaSP sonication at 0.6 MPa, but no delivery at RaSP sonication at 0.4 MPa. H&E staining of the brains for RaSP FUS at 0.6 MPa showed no damage while damage was observed for long pulses FUS at 0.4 MPa and 0.6 MPa. Cellular uptake of DPLs was observed only in microglia and neuronal cells. No astrocyte uptake was observed for both RaSP and long pulses. Conclusion: RaSP at 0.6 MPa showed localised delivery of fluorescent liposomes DPLs (~100 nm) across the BBB with a more diffused and safer profile compared to the long pulse ultrasound sequence. The safer delivery can be attributed to the lower energy transfer in RaSP compared to the long pulse sequence. This study could allow the targeted delivery of drugs via liposomes to neuronal cells and desired regions of the brain.

References: 1. S. Snipstad, E. Sulheim, C. de Lange Davies, C. Moonen, G. Storm, F. Kiessling, R. Schmid, T. Lammers. Expert Opin. Drug Deliv. 15 (2018) 1249–1261. 2. S. V. Morse, A.N. Pouliopoulos, T.G. Chan, M.J. Copping, J. Lin, N.J. Long, J.J. Choi. Radiology. (2019) 181625.

3. T.G. Chan, S. V. Morse, M.J. Copping, J.J. Choi, R. Vilar. ChemMedChem. 13 (2018) 1311–1314. 4. B. Baseri, J.J. Choi, Y.S. Tung, E.E. Konofagou. Ultrasound Med. Biol. 36 (2010) 1445–1459.

Image/Figure:

https://s3.amazonaws.com/amz.xcdsystem.com/1E8A4501-BB41-A02A-1D3B9882B798BFAA_abstract_File10351/GA333_ImageFigure_0513051255.png

Image/Figure Caption: (1) Ultrasound experimental setup: (Left) Ultrasound pulses were emitted from the therapeutic transducer (1 MHz) driven by one or two function generators. (Right) Ultrasound was focused through the intact scalp and skull onto the left hippocampus of the mouse's brain while the right hippocampus was used as a control (no ultrasound); (2) Fluorescence images of liposomal delivery with rapid short-pulse (RaSP) and long-pulse sequences at 0.35 and 0.53 MPa, at 0 h or 2 h after ultrasound treatment; (3) Tissue damage assessment in RaSP and long-pulse treated brains; (4) Fluorescence images of neuronal cell uptake assessment of liposomes (in red) within neurons, microglia and astrocytes (all in green) in RaSP and long-pulse treated brains

Full Name of Abstract's 1st Author : Aishwarya Mishra

First Name: Aishwarya

Last Name: Mishra

Email: aishwarya.mishra@kcl.ac.uk

Organization: King's College London

Country: United Kingdom

ID: GA334
[64Cu]TREM1-mAb imaging detects therapeutic response to fingolimod in a mouse model of multiple sclerosis

Aisling Chaney, Stanford University, aislingc@stanford.edu

Category: Neuroscience

Abstract Body : OBJECTIVES: Therapeutic selection and monitoring in relapsing-remitting multiple sclerosis (RR-MS) is impeded by the absence of sensitive biomarkers to track the presence, infiltration and/or activation of specific immune cells in the central nervous system (CNS). Although many FDA-approved immunomodulatory therapies are available for RR-MS1, response rates are highly heterogenous and determining an efficacious treatment strategy for individual patients remains challenging. Therefore, the ability to non-invasively assess therapeutic response in RR-MS patients in real-time is a critical unmet need to improve disease management and patient outcomes. Positron emission tomography (PET) imaging of the triggering receptor expressed on myeloid cells 1 (TREM1) is a sensitive approach to detect the infiltration of pathogenic peripheral myeloid cells (e.g., macrophages, monocytes, neutrophils) into the CNS in the context of neurological injury2. Moreover, TREM1-PET has been shown to identify active disease and distinguish it from periods of remission in a mouse model of RR-MS. Here, we aim to investigate the ability of [64Cu]TREM1-mAb imaging to monitor therapeutic response to prophylactic fingolimod (FTY720) treatment in the RR experimental autoimmune encephalomyelitis (RR-EAE) mouse model of MS. FTY720 is an immunotherapy widely used to treat RR-MS by preventing the activation and infiltration of lymphocytes into the CNS, and has also been shown to modulate myeloid cell responses3. We hypothesize that TREM1-PET will permit detection of early therapeutic response in FTY270-treated animals, as evidenced by reduced CNS [64Cu]TREM1-mAb signal. METHODS: Animals: RR-EAE was induced in female SJL mice using PLP139-151 emulsified in immune adjuvant. RR-EAE mice were randomly split into untreated and prophylactic FTY270 treatment (3mg/kg daily for 12 days) groups. Mice were scored daily for disease severity. Naïve (non-EAE) SJL mice were also used for these studies. TREM1-PET: PET/CT imaging was performed 18-20 h post-injection of a 64Cu-radiolabeled anti-TREM1 monoclonal antibody ([64Cu]TREM1-mAb: 82-99 μCi, >99% radiochemical purity). Ex vivo: Following PET, mice were perfused with saline and CNS tissues were analyzed via high-resolution autoradiography and gamma counting. Brain slices used for autoradiography were subsequently stained with cresyl violet to enable quantification of [64Cu]TREM1-mAb binding in specific brain regions. RESULTS: Prophylactic FTY270 treatment prevented the development of disease in RR-EAE induced mice, whereas untreated RR-EAE mice exhibited disease progression with significantly higher EAE scores seen from day 11 (Suppl. Fig1A). TREM1-PET images revealed high signal in the spinal cords of untreated RR-EAE mice (i.e., mice experiencing active EAE disease), which was markedly reduced in RR-EAE mice treated with FTY270 (Fig. 1A). Notably, RR-EAE FTY270-treated mice displayed similar CNS [64Cu]TREM1-mAb signal as naïve mice. PET data are supported by ex vivo autoradiography of CNS tissues following perfusion to remove unbound intravascular tracer. High-resolution autoradiography of spinal cords revealed significantly reduced [64Cu]TREM1-

mAb signal in the lumbar and thoracic regions of RR-EAE FTY270-treated and naïve mice compared to untreated RR-EAE mice (p Suppl. Fig.1B-C). These results were further corroborated by gamma counting of CNS tissues (Suppl. Fig.1D). CONCLUSION: [64Cu]TREM1-mAb imaging successfully identified therapeutic response in prophylactic FTY270-treated RR-EAE mice and distinguished it from an active disease state in untreated RR-EAE mice. TREM1-PET imaging has high potential for evaluating treatment efficacy in RR-MS, as well as the development and screening of novel immunotherapies targeting the CNS. Studies investigating the ability to detect responses to FTY270 in symptomatic RR-EAE mice are currently underway.

References: 1. Vargas DL., Tyor WR. Update on disease-modifying therapies for multiple sclerosis. J Investig Med., 2017; 65:883–891. 2. Liu, Q. et al. Peripheral TREM1 responses to brain and intestinal immunogens amplify stroke severity. Nat Immunol, 2019; 20(8):1023-1034 3. Di Dario et al. Myeloid cells as target of fingolimod action in multiple sclerosis. Neurol Neuroimmunol Neuroinflamm. 2015, 4;2(6):e157.

Image/Figure: https://s3.amazonaws.com/amz.xcdsystem.com/1E8A4501-BB41-A02A-1D3B9882B798BFAA_abstract_File10351/GA334_ImageFigure_0513052045.pdf

Image/Figure Caption: Fig. 1: In vivo TREM1 PET PET/CT imaging in RR-EAE mice 18-20 h following [64Cu]TREM1-mAb injection revealed high signal in the spinal cords (white arrow) of untreated RR-EAE mice exhibiting active EAE, which was markedly reduced in fingolimod (FTY270) treated mice (EAE+FTY270) (A). Tracer binding in the spinal cord was confirmed using ex vivo autoradiography (B). Quantification of [64Cu]TREM1-mAb autoradiographic images demonstratedsignificantly reduced signal in naïve and EAE+ FTY270 mice compared to untreated EAE mice. Statistics were performed using one-way ANOVAs with Tukey's multiple comparison tests (*=p < 0 .05, **=p < 0 .01).

Full Name of Abstract's 1st Author : Aisling Chaney

First Name: Aisling

Last Name: Chaney

Email: aislingc@stanford.edu

Organization: Stanford University

Country: United States

ID: GA335
Microbubble shape: a new design parameter in ultrasound-mediated drug delivery.

Anshuman Dasgupta, RWTH Aachen University, adasgupta@ukaachen.de

---

Category: New Chemistry, Materials & Probes

Abstract Body : Introduction: The blood-brain barrier (BBB) is a major physical barrier for drug delivery. Sonopermeation, which refers to the combination of ultrasound (US) and microbubbles (MB), has been used to permeabilize the BBB and improve drug delivery to the brain. In order to enhance sonopermeation, MB design parameters such as size, shell composition and active targeting have been investigated [1]. In this study, we investigated the role of MB shape, a new design parameter, to potentiate sonopermeation-mediated drug delivery across BBB. Methods: Spherical MB were synthesized by anionic polymerization of n-butyl cyanoacrylate [2]. Rod-shaped MB were synthesized by stretching spherical MB unidirectionally above their glass transition temperature [3]. Rod-shaped and spherical MB were studied to systematically compare their margination profiles, blood half-life and the magnitude of BBB permeation upon US treatment. Results: Cryo-SEM and confocal microscopy confirmed successful formation of spherical and rod -shaped MB. Upon flowing these MB in a microfluidic chip, we observed that rods showed stronger margination both in the absence and presence of blood. Real-time US monitoring in mice demonstrated that rods have a significantly higher blood half-life time than spheres. Likely as a direct result of these phenomena, rod-shaped MB in combination with focused US almost doubled the degree of BBB permeabilization and drug delivery as compared to spheres. Finally, via functionalizing the MB surface with brain endothelium-binding anti-CD71 antibodies, we demonstrate that active targeting of rod-shaped MB enhances BBB permeabilization and drug delivery even more, by up to a fourfold. Conclusion: This is the first study to exemplify the importance of MB shape in margination, circulation half-life and ultrasound-mediated drug delivery. These findings indicate that tailoring MB shape is a promising strategy for potentiating US-mediated opening of BBB to improve brain disorder treatment.

References: (1) Dasgupta et al. Drug Discov Today: Technologies. 2016:41-48. (2) Liu et al. Mol Pharmaceutics. 2020:2840-2848. (3) Champion et al. Proc Natl Acad Sci. 2007:11901-11904.

Image/Figure:

https://s3.amazonaws.com/amz.xcdsystem.com/1E8A4501-BB41-A02A-1D3B9882B798BFAA_abstract_File10351/GA335_ImageFigure_0513053119.jpg

Image/Figure Caption: Microbubble Shape: a new design parameter in ultrasound-mediated drug delivery. (A) Confocal, cryo-SEM and STED confirmed the fomation and morphology of spherical and rod-shaped microbubble. (B) In a microfluidic setup, rod-shaped microbubble tend

to marginate more strongly than spherical-shaped microbubble in the presence of blood. (C) Continuous ultrasound monitoring of intravenously injected microbubbles demonstrated that rod-shaped microbubble circulate longer than spheres. (D) Upon in-vivo application of focused ultrasound, rod-shaped microbubble almost doubled the BBB permeability and (E) this effect was further enhanced upon attaching anti-CD 71 targeting ligands.

Full Name of Abstract's 1st Author : Anshuman Dasgupta

First Name: Anshuman

Last Name: Dasgupta

Email: adasgupta@ukaachen.de

Organization: RWTH Aachen University

Country: Germany

ID: GA336

Multi-Tracer PET/CT to Monitor Response to Host-Directed Therapy in a Rabbit Model of TB Meningitis

Clara Erice, Johns Hopkins School of Medicine, clara.erice.j@gmail.com

---

Category: Immunology: Inflammation & Infection

Abstract Body : Background: Central nervous system (CNS) tuberculosis (TB) affects children disproportionately. It is the most aggressive form of extra-pulmonary TB and, despite antimicrobial treatment, mortality and morbidity remain high. Currently the only host-directed therapy recommended by the World Health Organization is corticosteroids (i.e. dexamethasone), but response to treatment is heterogenous (van Laarhoven et al 2017, Thuong et al 2017). Collectively, this highlights the need to develop new host-directed therapeutics to target neuroinflammation, a key determinant of pathophysiology (Jain et al 2018). N-acetyl-cysteine (NAC) has both antioxidant and anti-inflammatory properties and can cross the blood brain barrier (BBB) when conjugated to dendrimer nanodevices (D-NAC). Importantly, D-NAC has been shown to improve neurobehavioral outcomes in other models of neuroinflammation (Kannan 2012). We used a previously established rabbit model of TB meningitis mimicking disease in children, and performed 18F-FDG, 18F-py-albumin and 124I-DPA-713 (ligand for TSPO, which is upregulated on activated microglia/macrophages) positron emission tomography (PET) imaging and neurobehavioral scoring to noninvasively monitor response to D-NAC treatment over time. Objective: To noninvasively monitor response to host-directed treatment using PET imaging and neurobehavioral scoring in a pediatric model of TB meningitis. Methods: Young rabbits at post-natal day 5 were injected with live Mycobacterium tuberculosis H37Rv (TB-infected, n=13 rabbits) or PBS (uninfected control, n=6 rabbits) into the brain parenchyma. Intravenous treatment with D-NAC or PBS in TB-infected rabbits began 3 weeks post-infection, was blinded and continued weekly for 2 weeks. The same rabbits were imaged at day 0 and week 2 post-treatment with 18F-FDG (metabolic activity), 18F-py-albumin (vascular permeability) and 124I-DPA-713 (microglial activation) and compared to uninfected control. Regions of interest of brain lesion and unaffected brain were calculated and data was represented as ratios over time and fold change. Neurobehavioral studies and bacillary burden (CFU) were monitored during treatment. Results: We show that 18F-FDG, and 124I-DPA-713 signal correlated with brain lesions in TB-infected rabbits. Higher 18F-py-albumin PET signal was also observed at lesion sites suggesting increased BBB permeability. Brain lesion/unaffected ratios were significantly elevated in TB-infected rabbits compared to uninfected controls. Although TB-infected rabbits had similar brain bacillary burden ($P = 0.471$), the brain lesion/unaffected tissue ratios of all radiotracers decreased in TB-infected rabbits treated with D-NAC versus those treated with saline (controls). TB-infected rabbits treated with saline had significantly increased 124I-DPA-713 brain lesion/unaffected tissue ratios compared to uninfected rabbits ($P = 0.003$). This increase was not observed in TB-infected rabbits treated with D-NAC, indicating higher intracerebral inflammation in saline-treated TB-infected rabbits. Additionally, TB-infected rabbits treated with saline had significantly worse neurobehavioral scores compared to uninfected rabbits (P Conclusions: D-NAC treatment decreases intracerebral inflammation and

improves neurobehavioral scores in a rabbit model of TB meningitis. Multi-tracer PET imaging can be used to noninvasively monitor intracerebral responses to host-directed therapy. These data suggest that D-NAC is a promising host-directed therapy for TB meningitis that warrants further investigation in combinatorial studies with antimicrobials.

References: Jain, S. K., Tobin, D. M., Tucker, E. W., Venketaraman, V., Ordonez, A. A., Jayashankar, L., . . . Group, N. I. H. T. M. W. (2018). Tuberculous meningitis: a roadmap for advancing basic and translational research. Nat Immunol, 19(6), 521-525. doi:10.1038/s41590-018-0119-x Kannan, S., Dai, H., Navath, R. S., Balakrishnan, B., Jyoti, A., Janisse, J., . . . Kannan, R. M. (2012). Dendrimer-based postnatal therapy for neuroinflammation and cerebral palsy in a rabbit model. Sci Transl Med, 4(130), 130ra146. doi:10.1126/scitranslmed.3003162 Thuong, N. T. T., Heemskerk, D., Tram, T. T. B., Thao, L. T. P., Ramakrishnan, L., Ha, V. T. N., . . . Thwaites, G. E. (2017). Leukotriene A4 Hydrolase Genotype and HIV Infection Influence Intracerebral Inflammation and Survival From Tuberculous Meningitis. J Infect Dis, 215(7), 1020-1028. doi:10.1093/infdis/jix050 Tucker, E. W., Guglieri-Lopez, B., Ordonez, A. A., Ritchie, B., Klunk, M. H., Sharma, R., . . . Jain, S. K. (2018). Noninvasive (11)C-rifampin positron emission tomography reveals drug biodistribution in tuberculous meningitis. Sci Transl Med, 10(470). doi:10.1126/scitranslmed.aau0965 Tucker, E. W., Pokkali, S., Zhang, Z., DeMarco, V. P., Klunk, M., Smith, E. S., . . . Kannan, S. (2016). Microglia activation in a pediatric rabbit model of tuberculous meningitis. Dis Model Mech, 9(12), 1497-1506. doi:10.1242/dmm.027326 van Laarhoven, A., Dian, S., Ruesen, C., Hayati, E., Damen, M., Annisa, J., . . . van Crevel, R. (2017). Clinical Parameters, Routine Inflammatory Markers, and LTA4H Genotype as Predictors of Mortality Among 608 Patients With Tuberculous Meningitis in Indonesia. J Infect Dis, 215(7), 1029-1039. doi:10.1093/infdis/jix051

Image/Figure:

https://s3.amazonaws.com/amz.xcdsystem.com/1E8A4501-BB41-A02A-1D3B9882B798BFAA_abstract_File10351/GA336_ImageFigure_0513054022.png

Image/Figure Caption: Fig 1. A-D. Sagittal, coronal, and transverse PET/CT views of a representative TB-infected rabbit demonstrate a large brain lesion that is detected by (A) 18F-FDG, (B) 124I-DPA-713, and (C) 18F-py-albumin (upper panel) and correlates with (D) the lesion on gross pathology. All images correspond to the same rabbit. Lower panel quantifies the longitudinal changes in brain lesion/unaffected ratio of (A) 18F-FDG, (B) 124I-DPA-713, and (C) 18F-py-albumin of all TB-infected rabbits pre-treatment (day 0) and post-treatment (week 2) with D-NAC (blue, n=2 rabbits, n=5 ROIs) or saline (red, n=2 rabbits, n=6 ROIs). Data are represented as fold change of the brain lesion/unaffected ratio. PET signal of all radiotracers reduces more in TB-infected rabbits treated with D-NAC compared to those treated with saline. E. 124I-DPA-713 signal significantly increases in saline-treated rabbits (red, n=2 rabbits, n=6 ROIs) compared to uninfected rabbits (grey, n=2 rabbits, n=2 ROIs) which is not observed in D-NAC-treated rabbits (blue, n=2 rabbits, n=5 ROIs).

Full Name of Abstract's 1st Author : Clara Erice

First Name: Clara

Last Name: Erice

Email: clara.erice.j@gmail.com

Organization: Johns Hopkins School of Medicine

Country: United States

ID: GA337

Dual-isotope SPECT imaging of cytotoxic T-cells and tumor-associated macrophages in syngeneic animal models of melanoma

Alessandra Cavaliere, Yale University, alessandra.cavaliere@yale.edu

---

Category: Oncology

Abstract Body : Objectives. Advances in immunotherapy through immune checkpoint inhibitors have changed the paradigm for the treatment of patients with advanced melanoma(1). However, some patients do not respond and about 30% of patients respond initially but develop resistance. Mechanisms of resistance include poor penetration of T-cells in the tumor, and the immune-suppressive function of tumor-associated macrophages (TAMs)(2). Thus, there is a clinical need to monitor response to immunotherapy co-targeting these immune cells to spare potential non-responders from toxicity. SPECT is a non-invasive imaging modality that can image two radioisotopes concurrently. We aim to use dual-isotope SPECT imaging to track these immune cells through 99mTc-αCD8-cDb for imaging of cytotoxic T-cells and 111In-αCD68-IgG for imaging of TAMs, respectively, in syngeneic animal models of melanoma. Methods. 99mTc-αCD8-cDb was prepared via site specific conjugation of HYNIC(3) to the αCD8-cDb followed by radiolabeling with 99mTc. 111In-αCD68-IgG was prepared via conjugation of CHX-A''-DTPA to the αCD68-IgG followed by radiolabeling with 111In. Stability and binding affinity (Kd) of the SPECT agents were characterized. The optimal imaging timepoint and in vivo specificity of 111In-αCD68-IgG were determined via biodistribution studies of 0.37 MBq of the 111In-αCD68-IgG and compared with its isotype control in non-tumor bearing mice at 1, 5 and 24h p.i. (n = 3). YUMMER1.7 allografts characterized by high CD8+ T-cells, and high TAM(2) were used for imaging studies. 30 MBq of 99mTc-αCD8-cDb were injected in YUMMER1.7 allografts (n = 4) and single-isotope SPECT/CT was performed at 5h p.i. Imaging was repeated at 1, 10, 14 and 19 days post inoculation of tumor cells to monitor CD8+ T cell infiltration during tumor growth. Separately, YUMMER1.7 allografts (n = 5) were injected at 10 days post inoculation of tumor cells with 30 MBq of 111In-αCD68-IgG and single-isotope SPECT/CT was performed at 24h p.i. Dual-isotope SPECT imaging of a phantom composed of both 99mTc and 111In solutions was performed to determine feasibility of dual-isotope imaging studies. Results. 99mTc-αCD8-cDb was produced with a 80 μCi/μg specific activity, 100% radiochemical yield, and purity. The 99mTc-αCD8-cDb was determined to be stable in PBS and mouse serum with >74% monomer up to 5h post synthesis. 111In-αCD68-IgG was produced with a 10 μCi/μg specific activity, a 100% radiochemical yield, and 80% purity. 111In-αCD68-IgG was determined to be stable in PBS and mouse serum with >70% monomer up to 24h post synthesis. Affinity (Kd) of 111In-αCD68-IgG was found to be 35.5 nM. The 5-h imaging timepoint for 99mTc-aCD8-cDb was chosen based on previous studies(3). The optimal SPECT imaging time point for 111In-αCD68-IgG was determined via biodistribution studies and was found to be 24h p.i using the macrophage-rich spleen as in vivo standard. The highest spleen uptake of 40 ± 36 %ID/g was observed at 24h p.i. In contrast, the spleen uptake of the isotype control 111In-IgG2a was 4.5 ± 1.4 %ID/g. SPECT imaging quantification showed the greatest uptake of 99mTc-aCD8-cDb in the tumor relative to heart at 14 days (2.1 ± 0.9) of tumor growth but decreased at

19 days (0.8 ± 0.3), when the tumor volume decreased. This tumor model is dependent on T-cells, where tumor growth increases when CD4+ and CD8+ T-cells are depleted(2). SPECT imaging of 111In-αCD68-IgG showed a tumor:heart ratio of 4.9 ± 2.2. Dual-isotope SPECT imaging of the phantom showed distinct energies between 99mTc and 111In with 140 keV for 99mTc, and 170- and 245- keV for 111In. Dual-isotope SPECT imaging of 111In-aCD68-IgG and 99mTc-αCD8-cDb in YUMMER1.7 are currently ongoing. Conclusions. SPECT Imaging of 111In-aCD68-IgG or 99mTc-αCD8-cDb showed specificity for CD8+ T cells and CD68+ TAMs in YUMMER1.7 allografts. Future studies will consist in applying dual-isotope SPECT in the context of combination therapy.

References: 1. Siegel RL, Miller KD, Jemal A. Cancer Statistics, 2017. CA Cancer J Clin. 2017;67:7-30. 2. Wang J, Perry CJ, Meeth K, et al. UV-induced somatic mutations elicit a functional T cell response in the YUMMER1.7 mouse melanoma model. Pigment Cell Melanoma Res. 2017;30:428-435. 3. Tavare R, Escuin-Ordinas H, Mok S, et al. An Effective Immuno-PET Imaging Method to Monitor CD8-Dependent Responses to Immunotherapy. Cancer research. Jan 1 2016;76(1):73-82. doi:10.1158/0008-5472.can-15-1707

Full Name of Abstract's 1st Author : Alessandra Cavaliere

First Name: Alessandra

Last Name: Cavaliere

Email: alessandra.cavaliere@yale.edu

Organization: Yale University

Country: United States

ID: GA338
Dual imaging of the peripheral nerves with chlorin tracers

JUNIOR GONZALES, Memorial Sloan Kettering Cancer Center, gonzalj4@mskcc.org

---

Category: New Chemistry, Materials & Probes

Abstract Body : Background: Although chemotherapy-induced peripheral neuropathy (CIPN) represents a global, growing issue, affecting millions world-wide, no methods exist to quantitatively measure this dysfunction. 85% of patients in the form of intense burning, tingling, cramps, numbness and acute pain [1]. CIPN is the most common neurotoxic side-effect of antineoplastic agents such as cis-platin and paclitaxel, and it often has long lasting impact on a patient's quality of life [2]. To address this urgent medical challenge, we turned our awareness to an isolated venom peptide Hsp1a. Hsp1a was isolated from Homoeomma Spec. Peru (a tarantula from the rainforest of Peru), and it is highly selective for sodium channel, NaV1.7 [3]. In this work, we have synthesized a red fluorescent agent capable to as well chelate copper-64 that simultaneously features a novel NaV1.7-targeted peptide, Hsp1a. Our multi-modal imaging agent is a conjugate which is fluorescent and PET active. Combining these two imaging methods allowed us to determine selectivity of our agent not just on a whole-body level, but also at sub-cellular resolution. We also used human tissue (a human vagus nerve) to corroborate that our Hsp1a imaging agent is selective after topical administration. Herein, we report the first radiolabeled Hsp1a peptide, for the selective targeting of sodium channel NaV1.7, a previously validated marker of peripheral neuropathy. Methods: We synthesized ChL-Hsp1a by conjugating a chlorin tracer [4] to a Hsp1a peptide. ChL-Hsp1a was used to synthesize [64Cu]Cu-ChL-Hsp1a. Mice were intravenously injected with ChL-Hsp1a, PBS and block formulation or with [64Cu]Cu-ChL-Hsp1a and their sciatic nerves were exposed 30 min and then resected. For the fluorescence imaging, animals were intravenously injected with ChLHsp1a (10 μM, 1 nmol in 100 μL PBS) or a block formulation of ChLHsp1a (ChL-Hsp1a, 10 μM, 1 nmol, and Hsp1a, (204 μM, 21 nmol, in 100 μL of PBS), n = 6, or PBS (n = 6). Similarly, for the bioluminescence, animals were injected with [64Cu]Cu-ChL-Hsp1a (3.5−4.2 MBq) dissolved in 100 μL PBS and a block formulation [64Cu]Cu-ChL-Hsp1a (3.5−4.2 MBq), and Hsp1a (204 μM, 21 nmol in 200 μL of PBS, n = 6). Using a fluorescence stereoscope, we studied the fluorescence signal and accumulation in mouse sciatic and brachial plexus nerves 30 min after intravenous injection of ChL-Hsp1a (1 nmol, 10 μM of ChL-Hsp1a in 100 μL of PBS) or PBS (n=3/group). Results: We successfully labeled Hsp1a with a chlorin tracer to afford ChL-Hsp1a (25%). [64Cu]Cu-ChL-Hsp1a was obtained in >95% and in 40-50% radiochemical yield (ndc). We found that injections with ChL-Hsp1a (1 nmol, 10 μM in 100 μL of PBS) resulted in high fluorescence coming from the sciatic nerves with elevated 93-fold compared to sciatic nerves from mice injected with block. In a similar pattern, animals injected with [64Cu]Cu-ChL-Hsp1a (3.5−4.2 MBq) resulted in high bioluminescence signal coming from the sciatic nerves with elevated 48-fold compared to sciatic nerves from mice injected with block. We also found that mouse sciatic nerves were clearly visible with the Lumar fluorescence stereomicroscope (n=3/group). This data suggests that it is possible to delineate peripheral nerves with high contrast and that the same agent after radiolabeling can be used in Cerenkov bioluminescence.

Conclusions: ChL-Hsp1a and [64Cu]Cu-ChL-Hsp1a peptides accumulated and highlighted peripheral nerves in mice in vivo. The statistically significant fluorescence/Cerenkov signal observed in peripheral nerves in mice, as a result of using fluorescent/PET active Hsp1a peptides, is clear evidence of peripheral nerve localization. This fluorescent/PET approach could be especially beneficial to stratify patients, as treatments often continue to rely on subjective assessments of these symptoms by physicians after patients' self-reporting. ChL-Hsp1a and [64Cu]Cu-ChL-Hsp1a peptides are promising tools that could potentially help physicians to rapidly identify peripheral neuropathy in patients.

References: [1] Zajaczkowska, R., et al., Mechanism of Chemotherapy-Induced Peripheral Neuropathy. Int. J. Mol. Sci, 2019. 20 No. 1451. [2] Li, Y., et al., Drg voltage-gated sodium channel 1.7 is upregulated in paclitaxel-induced neuropathy in rats and in humans with neuropathic pain. J. Neurosci. 2018. 38, 1124-1136. [3] Gonzales, J., et al., Fluorescence imaging of peripheral nerves by a Nav1.7-targeted inhibitor cystine knot peptide. Bioconjugate Chem., 2019. 30(11): p. 2879-2888. [4] Gonzales, J., et al., Facile synthesis of chlorin bioconjugates by a series of click reactions. Chem. Commun., 2017. S3(11): p. 3773-3776.

Image/Figure: https://s3.amazonaws.com/amz.xcdsystem.com/1E8A4501-BB41-A02A-1D3B9882B798BFAA_abstract_File10351/GA338_ImageFigure_0513061042.pdf

Image/Figure Caption: Figure 1. Synthesis of ChL-Hsp1a and [64Cu]Cu-ChL-Hsp1a, and their corresponding accumulations in peripheral nerves with different modalities. A) Reaction scheme for the conjugation of the Hsp1a peptide with ChL-NHS ester dye. The ribbon model of ChL-Hsp1a shows disulfide bridges (in orange) and the covalent conjugation of the chlorin moiety and the radiochemical synthesis for the labeling of the ChL-Hsp1a peptide with 64Cu. B) Epifluorescence images of animals injected with 100 µL of PBS, ChL-Hsp1a (1 nmol, 10 µM ChL-Hsp1a in 100 µL of PBS), or a ChL-Hsp1a/Hsp1a formulation (ChL-Hsp1a, 10 µM, 1 nmol and Hsp1a, 204 µM, 21 nmol in 100 µL of PBS). Images were taken 30 min after tail vein injection. (C) Fluorescence intensity quantification of panel (B). D) Cerenkov luminescence (CL) images of mice injected with Hsp1a and [64Cu]Cu-ChL-Hsp1a (left) or [64Cu]Cu-ChL-Hsp1a alone (right). High radiance is observed after 30 min in mice injected with [64Cu]Cu-ChL-Hsp1a alone. E) CL quantification of panel (D). F) Representative fluorescence images of mice injected with ChL-Hsp1a using a Lumar stereoscope after 30 min tail vein injection.

First Name: JUNIOR

Last Name: GONZALES

Email: gonzalj4@mskcc.org

Organization: Memorial Sloan Kettering Cancer Center

Country: United States

ID: GA339

Copper-dopped responsive nanomaterials with improved Pt-based chemotherapy and chemodynamic therapy for cancer

Yuanyuan Ma, Southeast University, mayuanyuan.sun@gmail.com

Category: Oncology

Abstract Body : Cis-diamminedichloridoplatinum(II), known as cisplatin, and subsequent expansion of platinum-based chemotherapy drug family have been used against a wide range of tumors and achieved remarkable success for cancer therapy[1][2]. However, cisplatin shows its restricted clinical use because of the highly toxic nature, which will cause indiscriminate damage to both cancer cells and normal cells, further inducing severe side effects like nephrotoxicity and hepatotoxicity[3]. Moreover, rapid development of resistance is another major concern of cisplatin. Among all the effecting factors, overproduced glutathione(GSH) is an important one to induce resistance during the cancer therapy[4]. Thus, it is important to develop a novel method to enhance Pt-based chemotherapeutic effect and improve drug resistance, especially by depleting GSH. In this study, hollow-structured mesoporous organosilica nanoparticle(HMON) was used as the cisplatin carrier, owing to the large internal cavity and increased loading capacity[5]. Cu-based metal-organic framework(Cu-MOF) was used to encapsulate HMON to form a kind of hybrid nanomaterials(Hcis@Cu-MOF). MOF was responsive to the acid conditions and could be easily biodegraded[6], which enables the copper ions and loading cisplatin to release in a regulated manner. Moreover, copper ions within the framework of the nanometerials were capable of depleting intracullar GSH, leading to the enhanced cispaltin therapeutic effect. Additionally, copper ion was one kind of Fenton-like agent, which was able to react with intracellular hydrogen peroxide and subsequent produce highly toxic hydroxyl radicals(·OH), resulting in cell apoptosis, which was the chemodynamic therapy[7]. Thus, this synthesized nanomaterials could responsive to the mild acid conditions and release copper and cisplatin precisely. Additionally, the copper ions in the nanomaterials could enhance cisplatin therapeutic effect and combine chemodyamic therapy with chemotherapy via GSH consumption and ·OH production, achieving the improved cancer-killing efficacy. Figure 1a-b showed the uniform morphology of HMON and the synthesized Hcis@Cu-MOF monitored by transmission electron microscope. The HMON showed 40nm, while after encapsulation of Cu-MOFs, a thin layer of MOF structure could be observed evidently. In addition, the size of the nanomaterials would show great enhanced permeability and retention(EPR) effect. Copper ions and cisplatin could be released quickly at pH 5.5(Figure 1c-d). While at pH 7.4, copper ions and cisplatin could only release less than 30%, indicating the great pH responsiveness of Hcis@Cu-MOF. Figure 1e-f displayed the ability of GSH depletion and ·OH production, which were measured by 5,5′-Dithiobis(2-nitrobenzoic acid) and methylene blue(MB) degradation, showing the concentration/time-dependent manner. Cytotoxic effect was mesured by 3-(4,5-Dimethylthiazol-2-yl)-2,5-diphenyltetrazolium bromide as shown in Figure 1g. Compared to free cisplatin, Hcis@Cu-MOF showed higher cytotoxicity. Moreover, intracellular GSH level and ·OH production were also measured as shown in Figure 1h-i. Cells treated by Hcis@Cu-MOF showed a significant decrease of GSH, while the level of ·OH increased a lot. The

biodistribution of Cy-7 labeled Hcis@Cu-MOF in mice were displayed in Figure 1j. The results showed the nanomaterials possessed great EPR effect and could reach the tumor in 4 hours after intravenous administration. The in vivo results were shown in Figure 1k, showing that the tumor could be efficiently inhibited compared with free cisplatin. Moreover, mice treated by Hcis@Cu-MOF had a higher survival rate as shown in Figure 1l. To conclude, the synthesized Hcis@Cu-MOF could deliver cisplatin efficiently to the tumor site. In addition, the nanomaterals was pH-sensitive and could release cisplatin and copper ions within the cancer cells. Copper ions dopped in the nanomaterials could deplete intracellular GSH and improve cisplatin efficiency. Meanwhile, copper ions were able to react with the abundunt hydrogen peroxide, producing highly toxic □OH, leading to cell death and great chemodynamic therapeutic effect. Furthermore, Hcis@Cu-MOF could inhibit tumor growth in mice, indicating superior biomedical applications for cancer therapy in the future.

References: [1]Hu, Q., et al., Recent advances of cocktail chemotherapy by combination drug delivery systems. Advanced Drug Delivery Reviews, 2016. 98: p. 19-34. [2]Browning, R.J., et al., Drug Delivery Strategies for Platinum-Based Chemotherapy. ACS Nano, 2017. 11(9): p. 8560-8578. [3]Majumder, J., O. Taratula, and T. Minko, Nanocarrier-based systems for targeted and site specific therapeutic delivery. Advanced Drug Delivery Reviews, 2019. 144: p. 57-77. [4]Xu, Y., et al., Sulforaphane Mediates Glutathione Depletion via Polymeric Nanoparticles to Restore Cisplatin Chemosensitivity. ACS nano, 2019. 13(11): p. 13445-13455. [5]Llopis-Lorente, A., et al., Enzyme-Powered Gated Mesoporous Silica Nanomotors for On-Command Intracellular Payload Delivery. ACS Nano, 2019. 13(10): p. 12171-12183. [6]Advances in metal–organic framework coatings: versatile synthesis and broad applications. Chemical Society Reviews, 2020. 49(10): p. 3142-3186. [7]Ma, B., et al., Self-Assembled Copper-Amino Acid Nanoparticles for in Situ Glutathione "AND" H2O2 Sequentially Triggered Chemodynamic Therapy. J Am Chem Soc, 2019. 141(2): p. 849-857.

Image/Figure: https://s3.amazonaws.com/amz.xcdsystem.com/1E8A4501-BB41-A02A-1D3B9882B798BFAA_abstract_File10351/GA339_ImageFigure_0513062713.pdf

Image/Figure Caption: Figure 1a-b Representative TEM images of HMON and Hcis@Cu-MOF. Scale bar: 50μm. Figure 1c-d Copper ions and cisplatin release at different time points under various pH, respectively. Figure 1e GSH consumption of different concentrations of Hcis@Cu-MOF ex vivo at various time points, measured by DTNB. Figure 1f UV−vis spectra of MB solution treated with H2O2 plus Hcis@Cu-MOF(40μg/mL). Figure 1g Cytotoxicity of Hcis@Cu-MOF. MTT results of viability of A549 cancer cells with Hcis@Cu-MOF for 24h. Figure 1h Intracellular GSH level treated by different concentration of Hcis@Cu-MOF. Figure 1i Flow cytometry analysis showing the ·OH production in cancer cells after Hcis@Cu-MOF treatment. Figure 1j The biodistribution of Cy-7-labeled Hcis@Cu-MOF in mice at different time points after intravenous administration. Figure 1k-l Tumor size change during therapy in mice and survival rate of different treatments.

First Name: Yuanyuan

Last Name: Ma

Email: mayuanyuan.sun@gmail.com

Organization: Southeast University

Country: China

ID: GA340

Functionalization of Fluorocarbon Nanoemulsion with Fluorous Molecules for Multimodal Imaging

Chao Wang, UC SAN DIEGO, CHW124@UCSD.EDU

Category: New Chemistry, Materials & Probes

Abstract Body : Introduction. Fluorocarbon (FC) is both hydrophobic and lipophobic and has high biological inertness and gas-dissolving ability. In the clinic, FC colloids are routinely used as ultrasound contrast agents and have been widely studied for oxygen delivery, with a proven safety profile and well-characterized pharmacokinetics.1,2 FC-in-water nanoemulsion (NE) is actively being evaluated in clinical trials for in vivo cell detection by fluorine-19 (19F) MRI.3While the inertness of FC contributes to their low toxicity, it makes chemical functionalization challenging. The high electronegativity of fluorine imparts very low cohesive energy density and Lewis basicity to FC, making dissolution of other molecules difficult. Functionalization is further complicated by colloidal instability. We have designed new fluorous molecules, in particular chelators4,5 and fluorophores,6,7 that overcome solubility barriers to reside in the FC core, providing a platform for the development of multimodal imaging agents. This strategy minimizes the interaction of encapsulated molecules with biological systems and promotes agent stability in vivo. We have demonstrated the use of lipid FC NE formulations for visualization of macrophage infiltration in mouse models using multimodal imaging, including positron emission tomography (PET), 19F MRI and cryo-fluorescence tomography (CFT) (Figure 1). Materials & Methods. A fluorous octadentate hydroxamic acid chelator was synthesized and formulated into FC NE to capture 89Zr in NE for PET imaging.4 A fluorescent FC NE was also prepared by dissolving a fluorous Cy5 dye (lem = 672 nm) in FC.7 NE bearing the 89Zr chelator or Cy5 was formulated with lipid surfactants using a high-pressure homogenization process. The FC NE encapsulating 89Zr (3.7 MBq) or Cy5 was then intravenously injected into mice (8-10 weeks, female CD1 mice , Envigo, Indianapolis, IN) bearing acute inflammation at the left paw, induced by subcutaneous administration of λ-carrageenan (2% in saline, 50 μL). Images were acquired 24 h post NE injection on multiple imaging platforms, including PET/CT (Inveon, Siemens), 19F/1H MRI (11.7 T BioSpec, Bruker), fluorescence (IVIS Spectrum, PerkinElmer) and CFT (Xerra, Emit Imaging). Serial blood samples were collected to study the circulation time of NE in vivo. Histology was used to confirm the internalization of FC NE by macrophages. All animal experiments followed protocols that were approved by University of California San Diego's Institutional Animal Care and Use Committee. Results. Lipid FC NE containing fluorous 89Zr chelator or Cy5 dye in FC oil was formulated with a droplet diameter of ~150 nm and a polydispersity NE harboring fluorous chelator was readily labeled with 89Zr, giving a radiolabeling yield of ~60% after purification. Pharmacokinetic studies showed that the NE has a blood circulation half-life of 14.5 h. In PET/CT imaging, prominent signals are observed in the inflamed left paw, but not in the contralateral paw; signals are also observed in liver and spleen (Fig. 1b). Similarly, in 19F MRI, a hotspot is observed in the left paw (Fig. 1c), as is also observed superficially with in vivo fluorescence imaging using the fluorous Cy5 NE (Fig. 1d). The same mouse, subjected to

three-dimensional CFT, displays bright fluorescence signals in the left paw, liver, spleen and lymph nodes (Fig. 1e), where Fig. 1f shows the fluorescent signal overlaid on a white light image for anatomical reference. CFT is effective at yielding a high-resolution, 'ground truth' probe biodistribution at experimental endpoints. Conclusion. Synthesis of novel fluorous molecules, such as chelators and dyes, enable the functionalization of FC NE for multimodal imaging. A high degree of consistency is observed among PET, MRI and CFT in the visualization of local macrophage infiltration and agent biodistribution. Overall, these materials and methods are useful for imaging a broad range of preclinical inflammatory diseases.

References: References: (1) Wei, K.; Mulvagh, S. L.; Carson, L.; Davidoff, R.; Gabriel, R.; Grimm, R. A.; Wilson, S.; Fane, L.; Herzog, C. A.; Zoghbi, W. A.; Taylor, R.; Farrar, M.; Chaudhry, F. A.; Porter, T. R.; Irani, W.; Lang, R. M. The safety of deFinity and Optison for ultrasound image enhancement: a retrospective analysis of 78,383 administered contrast doses. J Am Soc Echocardiogr 2008, 21, 1202-1206. (2) Riess, J. G. Understanding the fundamentals of perfluorocarbons and perfluorocarbon emulsions relevant to in vivo oxygen delivery. Artif Cells Blood Substit Immobil Biotechnol 2005, 33, 47-63. (3) Ahrens, E. T.; Helfer, B. M.; O'Hanlon, C. F.; Schirda, C. Clinical Cell Therapy Imaging Using a Perfluorocarbon Tracer and Fluorine-19 MRI. Magn Reson Med 2014, 72, 1696-+. (4) Wang, C.; Leach, B. I.; Lister, D.; Adams, S. R.; Xu, H.; Hoh, C. K.; McConville, P.; Zhang, J.; Messer, K.; Ahrens, E. Metallo-Fluorocarbon Nanoemulsion for Inflammatory Macrophage Detection via PET and MRI. J Nucl Med 2020, DOI: 10.2967/jnumed.120.255273. (5) Kislukhin, A. A.; Xu, H.; Adams, S. R.; Narsinh, K. H.; Tsien, R. Y.; Ahrens, E. T. Paramagnetic fluorinated nanoemulsions for sensitive cellular fluorine-19 magnetic resonance imaging. Nat Mater 2016, 15, 662-668. (6) Janjic, J. M.; Srinivas, M.; Kadayakkara, D. K.; Ahrens, E. T. Self-delivering nanoemulsions for dual fluorine-19 MRI and fluorescence detection. J Am Chem Soc 2008, 130, 2832-2841. (7) Lim, I.; Vian, A.; van de Wouw, H. L.; Day, R. A.; Gomez, C.; Liu, Y.; Rheingold, A. L.; Campàs, O.; Sletten, E. M. Fluorous Soluble Cyanine Dyes for Visualizing Perfluorocarbons in Living Systems. J Am Chem Soc 2020, 142, 16072-16081.

Image/Figure:

https://s3.amazonaws.com/amz.xcdsystem.com/1E8A4501-BB41-A02A-1D3B9882B798BFAA_abstract_File10351/GA340_ImageFigure_0513064744.jpg

Image/Figure Caption: Figure 1. Functionalization of FC NE for multimodal imaging of macrophage infiltration in an acute inflammation murine model induced by λ-carrageenan in footpad. Panel (a) shows the structures of fluorous 89Zr chelator or Cy5 molecules incorporated into FC NE. In (b), we show a PET/CT image of mouse injected with 3.7 MBq 89Zr FC NE acquired 24 h post injection. (c) Displays composite 19F (hot-iron scale) /1H (grayscale) MRI in the same mouse as (b). Image (d) shows an in vivo fluorescent image of mouse injected with Cy5 FC NE acquired 24 h post injection. Panel (e) shows a representative CFT slice of the same mouse in (d), and (f) shows a CFT fluorescent and white light image overlay.

Full Name of Abstract's 1st Author : Chao Wang

First Name: Chao

Last Name: Wang

Email: CHW124@UCSD.EDU

Organization: UC SAN DIEGO

Country: United States

ID: GA341
A novel universal contrast agent for sensitive biomedical imaging

Neil Robertson, Michigan State University, robe1104@msu.edu

Category: New Chemistry, Materials & Probes

Abstract Body : Imaging is a powerful and rapidly growing field of biomedical research, proven indispensable for early detection, diagnosis and treatment of various cancer types and tracking cells of interest in vivo. Preclinical development of novel imaging agents and modalities helps to drive the way diseases are treated and diagnosed, and link interdisciplinary approaches. Individual imaging techniques have certain advantages in imaging biological objects, but at the same time each suffers from drawbacks that other modalities may overcome. As such, the formulation of a single universal contrast agent useful in multiple modalities was explored to help bridge specific gaps in information lost with any single modality and aid in enhancing collaboration between various imaging fields. Using a single agent removes the issue of co-administered agents having differing distribution and breakdown kinetics and ensures the ability to image the region of interest with all desired modalities. Furthermore, a universal agent would allow for the manual registration of different modalities from a single administration and work with or without artificial intelligence (A.I.) systems. Therefore, the goal of the study was to develop a contrast agent that combines magnetic resonance imaging (MRI), magnetic particle imaging (MPI), computed tomography (CT), fluorescence (FL), photoacoustic (PA), ultrasound (US) and positron emission tomography (PET)/single-photon emission computed tomography (SPECT) into a single formulation. Development of this agent, termed Omniparticle, was explored using a modified co-precipitation synthesis technique followed by conjugation of small molecule moieties to provide imaging potential in all modalities. The iron core, wrapped in a modified dextran polymer for stability and functionalization, provides the MR and MP imaging potential. The functionalized fluorophore component provides FL, PA and US imaging capabilities. Attachment of chelators, such as DOTA for PET or hynic for SPECT, provides the respective PET or SPECT imaging properties. Finally, attachment of thyroxine (T4) provides CT imaging potential and completes the MRI/MPI/FL/PA/US/CT and PET/SPECT contrast agent. The synthesized agent has the following parameters: core size 15-20 nm, overall size 25-35 nm, final zeta potential +10-15 mV, 100-150 functional amine groups per particle, and moieties include 7-10 Cy5.5/particle, 7-10 DOTA/particle and 5-10 Thyroxine (T4)/particle. Phantoms were imaged in each of the modalities to probe the presence of the individual functional moieties as well as gather information to adjust the ratio of loading on the contrast agent. Fig. 1 shows potent signal generation with each modality upon addition of corresponding moieties. To probe the in vivo functionality of our contrast agent, an initial pilot study was performed across multiple imaging modalities. Exploring a model of breast cancer, we imaged the ductal tree of naïve mice after an intraductal injection of the agent (40 μg Fe/duct), prior to moving into tumor bearing animals. Immediately post injection, the animal was imaged with a microCT, MPI and with the IVIS fluorescence imaging. As seen in Fig. 2, imaging of the intraductal injection was possible with each of the modalities, with the CT capable of resolving the ductal tree network (Fig. 2a). After rendering the slices we obtained a 3D view of the entire network (Fig. 2b).

Fluorescence imaging of Cy5.5 (Fig. 2c) as well as the simple 2D (Fig. 2e), and the 3D MPI scan co-registered with the mouse's skeleton, showed spatial localization of the injected agent (Fig. 2d). Ex-vivo histology showed accumulation of the agent in the ductal epithelial cells as expected. In the future we plan to utilize this agent to image tumor models along with tracking labeled cells (not shown here). We believe that by providing a universal tool to the biomedical imaging field we can corroborate registered signals and potentially enhance the information acquired in the clinic.

Image/Figure Caption: Figure 1. Initial characterization of the contrast agent core. a) TEM images depicting the relative size (10-20 nm) of the iron oxide core and crystalline structure. b) MRI scan with various contrast agent phantoms (MRI only, MRI/MPI, MRI/MPI, no signal expected and water, 1-5 respectively, see text for details). c) MPI scan of phantom shows positive signal generation (upper right is scan alone, lower is overlay of scan and image of phantom). Representative images of contrast agent phantoms after fluorophore conjugation with a) fluorescence (IVIS), b) photoacoustic (MSOT) and c) ultrasound (MSOT). Figure 2. Intraductal injection of the multimodal contrast agent as a proof of concept. The ductal tree is entirely visible in a) 2D and b) 3D CT scans, with similar contrast to bone. Injections were validated with c) fluorescence imaging (Cy5.5 channel, IVIS), d) a 3D co-registered MPI with CT scan or e) a 2D MPI scan.

Full Name of Abstract's 1st Author : Neil M Robertson

First Name: Neil

Last Name: Robertson

Email: robe1104@msu.edu

Organization: Michigan State University

Country: United States

ID: GA342

Using [18F]-FDG PET/CT to characterize liver dysfunction in people with HIV before and after antiretroviral treatment

Reema Patel, National Institutes of Health, rp5mg@virginia.edu

---

Category: Immunology: Inflammation & Infection

Abstract Body : Background: Liver disease is a leading cause of morbidity and mortality in people with human immunodeficiency virus (HIV) (PWH), even in those optimally-treated with antiretroviral therapy (ART) [1]. HIV itself can exert damaging effects on hepatocytes, liver-resident macrophages (Kupffer cells), and hepatic stellate cells. Immune cell depletion and other viral pathogenesis mechanisms can also contribute to liver dysfunction, inflammation, and fibrosis [2-7]. The extent of HIV-associated liver damage and recovery remains unclear. PET/CT is a valuable, non-invasive approach to elucidate liver dysfunction in PWH and establish a connection between imaging findings and hepatic changes that could provide additional guidance in HIV disease management. In this study, we used [18F]-fluorodeoxyglucose (FDG) PET/CT imaging to longitudinally evaluate hepatic structural and functional changes in ART-naïve PWH with advanced disease until two years after treatment initiation. Clinical, laboratory, and immune markers were also measured to identify other factors associated with liver injury and recovery. Methods: Forty-eight viremic PWH (33 males, 15 females), with CD4 counts Results: At baseline, PWH were younger than control participants with median ages of 36.25 and 52.55, respectively (p Conclusions: ART-naïve, late-presenting PWH demonstrated low baseline liver FDG uptake that increased two years after treatment but remained lower than healthy participants. These changes correlated with markers of immune recovery and decreased systemic inflammation following treatment. Our findings suggest a multifactorial model for liver injury in HIV that likely reflects CD4 depletion, monocyte/Kupffer cell activation, and hepatocyte dysfunction. While long-term ART seems to reverse many aspects of hepatic abnormalities, residual liver injury identified non-invasively through FDG PET/CT imaging may exist, at least within two years from treatment initiation, especially in PWH who present with low nadir CD4 counts.

References: 1. Croxford, S., et al., Mortality and causes of death in people diagnosed with HIV in the era of highly active antiretroviral therapy compared with the general population: an analysis of a national observational cohort. The Lancet Public Health, 2017. 2(1): p. e35-e46. 2. Ganesan, M., et al., Liver as a target of human immunodeficiency virus infection. World J Gastroenterol, 2018. 24(42): p. 4728-4737. 3. Kaspar, M.B. and R.K. Sterling, Mechanisms of liver disease in patients infected with HIV. BMJ Open Gastroenterol, 2017. 4(1): p. e000166. 4. Saeidi, A., et al., Functional role of mucosal-associated invariant T cells in HIV infection. Journal of Leukocyte Biology, 2016. 100(2): p. 305-314. 5. Dagur, R.S., et al., Human hepatocyte depletion in the presence of HIV-1 infection in dual reconstituted humanized mice. Biol Open, 2018. 7(2). 6. Hufert, F.T., et al., Human Kupffer cells infected with HIV-1 in vivo. J Acquir Immune Defic Syndr (1988), 1993. 6(7): p. 772-7. 7. Zhang, L. and M.B. Bansal, Role of

Kupffer Cells in Driving Hepatic Inflammation and Fibrosis in HIV Infection. Front Immunol, 2020. 11: p. 1086.

Image/Figure:

https://s3.amazonaws.com/amz.xcdsystem.com/1E8A4501-BB41-A02A-1D3B9882B798BFAA_abstract_File10351/GA342_ImageFigure_0513065248.jpg

Image/Figure Caption: (A) PET/CT imaging of liver FDG uptake in PWH at BL, ST, and LT time points (left to right). Representative axial images of PET and PET/CT fusion are shown. (B) Longitudinal changes in uptake across time points in PWH (median and IQR), with the solid and dotted black lines reflecting values of the control group (median and IQR, respectively).

First Name: Reema

Last Name: Patel

Email: rp5mg@virginia.edu

Organization: National Institutes of Health

Country: United States

ID: GA343
Exploring Dual Magnetic Particle Imaging (MPI) and Akaluc Bioluminescence Imaging (BLI) for In Vivo Cell Tracking

Ryan Williams, Robarts Research Institute, rwill27@uwo.ca

Category: Instrumentation

Abstract Body : Introduction: Cell tracking is a rapidly advancing field, providing critical insight on transplanted cell fate preclinically.1 This is essential for improving our understanding of biological mechanisms and developing cellular therapies.1 Prior to tracking, cells must be labelled either directly through endocytosis, or indirectly through the introduction of a reporter gene.1 To give complementary information, and limit the associated weaknesses of each method, this project will combine direct and indirect labelling for the tracking of cancer cells. Direct labelling is a highly sensitive method. However, the tracer is diluted upon cell division and may be expelled by cells where it is taken up by scavenger cells.1 Due to this, imaging based on direct labelling is limited to short term tracking.1 The novel Magnetic Particle Imaging (MPI) excels at short term tracking of cells directly loaded with iron nanoparticles due to its high sensitivity, positive signal contrast, and ability to directly quantify iron-loaded cells.2 Indirect labelling is less sensitive, however, as the reporter gene is passed equally to daughter cells during cell division, and is quickly denatured outside of living cells.1 Indirect labelling allows for long-term tracking of both cell viability and proliferation.1 Akaluc/Akalumine based Bioluminescence Imaging (BLI) has shown the ability to detect a single cell at depth in an animal model, due to the low biological attenuation of near-infrared light, released by the oxidation of Akalumine by Akaluc.3 BLI will therefore be used to image indirectly labelled cells in this project. This project will develop the first dual MPI/BLI system for tracking cancer cells, using the BLI reporter Akaluc, providing a more complete picture of cell fate in preclinical models. Methods: A mouse breast cancer cell line (4T1BR5) was transduced to express Akaluc, and the fluorescence reporter TdTomato (TdT). The expression level and stability of this construct was analyzed with flow cytometry over 10 passages. BLI of varying cell numbers was done to determine signal linearity. Cells were loaded with a commercial iron nanoparticle, Synomag-D. Loading efficiency was calculated through iron staining. Viability was assessed for loaded and unloaded cell populations through Zombie Violet staining and analysis with flow cytometry. Additionally, BLI signal intensity was compared for these cell populations following administration of Akalumine (n=9). The resolution and sensitivity of Synomag-D was assessed in comparison to Vivotrax (the industry standard) using in vitro MPI relaxometry (n=3). Calibration lines were created by imaging a range of Synomag-D concentrations, plotting signal versus concentration. Results: The TdT-Akaluc construct was successfully transduced and the percentage of cells (79%) stably expressing TdT did not change over 10 passages. Staining showed clear and efficient Synomag-D uptake, (98% of cells labelled, n=9). Viability and BLI expression were not significantly different for loaded and unloaded cell populations(n=9). BLI signal linearly and positively correlated with cell number (p=0.2). The sensitivity of Synomag-D was roughly 4x that of Vivotrax, with comparable resolutions (p Discussion: Here we developed the first dual MPI/BLI system for cell tracking with the highly sensitive BLI reporter Akaluc. The combined use of MPI

and BLI will give complementary information, leading to a more complete understanding of cell fate in the body. The stable expression of Akaluc, offers a highly sensitive marker for cell viability which is not affected by iron loading. As MPI and BLI signal are both linear, quantification of cells should be feasible in a mouse model, and is the focus of our current work

References: 1. Kircher, M. F., Gambhir, S. S., & Grimm, J. (2011). Noninvasive cell-tracking methods. Nature Reviews Clinical Oncology, 8(11), 677–688. https://doi.org/10.1038/nrclinonc.2011.141 2. Sehl, O. C., Gevaert, J. J., Melo, K. P., Knier, N. N., & Foster, P. J. (2020). A perspective on cell tracking with magnetic particle imaging. Tomography, 6(4), 315–324. https://doi.org/10.18383/j.tom.2020.00043 3.Iwano, S., Sugiyama, M., Hama, H., Watakabe, A., Hasegawa, N., Kuchimaru, T., Tanaka, K. Z., Takahashi, M., Ishida, Y., Hata, J., Shimozono, S., Namiki, K., Fukano, T., Kiyama, M., Okano, H., Kizaka-kondoh, S., Mchugh, T. J., Yamamori, T., Hioki, H., … Miyawaki, A. (2018). Moving Animals. 939(February), 935–939.

First Name: Ryan

Last Name: Williams

Email: rwill27@uwo.ca

Organization: Robarts Research Institute

Country: Canada

ID: GA344

MICROFLUIDIC PRODUCTION OF ULTRASOUND CONTRAST AGENTS FOR PD-L1 MOLECULAR IMAGING

Negar Sadeghipour, Stanford University, sadeghi@stanford.edu

Category: Oncology

Abstract Body : Purpose: Immune checkpoint inhibitors (ICIs) have had great success but remain ineffective in over 50% of patients due to several patient-specific response variabilities.1 The immunosuppressive effects of the endothelial 'barrier' (also termed EC anergy) have been related to EC surface expression of immunosuppressive markers (i.e. PD-L1) that deter effector T cells; identifying patients with such EC markers could help select patients for ICIs, and spare non-responders. Here, we present initial developments and validation of the first molecular ultrasound microbubble (MB) probes to image immunosuppressive markers on ECs. Method: MBs were fabricated by microfluidic procedure. Briefly, fixed-ratio of lipids i.e. DPPC, DPPA, and PEG5000 PE (Avanti Polar Lipids Inc.) (mole ratio 10:80:8) were hydrated with 2 mL buffer solution with propylene glycol, glycerol. The lipid suspension was then sonicated for 5 minutes and then homogenized by purging through LV1-microfluidic system (Microfluidics, Westwood, MA) operating at 30,000 psi. The homogenate was then supplemented with Pluronic® L-64 surfactant (0.3 mg/mL) and sealed in Wheaton vials pre-filled with perfluoropropane gas (6 mg/mL) and finally activated in a Vialmix (Lantheus Medical Imaging) to produce suspension of MB. The resulting MB were characterized by Accusizer for size distribution and concentration. Tissue-mimicking gelatin-agar based pipe phantoms were prepared as per procedure outlined by Shiying W et al.2 The inner lining of one of the conduit was surface functionalized with PDL-1 protein by EDC/NHS chemistry. PDL-1 targeted and non-targeted bubbles were infused into functionalized phantoms and imaged by linear array transducer MS250 (13–24 MHz) operated by Visualsonics (Vevo 2100) system. The presence of anti-PDL1 antibody on the lipid shells of microbubble and its binding affinity to 4T1 mouse endothelial cells was assessed in parallel plate inverted flow chamber system under steady state flow conditions outlined in earlier work.3 In vitro evaluation of anti-PDL1 and IFN-γ markers influence on T cell and Treg migration towards tumor cells was investigated with the dual chamber setup outlined in Fig 1g. Results: Conjugation of PDL-1 to PEG5000 PE was optimized and confirmed by detection of additional band in Anti-PEG immunoblot assay at 130 kDa (Fig 1a). FACS analysis of Alexa-647-anti PDL-1 engineered microbubbles led to prominent shift in fluorescent MBs as compared to rat-isotype conjugated MB which established the presence of anti-PDL1 antibody on lipid shell of MB (Fig 1b). Evaluation of concentration and size distribution of MB revealed presence of 4-5 x 108 microbubbles/mL with average size of 1.1 μm (±0.39 μm) which was consistent for both PDL-1 targeted and control MB (Fig 1c). Assessment of MB stability over time indicated that ~35% of MBs were stable after 4 hours of activation (Fig 1d). The PDL-1 specific binding affinity of MB was evaluated in PDL1-antigen functionalized tissue mimicking phantom, and revealed consistently higher level of acoustic signal (mean echo power) in PDL-1 antigen functionalized channel as compared to unfunctionalized channel which confirmed the ligand specific affinity and binding ability of anti-PD-L1 MB (Figure 1e/f). In order to identify the

implication of PDL-1 molecular imaging as potential screening agent for responders to ICI immunotherapy, we examined the role of immunomodulators (anti-PDL1 and IFN-γ) in altering the expression of CD47 and PDL-1 markers in CT-26 cells in the presence of murine bone marrow derived immune cells. Simultaneous treatment with anti-PDL-1 antibody and IFN- γ led to decline in CD47 and PDL-1 expression levels in CT26, and decline in viability of CT-26 seeded in the lower chamber (Figure 1g/h); these are consistent with literature indicating that co-blocking CD47 and PD-L1 increases innate and adaptive cancer immune responses and cytokine release.4 Conclusion: Here, we successfully demonstrate the first ever PD-L1 targeted microbubble fabricated with a

References: 1. Pramod D. et. al. Immune checkpoint inhibitors: recent progress and potential biomarkers, Exp Mol Med; 2018, 50(12), 1-11. 2. Shiying W. et. al. Pipe phantoms with applications in molecular imaging and system characterization, IEEE T Ultrason Ferr; 2016, 64(1), 39-52. 3. Lotfi A. E. et. al. Thy1-Targeted Microbubbles for Ultrasound Molecular Imaging of Pancreatic Ductal Adenocarcinoma, Clin Cancer Res. 2018, 24(7), 1574-1585. 4. Shu L. et. al. Simultaneous blocking of CD47 and PD-L1 increases innate and adaptive cancer immune responses and cytokine release, EBioMedicine; 2019, 42, 281–295.

Image/Figure:

https://s3.amazonaws.com/amz.xcdsystem.com/1E8A4501-BB41-A02A-1D3B9882B798BFAA_abstract_File10351/GA344_ImageFigure_0513070709.png

Image/Figure Caption: Figure 1: (a) Immunoblot analysis of anti-PDL-1 antibody conjugated PEG5000-PE with anti-PEG antibody at different molar ratios (b) Validation of Alexa-594 tagged anti-PDL1 antibody incorporation on the lipid shell of microbubbles by FACS analysis; (c) Estimation of size distribution and (d) stability of PDL-1 and Isotype antibody incorporated MB by Accusizer (NICOMP Particle Sizing Systems, Santa Barbara, CA) (e&f) Evaluation of targeted molecular imaging in tissue mimicking phantoms functionalized with PDL-1 protein by time decay analysis of MB contrast during constant flush with saline at flow rate of 0.3 ml/min; (g) Schematic representation of in vitro assay setup to measure immune cell infiltration across EC layer in response to ICI therapy assisted EC surface markers effects on T cell migration towards tumor cells. (h) Evaluation of immunomodulators IFN- γ and anti-PDL-1 effect in the invitro set up for expression of CD47 (do not eat me signal) and PDL-1 expression by CT26 cells in the presence of murine bone marrow derived immune cells by FACS analysis.

First Name: Negar

Last Name: Sadeghipour

Email: sadeghi@stanford.edu

Organization: Stanford University

Country: United States

ID: GA345

Combined 89Zr-panitumumab PET/CT and 18F-FDG-PET/CT improves detection of metastatic head and neck squamous cell carcinoma in humans

Yu-Jin Lee, Stanford University, yujinlee@stanford.edu

Category: Oncology

Abstract Body : INTRODUCTION The current standard of care preoperative imaging to stage head and neck squamous cell carcinoma (HNSCC) is performed using 18F-FDG-PET/CT, which nonspecifically highlights regions with significant metabolic activity. This lack of specificity for cancer presents challenges when incidental findings are identified and require additional invasive biopsy procedures. To address this, a highly specific PET radiotracer (89Zr-radiolabeled panitumumab) was tested for use in combination with conventional 18F-FDG-PET/CT diagnostic imaging of HNSCC in humans. Panitumumab is a monoclonal antibody targeting the epidermal growth factor receptor that is highly expressed in HNSCC. The current study investigated the safety and feasibility of this agent for detection of primary HNSCC and metastatic lesions. MATERIALS AND METHODS We enrolled 14 patients with HNSCC scheduled for surgical resection and cervical lymph node (LN) dissection in a single center study. Patients underwent 18F-FDG-PET/CT as standard of care preoperative imaging prior to study enrollment. 89Zr-panitumumab (1mCi) was administered intravenously 1-5 days prior to surgery, and 89Zr-PET/CT scans were performed prior to surgery. Both 18F-FDG-PET/CT and 89Zr-panitumumab-PET/CT scans were serially reviewed by a nuclear medicine physician. Surgical specimens were processed according to routine standard of care, assessed by a pathologist who was blinded to the imaging results, and used as gold standard for detection of local-regional HNSCC. Diagnostic statistics were evaluated using receiver operating characteristic curves, and logistic regression was performed to evaluate the combined ability of 18F-FDG-PET/CT and 89Zr-panitumumab-PET/CT to detect HNSCC. Likelihood ratio was used to compare the predictive model of 18F-FDG-PET/CT alone and the combined model of 18F-FDG-PET/CT and 89Zr-panitumumab-PET/CT scans to detect HNSCC. RESULTS A total of fourteen patients were enrolled and completed the study. Four patients (28.5%) had areas of high metabolic activity outside the head and neck region with SUVmax (maximum standardized uptake value; quantified PET signal) greater than 2.0 on 18F-FDG-PET/CT that were not detected on 89Zr-panitumumab-PET/CT. All four patients with incidental findings underwent further workup and were found to have no evidence of cancer on biopsy or follow-up. 89Zr-panitumumab-PET/CT imaging demonstrated uptake of 89Zr-panitumumab in the tumor lesions as early as 22 hours after study drug infusion (primary tumor SUVmax 4.0 ±2.6; mean ± standard deviation). A total of 47 lesions (primary tumor, LNs, incidental findings) with SUVmax signal (9.9 ± 6.1; mean ± SD) were visualized on 18F-FDG-PET/CT and 35 lesions on 89Zr-PET/CT (3.1 ± 2.5; mean ± SD). 89Zr-panitumumab-PET/CT had higher specificity (88.9%) and area under the curve (AUC; 0.89) compared to that of 18F-FDG-PET/CT (74.1%, 0.79, respectively) in detecting HNSCC using pathologic assessment as gold standard ($p > 0.05$; DeLong's test). The combined ability of 18F-FDG-PET/CT and 89Zr-panitumumab-PET/CT to detect HNSCC was significantly improved with higher specificity (96.3%) and AUC (0.91) (p

DISCUSSION/CONCLUSION 89Zr-panitumumab-PET/CT imaging was safe and identified metastatic lymph nodes, with the added ability of distinguishing HNSCC from incidental findings visualized on 18F-FDG-PET/CT. Larger studies with appropriate power are needed to evaluate the potential of 89Zr-panitumumab-PET/CT to accurately stage HNSCC in a minimally invasive manner.

Full Name of Abstract's 1st Author : Yu-Jin Lee

First Name: Yu-Jin

Last Name: Lee

Email: yujinlee@stanford.edu

Organization: Stanford University

Country: United States

ID: GA346

Automated Segmentation of T2-weighted MRI Brain Scans of Rats Exposed to Organophosphates using a Convolution Neural Network

Valerie Porter, University of California Davis, vporter@ucdavis.edu

---

Category: Computational & Data Science

Abstract Body : Introduction: Voxel-wise image segmentation is one of the most common tasks performed in preclinical brain MRI analysis pipelines [1]. Atlas co-registration protocols are useful; however, they are suboptimal in rodent models of acute organophosphate (OP) intoxication because of large deformations in brain regions over time post-exposure [2,3]. Manual segmentation is time consuming and may be subjective. Therefore, efficient and robust image segmentation tools are needed. The U-net convolutional neural network (CNN) [4] has been utilized for automated segmentation of rodent brain images [5], however previous studies have not employed these methods in the context of acute OP intoxication. We tested the hypothesis that the U-net CNN is capable of providing automated segmentation of rodent brain MRI scans in a longitudinal study of brain pathology in a rat model of acute OP intoxication. Methods: T2-weighted MRI brain scans (n=33, 59 slices/scan, acquired on a Bruker BioSpec 7T scanner, acquisition resolution 125x125x500 μm) of adult Sprague Dawley rats subjected to acute OP intoxication and follow-up treatments were manually segmented by an experienced human observer to delineate 8 brain regions, namely by hemisphere: hippocampus, lateral and medial thalamus, piriform cortex, and entorhinal cortex. Image data consisted of scans of rats from five treatment groups at three time points (3, 7, and 28 days post-exposure). Treatment groups included diisopropylfluorophosphate (DFP), DFP plus midazolam (MDZ), DFP plus allopregnanolone (ALO), DFP plus midazolam and allopregnanolone (DUO), and vehicle controls (VEH). The T2-weighted scans provide a range of both acute and chronic pathologies [6]. The training and test datasets consisted of 28 scans (DZP=5, MDZ=9, ALO=6, DUO=5, VEH=3, all five treatment groups) and 5 scans (DFP=1, MDZ=3, ALLO=1), respectively. The image data (size=280x200x59) were preprocessed by center-cropping the images and labels (size=200x200x59) to capture the entire brain and down sampling the in-plane resolution (128x128x59) to decrease the runtime. The U-net CNN used a learning rate of 0.002 with a batch size of 10 and 100 epochs. The image data was augmented by shifting each slice randomly between (-10,10) pixels in the x and y directions and randomly rotating the image between (-10,10) degrees. The augmentation also included the brightness levels of the image slices were increased or decreased by ± 20% of the original value, and Gaussian noise was added to each image slice. Dice coefficients of volumetric overlap were calculated between U-net CNN-generated labels and manually segmented labels. The results are reported as median (range). Results and Conclusion: The loss function did not change significantly beyond 30 epochs indicating that the network was able to quickly find robust segmentation features despite the heterogeneous presentation of lesions (Figure 1). The model accuracy however improved going from 20 epochs to 100 epochs from 84% to 93% (Figure 1), which suggests that additional epochs in future studies may be beneficial. The Dice coefficients were in the moderate range for most regions, being the highest for the right thalamus, 0.62 (0.39-0.68) (Table 1). Segmentation

accuracy was marginal for the right piriform cortex, 0.27 (0.20-0.28). The training took 15 minutes, while the generation of an individual segmentation took approximately 1 minute. We conclude that the U-net CNN-based segmentation approach was fully automated and efficient; however, its accuracy was in the low to moderate range. Future research will include examining the impact of adding more MRI scans of OP intoxicated rats with varying pathologies to the training data set, MRI bias correction, and skull stripping to improve the accuracy of the segmentation method. Supported by the National Institutes of Health via grants R21AG064599 and U54NS079202.

References: 1. R. Feo, et. al. “Towards an efficient segmentation of small rodents' brains: A short critical review.”Journal of Neuroscience Methods, 2019; 82-89. 2. M. Lyman, et. al. "Neuroinflammation: the role and consequences." Neuroscience Research, vol. 79, 2014; 1-12. 3. W. Chen, X. Zhang, & W. Huang. “Role of neuroinflammation in neurodegenerative diseases,” Molecular Medicine Reports. 2016; 3391-3396. 4. O. Ronneberger, P. Fischer, and T. Brox, “U-net: Convolutional networks for biomedical image segmentation,” in International Conference on Medical image computing and computer-assisted intervention. Springer, 2015; 234–241. 5. L. Hsu, et. al. “Automatic skull stripping of rat and mouse brain MRI data using U-net.” Frontiers in Neuroscience. 2020; 14. 6. B. Hobson, et. al. “Magnetic resonance imaging reveals progressive brain injury in rats acutely intoxicated with diisopropylfluorophosphate.” Toxicological Sciences. 2017; 342-53.

Image/Figure:

https://s3.amazonaws.com/amz.xcdsystem.com/1E8A4501-BB41-A02A-1D3B9882B798BFAA_abstract_File10351/GA346_ImageFigure_0513073543.png

Image/Figure Caption: Figure 1: A) The architecture of the U-net CNN.[4] B) The model accuracy and loss graphs over epochs. C) Images from two different test scans that were segmented manually and with the U-net CNN, where the first row is the anatomical image, second row is the manual segmentation of the anatomical image, and the last row is the U-net segmentation. Blue/Purple are the hippocampus, Yellow/Light Green are the lateral thalami, Dark Green is the medial thalamus, Red/Orange are the entorhinal cortexes, and Teal/Light Blue are the piriform cortexes. Table 1) Dice coefficients for each VOI from each test scan.

Full Name of Abstract's 1st Author : Valerie Alexandria Porter

First Name: Valerie

Last Name: Porter

Email: vporter@ucdavis.edu

Organization: University of California Davis

Country: United States

ID: GA347
Use of Self-Expanding Metal Stent to Treat Acute Esophageal Perforation in a 4 Year-Old Child

Kelly von Beck, Vanderbilt University School of Medicine,
kelly.n.vonbeck@vanderbilt.edu

Category: Instrumentation

Abstract Body : The patient is a 4 year-old male with a history prematurity (31-weeks), developmental delay, chronic lung disease, sleep apnea, gastroparesis, and dysphagia treated with two rounds of esophageal Botox injections of the lower esophageal sphincter (LES). He presented to the ED with acute abdominal pain three hours after an esophagogastroduodenoscopy (EGD) with dilation of the LES. He was ill-appearing on presentation with respiratory distress including audible grunting and diffuse subcutaneous emphysema. He underwent a chest x-ray which revealed pneumomediastinum and an esophagram that confirmed a distal esophageal perforation with contrast extravasation into the left pleural space. He was admitted to the PICU for resuscitation. He became febrile, tachycardic, and hypotensive overnight and was therefore taken to the OR due to concern for mediastinitis and septic shock. Bilateral chest tubes were placed under fluoroscopic guidance to drain inflammatory pleural fluid. An EGD was then performed which showed a large distal esophageal perforation. On-table esophagram revealed a linear 2cm posterolateral perforation along the distal 1/3rd of the esophagus with communication to the mediastinum. All contrast was then suctioned out, and the mediastinum was irrigated using a guidewire and kumpe catheter. The distal end of the perforation was located 2cm above the gastroesophageal (GE) junction, which was used as the landing zone for placement of an esophageal stent. External radiopaque markers were used to delineate the GE junction, as well as the distal and proximal ends of the perforation. A Boston scientific 18mm diameter x 10cm length covered self-expanding metal stent (SEMS) was chosen based on the gathered measurements. A kumpe catheter was advanced through the mouth into the stomach, which was then exchanged for a 0.035-inch Amplatz wire for delivery of the stent. The stent was advanced to 1 cm above the GE junction and slowly deployed, with the proximal end appropriately below the pharynx. Positioning was confirmed endoscopically and on x-ray. A catheter and guidewire were then used to place a distal jejunal feeding tube through the stent for enteral nutrition. On postoperative day (POD) 6, the patient failed extubation due to compression of the trachea by the esophageal stent. He remained intubated until the stent was removed on POD 13 with good healing of the esophagus and no evidence of perforation. The patient required prolonged intubation post-procedure given the small size of the child and the available SEMS options. Although frequently cited as a rare complication of esophageal balloon dilation, the risk of esophageal perforation has been shown to be as high as 12.5-14% in pediatric patients [1, 2]. While the application of esophageal stenting has been well established in adults, investigation on the use of SEMS in children has been limited to studies with small sample sizes. One retrospective case series reports the use of SEMS designed for trachea-bronchial use in the treatment of esophageal atresia, fistula, and corrosive ingestion in patients from 4 years to 16 months old [3]. The authors report the safety and efficacy of this approach as a secondary

treatment for benign esophageal strictures, citing stent migration as the only complication [3]. Similarly, Manfredi et al demonstrate a 100% technical success rate of placement and retrieval of esophageal stents and an 80% closure success rate in dilation-induced perforations in their cohort of pediatric patients [4]. Surgical repair of esophageal perforations is associated with significant perioperative risks. This case demonstrates that SEMS are a safe and effective alternative treatment in children with acute esophageal perforation. This treatment modality warrants further investigation in order to define criteria for placement in the pediatric population and increase experience with the procedure among pediatric surgeons and pediatric interventional radiologists.

References: 1. Kim, I.O., et al., Perforation complicating balloon dilation of esophageal strictures in infants and children. Radiology, 1993. 189(3): p. 741-4. 2. Yeming, W., et al., Balloon catheter dilatation in children with congenital and acquired esophageal anomalies. Journal of Pediatric Surgery, 2002. 37(3): p. 398-402. 3. Best, C., et al., Esophageal stenting in children: indications, application, effectiveness, and complications. Gastrointest Endosc, 2009. 70(6): p. 1248-53. 4. Manfredi, M.A., et al., Externally removable stents in the treatment of benign recalcitrant strictures and esophageal perforations in pediatric patients with esophageal atresia. Gastrointest Endosc, 2014. 80(2): p. 246-52.

Image/Figure:

https://s3.amazonaws.com/amz.xcdsystem.com/1E8A4501-BB41-A02A-1D3B9882B798BFAA_abstract_File10351/GA347_ImageFigure_0513080415.png

Image/Figure Caption: Fig. 1: Operative course of Esophageal Stenting. Esophageal perforation demonstrated by pneumomediastinum, subcutaneous emphysema (A) and extravasation of contrast into the left hemithorax (B) and mediastinum (C). Operative EGD showed a 2 cm posterolateral perforation in the distal esophagus (D) confluent with the mediastinum (E). Distal and proximal ends of the perforation were marked externally with radiopaque markers (F), and the stent was placed with the distal end lying between the perforation and GE junction (G). Chest x-ray shows placement of the stent (H) and resolution of the perforation after stent removal 13 days later (I).

First Name: Kelly

Last Name: von Beck

Email: kelly.n.vonbeck@vanderbilt.edu

Organization: Vanderbilt University School of Medicine

Country: United States

ID: GA348

Deuterated glucose-based assessment of the Warburg effect allows non-invasive imaging of tumor burden and treatment response in mutant IDH gliomas in vivo

Celine Taglang, University of California San Francisco, celine.taglang@ucsf.edu

---

Category: Oncology

Abstract Body : Introduction The Warburg effect, which is characterized by elevated glucose uptake and flux to lactate, is a metabolic hallmark of cancer1. Recent studies have identified deuterium (2H)-magnetic resonance spectroscopy (MRS) using [6,6'-2H]-glucose as a novel method of imaging the Warburg effect in high-grade primary glioblastomas (GBMs)2. However, its utility for imaging low-grade gliomas and for assessing treatment response has not been tested. The goal of this study was to determine whether [6,6'-2H]-glucose can be used for imaging tumor burden and treatment response in mutant isocitrate dehydrogenase (IDHmut) low-grade gliomas in vivo. Methods Orthotopic tumor implantation and treatment: We examined mice bearing orthotopic tumors of the BT257 model, which was derived from a patient carrying an IDHmut low-grade astrocytoma3. Eight 6-to-8-week-old female SCID mice were intracranially injected with ~3×105 BT257 cells. Once tumors reached a volume of ~20-25mm3 (day zero, D0), mice were randomized into treatment (100 mg/kg niraparib oral daily) or control (saline) groups. Anatomic MR imaging: MR studies were performed using a 14.1T vertical system (Agilent) equipped with a single-channel volume 1H coil. A spin echo multi-slice sequence was used for axial T2-weighted MRI (TE=20ms, TR=1200ms, field of view=30×30 mm2, matrix=256×256, slice thickness=1mm, number of averages=4). Tumor volume was evaluated as the sum of manually contoured tumor areas in each slice multiplied by slice thickness. 2H-MRS studies: Animals were positioned prone under a 16mm 2H surface coil (DOTY Scientific). Following injection of a bolus of [6,6'-2H]-glucose (1g/kg) via a tail-vein catheter over 25-35s, non-localized 2H-MR spectra were acquired over 66 minutes with a pulse-acquire sequence (TR=500ms, averages=500, complex points=512, flip angle=64, spectral width=2kHz, temporal resolution = 4min 10s). 2H spectra were referenced to semi-heavy water (HDO; 4.75 ppm, MestReNova). The area under the curve (AUC) for [3,3'-2H]-lactate was normalized to [6,6'-2H]-glucose and HDO for the sum of all spectra. For spatial localization, a 2D chemical shift imaging (CSI) sequence with TE/TR=1.35/250ms, FOV=30x30mm2, 7x7, 128 points, 2.5kHz spectral width, NA=20 was used and data analyzed using in-house Matlab codes. Statistical analysis: All results are expressed as mean±standard deviation. Statistical significance was assessed using an unpaired two-tailed Student's t-test with p Results 2H-MRS monitors tumor burden in IDHmut gliomas in vivo: In line with higher glucose uptake and lactate production in BT257 neurospheres relative to normal human astrocytes, [6,6'-2H]-glucose metabolism to lactate was observed in BT257 tumor-bearing mice. In contrast, tumor-free mice showed production of glutamate/glutamine, but not lactate. Importantly, 2D CSI confirmed spatial localization of lactate to the tumor vs. contralateral normal brain in mice bearing orthotopic BT257 tumors. 2H-MRS monitors early response to therapy in IDHmut gliomas in vivo: Poly-(adenosine 5′-diphosphate-ribose) polymerase inhibitors (PARPi) inhibit IDHmut glioma growth and are in clinical trials for IDHmut glioma patients4,5. Treatment of mice

bearing orthotopic BT257 tumors with niraparib induced tumor shrinkage as assessed by T2-weighted MRI, an effect that was apparent by D18 and resulted in significantly enhanced survival (Fig.4C). Importantly, [6,6'-2H]-glucose flux to lactate was reduced in BT257 tumor-bearing mice treated with niraparib relative to controls. Furthermore, this reduction was observed at early time-points (D4-5 and D8-9) when no difference in tumor volume could be detected by MRI pointing to the potential ability of [6,6'-2H]-glucose to assess pseudoprogression. Conclusions We show that IDHmut gliomas display the Warburg effect, which can be leveraged for non-invasive, non-radioactive 2H-MRS-based imaging of tumor burden in vivo. Importantly, [6,6'-2H]-glucose flux to lactate can be used for non-invasive visualization of IDHmut glioma response to therapy at early time-points when volumetric alterations cannot be detected by MRI, suggesting that [6,6'-2H]-glucose has the potential to assess pseudoprogression, which is a major challenge in glioma imaging6.

References: 1. Vander Heiden M et al. Understanding the Warburg Effect: The Metabolic Requirements of Cell Proliferation. Science, 324: 1029, 2009. 2. De Feyter H et al. Deuterium metabolic imaging (DMI) for MRI-based 3D mapping of metabolism in vivo. Sci. Adv. 2018; 4: eaat7314 22 August 2018. 3. Mazor T et al. Clonal expansion and epigenetic reprogramming following deletion or amplification of mutant IDH1. PNAS, 114(40): 10743–10748, 2017. 4. Sulkowski P et al. 2-Hydroxyglutarate produced by neomorphic IDH mutations suppresses homologous recombination and induces PARP inhibitor sensitivity. Sci Transl Med, 9(375):eaal2463, 2017. 5. Lu Y et al. Chemosensitivity of IDH1-Mutated Gliomas Due to an Impairment in PARP1-Mediated DNA Repair. Cancer Res, 77(7):1709-1718, 2017. 6. Villanueva-Meyer J et al. Current Clinical Brain Tumor Imaging. Neurosurgery 81:397-415, 2017.

Image/Figure: https://s3.amazonaws.com/amz.xcdsystem.com/1E8A4501-BB41-A02A-1D3B9882B798BFAA_abstract_File10351/GA348_ImageFigure_0513080420.pdf

Image/Figure Caption: A) After administration of 2H-labeled substrates (for example [6,6'-2H]glucose at 1g/kg over 30 seconds) and acquisition using Varian 14T (600MHz) NMR System and 16mm 2H surface coil, spectra are obtained with semi-heavy water (HDO), glucose, glutamate/glutamine (Glx) and lactate B) Representative metabolic heatmaps from 2D CSI studies in mice bearing orthotopic BT257 tumor xenografts following injection of a bolus of [6,6'-2H]-glucose. Left panel shows a representative axial T2-weighted MR image while the right panel shows a metabolic heatmap of the SNR of lactate produced from [6,6'-2H]-glucose. C) Representative T2-weighted MR images from mice bearing orthotopic BT257 tumor xenografts treated with niraparib (top panel) or vehicle-control (bottom panel) at day 0, day 5 and day 9. D) Quantification of lactate normalized to glucose and HDO following injection of a bolus of [6,6'-2H]-glucose in mice bearing orthotopic BT257 tumor xenografts treated with niraparib or vehicle-control at D0, D4-5 or D8-9.

First Name: Celine

Last Name: Taglang

Email: celine.taglang@ucsf.edu

Organization: University of California San Francisco

Country: United States

ID: GA349
Validation of nanoparticle delivery in primary and metastatic tumors using bioorthogonal chemistry

Neil Robertson, Michigan State University, robe1104@msu.edu

Category: New Chemistry, Materials & Probes

Abstract Body : Objectives: Validation of nanoparticle delivery to the tumor of interest is critical for the successful treatment of cancer. Nanoparticle-based technologies, including theranostic nanomedicine, are fast developing areas of biomedical research offering unprecedented potential for cancer treatment. The ability to image and follow nanoparticle accumulation in vivo, as well as observe clearance time, greatly enhances our ability to treat these tumors. An in vivo multimodal optical/MRI imaging probe was designed with a bioorthogonal chemistry activation and validation technique in mind. The nanoparticle utilizes the highly specific nature of the "click to release" reaction to label the particles taken up by the tumors with a secondary fluorophore, highlighting the location of the particle constructs within the body, validating delivery and activating therapeutic payloads. Bioorthogonal chemistry has previously been explored for potent pretargeting [1, 2] and toxicity studies in vivo [2-4], as well as clinical studies [5]. In this study we investigated in vivo function of a nanoparticle construct in combination with bioorthogonal chemistry to noninvasively image nanoparticle delivery to both primary and metastatic tumors. We hypothesized that uptake of the nanoparticle conjugated to trans-cyclooctene (TCO) would occur in the tumors after systemic injection, followed by accumulation of the non-toxic secondary labeling molecule tetrazine. This accumulation would only be possible due to reaction between trans-cyclooctene (TCO) and tetrazine and therefore, should occur only in the tissue with significant nanoparticle uptake. Methods: A dual modality (magnetic resonance and near infrared optical imaging) nanoparticle (MNP) construct labeled with Cy7 and a bioorthogonal TCO moiety (MNP-Cy7-TCO), as well as a fluorophore labeled small molecule probe, tetrazine labeled with Cy5.5, (Tet-Cy5.5) were synthesized. The construct consisted of a dextran-coated superparamagnetic iron-oxide nanoparticle (MNP), modified with amine termini and conjugated with the near-infrared fluorescent dye, Cy7, and the bioorthogonal trans-cyclooctene moiety. The small molecule probe synthesized was a dual amine tetrazine, which was conjugated with the near-infrared fluorescent dye, Cy5.5. The synthetic strategy employed for the particle was a co-precipitation technique as previously reported [6, 7]. For the small molecule tetrazine, a protected tetrazine intermediate was reacted with hydrazine to produce a dual amine probe easily conjugated. The synthesized construct, MNP-Cy7-TCO, was tested in a MDA-MB-231 mouse model of breast cancer. Animals with primary tumors and lymph node metastases were intravenously injected with the nanoparticles followed by intravenous injection of tetrazine 24 hrs later. Controls included tumor bearing mice injected with a non-clickable MNP construct, MNP-Cy7, followed by an injection with tetrazine 24 hrs later and mice who only received the tetrazine injection. Noninvasive imaging was performed with an IVIS Spectrum and verification of the nanoparticle presence was done with histology. Results: Characterization of the particle construct and the probe showed a particle size of roughly 30 nm with a zeta potential of +20-22 mV. The particles were also found to have approximately

7-10 Cy7 molecules per particle. The tetrazine product was characterized with FT- IR spectroscopy, which showed the presence of amine functional groups only post reaction and purification. In vivo studies demonstrated that the same nanoparticle construct was capable of imaging both primary and metastatic breast tumors in mice (Fig. 1). Fluorescence microscopy showed excellent co-localization of Cy7 and Cy5.5 signals, corroborating our imaging data (Fig. 2). Conclusions: The multimodal aspect of the nanoparticle construct is valuable for noninvasive imaging, while the biologically inert bioorthogonal reaction provides both an in vivo "tagging event" for validation and an operator-controlled approach to construct activation in future studies. Overall, the nontoxic nature of the explored system further validates future use of the chemistry coupled with therapeutic payloads.

References: 1. Haun, J.B., et al., Bioorthogonal chemistry amplifies nanoparticle binding and enhances the sensitivity of cell detection. Nat Nanotechnol, 2010. 5(9): p. 660-5. 2. Rossin, R., et al., Diels-Alder reaction for tumor pretargeting: in vivo chemistry can boost tumor radiation dose compared with directly labeled antibody. J Nucl Med, 2013. 54(11): p. 1989-95. 3. Devaraj, N.K. and R. Weissleder, Biomedical applications of tetrazine cycloadditions. Acc Chem Res, 2011. 44(9): p. 816-27. 4. Rossin, R., et al., Trans-cyclooctene tag with improved properties for tumor pretargeting with the diels-alder reaction. Mol Pharm, 2014. 11(9): p. 3090-6. 5. Peplow, M., Click chemistry targets antibody-drug conjugates for the clinic. Nat Biotechnol, 2019. 37(8): p. 835-837. 6. Medarova, Z., et al., In vivo imaging of siRNA delivery and silencing in tumors. Nat Med, 2007. 13(3): p. 372-7. 7. Yigit, M.V., et al., Context-dependent differences in miR-10b breast oncogenesis can be targeted for the prevention and arrest of lymph node metastasis. Oncogene, 2013. 32(12): p. 1530-8.

Image/Figure: https://s3.amazonaws.com/amz.xcdsystem.com/1E8A4501-BB41-A02A-1D3B9882B798BFAA_abstract_File10351/GA349_ImageFigure_0513080842.pdf

Image/Figure Caption: Figure 1) Fluorescence imaging after systemic injection of both the nanoparticle construct (MNP-Cy7-TCO) and small molecule probe trigger (Tet-Cy5.5). Upper panel, primary tumors: After validation of tumor formation with bioluminescent imaging (BLI), mice with MDA-MB-231 breast cancer were systemically injected with MNP-Cy7-TCO, followed by Tet-Cy5.5 24 hrs later. Accumulation of the particle construct and the small molecule trigger were apparent 24 hrs post injection, respectively. Lower panel, metastatic tumors: Validation of metastases was again performed with BLI, followed by systemic injection of both the MNP-Cy7-TCO and Tet-Cy5.5 probes, again 24 hrs in between. Accumulation became apparent 24 hrs post injection, after some clearance from the body. Figure 2) Histology slides representing nanoparticle uptake within the primary tumors imaged with microscopy. Heavy co-localization of the Cy7 and Cy5.5 fluorophores supports the function of bioorthogonal chemistry in vivo and in combination with nanoparticle constructs. Upper left to lower right: Intrinsic fluorescence of the MNP-Cy7 showing particle distribution within the tumor cells, fluorophore labeled Tet-Cy5.5 distribution within the tumor cells, DAPI staining showing the nuclei of the tumor cells, Overlay of the Cy7 and Cy5.5 channels showing co-localization of the dye and suggesting clicking by bioorthogonal chemistry, All channels overlaid.

Full Name of Abstract's 1st Author : Neil M Robertson

First Name: Neil

Last Name: Robertson

Email: robe1104@msu.edu

Organization: Michigan State University

Country: United States

ID: GA350
Fibrin Targeted Phase CHange Nanodroplets for Sonoreperfusion Therapy

Evan Unger, MVT Pharma LLC, e.unger@mvtpharma.com

Category: Cardiovascular & Pulmonary

Abstract Body : Cardiovascular disease is the leading cause of death and disability worldwide. Efforts to remove occlusive thrombi via thromboembolectomy or by mechanical disruption and/or biochemical dissolution have demonstrated efficacy; however, these therapeutic options are time consuming and are accompanied by substantial risk of hemorrhagic complications. Enhance safety and efficacy of thrombus removal have high potential clinical impact. Sonothrombolysis (SL) refers to the use of ultrasound (US) to disrupt thrombi. However, there is a trade-off between time/efficiency and damaging healthy tissue. Ultrasound mediated microbubble (MB) cavitation, which creates shear stress and induces biological response such as nitrite oxide release, can accelerate the disruption of the thrombi while keeping delivered energy low which can decrease the risk of damaging healthy tissue. Moreover, nanodroplets (NDs) can be better for SL than MBs due to their capacity to permeate better to the thrombi. In this study, we developed a safe and stable lipid-based MB and ND formulation. The formulation offers a targeted ND and MB with the capability to recognize fibrin through a fibrin binding peptide (FBP) ligand conjugated to the lipid surface of the MBs. We show in vitro that the targeted MB and ND bind to fibrin clots. We show in a rat hindlimb model of microvascular occlusion (MVO) that ultrasound therapy with NDs are able to disrupt the clots upon US mediated cavitation and relieve MVO (Fig. 1). These results are proof of concepts for the usage of ND to support further preclinical development and IND-enabling studies of these ND for MVO therapeutic indication.

References: 1. Nishioka, T., et al., Dissolution of thrombotic arterial occlusion by high intensity, low frequency ultrasound and dodecafluoropentane emulsion: an in vitro and in vivo study. J Am Coll Cardiol, 1997. 30(2): p. 561-8. 2. Chen, X., et al., New insights into mechanisms of sonothrombolysis using ultra-high-speed imaging. Ultrasound Med Biol, 2014. 40(1): p. 258-62. 3. Acconcia, C., Leung, BYC, Hynynen, K and Goertz, DE, Interactions between ultrasound stimulated microbubbles and fibrin clots. Applied Physics Letters, 2013. 4. Leeman, J.E., et al., Effect of acoustic conditions on microbubble-mediated microvascular sonothrombolysis. Ultrasound Med Biol, 2012. 38(9): p. 1589-98. 5. Villanueva, F.S., et al., Detection of coronary artery stenosis with power Doppler imaging. Circulation, 2001. 103(21): p. 2624-30. 6. Wei, K., et al., Quantification of myocardial blood flow with ultrasound-induced destruction of microbubbles administered as a constant venous infusion. Circulation, 1998. 97(5): p. 473-83. 7. Pacella, J.J., et al., Treatment of microvascular micro-embolization using microbubbles and long-tone-burst ultrasound: an in vivo study. Ultrasound Med Biol, 2015. 41(2): p. 456-64.

Image/Figure:

https://s3.amazonaws.com/amz.xcdsystem.com/1E8A4501-BB41-A02A-1D3B9882B798BFAA_abstract_File10351/GA350_ImageFigure_0513081230.jpg

Image/Figure Caption: Figure 1: Treatment of microcirculation obstruction (MVO) with US targeted MB cavitation using phase change contrast agent. During MVO stage, the blood flow to the hindlimb was substantially reduced as indicated by contrast specific ultrasound imaging. Post ultrasound treatment with infusion of NDs, the blood flow to the hindlimb was restored.

Full Name of Abstract's 1st Author : Evan C Unger

First Name: Evan

Last Name: Unger

Email: e.unger@mvtpharma.com

Organization: MVT Pharma LLC

Country: United States

ID: GA351

Quantifying S1PR1 Expression Changes of Brown Fat Adipose in Hindlimb Unloading Mice by Dynamic 18F-10a PET/CT

Min Yang, The Fifth Affiliation Hospital, Sun Yat-sen University, yangminyycm@sina.com

---

Category: Systemic Diseases (Kidney, Liver and Pancreas)

Abstract Body : Introduction: Sphingosine-1-phosphate (S1P) is a bioactive lipid mediator involved in many biological actions, including vascular homeostasis and immunosurveillance. S1PR1 plays the most important role in immunosurveillance. We speculated that S1P/S1PR1 axis would sense the homeostasis alternations under microgravity during the spaceflight. In this study, the molecular imaging quantification through PET/CT was used to explore the S1PR1 expression changes in hindlimb unloading (HU) model of simulated weightlessness. Methods: Eleven healthy Balb/c mice aged 8 weeks were randomly divided into the control group (CTR, n = 5) and the HU group (HU, n = 6). The preparation of the simulated weightless model was mainly based on the classic tail-suspension method proposed and improved by Morey-Holton and Chen Jie et al.1 After 4 weeks of modeling, dynamic PET/CT imaging was performed for 30 min including 25 frames (10×3s; 3×10s; 4×60s; 6×150s; 2 ×300s). The labeling and synthesis of radiopharmaceuticals (18F-10a) were based on previous published literature.2 The dynamic raw data was analyzed by Carimas software. With the time activity curve (TAC) of left ventricular as the input function, the original TAC of vital organs (including brain, lung, liver, spleen, renal, muscle, bone, brown adipose tissue) was fitted by Logan REF modeling to obtain corresponding distribution volume rate (DVR) and binding potential (BP).3 Area under the curve (AUC) of TACs, DVR and BP were compared between the CTR and HU group, and p Results: For the above indicators, there was no significant differences for most organs (including brain, lung, liver, spleen, renal, muscle, bone). However, we found that the AUC of the BAT TACs (2563.97 ± 594.34 vs 1714.76 ± 536.50, p) in the HU group was significantly higher than that of the CTR group. Simultaneously, the DVR (2.67 ± 0.30 vs 1.56± 0.32, p ± 0.30 vs 0.56 ± 0.32, p were significantly higher than that of the CTR group (Figure 1). Conclusions: After mid-term simulated weightlessness (hindlimb unloading 4 weeks), the specific association of S1PR1 in the BAT was significantly increased, indicating that hindlimb unloading may induced increased S1PR1 expression in BAT. Although the molecular mechanism behind this phenomenon remains to be explored, S1P/S1PR1 axis warrants further investigation regarding BAT metabolism under microgravity.

References: 1 Morey-Holton, E. R. & Globus, R. K. Hindlimb unloading rodent model: technical aspects. Journal of applied physiology (Bethesda, Md. : 1985) 92, 1367-1377, doi:10.1152/japplphysiol.00969.2001 (2002). 2 Luo, Z. et al. Syntheses and in vitro biological evaluation of S1PR1 ligands and PET studies of four F-18 labeled radiotracers in the brain of nonhuman primates. Organic & biomolecular chemistry 16, 9171-9184, doi:10.1039/c8ob02609b (2018). 3 Logan, J. et al. Distribution volume ratios without blood sampling from graphical analysis of PET data. Journal of cerebral blood flow and metabolism : official journal of the

International Society of Cerebral Blood Flow and Metabolism 16, 834-840, doi:10.1097/00004647-199609000-00008 (1996).

Image/Figure:

https://s3.amazonaws.com/amz.xcdsystem.com/1E8A4501-BB41-A02A-1D3B9882B798BFAA_abstract_File10351/GA351_ImageFigure_0513081345.jpg

Image/Figure Caption: Figure 1. Hindlimb unloading induced increased S1PR1 expression in BAT. A: Radiosynthesis of 18F-10a. B-C: Representative 18F-10a PET/CT imaging of control mice (B) and HU mice (C), the circle is where the classical brown adipose tissue is. D-E: TACs and AUC of BAT in both groups. F-G: PET quantitative analysis results of BAT by Logan REF modeling after 4 weeks of hindlimb unloading. Abbreviations: DVR: distribution volume rate BP: binding potential AUC: Area under curve

Full Name of Abstract's 1st Author : Min Yang

First Name: Min

Last Name: Yang

Email: yangminyycm@sina.com

Organization: The Fifth Affiliation Hospital, Sun Yat-sen University

Country: China

ID: GA352

Multimodality imaging of T cell infiltration and granzyme B activity in vivo predicts tumor response to checkpoint blockade and chimeric antigen receptor T-cell therapy

Jinghang Xie, Stanford University, jinghang@stanford.edu

Category: Oncology

Abstract Body : Immunotherapy is revolutionizing the management of many cancers. The lack of specific, non-invasive diagnostics monitoring tumor early response, however, remains an unmet clinical need in advancing precision immunotherapy. Granzyme B (gzm B) is a serine proteinase uniquely executing the cytotoxic T cell mediated cancer cell killing and tumor eradication and represents an ideal target for molecular imaging of patient early response to immunotherapy. Based on our highly translatable target-enabled in-situ ligand aggregation (TESLA) probe template, we designed and synthesized a novel gzm B activatable self-assembly small molecule probe G-SNAT for real-time imaging of gzm B activity in vivo. A series of studies in vitro confirmed the gzm B-specific probe activation. Cyanine 5 (Cy5) fluorophore conjugated probe (G-SNAT-Cy5) was highly retained in both activated cytotoxic T cells and CAR (chimeric antigen receptor) T-cell engaged cancer cells in correlation to gzm B expression and activity. In lymphoid tumor (A20) implanted BALB/c Rag2−/−γc−/− mice treated with CD19-targeted firefly luciferase expressing CAR T cells, bioluminescence imaging (D-luciferin) tracked the persistence of injected CAR T cells and G-SNAT-Cy5 successfully reported the cytotoxic response of tumors. To assess the clinical value of G-SNAT for imaging checkpoint blockade therapy and study associated immune cell trafficking, we constructed a colorectal cancer model with transgenic BALB/c mice expressing firefly luciferase in splenic cells and treated with a combined regimen of anti-PD-1 and anti-CTLA-4. Longitudinal bioluminescence imaging with D-luciferin and a gzm B specific luciferin substrate (GBLI2) developed by our group revealed the dynamics of immune cell infiltration and triggered cytotoxicity in responders. Further G-SNAT-Cy5 fluorescence imaging predicted the therapeutic outcomes before the difference of tumor volume was evident. These functional imaging studies also revealed tumors in nontreated and treated nonresponders an “immune desert” lacking immune cells and cytotoxic responses. These results support further development of G-SNAT for PET imaging of immune response to checkpoint blockade and CAR T-cell therapy in patients and highlight the role of multimodality imaging in understanding the fundamentals of immunotherapy.

References: 1. Xie J., Rice M. A., Chen Z., Cheng Y., Hsu E-C., Chen M., Song G., Cui L., Zhou K., Castillo J. B., Zhang A. C., Shen B., Chin F. T., Kunder C. A., Brooks J. D., Stoyanova T., Rao J. (2021) In vivo imaging of methionine aminopeptidase II for prostate cancer risk stratification. Cancer Research 81(9): 2510-2521 2. Chen M., Chen Z., Castillo J. B., Cui L., Zhou K., Shen B., Xie J., Chin F. T.., Rao J. (2021) [18F]-C-SNAT4: an improved caspase-3-sensitive nanoaggregation PET tracer for imaging of tumor responses to chemo- and immunotherapies. European Journal of Nuclear Medicine and Molecular Imaging 1-14 3. Chen Z., Chen M., Cheng Y., Kowada T., Xie J., Zheng X., Rao J. (2020) Exploring the condensation

reaction between aromatic nitriles and amino thiols to optimize in situ nanoparticle formation for the imaging of proteases and glycosidases in cells. Angewandte Chemie (International ed. in English) 132(8): 3298-3305 4. Palner, M., Shen B., Jeon J., Lin J., Chin F.T., and Rao J. (2015) Preclinical Kinetic Analysis of the Caspase-3 7 PET Tracer 18F-C-SNAT Quantifying the Changes in Blood Flow and Tumor Retention After Chemotherapy. The Journal of Nuclear Medicine 56: 1415-1421 5. Ye, D., Shuhendler A.J., Cui L., Tong L., Tee S.S., Tikhomirov G., Felsher D.W., and Rao J. (2014) Bioorthogonal cyclization-mediated in situ self-assembly of small-molecule probes for imaging caspase activity in vivo. Nature Chemistry 6(6): 519-26. 6. Shen, B., Jeon J., Palner M., Ye D., Shuhendler A.J., Chin F.T., and Rao J. (2013) Positron emission tomography imaging of drug-induced tumor apoptosis with a caspase-triggered nanoaggregation probe. Angewandte Chemie (International ed. in English) 52(40): 10511-4.

First Name: Jinghang

Last Name: Xie

Email: jinghang@stanford.edu

Organization: Stanford University

Country: United States

ID: GA353

Integration of Radiomic features from intra-tumoral and visceral fat regions on pre-treatment CT can predict response to immunotherapy in metastatic non-small cell lung cancer

Kaustav BERA, Case Western Reserve University, kxb413@case.edu

---

Category: Oncology

Abstract Body : Introduction – Artificial Intelligence (AI) enabled quantitative radiomic analysis1 which involves high-throughput extraction of sub-visual features from radiographic images has shown great potential in oncology. In non-small cell lung cancer (NSCLC), these radiomic features on CT scans have shown value in diagnosis, prognosis as well as predicting response to different therapies including chemotherapy, radiation as well as most recently immunotherapy2. These radiomic features have so far been derived from inside and immediately adjacent to the tumor. Meanwhile, recent studies have shown that estimation of fat from CT scans can prognosticate outcome in multiple different cancers3, including treatment prediction in NSCLC4. In this novel study, we have build an integrated model which combines traditional radiomic features from inside the tumor as well as radiomic features from different fat regions on multi-slice CT scans from pre-treatment PET/CT images in order to predict response to immune-checkpoint inhibition therapy ICI (nivolumab) in metastatic NSCLC. Methods- A retrospective database review at a single hospital between 2015-2020 after fulfilling inclusion criteria of availability of pre-treatment PET/CT as well as complete response information led to N=38 patients with Stage IV NSCLC treated with nivolumab. ICI response was defined as per RECIST 1.1 into responders(stable disease (SD), partial response (PR), complete response (CR)), and non-responders and non-responders (progressive disease (PD)). A total of 55 nodules were annotated on these scans by an expert radiologist. In addition to the tumor region, the regions associated with fat regions including total body fat, subcutaneous fat, visceral fat, intramuscular fat, and muscle volume region were also delineated using a semi-quantiative approach using in-house software along with radiologist input. From all of these annotated regions, radiomic textural features were extracted. These features included features from Gabor, Laws, Haralick, and Collage feature families2. The top performing features were then selected within 3-fold cross-validation settings with an embedded classifier for each fold. The mRMR feature selection algorithm5 was used in combination with the Random Forest classifier. Model performance was estimated using AUC, sensitivity, specificity and accuracy of predicting response Results- The three top features during the feature selection method included one from the intratumoral from Laws textural family and two from the visceral fat region from Gabor textural feature family. These texture features represent the degree of heterogeneity among the tumors with the feature values being higher in non-responders showing higher degree of heterogeneity as compared to responders. AUC of 0.72 +/- 0.06 was achieved with the integrated tumor+fat radiomics model with the accuracy of 0.72 +/- 0.05 and sensitivities and specificity of 0.72 +/- 0.14 and 0.71 +/- 0.14, respectively in predicting response. Using only the intra-tumoral radiomics model , the AUC of the model was 0.62 +/- 0.07 with an accuracy of 0.64 +/- 0.05. The addition of Radiomics features from the fat regions thus improved the overall performance of the model.

Conclusion- Radiomics analysis of semi-automatically derived visceral fat regions from multi-slice CT images of pre-treatment PET/CT in NSCLC patients treated with ICI has been shown preliminarily to accurately predict response to these agents. When integrated with traditional radiomic analysis, this can provide a robust method for response prediction. This proof-of-concept study will be further validated in larger multi-site data sets and finally deployed in a prospective clinical trial before being ready to be used clinically.

Image/Figure:

https://s3.amazonaws.com/amz.xcdsystem.com/1E8A4501-BB41-A02A-1D3B9882B798BFAA_abstract_File10351/GA353_ImageFigure_0513082816.png

Image/Figure Caption: Fig 1 –Representative slice from a multi-slice CT of PET/CT and corresponding quantitative feature maps for non-responders (top panel)and responders bottom panel) to ICI therapy A) Radiomic Laws feature maps from within the tumor of non-responders (top) and responders (bottom) to ICI therapy. B) Gabor textural Feature maps from semi-automatically delineated visceral fat on non-contrast CT scans of non-responders (top) and responders (bottom) to ICI therapy. Both intratumoral Laws and Visceral fat Gabor features show more heterogeneity in non-responders as compared to responders.

First Name: Kaustav

Last Name: BERA

Email: kxb413@case.edu

Organization: Case Western Reserve University

Country: United States

ID: GA354
Viral Encoding of Acoustic Reporter Genes for in situ Imaging of Mammalian Gene Expression

Shirin Shivaei, Caltech, sshivaei@caltech.edu

Category: Bioengineering, Synthetic Biology and Basic Biology

Abstract Body : While many cellular phenomena in mammalian organisms are studied in cell culture, these in vitro conditions often fail to reconstruct the complexity that cells experience in their native environment. However, studying mammalian cellular processes in a live intact organism requires noninvasive imaging tools that can penetrate deep inside the body. Commonly used light-based imaging techniques, while powerful in vitro, suffer from poor penetration into intact tissue. In contrast, ultrasound is a widely used biomedical technology that enables imaging of cells deep inside the body with high spatiotemporal resolution. Recent work has established gas vesicles (GVs), microbially derived gas-filled protein nanostructures, as genetically encodable acoustic reporter genes1, 2. However, the use of these proteins in mammalian cells has been limited by the need for tedious clonal expansions of sorted cell lines. To facilitate the use of acoustic reporter genes in a broader range of biological contexts such as primary cells and endogenous tissues, there is a need for an efficient, accessible, and a versatile platform to deliver these genes to cells both in vitro and in vivo. Here, we developed a modular viral delivery platform that efficiently integrates acoustic reporter genes into mammalian cells and tissues. This platform is based on viral vector architectures that successfully co-express more than 10 genes to produce strong ultrasound contrast. To demonstrate the modularity of this system, we expressed GVs with different promoters across several cell types, including neuronal and immune cells. We demonstrate the in vivo application of this technology by injecting our engineered viral vectors deep inside the brain and imaging the nonlinear acoustic contrast from in situ transduced cells transracially in live animals. Our viral GV delivery platform serves as a critical resource to greatly expand the in vivo imaging applications of acoustic reporter genes.

References: 1. R. W. Bourdeau, et al., Acoustic reporter genes for noninvasive imaging of microorganisms in mammalian hosts. Nature (2018). 2. Farhadi, A., et al., Ultrasound imaging of gene expression in mammalian cells. Science (2019).

First Name: Shirin

Last Name: Shivaei

Email: sshivaei@caltech.edu

Organization: Caltech

Country: United States

ID: GA356
Cyclooxygenase-2-induced tumor extracellular matrix stiffness

Mc Millan Ching, The Johns Hopkins University School of Medicine, mching5@jh.edu

---

Category: Oncology

Abstract Body : Cancer of the breast, with an estimated 279,100 new breast cancer cases for both men and women, is the most diagnosed cancer for the year 2020 in the United States. Despite advances in standard chemo and radiation therapies for breast cancer, patient morbidity and mortality from metastasis remains the most challenging to address. Current treatment paradigms are not yielding effective control or elimination of this lethal aspect of cancer. Critical to the understanding of metastasis are pathways that supply mechanical cues to cancer cells to migrate. Cancer cells invade and migrate through a complex network of collagen fibers and other extracellular matrix (ECM) components such as fibronectin, laminin and hyaluronan on their metastatic journey. In previous studies cyclooxygenase-2 (COX-2) downregulation resulted in a significant decrease of collagen 1 (Col1 fibers), numbers of cancer associated fibroblasts (CAFs), and metastasis, whereas COX-2 overexpression resulted in a significant increase of Col1 fibers, CAFs, and metastasis [1]. COX-2 catalyzes the production of prostaglandin E2 (PGE2) as a cellular response to inflammation via prostanoid receptors. COX-2 is overexpressed in 40% of human breast cancers and has a pleiotropic and multifaceted role in carcinogenesis. Upregulation of COX-2/PGE2 is associated with poor prognosis in many cancers, including breast cancer. Our purpose in this study was to determine if COX-2 driven changes in the ECM, including changes in Col1 fibers and their patterns, altered ECM stiffness. Altered ECM stiffness can provide mechanical cues to cancer cells through mechanotransduction pathways to modify migration and invasion. Establishment of pre-clinical triple negative SUM-149 human breast cancer cells that stably overexpress COX-2 (SUM-149-COX-2) or with an empty vector (SUM-149-EV) was achieved through cloning and construction of a lentivirus vector expressing the COX-2 gene. These cells were inoculated in the mammary fat pad of severe combined immunodeficient (SCID) mice. Nine weeks post-inoculation, excised xenograft tumors were measured using iNano nanoindenter (Nanomechanics Inc.) to measure tissue elastic modulus (i.e. stiffness). In parallel we evaluated molecular changes in ECM proteases such as MMP1, UPA and UPAR that actively play a dynamic role in the formation and degradation of ECM using western blot analysis. Indentation results were processed into resulting photomaps and heatmaps of indented regions and tissue stiffness, respectively (Fig. 1A). Representative photomap and heatmap of tissue stiffness measured in a SUM-149COX-2 tumor are shown in Figure 1A. Values for multiple indentation points measured per individual tumor and data summarized from elastic modulus-probed tumor tissues of SUM149EV Control (n=8) vs. SUM-149-COX-2 (n=9) are displayed in Figure 1B. Resulting indentation data identified, for the first time, a trend of reduction in tumor stiffness with COX-2 overexpression. COX-2 overexpression also altered the protein expressions of UPAR and MMP1 (Fig. 1C), which may be associated with the alterations of tumor tissue stiffness. These insights expand our understanding of the molecular interplay between inflammation and ECM remodeling during tumor development that

may lead to development of imaging probes and therapeutics to target mechanoresponsive proteins.

References: Krishnamachary B, Stasinopoulos I, Kakkad S, Penet MF, Jacob D, Wildes F, Mironchik Y, Pathak AP, Solaiyappan M, Bhujwalla ZM. Breast cancer cell cyclooxygenase-2 expression alters extracellular matrix structure and function and numbers of cancer associated fibroblasts. Oncotarget. 2017;8(11):17981-94.

Image/Figure:

https://s3.amazonaws.com/amz.xcdsystem.com/1E8A4501-BB41-A02A-1D3B9882B798BFAA_abstract_File10351/GA356_ImageFigure_0513084313.jpg

Image/Figure Caption: Figure 1: A) Representative photomap (left) and heatmap (right) of microindentation measurements of a SUM-149-COX-2 tumor. B) Number of indentation points per individual tumor section (left); data summarized from stiffness-probed tissues of SUM-149-EV Control (n=8) vs. SUM-149-COX-2 (n=9) tumors (right). C) Representative immunoblots of ECM degradation enzymes and GAPDH loading control

Full Name of Abstract's 1st Author : Mc Millan Ching

First Name: Mc Millan

Last Name: Ching

Email: mching5@jh.edu

Organization: The Johns Hopkins University School of Medicine

Country: United States

ID: GA357
MRI-visible biocompatible hydrogels as cell scaffolds for tissue engineering

Marc-André Fortin, Centre de Recherche du Centre Hospitalier Universitaire de Québec – Université Laval, marc-andre.fortin@gmn.ulaval.ca

---

Category: Bioengineering, Synthetic Biology and Basic Biology

Abstract Body : Introduction, hypothesis, and objectives: Adipose tissue engineering, often including hydrogels as cell scaffolds, is emerging as a promising alternative to autologous fat transfer, in particular for breast and facial reconstructive surgical procedures.1,2 However, in vivo implantation of voluminous reconstructed adipose tissue (AT) substitutes requires the development of imaging procedures addressing indicators such as volume retention and remodelling.3 In fact, excessive tissue remodeling in vivo is one of the main problematics occuring in AT grafts over time, and the development of in vivo imaging methodologies enabling their follow-up post-implantation appears timely. Reconstructed AT grafts are not always easy to delineate in MRI, and addition of MRI-visible additives into the hydrogels constituting the cell scaffolds, could facilitate delineation and segmentation of the implants.3 In this study, we postulated that the addition of ultra-small iron oxide nanoparticles (USPIONs) in alginate-based cell scaffolds could enhance their MRI-visibility, thus allowing their volume follow-up over a period of several weeks. The impact of hydrogel formulation on the differentiation potential of adipose-derived stromal cells (ASCs) is also demonstrated. Materials and methods: USPIONs (5 nm diam.) were synthesized by thermal decomposition and pegylated by phosphine-oxide PEG. The particles were characterized for size (DLS, TEM), molecular signatures (FTIR) and relaxometric properties (1H T1 and T2 at different fields). USPIONs were mixed with alginate formulations and jellified using a 3D-printing approach which allowed to build functional channels in the hydrogels (perspective of long-term implantation in vivo : oxygenation, vascular growth). Hydrogels with and without USPIONs were s.c. implanted in mice flanks (balb/c female mice, n = 6 each group), and MR-imaged at t = 0, 3, 10, and 14 days post-injection (T1-w. spin-echo; echo time/repetition time: 13.5/704.2 ms). Blood samples were analyzed for signs of inflammation (CBA cytokine test : IL-1, IL-10,IL-12p70; MCP-1; IFN-gamma; TNF). Finally, ASCs were incubated with the hydrogel, then induced into adipocytes in order to evaluate the impact of the formulation in the differentiation potential of ASCs, which is a key aspect in the preparation of AT grafts.4 Results: PEGylated USPIONs were successfully synthesized with a core size Conclusion: USPIO-alginate hydrogels can be implanted as cell scaffolds in vivo to provide a persistent visibility in MRI. The gel remains on the site of implantation after 2 weeks, with MRI-visibility preserved. The hydrogel has limited impact on ASCs differentiation, which confirms the potential of the technology for the development of reconstructed AT substitutes and their visualization over time in vivo by MRI (for volume retention quantification). Acknowledgements: Mr P. L. for his contribution to USPIO synthesis.

References: 1 - Patrick, C.W., Jr. Semin Surg Oncol 19, 302, 2000. 2 - Hsu, V.M., Stransky, C.A., Bucky, L.P., and Percec, I. Aesthet Surg J 32, 892, 2012 3 - Proulx, M., Fradette J., Fortin,

Met al. Tissue Engineering; part C; Volume 21, Number 7, 2015 4 - Vermette, M., Fradette., J. et al. Volume 28, Issue 18, pp 2850-2860, 2007.

Image/Figure: https://s3.amazonaws.com/amz.xcdsystem.com/1E8A4501-BB41-A02A-1D3B9882B798BFAA_abstract_File10351/GA357_ImageFigure_0513085755.pdf

Image/Figure Caption: Above: In vitro: alginate
hydrogels with and without USPIONs (picture – left; and MRI scans - right). Under: In vivo: alginate-USPION graft; T1-w. spin-echo MRI (with control: alginate only).

First Name: Marc-André

Last Name: Fortin

Email: marc-andre.fortin@gmn.ulaval.ca

Organization: Centre de Recherche du Centre Hospitalier Universitaire de Québec – Université Laval

Country: Canada

ID: GA358
Photoacoustic imaging guided photodynamic therapy with theranostic nanodroplets

Srivalleesha Mallidi, Tufts University, Srivalleesha.Mallidi@tufts.edu

---

Category: Oncology

Abstract Body : Photodynamic therapy (PDT) utilizes light and photosensitizer to generate cytotoxic species such as singlet oxygen. The effectiveness of PDT, especially the type II pathways, depends on the availability of oxygen in the vicinity. Many tumors lack oxygen, making them resistant to PDT and other therapies. Hence there is need to enhance the oxygen content of tumors while delivering sufficient photosensitizer dose. Here we employed a perfluorocarbon nanodroplets as an oxygen carrier along with the photosensitizer Benzoporphyrin Derivative (BPD) and a photoacoustic imaging contrast agent Indocyanine Green (ICG) to enhance the imaging signal. The PA signal provides information about the oxygen saturation and drug concentration accumulated in the tumor. In summary, this new nanodroplet platform has the capability to significantly enhance PDT while providing patient-specific treatment options.

First Name: Srivalleesha

Last Name: Mallidi

Email: Srivalleesha.Mallidi@tufts.edu

Organization: Tufts University

Country: United States

ID: GA359

Formulation and Collagen Binding Specificity of a Novel Human Protein-Based Collagen-Targeted Protein Contrast Agents

Dongjun Li, Georgia State University , a377682953@gmail.com

Category: Oncology

Abstract Body : The extracellular matrix protein collagen is a major biomarker for multiple diseases including fibrosis, metastasis, aortic aneurysms, cardiovascular diseases, and fibrotic stroma of cancer. Collagen's expression types, level and spatial pattern are largely dependent on locations, types of diseases and disease progression state. It is essential to develop a non-invasive imaging methodology to allow us to longitudinally map the dynamic changes of collagen expression during disease progression and upon treatment including radiation. Our group designed and developed a human protein-based contrast agent with a collagen-targeting moiety (hProCA32.collagen) based on key determinates for metal binding sites in proteins and relaxivity. In this study, we report our recent breakthrough in optimization, characterization, formulation, and production of a designed novel human protein-based contrast agent with strong collagen-targeting specificity (hProCA32.collagen) pioneered by our team. We have shown that hProCA32.collagen exhibits 6.7-fold and 13.7-fold higher binding affinity for collagen type I than type III and IV respectively. The expression and purification yield have been largely improved by fermentation and large-scale optimization with 2-fold increase in solubility and significantly improved shelf life (up to 12 months) with stable protein conformation and little to no aggregation. Meanwhile, hProCA32.collagen possesses high relaxivities per particle at both 1.4 and 7.0 T and high collagen binding affinity (Kd: 1.0 μM), which enables the robust detection of early-stage liver fibrosis via dual contrast modes. Furthermore, hProCA32.collagen has high Gd3+ binding affinity (2.0 ± 0.25 × 10-22 M) and up to 15-fold higher metal selectivity with r1 and r2 relaxivity of 27 mM-1s-1 and 41 mM-1s-1 per Gd3+. Our in vivo imaging studies and histological analysis revealed that the newly formulated hProCA32.collagen is able to detect tumors less than 2 cm in Hepatocellular carcinoma (HCC) mouse model as well as early-stage liver fibrosis with high sensitivity and specificity using magnetic resonance imaging (MRI). The newly formulated hProCA32.collagen is expected to have broad preclinical and clinical applications for various diseases.

References: 1. Xue S. Design of novel protein-based MRI contrast agernets with high relaxivity and stabilty for biomedical imaging. [Order No. 3591115]. Georgia State University; 2013. 2. Qiao, J., et al., HER2 targeted molecular MR imaging using a de novo designed protein contrast agent. PLoS One, 2011. 6(3): p. e18103 3. Xue, S., et al., Design of a novel class of protein-based magnetic resonance imaging contrast agents for the molecular imaging of cancer biomarkers. Wiley Interdiscip Rev Nanomed Nanobiotechnol, 2013. 5(2): p. 163-79. 4. Yang, J.J., et al., Rational design of protein-based MRI contrast agents. J Am Chem Soc, 2008. 130(29): p. 9260-7. 5. Yang, J.J., et al., Structural biology of the cell adhesion protein CD2: alternatively folded states and structure-function relation. Curr Protein Pept Sci, 2001. 2(1): p. 1-17.

Image/Figure: https://s3.amazonaws.com/amz.xcdsystem.com/1E8A4501-BB41-A02A-1D3B9882B798BFAA_abstract_File10351/GA359_ImageFigure_0513092121.pdf

Image/Figure Caption: Detection of Early-Stage HCC by hProCA32.collagen A: Binding specificity of hProCA32.collagen to collagen type I, III, and IV. B: Relaxivity of hProCA32.collagen C: T2 weighted fast spin echo MR imaging of DEN-induced HCC before and 24 hours after injection of hProCA32.collagen. Lesions not detected pre-injection showed up with high enhancement at 24 hours' time point. D: Hematoxylin and eosin stain of the HCC liver showed corresponding tumor detected by the MRI in the similar position. E: The tumor size detected by MRI has a positively linear correlation (R2=0.9832) with histology data. F: After injection of hProca32.collagen, a significant enhancement of tumor was observed compared to pre injection. (n=4).

Full Name of Abstract's 1st Author : Dongjun Li

First Name: Dongjun

Last Name: Li

Email: a377682953@gmail.com

Organization: Georgia State University

Country: United States

ID: GA360
In vivo phototheranostics of splenic myeloid-derived suppressor cells

James Barnett, The Johns Hopkins University School of Medicine, jbarne55@jhmi.edu

---

Category: Oncology

Abstract Body : Introduction: Myeloid-derived suppressor cells (MDSC) are a heterogeneous and functionally diverse population of cells that inhibit immune surveillance and compromise host-immune recognition in the tumor microenvironment (TME) 1. MDSC differentiate from immature myeloid progenitors during pathogenesis, and they are phenotypically characterized as CD11b+ and Ly6G+ polymorphonuclear cell-like PMN-MDSC or CD11b+ and Ly6C+ monocyte-like M-MDSC. Antibody mediated MDSC depletion using anti-mouse granulocyte receptor-1 antigen (Gr1) Clone RB6-8C5 (Ly6GHi/Ly6CLo) has been used to effectively eliminate MDSC in some tumor models, providing high selectivity for PMN-MDSC – the most abundant MDSC subset generated during tumorigenesis 2. To accomplish targeted near-infrared photoimmunotherapy (NIR-PIT) 3, we synthesized an IR700-labeled Gr1 antibody-photosensitizer conjugate to target Gr1+ cells. In this proof of principle study, we have previously demonstrated the specificity of the Gr1-IR700 conjugate to detect and eliminate splenic MDSC in culture. Here, we validate the effectiveness of Gr1-IR700-mediated PIT in vivo. Methods: Gr1-IR700 and IgG-IR700 synthesis was achieved through the attachment of an NHS-activated NIR phthalocyanine dye, IR700, to the free amine residues on the RB6-8C5 monoclonal antibody and rat IgG2b,κ isotype control. Previously, Gr1-IR700 specificity for spleen-derived Gr1+ cells from tumor-bearing mice was validated using CCK-8 viability assays. In this current work, we inoculated 4T1-luc mammary carcinoma cells in the mammary fat pad of 4-6 week old female BALB/c mice to induce the generation and expansion of MDSC. Intraperitoneal (i.p.) injection of IR700-conjugated antibodies was administered once tumors reached approximately 750 mm3. Biodistribution studies were carried out using this orthotropic tumor model and non-tumor-bearing (NTB) mice to determine the retention of Gr1-IR700 and IgG-IR700 at 24 hours. For NIR-PIT experiments, tumor-bearing (TB) mice were i.p. injected with 100 μg of Gr1-IR700 followed by NIR-PIT of the spleen at 200 J/cm2 48 hours post injection. Metabolite changes in PIT-treated spleens were identified through high resolution 1H magnetic resonance spectroscopy (MRS) of dual-phase extracts using a Bruker Avance III 750 MHz (17.6T) MR spectrometer. A 5 mm inverse triple-resonance (TXI) probe was used for data acquisition, and Topspin 3.5 software was used for data processing, analysis and quantification. In vivo Gr1-IR700-mediated MDSC cell death will be determined using CCK-8 viability assays and fluorescence-activated cell sorting (FACS) analysis of spleens in TB-Ctrl, Gr1-IR700 and Gr1-IR700+PIT-treated groups. Results and Discussion: The Gr1-IR700 and IgG-IR700 biodistribution data in Figure 1A and 1B illustrate a striking increase in mean fluorescence intensity (MFI) of the spleen and lungs of TB mice injected with Gr1-IR700 compared to Gr1-IR700-injected NTB mice and IgG-IR700-injected TB mice, indicating myeloid cell recruitment and binding of Gr1-IR700 in TB mice. Metabolite changes between the TB-Ctrl, Gr1-IR700 and Gr1-IR700+PIT groups were determined. The millimolar concentrations normalized to BALB/c mouse spleen weight presented in Figure 1C from 4T1-luc tumor-bearing TB-Ctrl (n=3), Gr1-

IR700 (n=3) and Gr1-IR700+PIT (n=3) groups demonstrate significant changes in valine, isoleucine, lactate, acetate, glutamate, succinate, glutamine, glutathione, aspartate, choline, creatine, P-choline, GPC, total choline, taurine and myoinositol with Gr1-IR700+PIT. The robust change in glutamine is of particular interest because of the role of glutamine in T cell metabolism. These findings, taken together with previous in vitro data, confirm the ability of Gr1-IR700 to eliminate MDSC, illustrating its potential application for MDSC theranostics in the TME.

References: 1. Gabrilovich DI. Cancer Immunol Res. 2017 2. Xing YF. et al. Ann Rheum Dis. 2016 3. Jin, J. et al. Sci.Rep. 2016

Image/Figure:

https://s3.amazonaws.com/amz.xcdsystem.com/1E8A4501-BB41-A02A-1D3B9882B798BFAA_abstract_File10351/GA360_ImageFigure_0513092910.jpg

Image/Figure Caption: Figure 1: (A) Representative in vivo and ex vivo fluorescence images of Gr1-IR700 and IgG-IR700 retention in non-tumor-bearing and tumor-bearing BALB/c mice – NTB-Gr1-IR700 (n=4), TB-IgG-IR700 (n=4) and TB-Gr1-IR700 (n=3) with (B) averaged mean fluorescence intensity of (left to right) the spleen, kidney, lungs, small intestine, liver, stomach, heart, blood and tumor. (C) Millimolar concentrations normalized to BALB/c mouse spleen weight from 4T1-luc tumor-bearing TB-Ctrl (n=3), Gr1-IR700 (n=3) and Gr1-IR700+PIT (n=3) groups illustrated respectively for (upper row: left to right) valine, isoleucine, lactate, acetate, glutamate, succinate, glutamine, glutathione and (lower row: left to right) aspartate, choline, creatine, P-choline, GPC, total choline, taurine and myoinositol. Values represent Mean ± SEM.

Full Name of Abstract's 1st Author : James D Barnett

First Name: James

Last Name: Barnett

Email: jbarne55@jhmi.edu

Organization: The Johns Hopkins University School of Medicine

Country: United States

ID: GA361
Pretargeting of [89Zr]Zr-DO3A-proteus radiohapten in a mouse orthotopic liver xenograft model of human colorectal cancer

Alexandre Le Roux, Memorial Sloan Kettering Cancer Center, lerouxa@mskcc.org

---

Category: Oncology

Abstract Body : Metastatic cancer is the leading cause of death for patients diagnosed with colorectal cancer (CRC), with the liver being the most common site of metastasis. The tumor microenvironment influences the growth, response to treatment and tumor immune responses in vivo, and subcutaneous tumors do not accurately represent the natural tumor microenvironment. Therefore, we used ultrasound-guided percutaneous inoculation to develop a pre-clinical orthotopic model of CRC liver metastasis. This orthotopic liver xenograft model was used to evaluate an anti-tumor/anti-DOTA bispecific antibody (bsAb) pretargeted radioimmunotherapy (PRIT) platform and radiohaptens developed for imaging and radiotherapy (lutetium-177). We used zirconium-89 (Zr-89) as an imaging surrogate due to its long physical half-life and imaging resolution, and effective half-life similar to the therapeutic radiohapten. A novel radiohapten precursor DO3A-proteus, mirroring the "gold standard" β-radiohapten [177Lu]LuDOTA-Bn was radiolabeled with [89Zr]ZrCl4, for theranostic imaging of the liver xenograft model. DO3A-proteus consists of a commercial 2,2',2''-(10-(17-amino-2-oxo-6,9,12,15-tetraoxa-3-azaheptadecyl)-1,4,7,10-tetraazacyclododecane-1,4,7-triyl) triacetic acid (NH2-PEG4-DO3A) and non-radioactive lutetium 2-(4-isothiocyanatobenzyl)-1,4,7,10-tetraazacyclododecane-tetraacetic acid (p-SCN-Bn-DOTA·Lu3+ complex) prepared from p-SCN-Bn-DOTA (Macrocyclics, Inc.) and 175LuCl3·6 H2O. For preparation of [89Zr]Zr-DO3A-proteus, DO3A-proteus (30 nmol) was mixed with [89Zr]ZrCl4 (UW-Madison Cyclotron Lab, 74 MBq/2 mCi) in 0.5M HEPES (pH 7.5). After 60 min at 95°C, the reaction was purified with a Strata-X SPE cartridge to obtain [89Zr]Zr-DO3A-proteus (RCY: 33%, AM= 0.93 MBq(25 µCi)/nmol, RCP by radio-RP-HPLC: >99%). GPA33-expressing human colorectal cancer SW1222 cells (40 µl bolus of 2 million cells suspended in PBS:Matrigel (1:1 v/v)) were inoculated percutaneously within the liver of athymic nude mice (n=10, female, 6-8 week-old) by freehand using the ultrasound monitor for reference (40 MHz transducer, Vevo 2100 high-resolution imaging system, Visualsonics). Adequate tumor growth was achieved in 5 weeks, and the mice were injected i.v. with bsAb huA33-C825 (250 µg, 1.19 nmol), followed 24 h later with i.v. injection of dendrimer-clearing agent (10% (w/w), 25 µg, 2.76 nmol), and long-lasting microCT contrast agent (10 mL/kg, Fenestra LC, Medilumine). Finally, [89Zr]Zr-DO3A-proteus was injected i.v. 4h after the clearing agent (0.37 MBq (10 µCi), 0.4 nmol). Imaging (Inveon PET/CT) was performed at ~4, 24h and 48h post-injection (p.i.). Ex vivo biodistribution assay of radioactivity was performed at 6h (n= 4 mice) and 48h (n= 6 mice) post-injection. 5 non tumor bearing athymic nude mice were also used as control and received the same doses of bsAb, clearing agent, microCT contrast agent and [89Zr]Zr-DO3A-proteus. [89Zr]Zr-DO3A-proteus showed rapid renal clearance, with minimal organ retention and demetallation. Following ex vivo biodistribution assay of radioactivity, the blood, SW1222 tumor, non-tumored liver and kidney uptakes at 6h p.i. were respectively 0.24 ± 0.07 %ID/g, 4.0 ± 1.2 %ID/g, 0.21 ± 0.03 %ID/g, and

0.6 ± 0.1 %ID/g. At 48h p.i, the blood, SW1222 tumor, non-tumored liver and kidney uptakes were respectively 0.08 ± 0.03 %ID/g, 3.1 ± 1.2 %ID/g, 0.17 ± 0.10 %ID/g, and 0.4 ± 0.2 %ID/g. At 6h p.i., the corresponding tumor-to-organ activity ratios (T:NT) for blood, non-tumored liver and kidney were respectively 17.6 ± 6.3, 19.4 ± 5.3, and 6.3 ± 1.3, and at 48h p.i. (n=6 mice), 32.5 ± 7.1, 21.7 ± 14.1, and 5.9 ± 1.4. The mean %ID/g for the control mice following ex vivo biodistribution at 48h was below 0.3%ID/g for all organs. Using serial image-based ROI data from 4-48h p.i., prospective Lu-177 dosimetry was estimated assuming complete local absorption of β particles only. The preliminary absorbed doses to tumor, blood, non-tumored liver, and kidney were respectively 175 mGy/MBq, 6 mGy/MBq (TI= 31), 47 mGy/MBq (TI= 3.7), and 41 mGy/MBq (TI= 4.3). [89Zr]Zr-DO3A-proteus had an excellent in vivo stability and radiopharmacology for imaging GPA33-expressing CRC liver metastasis, and appears to be an excellent radiohapten precursor for theranostic Zr-89/Lu-177 therapy.

References: McVeigh L.E., et al. Development of orthotopic tumour models using ultrasound-guided intrahepatic injection. Sci Rep, 2019, 9, 9904. Cheal S., et al. Alpha radioimmunotherapy using 225 Ac-proteus-DOTA for solid tumors - safety at curative doses. Theranostics, 2020;10(25):11359-11375

Image/Figure: https://s3.amazonaws.com/amz.xcdsystem.com/1E8A4501-BB41-A02A-1D3B9882B798BFAA_abstract_File10351/GA361_ImageFigure_0513093135.jpeg

Image/Figure Caption: Coronal multiplanar reconstruction (MPR) microCT (A) and PET (B) images, and maximum intensity projection (MIP) microCT/PET image (C) of a mouse ~ 4h after i.v. injection of ([89Zr]Zr-DO3A-proteus (0.37 MBq (10 μCi), 0.4 nmol). The SW1222 tumor (T.) can be seen as an hypoattenuating well-defined lesion in the liver on the microCT image (A) following long-lasting microCT contrast agent administration (Fenestra LC, Medilumine, 10 mL/kg), with high avidity of the tumor for the [89Zr]Zr-DO3A-proteus noted on the images (B) and (C). Table (D) is a summary of the estimated Lu-177 dosimetry for the tumor and abdominal organs, and corresponding therapeutic index. (E) and (F) are histograms and tables showing the tumor and abdominal organs %ID/g uptake (in vivo (E) and ex vivo (F)), and corresponding tumor-to-organs ratios.

First Name: Alexandre

Last Name: Le Roux

Email: lerouxa@mskcc.org

Organization: Memorial Sloan Kettering Cancer Center

Country: United States

ID: GA362

FLT3 is a major driver of [18F]FDG accumulation in squamous cell lung carcinoma cells

Peter Clark, UCLA, pclark@mednet.ucla.edu

Category: Oncology

Abstract Body : PET imaging with the glucose analogue 2-deoxy-2[18F]fluoroglucose ([18F]FDG) is foundational for the diagnosis and staging of many types of cancer including lung cancer. The biochemical pathway that enables [18F]FDG to concentrate in cancer cells is well described: [18F]FDG is transported across the cell membrane through the GLUT glucose transporters and phosphorylated by the hexokinase enzymes to [18F]FDG-6-phosphate. However, our understanding of the signaling pathways that activate the GLUT transporters and the hexokinase enzymes and that drive [18F]FDG accumulation in cancer cells is limited to a few major pathways in a limited number of cancer types. The full scope of pathways that regulate [18F]FDG accumulation in cancer cells remains largely unexplored. Squamous cell lung cancer (SqCLC) constitutes 30% of non-small cell lung cancer. SqCLC cells consume elevated levels of glucose compared to lung adenocarcinoma and surrounding lung tissue. However, few pathways have been identified that activate glucose consumption and drive [18F]FDG accumulation in SqCLC. The goal of this work is to discover new pathways that drive glucose consumption and [18F]FDG accumulation in SqCLC. To identify new pathways that drive glucose consumption and [18F]FDG accumulation in SqCLC, we used a high-throughput glucose consumption assay. In this assay, cells are treated with 2-deoxyglucose and 2-deoxyglucose-6-phosphate levels are measured using a coupled enzyme assay that quantitatively converts the 2-deoxyglucose-6-phosphate to a light output. We measured glucose consumption in three SqCLC cell lines – H520, SK-MES-1, and H596 – treated with 3555 bioactive small molecules. We further validated the results of the high-throughput screen and studied the mechanism by which one of the compounds identified regulates glucose consumption. We identified and validated >50 compounds that blocked glucose consumption in at least one of the SqCLC cell lines. We focused on validated compounds that were not previously known to affect glucose consumption in SqCLC, that significantly decreased glucose consumption by >70%, that blocked glucose consumption in more than one cell line, that had a glucose consumption IC50 M, and that had been in humans. Based on these criteria, we chose to further study the kinase inhibitor Pacritinib. Pacritinib strongly blocks glucose consumption with an IC50 of 2 μM in H520, SK-MES-1, and H596 cells in culture and blocks [18F]FDG accumulation in these cell lines in vivo while having no effect on [18F]FDG accumulation in other highly glycolytic tissue including the heart and brain. Pacritinib blocks mRNA and protein levels of Hexokinase 1 and 2, leading to a decrease in hexokinase activity. The effect of Pacritinib on glucose consumption was rescued by Hexokinase 1 overexpression. These data suggest that Pacritinib blocks glucose consumption by inhibiting Hexokinase 1 expression. Pacritinib targets various kinases, including FLT3, JAK2, and TYK2 with low nanomolar IC50 values. Additional small molecule inhibitors selective for JAK2 and TYK2 but not FLT3 had no effect on glucose consumption in the SqCLC cell lines. However, additional and selective FLT3 small molecule inhibitors blocked

glucose consumption, and FLT3 overexpression rescued the effect of Pacritinib on glucose consumption in SqCLC cell lines. These results suggest that Pacritinib blocks glucose consumption through the inhibition of FLT3. Our results demonstrate that FLT3 is a major driver of [18F]FDG accumulation in SqCLC by increasing Hexokinase 1 expression. The implications of this study are that [18F]FDG could potentially function as a pharmacodynamic biomarker of FLT3 inhibitor efficacy and that the degree of [18F]FDG accumulation could potentially serve as a measure of FLT3 pathway activity in SqCLC.

Image/Figure:

https://s3.amazonaws.com/amz.xcdsystem.com/1E8A4501-BB41-A02A-1D3B9882B798BFAA_abstract_File10351/GA362_ImageFigure_0513093600.png

Image/Figure Caption: [18F]FDG accumulation in H520 xenografts in mice treated with Pacritinib.

First Name: Peter

Last Name: Clark

Email: pclark@mednet.ucla.edu

Organization: UCLA

Country: United States

ID: GA363
High-precision noninvasive gene delivery to the brain

Manwal Harb, Rice University, mmh10@rice.edu

Category: Bioengineering, Synthetic Biology and Basic Biology

Abstract Body : Being able to noninvasively control any neural circuit with a combination of spatial, temporal, cellular, and molecular pathway precision could allow for more precise treatment of neuropsychiatric disorders with fewer side effects. Recently, a paradigm was developed that allows such neuromodulation to be performed noninvasively by combining focused ultrasound, viral vectors, and chemogenetics. In this approach called Acoustically Targeted Chemogenetics1, or ATAC, focused ultrasound (FUS) is used to briefly open tight junctions in the blood-brain barrier (FUS-BBBO) in spatially specific brain region(s)2, allowing localized delivery of adeno-associated viral vectors (AAVs) encoding chemogenetic receptors3-5 to neurons and enabling their subsequent excitation or inhibition with bio-orthogonal, orally bioavailable drugs. FUS targets both deep and cortical brain regions with millimeter precision6; AAVs allow for the selection of a neuronal population using cell-specific promoters7,8; and chemogenetic receptors3-5enable temporally-specific neuromodulation. Relative to what is currently being studied and tested, ATAC is the only neuromodulation technique that achieves temporal, spatial, cell-type, and molecular specificity noninvasively. However, its spatial precision is limited by the precision of FUS itself. While FUS allows for millimeter precision, many brain regions, such as a single layer of cortex or specific hypothalamic nuclei, are significantly smaller than the focus of FUS both in mice and larger animals. Such precision cannot be feasibly achieved in vivo with current FUS devices. To solve this limitation, a novel strategy is proposed that decouples the precision of FUS from noninvasive chemogenetic neuromodulation. Established tools for gene editing are combined with FUS delivery to achieve transduction precision comparable to an invasive intracranial injection. To achieve this, two independent sessions of FUS-BBBO are used, and a spatial overlap of expression between the fields expressing the gene-editing target and the gene-editing enzyme is enabled. The results of this intersectional ATAC strategy, or iATAC, show that expressing both of these components is safe in mice after a systemic delivery and show ~10-fold improvement in targeting precision.

References: [1] Szablowski, J. O., Lee-Gosselin, A., Lue, B., Malounda, D. & Shapiro, M. G. Acoustically targeted chemogenetics for the non-invasive control of neural circuits. Nature Biomedical Engineering 2, 475 (2018). [2] Hynynen, K., McDannold, N., Vykhodtseva, N. & Jolesz, F.A. Noninvasive MR imaging-guided focal opening of the blood-brain barrier in rabbits. Radiology 220, 640-646 (2001). [3] Armbruster, B.N., Li, X., Pausch, M.H., Herlitze, S. & Roth, B.L. Evolving the lock to fit the key to create a family of G protein-coupled receptors potently activated by an inert ligand. Proc Natl Acad Sci U S A 104, 5163-5168 (2007). [4] Roth, B.L. DREADDs for Neuroscientists. Neuron 89, 683-694 (2016). [5] Shapiro, M.G., Frazier, S.J. & Lester, H.A. Unparalleled control of neural activity using orthogonal pharmacogenetics. ACS Chem Neurosci 3, 619-629 (2012). [6] Elias, W.J. et al. A Randomized Trial of Focused Ultrasound Thalamotomy for Essential Tremor. N. Engl. J. Med. 375, 730-739 (2016). [7]

Dittgen, T. et al. Lentivirus-based genetic manipulations of cortical neurons and their optical and electrophysiological monitoring in vivo. Proc Natl Acad Sci U S A 101, 18206-18211 (2004). [8] Kugler, S., Kilic, E. & Bahr, M. Human synapsin 1 gene promoter confers highly neuron-specific long-term transgene expression from an adenoviral vector in the adult rat brain depending on the transduced area. Gene Ther 10, 337-347 (2003).

Image/Figure:

https://s3.amazonaws.com/amz.xcdsystem.com/1E8A4501-BB41-A02A-1D3B9882B798BFAA_abstract_File10351/GA363_ImageFigure_0513093635.png

Image/Figure Caption: Ultrasound-based gene delivery is limited in spatial precision because the FUS beam is too long and spans millimeters in length, leading to nonspecific viral transduction and gene expression. Moreover, when targeting near the base of the skull, there is reflection of the FUS beam, causing pressure build-up and undesired damage in the form of hemorrhage. To overcome these limitations, two separate gene delivery sessions can be performed with the gene-editing target delivered first followed by erasure of gene expression in undesired areas of the brain with the delivery of the gene-editing enzyme. By using this advance in precision targeting, desired gene expression will only be restricted to the intended site and allow for targeting difficult-to-reach areas of the brain such as a single layer of cortex.

Full Name of Abstract's 1st Author : Manwal Harb

First Name: Manwal

Last Name: Harb

Email: mmh10@rice.edu

Organization: Rice University

Country: United States

ID: GA364
[18F]DPA-714 PET delineating peripheral organ-level reactive changes in rat model of sepsis

Neysha Martinez-Orengo, NIH, neysha.martinez-orengo@nih.gov

Category: Immunology: Inflammation & Infection

Abstract Body : Background: Besides brain microglia, the translocator protein (TSPO) is expressed by macrophages and other peripheral immune cells, making it a potentially suitable biomarker for tracking reactive changes in peripheral organs in infectious/inflammatory diseases (e.g. lungs, liver, spleen, brain, and bone marrow), including sepsis. The bone marrow is especially important as it plays a central role during inflammatory/infectious events with secondary increased hematopoietic stem cell (HSC) differentiation (hematopoiesis). Still, only a handful of studies have used PET with TSPO specific ligands to evaluate peripheral organ inflammation in sepsis. In our study, using a rat model of LPS-induced inflammation (sepsis model), we performed whole body PET imaging with a TSPO tracer, [18F]DPA-714, to determine changes in TSPO expression in both the brain and lungs, liver, bone marrow, and spleen. In order to assess the physiologic relevance of TSPO upregulation, we correlated our imaging results with several serum and brain biomarkers of inflammation. Methods: Thirteen male Fisher rats (weight 0.32 ± 0.01 kg, age 3.96 ± 0.17 months) underwent dynamic PET scans with [18F]DPA-714 on an Inveon microPET/CT scanner. Scans were collected at baseline and 4 hours after intravenous LPS injection (5mg/Kg). Reconstructed PET images were analyzed using PMOD 3.8 to generate time activity curves (TACs) for brain, lungs, liver, bone marrow, and spleen. Mean Standardized Uptake Value (SUVmean) were calculated using emission data at equilibrium (26-40 mins). We measured serum cytokines and, following euthanasia and perfusion, assessed organ TSPO gene expression (qPCR) levels. Multiplex Immunofluorescence (IF) staining was done on the lung, spleen, and brain tissues for TSPO, CD68 (monocytes/macrophages), and Iba1 (microglia in brain only). In the brain, we measured microglial ramifications' length and cell body area. Paired t-tests were done to evaluate the differences in [18F] DPA-714 uptake between baseline and post LPS status. Repeated measures correlations between SUV values and serum cytokine levels were performed using the rmcorr package in R. Results: Mean TAC (n=13) for whole-brain, lungs, liver, and bone marrow showed increase in [18F]DPA-714 binding post-LPS compared to baseline. Post-LPS SUVmean were significantly higher for brain (p =0.006), lungs (p=0.02), liver (p Conclusion: Using noninvasive molecular imaging with [18F]DPA-714 PET in a rat model of sepsis, further validated by qPCR and IF microscopy, we demonstrated organ-level brain, liver and lung inflammatory changes as well as spleen immune cell efflux and activated hematopoiesis in the bone marrow. [18F]DPA-714 PET can be helpful in better understanding of the pathophysiology of systemic inflammation in sepsis and its organ-level effects.

Image/Figure:

https://s3.amazonaws.com/amz.xcdsystem.com/1E8A4501-BB41-A02A-1D3B9882B798BFAA_abstract_File10351/GA364_ImageFigure_0513094103.png

Image/Figure Caption: Figure 1. Representative images of [18F]DPA-714 uptake in the brain (A), bone marrow (B), and other peripheral organs (C) shown before and after LPS administration. (D) SUV mean pre- and post-LPS shown in the brain, liver, bone marrow, lungs, and spleen. (E) Fold difference of TSPO mRNA between control and LPS administration in the lungs, liver, spleen, and brain.

First Name: Neysha

Last Name: Martinez-Orengo

Email: neysha.martinez-orengo@nih.gov

Organization: NIH

Country: United States

ID: GA365
Phototheranostics of epithelioid sarcoma by targeting CD44 or EGFR

Jiefu Jin, Johns Hopkins University School of Medicine, jjin@jhmi.edu

---

Category: Oncology

Abstract Body : Introduction: Epithelioid sarcoma (ES) is a rare yet high-grade and highly aggressive soft tissue neoplasm first identified by Enzinger in 1970.1 ES has high reported recurrence and metastasis rates (around 70% and 50%, respectively).2 Unresectable locally advanced and metastatic ES are usually chemoresistant and generally fatal.3 Here, we extended a previous near-infrared photoimmunotherapy (NIR-PIT) study,4 to develop antibody photosensitizer conjugates based on two monoclonal antibodies (mAbs) binding to CD44 or EGFR, both overexpressed on ES tumor cell surface. We conducted cellular studies and established animal models to evaluate the specificity and efficacy of the two mAb conjugates in binding, detecting and eliminating ES. Method: CD44, EGFR mAb or its IgG isotype control was conjugated with a NIR phthalocyanine dye, IR700, to form CD44-IR700, EGFR-IR700 and IgG-IR700, respectively. A bilateral ES tumor model was established by inoculating 1×106 VAESBJ cells in 0.05 ml of Hank's balanced salt solution on either flank of athymic Balb/c (nu/nu) female mouse. Subsequently, 100 μg of CD44-IR700 or EGFR-IR700 or IgG-IR700 was injected intravenously (i.v.), and NIR fluorescence images of IR700 in mice were obtained over a 24-h period (n = 4 per group). For PIT, tumor-bearing mice (n = 4 or 5 per group) received two i.v. injections of 100 μg of CD44-IR700 or EGFR-IR700 at a one-week interval, and tumors were exposed to NIR light exposure at 200 J/cm2 at 24h p.i. Tumor diameters were measured over 3 weeks. IgG-IR700 and PBS-injected mice were used as controls. Results and Discussion: CD44 and EGFR overexpression in VA-ES-BJ cells and human ES sections were validated by flow cytometry and immunohistochemistry (Fig. S1). Both CD44-IR700 and EGFR-IR700 demonstrated concentration and exposure-dose dependence of cellular PIT and target-specific cell death of VA-ES-BJ cells. Compared to EGFR-IR700, CD44-IR700 exhibited a higher potency with cellular PIT and had a much lower IC50 value due to the higher expression level of CD44 on VA-ES-BJ cell surface (Fig. S2). CD44-IR700 and EGFR-IR700 both exhibited preferential accumulation in VA-ES-BJ tumors and showed approximately two to three-fold higher retention compared to IgG-IR700. EGFR-IR700 showed a higher tumor-to-normal ratio and less retention in organs than CD44-IR700 (Fig. S3). EGFR-IR700 injection combined with NIR light exposure resulted in significant tumor growth delay in VAESBJ tumors compared to the IgG-IR700 or PBS group or EGFR-IR700 without PIT group; CD44-IR700-PIT also resulted in significant tumor growth delay compared to the PBS group (Fig. 1). Reduction of CD44 and EGFR levels were observed in the CD44-IR700 or EGFR-IR700-treated tumors as evidenced by flow cytometry and western blotting studies (Fig. S4). Our data collectively demonstrate the specificity and efficacy of CD44 or EGFR-based PIT as novel therapeutic approaches that can be integrated into an intraoperative setting for achieving clear tumor margins in localized ES or applied as a standalone therapy for inoperable locally advanced and recurrent ES.

References: References: 1. Enzinger, F. et al. Cancer 1970; 2. Elsamna, S. et al. Acta Oncologica. 2020; 3. Wolf, P et al. Am J Surg. 2008; 4. Jin, J. et al. Sci Rep. 2016.

Image/Figure:

https://s3.amazonaws.com/amz.xcdsystem.com/1E8A4501-BB41-A02A-1D3B9882B798BFAA_abstract_File10351/GA365_ImageFigure_0513094120.png

Image/Figure Caption: Figure 1. In vivo CD44-IR700 and EGFR-IR700-PIT. (a) Growth curves of VA-ES-BJ tumors. 100 μg of CD44-IR700 or EGFR-IR700 or IgG-IR700 was injected i.v. on day 0 and on day 7. All the groups were monitored for three weeks after injection except for two weeks in the PBS group. PIT groups received light exposure at 200 J/cm2 24 h after each injection and no PIT groups were shielded from light exposure. Values represent Mean ± SEM from at least four mice per group ($n \geq 4$). EGFR-IR700 PIT group vs PBS group, ***$P < 0.001$; EGFR-IR700 PIT group vs No PIT group, ***$P < 0.001$. (b) Photograph of VA-ES-BJ tumors resected from different groups at the end of treatment.

First Name: Jiefu

Last Name: Jin

Email: jjin@jhmi.edu

Organization: Johns Hopkins University School of Medicine

Country: United States

ID: GA366

Derivation of optimal indicator to monitor sleep states using Monte Carlo Simulation of water molecules

Jehyeong Yeon, Yonsei University, yy77887@yonsei.ac.kr

Category: Computational & Data Science

Abstract Body : Introduction The glymphatic system (GS) is assumed to be a waste clearance system of the cerebrospinal fluid (CSF) through the perivascular and interstitial space of the brain [1]. Natural sleep is associated with about 60% increase in the interstitial space, resulting in a conspicuous increase in convective exchanges of CSF with interstitial fluid (ISF) [2]. To date, no studies have proposed a method of observing the influx of CSF into the interstitial space from non-surface to deep water using magnetic resonance diffusion tensor images along cellular space volume. In this study, we hypothesized that the extracellular space (ECS) volume fraction involved interstitial space expands from 30% to 50% during sleep, filling the dilated space with incoming CSF. The diffusion scalars of the corpus callosum (CC) were affected by sleep [3]. Therefore, using Monte Carlo simulation (MCS), we simulated diffusion tensor signals according to an increase in ECS volume ratio in the voxels of the corpus callosum and obtained a diffusion scalars: frcational anisotropy (FA), mean diffusivity (MD), radial diffusivity (RD) and axial diffusivity (AD). The purpose of this work was to detect the most sensitive diffusion scalars from the ECS volume changes using MCS. Methods For MCS, the voxel size of genu of CC was set to 20μm×20μm×20μm and the number of Axons was 420. Axons are acquired by fitting a gamma distribution to the histograms of axon radii as follows [4]. We integrated a three-dimensional diffusion motion by updating the position of each water molecule in every Δt during a diffusion time Tdiff. Details of the simulation parameters used in our study are shown in Table 1 [5-10]. Table 1. The MCS parameters Parameter Value Meaning θ 0.122 Scale parameter in radius gamma distribution k 3.5 Shape parameter in radius gamma distribution mxOD 2.6μm Maximum of outer diameter N 10000 Total water molecules Δt 1μm Update time Tdiff 120 ms Diffusion time ID/OD 0.63 (g-ratio) Inner diameter to outer diameter ratio Din 2.5×10-3mm2/s Intracellular space diffusivity Dout 3.5×10-3mm2/s Extracellular space diffusivity b 1000s/mm2 b-value G 80mT/m Gradient strength P 5 .5μm/s Permeability coefficient of water molecules The diffusion tensor signal was obtained by increasing gradually to about 5% of the initial ECS volume fraction from 30% to 50%. By adding noise to the obtained diffusion tensor signal, the diffusion scalars according to ECS volume fractions were obtained when SNR = 10, 20, 30, and infinite. MCS was performed using software developed by Sapkota et al [6]. Results The FA, MD, RD and AD ranges of the human corpus callosum were reported by Liu et el [8]. Our results are depicted in Figure 1. All diffusion scalars for the initial ECS volume fraction representing the non-sleep state were in the normal ranges mentioned above. As the ECS volume fraction increased, MD and RD increased and FA decreased, and AD did not change significantly. Regardless of the SNR, FA and MD can detect changes in ECS volume ratio of 10% or more, whereas RD can detect changes in ECS volume ratio of 5% or more. RD is very sensitive in changes of ECS volume because it can be distinguished even under 5% regardless of SNR. Discussion Decreased FA with increasing ECS volume may be caused by the disruption of

myelin and awakening was associated with widespread increases in white matter FA, which were mainly driven by RD reductions [11]. The result can be interpreted as a change in FA and RA because ECS volume was increased by shrinking myelin through MCS. FA and MD were not significantly different for ECS volume difference less than 10%. RD was most sensitive compared to other scalars, and ECS volume changes were discernable from more than 5%. Therefore, RD can be used as an appropriate index to monitor sleep states.

References: 1. Taoka T, Naganawa S. Glymphatic imaging using MRI. J Magn Reson Imaging. 2020;51:11–24. 2. Xie L, Kang H, Xu Q, et al. Sleep drives metabolite clearance from the adult brain, Science 2013, 342, 373-377. 3. Telzer EH, Goldenberg D, Fuligni AJ, Lieberman MD, Galvan A. Sleep variability in adolescence is associated with altered brain development. Developmental cognitive neuroscience. 2015;14:16–22. 4. Liewald, D., Miller, R., Logothetis, N., Wagner, H.J. & Schüz, A. Distribution of axon diameters in cortical white matter: an electron-microscopic study on three human brains and a macaque. Biol. Cybern. 108, 541–557 (2014). 5. M.G. Hall, D.C. Alexander, Convergence and parameter choice for Monte-Carlo simulations of diffusion MRI, IEEE Trans. Med. Imag. 28 (2009) 1354–1364 6. Nabraj Sapkota et al., Characterization of spinal cord white matter by suppressing signal from hindered space. A Monte Carlo simulation and an ex vivo ultrahigh-b diusion-weighted imaging study, Journal of Magnetic Resonance, Volume 272, November 2016, Pages 53-59 7. Stikov N, Campbell JSW, Stroh T, et al. In vivo histology of the myelin g-ratio with magnetic resonance imaging. Neuroimage. 2015; 118: 397- 405. 8. Liu, F, Vidarsson, L, Winter, JD, Tran, H, Kassner, A. 2010. Sex differences in the human corpus callosum microstructure: a combined T2 myelin-water and diffusion tensor magnetic resonance imaging study. Brain Res 1343:37–45. 9. Whittall KP, MacKay AL, Graeb DA, Nugent RA, Li DKB, Paty DW. In vivo measurement of T2 distributions and water contents in normal human brain. Magn Reson Med 1997; 27: 34– 43. 10. D.A. Dick The permeability coefficient of water in the cell membrane and the diffusion coefficient in the cell interior J. Theoretical. Biol., 7 (1964), pp. 504-531 11. T. Elvsashagen, L.B. Norbom, P.O. Pedersen, S.H. Quraishi, A. Bjørnerud, U.F. Malt, L.T. Westlye, et al. Widespread changes in white matter microstructure after a day of waking and sleep deprivation PLoS One, 10 (2015)

Image/Figure:

https://s3.amazonaws.com/amz.xcdsystem.com/1E8A4501-BB41-A02A-1D3B9882B798BFAA_abstract_File10351/GA366_ImageFigure_0513094503.JPG

Image/Figure Caption: Figure 1. Results (mean±SD) for (a)FA, (b)MD, (c)RD and (d)AD changes in ECS volume with different noise level: blue – noise free, red – SNR 10, green – SNR 20, purple – SNR 30

Full Name of Abstract's 1st Author : Jehyeong Yeon

First Name: Jehyeong

Last Name: Yeon

Email: yy77887@yonsei.ac.kr

Organization: Yonsei University

Country: South Korea

ID: GA367

Microbubble Shell Composition Alters Organ Biodistribution and Focused Ultrasound-Enabled Delivery to Orthotopic Breast Tumors: A Multimodal, Quantitative Evaluation of Lipid Microbubble Shell Fate

Alex Dhaliwal, University of Toronto, alex.dhaliwal@mail.utoronto.ca

---

Category: New Chemistry, Materials & Probes

Abstract Body : INTRODUCTION Microbubbles are ultrasound contrast agents used for diagnostic imaging. They derive their contrast from the expansion and contraction of a flexible shell around a gaseous core that occurs upon stimulation with acoustic waves. This interaction can also be manipulated to enhance local drug delivery using focused ultrasound (FUS), whereby interactions between microbubbles and their confining vasculature create openings at sites of ultrasound irradiation. This transient vasculature disruption allows for enhanced extravasation of drugs co-injected alongside the microbubbles or embedded within the microbubbles themselves 1–3. While microbubble-mediated FUS has been utilized to improve chemotherapy delivery to solid tumors 4, little is known about the impact of microbubble composition on important drug delivery parameters such as pharmacokinetics, biodistribution, and degree of FUS-enabled delivery enhancement to tumors. A thorough understanding of the interplay of these parameters is essential towards the intentional and optimal design of microbubble delivery systems. OBJECTIVE To quantitatively elucidate the effect of microbubble shell charge (+/- anionic phosphatidic acid lipids) and lipid chain length (C16, C18) on longitudinal organ biodistribution in the presence and absence of focused ultrasound in an orthotopic breast cancer model. METHODS A series of Definity®-analogue microbubbles was designed with varying lipid chain lengths (C16, C18) and the presence or absence of a negatively charged shell (+/- phosphatidic acid). These compositions were modified through the inclusion of porphyrin-lipid 5, a multifunctional imaging moiety capable of facilitating quantitative microbubble shell tracking in vivo through radionuclide chelation and fluorescence imaging. Microbubbles were coordinated to the radioisotope 64Cu using a simple, one-pot chelation strategy, after which they were injected into 4T1 tumor-bearing Balb/c mice and exposed to focused ultrasound (1 MHz, 300 kPa, 1% duty cycle, 2 minute total sonication time). Longitudinal biodistribution was assessed via PET imaging over 48 hours, while end-point quantification was assessed at 3.5 and 48 hours via gamma counting and hyperspectral fluorescence imaging. Degree of agent extravasation was assessed by comparing to mice perfused prior to dissection using both the porphyrin-microbubble platform and an Evans Blue standard. RESULTS Biodistribution was dominated by organs of the reticuloendothelial system, sequestering primarily within the liver, followed closely by the spleen. Uptake followed similar shell dependencies as seen with other lipid drug delivery platforms such as liposomes 6–8, but the degree of organ specificity was magnified – specifically, splenic uptake was greater for longer chain lengths, whereas liver uptake was greater for shorter chain lengths and negatively charged bubbles. Gamma counting of blood samples revealed that shell circulation follows a two-phase exponential decay with slow half-lives on the order of 4–10 hours depending upon shell composition. This was corroborated by biodistribution in perfusion-dominated organs (heart, lungs, kidneys), which followed the trends

set by the microbubble shell clearance kinetics. Importantly, focused ultrasound-mediated tumor delivery varied by shell composition, with an increase in shell extravasation only apparent for microbubbles constructed with C18 chain length lipids without phosphatidic acid. These differences were limited to microbubble shell extravasation and not to bulk changes in tumor vascular permeability as assessed by co-delivery of Evans Blue. IMPACT The trends and relationships uncovered in this robust exploration of microbubble shell biodistribution will better inform the design of microbubble-based delivery systems. Specifically, the use of charged lipids and tailoring of lipid chain length can alter organ selectivity of shell deposition and tumor uptake, providing a framework for those using microbubble-enabled FUS to enhance drug delivery to different tumor sites. Importantly, these quantitative longitudinal measurements revealed pharmacokinetic trends which were previously obscured in studies utilizing shorter study timeframes 9–11 or end-point metrics alone, highlighting the importance of thorough pharmacokinetic evaluation of microbubble platforms.

References: 1. Goertz, D. E. An overview of the influence of therapeutic ultrasound exposures on the vasculature: High intensity ultrasound and microbubble-mediated bioeffects. Int. J. Hyperth. 31, 134–144 (2015). 2. Kooiman, K., Emmer, M., Foppen-Harteveld, M., van Wamel, A. & de Jong, N. Increasing the Endothelial Layer Permeability Through Ultrasound-Activated Microbubbles. IEEE Trans. Biomed. Eng. 57, 29–32 (2010). 3. Juffermans, L. J. M. et al. Ultrasound and Microbubble-Induced Intra- and Intercellular Bioeffects in Primary Endothelial Cells. Ultrasound Med. Biol. 35, 1917–1927 (2009). 4. Dimcevski, G. et al. A human clinical trial using ultrasound and microbubbles to enhance gemcitabine treatment of inoperable pancreatic cancer. J. Control. Release 243, 172–181 (2016). 5. Huynh, E. et al. Porphyrin Shell Microbubbles with Intrinsic Ultrasound and Photoacoustic Properties. J. Am. Chem. Soc. 134, 16464–16467 (2012). 6. Yan, X., Scherphof, G. L. & Kamps, J. A. A. M. Liposome Opsonization. J. Liposome Res. 15, 109–139 (2005). 7. Harashima, H., Matsuo, H. & Kiwada, H. Identification of proteins mediating clearance of liposomes using a liver perfusion system. Advanced Drug Delivery Reviews 32, 61–79 (1998). 8. Shin, M. L., Paznekas, W. A. & Mayer, M. M. On the Mechanism of Membrane Damage by Complement: The Effect of Length and Unsaturation of the Acyl Chains in Liposomal Bilayers and the Effect of Cholesterol Concentration in Sheep Erythrocyte and Liposomal Membranes. J. Immunol. 120, (1978). 9. Warram, J. M. et al. Biodistribution of P-selectin targeted microbubbles. J. Drug Target. 22, 387–394 (2014). 10. Tartis, M. S. et al. Dynamic microPET imaging of ultrasound contrast agents and lipid delivery. J. Control. Release 131, 160–166 (2008). 11. Willmann, J. K. et al. Targeted Microbubbles for Imaging Tumor Angiogenesis: Assessment of Whole-Body Biodistribution with Dynamic Micro-PET in Mice. Radiology 249, 212–219 (2008).

Image/Figure:

https://s3.amazonaws.com/amz.xcdsystem.com/1E8A4501-BB41-A02A-1D3B9882B798BFAA_abstract_File10351/GA367_ImageFigure_0513095807.png

Image/Figure Caption: Porphyrin-lipid microbubbles enable longitudinal quantitative biodistribution measurements via PET imaging, hyperspectral fluorescence, and gamma counting. A) A series of microbubbles with varying lipid chain lengths (C16, C18) and shell charge (+/- anionic phosphatidic acid lipid) were designed and characterized. B) Exemplary data of serial PET and hyperspectral fluorescence images taken over 48 hours. The following plots

utilize PET data for which 3D contours for each individual organ were constructed and analyzed. C) Liver displays increased signal at early timepoints with dependence on both chain length and charge, showing highest signal for C16PA microbubbles. D) Spleen displays progressive and sustained increased signal for C18 microbubbles with or without PA compared to C16 microbubbles. E) In 4T1 orthotopic breast cancer tumors, C18nPA microbubbles displayed the greatest overall accumulation and degree of improvement following focused ultrasound treatment. F) Relative percentage change in tumor signal comparing FUS-treated and FUS-untreated tumours, illustrating that lipid composition has a substantial influence on the efficacy of a microbubble-based delivery system.

Full Name of Abstract's 1st Author : Alexander Dhaliwal

First Name: Alex

Last Name: Dhaliwal

Email: alex.dhaliwal@mail.utoronto.ca

Organization: University of Toronto

Country: Canada

ID: GA368
Protein L functionalized microparticles for detection of surface markers in heterogeneous colorectal lesions

Saleh Ramezani, The University of Texas MD Anderson Cancer Center UTHealth Graduate School of Biomedical Sciences, saleh.ramezani@uth.tmc.edu

---

Category: Oncology

Abstract Body : Introduction: Despite recent efforts to implement screening programs, colorectal cancer (CRC) remains the third leading cause of cancer-related deaths among both men and women in the United States (1). Because most colorectal lesions originate from the epithelial cells lining the luminal surface of the colon, biomarkers expressed on the polyp or lesion surface present an opportunity for early, real-time, in vivo detection of pre-cancerous lesions. Preliminary studies from our group have demonstrated the feasibility of using antibody-functionalized hyperpolarized (HP) silicon micro- and nano-particles to detect tumors expressing MUC1, a mucin glycoprotein aberrantly expressed in CRC (4). Although such surface-functionalized microparticles (MPs) have great potential value in identifying early polyps/lesions, the complex biological signatures of these lesions merit the concurrent use of multiple biomarkers, to increase specificity in detection. We envision that microparticles with a "universal" surface functionalization by the IgG-binding Protein L would enable modular incorporation of multiple antibodies, against multiple targets. In the present work, we demonstrate the utility of this method with our existing MUC1+ cell systems and tissues. We hypothesize that CRC-targeted microparticles will provide ultrasensitive, non-invasive molecular imaging agents for detection of the majority, if not all, of the CRC lesions. Methods: CRC cell lines (HT29-MTX, SW480, HCT116, and CACO2), and paraffin-embedded sections of primary polyp tissues representing the most common types of colorectal polyps (hyperplastic, sessile serrated, tubular, and villous/tubulovillous), were stained with various antibodies including EGFR, EpCAM, and MUC1 to determine the smallest subset of biomarkers that would collectively identify the most common subtypes of colorectal polyps. Micron-sized iron oxide magnetic beads, pre-coated with protein L, were used in this study as proof-of-concept particles for in vitro and ex vivo binding experiments. MUC1+ (HT29-MTX and SW480) and MUC1- (CACO2) cell lines were incubated with microparticles (MPs) conjugated to MUC1 antibody and a fluorescent dye. Cell lines were imaged with a confocal microscope after an hour of incubation and a wash step. In a separate strategy, the colon tissue of human (hu) MUC1-expressing, Apcmin/+ mice with colorectal tumors, and Apcmin/+ mice with colorectal tumors that do not express huMUC1 were removed, cut longitudinally, and fixed with 4% (v/v) PFA for 12 hours. The tissue then was incubated with MUC1 targeting particles and imaged with a confocal microscope. In all experiments, normal mouse IgG antibody served as control. Results: The primary polyp tissue staining showed differential expression of the cancer epitope of MUC1 across different polyp subtypes. In cell line binding assay, MUC1 antibody-conjugated MPs bound specifically to MUC1+ HT29-MTX and SW480 cells. There was no binding or minimal binding of MUC1 functionalized MPs to MUC1- CACO2 cell lines (Fig 1.). In fresh, fixed tissue, MUC1 functionalized MPs bound to huMUC1 colorectal tumors with minimal binding of

MPs to normal adjacent tissue in both targeting and control groups. Conclusion: Protein L coated MPs can be functionalized with antibodies to target CRC surface markers in vitro. Ongoing work seeks to functionalize MPs with additional CRC targeting antibodies to specifically recognize and target heterogeneous lesion surfaces to achieve early, real-time, and potentially non-invasive, detection of pre-cancerous lesions. Acknowledgments: This study was supported by the UTHealth Innovation for Cancer Prevention Research Training Program Pre-doctoral Fellowship (Cancer Prevention and Research Institute of Texas grant # RP160015); Cancer Prevention and Research Institute of Texas (CPRIT; RP180164); US National Cancer Institute (NCI; U01 CA214263 and R21 CA185536), Institutional Research Grants and a Startup grant from MD Anderson Cancer Center.

References: 1. Siegel RL, Miller KD, Jemal A. Cancer statistics, 2020. CA Cancer J Clin. 2020 Jan 1;70(1):7–30. 2. Ahn SB, Han DS, Bae JH, Byun TJ, Kim JP, Eun CS. The Miss Rate for Colorectal Adenoma Determined by Quality-Adjusted, Back-to-Back Colonoscopies. Gut Liver. 2012 Jan;6(1):64–70. 3. Nancy Baxter and Linda Rabeneck. ICES Report: New Findings about the Risks and Limitations of Colonoscopy Used in the Early Detection of Colorectal Cancer. Healthc Q. 2009 Apr 15;12(2):24–5. 4. Pudakalakatti S, Enriquez J, McGowan C, Ramezani S, Davis J, Zacharias N, et al. Hyperpolarized MRI with Silicon Micro and Nanoparticles: Principles and Applications. WIREs Nanomedicine Nanotechnolgoy. 2021;

Image/Figure:

https://s3.amazonaws.com/amz.xcdsystem.com/1E8A4501-BB41-A02A-1D3B9882B798BFAA_abstract_File10351/GA368_ImageFigure_0513095816.png

Image/Figure Caption: Figure 1. MUC1 functionalized MPs identify MUC1 positive cell lines. A. MPs functionalized with MUC1 antibody (black particles) bind specifically to MUC1+ HT29-MTX cell lines. B. Normal mouse IgG functionalized MPs do not bind to MUC1+ HT29-MTX cell lines. C. MUC1+ functionalized MPs do not bind to MUC1- CACO2 cell lines D. MPs functionalized with normal moue IgG antibody do not bind to CACO2 cell lines.

Full Name of Abstract's 1st Author : Saleh Ramezani

First Name: Saleh

Last Name: Ramezani

Email: saleh.ramezani@uth.tmc.edu

Organization: The University of Texas MD Anderson Cancer Center UTHealth Graduate School of Biomedical Sciences

Country: United States

ID: GA369

Exploring the effects of SBRT on the pancreatic tumor microenvironment using intravital fluorescence microscopy

Timothy Samuel, University Health Network, tim.samuel@mail.utoronto.ca

---

Category: Oncology

Abstract Body : Background: Despite decades of improvements in cytotoxic therapy, the current standard of care for locally advanced pancreatic cancer (LAPC) provides, on average, only a few months of survival benefit.1 Recently, Stereotactic Body Radiation Therapy (SBRT), a technique that accurately delivers high doses of radiation to tumors, has emerged as a promising therapy to improve local control of LAPC, however, its effects on the tumor microenvironment are still poorly understood.2 Our group and others have shown that high-dose radiotherapy can cause significant damage to tumor blood vessels.3,4 Thus, we hypothesize that this vascular damage may further lead to tumor hypoxia, which can potentially generate a more aggressive tumor phenotype. Exploring the effects of SBRT on the pancreatic tumor microenvironment (including hypoxia) can help guide the development of more effective treatments. Methods: NRG mice were orthotopically inoculated with a human pancreatic cancer cell line (BxPC3) engineered to constitutively express red fluorescent protein (RFP), as well as green fluorescent protein (GFP) under hypoxic conditions (driven by a 5x Hypoxia Response Element promoter). After five weeks of tumor growth, a glass imaging window was surgically implanted over the abdomen to provide optical access to the tumor. Mice were split into two groups (n=5/group), with one receiving SBRT (5x8Gy, given in daily fractions) using a small-animal irradiator (X-Rad 225Cx), and the other group being left untreated. Intravital fluorescence microscopy (Zeiss LSM710) was performed before and (1, 4, 7, and 14 days) after treatment to quantify changes in the pancreatic tumor microenvironment, including blood vessels and fibrillar collagen (using APC-CD31 and second harmonic generation, respectively). Immunohistochemical staining was also performed on tissues to validate in vivo findings. Results: Contrary to our hypothesis, a decrease in tumor hypoxia was observed following SBRT as compared to the control group. These results were validated immunohistochemically with CA9 staining. Reoxygenation of the tumor was observed with a decrease in both tumor growth and cell density in the SBRT group. No significant differences in tumor vascularization were detected between groups. Conclusions & Future Directions: Using intravital fluorescence microscopy, we were able to demonstrate a decrease in tumor hypoxia in pancreatic tumor xenografts following 5x8Gy SBRT. This reoxygenation of the tumor was likely due to reduced demand for oxygen as a result of significant cell death and growth arrest from treatment. Understanding how this reoxygenation phenomenon occurs in a dose-dependent manner will help optimize dose/fractionation schemes for clinical SBRT.

References: References: 1. Jung, J. et al. Stereotactic body radiation therapy for locally advanced pancreatic cancer. PLoS One 14, e0214970 (2019). 2. Arnold, K. M. et al. The Impact of Radiation on the Tumor Microenvironment: Effect of Dose and Fractionation Schedules. Cancer Growth Metastasis 11, 1179064418761639 (2018). 3. Maeda, A. et al. In Vivo Imaging

Reveals Significant Tumor Vascular Dysfunction and Increased Tumor Hypoxia-Inducible Factor-1α Expression Induced by High Single-Dose Irradiation in a Pancreatic Tumor Model. Int. J. Radiat. Oncol. Biol. Phys. 97, 184–194 (2017). 4. Castle, K. D. & Kirsch, D. G. Establishing the impact of vascular damage on tumor response to high-dose radiation therapy. Cancer Research 79, 5685–5692 (2019).

Image/Figure:

https://s3.amazonaws.com/amz.xcdsystem.com/1E8A4501-BB41-A02A-1D3B9882B798BFAA_abstract_File10351/GA369_ImageFigure_0513095941.png

Image/Figure Caption: (A) A laser-scanning confocal microscope (Zeiss LSM710) retrofitted with a custom, 3D-printed mouse imaging stage. (B) The pancreatic tumor microenvironment visualized using intravital fluorescence microscopy. Red = BxPC3 pancreatic cancer cells, green = HIF-activity (hypoxia), cyan = blood vessels, white = fibrillar collagen. (C) SBRT suppresses tumor hypoxia (as measured by GFP signal) 1-day post-SBRT (n=5/group, $p < 0$ .05).

Full Name of Abstract's 1st Author : Timothy Samuel

First Name: Timothy

Last Name: Samuel

Email: tim.samuel@mail.utoronto.ca

Organization: University Health Network

Country: Canada

ID: GA371

A Quantitative and Translational Biomarker for NAFLD Using 19F MRI

Deanne Lister, University of California San Diego, drlister@health.ucsd.edu

---

Category: Immunology: Inflammation & Infection

Abstract Body : Introduction Non-alcoholic fatty liver disease (NAFLD) affects ~25% of the global population, and can progress to non-alcoholic steatohepatitis (NASH), cirrhosis and hepatocellular carcinoma. Diagnostic imaging of NAFLD through ultrasound and elastography is routinely performed clinically, but diagnosis is subjective and occurs late in pathogenesis. Invasive liver biopsy remains the gold standard for assessing NAFLD/NASH. Quantitative, non-invasive biomarkers that are sensitive to early changes in liver pathology are needed for diagnosis and patient management, with particular interest in the early inflammatory response. Perfluorocarbon (PFC) nanoemulsion, administered systemically is taken up by phagocytic cells of the reticuloendothelial system including resident liver Kupffer cells, and peripheral macrophages that traffic to inflammatory sites. 19F MRI can then be used to detect PFCs in vivo. We assess the impact of high fat diet (HFD) on 19F PFC uptake in the liver using MRI, compared with proton MRI based proton density fat fraction (PDFF) (1) and T1 relaxation time (2). Methods NALFD was induced in 8-9-week-old female C57BL/6 mice HFD (40% fat, 2% cholesterol 20% fructose). Control animals received standard (Std) diet. MRI occurred at 6, 9 and 12 weeks post-diet start. A PFC imaging agent (VS-1000H, Celsense) was administered to mice two days before first imaging. Imaging was performed using an 11.7 T MRI system (Bruker) with a 1H/19F dual-tuned birdcage coil. A rapid relaxation enhancement (RARE) protocol was used to acquire 19F, and 1H anatomical images for co-registration and T1 maps. PDFF was quantified using a multi-gradient-echo (MGE) sequence. Analysis including fitting of MGE in/out of phase data (1) was accomplished in VivoQuant (Invicro) . Subsets of mice were sampled at each imaging time point for H&E and immunohistochemistry (IHC) staining. Results HFD mice show significant increases in liver volume compared to Std. diet mice (Fig. 1a). Moreover, the total amount of liver PFC remains significantly higher in HFD mice compared to controls at all time points (80-157%, Fig. 1b). When normalizing total liver PFC to tissue volume (Fig. 1c), HFD mice show a significant reduction in PFC density compared to Std diet mice at 9 weeks (41%) and 12 weeks (57%). The liver PDFF of Std diet mice treated with vehicle ranges from 5-8% (Fig. 1d). HFD mice show significantly higher PDFF at all time points (~36%). T1 relaxation times of Std diet mice treated with vehicle is ~2.35 s (Fig.1e). HFD mice show significantly reduced T1 values compared to Std diet at all time points (56-59%). H&E and IHC confirmed significantly higher steatosis and inflammation in HFD versus Std diet mice (data not shown). Discussion and Conclusions Overall, the MRI-based in vivo biomarkers studied detected the impact of HFD on liver with statistical significance; the total 19F-uptake increased, the 19F-density decreased (due to increased liver volume), PDFF increased and 1H T1 decreased. These findings are consistent with significant increases in steatosis as detected by PDFF, T1 values, and histology relative to normal mice. We speculate that the increase in total 19F-uptake with HFD is due to influx of inflammatory macrophages. However, the degree to which Kupffer cell activation occurs, which may also affect PFC uptake, or change in density

during disease course is unknown. Future experiments involving flow cytometry of liver tissues could resolve this question by separating Kupffer and peripheral cell populations that are PFC positive. Moreover, chronic administration of HFD resulted in marked disease in the liver of all animals prior to the start of imaging. Initiation of imaging earlier in the disease time course could enable detection of the onset of disease and provide a biomarker for protective effects of therapeutics prior to significant liver injury.

References: [1] Caussy C, Reeder SB, Sirlin CB, Loomba R. Non-invasive, quantitative assessment of liver fat by MRI-PDFF as an endpoint in NASH trials. Hepatol. 2018;68:763-772. [2] Marzola P, Boschi F, Moneta F, Sbarbati A, Zancanaro C. Preclinical In vivo Imaging for Fat Tissue Identification, Quantification, and Functional Characterization. Front. Pharmacol. 2016;7:336.

Image/Figure:

https://s3.amazonaws.com/amz.xcdsystem.com/1E8A4501-BB41-A02A-1D3B9882B798BFAA_abstract_File10351/GA371_ImageFigure_0513102943.PNG

Image/Figure Caption: MRI biomarkers for NALFD. HFD mice showed significant liver enlargement (a) compared to Std diet mice ($p < 0.05$). The total amount of liver PFC (b) remained significantly higher in HFD mice at 12 weeks ($p < 0.05$). When normalizing total liver PFC to tissue volume, liver PFC density (c) was significantly lower in HFD mice than Std diet controls at 9- and 12 weeks ($p < 0.05$). Proton MRI biomarkers confirmed significant increases in proton density fat fraction (d) in HFD mice ($p < 0.05$), and significantly reduced T1 relaxation times (e) compared to Std diet controls ($p < 0.05$).

First Name: Deanne

Last Name: Lister

Email: drlister@health.ucsd.edu

Organization: University of California San Diego

Country: United States

ID: GA372

Aortic Calcification in Prostate Cancer and Diabetes

Helene Chesnais, Penn Medicine, chesnais@sas.upenn.edu

Category: Oncology

Abstract Body : Introduction Type II diabetes mellitus has been known to be a significant risk factor for the development of cardiovascular disease (CVD). Amongst diabetics, CVD is the most prevalent cause for morbidity and mortality around the world. Studies have suggested that calcification is a key pathological feature of patients with diabetes and CVD. One such study found that patients with diabetic nephropathy had significantly greater prevalence of coronary artery calcification than normoalbuminuria diabetic patients. 18F-sodium fluoride (18F-NaF) positron emission tomography and computed tomography (PET/CT) is an imaging technique that has been used to investigate calcification activity in the human body. 18F-NaF PET/CT is also approved for the monitoring of bone metastases in prostate cancer. Research on the association between diabetes and prostate cancer suggests that patients with diabetes have a lower risk of developing prostate cancer. However, these studies have not investigated the effect of diabetes on aortic calcification in prostate cancer. Methods Our study included 101 males (ages 53-91) with prostate cancer who had undergone 18F-NaF PET/CT. The resulting mean (standard deviation) BMI was 29.1 (4.7) kg/m2. Mean tracer dose and time to scan were 7.8 (2.5) mCi 18F-NaF and 69.4 (14.8) minutes. Patients who had diabetes type II were identified from physician notes or lab values. An imaging processor (Fiji PET/CT Viewer) was used to manually segment each axial slice of the aorta from the top of the aortic arch to the end of the common iliac arteries, Figure 1. The CT segmentation was overlaid onto the PET images to calculate the mean and maximum Standard Uptake Values (SUVmean and SUVmax) of the aorta. Aortic SUVmean and SUVmax were compared with age and BMI. Aortic SUVmean and SUVmax were then compared between patients with and without type II diabetes. In order to correct for the effect of BMI or dose on uptake, a multiple regression analysis was performed to test for the effect of BMI, dose, and diabetes on SUVmean and SUVmax. Results We identified 21 cases of type II diabetes within the 101 patients. 71 patients did not have a history of type II diagnosis, and 9 had insufficient information in their charts to determine their diabetic status. Diabetic patients had higher aortic SUVmean ($p = 0.015$) and SUVmax ($p = 0.049$) than non-diabetic patients, Figure 2. SUVmean and SUVmax were correlated with BMI ($r = 0.24$, $p = 0.0199$ for mean; $r = 0.25$, $p= 0.0129$ for max) but not age. A diagnosis of type II diabetes was still correlated with higher SUVmean ($p = 0.026$) after correcting for BMI and tracer dose, whereas dose ($p=0.006$) and BMI ($p=0.016$) were stronger predictors of SUVmax than a diagnosis of diabetes. Conclusion Our results demonstrate a correlation between type II diabetes and increased calcification of the aorta as measured by higher 18F-NaF PET/CT aortic SUVmean in prostate cancer patients. This suggests that, while patients with diabetes have a lower risk of developing prostate cancer, patients who have both conditions may have a poorer cardiovascular profile than patients with prostate cancer and no diabetes. Future studies should elucidate the potential of 18F-NaF PET/CT to assess atherosclerosis in high-risk prostate cancer patients with diabetes.

Image/Figure:

https://s3.amazonaws.com/amz.xcdsystem.com/1E8A4501-BB41-A02A-1D3B9882B798BFAA_abstract_File10351/GA372_ImageFigure_0513104751.png

Image/Figure Caption: (Left). Sample aortic segmentation of the aortic arch, thoracic aorta, and abdominal aorta. (Right) Aortic SUVmean and SUVmax in diabetic versus non-diabetic patients with quantile pots. Diabetic patients have higher SUVmean ($p = 0.015$) and SUVmax ($p = 0.049$)

First Name: Helene

Last Name: Chesnais

Email: chesnais@sas.upenn.edu

Organization: Penn Medicine

Country: United States

ID: GA373

Automated segmentation and quantification of simultaneous PET/MRI for monitoring islet cell transplantation with Deep Learning

Hasaan Hayat, Michigan State University, hayathas@msu.edu

Category: Computational & Data Science

Abstract Body : Current methods of monitoring islet cell transplants for Type 1 diabetes (T1D) using MRI are limited by its low sensitivity and inability to differentiate signals between live and dead cells post-transplantation. Simultaneous PET/MRI has greater sensitivity and ability to visualize cell metabolism. However, this new dual modality tool currently faces two major challenges in its use for monitoring cell transplantation. Primarily, PET signal decay and spatiotemporal change in radioactivity hinder quantification of the transplant region and prediction of the transplanted cell number. Furthermore, selection bias from different radiologists renders human error in region of interest (ROI) selection. This calls for the development of artificial intelligence (AI) algorithms for the automated analysis of PET/MRI of cell transplantation. Here, we combined K-means++ for ROI segmentation with a Convolutional Neural Network (CNN) to predict radioactivity and cell number in the transplant ROI. To train the algorithm with in vitro data, 3D-printed phantoms were generated in varying shapes. BetaTC6 cell lines were sequentially labeled with VivoTrax (460ul of 5.5ug/ul stock solution per 25 cm² flask, 24 h @ 37 °C) and 18F-FDG (5.5mCi per 25 cm² flask, 1 h @ 37 °C) prior to imaging and dispersed in 1% agarose gel in the phantoms in various cell numbers. Radioactivity (uCi) measurements of the phantoms were recorded using a dose calibrator after labeling and before scanning. Static PET and T2Map MRI were acquired for all phantoms. Different k-values were tested for segmentation of in vitro data using the elbow method and raw PET volumes with radioactivity values were used to train the CNN on ground truth. The output from K-means++ on coregistered images used the segmented PET ROI as a mask to segment the MRI region. After scanning, inductively coupled plasma optical emission spectroscopy (ICP-OES) was used to determine actual iron content in the ROI of the phantoms. Iron staining was performed to confirm the presence of nanoparticles in the cells. Upon training the CNN to a minimum loss value and confirmation of dose prediction within 1μCi, the algorithm was programmed to estimate cell number by back-calculating to the initial timepoint labeling via F-18 half-life equation. In vivo data was then generated by transplanting the labeled betaTC6 cells under the left kidney capsule of mice (n=5). Image data and radioactivity values were acquired for all mice. The algorithm's performance was then tested on the in vivo data using intraclass correlation coefficient (ICC). Results from the elbow method showed that a k-value of 3 has the least sum-square errors (SSE) and was elected for PET image segmentation throughout the rest of the study (Fig. 1 A). Dose calibrator measurements of cell radioactivity after labeling indicated a linear correlation between cell number and dose response (Fig. 1 B). Initial training on ground truth indicates decreasing loss value (MSSE)in the activity range of 5 uCi to 60 uCi (Fig. 1 C). In vivo PET/MRI data indicates transplant location of cells with the overlay showing both MRI and PET signal from the cells under the left kidney capsule (Fig. 1 D). Testing of the algorithm indicates an ICC score with a high degree of agreement with the dose calibrator value

and actual transplanted cell number. Here, we observed the ability of combined machine learning and deep learning to segment a PET/MRI ROI and predict radioactivity and cell number in the image. This provides a novel tool for monitoring islet and other cell transplantation therapies through PET/MRI. It also unlocks a dynamic approach to automated, standardized segmentation and quantification of radioactivity of a ROI in simultaneous PET/MRI for radiolabeled nanodrug applications.

Image/Figure:

https://s3.amazonaws.com/amz.xcdsystem.com/1E8A4501-BB41-A02A-1D3B9882B798BFAA_abstract_File10351/GA373_ImageFigure_0513105036.png

Image/Figure Caption: Figure 1. Automated segmentation and quantification of simultaneous PET/MRI for monitoring islet cell transplantation with machine learning and deep learning. A. K-means++ segmentation of PET of 'M' shaped cell phantom using k-value of 2,3, and 4. B. Dose response measurements of increasing cell numbers (2.5M, 1.25M, 0.625M, 0.312M, 0.16M; M = million) measured from dose calibrator and used for training the CNN algorithm. C. Minimum Sum Squared Error for prediction of radioactivity (and cell number) after first round of algorithm training. D. (Left) Coronal slice of T2Map MRI of mouse transplanted with labeled cells under the left kidney capsule (indicated by red arrow); (Right) Merged PET/MRI Image showing the origination of the PET signal (algorithm predicted 4.2 uCi/0.625M cells in ROI) from the left kidney capsule region where MRI signal colocalized.

Full Name of Abstract's 1st Author : Hasaan Muhammad Hayat

First Name: Hasaan

Last Name: Hayat

Email: hayathas@msu.edu

Organization: Michigan State University

Country: United States

ID: GA374

Micro versus nano: Comparing supramolecular strategies for porphyrin theranostic probe delivery to infiltrative 9L rat glioblastoma tumours

Maneesha Rajora, University of Toronto, maneesha.rajora@mail.utoronto.ca

---

Category: Oncology

Abstract Body : Introduction Despite the use of aggressive surgical, radiation and chemo-therapies, glioblastomas remain highly lethal, incurable brain tumours with a mere 6.8% five-year survival rate.1 This poor prognosis is rooted in the diffuse infiltration of tumour cells beyond surgical margins, leading to incomplete tumour resection, inevitable tumour regrowth and patient death.2 There is consequently a dire clinical need for glioblastoma therapies that target tumour infiltrates; a need that can be addressed by porphryin theranostics. Porphyrins are multimodal organic probes whose preferential accumulation in tumour versus healthy tissue can be leveraged alongside their red/NIR fluorescence to 1) maximize tumour resection via fluorescence-guided surgery (FGS)3, 4 and 2) impart local, healthy tissue-sparing glioblastoma tumouricidal effects through photodynamic therapy (PDT). Despite these advantages, the clinical utility of porphyrins for glioblastoma treatment is limited by their poor transport across the intact blood-brain barrier (BBB) in infiltrative glioblastoma. Supramolecular porphyrin drug-delivery platforms, particularly nanoparticles and microbubbles, may address this limitation. Actively-targeted porphyrin nanoparticles (A-pNP) comprise surface ligands that target receptors at the BBB and tumour cells to facilitate glioblastoma-specific porphyrin delivery.5 This targeted delivery may be enhanced by microbubble-enabled MRI-guided focused ultrasound (MB-MRgFUS), an emerging platform that transiently and safely opens the BBB via ultrasound-triggered microbubble oscillation within target vasculature. This focal BBB disruption has been shown to enhance drug delivery to glioblastoma tumours using conventional co-delivery of lipid-microbubbles (MB) and drug agents, or via all-in-one drug-loaded microbubbles.6, 7 Collectively, A-pNPs, co-delivery MB-MRgFUS and all-in-one MB-MRgFUS strategies are thus promising avenues to explore for trans-BBB glioblastoma porphyrin delivery. Objective To compare the trans-BBB, glioblastoma-specific porphyrin delivery efficacy of three nano and micro-MRgFUS supramolecular platforms: 1) A-pNPs, 2) A-pNPs co-delivered with MB-MRgFUS, and 3) all-in-one porphyrin-loaded microbubbles (pMB-MRgFUS). Methodology A-pNPs, pMBs and porphyrin-devoid MBs were fabricated and characterized using literature protocols.5, 8 MRgFUS was administered to healthy or 9L dual-tumour-bearing rats using an established feedback-controlled system9 (see Figure below for details). Results Similarly effective MRgFUS BBB disruption was achieved by pMBs and MBs in both healthy and tumour tissue as evaluated by gadolinium-T1w MRI. Despite yielding similar bulk vasculature effects, the supramolecular platforms had distinct porphyrin delivery efficacies. In healthy rats, A-pNPs were able to facilitate similar levels of trans-BBB porphyrin delivery as when combined with MB-MRgFUS. This delivery was approximately six and two-fold higher than that via pMBs in unsonicated and sonicated tissue respectively. The A-pNPs also outperformed the pMBs when combined with MB-MRgFUS in delivering porphyrin to infiltrative 9L glioblastoma tumours, whereby the conventional A-pNP/MB-MRgFUS co-delivery strategy yielded an 8-fold higher

porphyrin tumour concentration and substantially higher fluorescence contrast at tumour sites compared to the all-in-one pMB/MRgFUS strategy. The porphyrin delivery efficacy of A-pNP/MB-MRgFUS could be amplified by increasing the A-pNP dose ten-fold while maintaining microbubble dose; dosing that was unfeasible for pMBs. Overall, co-delivery of A-pNP and MB-MRgFUS exhibited effective trans-BBB, glioblastoma-specific porphyrin delivery capabilities superior to A-pNP on its own or all-in-one pMB-MRgFUS. Impact This study overcomes the BBB as a primary barrier in delivering porphyrins to infiltrative glioblastoma via A-pNP/MB-MRgFUS, allowing the multitude of advantages of porphyrin-FGS and PDT to become clinically viable. Furthermore, given the increasing focus on using drug-loaded microbubbles within the field of MRgFUS, this study also has implications beyond porphyrin delivery. To the best of our knowledge this is the first in vivo orthotopic glioblastoma study to compare the trans-BBB, tumour-specific drug-delivery efficacy of drug-loaded microbubble-MRgFUS to conventional co-delivery MRgFUS. It highlights the advantages of the co-delivery strategy and demonstrates the limitation of drug dosing still faced by all-in-one microbubbles. This knowledge will invaluably inform more optimal design of microbubbles and MRgFUS for CNS applications.

References: 1. Q. T. Ostrom, G. Cioffi, H. Gittleman, N. Patil, K. Waite, C. Kruchko and J. S. Barnholtz-Sloan, Neuro Oncol., 2019, 21, v1-v100. 2. A. Giese, R. Bjerkvig, M. E. Berens and M. Westphal, J. Clin. Oncol., 2003, 21, 1624-1636. 3. H. Stepp, T. Beck, T. Pongratz, T. Meinel, F. W. Kreth, J. C. Tonn and W. Stummer, J. Environ. Pathol. Toxicol. Oncol., 2007, 26, 157-164. 4. W. Stummer, U. Pichlmeier, T. Meinel, O. D. Wiestler, F. Zanella and H.-J. Reulen, The Lancet Oncology, 2006, 7, 392-401. 5. M. A. Rajora, L. Ding, M. Valic, W. Jiang, M. Overchuk, J. Chen and G. Zheng, Chem. Sci., 2017, 8, 5371-5384. 6. T. Mainprize, N. Lipsman, Y. Huang, Y. Meng, A. Bethune, S. Ironside, C. Heyn, R. Alkins, M. Trudeau, A. Sahgal, J. Perry and K. Hynynen, Sci. Rep., 2019, 9. 7. C. Y. Ting, C. H. Fan, H. L. Liu, C. Y. Huang, H. Y. Hsieh, T. C. Yen, K. C. Wei and C. K. Yeh, Biomaterials, 2012, 33, 704-712. 8. E. Huynh, B. Y. Leung, B. L. Helfield, M. Shakiba, J. A. Gandier, C. S. Jin, E. R. Master, B. C. Wilson, D. E. Goertz and G. Zheng, Nat Nanotechnol, 2015, 10, 325-332. 9. N. McDannold, Y. Zhang, J. G. Supko, C. Power, T. Sun, C. Peng, N. Vykhodtseva, A. J. Golby and D. A. Reardon, Theranostics, 2019, 9, 6284-6299.

Image/Figure:

https://s3.amazonaws.com/amz.xcdsystem.com/1E8A4501-BB41-A02A-1D3B9882B798BFAA_abstract_File10351/GA374_ImageFigure_0514015338.png

Image/Figure Caption: The three porphyrin supramolecular platforms studied (a) included actively-targeted porphyrin nanoparticles (A-pNP), porphyrin microbubbles (pMB) and co-delivery of A-pNP and porphyrin-devoid microbubbles (MB). Porphyrin was incorporated into A-pNP and pMB as a lipid-conjugate within the particle shells. A-pNP/MB-enabled MRI-guided focused ultrasound (MB-MRgFUS) and pMB-MRgFUS displayed similar levels of BBB disruption (b) in healthy Wistar rats (2 sonication sites, indicated by yellow arrow) and 9L dual tumour-bearing Wistar rats (1 sonication site) as evident from (i) representative T1w MRI images post Gd contrast administration and (ii) associated quantification of Gd contrast enhancement relative to unsonicated regions. However, the strategies yielded differing degrees of porphyrin delivery (c) across the BBB to healthy brain parenchyma and 9L tumours as determined by tissue homogenate spectrofluorometry (i) and ex vivo Maestro fluorescence

imaging (ii; yellow and pink circles represent unsonicated and sonicated tumours respectively). MRgFUS was conducted using a feedback controlled acoustic cavitation setup to ensure sonication was matched by cavitation thresholds (0.56 MHz, 10 ms burst length, 1000 ms period, 120 s duration, 0.5 emission target) after the administration of either saline (n=3) A-pNP + MB (n=4) or pMB (n=4) (0.35 mg/kg porphyrin, 3x109 MB/kg). The two microbubbles were size matched via centrifugation size isolation. Animals were euthanized via transcardial perfusion to remove intravascular porphyrin, and transvascular porphyrin delivery was assessed with ex vivo hyperspectral fluorescence imaging (Maestro, red filter, 1000 ms exposure) and quantified by spectrofluorometry of tissue homogenates.

Full Name of Abstract's 1st Author : Maneesha Amrita Rajora

First Name: Maneesha

Last Name: Rajora

Email: maneesha.rajora@mail.utoronto.ca

Organization: University of Toronto

Country: Canada

ID: GA375

Comparative analysis of spatial image texture features for predicting response to therapy in molecular contrast-enhanced ultrasound of pre-clinical model of colorectal metastases

Cody Keller, Stanford University, cody.a.keller@gmail.com

Category: Oncology

Abstract Body : Introduction 3D molecular contrast-enhanced ultrasound (3D mCEUS) provides a powerful quantitative assessment for the functional monitoring of tumor response to oncologic therapy.1-4 Parameters commonly used employ the differential targeted enhancement (dTE), requiring a high mechanical index (MI) ultrasound pulse.2 This limits the feasibility of clinical translation of the technique given evidence of bioeffects in tissues exposed to high-MI ultrasound.5 In this study, quantitative image features (texture and histogram-based features) are extracted from static 3D parametric maps of 3D mCEUS cines with and without contrast destruction. By comparing statistical properties of extracted image features and performance predicting response to anti-angiogenic therapy, we promote furthering clinical translation of this technique in cancer treatment monitoring applications by obviating the need for contrast destruction. Methods Mice bearing LS174T tumors were randomized to serial treatment (n=8; Bevacizumab 10 mg/kg days 0, 1, 3, 7) or control (n=8; saline). A separate cohort with LS174T tumors (n=18) was used to assess repeatability of measurements through repeated acquisition. 3D mCEUS cine images with vascular endothelial growth factor receptor 2 targeted contrast were obtained on days 0, 1, 3, and 10 using Philips EPIQ 7 with an X6-1 transducer. 3D parametric maps were generated from 4D cines using intensity projection methods and other parameters obtained through a sliding window method6 then stratified by breadth of sliding window and requirement of destruction pulse. 91 image features extracted from each parametric map for each mouse, and each scan day were selected for repeatability (intraclass correlation coefficient; ICC≥0.8) and detection of response to therapy (Wilcoxon signed-rank test; p Results/Discussion 54 of 91 image features were repeatable in at least one parametric map as assessed in the separate repeatbility cohort. The average intensity projection (AIP) map had the most repeatable features at 47. Logistic regression and linear determinant analysis showed highest performance (AUC 1.0, AUC 1.0 respectively) predicting response to therapy with only features extracted from before contrast destruction. After recursive feature elimination, only AIP features remained and several demonstrated strong linear correlations (Spearman $\rho \geq 0.8$) with dTE parameters. Several of these AIP image features also showed separation of measured values between treated and control animals at scan day 1. Generating dTE maps involves taking the difference of AIP maps and a post-destruction baseline intensity projection to calculate the bound fraction of molecular contrast. While parameters extracted from dTE maps are the common standard in the literature, unintended bioeffects of high-MI pulses5 and 5+ minute acquisition times limit feasibility of clinical translation. Conclusion Utilizing image features attuned to spatial heterogeneities characteristic of tumor vasculature, we show promising performance in early prediction of response to oncologic therapy without contrast destruction. AIP image features driving model performance show strong evidence of mutual encoding of

information with the common dTE parameters in the literature. Further study with a larger sample size and in other contexts of tumor biology/therapy are merited.

References: [1] Zhou, J, Wang, H, Zhang H, et al. 2016, 'Vegfr2-targeted three-dimensional ultrasound imaging can predict responses to antiangiogenic therapy in preclinical models of colon cancer.', Cancer Res, 2016;76(14), 4081-4089 [2] Wang, H., Kaneko, O. F., Tian, L., Hristov, D. & Willmann, J. K. Three-dimensional ultrasound molecular imaging of angiogenesis in colon cancer using a clinical matrix array ultrasound transducer. Invest. Radiol. 50, 322–329 (2015). [3] Turco, S. et al. Pharmacokinetic Modeling of Targeted Ultrasound Contrast Agents for Quantitative Assessment of Anti-Angiogenic Therapy: a Longitudinal Case-Control Study in Colon Cancer. Mol. Imaging Biol. 21, 633–643 (2019). [4] Willmann, JK, Paulmurugan, R, Chen, K, et al 2008, 'US imaging of tumor angiogenesis with microbubbles targeted to vascular endothelial growth factor receptor type 2 in mice.', Radiology, 2008;246(2), 508-518 [5] Caruso, G, Valentino, B, Salvaggio, G, et al. 2005, 'Ultrastructural biologic effects of sonography with pulse inversion and microbubble contrast in rabbit liver.', J Clin Ultrasound, 2005;33(3), 106-111 [6] El Kaffas, A, Hoogi, A, Shou, J, et al. 2020, 'Spatial Characterization of Tumor Perfusion Properties from 3D DCE-US Perfusion Maps are Early Predictors of Cancer Treatment Response', Sci Rep, 2020;10(1), 6996

Image/Figure:

https://s3.amazonaws.com/amz.xcdsystem.com/1E8A4501-BB41-A02A-1D3B9882B798BFAA_abstract_File10351/GA375_ImageFigure_0513111225.png

Image/Figure Caption: AIP: Average intensity projection, MIP: maximum intensity projection, dTE: differential targeted enhancement, STD: standard deviation, LIP: lowest intensity projection, ICC: intra-class correlation coefficient, TIC: time-intensity curve Figure 1: A Schematic summary of US imaging data acquisition. B Representative TIC for molecular imaging demonstrates the sliding-window from which parametric maps are derived. C Stepwise statistical feature selection process leading to formation of feature sets reflecting size of image dataset and/or necessity of destruction pulse. D Summary of image feature sets based on expected clinical burden for obtaining after statistical feature selection and correlation elimination.

First Name: Cody

Last Name: Keller

Email: cody.a.keller@gmail.com

Organization: Stanford University

Country: United States

ID: GA376
Whole-Abdomen Metabolic Imaging in Healthy Volunteers Using Hyperpolarized 13C-Pyruvate MRI

Philip Lee, University of California, San Francisco, philip.lee2@ucsf.edu

---

Category: Systemic Diseases (Kidney, Liver and Pancreas)

Abstract Body : Purpose: Hyperpolarized (HP) 13C MRI is a novel metabolic imaging technique enabling real-time in vivo measurements of enzyme-catalyzed pyruvate metabolism being developed to address unmet clinical needs for prostate, brain, cardiac, and kidney imaging.1–4 Of primary interest are the conversions of pyruvate to lactate via lactate dehydrogenase (LDH), which is upregulated in cancers as well as animal models of inflammation and fatty liver disease,5 and of pyruvate to alanine via alanine aminotransferase (ALT). HP 13C MRI may provide valuable metabolic biomarkers for staging and assessing treatment response in these diseases. Human clinical research studies are underway at twelve sites around the world. However, whole-abdomen imaging with HP 13C maintains a challenge, mainly due to B0 and B1 inhomogeneities, respiratory motion, and the need for broad spatial coverage. In addition, there is little baseline data about HP 13C metabolite levels in healthy people. To investigate baseline energetics and the feasibility of whole-abdomen coverage, we studied HP 13C-pyruvate metabolism in multiple organs of healthy volunteers. Methods and Materials: After IRB approval, five healthy subjects underwent HP 13C MRI on a clinical 3 T scanner (MR750, GE Healthcare, Milwaukee, WI) with a volumetric transmitter and an 8-channel receiver array (Clinical MR Solutions, Brookfield, WI) to increase spatial coverage. T1- and T2-weighted images were acquired for anatomic registration. A volumetric multi-echo Dixon scan (IDEAL IQ) was used generate B0 field maps and correct off-centered metabolite frequencies due to in-plane B0 inhomogeneities. Localized shimming was used to correct for B0 inhomogeneities through-plane. After injection of 0.43 mL/kg of 250 mM HP [1-13C]pyruvate, signals from [1-13C]pyruvate and its downstream metabolites, [1-13C]lactate and [1-13C]alanine, were acquired using a multi-slice spectrally-selective echo planar imaging acquisition2 with flip angles of 30° for pyruvate, 60° for lactate and alanine. Total scan time was 1 minute with a 3 s temporal resolution, 2×2×2 cm3 voxels, and 7-14 slices extending from the diaphragm to the kidneys. Data were phase corrected, Fourier transformed, pre-whitened and coil-combined using pyruvate to estimate the coil weights.6 Metabolite signals were summed over the entire time course and ROIs were selected within the liver, both kidneys, the pancreas, and the spleen. Results and Discussion: Figure 1(A) shows area-under-the-curve (AUC) metabolite maps (summed over the entire time course) overlaid on a T2-weighted anatomical reference from a representative healthy volunteer data set. Figure 1(B) shows the average metabolite signals computed from the ROIs of each abdominal organ (liver, kidneys, pancreas, and spleen) averaged across the five subjects with standard error bars. Absolute metabolite signals (pyruvate, lactate, and alanine) from the kidneys and spleen were 3-6 times higher than those from liver and pancreas, likely reflecting differences in overall perfusion. Figure 1(C) shows the average metabolite ratios (lactate/pyruvate and alanine/pyruvate) for each organ averaged across the five subjects. Although absolute metabolite signals were lower,

lactate/pyruvate and alanine/pyruvate ratios were both higher in the liver than in other abdominal organs (L/P: 0.38 vs. 0.17-0.21, A/P: 0.25 vs. 0.02-0.10), indicating higher production of these metabolites. Right and left kidney metabolism were symmetric as expected. The pancreas showed higher levels of alanine production relative to other organs, possibly due to high levels of protein synthesis. Conclusions: We successfully acquired HP 13C metabolic images of multiple organs throughout the abdomen with excellent spatial and temporal resolution. This broad spatial coverage will be valuable in developing novel applications of HP 13C MRI. Establishing normal values for metabolite ratios and metabolic conversion rates will serve as an important baseline for imaging cancer as well as metabolic liver diseases. Acknowledgements: This work was supported by NIH grants NIDDK 5R01DK115987 and P41 EB013598.

References: 1. Chen HY, Aggarwal R, Bok RA, et al. Hyperpolarized 13C-pyruvate MRI detects real-time metabolic flux in prostate cancer metastases to bone and liver: a clinical feasibility study. Prostate Cancer Prostatic Dis. 2020;23(2):269-276. doi:10.1038/s41391-019-0180-z 2. Gordon JW, Chen HY, Autry A, et al. Translation of Carbon-13 EPI for hyperpolarized MR molecular imaging of prostate and brain cancer patients. Magn Reson Med. 2019;81(4):2702-2709. doi:10.1002/mrm.27549 3. Cunningham CH, Lau JYC, Chen AP, et al. Hyperpolarized 13C Metabolic MRI of the Human Heart: Initial Experience. Circ Res. 2016;119(11):1177-1182. doi:10.1161/CIRCRESAHA.116.309769 4. Tang S, Bok R, Qin H, et al. A metabolite-specific 3D stack-of-spiral bSSFP sequence for improved lactate imaging in hyperpolarized [1-13C]pyruvate studies on a 3T clinical scanner. Magn Reson Med. 2020;84(3):1113-1125. doi:10.1002/mrm.28204 5. Kurhanewicz J, Vigneron DB, Ardenkjaer-Larsen JH, et al. Hyperpolarized 13C MRI: Path to Clinical Translation in Oncology. Neoplasia (United States). 2019;21(1):1-16. doi:10.1016/j.neo.2018.09.006 6. Zhu Z, Zhu X, Ohliger MA, et al. Coil combination methods for multi-channel hyperpolarized 13 C imaging data from human studies. J Magn Reson. 2019;301:73-79. doi:10.1016/j.jmr.2019.01.015

Image/Figure:

https://s3.amazonaws.com/amz.xcdsystem.com/1E8A4501-BB41-A02A-1D3B9882B798BFAA_abstract_File10351/GA376_ImageFigure_0513113834.png

Image/Figure Caption: Figure 1. (A) Representative HP 13C-pyruvate data from a healthy volunteer showing area-under-the-curve (AUC) metabolite maps (summed over the entire time course) overlaid on a T2-weighted anatomical reference. (B) Average metabolite signals for each selected abdominal organ averaged across the five subjects with standard error bars. (C) Average metabolite ratios (lactate/pyruvate and alanine/pyruvate) for each selected abdominal organ averaged across the five subjects with standard error bars.

Full Name of Abstract's 1st Author : Philip Meng-en Lee

First Name: Philip

Last Name: Lee

Email: philip.lee2@ucsf.edu

Organization: University of California, San Francisco

Country: United States

ID: GA377
3D printed targets for fluorescence guided surgical systems

Alberto Ruiz, Dartmouth College & QUEL Imaging, alberto.j.ruiz.th@dartmouth.edu

---

Category: Instrumentation

Abstract Body : The 3D printing of fluorescent materials could help develop, validate, and translate imaging technologies, including systems for fluorescence-guided surgery. Despite advances in 3D printing techniques for optical targets, no comprehensive method has been demonstrated for the simultaneous incorporation of fluorophores and fine-tuning of absorption and scattering properties. Here, we introduce a photopolymer-based 3D printing method for manufacturing fluorescent targets with tunable optical properties. The results demonstrate the ability to 3D print various individual fluorophores at reasonably high fluorescence yields, including indocyanine green (ICG). Furthermore, tuning of the absorption and reduced scattering coefficients is demonstrated within the relevant mammalian soft tissue coefficient ranges of 0.005-0.05 mm-1 and 0.2-1.5 mm-1, respectively. Fabrication of fluorophore-doped biomimicking and complex geometric structures validated the ability to print feature sizes less than 200 μm. 3D printed fluorescence targets for performance comparison of ICG-imaging systems have been developed for determining concentration (1-1000 nM), depth (0.5 - 6 mm) and resolution sensitivity. The presented targets, methods, and optical characterization techniques provide the foundation for the manufacturing of solid 3D printed fluorescent structures, with direct relevance to biomedical optics and wide adoption of fluorescence guided surgery imaging standards for performance benchmarking and cross-system comparisons.

Image/Figure:

https://s3.amazonaws.com/amz.xcdsystem.com/1E8A4501-BB41-A02A-1D3B9882B798BFAA_abstract_File10351/GA377_ImageFigure_0513114851.PNG

Image/Figure Caption: 3D printed ICG-equivalent material with tuned optical properties. a-c White-light and 800nm channel fluorescence images of (a) MRI-scanned coronary artery tree structure, (b) complex geometrical lattice cube, and (c) resolution calibration cube with sub-200 μm feature sizes. d Fluorescence emission and excitation spectra of 3DP fluorescent material and ICG-in plasma showing close overlap in spectral features. e Linearity of fluorescent intensity output for increasing laser-dye concentrations in 3DP material. f, g Measured absorption and reduced scattering coefficient spectra of the 3DP material.

First Name: Alberto

Last Name: Ruiz

Email: alberto.j.ruiz.th@dartmouth.edu

Organization: Dartmouth College & QUEL Imaging

Country: United States

ID: GA378
Chain Formation is essential for Super-Resolution MPI

Caylin Colson, University of California, Berkeley, caylin.colson@berkeley.edu

---

Category: Instrumentation

Abstract Body : Introduction: Magnetic Particle Imaging (MPI) is an emerging tracer-based modality with promising applications in molecular imaging, in vivo cell tracking, and clinical angiography. Because its unique physics takes advantage of the electronic magnetization of superparamagnetic iron oxide particles (SPIOs), MPI has an excellent safety profile, superb linear "positive contrast", ideal tissue penetration, and a sensitivity of 200 cells [1,2,3]. However, the spatial resolution of MPI is currently limited to roughly 1 mm in high gradient (up to 7 T/m) preclinical scanners. Improved MPI resolution at human scale is essential for the clinical translation of MPI. Here we investigate a novel type of MPI tracer, which we call superferromagnetic nanoparticles (SFMIOs), that have experimentally yielded both a 10x improvement in resolution and a 100x improvement in SNR [4]. We hypothesize that when unchained SPIOs are in solution, we will observe signals comparable to typical SPIO magnetic responses. However, when the FWHM and SNR dramatically improve in the signal we observe, it should be indicative of SFMIO behavior: that is, interacting SPIOs being drawn to one another and increasing the magnetic field that each individual SPIO is exposed to. We test the hypothesis that "chaining" of strongly interacting SPIOs is essential for the dramatic improvement seen in our measurements by applying pre-polarization pulses to gauge their influence on the FWHM and SNR of our signal. An initial scan showing 100% SPIO behavior had a FWHM of 5.3 mT. The final scan with dominating SFMIO behavior had a FWHM of 1 mT. Materials and Methods: Single-core magnetite nanoparticles with an oleic acid coating were synthesized via thermal decomposition at UF and at UCB [5]. The estimated concentration of said particles is 12.6 mg/mL of Fe. The magnetization response of SFMIOs in toluene as a function of pre-polarization time was measured using the UCB arbitrary wave relaxometer (AWR) [6]. Spatial resolution was quantified via the Houston Criteria by calculating the full-width-at-half-maximum (FWHM) of the PSF. The pulse sequence used was made of 10 ms pre-polarizing magnetic fields (DC, 12 mT amplitude). The particles were then excited by a linear change in amplitude (from 12 mT to -12 mT) that occurred over 50 us (20 kHz). A chain of these pre-polarizing pulses followed by 20kHz excitation was created for a total scan time of 600 ms. Results: By applying pre-polarizing (DC) magnetic pulses before excitation, we successfully measured the "chain formation time", the time point when individual SPIOs form chains, thus causing SFMIO behavior. We also show that the total received signal we measure can linearly be decomposed into two independent portions - one from the decaying population of unchained SPIOs, and the other from the growing population of chained SFMIOs. Conclusion: These observations strongly support the hypothesis that chaining of SPIOs is responsible for dramatic improvement in spatial resolution and SNR responsible for Super-Resolution MPI.

References: References: [1] Gleich, Bernhard and Jurgen Weizenecker (2005). "Tomographic imaging using the nonlinear response of magnetic particles". In: Nature 435, pp. 1214–1217. [2]

Goodwill, P. W., & Conolly, S. M. (2010). The X-space formulation of the magnetic particle imaging process: 1-D signal, resolution, bandwidth, SNR, SAR, and magnetostimulation. IEEE Transactions on Medical Imaging, 29(11), 1851–1859. [3] Zheng, B., Vazin, T., Goodwill, P. W., Conway, A., Verma, A., Ulku Saritas, E., … Conolly, S.M. (2015). Magnetic particle imaging tracks the long-term fate of in vivo neural cell implants with high image contrast. Scientific Reports, 5. [4] Tay, Zhi Wei. (2018). Novel Scanning Strategies in x-Space Magnetic Particle Imaging for Improved Imaging Performance and Theranostic Applications. Dissertation. [5] Vreeland, E. C., Watt, J., Schober, G. B., Hance, B. G., Austin, M. J., Price, A. D., … Huber, D. L. (2015). Enhanced Nanoparticle Size Control by Extending LaMer's Mechanism. Chemistry of Materials, 27(17), 6059–6066. [6] Tay, Z. W., Goodwill, P. W., Hensley, D. W., Taylor, L. A., Zheng, B., & Conolly, S. M. (2016). A High-Throughput, Arbitrary-Waveform, MPI Spectrometer and Relaxometer for Comprehensive Magnetic Particle Optimization and Characterization. Scientific Reports,

Image/Figure:

https://s3.amazonaws.com/amz.xcdsystem.com/1E8A4501-BB41-A02A-1D3B9882B798BFAA_abstract_File10351/GA378_ImageFigure_0513115241.png

Image/Figure Caption: a) 1D Point Spread Functions showing experimental 6-fold improvement in spatial resolution (a to c) Conventional low-resolution MPI b) MPI scan with conventional single-core particles c) High Resolution SFMIO scan (d,e,f) Transition from individual SPIOs state to chains responsible for SFMIO behavior can be seen as a function of the length of a pre-polarizing pulse. (d,e) Received signal can be decomposed into two orthogonal signals that comprise the SFMIO and SPIO components. d) The SPIO component of our received signal drops as a function of pre-polarization time. The first scan shows 100% SPIO response with a FWHM of 5.3 mT.. e) As the pre-polarization time increases, the SPIO contribution drops and the SFMIO contribution increases with a final FWHM of 1 mT. f) An individual measured PSF and our reconstructed version from the two decomposed signals with a pre-polarization time of 30 ms. Good agreement between the two is seen. Note the small, sharper peak that occurs around ~17 us within the excitation scan - that is the beginning of SFMIO behavior within the sample. (a) 1.1 mg/mL Vivotrax, (b) (0.21 mg/mL LodeSpin-017) (c)(25 ug/mL UF-UC Berkeley Emulsion) (d,e,f) 12.6 mg/mL

Full Name of Abstract's 1st Author : Caylin Colson

First Name: Caylin

Last Name: Colson

Email: caylin.colson@berkeley.edu

Organization: University of California, Berkeley

Country: United States

ID: GA379

Computational modeling of superferromagnetism in finite-length chains of superparamagnetic Iron Oxide tracers for use in super-resolution Magnetic Particle Imaging

Chinmoy Saayujya, University of California, Berkeley, chinmoy@berkeley.edu

---

Category: Computational & Data Science

Abstract Body : Magnetic Particle Imaging (MPI) is an emerging positive-contrast imaging modality that directly images superparamagnetic iron oxide (SPIO) tracers in the body [1]. Pre-clinical MPI has demonstrated micromolar sensitivity for tracking of stem and white blood cells, as well as in imaging of cancer, lung perfusion and abdominal bleeding [2–5]. MPI resolution is determined by the ratio of the SPIO saturation strength and the gradient field strength [1,6,13]. MPI already has excellent sensitivity and ideal contrast, linearity and penetration depth. The only significant weakness is poor spatial resolution, now about 1.5 mm in a mouse [7, 8]. All MPI studies to date assume non-interacting SPIOs. Recently, Tay et al. experimented with interacting SPIOs to dramatically improve MPI resolution [9]. They showed experimentally that high local concentrations of SPIO tracers showed order-of-magnitude improvements in both SNR and resolution [9]. Several experiments support the hypothesis that the observed super-resolution behavior is due to the formation of SPIO particle chains [9, 10, 11]. We propose that these super-resolution chains of SPIOs exhibit "superferromagnetism,'' since superparamagnetism does not exhibit remanence or coercivity [12]. Objective: We performed computational modeling of finite-length linear chains of interacting single-domain superparamagnetic particles. We show that a linear chain of ≥ 2 SPIOs couples via a positive-feedback mechanism and demonstrates magnetic hysteresis. The saturation remanence and coercivity of the multi-particle system depend on its physical parameters such as chain length, particle size, separation and magnetic susceptibility. We show that the image-blurring effects of coercivity dispersion from varying chain lengths can be mitigated, facilitating simple yet robust synthesis. Methods: We consider identical and independent SPIO chains, allowing ensemble averaging across the nth SPIO in each chain. Each nodal SPIO feels an identical applied field plus the local dipole field from neighboring SPIOs. Ensemble averaging across chains permits the use of a Langevin saturator model for each node in the chain. This formulation generates a system of transcendental equations that describe positive feedback, which is consistent with the observed hysteretic behavior. The system is iteratively solved until an energetically stable, self-consistent solution is obtained. The external applied field is stepped, akin to a DC magnetometry study, to obtain the complete magnetization hysteresis curve. Relevant system parameters can be easily altered to accomodate particles of varying physical and magnetic properties. Results: We observe hysteresis in the magnetization curve for chains of ≥ 2 particles. Marked improvements in SNR (~70-fold) and resolution (~30-fold) are evident from the derived MPI point spread function (PSF). Parametric sweeps indicate that the coercive threshold does not vary with chain length above a certain size, allowing for generous practical tolerances in superferromagnetic iron oxide (SFMIO) chain synthesis. The simulation shows that dimers also display hysteresis, paving the way for dimeric tracers with superior sensitivity and resolution that should have negligible

magnetomotive drift, which could be a safety concern for longer chains. Simulated data shows the MPI harmonics necessary for MPI reconstruction [13]. We expect some resolution and SNR losses from particle relaxation. We can also incorporate coercivity dispersion, which will manifest as further PSF blurring. We find that coercivity is a monotonic function of SPIO shell thickness, vanishing for very thick shells as expected. Conclusion: We successfully simulated an ensemble of short-chains of SPIOs using a computational model of magnetic dipole-coupled Langevin saturators. The model accurately predicts hysteresis, and also predicts the experimentally measured 10-fold improvements in SNR and spatial resolution. These findings will be crucial for practical SFMIO synthesis and FDA safety. Indeed, the primary value of the simulation is to estimate uniformity constraints on chain length and shell coating thickness for SFMIO behavior.

References: [1] Gleich, Bernhard, and Jürgen Weizenecker. "Tomographic imaging using the nonlinear response of magnetic particles." Nature 435.7046 (2005): 1214-1217. [2] Zhou, Xinyi, et al. "White Blood Cell Tracking with Magnetic Particle Imaging." IWMPI (2019). [3] Zheng, Bo, et al. "Quantitative magnetic particle imaging monitors the transplantation, biodistribution, and clearance of stem cells in vivo." Theranostics 6.3 (2016): 291.(2018): 131- 138. [4] Yu, Elaine Y., et al. "Magnetic particle imaging for highly sensitive, quantitative, and safe in vivo gut bleed detection in a murine model." ACS nano 11.12 (2017): 12067-12076. [5] Zhou, Xinyi Y., et al. "First in vivo magnetic particle imaging of lung perfusion in rats." Physics in Medicine & Biology 62.9 (2017): 3510. [6] Goodwill, Patrick W., and Steven M. Conolly. "The X-space formulation of the magnetic particle imaging process: 1-D signal, resolution, bandwidth, SNR, SAR, and magnetostimulation." IEEE transactions on medical imaging 29.11 (2010): 1851-1859. [7] Goodwill, Patrick W., et al. "Projection x-space magnetic particle imaging." IEEE transactions on medical imaging 31.5 (2012): 1076-1085. [8] Saritas, Emine U., et al. "Magnetostimulation limits in magnetic particle imaging." IEEE transactions on medical imaging 32.9 (2013): 1600-1610. [9] Tay et al. Order-of-Magnitude Resolution and SNR improvement using Positive Feedback MNP chains in Magnetic Particle Imaging, WMIC 2019 [10] K. L. B. Fung, et al. “Dynamics of chain formation and decay for super-resolution Magnetic Particle Imaging,” inWorld Molecular Imaging Congress2019, WMIS, Sep. 2019. [11] C. Colson, et al. “Evidence that SPIO Chain Formation is Essential for Super-Resolution MPI,” in World Molecular Imaging Congress 2019, WMIS, Sep. 2019. [12] Rancourt, Denis G. "Magnetism of earth, planetary, and environmental nanomaterials." Reviews in mineralogy and geochemistry 44.1 (2001): 217-292. [13] Rahmer, Jürgen, et al. "Signal encoding in magnetic particle imaging: properties of the system function." BMC medical imaging 9.1 (2009): 4.

Image/Figure:

https://s3.amazonaws.com/amz.xcdsystem.com/1E8A4501-BB41-A02A-1D3B9882B798BFAA_abstract_File10351/GA379_ImageFigure_0514122802.png

Image/Figure Caption: Figure 1. (A) Experimental observations using 0.6 - 2mm Derenzo phantom showing marked improvement in resolution and sensitivity for novel Superferromagnetic Iron Oxide emulsion (SFMIOs, right) over commercial SPIOs (left); (B) Langevin (SPIO) and hysteretic (SFMIOs) responses are obtained in the magnetization curve. Experimental data from SFMIOs closely match curve predicted by theory; (C) Simulated MPI point spread function (PSF) shows order of magnitude improvements in both signal and full

width half-max (FWHM) resolution when moving from a single SPIO tracer to an SFMIO dimer; (D) Parametric sweeps indicate that chains larger than 7 particles show negligible coercive dispersion, mitigating the problem of resolution loss; (E) Coercivity as a function of center-to-center particle separation for 40nm particles shows that as particle separation within the chain increases, the ensemble behavior reverts to the Langevin response of non-interacting SPIOs; (F) Frequency spectrum of signal response of an SPIO (left) to a unit-amplitude RF excitation at 1 kHz shows odd harmonics associated with nonlinearity, used to reconstruct the MPI signal. The response of the SFMIO dimer (right) to an identical excitation shows stronger nonlinear harmonics, demonstrating the improved SNR and confirming that MPI reconstruction is viable.

First Name: Chinmoy

Last Name: Saayujya

Email: chinmoy@berkeley.edu

Organization: University of California, Berkeley

Country: United States

ID: GA380
A novel theranostic agent and nanoparticle for Boron Neutron Capture Therapy

Jacopo Sforzi, University of Turin, jacopo.sforzi@unito.it

Category: New Chemistry, Materials & Probes

Abstract Body : Boron Neutron Capture Therapy (BNCT)(1) is a promising option for tumoral treatment, relying on the selective delivery of boron atoms to cancer cells, followed by the irradiation with a neutron beam of the diseased organ. The innovation of this study lies on the development and test of a nanosized theranostic agent, able to maximize the selective uptake of boron atoms in tumor cells and, at the same time, to quantify (by MRI) the in vivo boron biodistribution that is crucial to determine the optimal neutron irradiation time and to calculate the delivered radiation dose. Methods: In this study we used the theranostic compound AT101(2) (10 B enriched ligand-C-[N-(DOTAMA-C6)carbamoylmethyl]C′-palmitamidomethyl-o-carborane), a compound containing a Gd atom for imaging purposes, and 10 Boron atoms organized in a carborane structure for BNCT. AT101 was internalized into PLGA (Poly,(lactic-co-glycolic acid) nanoparticles: these NPs, approved for clinical use, are coated with DSPE-PEG-2000 and produced with and w/o 50% of a PLGA conjugated with a polyhistidine chain(n=15). The NPs were dialyzed to remove the unbound AT101 and treated to remove unreacted compounds. These PLGA were incubated with mesothelioma (AB-22) and healthy mesothelium cell lines (MET-5α) for 24 h in a petri dish. The cells were collected and sonicated. A portion of each batch was mineralized to analyze Gd concentration with ICP-MS, the remaining portion is used to quantify proteins. Results: Preliminary studies on PLGA-poly-his nanoparticles were made using the compound Curcumin. After these preliminary steps, investigating the nanoparticle stability and compound retaining, PLGA NPs containing AT101 were characterized using Dynamic Light Scattering, showing an average size of 132±13 nm, with a Polydispersion index never superior to 0.15, suggesting the good quality and reproducibility of the preparations. Their reproducible Z-potential was also analysed. We observed no significant release of AT-101 from the NPs when incubated for 72 h with Hepes buffer at 37°C and different pH, suggesting good stability. Two different NPs were created, both containing AT-101 but with or w/o PLGA conjugated with poly-histidine, a feature that is, in theory, able to swell and alter the charge of the nanoparticle at different pH. They were incubated with AB-22 and MET-5α cell lines. We observed a significant increase in the nanoparticle uptake in the AB-22 cell line, compared with MET-5α, and interestingly, in AB-22 cells, the NP containing Poly-histidine has a double internalization rate compared to the one without the Poly-His feature. Moreover, both the cells lines showed no significant toxicity derived from the incubation with the nanoparticles. The evaluation of the corresponding contrast enhancement in the T1 weighted MR image is in progress. In vivo studies for BNCT mediated by the theranostic agent AT-101 conjugated with PLGA are also in progress. Conclusion: Our results show how stable PLGA nanoparticles with polyhistidine chains can be reliably produced, and how they can retain the theranostic agent AT-101. We showed how our nanoparticles can favourably enter tumoral cells, compared to healthy mesothelium. This therapy can potentially affect only tumour cells with a lethal dose of radiation, even in case of spreading and infiltrative cases. These

promising insights on the possibility to selectively direct a theranostic dual agent directly into the tumoral cell, with the possibility to analyze the drug uptake in a certain organ using MRI, may be an important, versatile and new starting point for the future of BNCT technology and cancer theranostics.

References: References: 1: Dymova, MA, Taskaev, SY, Richter, VA, Kuligina, EV. Boron neutron capture therapy: Current status and future perspectives. Cancer Communications. 2020; 40: 406– 421. https://doi.org/10.1002/cac2.12089 2: S. Geninatti-Crich, D. Alberti, I. Szabo, A. Deagostino, A. Toppino, A. Barge, F. Ballarini, S. Bortolussi, P. Bruschi, N. Protti, S. Stella, S. Altieri, P. Venturello, S. Aime MRI-guided neutron capture therapy by use of a dual gadolinium/boron agent targeted at tumour cells through upregulated low-density lipoprotein transporters Chemistry, 17 (2011), pp. 8479-8486

Image/Figure:

https://s3.amazonaws.com/amz.xcdsystem.com/1E8A4501-BB41-A02A-1D3B9882B798BFAA_abstract_File10351/GA380_ImageFigure_0514123352.png

Image/Figure Caption: Boron Neutron Capture Therapy (BNCT) is a radiation science emerging as a hopeful tool in treating cancer, by selectively concentrating boron compounds in tumor cells and then irradiating them with an epithermal neutron beam. BNCT relies on the nuclear reaction that occurs when Boron-10, a stable isotope, is irradiated with low-energy thermal neutrons to yield α particles(Helium-4) and recoiling lithium-7 nuclei. In our study, we exploit a dual imaging/therapy theranostic agent, AT-101, containing Boron and Gadolinium, encapsulated in PLGA nanoparticles, to perform Magnetic Resonance Imaging of the organ of interest and selectively damage tumoral cells. (Image made with Biorender.com)

Full Name of Abstract's 1st Author : Jacopo Sforzi

First Name: Jacopo

Last Name: Sforzi

Email: jacopo.sforzi@unito.it

Organization: University of Turin

Country: Italy

ID: GA381

Imaging Therapeutic Efficiency of Rationally Identified MicroRNAs in Improving Chemotherapy in Glioblastoma

Negar Sadeghipour, Stanford University, sadeghi@stanford.edu

Category: Oncology

Abstract Body : Glioblastoma (GBM) is a grade IV brain tumor and a deadly malignancy. Currently, surgery, radiotherapy, and chemotherapy are the standard line of treatment. Despite all improvements in GBM treatment, the survival rate of patients remains low, with a median of 14 months.1 One of the difficulties in the treatment of GBM patients is the delivery of chemotherapeutic drugs across the blood-brain barrier (BBB).2 As a result, the efficacy of GBM treatment is poor while acquiring resistance to chemotherapeutic drugs over time. Novel delivery solutions that improve drug dosage in GBM or supplementation therapy that sensitizes GBM to low dose chemotherapy can increase the survival rate of patients. Our goal was to find a combinatorial treatment option that improves the effectiveness of two chemotherapeutic drugs (temozolomide (TMZ) and doxorubicin (DOX)) in GBM. To this end, we established a methodology to select a panel of microRNAs (miRNA) that target genes with important therapeutic roles in GBM. MicroRNAs, the regulators of gene expressions, have been considered novel targets to reprogram GBM cells for effectively responding to chemotherapy. Since several mechanisms are involved in tumor cell survival and response to therapy, targeting multiple miRNAs regulating various cellular hallmarks of GBM was critical for achieving successful therapy. We defined four important therapeutic pathways to target: cell proliferation and apoptotic signaling, invasion and metastasis, cytokine signaling, and stemness. The abundance of the miRNAs and their target genes motivated us to use available online databases, including Gene Expression Omnibus (GEO) and The Cancer Genomic Atlas (TCGA), for a meta-analysis approach. We introduced a comprehensive method of therapeutic miRNA selection for sensitizing cancer cells to chemotherapy, and the assessment of these miRNAs in vitro in GBM cell lines and in vivo in mouse models by molecular imaging. The rationally identified panels were evaluated in GBM cells by delivering synthetic microRNAs using PLGA-PEG nanoparticles prior to treatment with TMZ and DOX drugs. A panel of five miRNAs (miR-218, miR-490, miR-138, miR-139, and antisense-miR-21) was identified as the most promising combination (Fig. 1a). STAT3, ZEB1, SMAD7, CDK6, and TGIF2 were identified among the most important genes that are targeted by these miRNAs, and they cover four different therapeutic signaling pathways identified earlier (Fig. 1b). Cell viability, apoptosis, and the expression of downstream genes were evaluated in cell culture using MTT, FACS, and western blot assays. Results of U87-MG cells treated with different combinations of miRNAs revealed that the panel of selected miRNAs significantly increased the apoptotic population compared to control conditions (~3 -fold higher). After optimizing the miRNA-mediated therapeutic evaluation in GBM cell lines of different phenotypes (U87-MG, T98g, and LN308), the cells were pretreated with the panel of miRNAs 24 hours before being treated with different concentrations of TMZ or DOX. TMZ is a pro-drug that became active upon addition to the medium with a neutral pH. It had higher efficiency when it was given in two consecutive doses

to the cells that were pre-treated with the panel of miRNAs loaded in PLGA-PEG-NPs. DOX showed a dose-dependent inhibition of cell viability upon pre-treatment with the microRNAs. Our results supported the hypothesis that we can achieve significant apoptosis induction with lower doses of drugs (Fig. 1c). Further evaluation in tumor xenografts of U87-MG GBM (expressing Fluc) in animals with the pre-treatment of miRNAs loaded PLGA-PEG-NPs by intravenous injections, and intraperitoneal doses of TMZ, resulted in a significant reduction in tumor volume by the group that received combinatorial treatment of miRNAs and TMZ after four cycles of treatment when compared to tumor growth in the group that received control nanoparticles (CNP) and TMZ, and miRNAs only treatment, $p < 0$ .05, (Fig. 1d).

References: 1. Koshy M, Villano JL, Dolecek TA, Howard A, Mahmood U, Chmura SJ, Weichselbaum RR, McCarthy BJ. Improved survival time trends for glioblastoma using the SEER 17 population-based registries. J Neurooncol. 2012;107(1):207-12. 2. Jain K. Use of nanoparticles for drug delivery in glioblastoma multiforme. Expert Rev Neurother. 2007;7(4):363-72.

Image/Figure:

https://s3.amazonaws.com/amz.xcdsystem.com/1E8A4501-BB41-A02A-1D3B9882B798BFAA_abstract_File10351/GA381_ImageFigure_0514010600.jpg

Image/Figure Caption: Figure 1. (a) Selected up- and down-regulated microRNAs target different therapeutic pathways in glioblastoma (GBM). (b) Target genes of each miRNAs in GBM were identified from Gene Expression Omnibus and The Cancer Genome Atlas and assigned to a specific therapeutic pathway. Genes are color-coded based on the therapeutic pathways: yellow is the proliferation and apoptotic signaling, red is invasion and metastasis, blue is cytokine signaling, and green is stemness including EMT. (c) FACS analysis showed a significant increase in the apoptosis percentages (red) after treatment of U87-MG cells with miRNAs than control nanoparticles (CNP). DOX is more effective in increasing apoptosis than TMZ, but it has difficulty in passing the blood-brain barrier. (d) Bioluminescence images of animals treated with control nanoparticles (CNP) and TMZ, miRNAs and saline or the combination of miRNAs and TMZ. Significant tumor shrinkage was observed in the group that was treated with the combination of miRNAs and TMZ after four cycles of therapy.

Full Name of Abstract's 1st Author : Negar Sadeghipour

First Name: Negar

Last Name: Sadeghipour

Email: sadeghi@stanford.edu

Organization: Stanford University

Country: United States

ID: GA383

Quantification of Sigma1 Receptor in Transgenic Mouse Model of Alzheimer's Disease by PET Imaging Using 18F-(+)-TZ3108

红军 金, 中山大学附属第五医院, **jinhj3@mail.sysu.edu.cn**

Category: Neuroscience

Abstract Body : Background: Alzheimer's disease (AD) is a neurodegenerative disorder characterized by a gradual decline in neurocognitive function. The ability of sigma-1 receptor (σ1R) to regulate cognitive impairment, especially its effect of delaying memory loss, has attracted increasing attention by more and more researchers[1]. Whether PET targeting σ1R can apply for the early diagnosis of AD remains to be explored. We aimed to evaluate a novel fluorine-18 labelled (+)-TZ3108 that specifically targets the σ1R to quantify the expression level of σ1R in the brain of mouse model of AD. Methods: Male APP/PS1 double-transgenic mice, expressed mutant human presenilin (Deltae9) and mouse amyloid precursor protein (APPswe) was assigned into transgenic group (Tg group, 5 month old, n = 3) for animal model of AD. Male age-matched C57BL/6 wild type mice was assigned into control group (Wt group, 5 month old, n =3). The fluorine-18 labelled (+)-TZ3108 was synthesized according previous published references[2,3]. Brain microPET imaging of (+)-[18F]TZ3108 was performed on a nanoPET scanner (Mediso Inc., Hungary). Anesthesia was maintained at 0.75–2.0% during the whole imaging session and core temperature was maintained at 37ºC. A 10 min CT scan was conducted to confirm positioning of the animal, followed by a 5 min transmission scan for attenuation correction. Thereafter, a 30 min dynamic (10×3s; 3×10s; 4×60s; 6×150s; 2 ×300s) emission scan was performed after i.v. injection of (+)-[18F]TZ3108 in 10% ethanol saline solution. PET emission data were corrected by related attenuation and reconstructed in manufactured software. The brain MRI image of each mouse was collected through 9.4T microMRI scanner (BioSpec 94/20USR, Bruker Inc.), and MRI images were co-registered to the PET/CT images in Carimas software manually. All volume of interest (VOI) were drawn on the MRI image using Carimas (Finland PET Center). Three dimensional VOIs were transformed to the PET space and then overlaid on all reconstructed PET images to obtain TACs. Activity measures were standardized to the mice body weight, and injected dose of radioactivity yielded SUV. With the time activity curve (TAC) of left ventricular as the input function, the original TAC of vital brain regions was fitted by 2TCM model to obtain binding potential (BP). Results: The quantification of (+)-[18F]TZ3108 PET/MRI revealed that the expression of σ1R in Tg group (BPTgWB = 2.41±0.10, BPTgCB = 0.95±0.10, BPTgFC = 1.04±0.10 BPTgHC = 0.92±0.10, BPTgST = 1.36±0.10, BPTgBS = 0.67±0.10, BPTgTHA = 0.63±0.10) was significantly lower than the Wt group (BPWtWB = 3.56±0.10, BPWtCB = 1.30±0.10, BPWtFC = 3.74, BPWtHC = 3.76±0.10, BPWtST = 1.95, BPWtBS = 1.98±0.10, BPWtTHA = 0.79±0.10) for whole brain (WB), cerebellum (CB), frontal cortex (FC), hippocampus (HC), striatum (ST), brain stem (BS), thalamus (THA) respectively.(Figure 1) Conclusion: Associated to the cognitive impairment, and effect of delaying memory loss, the expression of σ1R in the brain of 5-month old AD transgenic mice was significantly reduced compared to the Wt controls from this preliminary study indicated

that imaging σ1R via (+)-[18F]TZ3108 may be a potential biomarker for early diagnosis for AD. Funding This work was funded by the National Natural Science Foundation of China (No.81871382), the Key Realm R&D Program of Guangdong Province (2018B030337001), National Key R&D Program of China (2018YFC0910601), and Starting Fund from the Fifth Affiliated Hospital, Sun Yat-sen University.

References: 1. Niitsu T, Iyo M, Hashimoto K. Sigma-1 receptor agonists as therapeutic drugs for cognitive impairment in neuropsychiatric diseases. Curr Pharm Des. 2012;18(7):875-83. 2. Jin H, Fan J, Zhang X, Li J, Flores HP, Perlmutter JS, Parsons SM, Tu Z. Radiosynthesis and in vivo evaluation of a novel σ1 selective PET ligand. Medchemcomm. 2014 Nov 1;5(11):1669-1677. 3. Yue X, Jin H, Luo Z, Liu H, Zhang X, McSpadden ED, Tian L, Flores HP, Perlmutter JS, Parsons SM, Tu Z. Chiral resolution of serial potent and selective σ1 ligands and biological evaluation of (-)-[18F]TZ3108 in rodent and the nonhuman primate brain. Bioorg Med Chem. 2017 Feb 15;25(4):1533-1542.

Image/Figure:

https://s3.amazonaws.com/amz.xcdsystem.com/1E8A4501-BB41-A02A-1D3B9882B798BFAA_abstract_File10351/GA383_ImageFigure_0514080941.jpg

Image/Figure Caption: Figure 1. Quantification of brain expression σ1R via (+)-[18F]TZ3108 PET/MRI. Representative imagine with PET/MRI for Tg （Left） and Wt （Right） mouse. (Upper: Coronal slice; Middle: Transaxial slice; Lower: Sagittal slice); A,E,I: PET/MRI, B,F,J MRI only for Tg mouse; C,G,K: PET/MRI, D,H,L MRI only for Wt mouse; M:The BP value of vital brain regions was obtained after fitting by 2TCM model. WB, whole brain; CB, cerebellum; FC, frontal cortex; HC, hippocampus; ST, striatum; BS, brain stem; THA, thalamus).

First Name: 红军

Last Name: 金

Email: jinhj3@mail.sysu.edu.cn

Organization: 中山大学附属第五医院

Country: China

ID: GA384

Metal oxide-chitosan compounds as theranostic modular nano-cocktails for ROS and inflammatory related diseases

Yuao Wu, Griffith University - Queensland Micro Nanotechnology Centre, yuao.wu@griffith.edu.au

---

Category: New Chemistry, Materials & Probes

Abstract Body : Inflammation plays an essential role in the progression of many chronic diseases like hepatopathy, atherosclerosis and rheumatoid arthritis. Cytokines such as tumour necrosis factor-α (TNF-α), interleukin-6 (IL-6), cyclooxygenase-2 (COX-2) and inducible nitric oxide synthase (iNOS) play important roles in the regulation of the inflammation. In this study, modular two-in-one nano-cocktails were synthesised to provide treatment of inflammatory diseases and also enable tracking of their delivery to the disease sites. Chit-IOCO loaded with treatment module (cerium oxide nanoparticles) and imaging module (iron oxide nanoparticles) were synthesised by electrostatic self-assembly. Its MRI capability, anti-inflammatory and anti-fibrosis ability were investigated. Results demonstrated that Chit-IOCO significantly reduced the expression of ROS, TNF-α and COX-2 in the LPS-stimulated macrophages. Cytotoxicity studies showed that the nano-cocktails inhibited the proliferation of macrophages. Additionally, Chit-IOCO is a great MRI contrast agent in macrophages. It was possible to track the delivery of Chit-IOCO to the inflamed livers of CCl4-treated C57BL/6 mice, demonstrated by a shortened T2* relaxation time of the livers after injecting Chit-IOCO into mice. In vivo anti-inflammatory and blood tests demonstrated that Chit-IOCO reduced inflammation-related proteins (TNF-a, iNOS and Cox-2) and bilirubin in CCl4 treated C57BL/6. Histology images indicated that the nano-cocktails reduced fibrosis of CCl4-treated mouse liver and did not affect other organs of the mice. This is the first reported data on the anti-inflammation and anti-fibrosis efficacy of Chit-IOCO in C57BL/6 mouse liver inflammation model. Overall, Chit-IOCO nano-cocktails have shown great potential in MR imaging/detecting and treating/therapeutic capabilities for inflammatory diseases. Potentially, these nano-cocktails can be modified with antibodies or binding peptides, allowing these nanoparticles to target the inflammatory biomarkers for the diagnosis of diseases.

Full Name of Abstract's 1st Author : Yuao Wu

First Name: Yuao

Last Name: Wu

Email: yuao.wu@griffith.edu.au

Organization: Griffith University - Queensland Micro Nanotechnology Centre

Country: Australia

ID: GA385

Identifications of Malignant Lymph Nodes of Esophageal Squamous Cell Carcinoma by Quantified 18F-FDG PET/CT

红军 金, 中山大学附属第五医院, **jinhj3@mail.sysu.edu.cn**

Category: Oncology

Abstract Body : Background: Being the eighth most frequent cancer all over the world esophageal cancer can be histologically divided into two subtypes as esophageal squamous cell carcinoma (ESCC) and esophageal adenocarcinoma [1]. Most ESCC imaging diagnoses can be performed by computed tomography and ultrasound but it is difficult to detect suspicious minor lesions. However accurate diagnosis of disease progression and lesion location is of great significance for early diagnosis and the determination of neoadjuvant therapy. PET/CT becomes more and more popular in assessing tumors and lymph nodes, being a quantitative parameter the net uptake (influx) rate constant (Ki) may be more sensitive and specific than the max standardized uptake value (SUVmax) in different situations [2,3]. Methods: Thirty-two patients enrolled in this study were divided into two groups as N0 stage and non-N0 stage, who were examined by 18F-fluorodeoxyglucose (18F-FDG) positron emission tomography/computed tomography (PET/CT) dynamically. According to the CT imaging, primary tumors (PTs) and regional lymph nodes were collected to analysis. Respectively the SUVmax and Ki were statistic analyzed to identify primary tumors between N0 and non-N0 stages, as well as to distinguish suspicious malignant lymph nodes (sMLN), malignant lymph nodes (MLN) and benign lymph nodes (BLN) in different ranges and thoracic segments. Results: In this study, the number of lymph nodes found through CT were 84, of which 35 were malignant lymph nodes (MLN) and 49 were benign lymph nodes (BLN), which were affirmed by professional pathologists. Meanwhile the MLN was classified as sMLN (the LN pathologically verified as malignant but being suspicious by imageology) and cMLN (the LN verified as malignant both by pathologically and imageology). The p values of SUVmax and Ki in distinguishing sMLN (n=10) from BLN (n=42) were 0.7533 and 0.0247 indicating that for the potential suspicious minor lesions of MLN Ki had a more promising ability, while with a lower AUC value as 0.4607 SUVmax might not be a better parameter in this situation. Conclusion: It can be found that for more severe, activated and mature lesions with higher SUVmax and Ki, the parameters of SUVmax and Ki have the same ability to evaluate and filtrate. However when the lesions camouflage as a benign ones with lower SUVmax, Ki shows a more promising ability to scout them. Funding: This work was funded by the National Key R&D Program of China (2018YFC0910600), National Natural Science Foundation of China (81871382), the Key Realm R&D Program of Guangdong Province (2018B030337001), and Starting Fund from the Fifth Affiliated Hospital, Sun Yat-sen University.

References: 1.Zheng Y, Chen Z, Han Y, Han L, Zou X, Zhou B, Hu R, Hao J, Bai S, Xiao H, Li WV, Bueker A, Ma Y, Xie G, Yang J, Chen S, Li H, Cao J, Shen L. Immune suppressive landscape in the human esophageal squamous cell carcinoma microenvironment. Nat Commun. 2020;11(1):6268. 2.Yang M, Lin Z, Xu Z, Li D, Lv W, Yang S, Liu Y, Cao Y, Cao Q, Jin H.

Influx rate constant of 18F-FDG increases in metastatic lymph nodes of non-small cell lung cancer patients. Eur J Nucl Med Mol Imaging. 2020;47(5):1198-1208. 3.Hans FJ, Wei L, Bereczki D, Acuff V, Demaro J, Chen JL, Otsuka T, Patlak C, Fenstermacher J. Nicotine increases microvascular blood flow and flow velocity in three groups of brain areas. Am J Physiol. 1993;265(6 Pt 2):H2142-50.

Image/Figure:

https://s3.amazonaws.com/amz.xcdsystem.com/1E8A4501-BB41-A02A-1D3B9882B798BFAA_abstract_File10351/GA385_ImageFigure_0514075235.png

Image/Figure Caption: Figure. (A) and (B) were statistical analyses of SUVmax and Ki of total MLN and BLN; (C) and (D) were statistical analyses of SUVmax and Ki of sMLN and BLN with SUVmaxs; (E) was the correlation between SUVmax and Ki of MLN and BLN with SUVmax in different ranges; (F)-(K) were the typical imaging of a patient; (L) was the patlak fitting of Ki of MLN, sMLN and BLN.

First Name: 红军

Last Name: 金

Email: jinhj3@mail.sysu.edu.cn

Organization: 中山大学附属第五医院

Country: China

ID: GA386

Preclinical validation of [18F]MNI-1054 in non-human primates: A novel PET ligand for lysine-specific histone demethylase 1A (LSD1)

Paul McQuade, Takeda, paul.mcquade@takeda.com

Category: Neuroscience

Abstract Body : Introduction Lysine specific demethylase 1 (LSD1) is an enzyme involved in histone modification, with dysfunction implicated in the pathogenesis of neurodevelopmental diseases. Thus, inhibitors of LSD1 enzyme activity could have the potential to treat neurodevelopmental disorders. As part of a translatable biomarker strategy, the use of PET imaging to non-invasively assess target engagement of LSD1 inhibitors and establish a dose-occupancy relationship was desired. A rational PET tracer design effort was undertaken, with MNI-1054 identified as a potential PET candidate. Initial PET imaging studies with [18F]MNI-1054 indicated that it had specific binding in brain regions with known high LSD1 expression as well as displaying favorable kinetics for PET quantification. The ability of [18F]MNI-1054 to measure the target occupancy of a LSD1 inhibitor and establish a dose-occupancy relationship in non-human primates (NHP) was investigated, along with its whole-body distribution and dosimetry profile. Methods Rhesus monkeys were used as research subjects for both brain occupancy and whole body dosimetry studies. [18F]MNI-1054 brain scans were collected over 3 hours on a microPET Focus 220, with arterial blood samples taken throughout the scans for tracer kinetic modeling and quantification. Blocking studies with the LSD1 inhibitor TAK-418 (0.005-3.0 mg/kg) were performed. For these blocking studies TAK-418 was administered iv 3 hours prior to [18F]MNI-1054. As both [18F]MNI-1054 and TAK-418 bind irreversibly to LSD1, which was confirmed via displacement studies, the irreversible 2-tissue compartment model was used to estimate [18F]MNI-1054 Ki at baseline and post-TAK-418. Occupancy was calculated as the percent change in Ki from baseline to post-TAK-418. Due to the irreversible binding of these inhibitors to LSD1, the time taken for the enzyme to re-populate was investigated by imaging one subject with [18F]MNI-1054 at 24 h and 48 h post TAK-418 treatment (0.3 mg/kg). In addition, whole-body biodistribution scans were obtained in order to estimate the human radiation dosimetry of [18F]MNI-1054. Results Baseline PET scans with [18F]MNI-1054 were consistent with the known LSD1 regional brain distribution, with uptake highest in the cerebellum and lowest in the pons. A TAK-418 displacement study conducted 90 min post-[18F]MNI-1054 administration showed no observable change in the TACs, confirming the irreversible binding of [18F]MNI-1054. Blocking studies with TAK-418 showed a dose dependent decrease in LSD1 specific binding of [18F]MNI-1054, demonstrating the utility of [18F]MNI-1054 to establish a plasma concentration vs. enzyme occupancy relationship. Representative baseline and TAK-418-blocked co-registered PET/MRI scans are shown in Figure 1, along with the TAK-418 dose-occupancy curve in the cerebellum. From the re-population studies, there were no detectible levels of TAK-418 in plasma at either 24 or 48 h. By 24 h occupancy in cerebellum was measured at 30% which dropped to 6% by 48 h. This represents a significant repopulation of the LSD1 enzyme, as a dose of 0.3 mg/kg TAK-418 occupied 91% of the available enzyme at 3 h. From the dosimetry studies it was observed that

the elimination of [18F]MNI-1054 takes place via both hepatobiliary and urinary pathways. With the estimated whole-body effective doses scaled from NHP to human 0.0272 mSv/MBq and 0.0267 mSv/MBq for female and male respectively. Conclusions [18F]MNI-1054 showed good brain penetration and heterogenous distribution, which correlated with known LSD1 expression levels. It was found to bind irreversibly to LSD1, and determined to be a suitable PET tracer for determining the central LSD1 occupancy in NHP. There was also significant re-population of the LSD1 enzyme observed by 24 h, which by 48 h had almost returned to pre-block levels. The dosimetry profile of [18F]MNI-1054 is comparable to other 18F small molecule PET tracers, and the next step in its evaluation will be to conduct PET studies in humans.

Image/Figure: https://s3.amazonaws.com/amz.xcdsystem.com/1E8A4501-BB41-A02A-1D3B9882B798BFAA_abstract_File10351/GA386_ImageFigure_0514095454.docx

Image/Figure Caption: Figure 1: Representative 60-180 min summed PET/MRI image of [18F]MNI-1054 at baseline (A). and post 3mg/kg TAK-418 blocking (B). TAK-418 dose-occupancy relationship established with [18F]MNI-1054 in the cerebellum (C).

First Name: Paul

Last Name: McQuade

Email: paul.mcquade@takeda.com

Organization: Takeda

Country: United States

ID: GA387
FMISO-hypoxia monitoring during chemo-radiotherapy for outcome prediction in head and neck cancer.

Montserrat Carles, La Fe Health Research Institute, montserrat.carles@uniklinik-freiburg.de

---

Category: Oncology

Abstract Body : Radiotherapy constitutes a treatment mainstay for patients with head-and-neck squamous cell carcinomas (HNSCC) and is often combined with concomitant chemotherapy for locally advanced cancers. However, the radiation resistance of individual tumors has been shown to strongly depend on the presence and dynamics of tumor-associated hypoxia. Tumor hypoxia can be longitudinally monitored by 18F-Fluoromisonidazole (18F-FMISO)-PET/CT. The aim of our study was to evaluate radiomics changes of 18F-FMISO-hypoxia imaging during chemo-radiotherapy (CRT) as predictors for treatment outcome in head-and-neck squamous cell carcinoma (HNSCC) patients. HNSCC patients undergoing CRT were prospectively recruited. All obtained three FMISO-PET/CT scans at weeks 0, 2 and 5 during CRT (W0/W2/W5). Hypoxic subvolumes (HSV) within the tumor were segmented by a threshold of 1.4 times background uptake. Patients were classified based on variations during CRT of the HSV size (increasing, stable and decreasing) by the percentage relative volume deviation (ΔrV). Variations in the location of HSV (geographically-static and geographically-dynamic) were also quantified by a new classification parameter (CP) accounting for the spatial overlapping. Additionally, 130 radiomic features (RF) were extracted from HSV at W0, and their variations during CRT were quantified by relative deviations (ΔRF). The prediction of treatment outcome based on variation of FMISO-hypoxia quantification parameters was evaluated. To maximize generalizability in the prediction models, positive findings in outcome prediction were considered relevant if (i) they were statistically significant after Benjamin-Hochberg correction for multiple testing, (ii) their predictive value was observed for both time-points during CRT (W0-W2 and W0-W5) and (iii) the outcome prediction was confirmed in both cohorts (initial cohort of 25 patients and validation cohort of 15 patients). HV decreased in 64% of patients between W0 and W2 and in 80% between W0 and W5. Although an overall decrease of hypoxia for patients was observed in the sample, ΔrV did not shown predictive value for treatment outcome. CP distinguished earlier disease progression (geographically-dynamic) from later disease progression (geographically-static) in both time-points and confirmed for both cohorts. The texture feature low-grey-level-zone-emphasis predicted local recurrence with AUCW2 = 0.82 and AUCW5 = 0.81 in initial cohort and AUCW2 = 0.79 and AUCW5 = 0.80 in validation cohort. Radiomics analyses of FMISO-derived hypoxia dynamics and individual texture features were able to predict patient outcome during CRT for HNSCC.

Image/Figure:

https://s3.amazonaws.com/amz.xcdsystem.com/1E8A4501-BB41-A02A-1D3B9882B798BFAA_abstract_File10351/GA387_ImageFigure_0514101509.jpg

Image/Figure Caption: Figure 1. Graphical abstract of the study: (a) Patient cohort description, (b) analysis of variations in FMISO-hypoxia quantification parameters and (c) the most relevant treatement outcome predictions.

First Name: Montserrat

Last Name: Carles

Email: montserrat.carles@uniklinik-freiburg.de

Organization: La Fe Health Research Institute

Country: Spain

ID: GA388
Effect of crotamine on glucose uptake by brown fat - 18F-FDG PET evaluation in an experimental model

Marcelo Sapienza, FMUSP, mtsapienza@hotmail.com

Category: Systemic Diseases (Kidney, Liver and Pancreas)

Abstract Body : Brown adipose tissue (BAT) plays an important role in thermogenesis and thermoregulation. BAT metabolism is activated by sympathetic stimuli mediated by beta3-adrenergic receptors, triggered mainly by exposure to cold. Crotamine is a polypeptide isolated from the venom of the rattlesnake, that besides its antitumoral effect, has a recently described role on the differentiation and metabolic activation of BAT in rodents. Positron emission tomography with 18F-fluorodeoxyglucose (PET-FDG) allows the evaluation of BAT glycolytic activity. OBJECTIVE: to evaluate the effects on BAT metabolism of crotamine administration in rodents at basal conditions and after cold stimulus activation using PET-FDG. METHODS: PET-FDG studies were performed in a small -animal PET scanner (Triumph trimodality-Gamma Medica Ideas, california, USA), 45 min after intravenous administration of 18F-FDG in a group of 8 mice submitted to a cold stymulus at baseline, 10, and 21 days after daily oral administration of 10 μg of a synthetic crotamine (Group 1). PET-FDG ws performed after the same intervals in a control group also receiving crotamine but without cold stymulus (Group 2). Volumes of interest (VOI) were drawn over the interscapular fat on PET-FDG images, and metabolic activity was measured by SUVmax and SUVmean values in the VOI. RESULTS: Group 1 showed a significant reduction in uptake in BAT after 10 days of administration of crotamine when compared to the baseline study, both by analysis of medium SUV and SUVmax. There was no statistically significant difference in uptake after 21 days of treatment with crotamine compared to the baseline study, when the same parameters were analyzed (SUVmean: baseline 3.5+-0.5; T10 2;1+-0.7; T21 3.2+-0.8)(SUVmax baseline 5.2+-1.1;T10 3.2+-1.2; T21 5.3+-1.3). Group 2 (control) showed a significant increase in 18F-FDG uptake in BAT after 10 days of administration of crotamine when compared to the baseline study, both by analysis of SUVmean and SUVmax. There was no statistically significant difference in uptake after 21 days of treatment with crotamine compared to the baseline study when the same parameters were analyzed (SUVmean: baseline 1.2+-0.3; T10 1,6+-0.3; T21 1.2+-0.2)(SUVmax baseline 1.8+-0.5;T10 2.3+-0.4; T21 1.9+-0.5). PET-FDG with cold stimulus shows greater glycolytic activity than studies without stimulus at all intervals studied (baseline, 10 and 21 days with crotamine). CONCLUSION: This is the first study that has evaluated the effects of crotamine in BAT glycolitic metabolism in vivo. Crotamine induced a transient increase in the glycolytic activity of BAT and a transient reduction in the response to the cold stimulus after 10 days, with no significant change compared to baseline after 21 days in both groups.

References: • Batista da Cunha D, Pupo Silvestrini AV, Gomes da Silva AC, Maria de Paula Estevam D, Pollettini FL, de Oliveira Navarro J, Alves AA, Remédio Zeni Beretta AL, Annichino Bizzacchi JM, Pereira LC, Mazzi MV. Mechanistic insights into functional

characteristics of native crotamine. Toxicon. 2018;146:1-12. • Campeiro JD, Marinovic MP, Carapeto FC, Dal Mas C, Monte GG, Carvalho Porta L, Nering MB, Oliveira EB, Hayashi MA (2018) Oral treatment with rattlesnake native toxin crotamine efficiently inhibits the tumor growth with no potential toxicity for the host animal and with suggestive positive effects on animal metabolic profile. Amino Acids 50: 267-278. • Hayashi MA, Oliveira EB, Kerkis I, Karpel RL (2012) Crotamine: a novel cell-penetrating polypeptide nanocarrier with potential anti-cancer and biotechnological applications. Methods Mol. Biol. 906: 337–52. • Lima SC, Porta LC, Lima ÁDC, Campeiro JD, Meurer Y, Teixeira NB, Duarte T, Oliveira EB4, Picolo G, Godinho RO, Silva RH, Hayashi MAF. Pharmacological characterization of crotamine effects on mice hind limb paralysis employing both ex vivo and in vivo assays: Insights into the involvement of voltage-gated ion channels in the crotamine action on skeletal muscles. PLoS Negl Trop Dis. 2018 6;12(8):e0006700. • Marinovic MP, Campeiro JD, Lima SC, Rocha AL, Nering MB, Oliveira EB, Mori MA, Hayashi MAF. Crotamine induces browning of adipose tissue and increases energy expenditure in mice. Sci Rep. 2018 22;8(1):5057. • Nascimento FD, Hayashi MA, Kerkis A, Oliveira V, Oliveira EB, Rádis-Baptista G, Nader HB, Yamane T, Tersariol IL, Kerkis I. Crotamine mediates gene delivery into cells through the binding to heparan sulfate proteoglycans. J Biol Chem. 2007; 282(29):21349-60.

Image/Figure:

https://s3.amazonaws.com/amz.xcdsystem.com/1E8A4501-BB41-A02A-1D3B9882B798BFAA_abstract_File10351/GA388_ImageFigure_0520095507.jpg

Image/Figure Caption: Delimitation of volume of interest (VOI) in the interscapular BAT of a mice form Group 1, shown in transverse, coronal and sagital planes:

First Name: Marcelo

Last Name: Sapienza

Email: mtsapienza@hotmail.com

Organization: FMUSP

Country: Brazil

ID: GA389

Prostate-specific membrane antigen (PSMA)-targeted photodynamic therapy enhances the delivery of PSMA-targeted magnetic nanoparticles to PSMA-expressing prostate tumors

Ethel Ngen, Johns Hopkins University School of Medicine, engen1@jhmi.edu

---

Category: Oncology

Abstract Body : Introduction: Magnetic nanoparticle-induced hyperthermia (MNP-IH) is a less morbid focal therapy that is currently being explored to treat localized, intermediate, and high-risk prostate cancers (PCs).1 MNPs (≥100 nm), have been shown to possess both thermal and magnetic properties ideal for magnetic resonance image (MRI)-guided MNP-IH.2 However, the delivery of both receptor-targeted and non-targeted nanoparticles to tumors, after intravenous administration is still a challenge, especially nanoparticles ≥ 100 nm.3 Current preclinical and clinical practices to deliver high doses of magnetic nanoparticles (MNPs) to tumors for MNP-IH, involve direct intra-tumoral injections.4,5 However, this is an invasive procedure that can cause treatment-related morbidity, and negatively impact patient quality of life after treatment.6 Additionally, given the multi-focal nature of PC lesions, direct tumor injections could miss remote or nearby foci, which could lead to disease recurrence after therapy. Consequently, there is a need for nanoparticle delivery systems capable of increasing tumor-specific accumulation of MNPs, after intravenous administration.7-9 Hypothesis: Enhanced vascular permeability plays an essential role in the delivery of nanoparticles to tumors, through the enhanced permeability and retention (EPR) effect. However, the EPR effect varies greatly within tumors and also between patients.3 The poor clinical performance of some targeted and non-targeted nanoparticles has been partially attributed to this variable EPR effect.3 Consequently, tumor re-engineering approaches designed to specifically enhance the tumor EPR effect and subsequently increase nanoparticle delivery, are currently being explored.10, 11 Prostate-specific membrane antigen (PSMA) is overexpressed on the epithelium of aggressive prostate cancers (PCs) and has been targeted for imaging and therapy.8,9 Objective: Here, we evaluated the feasibility of using low dose PSMA-targeted photodynamic therapy (PDT), as a tumor re-engineering approach, to enhance the EPR effect and subsequently increase the delivery of PSMA-targeted MNPs to human PSMA(+) PC tumor xenografts, in a preclinical mouse model. Method: Human PSMA(+) PC3 PIP tumor-bearing NSG mice (Group 1) were intravenously administered 3.3 nmol of a low-molecular-weight PSMA-targeted photosensitizer and treated with fluorescence image-guided PDT, 4 h after. Briefly, the mice were irradiated with NIR light from a 690 ± 20 nm light-emitting diode, at a total fluence of 200 J/cm2.12 The mice were then intravenously administered 50 mg/kg of a PSMA-targeted MNP, immediately after PDT and monitored with both fluorescence imaging and T2-weighted MRI 18 h, 42 h, and 66 h after that.8,9 While the PSMA-targeted photosensitizer was imaged using its 700 nm fluorescence signal; the PSMA-targeted MNP was imaged using its 800 nm fluorescence signal. Additionally, T2-weighted MRI was used to image the PSMA-targeted MNP core. Human PSMA(+) PC3 PIP tumor-bearing NSG mice, not pretreated with PDT and only intravenously administered the PSMA-targeted MNP, were used

as primary negative controls (Group 2). Additional control groups were also used to investigate the specificity of the PSMA-targeted photosensitizer and the EPR enhancement effect. Results: An 8-fold increase in the delivery of the PSMA-targeted MNPs was detected using T2-W MRI in the PDT-pretreated PSMA(+) PC3 PIP tumors of the Group 1 mice, 42 h after PDT; compared to the untreated PSMA(+) PC3 PIP tumors of the control Group 2 mice. This finding was validated with fluorescence imaging which showed similar results. Additionally, T2-W MRIs revealed enhanced peripheral intra-tumoral delivery of the PSMA-targeted MNPs. That finding was in keeping with two-photon microscopy, which revealed higher vascular densities at the tumor periphery. Conclusion: These results suggest that PSMA-targeted PDT enhances the delivery of PSMA-targeted MNPs to PSMA(+) tumors by enhancing the EPR effect of PSMA(+) PC3 PIP tumors. Clinical Significance: MNP-IH and vascular-targeted PDT are both focal therapies currently being evaluated for the treatment of localized intermediate, and high-risk PCs. Consequently, the use of low dose PSMA-targeted PDT to enhance the delivery of PSMA-targeted MNPs could contribute synergistically to effective long-term control of localized intermediate, and high-risk PCs.13

References: 1. Johannsen, M., et al. Magnetic nanoparticle hyperthermia for prostate cancer. Int J Hyperther 26, 790-795,(2010). 2. Wabler, M. et al. Magnetic resonance imaging contrast of iron oxide nanoparticles developed for hyperthermia is dominated by iron content. Int J Hyperther 30, 192-200, (2014). 3. Wilhelm, S. et al. Analysis of nanoparticle delivery to tumors. Nat Rev Mater 1, 16014, 2016. 4. Attaluri, A. et al. Nanoparticle distribution and temperature elevations in prostatic tumours in mice during magnetic nanoparticle hyperthermia. Int J Hyperther 27, 491-502, (2011). 6. Johannsen, M. et al. Morbidity and quality of life during thermotherapy using magnetic nanoparticles in locally recurrent prostate cancer: Results of a prospective phase I trial. Int J Hyperther 23, 315-323,(2007). 7. Albarqi, H. A. et al. Biocompatible nanoclusters with high heating efficiency for systemically delivered magnetic hyperthermia. ACS Nano 13, 6383-6395, (2019). 8. Behnam Azad, B. et al. Evaluation of a PSMA-targeted BNF nanoparticle construct. Nanoscale 7, 4432-4442, (2015). 9. Ngen, E. J. et al. MRI assessment of prostate-specific membrane antigen (PSMA) targeting by a PSMA-targeted magnetic nanoparticle: Potential for image-guided therapy. Mol Pharm 16, 2060-2068, (2019). 10. Nakamura, Y., et al. Nanodrug delivery: Is the enhanced permeability and retention effect sufficient for curing cancer? Bioconjug Chem 27, 2225-2238, (2016). 11. Stylianopoulos, T., et al. Reengineering the Physical Microenvironment of Tumors to Improve Drug Delivery and Efficacy: From Mathematical Modeling to Bench to Bedside. Trends in Cancer 4, 292-319, (2018). 12. Chen, Y. et al. A PSMA-targeted theranostic agent for photodynamic therapy. J Photochem Photobiol B 167, 111-116, (2017). 13. Ngen, E. J. et al. Prostate-specific membrane antigen (PSMA)-targeted photodynamic therapy enhances the delivery of PSMA-targeted magnetic nanoparticles to PSMA-expressing prostate tumors. Nanotheranostics 5, 182-196, (2021).

Image/Figure: https://s3.amazonaws.com/amz.xcdsystem.com/1E8A4501-BB41-A02A-1D3B9882B798BFAA_abstract_File10351/GA389_ImageFigure_0514085702.pdf

Image/Figure Caption: A) Schematic representing the experimental design for Group 1 and Group 2 mice, respectively. B) 800 nm in vivo fluorescence images of representative male NSG mice bearing human PSMA(+) PC3 PIP tumor xenografts, from Group 1 and Group 2,

respectively. Group 1 mice were pretreated with PDT before the intravenous administration of the PSMA-targeted MNPs, while Group 2 mice were not pretreated with PDT before the administration of the PSMA-targeted MNPs. A significant increase in the delivery of PSMA-targeted MNPs was detected in the tumors of Group 1 mice compared to Group 2 mice (controls). C) Quantification of the 800 nm in vivo fluorescence signal from the PSMA-targeted MNPs in PSMA(+) tumors of Group 1 mice compared to Group 2 mice, over 66 h post-MNP administration ($P \leq 0.019$; $n = 3$). This confirmed that a significant increase in the delivery of PSMA-targeted MNPs was detected in the tumors of Group 1 mice compared to Group 2 mice. D) In vivo T2W MRI of representative male NSG mice bearing human PSMA(+) PC3 PIP tumor xenografts, from Group 1 and Group 2 mice, respectively, 0 h, 18 h, 42 h, and 66 h after the intravenous administration of PSMA-targeted MNPs. A significant increase in the delivery of PSMA-targeted MNPs was detected in the tumors of Group 1 mice compared to Group 2 mice. E) T2W MRI signal change ratios of PSMA(+) PC3 PIP tumors in Group 1 mice compared to those of PSMA(+) PC3 PIP tumors in Group 2 mice, 0 h, 18 h, 42 h, and 66 h after MNP administration ($P \leq 0.008$; $n = 3$). This confirmed that a significant increase in the delivery of PSMA-targeted MNPs was detected in the tumors of Group 1 mice compared to Group 2 mice.

First Name: Ethel

Last Name: Ngen

Email: engen1@jhmi.edu

Organization: Johns Hopkins University School of Medicine

Country: United States

ID: GA390

Targeting Prostate Specific Membrane Antigen For Fluorescence Image Guided Surgery Of Breast Cancer

Aditi Shirke, Case Western Reserve University, aas151@case.edu

---

Category: Oncology

Abstract Body : Breast cancer is the most common cancer in women with cancer.org projecting 276,480 new cases of invasive breast cancer and 42,170 deaths in 2020. With current screening techniques, cancers are caught earlier and most patients are candidates for breast conserving surgery (BCS) to remove the cancer1. The success of the BCS is assessed post-operatively by pathology to determine cancerous tissues at or near the margins of the excised specimen, i.e. Positive Surgical Margins (PSM). Incomplete resections occur in 20-60% of BCS using current surgical tumor visualization technologies often leading to repeat surgeries2-10. This data demonstrates that there is an unmet clinical need for technologies that identify cancerous tissues in the margins of BCS specimens and real-time surgical methods of cancer tissue resection. Prostate Specific Membrane Antigen (PSMA) is known to be overexpressed in prostate cancer and has also be found to be significantly overexpressed on neovasculature of many solid human tumors, including breast tumor neovasculature and breast cancer cells2. Previously, we combined a potent Photo Dynamic Therapy (PDT), Pc413, and a highly selective PSMA inhibitor, PSMA-1, invented in our lab, to develop a theranostic agent that can selectively identify and destroy prostate cancer (PCa) both in vitro and in vivo to improve fluorescence image guided surgery (FIGS) for prostate cancer3. We recently demonstrated that PDT can be used as an effective adjuvant therapy after FIGS of prostate cancer resulting in reduced PSMs, lower tumor recurrence and extended animal survival following surgery. In this application we will utilize PSMA-Pc413, a theranostic agent, to determine if FIGS followed by PDT can improve the approach to breast cancer management. To confirm PSMA expression in breast cancer cells, adult, female BALB/c mice inoculated with 5x103 cells were allowed to grow until tumors reached ~100mm3 in volume. They then received 0.5mg/kg of PSMA-1-Pc413 through tail vein injection. Fluorescence images were taken at 24-hour post injection – previously determined peak time of PSMA-1-Pc413 – and the tumor was subsequently excised for histological analysis. To validate PSMA expression in the 4T1 model, orthotopic tumor tissue underwent immunofluorescence staining. Tumor tissues were co-incubated with PSMA-1- Alexa488 (synthesized in the lab) and goat anti-rabbit CD31-specific antibody overnight at 4oC. After washing, tissues were incubated with goat anti-rabbit AlexaFluor594 and analyzed11. We have demonstrated an orthotopic syngeneic mouse model of breast cancer where PSMA is overexpressed on the neovasculature of 4T1 breast cancers in BALB/c mice. Strong PSMA expression was observed in tumor tissues, which was blocked in the presence of excess amount of PSMA-1 ligand (Fig.1A). PSMA expression was found to be co-localized with CD31, indicating PSMA's expression in tumor vasculature. When PSMA-1-Pc413 was given via IV to female BALB-C mice bearing orthotopic 4T1 tumor, selective accumulation in the tumor was observed (Fig.1B). These data support the feasibility to use PSMA-1-Pc413 to highlight tumor for FIGS and PDT of breast cancer. This work will lay the foundation for development of this

agent towards clinical BCS and has the potential to dramatically impact current surgical procedures. In the next stage, we will then utilize this optimized model to investigate the efficacy of FIGS followed by PDT. After tumor implantation into breast fat pads, we will inject the PSMA targeted Pc413 agent and perform FIGS followed by PDT therapy to the resection cavity. Mice will be assessed for survival, local recurrence, metastatic spread to the lungs and elicited immunological response, which, in the future, may allow combination therapy with immune modulators. These studies will result in the use PSMA-1-Pc413 as a theranostic molecular imaging probe provide image guidance for breast tumor resection and ablative therapy to cancer tissues missed during surgery.

References: [1] Katipamula, R., et al. Trends in mastectomy rates at the Mayo Clinic Rochester: effect of surgical year and preoperative magnetic resonance imaging. J Clin Oncol 27, 4082-4088 (2009). [2] Jeevan, R., et al. Reoperation rates after breast conserving surgery for breast cancer among women in England: retrospective study of hospital episode statistics. BMJ 345, e4505 (2012). [3] Wang, X., et al. Photodynamic Therapy Is an Effective Adjuvant Therapy for Image-Guided Surgery in Prostate Cancer. Cancer research 80, 156-162 (2020) [4] Aziz, D., et al. The role of reexcision for positive margins in optimizing local disease control after breast-conserving surgery for cancer. Breast J 12, 331-337 (2006). [5] Gibson, G.R., et al. A comparison of ink-directed and traditional whole-cavity re-excision for breast lumpectomy specimens with positive margins. Ann Surg Oncol 8, 693-704 (2001). [6] Fleming, F.J., et al. Intraoperative margin assessment and re-excision rate in breast conserving surgery. Eur J Surg Oncol 30, 233-237 (2004). [7] Kotwall, C., Ranson, M., Stiles, A. & Hamann, M.S. Relationship between initial margin status for invasive breast cancer and residual carcinoma after re-excision. Am Surg 73, 337-343 (2007). [8] Waljee, J.F., Hu, E.S., Newman, L.A. & Alderman, A.K. Predictors of re-excision among women undergoing breast-conserving surgery for cancer. Ann Surg Oncol 15, 1297-1303 (2008). [9] Celli, J.P., et al. Imaging and photodynamic therapy: mechanisms, monitoring, and optimization. Chem Rev 110, 2795-2838 (2010). [10] McCahill, L.E., et al. Variability in reexcision following breast conservation surgery. JAMA 307, 467-475 (2012). [11] Pleijhuis, R.G., et al. Obtaining adequate surgical margins in breast-conserving therapy for patients with early-stage breast cancer: current modalities and future directions. Ann Surg Oncol 16, 2717-2730 (2009).

Image/Figure:

https://s3.amazonaws.com/amz.xcdsystem.com/1E8A4501-BB41-A02A-1D3B9882B798BFAA_abstract_File10351/GA390_ImageFigure_0514092911.jpg

Image/Figure Caption: Fig1.: PSMA as a target for breast cancer (A) Expression of PSMA (green) on 4T1 tumor vasculature (CD31, red) as indicated by the yellow color. (B) Selective uptake of PSMA-1-Pc413 in 4T1 tumor.

First Name: Aditi

Last Name: Shirke

Email: aas151@case.edu

Organization: Case Western Reserve University

Country: United States

ID: GA391
Coupled plasmonic gold nanoparticle-coated nanobubbles - multimodal imaging agent for atherosclerosis

Sourabh Mehta, IITB Monash research academy, sourabh.mehta@monash.edu

---

Category: Cardiovascular & Pulmonary

Abstract Body : Cardiovascular diseases (CVDs) contribute to 31% of global deaths, with atherosclerosis-related CVDs being the major contributor1. In high-risk CVDs, like atherosclerosis, real-time information about disease status plays a crucial role in designing treatment strategies. For the detection of atherosclerosis imaging technologies such as ultrasound, computer tomography (CT), and magnetic resonance imaging are approved diagnostic modalities. However, each has its own limitations; thus, multimodal imaging could be a potential solution2. We designed and developed gold nanoparticle (AuNP)-coated nanobubbles (AuNB) by assembling and growing gold nanoparticles on the lipidic nanobubble (NB) template. The synthesized AuNBs exhibit coupled plasmonic resonance at a wavelength of 630 nm, whereas free nanoparticles show plasmonic resonance at a wavelength of 520 nm. Further, the transmission electron microscopy images show AuNP coating on the NB surface to form spherical AuNB of 300-400 nm size, and the X-ray photoelectron spectroscopic (XPS) analysis confirms the presence of AuNP on the NB surface. Furthermore, we observed that the AuNPs did not leak from the AuNBs surface when incubated at 37 oC at 300 RPM for 72 hours. Next, we studied the echogenicity of AuNBs in various conditions such as depth, pH, and dilutions; the results indicated the AuNBs show contrast enhancement in tissue-mimicking phantom in vitro. Also, the AuNBs show contrast enhancement in CT imaging in vitro; thus, AuNBs can be used as a multimodal imaging agent (US/CT). We functionalized AuNB with Biotin for making AuNBs molecular imaging ready. Further, to test the proof of concept, we added Streptavidin-FITC. The absorbance measured at 488 nm indicated the AuNBs successful conjugation of AUNB-Biotin-Streptavidin-FITC. For molecular imaging of atherosclerosis, we tagged scFv-anti-GPIIb/IIIa, which binds specifically to activated GP IIb/IIIa on activated platelets at the thrombus site or the atherothrombotic site3, 4. Flow cytometric analysis indicates the successful detection of activated platelets. Hence, the AuNBs can be used as a potential contrast agent for multimodal molecular imaging of thrombosis and atherosclerosis.

References: 1. Yusuf, S.; Reddy, S.; Ôunpuu, S.; Anand, S. Circulation 2001, 104, (22), 2746-2753. 2. Di Carli Marcelo, F.; Geva, T.; Davidoff, R. Circulation 2016, 133, (25), 2640-2661. 3. Ta, H. T.; Li, Z.; Hagemeyer, C. E.; Cowin, G.; Zhang, S.; Palasubramaniam, J.; Alt, K.; Wang, X.; Peter, K.; Whittaker, A. K. Biomaterials 2017, 134, 31-42. 4. Wang, X.; Hagemeyer Christoph, E.; Hohmann Jan, D.; Leitner, E.; Armstrong Paul, C.; Jia, F.; Olschewski, M.; Needles, A.; Peter, K.; Ahrens, I. Circulation 2012, 125, (25), 3117-3126.

Full Name of Abstract's 1st Author : Sourabh Mehta

First Name: Sourabh

Last Name: Mehta

Email: sourabh.mehta@monash.edu

Organization: IITB Monash research academy

Country: India

ID: GA392

CD19-PET imaging of B cell depletion in a mouse model of multiple sclerosis: a clinically translatable technique to improve patient outcomes

Samantha Reyes, Stanford University SoM, levines@stanford.edu

---

Category: Neuroscience

Abstract Body : Objectives: Multiple sclerosis (MS) is a highly debilitating, immune-mediated disease characterized by demyelination in the central nervous system (CNS). Currently, there are over 15 FDA-approved MS therapies with variable responses in patients, but no reliable method to select the most appropriate treatment for a given patient. Moreover, standard-of-care techniques (e.g., blood tests and magnetic resonance imaging) yield little insight as to why a therapy might have failed since they cannot provide specific information on immune cell burden in the CNS. Positron emission tomography (PET) is a powerful imaging technique that can detect and quantify specific immune cells in the whole body/CNS, thus permitting accurate monitoring of therapeutic effectiveness in real time. Recently, a PET tracer was developed for tracking pathogenic human CD19+ B cells in a mouse model of MS, experimental autoimmune encephalomyelitis (EAE). Here we aim to assess the ability of this tracer ([64Cu]hCD19-mAb) to detect B cell depletion in EAE mice following treatment with an anti-CD19 therapy. Methods: Female hCD19-tg C57/BL6 mice (n=18) were induced with EAE through subcutaneous inoculation of 100-200 µg myelin oligodendrocyte glycoprotein (MOG1-125). Animals were observed daily for signs of paralysis and disease progression was scored on a 1-5 scale. On day 7 post-induction, mice received 250 µg of anti-CD19 mAb, MDX-1342, or control mAb intraperitoneally (n=9/group). On day 14, control and treated mice (n=4/group) were intravenously injected with 3.44±0.37 MBq [64Cu]hCD19-mAb and imaged using PET/CT 18-20h later; these animals were perfused post-scan and organs dissected to determine percent injected dose per gram (%ID/g). CNS tissues were further analyzed using ex vivo autoradiography. PET signal was quantified in the whole brain, cerebellum, pons and medulla using a brain atlas, and normalized to ex vivo blood signal. Finally, on day 16, CNS tissues and spleen were harvested for flow cytometry (n=5/group) to quantify B cells. Results: [64Cu]hCD19-PET imaging enabled highly sensitive in vivo detection of B cell burden in different tissue compartments of EAE mice after MDX-1342 treatment. Although the disease severity of treated and control groups did not statistically differ (Fig. S1a), CD19-PET results helped provide insights into why this therapy might not have worked. Notably, PET images showed a marked decrease in [64Cu]hCD19-mAb binding in the spleen (Fig 1a), but a strikingly incomplete reduction in bone marrow and brain signal in the medulla, pons and cerebellum (Figs. 1b&S1b). Peripheral PET findings were mirrored by ex vivo gamma counting, showing significant signal reduction in spleen (97%, p 0.1 for all). Importantly, flow cytometry verified the dramatic depletion of CD19+, CD45R/B220+, and CD20+ B cell populations in the spleen of treated mice (p Conclusion: Taken together, our CD19-specific PET tracer accurately detected the incomplete depletion of B cells in the CNS and peripheral tissues of mice treated with an anti-B cell therapy. Accordingly, incomplete depletion of B cells may be the reason this particular therapy was not successful in treating these EAE mice. The ability to track CD19+ B

cells in the whole body and CNS, both preclinically and clinically, will help provide a more complete picture of the in vivo B cell load during MS pathogenesis, and has the potential to greatly enhance understanding, diagnosis, and treatment of this disease. Such whole-body molecular information is critical to optimize the dose and timing of immunomodulatory therapies and ultimately improve clinical outcomes for MS patients.

References: 1. Chen, D. et al. J. Immunol. 196, 1541–1549 (2016).

Image/Figure: https://s3.amazonaws.com/amz.xcdsystem.com/1E8A4501-BB41-A02A-1D3B9882B798BFAA_abstract_File10351/GA392_ImageFigure_0518010629.pdf

Image/Figure Caption: Figure 1. (A) Representative [64Cu]hCD19-PET images of a treated and untreated mouse showing depletion of CD19+ cells in the spleen and bone marrow. Arrows indicate lymph nodes and BM is abbreviated for bone marrow. (B) Atlas-based PET quantification revealed significant decrease in binding of the [64Cu]hCD19-mAb in the whole brain in the mice given the anti-hCD19 mAb when compared to mice given a control mAb. PET analysis normalized to ex vivo blood signal. (C) Ex vivo gamma counting shows significantly lower signal in both the spleen and bone marrow in treated mice compared to control mice which mirrors the PET images. ***p-value ≤ 0.001, **p-value ≤ 0.01, **p-value ≤ 0.05, nsp-value > 0.05.

Full Name of Abstract's 1st Author : Samantha Reyes

First Name: Samantha

Last Name: Reyes

Email: levines@stanford.edu

Organization: Stanford University SoM

Country: United States

ID: GA394
Imaging of Covid-19 non-human primate models

Ian Crozier, Clinical Monitoring Research Program Directorate, Frederick National Laboratory for Cancer Research sponsored by the National Cancer Institute, ian.crozier@nih.gov

---

First Name: Ian

Last Name: Crozier

Email: ian.crozier@nih.gov

Organization: Clinical Monitoring Research Program Directorate, Frederick National Laboratory for Cancer Research sponsored by the National Cancer Institute

Country: United States

ID: GA395

Syrian hamsters as a small animal model for SARS-CoV-2 infection and countermeasure development

Samantha Loeber, University of Wisconsin Madison School of Veterinary Medicine, sloeber@wisc.edu

---

First Name: Samantha

Last Name: Loeber

Email: sloeber@wisc.edu

Organization: University of Wisconsin Madison School of Veterinary Medicine

Country: United States

ID: GA396
TBD

Junjie Yao, Duke University Photoacoustic Imaging Lab, junjie.yao@duke.edu

---

First Name: Junjie

Last Name: Yao

Email: junjie.yao@duke.edu

Organization: Duke University Photoacoustic Imaging Lab

Country: United States

ID: GA397
TBD

Youssef Wadghiri, NYU Grossman School of Medicine, wadghiri@med.nyu.edu

---

First Name: Youssef

Last Name: Wadghiri

Email: wadghiri@med.nyu.edu

Organization: NYU Grossman School of Medicine

Country: United States

ID: GA398
TBD

Shawn Wagner, Cedars-Sinai Medical Center, wagners@cshs.org

First Name: Shawn

Last Name: Wagner

Email: wagners@cshs.org

Organization: Cedars-Sinai Medical Center

Country: United States

ID: GA399
TBD

James Mansfield, Visiopharm, jim@visiopharm.com

First Name: James

Last Name: Mansfield

Email: jim@visiopharm.com

Organization: Visiopharm

Country: United States

ID: GA400
OSN Plenary

James Basilion, Case Western Reserve University, jxb206@case.edu

---

First Name: James

Last Name: Basilion

Email: jxb206@case.edu

Organization: Case Western Reserve University

Country: United States

ID: GA401
TBD

Alexander Vahrmeijer, Leiden University Medical Center, a.l.vahrmeijer@lumc.nl

---

First Name: Alexander

Last Name: Vahrmeijer

Email: a.l.vahrmeijer@lumc.nl

Organization: Leiden University Medical Center

Country: Netherlands

ID: GA402
OTL38

Sunil Singhal, University of Pennsylvania School of Medicine,
Sunil.Singhal@uphs.upenn.edu

First Name: Sunil

Last Name: Singhal

Email: Sunil.Singhal@uphs.upenn.edu

Organization: University of Pennsylvania School of Medicine

Country: United States

ID: GA403
Updates on Clinical Trials (Tracers)

Gooitzen van Dam, TRACER BV, go@tracercro.com

First Name: Gooitzen

Last Name: van Dam

Email: go@tracercro.com

Organization: TRACER BV

Country: Netherlands

ID: GA404
Updates from Upenn

Jim Delikatny, University of Pennsylvania, delikatn@pennmedicine.upenn.edu

---

First Name: Jim

Last Name: Delikatny

Email: delikatn@pennmedicine.upenn.edu

Organization: University of Pennsylvania

Country: United States

ID: GA405
PSMA (IS-002)

Jonathan Sorger, Intuitive Surgical, Jonathan.Sorger@intusurg.com

---

First Name: Jonathan

Last Name: Sorger

Email: Jonathan.Sorger@intusurg.com

Organization: Intuitive Surgical

Country: United States

ID: GA406
Discussion: OncoNano

Baran Sumer, University of Texas Southwestern Medical Center, Baran.Sumer@utsouthwestern.edu

---

First Name: Baran

Last Name: Sumer

Email: Baran.Sumer@utsouthwestern.edu

Organization: University of Texas Southwestern Medical Center

Country: United States

ID: GA407
TBD

John Frangioni, Curadel, jvfrangioni@curadel.com

First Name: John

Last Name: Frangioni

Email: jvfrangioni@curadel.com

Organization: Curadel

Country: United States

ID: GA408
TBD

Viktor Gruev, , vgruev@wustl.edu

First Name: Viktor

Last Name: Gruev

Email: vgruev@wustl.edu

Country: United States

ID: GA409
TBD

Tulio Valdez, Stanford University, tvaldez1@stanford.edu

First Name: Tulio

Last Name: Valdez

Email: tvaldez1@stanford.edu

Organization: Stanford University

Country: United States

ID: GA410
TBD

Jonathan Liu, University of Washington, jonliu@uw.edu

First Name: Jonathan

Last Name: Liu

Email: jonliu@uw.edu

Organization: University of Washington

Country: United States

ID: GA411
Unnamed Speaker Presentation

**Sunil Singhal, University of Pennsylvania School of Medicine,
Sunil.Singhal@uphs.upenn.edu**

First Name: Sunil

Last Name: Singhal

Email: Sunil.Singhal@uphs.upenn.edu

Organization: University of Pennsylvania School of Medicine

Country: United States

ID: GA413
Poster Test

Daria Cohen, , daria.locke@gmail.com

First Name: Daria

Last Name: Cohen

Email: daria.locke@gmail.com

Country: Canada